Food Mixing: Principles and Applications

Edited by

P.J. Cullen
School of Food Science and Environmental Health
Dublin Institute of Technology
Dublin 1
Ireland

WILEY-BLACKWELL
A John Wiley & Sons, Ltd., Publication

This page intentionally left blank

Food Mixing: Principles and Applications

Edited by

P.J. Cullen
School of Food Science and Environmental Health
Dublin Institute of Technology
Dublin 1
Ireland

WILEY-BLACKWELL

A John Wiley & Sons, Ltd., Publication

This edition first published 2009

Blackwell Publishing was acquired by John Wiley & Sons in February 2007. Blackwell's publishing programme has been merged with Wiley's global Scientific, Technical, and Medical business to form Wiley-Blackwell.

Registered office
John Wiley & Sons Ltd, The Atrium, Southern Gate, Chichester, West Sussex, PO19 8SQ, United Kingdom

Editorial offices
9600 Garsington Road, Oxford, OX4 2DQ, United Kingdom
2121 State Avenue, Ames, Iowa 50014-8300, USA

For details of our global editorial offices, for customer services and for information about how to apply for permission to reuse the copyright material in this book please see our website at www.wiley.com/wiley-blackwell.

Library of Congress Cataloging-in-Publication Data

Food mixing : principles and applications / edited by P.J. Cullen.
p. cm.
Includes bibliographical references and index.
ISBN 978-1-4051-7754-2 (hardback : alk. paper) 1. Food industry and trade—Mathematical models. 2. Mixing—Mathematical models. 3. Food mixes. I. Cullen, P. J. (Patrick J.)
TP370.9.M38F66 2009
664'.024—dc22

2009012285

A catalogue record for this book is available from the British Library.

Set in 10/12 pt Times by Macmillan Publishing Solutions, Chennai, India
Printed in Singapore

1 2009

Contents

Contributors

Bharani Ashokan
Department of Food Science
School of Environmental and Biological Sciences
Rutgers University
New York, NY, USA

Mostafa Barigou
Department of Chemical Engineering
University of Birmingham
Birmingham, UK

Robin K. Connelly
Food Science and Biological Systems Engineering
University of Wisconsin
Madison, WI, USA

P.W. Cox
Department of Chemical Engineering
University of Birmingham
Birmingham, UK

P.J. Cullen
School of Food Science and Environmental Health
Dublin Institute of Technology
Dublin, Ireland

David S. Dickey
MixTech, Inc.
Dayton, OH, USA

Maureen Evans
Department of Food Science
School of Environmental and Biological Sciences
Rutgers University
New York, NY, USA

Colette C. Fagan
UCD School of Agriculture
Food Science and Veterinary Medicine
University College Dublin
Dublin, Ireland

John J. Fitzpatrick
Department of Process and Chemical Engineering
University College Cork
Cork, Ireland

Jolius Gimbun
Department of Chemical Engineering
Loughborough University
Loughborough, UK

Jozef L. Kokini
Department of Food Science and Human Nutrition
University of Illinois
Illinois, IL, USA

Kasiviswanathan Muthukumarappan
Department of Agricultural and Biosystems Engineering
South Dakota State University
Brookings, SD, USA

Keshavan Niranjan
Department of Food Biosciences
University of Reading
Reading, UK

Ian T. Norton
Department of Chemical Engineering
University of Birmingham
Birmingham, UK

Colm P. O'Donnell
UCD School of Agriculture
Food Science and Veterinary Medicine
University College Dublin
Dublin, Ireland

Chris D. Rielly
Department of Chemical Engineering
Loughborough University
Loughborough, UK

J.K. Sahu
School of Food Biosciences
University of Reading
Reading, UK

Fotis Spyropoulos
Department of Chemical Engineering
University of Birmingham
Birmingham, UK

Brijesh Tiwari
UCD School of Agriculture
Food Science and Veterinary Medicine
University College Dublin
Dublin, Ireland

Kiran Vyakaranam
Department of Food Science
School of Environmental and Biological Sciences
Rutgers University
New York, NY, USA

1 Mixing in the food industry: trends and challenges

P.J. Cullen and Colm P. O'Donnell

1.1 Role of mixing

Mixing is a fundamental unit operation in the chemical, pharmaceutical and food process industries. Mixing increases the homogeneity of a system by reducing non-uniformity or gradients in composition, properties or temperature. Besides the primary objective of homogeneity, secondary objectives of mixing include control of heat and mass transfer rates, reactions and structural changes (Harnby *et al*. 2001). In food processing applications, additional mixing challenges include sanitary design, complex rheology, desire for continuous processing and the effects of mixing on final product texture and sensory profiles.

The mixing of liquids, solids and gases is one of the most common unit operations in the food industry. Mixing is frequently employed to develop the desired product characteristics such as texture rather than simply ensure product homogeneity. If mixing fails to achieve the required product yield, quality, and organoleptic or functional attributes, production costs may increase significantly.

1.2 Design criteria for mixing

As described earlier, mixing is rarely a process with a sole intended effect; a number of physico-chemical processes may occur simultaneously within a mixer. Consequently, numerous mixer designs are proposed to meet these demands (Chapter 5). Although categorisation of mixing equipment is difficult, some mixers are used primarily for either liquids or powders, whereas others are employed for combinations of liquids and powders. Many unique design challenges apply to food mixing as food properties such as texture, flavour, shelf-life and safety must also be considered. The effectiveness of mixing can be assessed only in the context of the quality of the end product.

Within the food industry, relationships established between the quality of mixed products and the operating parameters of mixing are often empirical, and consequently, the design of mixing systems are frequently not based upon well-established scientific principles. Patwardhan and Joshi (1999) indicated an enormous scope for improvement in the efficiency of mixing processes (mixing time per unit power consumption). Mixer design is slowly changing from a complete experimental process to a partially numerical and experimental one. Consequently, the design of new mixing devices is more efficient. On-going demand for improved impeller designs usually comes from the users of industrial mixing equipment when vessels are to be designed for new plants or improvement in the existing design is

desired for enhancing quality, capacity, process efficiency and energy efficiency. For meeting these objectives, it is imperative that the relationship between the flow pattern and the design objective is understood (Patwardhan & Joshi 1999).

There is a need to develop and evaluate new in-line mixers to meet the requirements of the food industry, where there is an increasing trend towards high-capacity continuous processes. Irrespective of the type of mixer used, hygienic design and suitability for cleaning-in-place are critical. Static mixers may be employed for continuous processing, making them an attractive alternative to stirred tanks, as similar and sometimes better performance can be achieved at lower cost. Motionless mixers, typically, have lower energy consumptions and are of sanitary design due to the absence of moving parts (Thakur *et al*. 2003).

The energy requirements for food mixing applications can vary significantly. For example, emulsification requires high energy levels, whereas dispersion of delicate particulate matter in shear sensitive liquids requires much lower energy levels. Mechanical damage to food particles in suspension can result from the stirring action of an impeller. It is possible that resultant comminution or attrition of the particles might be such that the overall quality of the product is affected.

Given the wide variety and complexity of mixing tasks, careful design and scale-up studies are required to ensure that effective mixing is achieved in an efficient manner. Mixing scale-up is an empirical process that begins when the first ingredient is chosen, and continues until a successful process is in production (Chapter 6). The challenge is to scale up the equipment and ingredients to an effective size for production, while duplicating the results obtained during development. Failure to adequately consider mixing issues at laboratory or pilot scale may result in significant problems on scale-up. The costs incurred in solving these problems may be significantly more than the cost of investigating and solving mixing problems during the process development phase.

1.3 Specific challenges in food mixing

Significant advances in food mixing have been derived from chemical engineering research. Consequently, the complex rheological challenges arising from non-Newtonian food materials and the inclusion of large particles have not been sufficiently investigated. The complex rheology of food products can influence the effectiveness of a given geometry to achieve the desired mixing outcomes (Chapter 3). Food mixing can involve ingredients of different physical properties and quantities. Food materials mixed may range from nano-emulsions, to large particulate suspensions, to highly viscous pastes or dry powders.

The wide variety of particulates with different sizes, shapes and strengths used in the food industry can result in major segregation issues. Producing particulates with similar sizes, agglomerating ingredients, or reducing vibration during transport can all help reduce these segregation problems (Chapter 13).

Also, as food safety is of critical importance in the food industry, mixing processes should not contaminate the product or allow conditions facilitating microbial growth. Consequently, it is important to use appropriate cleaning regimes and equipment with adequate hygienic design (Chapter 13).

1.3.1 Quality assurance compliance through mixing

The evolution of the food industry towards higher level processing, increasing consumer expectations and the recent growth of nutraceuticals necessitates a more scientific understanding of mixing within the food industry. New quality assurance risks are emerging

with mixed food products due to the addition of functional ingredients and increasingly stringent labelling legislation. In 2006 the EU passed Regulation (EC) No. 1925/2006 to regulate the addition of vitamins, minerals and other substances to foods which have a nutritional or physiological effect. The total amount of such additives present in the food may not exceed the regulated maximum levels listed on the label. In 2007 the U.S. Food and Drug Administration (FDA) issued a final rule for current good manufacturing practices (CGMPs) for dietary supplements, requiring that proper controls are in place to ensure such products are processed in a consistent manner, and meet quality standards including purity, strength, and composition. The blurring of the line between the food and pharmaceutical industries is resulting in novel opportunities for each sector coupled with new challenges. Consequently, the food industry can no longer afford to depend upon a 'black box' approach to mixing.

As the food industry is increasingly governed by legislation, it is imperative that unit operations such as mixing are effectively controlled to reduce product variability. The objective is to move from a paradigm of 'testing quality in' to 'building quality in by design'. Fundamental understanding and optimisation of food mixing will facilitate the evolution of the industry towards higher level processing and novel products with added value.

As stated the food industry has adopted its understanding of mixing from other process industries, including chemical and pharmaceutical. For pharmaceuticals, active ingredients are typically dispersed at relatively low concentrations throughout a dispersion media, making the objective of homogeneity difficult. Pharmaceuticals are similar to nutraceuticals or functional foods with regard to the objective of dispersing such active ingredients equally throughout a carrier; however, there are significant differences. Health-promoting properties of foods are not necessarily due to single components, but rather a few or several active ingredients. This creates a significant paradigm shift from the pharmaceutical model, which is based on the efficacy of single agents. Also, pharmaceutical carriers (excipients) are generally not limited by consumer acceptance criteria of taste, nutrition and texture.

1.3.2 Engineering texture through mixing

Mixing in the food industry is employed not only to combine multiple ingredients, but also to modify the structure of foods. The unique aspect of the food industry is the development of texture through mixing and the influence of mixing on the sensory characteristics of foods. Complex food structures influenced by mixing include dough, where shear and extensional forces generated by the mixer may be used to develop flour and water into a viscoelastic protein matrix that is capable of retaining the gas produced during proving and baking (Rielly 1997). Other examples of structured fluids produced by mixing include creams and margarines, where the flow field developed in the mixer is used to disperse one liquid phase in another, forming a stable emulsion with the desired rheological and organoleptic properties (Rielly 1997).

Another unique aspect of mixing within the food industry is where gas bubbles are incorporated into liquid or viscoelastic matrices to impart novel and functional properties. Bubble incorporation in processes such as the manufacture of ice creams and chocolate confectionery is now so widely practised that air and gases are increasingly recognised as food ingredients (Chapter 12). In contrast, bubble incorporation—which inevitably accompanies mixing of viscous recipes such as sauces and salad cream—is undesirable, as this can result in inconsistent filling of packages and can also accelerate spoilage. De-aeration or bubble exclusion can be classified as a food mixing operation, as the end product of their exclusion results in a greater level of homogeneity.

The development of food micro- or nano-emulsions facilitates the addition of novel sensory characteristics to foods (Chapter 9). This can be achieved via a reduced calorific food in which emulsions are designed to give all the sensory properties of high-fat products with lower calorific content. The addition and delivery of micronutrients in this manner is not detectable to the consumer.

1.4 Advances in the science of mixing

The food industry must continually seek improvement in process design to increase efficiency and facilitate the development of novel products. Despite the ubiquity of mixing processes and the vast quantities of materials mixed every day, mixing processes are not fully understood scientifically. Although there is broad agreement that mixing is complicated, there is no agreement as to the source of the complications; from a rheology perspective, the constitutive equation is of paramount importance, whereas from a fluid mechanics viewpoint, the complexities of the flow field are of interest (Ottino 1990).

Advances in computational techniques have facilitated a more fundamental understanding of the mixing process for both complex fluids and mixer designs. Computational fluid dynamics (CFD) provides explanations for fluid flow, heat and mass transfer phenomena, potentially leading to better equipment design and process control for food mixing. Although very significant advances have been made over the last few years in the numerical solution of the equations of fluid motion using CFD methods, relatively few studies have been carried out on food mixing. It is likely that CFD modelling will be increasingly employed for optimisation of food processes including mixing.

Perfect mixing is rarely possible; consequently, mixing will be a source of variability within the manufacturing process. There is an increasing trend in the food industry to adopt a process analytical technology (PAT) framework for innovative process manufacturing and quality assurance. This framework facilitates a move from a paradigm of 'testing quality in' post manufacture to 'designing quality in' during manufacture. Recent developments in imaging and monitoring technologies facilitate the mapping of flow within processing vessels, enabling the identification of regions of poor mixing. Sensing technologies such as NIR spectrometry and NIR chemical imaging have been proposed as control systems for determining the optimum mixing time. NIR chemical imaging is an emerging technique that integrates conventional imaging and spectroscopy to attain both spatial and spectral information from an object. Recently, this technology has shown promise for monitoring the blending of pharmaceutical ingredients. Monitoring and control of the mixing processes in the food industry is critical, as incomplete or over-mixing of a product may result in product separation, attrition and undesirable product texture (Chapter 7). In some applications, the effects of mixing can continue well after the mixing action has ceased, and it could be quite some time before the end point is reached. In such situations, on-line monitoring and process control can be very challenging. Monitoring of mixing in many food applications is particularly challenging, especially in processes involving gas inclusion and crystallisation, where the effects of mixing can continue even after agitation has stopped.

1.5 Book objectives

This book addresses an identified gap in the literature by providing a dedicated and in-depth reference for mixing processes within the food industry. Although there are a

number of creditable references covering general mixing, such publications are often biased towards the chemical industry; therefore, topics specific to food mixing and unique food applications are often neglected. This book brings together essential information on the principles and applications of mixing within food processing.

This book covers the underlying principles of mixing, equipment design, novel monitoring techniques and numerical techniques available to advance the scientific understanding of food mixing. Food mixing applications are described in detail. This book will be useful for engineers and scientists who need to specify and select mixing equipment for specific processing applications. It will also assist with the identification and solving of the wide range of mixing problems that occur in industry.

References

Harnby, M., Edwards, M.F. & Nienow, A.W. (2001). *Mixing in the Process Industries.* Butterworth-Heinemann, Oxford.

Ottino, J.M. (1990). Mixing, chaotic advection and turbulence. *Annual Reviews in Fluid Mechanics*, **22**, 207–253.

Patwardhan, A.W. & Joshi, J.B. (1999). Relation between flow pattern and blending in stirred tanks. *Industrial and Engineering Chemistry Research*, **38**, 3131–3143.

Rielly, C.D. (1997). Mixing in food processing. In: *Chemical Engineering for the Food Industry* (eds P.J. Fryer, D.L. Pyle & C.D. Rielly). Chapman & Hall, London.

Thakur, R.K., Vial, C., Nigam, K.D., Nauman, E.B. & Djelveh, G. (2003). Static mixers in the process industries – a review. *Transactions of the Institution of Chemical Engineers*, **81**, 787–826.

2 Mixing fundamentals

Kasiviswanathan Muthukumarappan

2.1 Introduction

Mixing is a fundamental process in many food processing operations such as the preparations of ingredients, the addition of solids to liquids, the development of structure and incorporation of air in the mixing process. More and more processed and manufactured foods are being produced in which mixing has an important role. A complete mixing process produces a uniform mixture in minimum time with minimum cost for processing. The food processing industry relies heavily on mixing to ensure delivery of a product with constant properties. For example, consumers expect all containers of soups, breakfast cereals, fruit mixes, etc., to have the same amount of each ingredient to meet their nutritional needs.

The mixing and/or agitation of solids, liquids and gases is one of the key unit operations in the food processing industry. Different types of system are required for different mixing operations in the food industry.

- *Solid–solid mixing*: Ensuring that all the ingredients in a cereal box are mixed uniformly to provide consistent nutrition according to labelling, for textural effects, or to give a specific taste.
- *Solid–liquid mixing*: The addition of solids to liquids is involved in the reconstitution of fluids, such as addition of coffee, milk and sugar to hot water. The addition of liquid to solid systems is the key to the production of many food batters, pastes and doughs.
- *Liquid–liquid mixing*: The creation of liquid–liquid emulsions is central to the manufacture of margarines and spreads.
- *Gas–liquid mixing*: Ascertaining that enough air is mixed into a fermentor liquid to ensure microbial growth is not oxygen limited.

It is important to define exactly the meaning of the terms ‘agitation’ and ‘mixing’, and it is perhaps much easier to do by considering liquid–liquid systems. The agitation of a liquid may be defined as the establishment of a particular flow pattern within the liquid, usually a circulatory motion within a container. On the other hand, mixing implies the random distribution of two or more ingredients throughout a system. In general, mixing is brought about by agitation. However, it would be difficult to continue to use both words according to their precise meaning, and therefore, in this chapter, the term ‘mixing’ will be used to mean both the random distribution of components and the means for bringing about that randomness, that is, the mechanisms of agitation.

2.2 Defining mixing

The primary objective in mixing is to achieve a homogenous mixture; generally, this means, attaining a nearly uniform distribution of the ingredients. A distinction may be drawn between batch and continuous processes. In a batch process, the objective is to produce a spatially homogenous mixture and, up to a point, an increase in batch time leads to an improvement in mixture uniformity. In contrast, the outlet stream from a continuous mixing process should contain the same proportions of the ingredients and should have received the same treatment within the process. Overall, the concentrations of the ingredients should be uniformly distributed in the output stream, should not vary with time and the processing of each part of the mixture should be the same.

Consider that the mixture is divided into a number of samples or sub-mixtures. If the mixture is homogeneous, then the composition of sample or sub-mixtures would be exactly the same. Figure 2.1a shows a homogeneous but non-random distribution of particles containing 50% black and 50% white particles. The mixture is divided into sub-mixtures, each containing 16 particles, and clearly, there are eight white particles in each sample. The random probability of producing the ordered structure shown in Figure 2.1a is extremely small (Brennan *et al.* 1976). In general, the best that a mixer can achieve is to distribute the white particles randomly in space, as shown in Figure 2.1b. Now, each sub-mixture of 16 particles contains different number of white particles (8, 10, 7 and 7). But on an average, there are eight whites in each sample. It may appear that the material is not fully mixed, but further random distribution of the particles would not result in any improvement in mixture (Rielly *et al.* 1994).

Complete mixing could be defined as the case wherein all the sub-mixtures are found to contain the components in the same proportion as the original mixture (Earle 1983). On this basis, the mixture shown in Figure 2.1a would be completely mixed, which is rather impossible in reality. In contrast, the mixture shown in Figure 2.1b does not contain eight white particles in each sub-mixture, even though the particles are entirely randomly distributed. In the following sections, methods are described for quantifying the variation in concentration and comparing it with the random mixture.

A clear distinction between ‘dispersive’ and ‘non-dispersive’ mixing mechanisms will be the key to a fundamental understanding of the mixing process and its optimisation. In a multi-phase food system, dispersive mixing involves the reduction in size of a cohesive

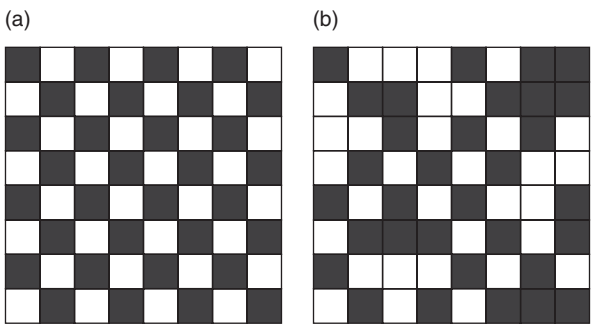

Fig. 2.1 (a) Non-random mixture of particles. (b) Random mixture of particles. In both cases, the mixture contains 50% black and 50% white particles.

minor component such as clusters of solid particle or droplets of liquid. Distributive mixing is the process of spreading the minor component throughout the matrix in order to obtain a good spatial distribution. In any mixing device, these two mechanisms may occur simultaneously or stepwise. Figure 2.2 depicts these two mixing mechanisms schematically. The conditions under which dispersive mixing occurs are determined by the balance between the cohesive forces holding agglomerates or droplets together and the disruptive hydrodynamic forces. Quantitative studies of droplet break-up in simple shear and pure elongational flows have shown that elongational flows are more effective than simple shear flows, especially in the case of high viscosity ratios and low interfacial tensions (Bentley & Leal 1986; Elemans *et al.* 1993).

These effects are most intense near the blades of the mixer. The distorted fluid elements are convected into the bulk flow, where they are re-oriented before passing once more through the region of high shear or accelerated flow. Molecular diffusion is required to bring about homogeneity on a molecular scale, but this is a very slow process in viscous liquid foods, and typically, the criterion for mixer design is to reduce average scale of segregation until in-homogeneities are not visible at the required scale of scrutiny. In static mixers, the mixer blades or elements physically cut and twist the fluid elements and re-orient them in the flow. Figure 2.3 shows the effect of a series of cutting and twisting operation that reduces the scale of segregation until the required degree of homogeneity is achieved.

Most of the food processes are essentially molecular-level processes, so only mixing on that level can directly influence their course, whereas mixing mechanisms on larger scales

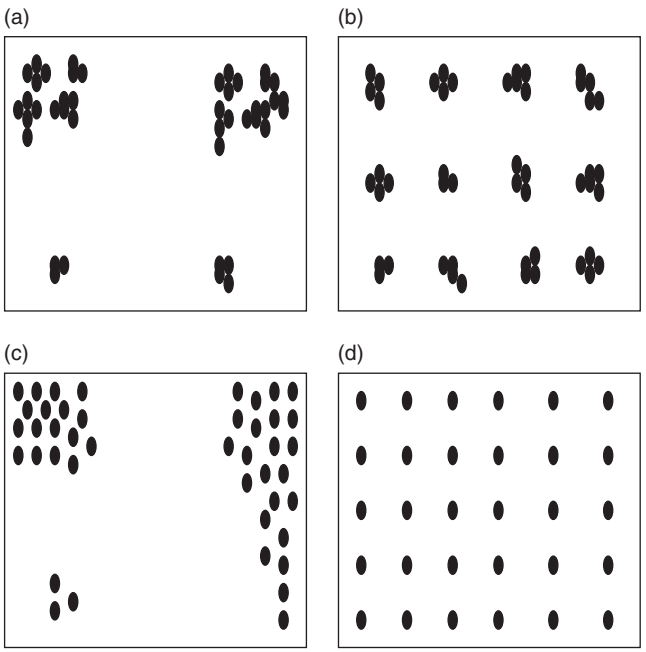

Fig. 2.2 Schematic of dispersive and distributive mechanisms: (a) bad dispersion with bad distribution; (b) bad dispersion with good distribution; (c) good dispersion with bad distribution; (d) good dispersion with good distribution.

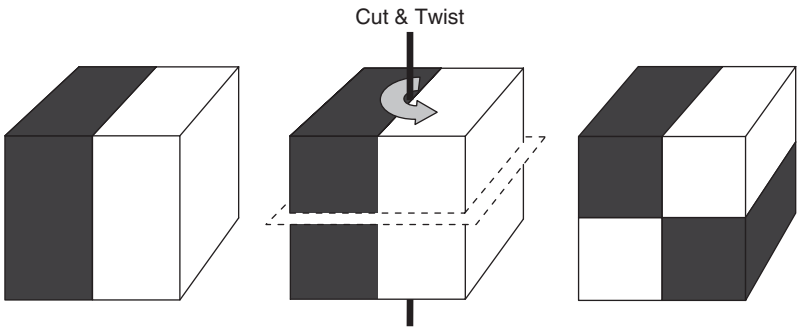

Fig. 2.3 Distributive mixing.

have an indirect influence by changing the environment for local mixing. Mixing mechanisms can be grouped into three main categories, depending on their characteristic length scale. Small scale mixing, close to the molecular level, is referred to as micromixing; mixing on a large scale is referred to as macromixing and intermediate scale mixing is called mesomixing.

2.2.1 Macromixing

For a process carried out in a stirred tank of volume (V), the largest scale of mixing is the scale of the whole reactor. Macromixing refers to flow processes controlling the mean concentration and the residence time distribution, that is, the mean convective flow in the vessel. Macromixing can be characterised by the circulation time τ_C, which can be estimated as:

$$\tau_C = \frac{V}{Q_C} \tag{2.1}$$

where $Q_C = C_1 N d_{imp}^3$, N is the stirring rate, d_{imp} is the impeller diameter, Q_C is the circulation capacity, and $C_1 = 1.5$ is a constant depending on the pumping capacity of the impeller (e.g., Rushton turbine).

2.2.2 Mesomixing

Mesomixing refers to the coarse scale turbulent exchange between the fresh feed and its surroundings. A fast chemical reaction is usually localised near the feed point, where a plume of fresh feed is formed. This plume is of a coarse scale relative to the micromixing scales, but of a fine scale relative to the scale of the system. Spatial evolution of the plume can be identified with the mechanism of turbulent diffusion. A characteristic time for turbulent diffusion τ_D can be defined through the feed addition rate Q_{feed}, the velocity u close to the feed point and the turbulent diffusivity D_T.

$$\tau_D = \frac{Q_{feed}}{u^* D_T} \tag{2.2}$$

Another aspect of mesomixing is related to the inertial-convective process of disintegration of large eddies, with a size r larger than the Kolmogorov microscale η but smaller than the

large energy-containing eddies of size L. Inertial-convective disintegration proceeds without being influenced by molecular mixing, but it influences itself the micromixing since the structure of the large eddies determines the environment for small scale mixing. When assuming equal integral scales for velocity and concentration, a characteristic time constant τ_s for the inertial-convective mixing can be estimated as:

$$\tau_s = \frac{k}{2\varepsilon} = \frac{3L^{2/3}}{4\varepsilon^{1/3}} \tag{2.3}$$

where k is the turbulent kinetic energy and ε is the energy dissipation rate.

2.2.3 Micromixing

Small scale mixing in liquids is driven by the mechanism of the viscous-convective deformation of fluid elements, followed by molecular diffusion. An important feature of micromixing is the accelerating effect of viscous-convective deformation on molecular diffusion. A characteristic time constant for viscous-convective mixing (for $r < \eta$), τ_E, is known as the engulfment time constant:

$$\tau_E = \frac{1}{E} = 17.24\ (\nu/\varepsilon)^{1/2} \tag{2.4}$$

where E is the engulfment parameter and v is the kinematic viscosity.

2.3 Scale of scrutiny

The quality of a mixture depends heavily on the scale at which it is examined. For example, a sample of milk may appear to be a homogeneous mixture when viewed by naked eye; but, it becomes apparent that it is composed of fat globules of varying size entrapped in a protein matrix, when observed under a microscope. Thus, the degree of homogeneity can only be determined once a suitable scale of scrutiny has been established, and the scale of scrutiny itself depends on the end use of the mixture. A second example to validate this point would be of mixing ingredients (nutrients/calories) to make a cake for human consumption in a weight watchers programme. If the main objective is to ensure that each person receives the correct amount of calories daily from the cake, then the appropriate scale of scrutiny for that mixture would be the daily consumption of the cake. However, if the criterion is that the nutrient/calorie intake should be controlled on a weekly basis, then the scale of scrutiny should be chosen as the weekly consumption of the cake. In the latter case, there might be considerable variations in nutrient concentration between daily consumptions to allow for variations in metabolic activities of each person. However, if the consumer expects the cake to be uniform in colour and texture, then the scale of scrutiny would be much reduced.

Danckwerts (1953) explained the importance of establishing the scale of scrutiny, and defined it as the minimum size of the regions of segregation which would cause the mixture to be regarded as imperfectly mixed. The situation is much more complex, as 'mixedness' is determined not only by the size of the regions of imperfectly mixed material, but also by the intensity of segregation between these regions. In practice, it may not be possible to make more than an approximate estimate of the scale of scrutiny, but the concept is useful in defining the quality of any mixture. Establishing a scale of scrutiny appropriate

to the end use of the mixed product fixes the size or volume of the samples to be used to assess the mixture quality.

2.4 Quantifying mixedness

The purpose of mixing is to obtain a randomisation of the particles, by which variation in concentration between samples should fall below a prescribed value. A distinction can be made between coarse and fine grained mixtures. Coarse grained mixtures normally have few particles which can be easily identified, when examined on a scale of scrutiny comparable with the particle size, and they are highly segregated as shown in Figure 2.1. Fine grained mixtures have large number of particles, and existence of concentration gradient at a given scale of scrutiny is normal. In solids mixing, there is no intrinsic motion, so there are a number of discrete units; whereas, in mixing of fluids, there are a large number of mixing units, molecules are capable of random motion and diffusion processes produce uniform mixture in due course of time. The following discussion applies to fine and coarse grained mixtures; for simplicity, binary mixtures are considered.

Scale of segregation (to describe the size of unmixed region) and intensity of segregation (concentration variation) are two measures to quantify the quality of mixtures proposed by Danckwerts (1953). Consider a mixture containing components A and B with concentrations a and b, respectively. The quantity 'a' denotes a mass fraction, such that $a = 1$ represents pure component A at a point and $a = 0$ represents pure component B; hence $a + b = 1$ and $\overline{a} + \overline{b} = 1$, where overbar represents an average spanning the whole mixture. A correlation coefficient may be defined as given below, which gives information on the average of the product of the concentration differences from the mean, at a position x and at positions a distance r away.

$$R(r) = \overline{(a(x)-\overline{a})(a(x+r)-\overline{a})} \,/\, \overline{(a(x)-\overline{a})^2} = \overline{(b(x)-\overline{b})(b(x+r)-\overline{b})} \,/\, \overline{(b(x)-\overline{b})^2} \tag{2.5}$$

Scale segregation within a mixture can be measured in two ways, namely, on a distance and volume basis. Danckwerts (1953) defined length (S) and volume (V) scale of segregation, using the above correlation coefficient.

$$S = \int_0^\infty R(r)\mathrm{d}r \quad \text{and} \quad V = 2\pi \int_0^\infty r^2 R(r)\mathrm{d}r \tag{2.6}$$

For linear function, it is easy to show that

$$V = \frac{4\pi}{3} S^3 \tag{2.7}$$

The length and volume scale of segregation represents the maximum length and volume, respectively, at which the unmixed material can be detected within the mixture. It can be shown that these two scales are independent of component fractions present in the mixture.

In fluid mixture, the diffusion process nullifies the concentration gradient. Danckwerts (1953) proposed a second measure of mixedness based on the concentration variance

of a given component in the mixture. Mean concentration and variance are given below:

$$\bar{a} = \frac{1}{n}\sum_{i=1}^{n} a_i \tag{2.8}$$

$$\sigma^2 = \frac{1}{n-1}\sum_{i=1}^{n} (a_i - \bar{a})^2 \tag{2.9}$$

where a_i is the concentration of a in sample i and n is the number of samples analysed from the mixture; $n - 1$ ensures that estimate is unbiased. Perfect and completely segregated mixtures have variance of zero and maximum value, respectively. The variance of completely segregated mixture of particles is given as $\sigma_0^2 = \bar{a}(1-\bar{a})$, where $\bar{a}$ is the fraction of one of the components in the mixture.

Danckwerts (1953) defined intensity of segregation as:

$$I = \frac{\sigma^2}{\sigma_0^2} = \frac{\sigma^2}{\bar{a}(1-\bar{a})} \tag{2.10}$$

so that completely segregated mixture has $I = 1$ and uniform mixture has $I = 0$. The impact of changes in the length scale and intensity of segregation on mixture quality is presented schematically in Figure 2.4. By decreasing intensity of segregation, the mixture becomes more diffuse; wherein, decreasing the length scale of segregation reduces the size of the non-homogeneities.

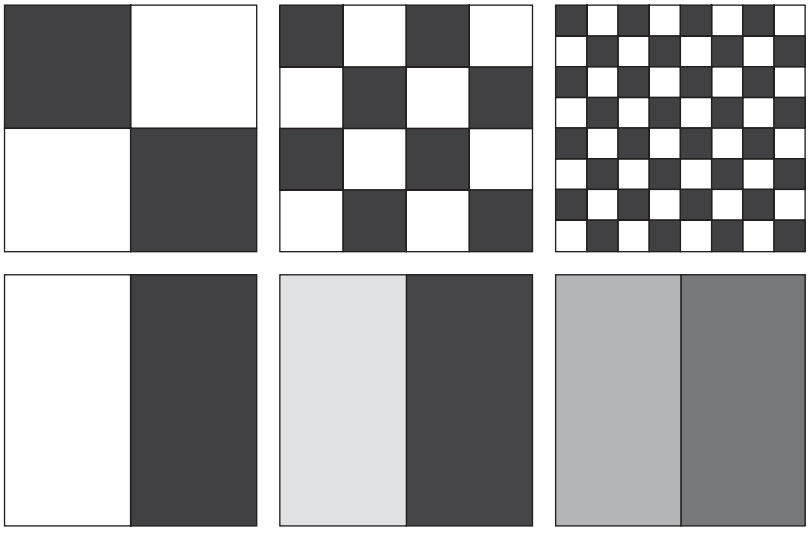

Fig. 2.4 The effects of scale and intensity of segregation on mixedness.

2.4.1 Inference of mixing indices

According to Lacey (1954), statistics can be used to measure the status of a mixture. Many researchers have also proposed the use of mixing indices, which is similar to the intensity of segregation, as given earlier by Danckwerts (1953). There is a practical difficulty in using length scale of segregation because it requires a large number of measurements of pairs of concentrations to estimate the correlation coefficient, and hence it is no longer used. Many researchers have proposed to measure mixedness based on concentration variance from a number of samples of the mixture. Lacey (1943) proposed the following equation for concentration variance of a fully randomized binary mixture of the same-sized particles:

$$\sigma_{\mathrm{R}}^2 = \frac{\overline{a}(1-\overline{a})}{n_{\mathrm{p}}} \tag{2.11}$$

where n_{p} is the number of particles within each sample and $\overline{a}$ is the mean fraction of component A in the mixture. As the number of particles increase, the random variance decrease; again, n_{p} depends on the scale of scrutiny of mixture and the particle size. If the particle size is decreased, there will be an improvement in degree of homogeneity of the mixture. However, agglomerates are produced when particle size decreases below 1 μm due to an increase in cohesive interactions between the particles, so approaching a zero variance mixture is difficult in practice.

Lacey (1954) assumed that initially the binary components are fully segregated with a concentration variance σ_0^2, and proposed a different mixing index to represent the closeness of approach to the random mixture, as given below.

$$M = \frac{\sigma_0^2 - \sigma^2}{\sigma_0^2 - \sigma_{\mathrm{R}}^2} \tag{2.12}$$

M is the ratio of the mixing that has occurred to the amount of mixing that could occur. M values vary between 0 for a completely segregated mixture and 1 for a fully randomised mixture. Table 2.1 summarises the definition of mixing indices proposed by various researchers. Most of the equations are based on variance whereas equations H and K are based on standard deviation. Choosing a definition of mixing index for a given application depends on its ability to correlate mixedness with time by a simple linear relationship.

Let us consider equation J, where the driving force for mixing is the difference in variance between a given time t and end point. Hence, the rate of change of variance can be written as:

$$\frac{\mathrm{d}(\sigma^2)}{\mathrm{d}t} = -k(\sigma^2 - \sigma_{\mathrm{R}}^2) \tag{2.13}$$

where k is a rate constant representing the rate at which the mixing proceeds. Integrating this equation between the variance of σ_0^2 at time 0 and σ^2 at time t, we get the following equation.

$$\int_{\sigma_0^2}^{\sigma^2} \frac{\mathrm{d}(\sigma^2)}{\sigma^2 - \sigma_{\mathrm{R}}^2} = -k\int_0^t \mathrm{d}t \quad \text{and} \quad \ln\left|\frac{\sigma^2 - \sigma_{\mathrm{R}}^2}{\sigma_0^2 - \sigma_{\mathrm{R}}^2}\right| = -kt \tag{2.14}$$

Table 2.1 Definitions of mixing index.

	Mixing index definition	Range of values		Reference
		Fully segregated	Fully mixed	
A	$M = 1 - \frac{\sigma}{\sigma_0}$	0	1	Rose and Robinson (1965)
B	$M = 1 - \frac{\sigma^2}{\sigma_0^2}$	0	1	Miles (1962)
C	$M = \frac{\sigma_0^2 - \sigma^2}{\sigma_0^2 - \sigma_R^2}$	0	1	Lacey (1954)
D	$M = \frac{\sigma_R}{\sigma}$	$\frac{\sigma_R}{\sigma_0}$	1	Wiedenbaum and Bonilla (1955)
E	$M = \frac{\sigma}{\sigma_0}$	1	$\frac{\sigma_R}{\sigma_0}$	Yano *et al*. (1956)
F	$M = \frac{(\sigma_0 / \sigma) - 1}{(\sigma_0 / \sigma_R) - 1}$	0	1	Beaudry (1948)
G	$M = \sqrt{\frac{\ln \sigma_0^2 - \ln \sigma^2}{\ln \sigma_0^2 - \ln \sigma_R^2}}$	0	1	Ashton and Valentin (1966)
H	$M = \frac{\sigma_0 - \sigma}{\sigma - \sigma_R}$	0	1	Lacey (1943)
I	$M = \frac{\sigma^2}{\sigma_0^2}$	1	$\frac{\sigma_R^2}{\sigma_0^2}$	Westmacott and Lineham (1960)
J	$M = \frac{\sigma^2 - \sigma_R^2}{\sigma_0^2 - \sigma_R^2}$	0	1	Smith (2003)
K	$M = \frac{\sigma - \sigma_R}{\sigma_0 - \sigma_R}$	0	1	Smith (2003)
L	$M = \frac{\ln \sigma - \ln \sigma_R}{\ln \sigma - \ln \sigma_R}$	0	1	Smith (2003)

If we substitute from equation J of mixing index:

$$M = \exp(-kt) \tag{2.15}$$

The time required to get the desired degree of mixing can be found by plotting the log of experimental values of the mixing against time. The existence of a linear relationship validates the choice of mixing index.

2.5 Determining the end point of mixing

In any mixing operation, the state of mixture at the end of the operation is known as the end point. The concentration of one or more of the components in a mixture is measured

by calculating the intensity of segregation, mixing index, etc. These parameters are used to determine the end point of a mixing operation. The methods used to determine the end point generally rely on measuring the concentration of one or more components in the mixture. In the food processing industry, the technique used to measure end point should be non-intrusive, easily cleaned, should not contaminate the product and simple to operate.

2.5.1 Solids mixing

End point during solids mixing process is assessed by sampling as the appropriate scale of scrutiny. Analysis of the samples yields information on fraction component. The variance for a number of samples analysed can be calculated using the following equation (Rielly *et al*. 1994):

$$\sigma^2 = \frac{1}{n-1}\sum_{i=1}^{n}(C_i - \bar{C})^2 \tag{2.16}$$

where C_i is the concentration of a component C in sample i and n is the number of samples analysed from the mixture. The variance given by the equation describes how the concentration of C in various regions of the mixture differs from the mean concentration—a perfect mixture will have this value as 0. The maximum variance occurs for a segregated mixture, in which the concentration of component C at a particular point would be either 0 or 1. The variance of a completely segregated mixture is given by the following equation.

$$\sigma^2 = \bar{C}(1-\bar{C}) \tag{2.17}$$

Using this variance, one of the mixing indices, as given below, will be calculated to identify the end point or extent of mixing in solids mixing operation (Fellows 2000):

$$M_1 = \frac{\sigma_\mathrm{m} - \sigma_\infty}{\sigma_0 - \sigma_\infty} \tag{2.18}$$

$$M_2 = \frac{\log\sigma_\mathrm{m} - \log\sigma_\infty}{\log\sigma_0 - \log\sigma_\infty} \tag{2.19}$$

$$M_3 = \frac{\sigma_\mathrm{m}^2 - \sigma_\infty^2}{\sigma_0^2 - \sigma_\infty^2} \tag{2.20}$$

where σ_∞ is the standard deviation of a perfectly mixed sample, σ_0 is the standard deviation of a sample at the start of mixing and σ_m is the standard deviation of a sample taken during mixing. σ_0 can be found using:

$$\sigma_0 = \sqrt{V_1(1-V_1)} \tag{2.21}$$

where V is the average fractional volume or mass of a component in the mixture. The mixing index M_1 is used when approximately equal masses of components are mixed and/or at

relatively low mixing rates, M_2 is used when a small quantity of one component is incorporated into a larger bulk of material and/or at higher mixing rates and M_3 is used for liquids or solids mixing. The mixing time is related to mixing index as:

$$\ln M = -Kt_{\mathrm{m}} \tag{2.22}$$

where K is a mixing rate constant, which varies with the type of mixer and the nature of the components, and t_{m} is mixing time.

A set of samples taken at definite intervals during mixing gives information on the rate of mixing and closeness to randomly mixed state. In practice, the end point of the mixture would be chosen as somewhat away from a fully random state, taking into account the errors introduced during sampling and analysis. The overall concentration variance may be calculated from:

$$\sigma^2 = \sigma_{\mathrm{m}}^2 + \sigma_{\mathrm{a}}^2 + \sigma_{\mathrm{s}}^2 + \sigma_{\mathrm{p}}^2 \tag{2.23}$$

where $\sigma_{\mathrm{a}}^2, \sigma_{\mathrm{s}}^2$ and σ_{p}^2 represent variances due to analytical errors, sampling errors and purity differences, respectively. σ_{m}^2 represents the variance due to imperfect mixing and reduces to a value σ_{r}^2 in fully random state. The variance calculated using the above equations is for a finite number of samples and is only an unbiased estimate of the true concentration variance of the mixture. The larger the number of samples extracted, the better is the estimate of the concentration variance. A higher number of samples collected should give a better estimate of the concentration variance, and generally, 20–40 samples are required to give correct information on homogeneity. Moreover, the samples should be withdrawn from different locations within the mixer to get an overall measure of mixedness. Samples can be removed by a variety of probes (e.g., a *thief* probe) or can be inspected by fibre optic probes, image analysis, etc. The samples are analysed by particle counting, gravimetric methods and sieve analysis methods.

2.5.2 Fluid mixing

Concepts of scale and intensity of segregation are used to characterise fluid mixing operations. As homogeneity is approached, the length scale of segregation is expected to decrease to a small value, and it is difficult to measure very small length scales. To calculate this small value, it is necessary for concentration measurements to be made on a very fine scale, less than the scale of segregation. All the probes have finite measurement volumes, and a mixture containing heterogeneities on a length scale which are much less the probe resolution scale would appear from the measurement device as well mixed. In fluid mixing operations, various tracers such as dye, electrolyte, temperature refractive index, acid base reaction, etc., are used to express the mixedness of the fluid. Visual/light absorption, conductivity probe, thermocouple, colour change of pH indicator, etc., are used as measuring techniques when the aforementioned tracers are used to measure the mixedness of the fluid. In fluid mixing, a sample variance, or simply comparing the variance of concentration at a point with mean, is generally preferred in order to avoid difficulties associated with measuring the scale of segregation.

A common method in the batch mixing process of various fluids is to measure the concentration of an inert tracer component in the flow and say that the system is well mixed when fluctuations in the concentration fall within prescribed limits. A 95% mixing time is defined as the time at which the tracer concentration falls and stays within $\pm 5\%$ of the

final mean concentration (Rielly *et al*. 1994). The difficulties in batch mixing operations are related to tracer volume, resolution scale of the measurement probe, location of tracer addition and that of the probe. In turbulent flow, the measured 95% time is independent of the position of the probe. However, in laminar flow, the measured time depends on the location of the probe within the vessel. In this case, a global mixing time can be measured by locating measurement probes at a number of representative positions within the flow. The time variation of concentration variance may be calculated for n number of probes as:

$$\sigma^2(t) = \frac{1}{n-1}\sum_{i=1}^{n}[C_i(t) - C_\infty]^2 \tag{2.24}$$

where $C_i(t)$ is the concentration measured by probe i and C_∞ is the mean concentration in the tank. In continuous processing, it is the residence time within the mixer that determines the mixture quality in the output streams. The ratio of standard deviation and the mean of the tracer element in the output stream are often used to describe the degree of mixing in static mixers. In these mixers, pipeline inserts cause flow splitting and re-orientation, giving a form of distributive mixing.

In case of high-viscosity liquids agitated by high-speed dual impellers, flow visualisation using neutrally buoyant particles can be used. For high-viscosity, shear-thinning fluids such as xanthan gum and sodium carboxy methyl cellulose, the fluid in the region close to the agitator experiences high shear stress. At some distance from the impeller, the shear stress is low and the apparent viscosity is high; the liquid is almost stationary. Moreover, Bingham plastic liquids have a yield stress requiring two impellers to generate flow in the whole vessel. Dilatant foods like corn flour and chocolate should be mixed with great care. If adequate power is not available in the mixer, the increase in viscosity causes damage to the drive mechanism. A folding or cutting action prevalent in some planetary mixers or paddle mixers is suitable for this type of food (Fellows 2000). In these cases, the liquid flow is defined by a series of dimensionless numbers: the Reynolds number, $Re(D^2N\,\rho_m/\mu_m)$, the Froude number, $Fr(DN^2/g)$ and the Power number, Po $(P/\rho_m N^3 D^5)$, where P is power transmitted via the agitator, ρ_m is density of mixture and μ_m is viscosity of the mixture. These are related as:

$$Po = K(Re)^n\,(Fr)^m \tag{2.25}$$

where K, n and m are factors relating to the geometry of the agitator, which are found by experiment. The density of the mixture is found by addition of component densities of the continuous and dispersed phases:

$$\rho_m = V_1\,\rho_1 + V_2\,\rho_2 \tag{2.26}$$

where V is the volume fraction, and 1, 2 refer to continuous and disperse phases, respectively. The viscosity of a mixture is found by using the following equations.

$$\mu_{m\ \text{unbaffled}} = \mu_1^{V_1}\mu_2^{V_2} \tag{2.27}$$

$$\mu_{m\ \text{baffled}} = \frac{\mu_1}{V_1}\left(\frac{1+1.5\,\mu_2 V_2}{\mu_1+\mu_2}\right) \tag{2.28}$$

2.5.3 Multi-phase mixing

Multi-phase mixing operations include dispersion of gas in a liquid, suspension of solids in a liquid during dissolution, dispersion of one liquid in another to promote interface mass transfer, etc. In these cases, the phases have a natural tendency to separate. In batch processing, these mixtures can be maintained in a well-mixed state only by a continuous supply of energy through agitation. The distribution of the dispersed phase in the continuous phase in the equilibrium state depends on the intensity of agitation. For example, during suspension of food particles in a viscous sauce, increasing rotational speed of the agitator blades leads to more uniform distribution. The quality of mixture is often judged visually through a transparent window. For gas–liquid mixtures, the minimum impeller speed, N_{CD}, given by the following equation can be used to describe complete dispersion of the gas for pipe spargers:

$$N_{CD} = \frac{4V_G^{0.5}T^{0.25}}{D^2} \tag{2.29}$$

where, V_G is mean volumetric gas flow rate, T is tank diameter and D is impeller diameter. For solid–liquid mixtures, when all the particles are in motion and none remains at the bottom of the tank for more than 1–2 s, then this condition is known as *just suspended*. The impeller speed for just-suspended condition is given as:

$$N_{JS} = s\,\mathrm{v}^{0.1}d_p^{0.2}\left(\frac{g\,\Delta\rho}{\rho}\right)^{0.45}x^{0.13}\,D^{-0.85} \tag{2.30}$$

where d_p is particle diameter, x is the percentage solids fraction by mass, D is the impeller diameter and s is a constant that depends on impeller and tank geometry. In food processing, it is quite common to have to draw-down and homogenise floating solids, for example, hydration of dried vegetables or meat. A partially baffled tank to draw-down solids through a central vortex can be used for this type of application.

2.5.4 Alternative measures of mixedness in industrial practice

In food processing applications, several other criteria are used to define the well-mixed or uniformly dispersed condition, and not all of them are directly related to the distribution of concentration or phase fraction within the mixture. Organoleptic or textural qualities are often used as indicators of product quality or the state of mixing. The combination of mouth feel, flavour and odour is complex to measure using instrumentation. These properties are commonly assessed by a sensory panel consisting of a number of experienced tasters, who individually rate perceived qualities of the food material in different categories. These methods are reliable and consistent, but cannot be routinely implemented to assess the mixedness of a significant fraction of the product output; rather, they are used as a measure for occasionally checking product quality and for detecting long-term changes in the manufacturing process. Moreover, mixing of food products may involve a number of simultaneous processing objectives.

2.6 Residence time distributions

In general, mixing can be accomplished using a batch process or a continuous process. The batch operation aims to achieve spatial mixing as described in Section 2.2, whereas continuous operations are able to produce mixing in space and mixing in time (also called axial mixing). For example, in the continuous operation of a well-mixed stirred tank, inside the vessel, the mixture is perfectly homogeneous in space, such that the outlet stream contains exactly the same composition as in the vessel. In this case, the mixing in time is characterised by a residence time distribution as follows:

$$E(t) = \frac{1}{\tau}\exp\left(-\frac{t}{\tau}\right) \tag{2.31}$$

where τ is the mean residence time given by vessel volume/volumetric flow rate, $E(t)\ \mathrm{d}t$ is the probability that the material residence time is between t and $(t+\mathrm{d}t)$ in the mixer. Equation (2.31) shows that there is a wide distribution of residence times in a well-mixed vessel, such as 10% of the material is retained for $t < 0.11\tau$ and 10% resides for $t > 2.3\tau$, indicating that there is a non-homogeneity in the time histories of the materials leaving the vessel. Therefore, the two concepts of mixing in space and in time are not always helpful, and the use of a residence time distribution to evaluate mixing quality can be misleading. Moreover, increasing the degree of back-mixing in a vessel generally increases the spread of residence times and non-homogeneity of processing histories.

2.6.1 Modelling of residence time distributions

A typical mixing process can be visualised as moving of individual particles relative to a fixed reference. This is a three-dimensional flow problem. If the movement of each particle could be analysed separately and then the mass integrated, the mixing or residence time can be modelled. The main problem in doing this is determining the forces acting on a particle (Lindley 1991). A driving force is imparted by the mixer, but this force is applied directly on only relatively few particles, and particle movement is resisted by unknown forces from the reminder of the particulate matter. Applying the concepts of mathematical modelling that includes fundamental laws of mixing and performance parameters would allow quick and easy investigation of residence time distributions. For example, the mean residence time in a screw type mixer can be expressed as a function of t_i and $E(t)$ (Gautam & Choudhury 1999):

$$T_\mathrm{mean} = \int_0^\mathrm{t} t_\mathrm{i} E(t)\mathrm{d}t \tag{2.32}$$

$$= \frac{\sum_0^\infty t_\mathrm{i} c_i \Delta t_i}{\sum_0^\infty t_\mathrm{i} \Delta t_i} \tag{2.33}$$

where, c_i is the tracer concentration in the sample producing the observed voltage response across the resistor at time t_i, and Δt_i is the time interval between successive samplings.

Acknowledgement

This work was funded by Agricultural Experimental Station (AES), South Dakota State University, Brookings, SD, USA.

References

Ashton, M.D. & Valentin, F.H.H. (1966). The mixing of powders and particles in industrial mixers. *Transactions of the Institute of Chemical Engineers*, **44**, 166–188.

Beaudry, J.P. (1948). Blender efficiency. *Chemical Engineering*, **55**, 112–113.

Bentley, B.J. & Leal, L.G. (1986). A computer-controlled four-roll mill for investigations of particle and drop dynamics in two-dimensional linear shear flows. *Journal of Fluid Mechanics*, **167**, 219–240.

Brennan, J.G., Butters, J.R., Cowell, N.D. & Lilly, A.E.V. (1976). *Food Engineering Operations*, 2nd edn. Elsevier, London.

Danckwerts, P.V. (1953). Theory of mixtures and mixing. *Research (London),* **6**, 355–361.

Earle, R.L. (1983). *Unit Operations in Food Processing*. Pergamon Press, Oxford, London.

Elemans, P.H.M., Bos, H.L., Janssen, J.M.H. & Meijer, H.E.H. (1993). Transient phenomena in dispersive mixing. *Chemical Engineering Science*, **48**, 267–276.

Fellows, P. (2000). *Food Processing Technology*, 2nd edn. CRC Press, NewYork.

Gautam, A. & Choudhury, G.S. (1999). Screw configuration effects on residence time distribution and mixing in twin screw extruders during extrusion of rice flour. *Journal of Food Process Engineering*, **22**, 263–285.

Lacey, P.M.C. (1943). The mixing of solid particles. *Transactions of the Institution of Chemical Engineers*, **21**, 53–59.

Lacey, P.M.C. (1954). Developments on the theory of particle mixing. *Journal of Applied Chemistry*, **4**, 257–268.

Lindley, J.A. (1991). Mixing processes for agricultural and food materials: 1, fundamentals of mixing. *Journal of Agricultural Engineering Research*, **48**, 153–170.

Miles, S.R. (1962). Heterogeneity of seed lots. *Proceedings of the International Seed Testing Association*, **27**(2), 407–413.

Rielly, C.D., Smith, D.L.O., Lindley, J.A., Niranjan, K. & Phillips, V.R. (1994). Mixing processes for agricultural and food materials: 4, assessment and monitoring of mixing systems. *Journal of Agricultural Engineering Research*, **59**, 1–18.

Rose, H.E. & Robinson, D.J. (1965). The application of the digital computer to the study of some problems in the mixing powders. *American Institute of Chemical Engineers Symposium Series*, **10**, 61.

Smith, P.G. (2003). *Introduction to Food Process Engineering*. Kluwer Academic/Plenum Publishers, London.

Westmacott, M.H. & Lineham P.A. (1960). Measurement of uniformity in seed bulk. *Proceedings of the International Seed Testing Association*, **25**, 151.

Wiedenbaum, S.S. & Bonilla C.F. (1955). A fundamental study of the mixing of particulate solids. *Chemical Engineering Progress*, **51**, 27–36.

Yano, T., Kanise, I. & Tanaka, K. (1956). Mixing of powders by the V-type mixer. *Kagaku Kogaku*, **20**, 20–25.

3 Kinematics of flow and mixing mechanisms

Brijesh Tiwari and P.J. Cullen

3.1 Introduction

Mixing theory has attracted the interest of fluid dynamicists and engineers for its relevance in understanding some of the most fundamental problems involving fluid flows, and for its practical impact in connection with the chemical, pharmaceutical and food processing industries (Baldyga & Bourne 1999). The first quantitative approach to mixing dates back to Danckwerts (1952, 1958), who introduced global indices of the 'degree of mixedness' such as the intensity of segregation, which essentially corresponds to the concentration variance of an advecting–diffusing dye carried by the flow, and the linear scale of segregation, yielding the average 'diameter' of the partially mixed structures.

About two decades ago, a new approach to characterise mixing in flow systems spread out in the fluid dynamics community (Aref 1984; Ottino 1989). This approach originated from the observation that even simple, large-scale velocity fields can generate mixing structures at arbitrarily small scale. This theory constituted a breakthrough in fluid mixing. In fact, until then, the wordings 'mixing flow' and 'turbulent flow' were used almost interchangeably (Cerbelli *et al*. 2006). Methods and quantities derived from dynamical system theory were directly applied to simple flows, laboratory equipment, stirred tanks, static mixers and constituted what is now referred to as the Lagrangian or kinematic theory of laminar mixing (Ottino 1989; Beigie *et al*. 1994).

Our understanding of fluid mixing is advancing by developments in turbulence and chaos theory, along with advances in complimentary fields of imaging and computation. However, there is still no complete description of turbulence, with flows within mixing systems complicated by recirculation, geometric effects and instabilities on several scales of motion (Kresta & Brodkey 2004). Turbulence plays a central role in many mixing processes and is commonly induced by the process industries in mixers to facilitate effective mixing. However, the food industry regularly deals with viscous fluids, which necessitate mixing in the laminar flow regime, where effective mixing may prove challenging. This chapter discusses the role of turbulent and laminar flow in fluid mixing. Comparably, the influence of particulate flow on the mixing of solids is also reviewed.

3.2 Fluid mixing

The modern approach to the study of mixing in laminar fluid flows applies dynamical systems theory and concepts to the Lagrangian description of fluid flow. The Lagrangian

description uses Cartesian coordinates that move with a particle. When we speak of a fluid particle, we mean an element of fluid of negligible dimensions. The equations of fluid motion are obtained by applying the principles of mechanics to a fluid particle. In the case of an incompressible viscous (Newtonian) fluid of uniform density, the following equations are obtained (King 1998).

Considering the Navier–Stokes equations for an incompressible fluid:

$$\frac{\partial u}{\partial t}+\omega\times u+\frac{1}{2}\nabla u^2=-\nabla\left(\frac{p}{\rho}\right)+\nu\nabla^2 u \tag{3.1}$$

$$\nabla\cdot u=0$$

where $\omega=\nabla\times u$ is the vorticity, $\omega\times u$ is the lamb vector, p is the pressure, ρ is the density and $\nabla^2 u$ is the dissipation field. Solving these *Navier–Stokes* equations, we obtain the velocity field $u(x, t)$. The dynamical systems setting for the study of the transport and mixing of a fluid particle is the study of the trajectories of:

$$\dot{x}=u(x,t) \tag{3.2}$$

where each initial condition corresponds to a different fluid particle. A trajectory is the path the fluid particle takes through the fluid, and the phase space is physical space (King 1998).

To investigate the mixing in a fully three-dimensional laminar flow, it is difficult to obtain $u(x, t)$ because the majority of studies have been restricted to time-dependent forcing of 2D velocity fields (Ottino 1989) and 3D flows based on qualitative or kinematic models which mimic a velocity field but do not satisfy equations (3.1) (Feingold *et al.* 1988; Bajer & Moffatt 1990; Holm & Kimura 1991; Stone *et al.* 1991; Jones & Young 1994). Only by studying the kinematics of velocity fields satisfying the Navier–Stokes equations can an understanding be achieved of how inertia and viscosity influence the mixing properties throughout the fluid—a question of both fundamental and practical interest.

The Navier–Stokes equations for a Newtonian fluid are simply equations for the velocity *vector* field, whereas the rheological equations for a visco-elastic fluid involve a non-linear 'constitutive equation' for the stress *tensor*. Any calculation is therefore much harder for visco-elastic flow, and even conceptually simple approximation schemes often lead to cumbersome expressions with many terms. Secondly, the structure of these equations is such that in flow regions with significant shear, components of the stress tensor tend to grow exponentially, making extension of numerical techniques to significant Weissenberg numbers (*Wb*) difficult, resulting in it being termed the high Weissenberg number problem (HWNP) (Owens & Phillips 2002; Fattal & Kupferman 2004; Hulsen *et al.* 2005). The HWNP has been the major stumbling block in computational rheology for the last three decades. The term 'HWNP' refers to the empirical observation that all numerical methods break down when the Weissenberg number exceeds a critical value (Hulsen *et al.* 2005).

3.2.1 Kinematics of fluid flow

Fluid flow can be expressed by either one of two ways viz. Lagrangian or Eulerian approaches. To express fluid velocity with the Eulerian approach, a point in a flow field is

selected using the Cartesian coordinate system (x, y, z), and observed changes in properties such as velocity, pressure and/or temperature as the fluid passes through this particular point are measured. However, in the steady state condition, the flow properties are no longer a function of time. The Eulerian viewpoint is commonly used, and it is the preferred method in the study of fluid mechanics. In this case, velocity depends upon the point in space and time. In the Lagrangian viewpoint, an individual fluid particle is considered for all time. The Lagrangian description of fluid mechanics is based on an observer following the trajectories of fluid particles, which are moving mathematical fluid points of infinitesimal size but large compared to molecular dimensions as required by continuum assumptions (Yeung 2002). This viewpoint is widely used in dynamics and statics and easy to use for a single particle and works well for solid particle tracking techniques (Chapter 7). In this approach, as the fluid particle travels about the flow field, the changes in flow properties such as velocity is obtained by differentiating the position vector [$\boldsymbol{r}(t)$] with respect to time:

$$\boldsymbol{r}(t) = x\boldsymbol{i} + y\boldsymbol{j} + z\boldsymbol{k} \tag{3.3}$$

$$\boldsymbol{V}(t) = \frac{\mathrm{d}x}{\mathrm{d}t}\boldsymbol{i} + \frac{\mathrm{d}y}{\mathrm{d}t}\boldsymbol{j} + \frac{\mathrm{d}z}{\mathrm{d}t}\boldsymbol{k} \tag{3.4}$$

$$\boldsymbol{V}(t) = u\boldsymbol{i} + v\boldsymbol{j} + w\boldsymbol{k} \tag{3.5}$$

where $\boldsymbol{i}$, $\boldsymbol{j}$, $\boldsymbol{k}$ are unit vectors in x, y, z directions and u, v, w are the respective component velocities.

It is not practical to keep track of the positions of all particles in a flow field; consequently, the Eulerian approach is often preferred over the Lagrangian approach. However, both the approaches can be used in the study of fluid mechanics. A Lagrangian approach following the motion of infinitesimal material fluid elements (which by definition move with the local instantaneous flow) is conceptually natural and practically useful for describing turbulent transport (Yeung 2002). Important early contributions in this line of research include those of Taylor (1921) who studied the statistics of displacement of a single fluid particle, Richardson (1926) who studied the dispersion of particle pairs relative to each other and Batchelor (1949, 1952) who established formal connections between the statistics of fluid particle motion and the concentration field of a diffusing contaminant. The kinematic approach has contributed to a better understanding of existing mixing devices as well as to the rational design of new ones (Harvey & Rogers 1996; Zalc *et al*. 2001).

Motion of individual particles in a fluid can be either regular, that is integrable (terminology used by fluid dynamicist for regular flow), or chaotic. A laminar flow field is one in which velocity, pressure and other flow parameters do not vary irregularly with time. A chaotic flow field is one in which the path and final position of a particle placed within the field are extremely sensitive to their initial position (Rothstein *et al*. 1999). Chaotic advection is the process of mixing using flow fields that are entirely regular in space and time, yet which cause particles initially close together, to become widely separated, and the flow as a whole well mixed (see Section 3.3). Chaotic flows have been proven to be the only effective route to destroy segregation rapidly in viscous mixing applications, which are particularly prone to remain inhomogeneous for long periods of time (Lamberto *et al*. 1996; Avalosse & Crochet 1997; Hobbs *et al*. 1997; Unger & Muzzio 1999). Before discussing mixing in various flow regimes, it is important to quantify the flow regime.

3.2.2 Quantification of flow regimes

Hydrodynamic flow in classical and quantum fluid mechanics can be classified into one of two broad categories or regimes, namely, laminar and turbulent flows. The flow regime, whether laminar or turbulent, is important in understanding the mixing mechanism. Laminar flow exists over a very low range of velocities, whereas turbulent flow occurs at higher velocities. When viscous forces predominate, the flow is laminar. Conversely, in turbulent flow, inertial forces dominate and the fluid forms eddies with widely different length and time scales. However, such predictions are valid only for constant flow and become more difficult where flow is pulsatile or radial. The situation is further complicated if the contained fluid is non-Newtonian (Janssen *et al.* 2007). In general, the pattern of the flow varies with the velocity, the physical properties of the fluid and the geometry of the surface, for example tube or an open surface. In the majority of moderate and high-speed flow problems, some form of random variation of flow variables exists. The laminar treatment is generally not applicable when such variations occur. Turbulent flow is defined as a flow with random variation of various flow quantities such as velocity, pressure and density. Turbulence is a property of a flow, not that of a fluid (Zienkiewicz *et al*. 2005). In turbulent flow, the inertia stresses dominate over the viscous stresses, leading to small-scale chaotic behaviour in the fluid motion. Turbulent flow is generally dominated by recirculation, swirling of a fluid or apparent randomness. Recirculation or randomness does not necessarily indicate turbulent flow, and it may also be present in laminar flow.

Flows of visco-elastic fluids are characterised by the Weissenberg number (*Wb*) which measures the importance of relaxation, elasticity and anisotropy effects due to the visco-elasticity. The Reynolds number (*Re*) and *Wb* behave in a similar fashion. However, transformation towards turbulent flow for either case largely depends upon flow geometry (Morozov & van Saarloos 2007).

Flow regimes can be quantified based on the type of mixer employed, including stirred tank, static mixer, bubble column reactor or flow in a pipe or a duct.

3.2.2.1 *Tube flow and static mixers*

The flow rate and physical properties of a Newtonian fluid may be used to predict its pattern of flow in a simple circular pipe. The parameters determining the type of flow present is expressed by the Reynolds number given by:

$$Re = \frac{\rho V D}{\mu} \tag{3.6}$$

where V, D, ρ and μ are fluid velocity, pipe diameter, fluid density and fluid viscosity, respectively.

Laminar flow: $Re < 2{,}000$
Transitional flow: $2{,}000 < Re < 4{,}000$
Completely turbulent: $Re > 4{,}000$

By inserting a series of flow orientation elements along the axis of a straight pipe, the flow can be periodically split and remixed at the junctions along with stretching and folding

within the elements. Static mixers may function in either the laminar, transitional or turbulent flow regimes.

The same general concepts of an open type apply to flows in static mixers except that the transition values for *Re* are lower by a factor of about 2 (Regner *et al*. 2006). Flows are generally laminar for $Re < 50$ and turbulent for $Re > 1{,}000$. The inserts cause systematic disturbances to the flow field so that complex but fairly reproducible flow behaviour can be expected in the intermediate range $50 < Re < 1{,}000$ (Regner *et al*. 2006). More exact numbers depend on the design of the elements including their aspect ratio (length-to-diameter ratio) of the elements.

Apart from the primary flows, which follow the curvature of the mixer elements, additional structures in the flow (secondary flows) may significantly influence the mixing process. Vortices have been reported to occur at flow rates above certain Reynolds numbers (*Re*) (Jaffer & Wood 1998; Ujhidy *et al*. 2003). For a given geometry, this critical Reynolds number is dependent on the aspect ratio, that is, short elements lead to a low critical Reynolds number (Regner *et al*. 2006). Figure 3.1 shows how a striation is rotated and

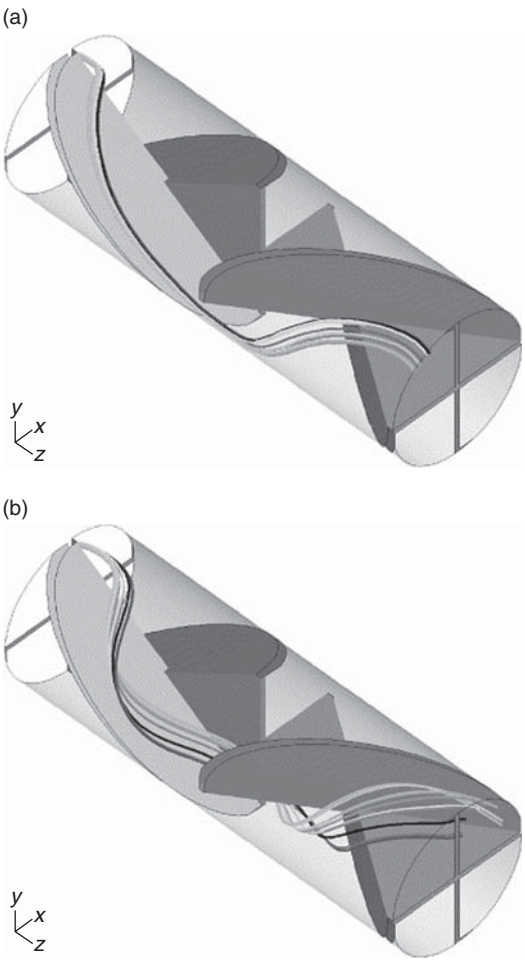

Fig. 3.1 The rotation and stretching of a striation in a Lightnin Series 45 static mixer: (a) due to primary flow at a Reynolds number of 1 and (b) due to primary and secondary flows at a Reynolds number of 80. [Reprinted from Regner *et al*. (2006) with permission from Elsevier.]

stretched at a Reynolds number of 1 and 80, respectively, by the trajectories of particles. At $Re = 1$, the striation is only affected by the primary flow, whereas at $Re = 80$, any additional rotation and stretching occurs due to vortices in the middle of the mixer elements and at the element intersection (Regner *et al*. 2006).

Table 3.1 shows the flow regime for a number of commercially available static mixers.

3.2.2.2 *Stirred tanks*

The stirred tank is the most common industrial mixer used by the processing industries of detergents, creams, drugs, foods, vaccines and chemicals. A modified Reynolds number is employed for stirred tanks, based upon the impeller diameter (d) and rotational speed (N).

$$Re = \frac{\rho d^2 N}{\mu} \tag{3.7}$$

The flow patterns within a stirred tank will be governed by the type of impeller employed. The flow patterns include: (a) axial flow which coincides with the axis of the impeller shaft, (b) radial flow which is parallel to the impeller radius toward the vessel wall, and (c) tangential flow which is induced by swirling or by formation of a vortex. Mixing in tangential flow pattern is limited due to small velocity gradients. Figure 3.2 shows the flow regime transition with change in Re number in a stirred tank agitated by an impeller. Figures 3.2a and 3.2b show the region where Reynolds number is small and is in laminar flow, whereas Figure 3.2c shows the transition region from laminar to completely turbulent flow. For stirred vessels, the flow is laminar for $Re < 10$ and fully turbulent for $Re < 10^4$.

For viscous fluids the laminar flow regime dominates, where even small disturbances are dampened out by the viscous forces. If we attempt to induce turbulence with high rotational speed impellers, the flow velocities decay rapidly at distances from the impeller. Caverns of well-mixed regions are formed, surrounded by the regions of unmixed or stationary fluid. Consequently, numerous mixing designs operate in the laminar regime such as close clearance impellers including helical ribbons and anchors.

Quantification of the flow regime in a stirred tank has not been accurately characterised in the laminar regime neither with the Eulerian velocity field nor with the Lagrangian particle trajectories (Harvey & Rogers 1996; Harvey *et al*. 1997; Ranade 1997; de la Villéon *et al*. 1998; Tanguy *et al*. 1998; Lamberto *et al*. 2001). Alvarez-Hernández *et al.* (2002) examined the transport of fluorescent dye in a tank stirred by three co-axial 'Rushton' impellers, each with six equally spaced vertical vanes. The experiment showed that a small aliquot of dye would ultimately spread to cover approximately 80% of the cross-sectional area of the tank. If the impellers are replaced by disks of the same outer diameter, a very similar flow is generated, but essentially no convective mixing occurs. Dye injected anywhere in the flow becomes trapped in toroidal recirculating regions. Alvarez-Hernández *et al*. (2002) reported that the stirring action alone does not generate detectable global mixing. They demonstrated that the flow in stirred tank mixers is almost identical to a dominant non-chaotic circulatory flow. Mixing occurs only due to small perturbations to a non-chaotic flow that leads to the emergence of 3D horseshoes. Horseshoes indicate that the system is chaotic which involves repetitive stretching and folding (Ottino 1989), an operation referred to as a horseshoe map in mathematics.

Table 3.1 Industrial applications of static mixers along with flow regime.

Mixer	Flow regime	Area of application	References/ Company
Kenics	Laminar/ turbulent	Thermal homogenisation of polymer melt Gas–liquid dispersion Dilution of feed to reactor	Chen (1975) Smith (1978)
	Turbulent	Dispersion of viscous liquids	Berkman and Calabrese (1988)
	$980 < Re < 8{,}500$	Enhancement of forced flow boiling heat exchanger	Azer and Lin (1980)
SMX	Laminar	Mixing of high-viscosity liquids and liquids with extremely diverse viscosity, homogenisation of melts in polymer processing	Koch-Glitsch Inc. (2001)
SMV	Turbulent	Low-viscosity mixing and mass transfer in gas–liquid systems	Koch-Glitsch Inc. (2001)
SMXL	Laminar	Liquid–liquid extraction Homogeneous dispersion and emulsions Heat transfer enhancement for viscous fluids	Koch-Glitsch Inc. (2001)
SMF		Sludge conditioning, pulp stock blending, bleaching and dilution, bleaching of suspension and slurries	Koch-Glitsch Inc. (2001)
SMR	Laminar	Polystyrene polymerisation and devolatilisation	
HEV	Turbulent	Low-viscosity liquid–liquid blending, gas–gas mixing	Chemineer Inc. (1988)
LPD	Laminar	Blend two resins to form a homogeneous mixture	
	Turbulent	Blending grades of oil or gasoline	Ross Engineering Inc. (2001)
LLPD	Turbulent	Liquid–liquid dispersions	Ross Engineering Inc. (2001)
	Laminar	Blend out thermal gradient in viscous streams	Ross Engineering Inc. (2001)
ISG	Laminar	Blending catalyst, dye or additive into viscous fluid Homogenisation of polymer dope Pipeline reactor to provide selectivity of product	Ross Engineering Inc. (2001)
	Turbulent	Wastewater neutralisation	
Inliner mixer series 45	Turbulent	Fast reaction and blending application including widely differing viscosity, densities and fluid with unusual properties, such as polymer Chemical and petrochemical systems, hydrocarbon refining, caustics, pulp and fast reactions	Lightnin (2001)
Inliner mixer series 50 SMV-4	$1{,}400 < Re < 3{,}700$	Fine liquid–liquid dispersions (water–kerosene)	
	$16{,}000 < Re < 58{,}000$	Dispersion of immiscible fluids, for example, water–kerosene Phase inversion in liquid–liquid system, for example, water–organic, water–CCl_4	Al-Taweel and Walker (1983), Sembira *et al*. (1986), Tidhar *et al*. (1986)
Static-mixer woven screen Komax SM	Turbulent	Dispersion of kerosene in water. Mixing food products such as margarine and tomato pastes, viscous liquids like syrups and light fluids like juices	Al-Taweel and Walker (1983), Komax Systems Inc. (2001)

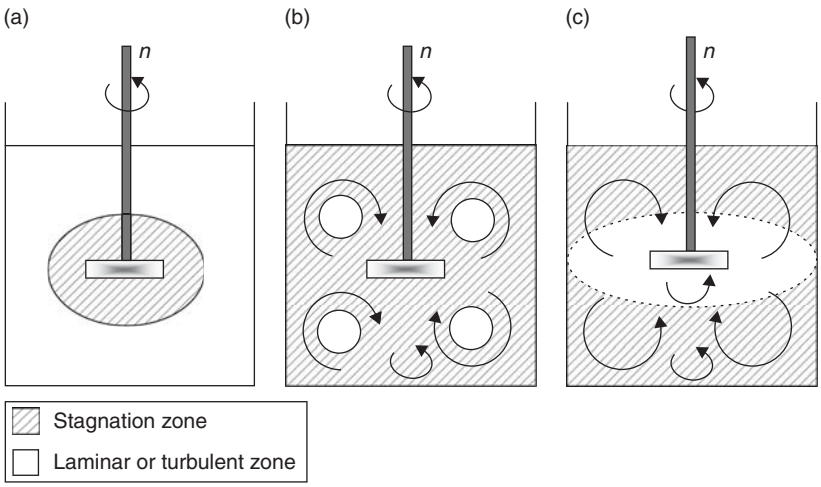

Fig. 3.2 Transition of flow regime in stirred tank: (a) laminar and stagnation, (b) laminar with stagnation and (c) transitional region.

3.2.2.3 *Bubble columns*

In bubble column reactors, a commonly used device in the process industries, a dispersed gas phase moves in a continuous liquid phase, and accordingly, the flow conditions in the gas phase are of essential importance for understanding and modelling of these reactors. The flow regime in a bubble column reactor can be defined based on the nature of dispersion. In general, based on the bubble size distribution, the radial distribution of gas hold-up and the macro-scale liquid circulations, two different flow regimes have been identified in bubble columns: the dispersed bubble (homogeneous) and coalesced bubble (heterogeneous) flow regimes (Deckwer 1992; Tzeng *et al.* 1993; Chen *et al.* 1994; Lin *et al.* 1996; Zahradnik *et al.* 1997; Ruzicka *et al.* 2001; Mouza *et al.* 2005). These two regimes along with the transition regime are shown in Figure 3.3. The two flow regimes can be clearly distinguished visually and can be simply identified from the dependence of gas hold-up on the superficial gas velocity demonstrated schematically (Zahradnik *et al.* 1997) (Figure 3.4). The homogeneous bubbling regime, represented by the line AB in Figure 3.4, is characterised by the almost uniform size of bubbles and by radially uniform gas hold-up. The bubbles generated at the sparger rise undisturbed vertically or with small-scale transverse and axial oscillations. The extent of bubble coalescence and break-up in the bed is negligible, and hence, the sizes of bubbles and the value of the bubble-bed voidage are entirely governed by the type and design of the gas sparger and by physical properties of the gas–liquid system. There is no large-scale liquid circulation in the bed. The liquid phase turbulence is not isotropic and its scale is of the order of the bubble size. Conversely, the heterogeneous bubbling regime is characterised by the wide distribution of bubble sizes and by the existence of a radial gas hold-up profile. A portion of gas throughput, which increases with increasing gas velocity, is transported through the bed in the form of fast-rising large bubbles. Macro-scale circulation of the liquid phase is induced by the voidage profile, with velocities one to two orders of magnitude higher than the common range of superficial liquid velocities. The turbulence characteristics are assumed to be isotropic,

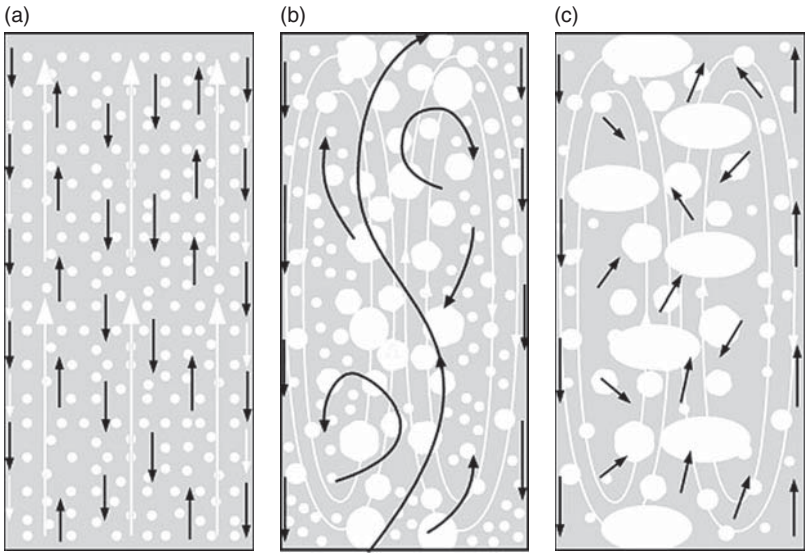

Fig. 3.3 Schematic representation of the flow regimes in a bubble column: (a) dispersed bubble flow regime, (b) vortical flow regime and (c) turbulent flow regime. *White arrows*: time-averaged liquid flow patterns; *black arrows*: instantaneous liquid flow patterns; *grey colour*: liquid phase; *white circles/ellipses*: gas phase. [Reprinted from Díaz *et al*. (2008) with permission from Elsevier.]

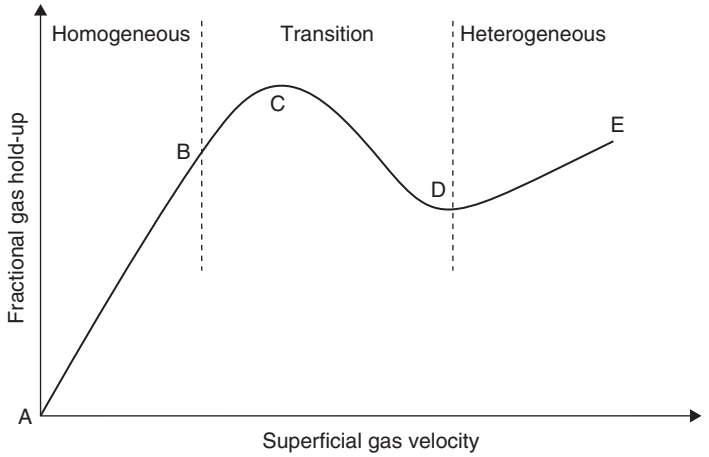

Fig. 3.4 Schematic diagram showing relationship between flow regime, superficial gas velocity and fractional gas hold-up.

and the scale of turbulence is proportional to the column diameter. The limits of the transition region between the homogeneous and the heterogeneous bubbling regimes (B and D in Figure 3.4) are characterised by the onset and the complete development of liquid circulation patterns in the bed. In the transition regime, dependence fractional gas hold-up and superficial velocity typically exhibit a clearly pronounced maximum, reflecting the increasingly negative effect of the developing liquid circulation on the gas hold-up values (Zahradnik *et al.* 1997).

Dispersed bubble flow regime (homogeneous)

This is also known as the laminar, uniform, dispersed, bubbly flow regime. It generally takes place at low values of superficial gas velocity and is characterised by: (a) a narrow bubble size distribution with bubbles rising vertically; (b) a time-averaged uniform radial distribution of both the gas hold-up and the liquid velocity and (c) the inexistence of large-scale liquid circulations (although small liquid vortices are detected). The bubbles rise almost vertically and lift up a considerable amount of liquid to the top of the column. The liquid thus carried up must return down, as there is zero net liquid flow in the column. The liquid counter-current delays the bubble rise, hence increasing the gas hold-up. This small-scale liquid velocity field is unsteady and highly fluctuating on short time scales; however, the long-time radial profiles of velocity (Hills 1974; Lapin & Lubbert 1994) and voidage (Kumar *et al*. 1997) are flat.

Coalesced bubble flow regime (heterogeneous)

This is also known as the turbulent, circulation, clustered, churn-turbulent regime. It is produced by either (a) plates with small and closely spaced orifices at high gas flow or (b) plates with large orifices at any gas flow. The former case results from the instability of a dispersed bubble flow regime and the subsequent transition. This flow regime exists for higher values of superficial gas and presents a wide bubble size distribution due to the now significant influence of the coalescence and break-up processes. Both the gas hold-up and the liquid velocity exhibit a remarkable radial profile when their values are time-averaged. Additionally, the liquid phase develops highly chaotic and dynamic macro-scale circulation patterns. As in case of homogeneous flow regimes, the liquid circulations in heterogeneous flow regimes are highly non-stationary in short time scales (Chen *et al*. 1994; Devanathan *et al*. 1995). However, the long-time radial profiles of velocity and voidage are not flat as in case of homogeneous flow regimes, and display roughly parabolic dependence on the column radius with a maximum on the centreline (Franz *et al*. 1984).

In both the dispersed bubble and coalesced bubble flow regimes, the liquid vortices are highly unsteady, but their dimension determines the resulting time-averaged liquid velocity and gas hold-up profiles, as only bubble column size flow structures contribute to the time-averaged calculations (Mudde & Van Den Akker 1999; Ruzicka *et al.* 2001b). Therefore, when the dispersed bubble regime prevails, the radial profiles of the time-averaged values of gas hold-up and liquid velocity time are flat. Those profiles become approximately parabolic as the coalesced bubble regime gets established. Table 3.2 shows the difference between two flow regimes.

Owing to the different behaviour of bubble-bed reactors in the homogeneous and heterogeneous bubbling regimes, the dependences of the rates of momentum, mass and heat transfer on the design and operating parameters of these reactors (such as reactor geometry, gas and liquid flow rates, and gas and liquid phase properties) are also substantially different. For rational reactor design, it is of essential importance to know the range of parameters over which a particular regime prevails and the conditions under which the regime transition occurs (Zahradnik *et al.* 1997).

Following the pioneering papers of Aoyama *et al*. (1968) and Ohki and lnoue (1970), numerous experimental studies have examined the conditions of formation and stability of homogeneous and heterogeneous bubbling regimes in bubble column reactors and/or determined the critical values of superficial gas velocity at which the transition between the two respective regimes occurs (Zahradnik & Kastanek 1979; Pilhofer 1980; Joshi & Lali 1984;

Table 3.2 Qualitative comparison of homogeneous and heterogeneous flow regimes in bubble columns.

		Flow regime	
		Homogeneous	**Heterogeneous**
Plate	Orifice size	Small	Large
	Orifice pitch	Small	Large
	Number of orifice	Large	Small
Bubbles	Size	Small	Large
	Formation	Break-up of fine jets	Break-up of strong jets
	Coalescence	No	Yes
	Rise	Almost vertically	Irregular path
Voidage	Mean value	Low	High
	Non-uniformity	Small	Large
	Mean radial profile	Zero	Non-zero
	Voidage gas flow rate graph	Convex	Concave
Liquid flow	Scales excited	~Bubble size	~Column size
	Circulations	No	Yes
	Mean radial profile	Zero	Non-zero
Boundaries	Importance	High	Low

Jamialahmadi & Mueller-Steinhagen 1989; Krishna *et al*. 1991). In their comprehensive treatise on bubble column hydrodynamics, Ranade and Joshi (1987) developed a mathematical description of the gas hold-up structure in the homogeneous and heterogeneous bubbling regimes, and subsequently, proposed relations predicting transition values of gas hold-up for small ($\leqslant$2 mm) and large ($\geqslant$2 mm) diameter bubbles. Following their work, an attempt at theoretical analysis of the transition from the homogeneous to the heterogeneous bubbling regime in two-dimensional bubble columns was made by Shnip *et al*. (1992), who eventually developed quantitative transition criteria for both semibatch and continuous column operations. An empirical correlation for the transition from the homogeneous to the heterogeneous regime has been developed by Wilkinson *et al*. (1992), taking into account the effect of gas phase density and physical properties of the liquid phase (for pure coalescing liquids). Research on the bubbling regime duality has been given a new impulse with the work of Biesheuvel and Gorissen (1990), who derived one-dimensional conservation equations governing gas–liquid flow at small deviations from the uniform state and used them subsequently to describe the features of propagation of void fraction disturbances and to investigate the stability of the uniform (homogeneous) bubbly flow. Their analysis has been modified by Krishna *et al*. (1993) to examine the effect of gas density on the delay in the regime transition observed with the increase in gas density. In the wake of the attempts at general treatment of the transition phenomena, a new generation of experimental works appeared lately, aimed at characterising the homogeneous and the heterogeneous bubbling regimes and identifying regime transition, with the help of sophisticated experimental methods as well as evaluating procedures of non-linear dynamics (Thimmapuram *et al*. 1992; Bakshi *et al*. 1995; Letzel *et al*. 1996; Hyndman *et al*. 1997). In spite of the long-term activities of numerous researchers, the attempts at a general treatment of the bubbling regime duality do not seem to be adequately backed by the experimental evidence characterising the influence of design and operating parameters of bubble column reactors on the regime stability and transition and/or on the behaviour of gas–liquid beds in the respective bubbling regimes. In particular, inspection of the literature clearly indicates

the lack of quantitative information on the effect of column (and to a lesser extent even distributor) geometry on the bubbling regime characteristics and the transition conditions in non-coalescent media. Accordingly, the effect of apparatus and sparger geometry has not been adequately reflected in the criteria proposed in the literature for regime transition (Ranade & Joshi 1987; Wilkinson *et al*. 1992), or, as in the case of Shnip *et al*. (1992), implications of such an effect have not been appropriately verified. Similarly, correlation of the effect of liquid phase properties has been limited to pure coalescent liquids (Wilkinson *et al*. 1992), though it has been acknowledged that coalescence hindering in aqueous solutions of electrolytes or alcohols may result in a delay of the regime transition to higher superficial gas velocities and gas hold-up values. It has therefore been felt that, in parallel with the attempts at general theoretical treatment of bubbling regime duality in bubble column reactors, it might be useful to present comprehensive experimental evidence mapping the changes of bubble-bed characteristics with bubbling regime transition and demonstrating the multifaceted effects of design parameters and liquid phase properties on the formation and stability of respective bubbling regimes and on the conditions of their mutual transition.

Factors influencing formation and stability of bubbling regimes

Stability of the bubbling regime and respective values of bubble-bed voidage are strongly influenced by the type and geometry of a gas distributor, in the case of the most common perforated distributing plates (Zahradnik *et al.* 1997). Table 3.3 shows the effects of operating and design parameters on flow regime transition and the stability of bubbling regimes. At a constant value of the aspect ratio (height/diameter of bubble column), both the stability region of the homogeneous bubbling regime and the maximum value of the homogeneous gas hold-up are negatively influenced by increasing the column diameter. Conversely, for heterogeneous bubble beds, gas hold-up is independent of the column diameter for $D \geqslant 0.15\,\text{m}$ (Zahradnik *et al.* 1997). These may not be true in large-diameter units, which may require experimental validation to clarify the scale-up issue under the homogeneous and transition bubbling conditions.

3.2.3 Chaotic advection

Mixing in the laminar flow regime is accomplished very slowly by molecular diffusion, and mixing rate is greatly accelerated by turbulence. Turbulence is associated with large velocity gradients, especially, in the small scales (eddies) and high shear rates (Bagtzoglou *et al.* 2006). Hence, in food mixing, use of turbulence may not be desirable in certain cases. For example, the high shear rates could modify rheological and functional properties of proteins and may damage enzymes or beneficial microorganisms such as yeasts involved in fermentation. In other situations such as flows of very viscous fluids, including viscous suspensions and pastes, the flow remains laminar. A fundamental mixing process, namely, chaotic advection has been proposed in fluid dynamical systems theory based on the pioneering work of Aref (1984). Chaotic advection causes simple, non-turbulent flows to exhibit very complicated particle trajectories that result in enhanced mixing. Several studies demonstrate chaotic advection in low Reynolds number flows. Since the mid-1980s, a substantial number of investigators have demonstrated that chaotic advection can occur in a wide variety of laminar flows, from creeping flow to potential flow, and in a number of different flow systems, including unsteady two-dimensional flow and both steady and time-periodic three-dimensional flows (Stremler *et al*. 2004). Chaotic advection occurs

Table 3.3 Generalised effect of operating and design parameters on flow regime transition.

Parameter	Effect on flow regime transition	References
Pressure	In general, an increase in pressure results in an increase in transition velocity	Krishna *et al*. (1991), Wilkinson *et al*. (1992), Reilly *et al*. (1994), Lin *et al*. (1999), Shaikh and Al-Dahhan (2005)
Temperature	An increase in temperature increases the transition velocity and delays flow regime transition	Bukur *et al*. (1987), Lin *et al*. (1999)
Viscosity	An increase in viscosity, in general, advances flow regime transition	Wilkinson (1991), Ruzicka *et al*. (2001)
Surface tension	Reduction in surface tension increases transition velocity	Urseanu (2000)
Solids loading	An increase in solids loading, in general, decreases transition velocity	Krishna *et al*. (1999), Vandu (2005), Mena *et al*. (2005), Shaikh and Al-Dahhan (2006)
Sparger (hole size)	Transition velocity decreases with an increase in hole size up to certain hole size	Sarrafi *et al*. (1999), Jamialahmadi *et al*. (2000)
Sparger (perforation pitch)	Transition velocity increases with perforation pitch and then remains the same after certain critical value	Sarrafi *et al*. (1999), Jamialahmadi *et al*. (2000)
Liquid height	An increase in liquid height reduces the transition velocity	Sarrafi *et al*. (1999), Ruzicka *et al*. (2001)
Column diameter	Conflicting results. An increase in column diameter increases transition velocity (Group 1) while column diameter advances flow regime transition (Group 2)	Group 1: Ohki and Inoue (1970), Sarrafi *et al*. (1999), Jamialahmadi *et al*. (2000), Urseanu (2000) Group 2: Zahradnik *et al*. (1997), Ruzicka *et al*. (2001)
Aspect ratio	Aspect ratio decreases the transition velocity. However, it alone is not sufficient to provide reliable information on flow regime stability	Ruzicka *et al*. (2001), Thorat and Joshi (2004)

when highly complicated particle trajectories are observed in the Lagrangian frame of reference even for simple, well-behaved velocity fields. Aref (1984) made the fundamental observation that the stream function (ψ) in 2D incompressible flows plays the role of a Hamiltonian in classical mechanics. If ψ were to be time dependent, it is possible for the system to exhibit chaotic particle trajectories. The required time dependence of the stream function need not be due to the effects of high Reynolds number flows in which the velocities fluctuate stochastically, but may be caused by some simple, external modulation of the flow system. The role of diffusion and transient velocities has been studied numerically and experimentally in the dispersal of passive scalars produced in a low Reynolds number journal-bearing flow by Dutta and Chevray (1995). The ability of chaotic advection to enhance mixing in laminar flows on the macroscale and the fact that chaotic advection occurs in numerous geometries (Table 3.4) and under a variety of flow conditions make it an obvious tool for designing devices that mix well on the microscale.

Table 3.4 Application of chaotic advection.

Applications	References
Tendril–whorl flow	Khakhar *et al*. (1987)
Pulsed source-sink systems	Jones and Aref (1988)
Eccentric journal-bearing flow	Aref and Balachandar (1986), Chaiken *et al*. (1986, 1987)
Lid-driven cavity flow	Chien *et al*. (1986), Leong and Ottino (1989)
Twisted-pipe flow	Jones *et al*. (1989)
Pulsed source-sink flow	Jones and Aref (1988)
Taylor–Couette flows	Ashwin and King (1995), Mezid (2001)
Two-dimensional vortex flows	Rom-Kedar and Poje (1999), Krasny and Nitsche (2002), Boyland *et al*. (2003)
Three-dimensional vortex flows	MacKay (1994), Solomon and Mezid (2003)
Time-periodic vortex flows	Rothstein *et al*. (1999)
Two-dimensional cellular flow	Rothstein *et al*. (1999)
Open cavity flow	Horner *et al*. (2002)
Stirred tanks	Meleshko and Aref (1996), Boyland *et al*. (2000), Finn *et al*. (2003)
Heat transfer enhancement	Ghosh *et al*. (1992), Bryden and Brenner (1996), Ganesan *et al*. (1997), Mokrani *et al*. (1997)
Enhanced heat transfer for heat exchangers	Sen and Chang (1991)
Fuel cell cooling	Lasbet *et al*. (2007)
Novel polymer processing	Zumbrunnen and Inamdar (2001), Kwon and Zumbrunnen (2001)
Field of medicine (low R_E mixing enabled human plasma mixing without damaging the cells)	Omurtag *et al*. (1996)
To create long-chain polymers as low velocities prevent the viscous disunion of such molecules	Miles *et al*. (1994)

Chaotic advection can be used to control the rate and quality of mixing (D'Alessandro *et al.* 1999). The two controlling mechanisms of the convective mixing process, stretching and folding, occur simultaneously at different rates in each portion of the flow, creating complex patterns (Szalai *et al.* 2003). Figure 3.5 shows the characteristic of chaotic advection.

In two dimensions, chaotic advection (Rothstein *et al*. 1999) requires a time-dependent flow. In three dimensions, it can occur in steady flow. Chaotic advection enhances the quality of mixing because one of the hallmarks of chaos is the exponential separation of initially nearby points. If all pairs of points in some region of the flow separate exponentially, interfaces stretch dramatically and the end result for the bulk fluid is improved mixing. Over the past two decades, chaotic advection has become a mainstay of the literature on fluid stirring and mixing. The immediate applications to the mixing of viscous fluids in chemical engineering have been supplemented by more esoteric examples (Ottino 1989; Aref & El Naschie 1995) such as mixing in physiological flows, in microfluidic channels, in geophysical fluids such as molten rock, and even in tidal flows in shallow waters.

Even though the first theoretical example of chaotic advection was a 3D flow (Hénon 1966), the number of theoretical studies addressing chaos and mixing in such flows is

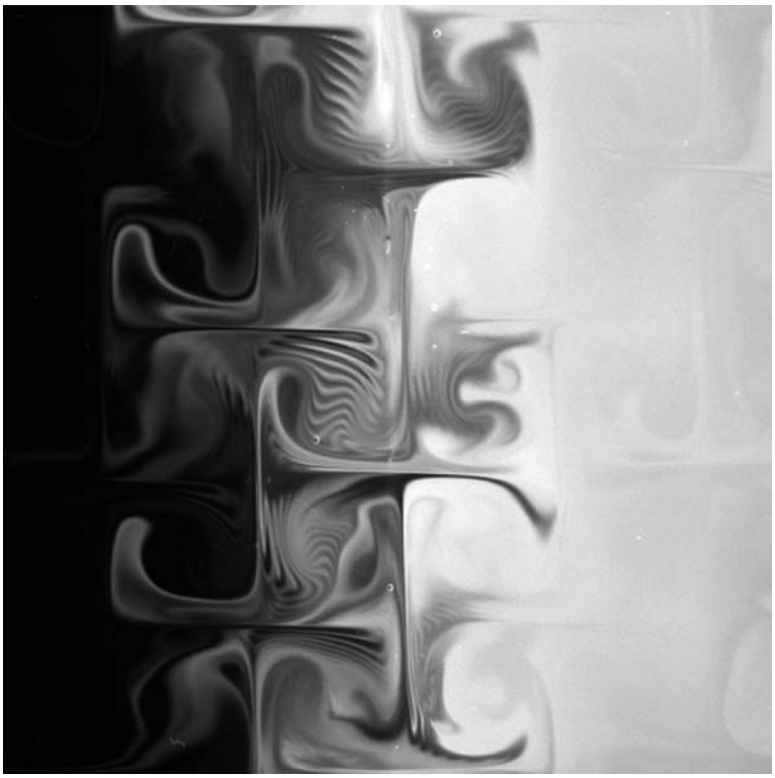

Fig. 3.5 Fluid labelled with fluorescein was initially confined to the right half of a cell. Forcing occurs by a time-periodic electric current in the presence of a spatially periodic magnet array. The repetitive stretching and folding that is characteristic of chaotic advection is evident. [Reprinted from Rothstein *et al.* (1999) with permission from Macmillan Publishers Ltd.]

small (MacKay 1994; Ashwin & King 1995; Haller & Mèzic 1998). Most chaotic mixing experiments have been restricted to two-dimensional, time-periodic flows, and this has shaped advances in theory as well. A prototypical, bounded, three-dimensional flow with a moderate Reynolds number was reported by Fountain *et al.* (1998), which reveals detailed chaotic structures with high-period islands. Islands are unmixed regions, which translate, stretch and contract periodically, and they represent the primary obstacle to efficient mixing. Particle trajectories in chaotic regions separate exponentially fast, and material filaments are continuously stretched and folded by means of horseshoes (Leong *et al.* 1988). Formally, the advection equations are a Hamiltonian system (Aref 1984), for which considerable theory already exists (Wiggins 1992).

3.2.4 Fluid mixing mechanisms

Mixing in the food industry implies not only a stirring process in stirred tank, where fluid particles are transported mechanically and distributed more uniformly, but also involves diffusion, which smoothes the concentration gradients created by advection (Raynal & Gence 1997). As discussed in Chapter 2, the scale and intensity of segregation are important when evaluating mixing. Molecular diffusion is needed to reduce segregation intensity.

It will occur in all flow regimes; however, turbulence decreases the scale of segregation by dramatically increasing the interfacial area available for molecular diffusion to occur. Turbulent mixing can be viewed as a three-stage process (Eckart 1948) of entrainment, dispersion (or stirring) and diffusion, spanning the full spectrum of space-time scales of the flow. In liquids, where mass diffusivities are much smaller than kinematic viscosities, it is useful to further split diffusive action into two steps, one in which viscosity acts (acquisition of small-scale vorticity) and the second where mass diffusion takes place (Batchelor 1959; Dimotakis 1986). In the simplest case, mixing is passive, as occurs between passive scalars. A passive scalar is a diffusive contaminant in a fluid flow and is present in such low concentration that it has no dynamical effect on the fluid dynamics itself. Passive scalar behaviour is important in turbulent mixing, combustion and pollution and provides impetus for the study of turbulence itself (Warhaft 2000). Examples of such mixing include: mixing of density-matched gases; the dispersion and mixing of non-reacting trace markers such as pollutants, small temperature differences, small-particle smoke/clouds, or ink; and other low-concentration dyes in a liquid. Such mixing does not couple back on the flow dynamics; although dispersion and mixing are driven by the turbulent flow, a correct accounting of mixing is not required to describe the flow dynamics (Dimotakis 2005). Whereas, mixing of different-density fluids in an acceleration/gravitational field, as in Rayleigh–Taylor (Rayleigh 1883; Taylor 1950) and Richtmyer–Meshkov (Richtmyer 1960; Meshkov 1969) instability flows, and mixing of the temperature and salinity fields in large-scale ocean currents and the thermohaline circulation (Adkins *et al*. 2002; Wunsch 2002; Wunsch & Ferrari 2004) are coupled to the flow dynamics. Progress in the study of turbulent mixing has mostly been confined to a process, which does not describe fluid dynamics, with results for high Reynolds number flows mostly limited to a few canonical cases (e.g., grid/isotropic turbulence, channel and pipe flows, and free shear layers and jets) and largely based on empirical data (Dimotakis 2005).

Laminar mixing is proposed for slow flows compared to turbulent mixing. The task is how to achieve efficient laminar mixing. A general question asked for mixing is 'how to mix' and possible common answer would be to make the flow turbulent. This choice of making flow turbulent may not be the best choice. For example, if suppose we have to mix a food hydrocolloid in a Newtonian fluid (water or a juice), to prepare a solution of $>1\%$ w/v will be very viscous, and then making the flow turbulent implies a large energy dissipation rate (Raynal & Gence 1997). On the other hand, the energy dissipation required in a Stokes flow is very small (advective inertial forces are significantly small compared with viscous forces; $R_E << 1$), but complete mixing takes longer time.

3.2.4.1 *Turbulent mixing*

Effective mixing occurs in turbulent flows, where the flow field itself is composed of a complex hierarchy of interacting eddies of various sizes. As a three-dimensional eddy moves with the bulk flow, it rotates, exchanging material with its surroundings, leading to changes in size and shape. It is this dynamic behaviour that leads to the effective mixing observed with turbulence. The presence of particulate matter, walls, baffles, impeller blades, etc., may result in the formation of highly distorted eddies, further enhancing its dynamic life cycle.

Turbulence results in the formation of eddies of various length scales. A significant proportion of the kinetic energy of the turbulent motion is contained within the large-scale structures. This energy is transferred from these large-scale structures to decreasingly

smaller scales, resulting in the hierarchy of eddies. These eddies will mix fluid on their own scale (Aref 1999). For example, if a large eddy encounters an immiscible drop much smaller than itself, it may simply incorporate the drop without any significant deformation of the drop. However, if the eddy is of similar scale to the drop, significant distortion occurs, where the drop is either torn apart by two counter-rotating eddies or elongated by two co-rotating eddies (Kresta & Brodkey 2004). If the drop encounters eddies smaller than itself, components of the drop may be torn from it. Eventually, this process creates structures that are sufficiently small to allow molecular diffusion to become significant, and the viscous dissipation of energy finally takes place. The scale at which this occurs is known as the Kolmogorov length scale (η). These smallest scales of turbulence are considered to be similar for all turbulent flows and simply depend on the rate of turbulent kinetic energy dissipation (ε) and kinematic viscosity (ν).

$$\eta = \left(\frac{\nu^3}{\varepsilon}\right)^{1/4} \tag{3.8}$$

The time taken to dissipate the energy contained within this small eddy is given as the Kolmogorov time scale (equation 3.9).

$$t_{\mathrm{K}} = \left(\frac{\nu}{\varepsilon}\right)^{1/2} \tag{3.9}$$

3.2.4.2 *Laminar mixing*

As shown in the previous section, turbulence is intrinsically time dependent, with continual reorientation of the fluid particle. However, mixing in the laminar flow regime, as observed with pipe flow, depends on molecular diffusion and is consequently relatively poor. The flow will be dominated by viscous forces, not non-linear inertia forces, resulting in time independence. Fluid particles will be confined within streamlines, resulting in limited mixing. For liquid mixing, considerable time will be required to ensure proper mixing owing to the slow rate of molecular diffusion. However, with design we can initiate periodic forcing of the fluid. For stirred tanks, the impeller speed may be constant; however, as it sweeps through the fluid, it disturbs the fluid periodically (Szalai *et al*. 2003). The resultant chaotic flow gives rise to effective mixing, where fluid elements are exponentially stretched.

The mechanism for laminar mixing for such viscous fluids includes reorientation and redistribution of the material. Mixing in laminar flows can be enhanced through chaotic advection, the phenomenon in which passive particles advected by a periodic velocity field exhibit chaotic trajectories (Aref 1984, 1990, 2002; Ottino 1989). Relative to integrable advection, chaotic advection enhances stretching and folding of material interfaces. Figure 3.6 shows the principle of chaotic mixing, where a fluid element is stretched and subsequently folded. The process is repeated ($n = 2, 3, 4, \ldots$) and an exponential increase in the interfacial area is observed, leading to increased diffusion and homogenisation.

Rothstein *et al.* (1999) demonstrated a major difference between chaotic, laminar and turbulent mixing. They reported that there is relative order in chaos. For example, a complex spatial pattern created by chaotic advection due to periodic stirring of the fluid has a simple time dependence. Chaotic advection produces a complex spatial structure with

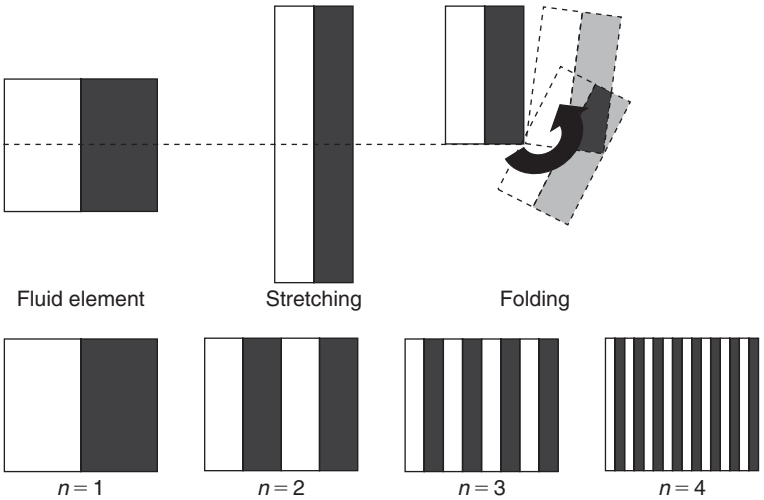

Fig. 3.6 Stretching and folding as observed in chaotic mixing showing an exponential increase in the contact area as the sequence is repeated.

simple time dependence, whereas in turbulent advection, there is complexity both in space and time. Chaotic advection of a fluid can cause an initially inhomogeneous impurity (a passive scalar field) to develop a complex spatial structure as the elements of the fluid are stretched and folded, even if the velocity field is periodic in time (Aref 1984; Ottino 1990; Fountain *et al.* 1998). In chaotic advection, an interesting event is the development of persistent spatial patterns, whose amplitude decays slowly with time but without change of form. Rothstein *et al.* (1999) observed the formation of structurally invariant but slowly decaying mixing patterns. Advective stretching of the fluid elements and molecular diffusion work together to produce effective mixing. Chaotic mixing occurs by time-periodic cellular flows, leading to a persistent spatial structure, a complex pattern that recurs periodically while its amplitude decays slowly with time owing to a delicate balance of two distinct processes, stretching and diffusion (Rothstein *et al.* 1999).

3.2.4.3 *Mixing transition*

Flow regime transition is the dynamical events occurring sequentially during the process of transition from a laminar state of stratified parallel flow to a state of intense three-dimensional turbulence. There are essentially three distinct phases in the evolution of such flows: (a) initial parallel shear instability and subsequent Kelvin–Helmholtz (KH) stage of flow evolution, (b) the stage of onset and growth of the three-dimensional secondary instability through which shear aligned convective rolls are nucleated in the region surrounding the KH billow cores and, finally, (c) the stage of turbulent-mixing layer collapse characterised by intense viscous dissipation and triggered fundamentally by the breakdown of the shear aligned convective rolls that grow on, and then destroy, the primary KH billow (Peltier & Caulfield 2003). A KH instability may occur when a velocity shear is present within a continuous fluid or when there is sufficient velocity difference across the interface between two fluids. The onset of the KH instability is given by a suitably defined Richardson number, *Ri* (equation 3.10). These three stages of the mixing transition are illustrated qualitatively in Plate 3.1. Isosurfaces of cross-stream and streamwise vorticity from a direct numerical simulation (DNS) are

shown, in which the streamwise length of the domain is restricted to a single wavelength of the fastest growing mode of the linear instability through which the transition process is initially engendered:

$$Ri = \frac{N^2}{(\mathrm{d}V/\mathrm{d}z)^2} \tag{3.10}$$

where N^2 is the square of the Brunt–Vaisala frequency and $V(z)$ is the initial height variation of background horizontal velocity.

Carpenter *et al.* (2007) performed a series of DNSs. DNS has the advantage of directly resolving the smallest scales of variability present in the flow such that the turbulence and mixing characteristics do not require parameterisation. In this way, the mixing behaviour is modelled without relying on a turbulence closure scheme. The simulation results of Carpenter *et al.* (2007) show that there are two different mixing mechanisms present. The first is a feature of KH instabilities and is characterised by a significant overturning of the density interface. This leads to the mixing and production of intermediate density fluid causing a final density profile that is layered. The second mixing mechanism is found in Holmboe instabilities and consists of regions of mixing and turbulence production that are located on one or both sides of the density interface. It is comprised of a cusp-like wave that periodically ejects partially mixed fluid from the top or bottom of the interface. As the instability does not generate overturning, the density interface is able to 'retain its identity' throughout the mixing event. The amount of mixing that takes place is found to be strongly dependent on the degree of asymmetry in the flow. As the asymmetry is increased, the amount of mixing also increases; however, this is not necessarily an accurate representation of natural conditions as the pairing mechanism is expected to play a role in the dynamics of the flow. The development of three-dimensional secondary structure showed by Carpenter *et al.* (2007) agrees with previous studies by Caulfield and Peltier (2000), Peltier and Caulfield (2003) and Schowalter *et al.* (1994) and consists of the formation of streamwise vortices, particularly in the gravitationally unstable regions. The presence of the density interface and the periodic ejection of interfacial fluid were also found to influence the development of these vortices. The formation and breakdown of streamwise vortices appears to be an important step in the transition to turbulence.

3.2.4.4 *Improving mixing efficiency*

The fluid dynamicist faces an open challenge to enhance the mixing rate or entrain fluids at low Reynolds number (laminar flow regime). It has been shown that crossing two laminar flows of fluid at a small angle can aid mixing by invoking a transition to turbulent flow and can hence improve the mixing performance (Milojevic & Schneider 1993). Woodfield *et al.* (2003) reported improved mixing by the introduction of a multi-holed baffle plate, which dramatically improves laminar mixing. The mechanism by which mixing is enhanced is that of structure generation. The liquid flows issuing from the holes create recirculation zones (vortical structures), which promote interaction between the liquids. The mixing performance is strongly dependent on the formation of vortical structures generated by the baffle plate which are dependent on geometrical parameters such as the vessel diameter and position of the baffle (Moghtaderi *et al.* 2006). Further, smaller baffle spacing results in better mixing due to stronger vortex motion and shear mixing (Wang *et al.* 2005).

The addition of baffles is beneficial to enhance mixing effectiveness. As mixing occurs at the interface of the two fluids through molecular diffusion, in order to improve mixing, one must increase the interfacial area between the two fluids. Recently, approaches have been identified to improve mixing in the laminar flow regime.

3.3 Solids mixing

Mixing of solids or granular materials is no doubt important. However, it is less developed compared to fluids (Ottino 1990) and certainly is not yet at a point where a first-principles modelling approach is either realistic or possible (Ottino & Khakhar 2000).

Lacey (1954) first attempted to describe solid mixing based on analogies with fluid mixing by developing physical concepts. He classified the solid mixing mechanism as: (a) convective mixing, (b) dispersive mixing and (c) shear mixing, all in the context of granular flows. The understanding of mixing of granular matter is more complex than that of regular fluids, and modelling of the mixing of granular materials requires a confluence of several tools, including continuum and discrete descriptions such as particle dynamics, Monte Carlo (MC) simulations, and cellular automata calculations combined with considerable geometrical insight. Moreover, continuum and discrete descriptions of granular flows are regime dependent, which may require adopting different sub-viewpoints. The grain inertia regime is dominated by binary collisions. The quasi-static regime is characterised by lasting particle contacts (Jackson 1986). MC simulations and cellular automata algorithms are often too idealised to mimic realistic situations. Shortcomings of continuum descriptions manifest on macroscopic scales; particle segregation is an instance in which physical mesoscale processes are imperfectly understood. Although particle dynamics simulations, akin to molecular dynamics (Cundall & Strack 1979), are exact in principle, they require precise physical properties and interaction models, and the results may provide little insight because they are as specific as those originated by a single well-controlled experiment (Cleary *et al.* 1998).

3.3.1 Mixing flow in solids

Consider a rotating cylinder as a mixing system. In this case, a flow is well defined and can be classified into different regimes (Henein *et al.* 1983; Rajchenbach 1990). Henein *et al.* (1983) confirmed experimentally the existence of different regimes for bed movement.

- Avalanching or slumping.
- Continuous-flow, rolling or cascading regime.
- Cataracting and centrifuging.

Henein *et al.* (1983) studied the boundaries between some of these regimes. At low rotational speeds (quantified in terms of the Froude number, $Fr = \omega L2/g$, where g is the acceleration due to gravity, L is the length scale of the system and ω is the rotational speed), the flow comprises discrete avalanches; one stops before the next one begins (the avalanching or slumping regime). At higher speeds, a steady flow is obtained with a thin cascading layer at the free surface of the rotating bed (continuous-flow, rolling or cascading regime); if inertial effects are small, the free surface is nearly flat. At still higher speeds, particle inertia effects become important, and particles may become airborne (cataracting regime). $Fr = 1$ corresponds to the critical speed for centrifuging (Figure 3.7). In the slumping regime, the motion of the solids is similar but it is not continuous; sliding movement is achieved by slumps

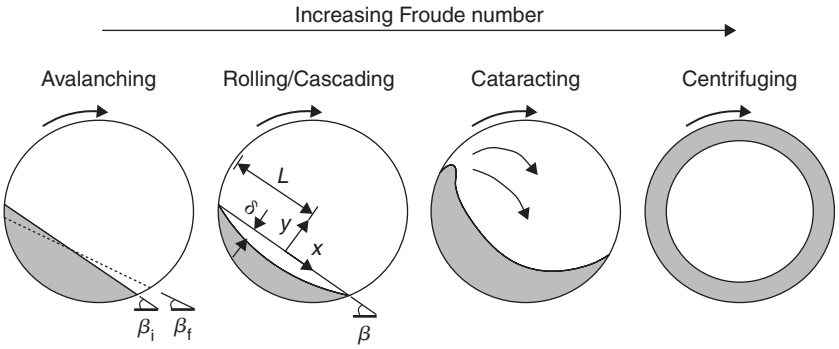

Fig. 3.7 Schematic view of flow regimes in a rotating cylinder with increasing rotational speed (ω). In the avalanching regime, the dashed line shows the position of the interface after an avalanche, and β_i and β_f are the free surface angles just before and after an avalanche. The angle β in the rolling/cascading or continuous-flow regime is the dynamic or equilibrium angle of repose. (With kind permission of Springer Science and Business Media.)

that may be local and sporadic (Gonzalez & Romero 2005). The flow of particles during an avalanche is complex and determines the extent of mixing (Ottino & Khakhar 2000).

3.3.2 Solids mixing mechanism

The rate of the mixing process and the achievable homogeneity are significantly influenced by the mixing mechanism (Gyenis 1999). Therefore, insight into the mechanism of mixing gives a possibility to improve and control the operation. To achieve an effective mixer, one should have fair knowledge of the fundamentals of mixing and the mechanism involved. The mechanism involved can be considered as a qualitative feature, which characterises the intermingling of components. Visual observation is the simplest tool to achieve information on the mechanism (Gyenis 1999). But in the case of different mixing mechanisms acting simultaneously, it is important to assess their relative contribution to the global result of operation or to determine the dominant ones. Lacey (1954) pointed out the following three mixing mechanisms of dry granular materials.

Convective mixing: This involves the transfer of larger particle groups from one location to another. Convection generally causes certain shear between the adjacent regions moving at different velocities, and vice versa; shear cannot exist without relative displacements, that is, convection.

Diffusive mixing: This involves the distribution of particles over a freshly developed surface. Diffusive particle mixing is analogous to molecular diffusion, taking place in fluids, with respect to the random walk of particles. This analogy is not faultless because, in addition to great differences between their size and physical properties, the crucial difference is that molecular diffusion takes place spontaneously, while particles should be energised to move. In some particle systems, random movements of particle groups may also occur, together with their dispersion and combination, analogously to turbulent dispersion or eddy diffusion in fluids.

Shear mixing: This involves the development of slipping planes within the grain packing.

3.4 Identification of mixing mechanisms

3.4.1 Solids

There are two principal possibilities to identify the mechanism of mixing: (a) direct methods, by observing the movement of the particle bed or individual constituents during operation and/or (b) indirect methods, by analysing the spatial distribution of components after given mixing times. In principle, spatial distribution is the consequence of the relative movements of constituents; therefore, the results obtained by these methods can be mutually reconstructed from each other and must be equivalent. Selection between them depends on the available measurement techniques and the nature of the studied system. From another respect, investigations very often have to be carried out at different levels to elucidate microscopic and macroscopic mechanisms.

From several experimental studies, it has been demonstrated that the mixing process occurred through a diffusion mechanism in different transport devices (Scott & Bridgewater 1976; Hwang & Hogg 1980; Buggish & Löffelmann 1989; Zik & Stavans 1991; Hsiau & Hunt 1993a,b; Hunt *et al*. 1994; Natarajan *et al*. 1995; Hsiau & Shieh 1999; Hsiau *et al*. 2005). Computer simulation has been employed to study the mixing behaviours in different granular-flow systems. Cleary *et al*. (1998) delivered a simulation study of granular mixing to demonstrate that the amount and nature of the mixing were quite sensitive to a range of physical properties. Henrique *et al*. (2000) used computer simulation to examine the influence of granular temperature gradient on the mixing condition.

3.4.2 Fluids

Many computational studies have been done, for laminar flow and mixing of Newtonian fluids in static mixers, using finite element and finite volume models. Static mixers produce a multitude of striation layers in laminar flow. A very fine mesh for a computational simulation is necessary to get a good representation of the concentration field, but this requires substantial computer resources. Particle tracking is often used to visualise mixing performance because numerical diffusion in a pseudo-concentration method to track changes in mixing quality displays much faster mixing than the real physical diffusion in laminar flow (Bakker & Laroche 1993; Fleischli *et al*. 1997). Fleischli *et al*. (1997) simulated the velocity fields and concentration fields in both Kenics and SMX static mixers. They found that the results from particle tracking show much better agreement with concentration measurements than those obtained from solving mass transfer equation in the same grid. Rauline *et al*. (1998, 2000) simulated the velocity fields for creeping flow conditions in Kenics, Inliner, LPD, Cleveland, SMX and ISG static mixers. Pressure drop, extensional efficiency, stretching, mean shear rate and the coefficient of variation in the particle distribution were used to compare the performance of the static mixers. The SMX mixer is the most efficient among the six mixers studied. Fourcade *et al*. (2001) simulated mixing in a Kenics static mixer and an SMX static mixer. They defined an average rate of striation thinning to describe the mixing performance in static mixers. They used laser-induced fluorescence (LIF) (Chapter 7) experiments to qualitatively verify the computational striation patterns. Recently, Zalc *et al*. (2002) simulated the flow and mixing in an SMX static mixer at several values of Reynolds number. Their simulations showed that lower Reynolds number flow condition shows better mixing efficiency and centreline injection is better than off-centre injection. They found that the pressure drop ratio at $R_E \leqslant 10$ is constant and it increases quickly with increasing Re when $R_E > 10$.

References

Adkins, J.F., McIntyre, K. & Schrag, D.P. (2002). The salinity, temperature, and δ18O of the glacial deep ocean. *Science*, **298**, 1769–1773.

Al-Taweel, A.M. & Walker, L.D. (1983). Liquid dispersion in static in-line mixers. *Canadian Journal of Chemical Engineering*, **61**, 527–533.

Alvarez-Hernández, M.M., Shinbrot, T., Zalc, J. & Muzzio, F.J. (2002). Practical chaotic mixing. *Chemical Engineering Science*, **57**, 3749–3753.

Aref, H. (1984). Stirring by chaotic advection. *Journal of Fluid Mechanics*, **143**, 1–21.

Aref, H. (1990). Chaotic advection of fluid particles. *Proceedings of the Royal Society of London. Series A*, **434**, 273–289.

Aref, H. (1999). Order in chaos. *Nature*, **401**, 756–758.

Aref, H. (2002). The development of chaotic advection. *The Physics of Fluids*, **14**, 1315–1325.

Aref, H. & Balachandar, S. (1986). Chaotic advection in a Stokes flow. *The Physics of Fluids*, **29**, 3515–3521.

Aref, H. & El Naschie, M.S. (1995). *Chaos Applied to Fluid Mixing.* Pergamon, Oxford.

Ashwin, P. & King, G.P. (1995). Streamline topology in eccentric Taylor vortex flow. *Journal of Fluid Mechanics*, **285**, 215–247.

Avalosse, T.C. & Crochet, M.J. (1997). Finite-element simulation of mixing: 1. Two-dimensional flow in periodic geometry. *AIChE Journal*, **43**, 577–587.

Aoyama, K., Ogushi, K., Koide & Kubota, H. (1968). Liquid mixing in concurrent bubble columns. *Journal of Chemical Engineering of Japan*, **1**, 158–163.

Azer, N.Z. & Lin, S.T. (1980). Augmentation of forced flow boiling heat transfer with Kenics motionless mixers. *Industrial and Engineering Chemistry Process Design and Development*, **19**, 246–250.

Bagtzoglou, A.C., Assaf-Anid, N. & Chevray R. (2006). Effect of chaotic mixing on enhanced biological growth and implications for wastewater treatment: a test case with *Saccharomyces cerevisiae*. *Journal of Hazardous Materials*, **136**, 130–136.

Bajer K. & Moffatt, H.K. (1990). On a class of steady confined Stokes flows with chaotic streamlines. *Journal of Fluid Mechanics*, **212**, 337–363.

Bakker, A. & Laroche, R. (1993). Flow and mixing with Kenics static mixers. *Cray Channels*, **15**(3), 25–28.

Bakshi, B.R., Jiang, P. & Fan, L.S. (1995). Analysis of flow in gas–liquid bubble columns using multiresolution methods. *Chemical Engineering Research Design*, **73**, 608–614.

Baldyga, J. & Bourne, J.R. (1999). *Turbulent Mixing and Chemical Reaction*. Wiley, Chichester.

Batchelor, G.K. (1949). Diffusion in a field of homogeneous turbulence. I. Eulerian analysis. *Australian Journal of Scientific Research*, **2**, 437–450.

Batchelor, G.K. (1952). Diffusion in a field of homogeneous turbulence. II. The relative motion of particles. *Proceedings of the Cambridge Philosophical Society*, **48**, 345–361.

Batchelor, G.K. (1959). Small-scale variation of convected quantities like temperature in a turbulent field. Part 1. General discussion and the case of small conductivity. *Journal of Fluid Mechanics*, **5**, 113.

Beigie, D., Leonard, A. & Wiggins, S. (1994). Invariant manifold templates for chaotic advection. *Chaos, Solitons and Fractals*, **4**, 749–868.

Berkman, P.D. & Calabrese, R.V. (1988). Dispersion of viscous liquids by turbulent flow in a static mixer. *AIChE Journal*, **34**, 602–609.

Biesheuvel, A. & Gorissen, W.C.M. (1990). Void fraction disturbances in a uniform bubbly fluid. *International Journal of Multiphase Flow*, **16**, 211–231.

Boyland, P.L., Aref, H. & Stremler, M.A. (2000). Topological fluid mechanics of stirring. *Journal of Fluid Mechanics*, **403**, 277–304.

Boyland, P.L., Stremler, M.A. & Aref, H. (2003). Topological fluid mechanics of point vortex motions. *Physica D*, **175**, 69–95.

Bryden, M.D. & Brenner, H. (1996). Effect of laminar chaos on reaction and dispersion in eccentric annular flow. *Journal of Fluid Mechanics*, **325**, 219–237.

Buggish, H. & Löffelmann, G. (1989). Theoretical and experimental investigation into local granulate mixing mechanism. *Chemical Engineering Process*, **26**, 193–200.

Bukur, D.B., Petrovic, D. & Daly, J.G. (1987). Flow regime transitions in a bubble column with a paraffin wax as the liquid medium. *Industrial & Engineering Chemistry Research*, **26**, 1087–1092.

Carpenter, J.R., Lawrence, G.A. & Smyth, W.D. (2007). Evolution and mixing of asymmetric Holmboe instabilities. *Journal of Fluid Mechanics*, **582**, 103–132.

Caulfield, C.P. & Peltier, W.R. (2000). The anatomy of the mixing transition in homogeneous and stratified free shear layers. *Journal of Fluid Mechanics*, **413**, 1–47.

Cerbelli, S., Adrover, A., Creta, F. & Giona, M. (2006). Foundations of laminar chaotic mixing and spectral theory of linear operators. *Chemical Engineering Science*, **61**, 2754–2761.

Chaiken, J., Chevray, R., Tabor, M. & Chan, Q.M. (1986). Experimental study of Lagrangian turbulence in a Stokes flow. *Proceedings of the Royal Society of London. Series A*, **408**, 165–174.

Chaiken, J., Chu, C.K., Tabor, M. & Tan, Q.M. (1987). Lagrangian turbulence and spatial complexity in Stokes flow. *The Physics of Fluids*, **30**, 687–694.

Chen, R.C., Reese, J. & Fan, L.S. (1994). Flow structure in a three-dimensional bubble column and three-phase fluidized bed. *AIChE Journal*, **40**, 1093–1104.

Chen, S.J. (1975). Static mixing of polymers. *Chemical Engineering Progress*, **71**, 80–83.

Chien, W.I., Rising, H. & Ottino, J.M. (1986). Laminar mixing and chaotic mixing in several cavity flows. *Journal of Fluid Mechanics*, **170**, 355.

Cleary, P.W., Metcalfe, G. & Liffman, K. (1998). How well do discrete element granular flow models capture the essentials of mixing processes? *Applied Mathematical Modelling*, **22**, 995–1008.

Cundall, P.A. & Strack, D.L. (1979). A discrete numerical model for granular assemblies. *Geotechnique*, **29**, 47–65.

D'Alessandro, D., Dahleh, M. & Mezic, I. (1999). Control of mixing in fluid flow: a maximum entropy approach. *IEEE Transactions on Automatic Control*, **44**, 1852–1863.

Danckwerts, P.V. (1952). The definition and measurements of some characteristics of mixtures. *Applied Science Research A*, **3**, 279–296.

Danckwerts, P.V. (1958). The effect of incomplete mixing on homogeneous reactions. *Chemical Engineering Science*, **8**, 93–99.

de la Villéon, J., Bertrand, F., Tanguy, P.A., Labrie, R., Bousquet, J. & Lebouvier, D. (1998). Numerical investigation of mixing efficiency of helical ribbons. *AIChE Journal*, **44**, 972–977.

Deckwer, W.D. (1992). *Bubble Column Reactors.* John Wiley & Sons, New York.

Devanathan, N., Dudukovic, M.P., Lapin, A. & Lubbert, A. (1995). Chaotic flow in bubble column reactors. *Chemical Engineering Science*, **50**, 2661–2667.

Díaz, M.E., Montes, F.J. & Galán, M.A. (2008). Experimental study of the transition between unsteady flow regimes in a partially aerated two-dimensional bubble column. *Chemical Engineering and Processing: Process Intensification*, **47**(9–10), 1867–1876.

Dimotakis, P.E. (1986). Two-dimensional shearlayer entrainment. *The American Institute of Aeronautics and Astronautics Journal*, **24**, 1791–1796.

Dimotakis, P.E. (2005). Turbulent mixing. *Annual Review of Fluid Mechanics*, **37**, 329–356.

Dutta, P. & Chevray, R. (1995). Inertial effects in chaotic mixing with diffusion. *Journal of Fluid Mechanics*, **285**, 1–16.

Eckart, C. (1948). An analysis of the stirring and mixing processes in incompressible fluids. *Journal of Marine Research*, **7**, 265–275.

Fattal, R. & Kupferman, R. (2004). Constitutive laws for the matrix-logarithm of the conformation tensor. *Journal of Non-Newtonian Fluid Mechanics*, **123**, 281–285.

Feingold, M., Kadanoff, L.P. & Piro, O.J. (1988). Passive scalars, three-dimensional volume-preserving maps, and chaos. *Journal of Statistical Physics*, **50**, 529–565.

Finn, M.D., Cox, S.M. & Byrne, H.M. (2003). Topological chaos in inviscid and viscous mixers. *Journal of Fluid Mechanics*, **493**, 345–361.

Fleischli, M., Wehrli, M., Streiff, F.A. & Lang, E. (1997). Effect of diffusion and heat conduction on homogeneity in laminar static mixing. *Recents Progres en Genie des Procedes*, **11**(51, Mixing 97: Recent Advances in Mixing), 283–290.

Fountain, G.O., Khakhar, D.V. & Ottino, J.M. (1998). Visualization of three-dimensional chaos. *Science*, **281**, 683–686.

Fourcade, E., Wadley, R., Hoefsloot, H.C.J., Green, A. & Iedema, P.D. (2001). CFD calculation of laminar striation thinning in static mixer reactors. *Chemical Engineering Sciences*, **56**, 6729–6741.

Franz, K., Borner, T., Kantorek, H.J. & Buchholz, R. (1984). Flow structures in bubbly columns. *German Chemical Engineering*, **7**, 365–374.

Ganesan, V., Bryden, M.D. & Brenner, H. (1997). Chaotic heat transfer enhancement in rotating eccentric annular-flow systems. *The Physics of Fluids*, **9**, 1296–1306.

Ghosh, S., Chang, H.C. & Sen, M. (1992). Heat transfer enhancement due to slender recirculation and chaotic transport between counter rotating eccentric cylinders. *Journal of Fluid Mechanics*, **238**, 119–154.

Gonzalez, L.M. & Romero, J.J.B. (2005). Solids movement in rotary kilns in the slumping regime: model using a control plane parallel to the steepest descent. *Particle & Particle Systems Characterization*, **22**(2), 119–132.

Gyenis, J. (1999). Assessment of mixing mechanism on the basis of concentration pattern. *Chemical Engineering Process*, **38**, 665–674.

Haller, G. & Mézic, I. (1998). Reduction of three-dimensional, volume preserving flows with symmetry. *Nonlinearity*, **11**, 319–339.

Harvey, A.D. & Rogers, S.E. (1996). Steady and unsteady computation of impeller-stirred reactors. *AIChE Journal*, **42**, 2701–2712.

Harvey, A.D., Wood, S.P. & Leng, D.E. (1997). Experimental and computational study of multiple impeller flows. *Chemical Engineering Science*, **52**, 1479–1491.

Henein, H., Brimacomble, J.K. & Watkinson, A.P. (1983). Experimental study of transverse bed motion in rotary kilns. *Metallurgical and Materials Transactions B*, **14**, 191–205.

Hénon, M. (1966). Sur la topologie des lignes de courant dans un cas particulier. *Comptes rendus de l'Académie des sciences, Paris A*, **262**, 312–314.

Henrique, C. Batrouni, G. & Bideau, D. (2000). Diffusion as a mixing mechanism in granular materials, *Physical Review E*, **6301**, 1304–1311.

Hills, J.H. (1974). Radial non-uniformity of velocity and voidage in a bubble column. *Transactions of the Institution of Chemical Engineering*, **52**, 1–9.

Hobbs, D.M., Alvarez, M.M. & Muzzio, F.J. (1997). Mixing in globally chaotic flows: a self-similar process. *Fractals*, **5**, 395–425.

Holm, D.D. & Kimura, Y. (1991). Zero-helicity Lagrangian kinematics of three-dimensional advection. *Physics of Fluids A*, **3**, 1033–1038.

Horner, M., Metcalfe, G., Wiggins, S. & Ottino, J.M. (2002). Transport enhancement mechanisms in open cavities. *Journal of Fluid Mechanics*, **452**, 199–229.

Hsiau, S.S. & Hunt, M.L. (1993a). Kinetic theory analysis of flow-induced particle diffusion and thermal conduction in granular material flows. *Journal of Heat Transfer*, **155**, 541–548.

Hsiau, S.S. & Hunt, M.L. (1993b). Shear-induced particle diffusion and longitudinal velocity fluctuations in a granular-flow mixing layer. *Journal of Fluid Mechanics*, **251**, 299–313.

Hsiau, S.S. & Shieh, Y.H. (1999). Fluctuations and self-diffusion of sheared granular material flows. *Journal of Rheology*, **43**, 1049–1066.

Hsiau, S.S., Lu, L.S., Chen, J.C. & Yang, W.L. (2005). Particle mixing in a sheared granular flow. *International Journal of Multiphase Flow*, **31**, 793–808.

Hulsen, M.A., Fattal, R. & Kupferman, R. (2005). Flow of viscoelastic fluids past a cylinder at high Weissenberg number: stabilized simulations using matrix logarithms. *Journal of Non-Newtonian Fluid Mechanics*, **127**, 27–39.

Hunt, M.L., Hsiau, S.S. & Hong, K.T. (1994). Particle mixing and volumetric expansion in a vibrated granular bed. *Journal of Fluids Engineering*, **116**, 785–791.

Hwang, C.L. & Hogg, R. (1980). Diffusive mixing in flowing powders. *Powder Technology*, **26**, 93–101.

Hyndman, C.L., Larachi, F. & Guy, C. (1997). Understanding gas phase hydrodynamics in bubble columns: a convective model based on kinetic theory. *Chemical Engineering Science*, **52**, 63–77.

Jackson, R. (1986). Some features of the flow of granular materials and aerated granular materials. *Journal of Rheology*, **30**, 907–930.

Jaffer, S.A. & Wood, P.E. (1998). Quantification of laminar mixing in the Kenics static mixer: an experimental study. *Canadian Journal of Chemical Engineering*, **76**, 516–521.

Jamialahmadi, M. and Mueller-Steinhagen, H. 1989. Bubble formation and coalescence in bubble columns. *Chemie lngenieur Technik*, **61**, 715–718.

Jamialahmadi, M., Muller-Steinhagen, H., Sarrafi, A. & Smith, J.M. (2000). Studies of gas holdup in bubble column reactors. *Chemical Engineering & Technology*, **23**, 919–921.

Janssen, P.W.M., Lentle, R.G., Asvarujanon, P., Chambers, P., Stafford, K.J. & Hemar, Y. (2007). Characterization of flow and mixing regimes within the ileum of the brushtail possum using residence time distribution analysis with simultaneous spatio-temporal mapping. *The Journal of Physiology*, **582**(3), 1239–1248.

Jones, S.W. & Aref, H. (1988). Chaotic advection in pulsed source–sink systems. *The Physics of Fluids*, **31**, 469–485.

Jones, S.W. & Young, W.R. (1994). Shear dispersion and anomalous diffusion by chaotic advection. *Journal of Fluid Mechanics*, **280**, 149–172.

Joshi, J.B. & Lali, A.M. 1984. Velocity-holdup relationship in multiphase contactors—a unified approach. In: *Frontiers in Chemical Reaction Engineering* (eds L.K. Doraiswamy & R.A. Mashelkar), Vol. 1. Wiley Eastern, New Delhi, pp. 314–329.

Khakhar, D.V., Franjione, J.G. & Ottino, J.M. (1987). A case study of chaotic mixing in deterministic flows: the partitioned pipe mixer. *Chemical Engineering Science*, **42**, 2209.

King, G. (1998). Mixing with Chaos. *UK Nonlinear News*, **12**, available online: http://www.amsta.leeds.ac.uk/Applied/news.dir/

Krasny, R. & Nitsche, M. (2002). The onset of chaos in vortex sheet flow. *Journal of Fluid Mechanics*, **454**, 47–69.

Kresta, S.M. & Brodkey, R.S. (2004). Turbulence in mixing applications. In: *Handbook of Industrial Mixing: Science and Practice*. (eds E.L. Paul, V.A. Atiemo-Obeng & S.M. Kresta). John Wiley & Sons, Hoboken, NJ.

Krishna, R., Wilkinson, P.M. & Van Dierendonck, L.L. (1991). A model for gas holdup in bubble columns incorporating the influence of gas density on flow regime transitions. *Chemical Engineering Science*, **46**, 2491–2496.

Krishna, R., Ellenberger, J. & Hennephof, D.E. (1993). Analogous description of the hydrodynamics of gas-solid fluidized beds and bubble columns. *Chemical Engineering Journal*, **53**, 89–101.

Krishna, R., Ellenberger, J. & Maretto, C. (1999). Flow regime transition in bubble columns. *International Communications in Heat and Mass Transfer*, **26**(4), 467–475.

Kumar, S.B., Moslemian, D. & Dudukovic, M. (1997). Gas-holdup measurements in bubble columns using computed tomography. *AIChE Journal*, **43**, 1414–1425.

Kwon, O. & Zumbrunnen, D.A. (2001). Progressive morphology development to produce multilayer films and interpenetrating blends by chaotic mixing. *Journal of Applied Polymer Science*, **82**, 1569–1579.

Lacey, P.M. (1954). Developments in the theory of particle mixing. *Journal of Applied Chemistry*, **4**, 257–268.

Lamberto, D.J., Muzzio, F.J., Swanson, P.D. & Tonkovic, A.L. (1996). Using time-dependent RPM to enhance mixing in stirred vessels. *Chemical Engineering Science*, **51**, 733.

Lamberto, D.J., Alvarez, M.M. & Muzzio, F.J. (2001). Computational analysis of regular and chaotic mixing in a stirred tank reactor. *Chemical Engineering Science*, **56**, 4887–4899.

Lapin, A. & Lubbert, A. (1994). Numerical simulation of the dynamics of two-phase gas–liquid flows in bubble columns. *Chemical Engineering Science*, **49**, 3661–3674.

Lasbet, Y., Auvity, B., Castelain, C. & Peerhossaini, H. (2007). Thermal and hydrodynamic performances of chaotic mini-channel: application to the fuel cell cooling. *Heat Transfer Engineering*, **28**(8–9), 795–803.

Leong, C.W. & Ottino, J.M. (1989). Experiments on mixing due to chaotic advection in a cavity. *Journal of Fluid Mechanics*, **209**, 463–499.

Leong, C.W., Rising, H. & Swanson, P.D. (1988). Morphological structures produced by mixing in chaotic flows. *Nature*, **333**, 419.

Letzel, H.M., Schouten, J.C., Krishna, R. & van den Bleek, C.M. (1996). Characterization of regimes and regime transition in bubble columns by chaos analysis of pressure signals. *Presented at 12th International Congress of Chemical and Process Engineering CHISA'96*, Prague, 25–30 August, Paper J4.2.

Lin, T.J., Reese, J., Hong, T. & Fan, L.S. (1996). Quantitative analysis and computation of two-dimensional bubble columns. *AIChE Journal*, **42**, 301–318.

Lin, T.J., Tsuchiya, K. & Fan, L.-S. (1999). On the measurements of regime transition in high-pressure bubble columns. *Canadian Journal of Chemical Engineering*, **77**, 370–374.

MacKay, R.S. (1994). Transport in 3D volume-preserving flows. *Journal of Nonlinear Science*, **4**, 329–354.

Meleshko, V.V. & Aref, H. (1996). A blinking rotlet model for chaotic advection. *The Physics of Fluids*, **8**, 3215–3217.

Mena, P.C., Ruzicka, M.C., Rocha, F.A., Teixeira, J.A. & Drahos, J. (2005). Effect of solids on homogeneous–heterogeneous flow regime transition in bubble columns. *Chemical Engineering Science*, **60**, 6013–6026.

Meshkov, E.E. (1969). Instability of the interface of two gases accelerated by a shock wave. *Fluid Dynamics*, **4**, 101–104.

Mezid, I. (2001). Chaotic advection in bounded Navier–Stokes flows. *Journal of Fluid Mechanics*, **431**, 347–370.

Miles, K.C., Nagarajan, K.C. & Zumbrunnen, D.A. (1994). 3D chaotic mixing of fluids in a cylindrical cavity. In: *Chaos in Heat Transfer and Fluid Mechanics* (ed. V.S. Arpaci). ASME, Chicago, Illinois. pp. 298

Milojevic, D.K. & Schneider, W. (1993). Free and confined jets at low Reynolds numbers. *Fluid Dynamics Research*, **12**, 307–322.

Moghtaderi, B., Shames, I. & Djenidi, L. (2006). Microfluidic characteristics of multi-holed baffle plate micro-reactor. *International Journal of Heat and Fluid Flow*, **27**, 1069–1077.

Mokrani, A., Castelain, C. & Peerhossaini, H. (1997). The effect of chaotic advection on heat transfer. *International Journal of Heat and Mass Transfer*, **40**, 3089–3104.

Morozov, A.N. & van Saarloos, W. (2007). An introductory essay on subcritical instabilities and the transition to turbulence in visco-elastic parallel shear flows. *Physics Reports*, **447**(3–6), 112–143.

Mouza, A.A., Dalakoglou, G.K. & Paras, S.V. (2005). Effect of liquid properties on the performance of bubble column reactors with fine pore spargers. *Chemical Engineering Science,* **60**, 1465–1475.

Mudde, R.F. & Van Den Akker, H.E.A. (1999). Dynamic behavior of the flow field of a bubble column at low to moderate gas fractions. *Chemical Engineering Science*, **54**, 4921–4927.

Natarajan, V.V.R., Hunt, M.L. & Taylor, E.D. (1995). Local measurements of velocity fluctuations and diffusion coefficients for a granular material flow. *Journal of Fluid Mechanics*, **304**, 1–25.

Ohki, Y. & Inoue, H. (1970). Longitudinal mixing of the liquid phase in bubble columns. *Chemical Engineering Science*, **25**, 1–16.

Omurtag, A., Stickel, V. & Chevray, R. (1996). Chaotic advection in a bioengineering system, *Proceedings of the Eleventh ASCE Engineering Conference*, Fort Lauderdale, FL.

Ottino, J.M. (1989). *The Kinematics of Mixing: Stretching, Chaos and Transport*. Cambridge University Press, Cambridge.

Ottino, J.M. (1990). Mixing, chaotic advection, and turbulence. *Annual Reviews in Fluid Mechanics*, **22**, 207–253.

Ottino, J.M. & Khakhar, D.V. (2000). Mixing and segregation of granular materials. *Annual Reviews in Fluid Mechanics*, **32**, 55–91.

Owens, R.G. & Phillips, T.N. (2002). *Computational Rheology*. Imperial College Press, London.

Peltier, W.R. & Caulfield, C.P. (2003). Mixing efficiency in stratified shear flows. *Annual Review of Fluid Mechanics*, **35**, 135–167.

Pilhofer, T. (1980). Effect of plate geometry on gas holdup in bubble columns. *Chemical Engineering Communication*, **5**, 69–72.

Rajchenbach, J. (1990). Flow in powders: from discrete avalanches to continuous regime. *Physics Review Letters*, **65**, 2221–2224.

Ranade, V.V. (1997). An efficient computational model for simulating flow in stirred vessels: a case of Rushton turbine. *Chemical Engineering Science,* **52**, 4473–4484.

Ranade, V.V. & Joshi, J.B. (1987). Transport processes in multiphase systems: momentum, mass and heat transfer in bubble column reactors. *Transfer Processes in Multi-Phase Systems, Proceedings of International Symposium on Transport Phenomena in Multiphase Systems*, BHU Press, Varanasi, India, pp. 113–196.

Rauline, D., Tanguy, P.A., LeBlevec, J. & Bousquet, J. (1998). Numerical investigation of the performance of several static mixers. *Canadian Journal of Chemical Engineering*, **76**, 527–535.

Rauline, D., Le Blévec, J.M., Bousquet, J. & Tanguy, P.A. (2000). A comparative assessment of the performance of the Kenics and SMX static mixers. *Transactions IChemE, Part A*, **78**, 389–395.

Rayleigh, L. (1883). Investigation of the character of the equilibrium of an incompressible heavy fluid of variable density. *Proceedings of the London Mathematical Society*, **14**, 170–177.

Raynal, F. & Gence, J. (1997). Energy saving in chaotic laminar mixing. *International Journal of Heat and Mass Transfer*, **40,** 3267–3273.

Regner, M., Östergren, K. & Trägårdh, C. (2006). Effects of geometry and flow rate on secondary flow and the mixing process in static mixers—a numerical study. *Chemical Engineering Science*, **61**, 6133–6141.

Reilly, I.G., Scott, D.S., DeBruijn, T.J.W. & MacIntyre, D. (1994). The role of gas phase momentum in determining gas holdup and hydrodynamic flow regimes in bubble column operations. *Canadian Journal of Chemical Engineering*, **72**, 3–12.

Richardson, L.F. (1926). Atmospheric diffusion shown on a distance-neighbor graph. *Proceedings of the Royal Society of London Series* A, **110**, 709–737.

Richtmyer, R.D. (1960). Taylor instability in shock acceleration of compressible fluids. *Communication in Pure and Applied Mathematics*, **13**, 297–319.

Rom-Kedar, V. & Poje, A.C. (1999). Universal properties of chaotic transport in the presence of diffusion. *The Physics of Fluids*, **11**, 2044–2057.

Rothstein, D., Henry, E. & Gollub, J.P. (1999). Persistent patterns in transient chaotic fluid mixing. *Nature*, **401**, 770–772.

Ruzicka, M.C., Drahos, J., Fialova, M. & Thomas, N.H. (2001a). Effect of bubble column dimensions on flow regime transition. *Chemical Engineering Science*, **56**, 6117–6124.

Ruzicka, M.C., Zahradnik, J., Drahoš, J. & Thomas, N.H. (2001b). Homogeneous–heterogeneous regime transition in bubble columns. *Chemical Engineering Science*, **56**, 4609–4626.

Sarrafi, A., Jamialahmadi, M., Muller-Steinhagen, H. & Smith, J.M. (1999). Gas holdup in homogeneous and heterogeneous gas–liquid bubble column reactors. *Canadian Journal of Chemical Engineering*, **77**, 11–21.

Schowalter, D.G., Van Atta, C.W. & Lasheras, J.C. (1994). A study of streamwise vortex structure in a stratified shear layer. *Journal of Fluid Mechanics*, **281**, 247–291.

Scott, A.M. & Bridgewater, J. (1976). Self-diffusion of spherical particles in a simple shear apparatus. *Powder Technology*, **14**, 177–183.

Sembira, A.N., Merchuk, J.C. & Wolf, D. (1986). Characteristics of a motionless mixer for dispersion of immiscible fluids—II. A modified electro-resistivity probe technique. *Chemical Engineering Science*, **41**, 457–462.

Sen, M. & Chang, H.C. (1991). Heat transfer enhancement by chaotic mixing, *GRI Annual Report.* Corporate Source: University of Notre Dame, p. 103.

Shaikh, A. & Al-Dahhan, M. (2005). Characterization of the hydrodynamic flow regime in bubble columns via computed tomography. *Flow Measurement and Instrumentation*, **16**, 91–98.

Shaikh, A. & Al-Dahhan, M. (2006). Hydrodynamics of slurry bubble column reactors, *CREL Internal Report*.

Shnip, A.I., Kolhatkar, R.V., Swamy, D. & Joshi, J.B. (1992). Criteria for the transition from the homogeneous to the heterogeneous regime in two-dimensional bubble column reactors. *International Journal of Multiphase Flow*, **18**, 705–726.

Smith, J.M. (1978). Gas dispersion in viscous liquids with a static mixer. *Chemical Engineering*, November, 827–830.

Solomon, T.H. & Mezid, I. (2003). Uniform resonant chaotic mixing in fluid flows. *Nature*, **425**, 376–380.

Stone, H.A., Nadim, A. & Strogatz, S.H. (1991). Chaotic streamlines inside droplets immersed in steady linear Stokes flows. *Journal of Fluid Mechanics*, **232**, 629–646.

Stremler, M.A., Haselton, F.R. & Aref, H. (2004). Designing for chaos: applications of chaotic advection at the microscale. *Philosophical Transactions of the Royal Society A-Mathematical Physical and Engineering Sciences*, **362**(1818), 1019–1036.

Szalai, E.S., Kukura, J., Arratia, P.E. & Muzzio, F.J. (2003). Effect of hydrodynamics on reactive mixing in laminar flows. *AIChE Journal*, **49**, 168–179.

Tanguy, P.A., Thibault, F., Brito-de la Fuente, E., Espinosa-Solares, T. & Tecante, A. (1998). Mixing performance induced by coaxial flat blade-helical ribbon impellers rotating at different speeds. *Chemical Engineering Science*, **52**, 1733–1741.

Taylor, G.I. (1921). Diffusion by continuous movements. *Proceedings of the London Mathematical Society*, **20**, 196–211.

Taylor, G.I. (1950). The instability of liquid surfaces when accelerated in a direction perpendicular to their planes. *Proceedings of the Royal Society of London Series* A, **201**, 192–196.

Thimmapuram, P.R., Rag, N.S. & Saxena, S.C. (1992). Characterization of hydrodynamic regimes in a bubble column. *Chemical Engineering Science*, **47**, 3355–3362.

Thorat, B.N. & Joshi, J.B. (2004). Regime transition in bubble columns: experimental and predictions. *Experimental Thermal and Fluid Science*, **28**, 423–430.

Tidhar, M., Merchuk, J.C., Sembira, A.N. & Wolf, D. (1986). Characteristics of a motionless mixer for dispersion of immiscible fluids. Part II. Phase inversion of liquid–liquid systems. *Chemical Engineering Science*, **41**, 457–462.

Tzeng, J.W., Chen, R.C. & Fan, L.S. (1993). Visualization of flow characteristics in a 2-D bubble column and three-phase fluidized bed. *AIChE Journal*, **39**, 733–744.

Ujhidy, A., Németh, J. & Szépvölgyi, J. (2003). Fluid flow in tubes with helical elements. *Chemical Engineering and Processing*, **42**, 1–7.

Unger, D.R. & Muzzio, F.J. (1999). Laser-induced fluorescence technique for the quantification of mixing in impinging jets. *AIChE Journal*, **45**, 2477–2486.

Urseanu, M. (2000). Scaling up bubble column reactors. Ph.D. Thesis, University of Amsterdam, Amsterdam, The Netherlands.

Vandu, C. (2005). Hydrodynamics and mass transfer in multiphase reactors. Ph.D. Thesis, University of Amsterdam, Amsterdam, The Netherlands.

Wang, S.J., Devahastin, S. & Mujumdar, A.S. (2005). A numerical investigation of some approaches to improve mixing in laminar confined impinging streams. *Applied Thermal Engineering*, **25**(2–3), 253–269.

Warhaft, Z. (2000). Passive scalars in turbulent flows. *Annual Review of Fluid Mechanics*, **32**, 203–240.

Wiggins, S. (1992). *Chaotic Transport in Dynamical Systems.* Springer-Verlag, New York.

Wilkinson, P.M. (1991). Physical aspects and scale-up of high pressure bubble columns. Ph.D. Thesis, University of Groningen, Netherlands.

Wilkinson, P.M., Spek, A.P., Van, D. & Laurent L. (1992). Design parameters estimation for scale-up of high-pressure bubble columns. *AIChE Journal*, **38**, 544–554.

Woodfield, P.L., Kazuyoshi, N. & Suzuki, K. (2003). Numerical study for enhancement of laminar flow mixing using multiple confined jets in a micro-can combustor. *International Journal of Heat and Mass Transfer*, **46**, 2655–2663.

Wunsch, C. (2002). What is the thermohaline circulation? *Science*, **298**, 1179–1181.

Wunsch, C. & Ferrari, R. (2004). Vertical mixing, energy, and the general circulation of the oceans. *Annual Reviews of Fluid Mechanics*, **36**, 281–314.

Yeung, P.K. (2002). Lagrangian investigations of turbulence. *Annual Review of Fluid Mechanics*, **34**, 115–142.

Zahradnik, J. & Kastanek, F. (1979). Gas holdup in uniformly aerated bubble column reactors. *Chemical Engineering Communication*, **3**, 413–429.

Zahradnik, J., Fialova, M., Ruzicka, M., Drahos, J., Kastanek, F. & Thomas, N.H. (1997). Duality of the gas–liquid flow regimes in bubble column reactors. *Chemical Engineering Science*, **52**, 3811–3826.

Zalc, J.M., Alvarez, M.M., Muzzio, F.J. & Arick, B.E. (2001). Extensive validation of computed laminar flow in a stirred tank with three Rushton turbines. *AIChE Journal*, **47**, 2144–2154.

Zalc, J.M., Szalai, E.S. & Muzzio, F.J. (2002). Characterization of flow and mixing in the SMX static mixer. *AIChE Journal*, **48**, 427–436.

Zienkiewicz, O.C., Taylor R.L. & Zhu, J.Z. (2005). Turbulent flows. *The Finite Element Method Set* (eds O.C. Zienkiewicz, R.L. Taylor & P. Nithiarasu). 6th edn., pp. 248–273.

Zik, O. & Stavans, J. (1991). Self-diffusion in granular flows. *Europhysics Letters*, **16**, 255–258.

Zumbrunnen, D.A. & Inamdar, S. (2001). Novel sub-micron highly multilayered polymer films formed by continuous flow chaotic mixing. *Chemical Engineering Science*, **56**, 3893–3897.

4 Rheology and mixing

P.J. Cullen and Robin K. Connelly

4.1 Introduction

Rheology is defined as the science of deformation and flow (Morrison 2004). It provides insight into material phenomena, which are governed by the microscopic scale at a macroscopic level. Rheology entails the study of materials with properties described by relationships between force and deformation. A viscous liquid may be defined as a medium in which the energy needed to deform it is completely dissipated in the process of deformation. Consequently, it will not recover from the deformation. Conversely, an elastic solid is a material which stores the work from the deformation process and returns energy after removal of the deformation forces. In this sense, the ideal behaviour of solid and fluid as described by Newton–Stokes and Hooke laws lies on the boundaries of rheology (Figure 4.1).

As rheology describes how matter responds to applied stress or strain, it finds application in diverse areas such as product development, process engineering calculations, quality control, stability studies and correlations to sensory data. Many processed foods are formulated to display desired rheological behaviour under specific stress conditions such as gravity, pouring, mouth feel, etc. However, it is unlikely that one of these will be to facilitate ease of mixing.

With regard to mixing, rheology plays a critical part in the ease at which mixing proceeds and is a primary factor governing the design of mixing geometries. Food displays a vast array of rheological behaviour such as shear thinning, plasticity and viscoelasticity, which may influence mixing either positively or negatively. Apart from rheology influencing the mixing process, the mixing process may in turn significantly influence food rheology, and ultimately, consumer acceptability. This chapter provides an overview of food rheology with particular reference to the influence of rheology on fluid mixing.

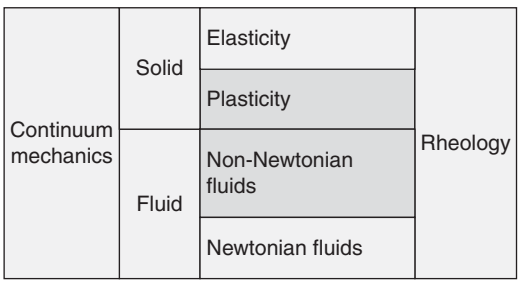

Fig. 4.1 Rheology within continuum mechanics.

4.2 Dispersion rheology

Dispersions are defined as homogeneous or heterogeneous systems in which a solid (rigid or deformable) or liquid phase is dispersed in a liquid medium. Dispersions may destabilise or transform over time under a range of forces including inter-particle, gravitational and shear. Dispersion behaviour will be influenced by both the characteristics of the dispersed phase (particles) and the dispersing medium. A vast range of dispersions and concentrated (high percentage total solids) suspensions are found in the food industry ranging from low-viscosity Newtonian colloidal suspensions (solids < 1 μm) to highly concentrated non-Newtonian liquids containing large suspended matter (Cullen & O'Donnell 2003).

4.2.1 Forces acting on dispersed particles

To understand the flow behaviour of dispersions, a survey of the forces acting on the dispersed particles is required. Such forces include colloidal forces, gravitational forces and hydrodynamic forces.

4.2.1.1 *Colloidal forces*

Inter-particle forces, which may be attractive (van der Waal) or repulsive (electrostatic) in nature, become significant for colloidal particles. If the net result of the forces is attractive, the particles tend to flocculate. To develop stability in a counteracting repulsive force, a surfactant material or electrostatic charge on the particle's surface is required. Brownian forces randomise particle spatial distribution, which may overcome sedimentation problems where flocculation can be prevented.

4.2.1.2 *Gravitational forces*

Particles greater in size than colloidal tend to settle under the influence of gravity unless the relative densities of the particle and the suspending medium are comparable. Stokes' equation (4.1) describes the rate of sedimentation or creaming (v) of an isolated particle in a Newtonian fluid of viscosity (μ) as a function of particle radius (r), the force of gravity (g) and the density difference between the particle (ρ_p) and the suspending fluid (ρ_s).

$$v = \frac{2r^2(\rho_p - \rho_s)g}{9\mu} \tag{4.1}$$

Stokes' law applies where particle settling is independent of neighbouring particles. As particle phase fraction increases, there is appreciable interference of the flow patterns surrounding the falling particles. However, where a minimum level of concentration is reached and where particle size distribution is not greater than 10:1, particles tend to settle at similar rates.

4.2.1.3 *Hydrodynamic forces*

The orientation distribution of non-spherical particles depends upon the ratio of the hydrodynamic forces to randomisation effects caused by Brownian forces. Hydrodynamic forces, which are viscosity dependent, cause the alignment of a particle's major axis with the

direction of flow, reducing frictional resistance (Figure 4.2). The Peclet number (*Pe*) quantifies the contribution of each term as a dimensionless shear rate:

$$Pe = \frac{\mu_s \dot{\gamma} r^3}{k'T} \tag{4.2}$$

where r is particle radius, T is absolute temperature, k' is Boltzmann constant, μ_s is viscosity of suspending fluid and $\dot{\gamma}$ is shear rate. The Peclet number ranges from $Pe = 0$, which indicates randomisation of the particle orientation by Brownian forces, to $Pe \rightarrow \infty$, which indicates alignment of the particles with the flow.

4.2.2 Parameters affecting suspension rheology

4.2.2.1 *Concentration*

Suspended particulate matter causes small increases in viscosity at low concentrations with the effect becoming significantly more pronounced at high concentrations. Suspended particles disturb the flow field under shear, squeezing the flow stream between adjoining particles (Figure 4.2). Viscosity for Newtonian suspensions may be described by equation (4.3), which can be seen to depend primarily on the ratio of particle volume fraction (ϕ) to maximum packing (ϕ_m).

$$\mu = \mu_s \left(1 - \frac{\phi}{\phi_m}\right)^{-2} \tag{4.3}$$

Concentration increases particle phase volume, resulting in increased particle–particle interaction. The effect of concentration on apparent viscosity may be described by an exponential relationship.

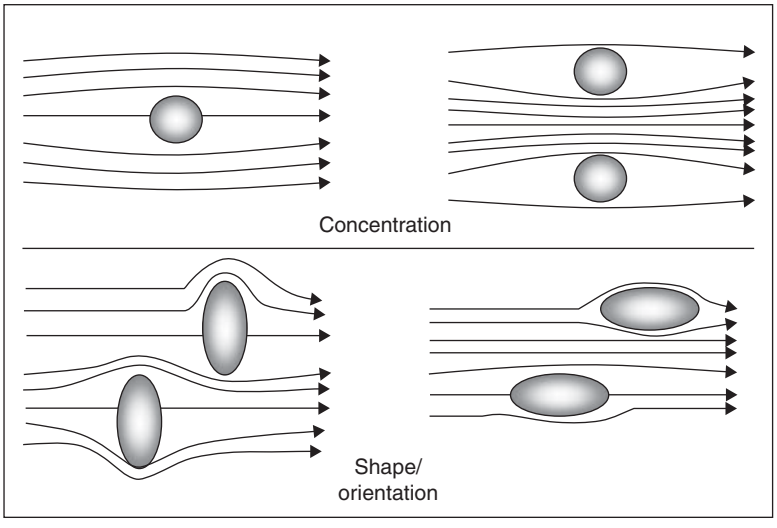

Fig. 4.2 Effects of particle concentration and orientation on fluid viscosity.

The exhibition of a yield stress occurs where inter-particle attraction forms flocs that in turn develop a three-dimensional network throughout the fluid. Such a network provides additional structure to a fluid, resulting in solid-like behaviour under low stresses. A minimum stress is required for sufficient structural breakdown and the initiation of flow. Hydrocolloids are widely used as structuring agents to control suspension stability of large particulates along with organoleptic and processing parameters of foods. Such rheology modifiers often display pseudoplastic and viscoelastic behaviour resulting in solid-like behaviour of a suspension under low-stress environments, providing improved particle suspension ability to the continuous phase.

If particle concentration approaches the maximum packing volume, particle interaction results in large aggregates that make homogeneous flow increasingly difficult. Inter-particle friction then becomes less viscous in nature, which may result in cracks under shear.

4.2.2.2 *Particle geometry*

Most food suspensions do not have a regular or simple geometry that can be characterised by size and shape. Viscosity increases as shape diverges from that of a sphere, and particle rotation increases with particle size. The effects of the particle size distribution on suspension behaviour may be pronounced with significantly different particle diameters, resulting in a marked decrease in viscosity. As smaller particles interpose larger ones, the void fraction is decreased resulting in increased maximum packing.

Suspension rheology will be affected by the motion and orientation of the particles. Hydrodynamic forces, caused by the difference in velocity of the suspending fluid and the particle, act on the particle or aggregated particles. Thus, the flow behaviour of the system is a function of the relative motion and orientation of the particles. Under low shear conditions, hydrodynamic forces may not be sufficient to disrupt flocs, which act as particles with fixed size and shape, resulting in a constant viscosity. Larger forces under increasing shear rates will cause the flocs to deform and disrupt. Alignment with the shear field results in shear thinning behaviour (Figure 4.3). A constant viscosity may be exhibited at high shear rates where flocs are completely disrupted or the rate of floc formation equals the rate of floc disruption. Complex rheological behaviour such as shear thinning and time-dependency effects may be associated with the shear-induced breakdown and possible rebuilding of structure.

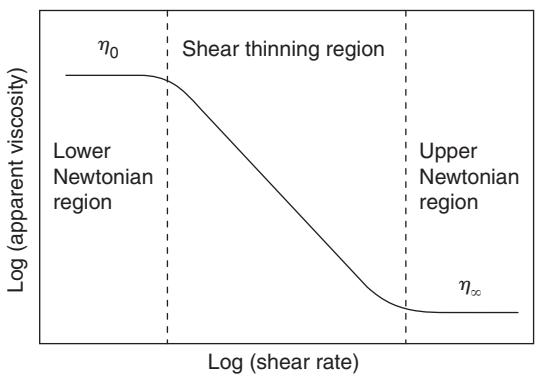

Fig. 4.3 Typical shear thinning behaviour for plot of shear rate versus apparent viscosity.

4.3 Fluid rheology and mixing

4.3.1 Shear flow

Shear flows occur when force is applied parallel to a face of a fluid element (shear stress, σ) and results in a shear deformation where there is an angular displacement of parallel surfaces in the fluid element (shear strain, γ). The rate at which the shear deformation occurs is the shear rate ($\dot{\gamma}$). Shear flow is the dominate flow type found in most mixers.

The typical rheological behaviours of fluid foods under steady shear conditions are depicted in the rheogram in Figure 4.4. The most basic behaviour is the case in which the shear stress is proportional to the shear rate as seen in curve 4, where the slope is the Newtonian viscosity (μ) as was originally defined by Newton's viscosity law. Curves 3 and 5 describe shear thinning (or pseudoplastic) and shear thickening (or dilatant) behaviours, respectively, and are both described by the power law model. Curves 1 and 2 describe fluids that have a dynamic yield stress (σ_y) that must be overcome before fluid flow commences. At stress levels greater than the yield stress, Bingham fluids (curve 2) exhibit shear stress that is proportional to shear rate with the slope described as the plastic viscosity (μ_{pl}), whereas fluids exhibiting continued shear thinning behaviour are described as viscoplastic (curve 1). This range of behaviours can be generally described using the Herschel–Bulkley model (Steffe 1996):

$$\sigma = \sigma_y + K\dot{\gamma}^n \tag{4.4}$$

where K is the consistency coefficient and n is the flow behaviour index. It directly describes the behaviour seen in curve 1 of Figure 4.4 as well as that in curve 2 when $n = 1$ to give the Bingham model, where $K = \mu_{pl}$. When the yield stress is zero ($\sigma_y = 0$), equation (4.4) takes the form of the power law model with the pseudoplastic behaviour of curve 3 modelled when $n < 1$ and dilatant behaviour of curve 5 modelled when $n > 1$. In the case where both $\sigma_y = 0$ and $n = 1$, equation (4.4) reduces to the Newtonian case of curve 4 where K becomes the Newtonian viscosity (μ).

4.3.1.1 *Shear thinning flow*

Shear thinning behaviour is observed with structured foods, where viscosity decreases with applied shear. Consequently, the viscosity at any given shear rate must be reported

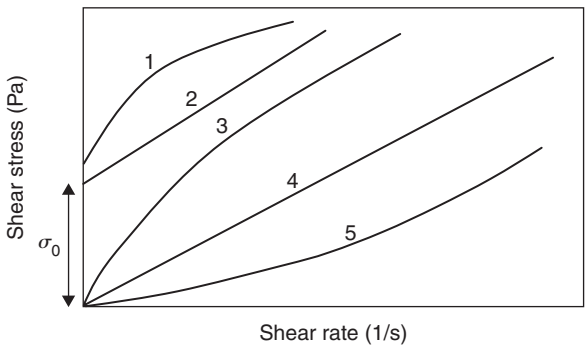

Fig. 4.4 Flow curves for typical time-independent fluids. 1—viscoplastic fluid, 2—bingham fluid, 3—pseudoplastic fluid, 4—Newtonian fluid and 5—dilatant fluid.

as apparent viscosity ($\eta_a = \sigma / \dot{\gamma}$). The fluid's microstructure, which may be due to either macromolecule entanglement or particle–particle interaction, is broken down under shear. Rheograms of such complex fluids typically display two regions of near constant viscosity connected by a shear thinning region. The zero shear viscosity (η_0) corresponds to a region where the fluid is completely structured. The intermediate shear thinning region, typically characterised by the power law, corresponds to structural breakdown. The second Newtonian infinite shear viscosity (η_∞) region corresponds to complete structural breakdown. Where a fluid structure can recover, the shear thinning behaviour may be independent of time, as at a constant shear rate there is an equilibrium between the rate of structural breakdown and recovery. Fortunately, the rheological behaviour of these structured fluid food materials can generally be considered to fall entirely in the shear thinning region for the shear rate range of interest during mixing.

The shear stresses responsible for the mixing process will naturally be governed by the shear rate. However, the shear rate will be defined by both the impeller and fluid properties. Figure 4.5 shows a typical velocity profile near a rotating impeller. The shear rate may be determined from the local slope. High shear rates will be generated near the impeller. However, the volume of fluid exposed to these rates may be relatively small; consequently, it is important to quantify mixing in terms of shear rate and fluid volume. For power law fluids, the apparent viscosity will increase from a minimum value close to the impeller to a maximum value far away from the impeller. Metzner and Otto (1957) proposed equation (4.5) in which an apparent viscosity is evaluated at an average shear rate, based on the assumption that the average shear rate is directly proportional to the rotational speed of the impeller.

$$\dot{\gamma}_a = k_s N \tag{4.5}$$

The shear rate constant of proportionality k_s is dependent upon the impeller geometry, but is usually found to be independent of fluid properties and impeller speed (Shamlou & Edwards 1985).

At first glance, it is logical to expect an increase in the ease of mixing with increased shear rate and time for shear thinning fluids, similar to the benefits often found when

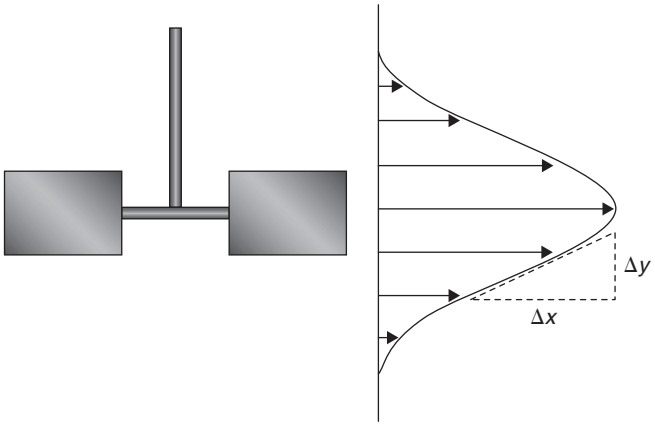

Fig. 4.5 Typical velocity profile near a rotating impeller.

pumping such fluids. However, this is not necessarily the case. Anderson *et al*. (2000) showed that shear thinning may have both positive and negative effects on mixing efficiency. The viscosity of such fluids may change dramatically at high shear rates, whereas mixing equipment is generally designed to work effectively only within a limited viscosity range.

It is also possible for the viscosity of fluids to increase as a function of shear. Shear thickening (or dilatant) fluids are frequently solid suspensions, such as concentrated raw corn starch in water (Steffe 1996). As observed with shear thinning, the shear thickening phenomena occurs due to the rearrangement of the fluid's microstructure. For example, in the case of concentrated raw corn starch in water, at low shear rates the water has a lubricating effect such that the starch particles can slide past each other easily, thus exhibiting a low apparent viscosity. However, as the shear rate increases, increased resistance caused by particle–particle interactions causes the apparent viscosity to increase substantially (Steffe 1996). During mixing, the shear thickening behaviour can actually cause the material near the impeller to behave as a solid, and thus effectively change the geometry of the impeller (Delaplace *et al.* 2000). The design of mixers for shear thickening solid suspensions can still be done using the Metzner and Otto concept, but requires the use of geometrically similar mixing elements in the rheometer for the calculation of the apparent viscosity curve used in the calibration process in order to determine an appropriate value for k_s (Jomha *et al.* 1990). Care should be taken when mixing shear thickening fluids, as the development of increased resistance to flow may damage the mixer, if the apparent viscosity exceeds the limits for which the mixer was designed for.

4.3.1.2 *Yield stress*

Materials with a yield stress do not flow until a minimum yield stress (σ_y) is exceeded. Below this minimum stress, the structure of the materials is sufficiently rigid to prevent flow and instead stores the applied energy (Figure 4.4). Upon breach of the yield stress value, the structure disintegrates and flow is initiated. Although the existence of a yield stress may be argued (Barnes & Walters 1985) based on the theory that everything flows given sufficient time or sufficiently sensitive measurement equipment, it is an engineering reality influencing process design, product stability and sensory assessment. The ability to build in a yield stress within food systems is one of the most valuable strategies available in food product development. The use of structure-modifying ingredients such as biopolymers allows the design and control of desired rheological behaviour at varying applied stress conditions within food systems.

Mixing of shear thinning fluids that exhibit yield stresses may result in the formation of a well-mixed region around the impeller and stagnant fluid elsewhere within the vessel. Wichterle and Wein (1981) showed that fluids with a yield stress are mobile around the impeller where shear stresses are high, whereas the same fluid is stagnant away from the impeller. The term 'cavern' was used from this work to describe a region of good mixing. Numerous studies have focused on the influence of various impeller designs on the mixing of yield stress fluids (Elson 1990; Galindo & Nienow 1993; Amanullah *et al*. 1997). Prediction of the cavern properties is critical in the mixing of shear thinning fluids with yield stresses, to ensure optimal mixing. Several studies have correlated cavern size to energy introduced to the system via torque measurements. Solomon *et al*. (1981) developed the following mathematical model for a spherical cavern during impeller mixing of a yield stress fluid based on a momentum balance. This model assumes that the power dissipated

by the impeller is transmitted through the fluid to the cavern wall, the shear stress at the cavern boundary equals the fluid yield stress and the predominant motion of the fluid within the cavern is tangential:

$$\left(\frac{D_C}{D}\right)^3 = \left(\frac{4Po}{\pi^3}\right)\left(\frac{N^2D^2\rho}{\sigma_y}\right) \tag{4.6}$$

where D_C, D, N, ρ, σ_y and Po are cavern diameter, impeller diameter, impeller speed, fluid density, fluid yield stress and power number, respectively.

Similar models have been developed for different cavern shapes (spherical, cylindrical and toroidal), different flow regimes within the cavern and for various rheological models. Tanguy *et al*. (1994) and Bertrand *et al*. (1996) showed the influence of viscoplasticity on the flow pattern and power consumption for anchor impellers. Wilkens *et al*. (2005) developed and experimentally validated a model to predict the elliptical torus cavern shape for radial impellers and axial flow impellers at low speeds mixing ketchup that exhibited Bingham behaviour. Arratia *et al*. (2006) showed robust segregation between caverns for yield stress fluids in multi-impeller systems, leading to poor global mixing. Such insight will facilitate more efficient design for dealing with yield stress fluids, such as breaking the special symmetry by positioning the impeller off-centre resulting in weaker cavern segregation.

Until recently, the majority of studies on mixing of yield stress fluids has focused on 2-D flows, and indeed, much remains to be learned about mixing on non-Newtonian fluids in 3-D. Computational fluid dynamics (CFD) (Pakzad *et al*. 2008a) and novel measurement techniques (Chapter 7) including x-ray (Elson *et al*. 1986), electrical resistance tomography (Pakzad *et al*. 2008b), planar laser-induced fluorescence (PLIF) (Arratia *et al*. 2006) and positron emission particle tracking (PEPT) (Chapter 10) are providing increased insight into cavern formation in the mixing of fluids possessing yield stresses. Such developments have facilitated research into 3-D flows within mixing systems for fluids displaying complex rheology.

4.3.1.3 *Thixotropy*

Thixotropy is defined as the progressive decrease in viscosity with time for a constant applied shear stress, followed by a gradual recovery when the stress is removed. The mechanical properties of thixotropy systems result from the competition between the spontaneous restructuring of the microstructure at rest and its destruction under shear. Such materials exhibit a complex rheological behaviour comprising shear thinning, time-dependent viscosity and a yield stress (Couerbe *et al.* 2008). Despite the importance of mixing of thixotropy fluids, there are few studies in the literature. Edwards *et al*. (1976) studied the effects of various mixing impellers on the structural breakdown of a range of fluids including ketchup, salad cream and yoghurt. They reported that average shear rates from the mixers using the Metzner and Otto (1957) technique compared well to shear rate viscometry data. Similarly, Sestak *et al*. (1986) used the technique to predict power consumption by various anchor impellers for thixotropy fluids in their equilibrium state after breakdown. Maingonnat *et al*. (2005) modelled the build-up of a thixotropic fluid under viscometric conditions. They employed the stretched exponential model to describe the rheological build-up:

$$\eta(t) = \eta_0 + (\eta_\infty - \eta_0)(1 - e^{-(t/\sigma)}) \tag{4.7}$$

where t is a characteristic time. η_∞ is the viscosity value at equilibrium and η_0 is the fluid viscosity when the structure is completely broken down. They applied the Metzner and Otto concept to experimental data obtained with a small-scale mixing device and reported accurate predictions of the initial and equilibrium viscosities. However the build-up kinetics were not described precisely, especially for low shear rates. Recently, Couerbe *et al.* (2008) studied the impact of thixotropy on flow patterns induced in a stirred tank. They employed particle image velocimetry (PIV) to characterize the steady state flow fields in the stirred tank with the mixing efficiency of the impeller quantified in terms of its pumping capacity, cavern volume and the ratio of the axial to radial flow rates. The authors also employed CFD to predict 3D flows of the fluids.

4.3.1.4 *Viscoelasticity*

In order to conceptualise viscoelasticity, analogies with simple mechanical models consisting of a spring of modulus (E) representing elastic behaviour and a dashpot representing a Newtonian fluid of viscosity (η) are useful. These analogues provide insight into the physical behaviour of such materials by breaking down the dissipative viscous processes (time-dependent) and energy-storage processes. These terms may be arranged in series (Maxwell model) or parallel (Kelvin–Voigt model) (Figure 4.6). In the Maxwell model, for slow motions, the viscous dashpot will dominate (Rao 2007). However, for rapid stress changes, the model approaches elastic behaviour.

Mixing difficulties involved in the mixing viscoelastic materials are due to energy storage and release. Elastic effects result in normal forces being generated within the fluid as well as the shear forces from the viscous component. Such normal forces may give rise to rod climbing (Weissenberg effect) and flow reversal. However, there is no comprehensive understanding of the effects of viscoelasticity on mixing. Difficulties arise in experimentation with completely separating the effects caused by shear thinning from viscoelasticity and in simulations with the use of viscoelastic models. Literature reveals contradictions in the effects of viscoelasticity, with Niederkorn and Ottino (1993) reporting that even mildly elastic model fluids caused a significant negative impact on mixing. However Fan *et al.* (2000) reported that similar elastic fluids gave results that were comparable to Newtonian fluids. Carreau *et al.* (1993) investigated the influence of shear thinning and elasticity on power consumption for the mixing of viscous fluids using helical ribbon agitators. They reported that power consumption increases appreciably with fluid elasticity. They observed

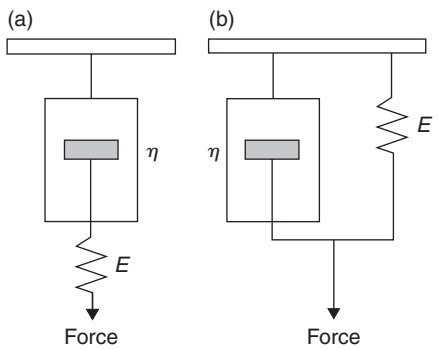

Fig. 4.6 Analogues of visco-elastic behaviour: (a) Maxwell model and (b) Kelvin–Voigt model.

that the departure from the generalised Newtonian power curve occurred at smaller Reynolds numbers for viscoelastic fluids as compared with inelastic non-Newtonian or Newtonian fluids. Conversely, Zhou *et al*. (2000) found that fluid elasticity had no clear effects on the power consumption of a double planetary mixer. They suggested that this finding may be due to the specific configuration of the two intermeshing blades.

Connelly and Kokini (2003) studied the effects of viscoelasticity on mixing flows from kneading paddles in a single-screw continuous mixer, using 2-D finite element numerical simulations. Viscoelasticity caused the shear and normal stresses to vary greatly from the viscous results, with a resulting loss of symmetry in the velocity and pressure profiles in the flow region. Connelly and Kokini (2004) showed that viscoelasticity changes the shear stress distributions around the impeller blades as seen in Plate 4.1. They also reported that shear thinning behaviour led to an increase in the size of plug flow regions whereas viscoelasticity increased the size of the elongational flow regions.

A group at the University of Wales has studied simplified single and double concentric cylinder model mixers in filled and partially filled conditions using a combination of numerical modelling and experimental results in model mixers to better understand dough kneading in order to improve performance of industrial dough mixers (Baloch *et al*. 2002; Binding *et al*. 2003; Couch & Binding, 2003; Sujatha *et al*. 2003). Their wall-driven mixer finite element method (FEM) simulation results include Carreau flow model simulations of partially filled conditions with concentric and eccentric stirrers using an arbitrary Lagrangian–Eularian scheme to model the free surface, as well as viscoelastic Oldroyd-B and Phan-Thien/Tanner simulations of the fully filled case with concentric, eccentric and double eccentric stirrers. They found the asymmetrical stirrer positioning of a single stirrer provided the best mixing of viscoelastic fluids. Their experimental techniques included laser scatter technology, laser doppler anemometry (LDA) and a video capture technique to determine velocity profiles and peeling stresses in a prototype industrial mixer allowing both horizontal and vertical orientations and mixing speeds between 25 and 450 rpm with the cylindrical bowl and stirring rods fashioned from Perspex. Close agreement was found between numerical and experimental flow fields and free surface profiles.

4.3.2 Elongational flow

Figure 4.7 shows a fluid element within converging streams undergoing stretching at a constant rate along the x axis. In pure extensional flow, all the shear stresses are zero and the normal stresses are equal in the y and z directions. The elongational viscosity depends on

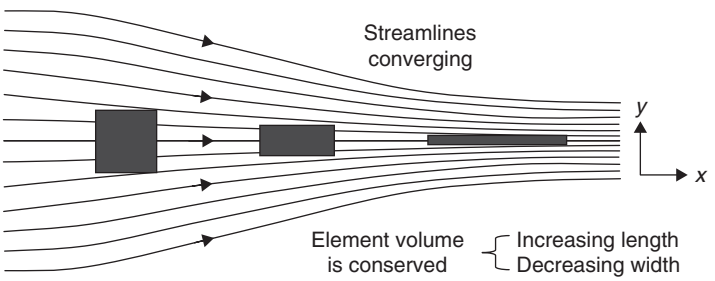

Fig. 4.7 A fluid element within converging streams undergoing stretching at a constant rate along the x axis.

the elongational strain rate and time. Assuming fluid incompressibility, the volume will be conserved and the elongational strain rate is calculated as follows.

$$\dot{\varepsilon} = \frac{\partial v_x}{\partial x} \tag{4.8}$$

The normal viscous stress differences are:

$$\sigma_{xx} - \sigma_{yy} = \sigma_{xx} - \sigma_{zz} = \eta_E \, \varepsilon \tag{4.9}$$

where η_E is the elongational viscosity. The elongational viscosity will depend upon the strain rate and time. The Trouton ratio gives the ratio of the elongational viscosity to the shear viscosity.

$$T_R = \frac{\eta_E}{\eta} \tag{4.10}$$

For Newtonian fluids, the Trouton ratio is 3. However, for some non-Newtonian fluids, the Trouton ratio may be magnitudes greater than Newtonian fluids.

Elongational flow may result in significantly different effects than shear flow on fluid behaviour. This is due to the way the flow fields orientate long molecules of high molecular weight. With shear flow, the presence of a differential velocity across the flow field encourages molecular chains to rotate rather than stretch (Figure 4.8). The tendency of molecules to rotate rather than elongate depends on the magnitude of the shear field, with relatively more elongation and less rotation at high shear rates (Steffe 1996). However, with elongational flow, the molecular orientation tends to be in the direction of the flow field as there are no competing forces to cause rotation. Therefore, extensional flow induces the maximum stretching of molecular chains resulting in large resistances to deformation. The nature of the molecule, branched versus linear, may significantly influence the flow behaviour during elongational flow.

Elongational flow plays an important role in many food process applications such as dough mixing with helical ribbons (Steffe 1996). Elongational flow may be more effective than simple shear flow for dispersive mixing, especially at high viscosities and low interfacial tensions (Elemans *et al*. 1993). The presence of non-zero vorticity in shear flow causes the portion of the agglomerates whose fracture surface lies nearly in the plane formed by principal strain and compression directions to orbit as a rigid body and not rupture (Manas-Zloczower & Feke 1989).

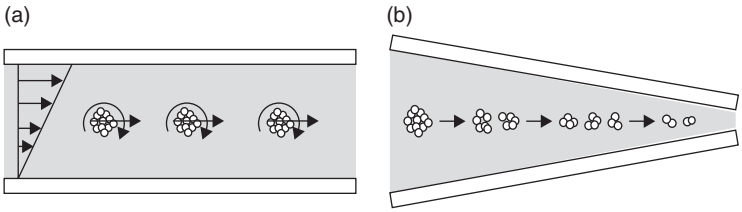

Fig. 4.8 Dispersion in (a) shear and (b) elongational flows.

Dispersive mixing involves the rupture of clumps or agglomerates by forcing the mixture to pass through high shear zones generated in narrow clearances (Prakash & Kokini 2000). Using a rigid dumbbell model, the maximum force acting on an agglomerate for steady shear flow may be expressed as:

$$F_{\max} = 3\pi\eta\dot{\gamma}r^2 \tag{4.11}$$

where r is the radius of the agglomerate. Comparatively, the maximum force for steady elongational flow is as follows.

$$F_{\max} = 6\pi\eta\dot{\varepsilon}r^2 \tag{4.12}$$

When elongational flow is present, the maximum forces trying to disperse an agglomerate is twice as large as the ones present in shear flow. Elongational flow may not only result in more effective dispersion, but may also result in less viscous dissipation than shear flow, requiring less power consumption and temperature rises. However, in practice, with shear flow very large shear rates are obtainable, whereas for elongational flow large rates are hard to obtain. Hence, virtually, all dispersive mixers are based on shear dispersion in narrow clearances.

4.4 Effects of mixing on fluid rheology

The effects of the mixing process on food rheology may be significant, resulting in both positive and negative changes. Factors that influence the rheological properties of mixed fluids include processing variables such as speed and time of mixing, impeller geometry, processing temperature, and intrinsic fluid characteristics including solids volume fraction and time-dependency effects. During mixing, material elements undergo continuous transient changes because shear and extensional rates vary a great deal from location to location (Prakash & Kokini 2000). Positive effects of high shear mixing include the manufacture of emulsions (Chapter 9). Negative effects include the breakdown of desired structure and particle attrition for suspensions (Chapter 10). To minimise such negative effects, it is important to prevent over- or under-mixing by monitoring the mixing process (Chapter 7) and using suitable mixer designs (Chapter 5) when mixing fluids that are succeptible to structural damage.

The effects of mixing time have been extensively examined for dough mixing. Mixing time is found to be a critical factor influencing dough rheological properties, including compliance, elastic recovery, cohesiveness, adhesiveness, extensional viscosity along with the consistency and hardness of final products such as biscuits (Manohar & Rao 1997). Glutenin and, particularly, the glutenin macropolymer (GMP) fraction are considered to play a pivotal role in the manufacture of dough-based products (Wang *et al*. 2007). Don *et al*. (2005) and Weegels *et al*. (1997) showed that the structure of gluten protein changes during dough mixing and is associated with changes in ultrastructural characteristics of gluten and viscoelastic properties of dough. Weegels *et al*. (1997) showed that mixing changes the physicochemical properties of glutenin. After resting, dough viscoelasticity is influenced by glutenin particle properties (Don *et al*. 2005). However, there is no clear consensus on how mixing induces the formation of a viscoelastic network in dough (Hoseney & Rogers 1990; Wang *et al*. 2007).

Two of the most common empirical mixing instruments which follow rheological changes due to the development of the viscoelastic network in dough during mixing are the twin sigma blade Farinograph (C.W. Brabender, Hackensack, NJ) and the planetary pin mixing Mixograph (National Manufacturing, TMCO, Inc., Lincoln, NE). They measure the torque taken to mix the dough, and the dough is considered fully mixed or developed when the torque is at a peak or just beyond a peak value. However, the intensity of the mixing in the two instruments is not the same because they use completely different geometry and mixing actions (Connelly & Kokini 2006a,b). It has been shown that for some very hard or strong flours, the less-intensive Farinograph is never able to fully develop the dough (Rao *et al*. 2000). In addition, researchers using the Mixograph have found the strain to peak at high speeds to be only a function of work input by the mixers and therefore independent of mixing speed (Anderssen *et al.* 1998), whereas others using the Farinograph have found that the strain to peak is dependant on mixer speed as well as work input (Zounis & Quail 1997).

A reason for the differing results in these two standard empirical mixing rheometers is that a minimum intensity is required to develop dough (Kilborn & Tipples 1972). An indication of why this may be the case is the fact that during fundamental rheological testing at the low strains ($<1.0\%$) that are required to be in the linear range for dough, the behaviour of dough is that of a viscoelastic solid, whereas the behaviour of dough at higher strains is that of an elastoviscous liquid (Faubion & Hoseney 1989; Connelly & McIntier 2008). Factors that affect the intensity likely include the mixing speed or rate of strain and the mixing effectiveness of the particular test geometry, with the minimum intensity for dough made from a particular flour also dependent on the flour strength and dough composition. The effectiveness of the mixing geometry is related to the strain rate distribution and elongation or flow type distribution, as well as the overall distributive mixing ability (Connelly & Kokini 2006a,b). There are also indications (Schluentz *et al*. 2000; Lee *et al*. 2001) that dough development may be a function of both energy input and type of deformation, with pure elongational flow developing the protein matrix more efficiently than pure shear flow for a given energy input, in a fashion similar to the effect of flow type or strength on dispersive mixing of cohesive clumps or agglomerates (Manas-Zloczower & Feke 1989; Elemans *et al*. 1993).

Ross *et al*. (2006) examined the effects of mixing on the rheological properties of an agar gel and found that mixing resulted in stronger gels. They reported that mixing affected the degree of porosity induced in the system by incorporation of air bubbles, but these bubbles did not weaken the gel's macrostructure. Similarly, for alginate pastes, greater gel strength was found for high shear mixing when compared to low shear mixing (Inoue *et al*. 2002). Conversely, the authors propose that the high shear mixing may result in air removal. Given the critical role air plays on the quality of dough-based products, the effects of mixing on the incorporation of air bubbles has been studied extensively for dough rheology. Literature indicates that mixing increases the number of bubbles more than the size of the bubbles in the system (Scanlon & Zghal 2001). Overall control of the mixing process will govern product macrostructure as influenced by pore size and porosity due to the number and size of air bubbles. However, mixing speed was reported to decrease bubble size in whey protein isolate foams (Hanselmann & Windhab 1999). The authors reported that as the flow field around the mixing blades transitioned from laminar to turbulent, an increased break-up of bubbles was found resulting in a larger number of smaller bubbles. Improved gas dispersion in the laminar flow field was also achieved with a higher-viscosity fluid and, consequently, an increase in the mechanical energy input.

The effects of mixing time on the rheology and coating characteristics of batter was studied by Lee *et al*. (2002), who reported that the maximum retention of batter could be controlled by inputting the corrected amount of energy during the mixing process. They also found that foods coated with undermixed batter resulted in lower quality attributes than those coated with overmixed batter.

4.5 Mixer rheometry

4.5.1 Theory

The rotational rheometer is the most widely used instrument for fluid characterisation. Conventional geometries such as Couette, parallel plate, and cone and plate, which display well-defined shear rates, should ideally be used for rheological characterisation. The theory of such geometries is effectively reviewed by Steffe (1996). However, such geometries are frequently limited due to the effects of the solid phase, including wall effects and particle settling. Geometries based on mixing impellers allow the study of fluids displaying complex characteristics including large particulates, settling problems, slip and time dependency. Geometries that facilitate mixing, such as helical ribbons, vanes, anchors and paddles, can overcome settling out problems and errors due to slip. As with conventional rotational techniques, the fundamental principle of operation is the determination of shaft torque as a function of rotational speed. Owing to complex flow patterns, and hence shear rates, absolute rheological data may be difficult to obtain. However, such data may be representative of a fluid's rheological characteristics (Cullen *et al*. 2003).

A technique developed for the determination of power consumption during fluid mixing and adopted for rheological analysis has been widely used and is generally referred to as 'mixer viscometry' (Rao 1975). Power consumption for Newtonian fluids within a mixing system may be expressed in terms of power number $Po = (P/\rho d^5 N^3)$ and mixing Reynolds number $Re = (\rho d^2 N/\mu)$, which may be empirically related to each other in the laminar flow region ($Re < 10$) by the equation:

$$Po = \frac{A}{Re} \tag{4.13}$$

where A is a geometric constant. An average shear rate may be determined using the Metzner and Otto technique. The shear rate constant of proportionality k_s is dependent upon impeller geometry, but is usually found to be independent of fluid properties and impeller speed (Shamlou & Edwards 1985). There are a number of techniques for determining the constant k_s. Rieger and Novak (1973) demonstrated that if equation (4.13) is valid, a plot of $(1 - n)$ versus $\log_{10}(P/K\Omega^{n+1}d^3)$ results in a straight line of slope $-k_s$ for the impeller geometry. This technique is commonly referred to as the slope method. For any given impeller geometry, the variables required include power, rotational speed, impeller diameter and the power law parameters for a number of test fluids spanning the flow behaviour index (n) spectrum. A second technique, referred to as the matching viscosity technique, matches the power consumption/torque developed for non-Newtonian test fluids with a Newtonian fluid. Comparisons between the different calculation methods are discussed in detail by Castell-Perez and Steffe (1992).

Shear stress/shear rate curves can also be determined from torque and rotational speed data for mixing geometries using a Couette analogy (Castell-Perez *et al*. 1991; Steffe 1996). In the case of a power law fluid in the concentric cylinder viscometer (Steffe 1996):

$$\sigma_a = m(\dot{\gamma})^n = \frac{M}{2\pi r^2 h} \tag{4.14}$$

$$\Omega = \frac{n}{2m^{1/n}}\left(\frac{M}{2\pi h R_b^2}\right)^{1/n}\left[1-\left(\frac{R_b}{R_c}\right)^{2/n}\right] = \frac{nr^{2/n}}{2}\left(\frac{M}{2\pi r^2 hm}\right)^{1/n}\left[\frac{1}{R_b^{2/n}}-\frac{1}{R_c^{2/n}}\right] \tag{4.15}$$

$$\dot{\gamma}_a = \left(\frac{M}{2\pi r^2 hm}\right)^{1/n} = \frac{2\Omega}{nr^{2/n}[(1/R_b^{2/n})-(1/R_c^{2/n})]} \tag{4.16}$$

$$n = \frac{\mathrm{d}(\ln \tau_b)}{\mathrm{d}(\ln \Omega)} = \frac{\mathrm{d}(\ln M)}{\mathrm{d}(\ln N)} = \text{the slope of the ln } M \text{ versus ln } N \text{ curve} \tag{4.17}$$

where σ_a is the average shear stress (Pa), M is the torque (N m), $\dot{\gamma}_a$ is the average shear rate (s^{-1}), $\Omega = 2\pi N/60$ is angular velocity (rad/s), N is the blade speed (rpm), R_b and R_c (m) are the radii of the inner (bob or mixing element) and the outer (cup) cylinders, respectively, r (m) is an arbitrary radius between R_b and R_c, and h (m) is the immersed height of the mixing element. Also, n is the flow behaviour index, which can be determined directly from the torque versus blade speed results, and m is the consistency coefficient (Pa·s^n), which becomes the viscosity when $n = 1$. The assumptions of these equations are that the flow is laminar and steady, end effects are negligible, the test fluid is incompressible, properties are not a function of pressure, temperature is constant, no slip occurs at the walls, and radial and axial velocity components are zero. They are valid only for fluids without a yield stress.

Using this analogy, an equivalent radius for a Couette cylinder having the same length and providing the same torque and rotational speed as the cylindrical complex geometry, such as a helical ribbon or a vane, for fluids that have $n > 0.5$ is determined (Figure 4.9). In this case, equation (4.20) for a Newtonian fluid generally takes the form (Steffe 1996):

$$\Omega = \left[\frac{M}{4\pi(h+h_e)\eta}\right]\left[\frac{1}{R_{b,equf}^2}-\frac{1}{R_c^2}\right] \tag{4.18}$$

where the value of R_b is generally replaced with an effective radius $R_{b,equ}$. A Newtonian fluid may be used with its corresponding torque and rotational speed to solve equation (4.18) for the equivalent radius, $R_{b,eq}$, which will be smaller than the radius of the mixing element because the streamlines of Newtonian and mildly shear thinning materials are not circular, but instead dip inside the cylinder cut out by the complex mixing geometry (Barnes & Carnali 1990; Martínez-Padilla & Quemada 2007). End effects can be taken into account by adding a factor to the length of the cylinder (h_e) determined by immersing the

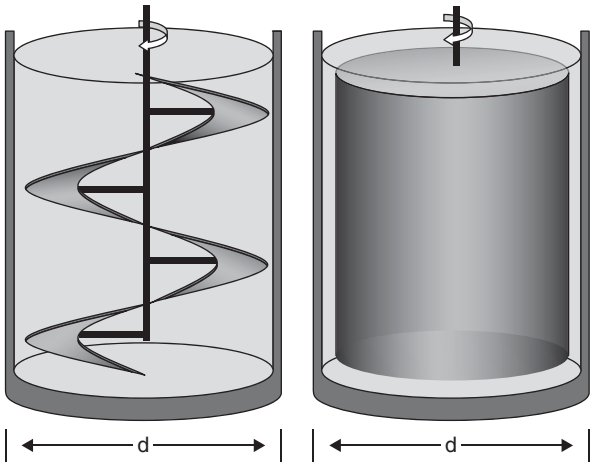

Fig. 4.9 Helical ribbon and cylinder geometries with geometrically similar dimensions.

mixing element to different levels (h) using a Newtonian fluid, which has been shown to depend on the distance the mixing element is from the bottom for the four-vane geometry (Martínez-Padilla & Quemada 2007).

Once $R_{b,equ}$ has been determined, shear rate in the virtual gap of the hypothetical rheometer may be determined using equation (4.19) as a function of radius r and flow behavioural index n.

$$\dot{\gamma} = \left[\frac{\dfrac{4\pi}{n}\left(\dfrac{R_i}{r}\right)^{2/n}}{1-\left(\dfrac{R_i}{R_{b.equ}}\right)^{2/n}} \right] N = K_s N \tag{4.19}$$

A position within this gap where shear rate at a constant speed is nearly independent of the rheology for flow behaviour is chosen (Aerts & Verspaille 2001). Bousmina *et al*. (1999) showed that at $r = R_a = (R_{b,equ} + R_c)/2$, the shear rate is nearly independent of the flow behaviour index n, when $R_{b,equ}/R_c > 0.85$ and $n > 0.2$. The proportionality constant K_s can be determined directly if the rotational speed of the mixer is chosen as $N = 1$.

This analogy has also been applied to the differential-speed, twin-blade mixing torque rheometers used to measure the changes occurring during mixing and processing of dough, thick pastes and polymeric materials by considering the mixing blades to be two adjacent cylinders (Blyler & Daane 1967; Goodrich & Porter 1967; Lee & Purdon 1969; Menjivar *et al*. 1990; Bousmina *et al*. 1999). In this situation, the measured torque on the drive shaft is a combination of the torques from the two elements where, according to conservation of energy (neglecting energy dissipation), for any type of fluid:

$$\Omega_d M_d = \Omega_s M_s + \Omega_f M_f \tag{4.20}$$

where d refers to the drive shaft, and s and f refer to the slow and fast blades, respectively. However, in the case of a power law type fluid, the torque is not proportional to the angular velocity, but the relationship is as given below.

$$\frac{M_f}{M_s} = \left(\frac{\Omega_f}{\Omega_s}\right)^n \tag{4.21}$$

The drive/driven gear ratio, b, and the driven blade speed are then used to determine the final relationships of the torque to the angular velocity for each blade. Inputting the results into equation (4.22), Bousmina *et al*. (1999) obtained the following expression for determining the effective blade radius in a twin-blade mixer using a Newtonian or power law fluid with known properties:

$$R_{b,equ} = \frac{R_c}{\left[1+\frac{2\Omega_d}{n}\left(2\pi h R_c^2 m \frac{(1+b^{n+1})}{M_d}\right)^{1/n}\right]^{n/2}} \tag{4.22}$$

where the shear rate has been determined at the average radius $r = (R_{b,equ}+R_c)/2$ and the value of n has been predetermined from the slope of ln M versus ln N.

In the case of a fluid with a yield stress, σ_o, the situation becomes more complicated. There are three possible scenarios.

1. The yield stress is not overcome anywhere in the fluid and there is no motion.
2. The yield stress is overcome in only part of the flow.
3. The yield stress is overcome everywhere in the fluid, so all the fluid is moving.

The vane method for yield stress determination uses the point of transition between scenarios 1 and 2. In such case, assuming that the yield surface is the cylinder cut out by the blades, it has been shown that for the vanes with four or more blades (Yoshimura & Purd'homme 1987; Steffe 1996):

$$M_o = \frac{\pi d}{2}\left(\frac{h}{d}+\frac{1}{6}\right)\sigma_o \tag{4.23}$$

where M_o is the torque required to overcome the yield stress, d is the diameter of the cylinder cut out by the vane and as the top of the vane is in level with the fluid surface, there is no top end effect. The 1/6 factor can vary; so for the most accurate yield stress determination, tests with varying vane heights should be done and the yield stress can be determined from the slope of M_o versus h (Steffe 1996).

4.5.2 Mixer rheometry applications

Flow curves from such geometries may correspond satisfactorily with the Couette-determined equivalents in the creeping flow regime (Figure 4.10). Obtaining rheological

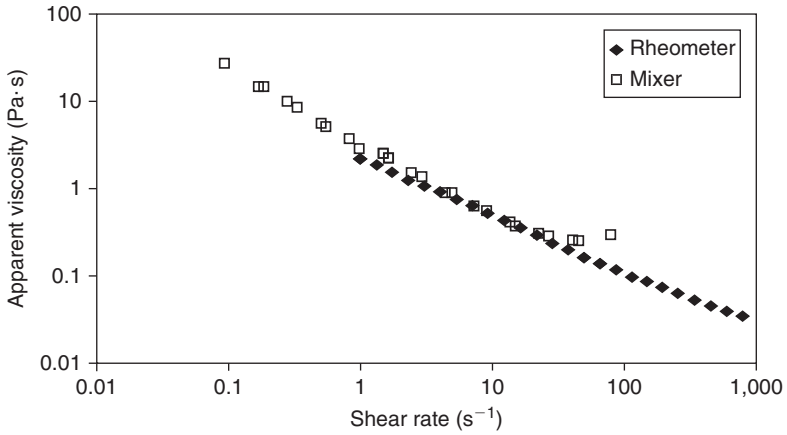

Fig. 4.10 Apparent viscosity versus shear rate for fruit pulp samples as determined from a helical ribbon mixer and rheometer.

measurements using mixer geometries offers numerous benefits in fluid food analysis, facilitating improved product characterisation and the provision of previously unmeasurable data.

Choplin (2000) employed such geometries combined with a rheometer (termed rheoreactor) to track the structural evolution during both emulsification and ice cream manufacturing process. In the emulsification application, a helical ribbon mixer geometry connected to a rheometer, coupled with a high stress device to mimic a standard reactor, provided macromixing and rheological fluid analysis. This technique allowed monitoring of viscosity evolution, which was evaluated at an effective shear rate. The structural build-up of ice cream was monitored in the ice cream manufacturing process application, using a close clearance helical ribbon, during foaming and freezing in a reactor. The procedure allowed the monitoring of the evolution of the mechanical spectrum (G′, G″) of the product as freezing proceeded by intermittingly carrying out oscillation tests during macromixing. Vivar-Vera *et al*. (2008) studied the evolution of the rheological properties of chocolate mass during conching using a mixing rheometry approach. Nachbaur *et al*. (2001) examined the evolution of cement and tricalcium pastes from mixing to setting using dynamic mode rheology data obtained using a helical ribbon geometry connected to a rheometer. They concluded that the main evolution of structure in the products occurs within a few minutes post mixing. Analysis in this period is unattainable with conventional geometries due to the time delay encountered in sample presentation.

Mixing geometries may also be used with less sophisticated instrumentation such as the common Brookfield viscometer. Dolan and Steffe (1990) and Steffe *et al*. (1989) used such a viscometer coupled with a flag impeller to examine the rheological behaviour of gelatinising starch solutions carried out under continual mixing conditions.

Owing to the complex nature of many foods, only empirical testing devices have proven capable of characterizing these composite products. Such instruments are widely used within the food industry (Steffe 1996) and a number of instruments are based on measuring torque developed due to rotating elements, including dough mixers (Farinograph and Mixograph), gelatinisation effects (Visco-Amylograph, Rapid Visco Analyser) and pastes (Brabender FMC Consistometer). Efforts have been made to determine the average shear rates and apparent viscosity for some of these instruments using mixer viscometry methods

(Wood & Goff 1973; Lai *et al*. 2000) with some success. Menjivar *et al*. (1990) were able to calibrate various paddle geometries in a C.W. Brabender Do-corder using the Couette analogy (Goodrich & Porter 1967) in order to predict the flow properties of fruit pastes that were difficult to measure in a standard rotational rheometer due to the presence of seeds. Aerts and Verspaille (2001) utilised the Couette analogy of Bousmina *et al*. (1999) to produce flow curves from a C.W. Brabender Viscograph. This absolute data compared favourably with a concentric cylinder rheometer, with a maximum deviation of only 4% in flow curves. Such an approach allows the instrument to quote in absolute rather than empirical units.

A commercial mixer torque rheometer (Caleva MTR, Caleva Process Solutions, UK) was developed and was proven popular for rheological monitoring of wet masses. The technique has been found capable of quantifying the effects of formulation including substrate source, binder type and concentration (Parker & Rowe 1991, Parker *et al*. 1991, 1992; Hancock *et al*. 1994) and processing effects (Janin *et al*. 1990). A more detailed review of the technique is given by Rowe and Parker (1994) and Rowe (1996).

The effects of rheological properties on mixing may be used to predict flow patterns, mixing times and power requirements within mixing vessels. Rheological data have been used widely to predict power requirements in mixing vessels for Newtonian and shear thinning fluids which lend themselves to characterisation by conventional geometries. However, for more rheologically complex media such as concentrated solid–liquid suspensions, difficulties were reported in determining meaningful data from concentric cylinders due to gap effects (Edwards *et al*. 1986; Edwards & Jomha 1987). In an effort to overcome such problems with shear thickening suspensions, Jomha *et al*. (1990) used helical ribbon and anchor geometries which were geometrically similar to full-scale mixing devices, coupled with rotational viscometry. Such geometries proved successful in predicting power consumption with the ratio to measured power close to unity. They concluded that fairly accurate power consumption data for mixing vessels may be obtained by replacing the bob of Couette geometries with an impeller of geometrical similarity.

Sestak *et al*. (1982) used a small-scale anchor impeller with a rheometer to develop a technique to facilitate torque predictions for the mixing of inelastic thixotropic fluids. Cheng's thixotropy model was successfully applied in the calculation of impeller torque-time variations resulting from arbitrary past deformation history of a thixotropy material within a mixing process.

Hugelshoffer *et al*. (2000) studied the rheological and structural changes occurring during the mixing of suspensions and emulsions. A helical ribbon was attached to a rheometer allowing phase interactions and surfactant influences to be described in terms of their effect on representative viscosity of the mixture. Evaluation of plug flow was also described during the mixing process for high-suspension concentrations.

Such techniques could be used to optimise impeller design, predict power requirements and analyse mixing performance for rheologically complex fluids. Benefits from scaled-down experiments include ease of impeller geometry variation, reduced product volumes combined with increased measurement sensitivity from viscometers/rheometers and improved temperature control.

4.6 Conclusion

This chapter has highlighted the research that has been done and the theory that has been developed in order to understand and utilise the effect of rheology on mixing. Not only is

mixing used in food processing to distribute the ingredients throughout the material being mixed, but it is also used to build structure by inputting energy and enhance the chemical reactions taking place as the ingredients interact. The rheology of the fluid phases can change the effectiveness of a given geometry to cause these required mixing outcomes. Also, the rheology has effects on the power input required and torque generated to turn the mixing elements during the mixing process. These effects, once understood, can then be used to determine the rheological properties, and more importantly, follow the evolution of the rheological properties throughout the mixing process.

References

Aerts, L. & Verspaille, M. (2001). Absolute rheometry in Brabender Viscograph by mixer viscometry calibration. *Starch*, **53**, 59–63.

Amanullah, A., Hjorth S.A. & Nienow, A.W. (1997). Cavern sizes generated in highly shear thinning viscous fluids by Scaba 3SHP1 impeller. *Transactions of the Institution of Chemical Engineers*, **C75**, 232–238.

Anderson, P.D., Galaktionov, O.S., Peters, G.W.M., van de Vosse, F.N. & Meijer, H.E.H. (2000). Mixing of non-Newtonian fluids in time-periodic cavity flows. *Journal of Non-Newtonian Fluid Mechanics*, **93**, 265–286.

Anderssen, R.S., Gras, P.W. & Mac Ritchie, F. (1998). The rate-independence of the mixing of wheat flour dough to peak dough development. *Journal of Cereal Science*, **27**, 167–177.

Arratia, P.E., Kukura, J., Lacombe, J. & Muzzio, F.J. (2006). Mixing of shear thinning fluids with yield stress in stirred tanks. *AIChE Journal*, **52**(7), 2310–2322.

Baloch, A., Grant, P.W. & Webster, M.F. (2002). Parallel computation of two-dimensional rotational flows of viscoelastic fluids in cylindrical vessels. *Engineering Computations*, **19**(7–8), 820–853.

Barnes, H.A. & Carnali, J.O. (1990). The vane-in-cup as a novel rheometer geometry for shear thinning and thixotropic materials. *Journal of Rheology*, **34**, 841–866.

Barnes, H.A. & Walters, K. (1985). The yield stress myth? *Rheologica Acta*, **24**(4), 323.

Bertrand, F., Tanguy, P.A. & Brito de la Fuente, E. (1996). A new perspective for the mixing of yield stress fluids with anchor impellers. *The Canadian Journal of Chemical Engineering*, **74**, 51–58.

Binding, D.M., Couch, M.A., Sujatha, K.S. & Webster, M.F. (2003). Experimental and numerical simulation of dough kneading in filled geometries. *Journal of Food Engineering*, **58**(2), 111–123.

Blyler, L.L. & Daane, J.H. (1967). An analysis of Brabender torque rheometer data. *Polymer Engineering & Science*, **7**(7), 178–181.

Bousmina, M., Ait-kadi, A. & Faisant, J.B. (1999). Determination of shear rate and viscosity from batch mixer data. *Journal of Rheology*, **43**, 415–433.

Carreau, P.J., Chabra, R.P. & Cheng, J. (1993). Effect of rheological properties on power consumption with helical ribbon agitators. *AIChE Journal*, **39**, 1421–1430.

Castell-Perez, M.E. & Steffe, J.F. (1992). Using mixing to evaluate rheological properties. In: *Viscoelastic Properties of Food* (eds A.M. Rao & J.F. Steffe). Elsevier Applied Science Publishing Ltd, Barking, England, pp. 247–284.

Castell-Perez, M.E., Steffe, J.F. & Moreira, R.G. (1991). Simple determination of power law flow curves using a paddle type mixer viscometer. *Journal of Texture Studies*, **22**, 303–316.

Choplin, L. (2000). *In situ* rheological follow-up of food processes: application to emulsification and ice cream fabrication processes. In: *Proceedings of the 2nd International Symposium on Food Rheology and Structure*, Zurich, Switzerland (eds P. Fisher, I. Marti & E.J. Windhab), pp. 63–68.

Connelly, R.K. & Kokini, J.L. (2003). 2-D numerical simulation of differential viscoelastic fluids in a single-screw continuous mixer: application of viscoelastic finite element methods. *Advances in Polymer Technology*, **22**(1), 22–41.

Connelly, R.K. & Kokini, J.L. (2004). The effect of shear thinning and differential viscoelasticity on mixing in a model 2D mixer as determined using FEM with particle tracking. *Journal of Non-Newtonian Fluid Mechanics*, **123**, 1–17.

Connelly, R.K. & Kokini, J.L. (2006a). 3D numerical simulation of the flow of viscous Newtonian and shear thinning fluids in a twin sigma blade mixer. *Advances in Polymer Technology*, **25**(3), 182–194.

Connelly, R.K. & Kokini, J.L. (2006b). Mixing simulation of a viscous Newtonian liquid in a twin sigma blade mixer. *AIChE Journal*, **52**(10), cover, 3383–3393.

Connelly, R.K. & McIntier, R. (2008). Rheological properties of yeasted and non-yeasted wheat dough developed under different mixing conditions. *Journal of the Science of Food and Agriculture*, **88**, 2309–2323.

Couch, M.A. & Binding, D.M. (2003). An experimental study of the peeling of dough from solid surfaces. *Journal of Food Engineering*, **58**(4), 299–309.

Couerbe, G., Fletcher, D.F., Xuereb, C. & Poux, M. (2008). Impact of thixotropy on flow patterns induced in a stirred tank: numerical and experimental studies. *Chemical Engineering Research and Design*, 42.

Cullen, P.J. & O'Donnell, C.P. (2003). Viscosity of suspensions and concentrates. In: *Encyclopedia of Agricultural, Food, and Biological Engineering* (ed. D.R. Heldman). Taylor & Francis, London.

Cullen, P.J., O'Donnell, C.P. & Houska, M. (2003). Rotational rheometry using complex geometries – a review. *Journal of Texture Studies*, **34**(1), 1–20.

Delaplace, G., Leuliet, J.-C., Ronse, G. (2000). Power requirement when mixing a shear-thickening fluid with a helical ribbon impeller type. *Chemical Engineering & Technology*, **23**(4), 329–336.

Dolan, K.D. & Steffe, J.F. (1990). Modeling rheological behaviour of gelatinizing starch solutions using mixer viscometry data. *Journal of Texture Studies*, **21**, 265–294.

Don, C., Lichtendonk, W.J., Plijter, J.J., Vliet, T.V., Rob, J. & Hamer, R.J. (2005). The effect of mixing on glutenin particle properties: aggregation factors that affect gluten function in dough. *Journal of Cereal Science*, **41**, 69–83.

Edwards, M.F. & Jomha, A.I. (1987). *Dispersions and Emulsions*. Institute of Chemical Engineering, Delft, Netherlands.

Edwards, M.F., Godfrey, J.C. & Kashani, M.M. (1976). Power requirement for the mixing of thixotropic fluids. *Journal of Non-Newtonian Fluid Mechanics*, **1**, 309–322.

Edwards, M.F., Jomha, A.I., MacSporran, W.C. & Woodcock, L.V. (1986). The power requirement for mixing concentrated solid/liquid suspensions. Institution of Chemical Engineers Annual Research Meeting, 14–15 April, Bradford, UK.

Elemans, P.H., Bos, H.L., Janssen, J.M.H. & Meijer, H.E.H. (1993). Transient phenomena in dispersive mixing. *Chemical Engineering Science*, **48**, 267.

Elson T.P. (1990). The growth of caverns formed around rotating impellers during the mixing of a yield stress fluid. *Chemical Engineering Communications*, **41**, 2555–2562.

Elson, T.P., Cheesman, D.J. & Nienow, A.W. (1986). X-ray studies of cavern sizes and mixing performance with fluids possessing a yield stress. *Chemical Engineering Science*, **41**(10), 2555–2562.

Fan, Y.R., Tanner R.I. & Phan-Thien, N. (2000a). A numerical study of viscoelastic effects in chaotic mixing between eccentric cylinders. *Journal of Fluid Mechanics*, **412**, 197.

Faubion, J.M. & Hoseney, R.C. (1989). The viscoelastic properties of wheat flour doughs. In: *Dough Rheology and Baked Products Texture* (eds H. Faridi & J.M. Faubion). Van Nostrand, Reinhold, New York.

Galindo, E. & Nienow, A.W. (1993). The performance of the Scaba 6SRGT agitator in the mixing of simulated xanthan gum broths. *Chemical Engineering & Technology*, **16**, 102–108.

Goodrich, J.E. & Porter, R.S. (1967). A rheological interpretation of torque-rheometer data. *Polymer Engineering & Science*, **7**(1), 1–7.

Hancock, B.C., York, P. & Rowe, R.C. (1994). An assessment of substrate binder interactions in model wet masses. 1. Mixer torque rheometry. *International Journal of Pharmaceutics*, **102**, 167–176.

Hanselmann, W. & Windhab, E. (1999). Flow characteristics and modelling of foam generation in a continuous rotor/stator mixer. *Journal of Food Engineering*, **38**, 393–405.

Hoseney, R.C. & Rogers, D.E. (1990). The formation and properties of wheat flour doughs. *Critical Reviews in Food Science and Nutrition*, **29**, 73–93.

Hugelshofer, D., Windhab, E.J. & Wang, J. (2000). Rheological and structural changes during the mixing of suspensions and emulsions. *Applied Rheology*, **10**(1), 22–30.

Inoue, K., Song, Y.X., Kamiunten, O., Oku, J., Terao, T. & Fugii, K. (2002). Effect of mixing method on rheological properties of alginate impression materials. *Journal of Oral Rehabilitation*, **29**, 615–619.

Janin, V., Parker, M.D. & Rowe, R.C. (1990). Monitoring production scale granulation process using an instrumented mixer torque rheometer. *STP Pharma Sciences*, **6**, 233–237.

Jomha, A.I., Edwards, M.F. & Woodcock, L.V. (1990). New method for predicting the power requirement for mixing shear thinning suspensions. *Chemical Engineering Science*, **45**(5), 1389–1396.

Kilborn, R.H. & Tipples, K.H. (1972). Factors affecting mechanical dough development. I. Effect of mixing intensity and work input. *Cereal Chemistry*, **49**, 34–47.

Lai, K.P., Steffe, J.F. & Ng, P.K.W. (2000). Average shear rates in the rapid visco analyser (RVA) mixing system. *Cereal Chemistry*, **77**(6), 714–716.

Lee, G.C.N. & Purdon, J.R. (1969). Brabender viscometry: 1. Conversion of Brabender curves to Instron flow curves. *Polymer Engineering & Science*, **9**(5), 360–364.

Lee, L., Ng, P.K.W., Whallon, J.H. & Steffe, J.F. (2001). Relationship between rheological properties and microstructural characteristics of nondeveloped, partially developed, and developed doughs. *Cereal Chemistry*, **78**(4), 447–452.

Lee, S., Ng, P.K.W. & Steffe, J.F. (2002). Effects of controlled mixing on the rheological properties of deep fat frying batters at different percent solids. *Journal of Food Process Engineering*, **25**, 381–394.

Maingonnat, J.F., Muller, L. & Leuliet, J.C. (2005). Modelling the build-up of a thixotropic fluid under viscosimetric and mixing conditions. *Journal of Food Engineering*, **71**, 265–272.

Manas-Zloczower, I. & Feke, D.L. (1989). Agglomerate rupture in linear flow fields. International Polymer Processing, **IV**, 3–8.

Manohar, R.S. & Rao, P.H. (1997). Effect of mixing period and additives on the rheological characteristics of dough and quality of biscuits. *Journal of Cereal Science*, **25**, 197–206.

Martínez-Padilla, L.P. & Quemada, D. (2007). Baffled cup and end-effects of a vane-in-a-large cup rheometer for Newtonian fluids. *Journal of Food Engineering*, **80**, 24–32.

Menjivar, J., Connelly, R.K. & Hsu, K. (1990). Application of a mixing recorder to determine fundamental rheological properties of food materials. *Proceedings of the 5th International Congress on Engineering & Food*, Cologne, FRG, 28 May–3 June 1989, pp. 49–58.

Metzner, A.B. & Otto, R.E. (1957). Agitation of non-Newtonian fluids. *AIChE Journal*, **3**(1), 3–10.

Morrison, F.A. (2004). What is rheology anyway? *The Industrial Physicist*, **10**(2), 29–31. http://www.aip.org/tip/INPHFA/vol-10/iss-2/p29.html

Nachbaur, L., Mutin, J.C., Nonat, A. & Choplin, L. (2001). Dynamic mode rheology of cement and tricalcium silicate pastes from mixing to setting. *Cement and Concrete Research*, **31**, 183–192.

Niederkorn, T.C. & Ottino, J.M. (1993). Mixing of a viscoelastic fluid in a time-periodic flow. *Journal of Fluid Mechanics*, **256**, 243.

Pakzad, L., Ein-Mozaffari, F. & Chan, P. (2008a). Using computational fluid dynamics modeling to study the mixing of pseudoplastic fluids with a Scaba 6SRGT impeller. *Chemical Engineering Process*, doi:10.1016/j.cep.2007.12.003.

Pakzad, L., Ein-Mozaffari, F. & Chan, P. (2008b). Using electrical resistance tomography and computational fluid dynamics modeling to study the formation of cavern in the mixing of pseudoplastic fluids possessing yield stress. *Chemical Engineering Science*, **63**, 2508–2522.

Parker, M.D. & Rowe, R.C. (1991). Source variation on the wet massing (granulation) of some microcrystalline celluloses. *Powder Technology*, **65**, 273–281.

Parker, M.D., York, P. & Rowe, R.C. (1991). Binder–substrate interactions in wet granulation II. The effect of binder molecule weight. *International Journal of Pharmaceutics*, **72**, 242–249.

Parker, M.D., York, P. & Rowe, R.C. (1992). Binder–substrate interactions in wet granulation III. The effect of substrate source variation. *International Journal of Pharmaceutics*, **80**, 179–190.

Prakash, S. & Kokini, J.L. (2000). Estimation and prediction of shear rate distribution as a model mixer. *Journal of Food Engineering*, **44**, 135.

Rao, M.A. (1975). Measurement of flow properties of food suspensions with a mixer. *Journal of Texture Studies*, **6**, 533–539.

Rao, M.A. (2007). *Rheology of Fluid and Semisolid Foods*, 2nd edn. Springer, New York.

Rao, V.K., Mulvaney, S.J. & Dexter, J.E. (2000). Rheological characterization of long- and short-mixing flours based on stress-relaxation. *Journal of Cereal Science*, **31**, 159–171.

Rieger, F & Novak, V. (1973). Power consumption of agitators in highly viscous non-Newtonian liquids. *Transactions of the Institution of Chemical Engineers*, **51**, 105–111.

Ross, K.A., Pyrak-Nolte, L.J. & Campanella, O.H. (2006). The effect of mixing conditions on the material properties of an agar gel—microstructural and macrostructural considerations. *Food Hydrocolloids*, **20**, 79–87.

Rowe, R.C. (1996). Mixer torque rheometry – further advances. *Pharmaceutical Technology Europe*, **8**(8), 38–48.

Rowe, R.C. & Parker, M.D. (1994). Mixer torque rheometry – an update. *Pharmaceutical Technology Europe*, **6**(3), 24–27.

Scanlon, M.G. & Zghal, M.C. (2001). Bread properties and crumb structure. *Food Research International*, **34**, 841–864.

Schluentz, E.J., Steffe, J.F. & Ng, P.K.W. (2000). Rheology and microstructure of wheat dough developed with controlled deformation. *Journal of Texture Studies*, **31**, 41–54.

Sestak, J., Houska, M. & Zitny, R. (1982). Mixing of thixotropic fluids. *Journal of Rheology*, **26**(5), 459–475.

Sestak, J., Zitny, R. & Houska, M. (1986). Anchor-agitated systems: power input correlation for pseudoplastic and thixotropic fluids in equilibrium. *AIChE Journal*, **32**, 155–158.

Shamlou, P.A. & Edwards, M.F. (1985). Power consumption of helical ribbon mixers in viscous Newtonian and non-Newtonian fluids. *Chemical Engineering Science*, **40**(9), 1773–1781.

Solomon, J., Elson, T.P. & Niewnow, A.W. (1981). Cavern sizes in agitated fluids with a yield stress. *Chemical Engineering Communications*, **11**, 143–164.

Steffe, J.F. (1996). *Rheological Methods in Food Process Engineering*, 2nd ed. Freeman Press, Michigan.

Steffe, J.F., Castell-Perez, M.E., Rose, K.J. & Zabik, M.E. 1989. Rapid testing method for characterizing the rheological behaviour of gelatinizing corn starch slurries. *Cereal Chemistry*, **66**, 65–68.

Sujatha, K.S., Webster, M.F., Binding, D.M. & Couch, M.A. (2003). Modeling and experimental studies of rotating flows in part-filled vessels: wetting and peeling. *Journal of Food Engineering*, **57**(1), 67–79.

Tanguy, P.A., Bertrand, F. & Brito de la Fuente, E. (1994). Mixing of viscoplastic fluids with anchor impellers. *Chemical Engineering Symposium Series*, 525–532.

Vivar-Vera, G., Torrestiana-Sanchez, B., Monroy-Rivera, J.A. & Brito de la Fuentel, E. (2008). Chonching – rheological and structural changes of chocolate mass. *Deutsche Lebensmittel-Rundschau*, **104**(8), 376–382.

Wang, J., Zhao, M. & Zhao, Q. (2007). Correlation of glutenin macropolymer with viscoelastic properties during dough mixing. *Journal of Cereal Science*, **45**, 128–133.

Weegels, P.L., Hamer, R.J. & Schofield, J.D. (1997). Depolymerisation and re-polymerisation of wheat glutenin during dough processing. II. Changes in composition. *Journal of Cereal Science*, **25**, 155–163.

Wichterle, K. & Wein, O. (1981). Threshold of mixing of non-Newtonian fluids. *International Chemical Engineering Journal*, **21**, 116–120.

Wilkens, R.J., Miller, J.D., Plummer, J.R., Dietz, D.C. & Myers, K.J. (2005). New techniques for measuring and modeling cavern dimensions in a Bingham plastic fluid. *Chemical Engineering Science*, **60**, 5269–5275.

Wood, F.W. & Goff, T.C. (1973). The determination of effective shear rate in the Brabender Viscograph and in other systems of complex geometries. *Staerke*, **25**, 89–91.

Yoshimura, A.S. & Prud'homme, R.K. (1987). Response of an elastic Bingham fluid to oscillatory shear. *Rheologica Acta*, **26**, 428–436.

Zhou, G., Tanguy, P.A. & Dubois, C. (2000). Power consumption in a double planetary mixer with non-Newtonian and viscoelastic materials. *Transactions of the Institution of Chemical Engineers*, **78**, 445–453.

Zounis, S. & Quail, K.J. (1997). Predicting test bakery requirements from laboratory mixing tests. *Journal of Cereal Science*, **25**, 185–196.

5 Equipment design

David S. Dickey

5.1 Introduction

The equipment used for food mixing can be either application specific or general purpose. Unique design challenges apply to food mixing where food properties such as texture, flavour, shelf-life, and safety must be considered. The equipment must handle different rheological properties and still be effectively cleaned. Although categorisation of mixing equipment is difficult, some mixers are used primarily for either liquids or powders, whereas others are employed for combinations of liquids and powders.

This chapter will focus on the range of mixers employed in typical food processing applications. However, unique products or processes may necessitate the use of customised mixers. Manufacturers of food mixing equipment range from major food application focused companies to independent fabricators that make both common and specialized mixers. All types of mixers work for some applications, but choosing the best mixer with the most appropriate features is more likely to give optimum results. Other equipment, such as pumps, grinders, and even packaging equipment, may provide some degree of mixing. Additionally, mixing equipment must operate safely and without mechanical failures to be a success.

5.2 Liquid mixing equipment

Liquid mixing applications include everything from water-like to high viscous formulations.

5.2.1 Portable mixers

The most common industrial mixer is the ubiquitous portable mixer. As with most food mixing equipment, basic design criteria include stainless steel wetted parts and stainless housings, or painted surfaces resistant to corrosion resulting from frequent cleaning. Portable mixers are available in different sizes. Small, fractional power mixers with small impellers and high motor speeds are used in small containers, and for laboratory applications. Larger portables with motors as large as 2.2 kW have gear reduced speeds with larger impellers and can handle sizeable batches of liquid, depending on fluid viscosity and mixing requirements. These larger mixers may be portable, but only with the assistance of a crane or other lifting devices.

An adjustable mounting is a common feature of portable mixers, allowing the mixer to be angled both vertically and horizontally. This flexibility facilitates mixing in different size tanks, which have various support characteristics. For instance, tanks made of polymer materials are not likely to provide sufficient rigidity for attaching a mixer directly to the tank wall. Similarly, the depth and diameter of the tank could require adjustment of the mixer shaft angle for optimum mixing.

Contrary to a common misconception, a strong surface vortex does not provide good mixing. As tanks mixed with portable mixers rarely have baffles to control swirling, the adjustable mounting is available to create the best flow pattern for the application. A strong or deep surface vortex probably indicates that the tank contents are swirling in a circular pattern, resulting in solid-body rotation with poor mixing. A swirling flow pattern does not provide good movement from the top to the bottom or from the centre to the sides of the tank. Typically, swirling will allow solids to settle at the centre of the tank. Proper mounting of a portable mixer can more than double the effectiveness of the mixer.

The angled offset of the portable mixer is typically about 15° from the vertical; consequently, the impeller is located in the same half of the tank from which the mixer is mounted. Most portable mixers have a shaft and impeller that rotate clockwise, when viewed from behind the motor.

When mounted with the shaft aimed across the centre of the tank, the rotation of the impeller creates an inherent flow pattern with a clockwise rotation (Figure 5.1). Typically, the impeller is either a marine-style propeller or a hydrofoil impeller which creates an axial flow. By angling the portable mixer far enough to the right of the tank centreline, the resultant axial flow can counteract the induced flow and even create an opposite rotation, shown as 'induced flow' in Figure 5.1. Optimum mixing is usually created when the axial flow counteracts the inherent rotation, resulting in little, if any, vortex on the surface. This condition gives good top-to-bottom motion in the tank.

Where powders or immiscible liquids are added on the liquid surface, an inherent swirl may be advantageous in creating more surface motion. However, only a moderate surface vortex is required. A strong vortex extending to the impeller region is not desirable from either a mechanical or processing perspective. A vortex to the impeller is likely

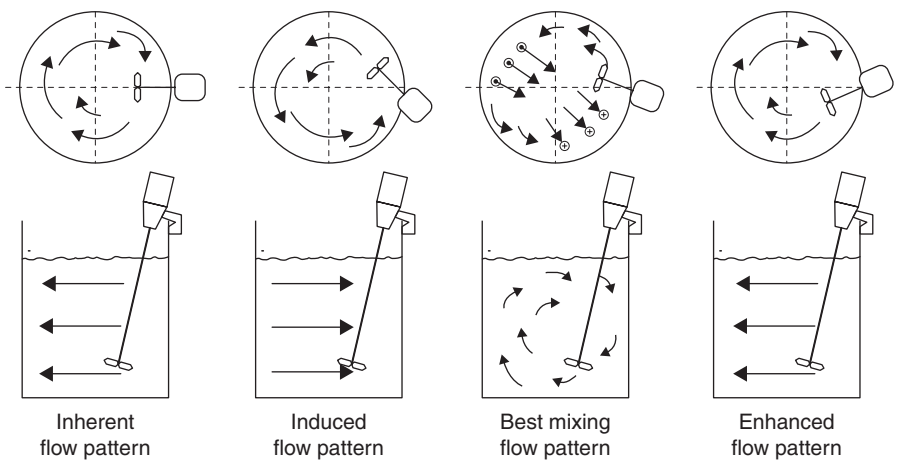

Fig. 5.1 Portable mixer flow patterns.

to cause excessive loads on the mixer shaft and mountings. A deep vortex will also draw air bubbles into the product, which will reduce the mixing effectiveness. Swirling may be advantageous for the mixing of viscous fluids. With high-viscosity fluids (>1,000 mPa s), vortexing becomes less of a problem. In such cases, 'enhanced flow' pattern, shown in Figure 5.1, may be optimal.

5.2.2 General purpose liquid mixers

For larger tanks and batches with a range of viscosities, various types of vertical, centre-mounted mixers are commonly used. For lower viscosities, typically <1,000 mPa s, tanks have wall baffles to prevent or limit the swirling created with centre-mounted mixers. Mixer tanks can be short or tall, with a wide range of diameters. Typically, a cover with an opening to facilitate the addition of ingredients is employed to reduce contamination. The internals of the typical food mixer can have a single shaft with single or multiple mixing impellers, or may have multiple shafts and impellers, to provide different mixing capabilities.

One of the most common and versatile mixing impellers is the pitched-blade turbine impeller (Figure 5.2). The pitched-blade impeller is both easy to manufacture and effective for a wide range of mixing applications. Typically, such impellers have four blades, made of flat plates, mounted at 45º angle, with blade width approximately one-fifth of the impeller diameter. The impeller is rotated to pump downward, which requires clockwise rotation as shown in Figure 5.2a. The down-pumping flow in a baffled tank creates good fluid motion along the bottom of the tank with circulation up the sides and back to the impeller. Motion across the tank bottom helps to prevent particle settling. The straight-blade turbine impeller (Figure 5.2b) creates radial flow. Radial flow is less effective for bulk mixing, but may be appropriate for dispersion or high-power input applications. The straight-blade or pitched-blade impellers may be placed close to the bottom of a tank to ensure adequate mixing during filling or emptying. Hydrofoil impellers (Figure 5.3) are effective for the bulk blending of liquids and the suspension of solids in liquids. Strong axial flow and a low power number create effective motion across the bottom of the tank and good circulation.

Comparisons of impeller efficiency are rather difficult, as different impeller designs are appropriate to particular applications. However, comparisons can be made by considering mixing effectiveness for impellers, when rotated at the same speed with the same power input. To achieve the same power input, the pitched-blade impeller must be larger than the straight-blade impeller and the hydrofoil impeller must be larger than either of the other

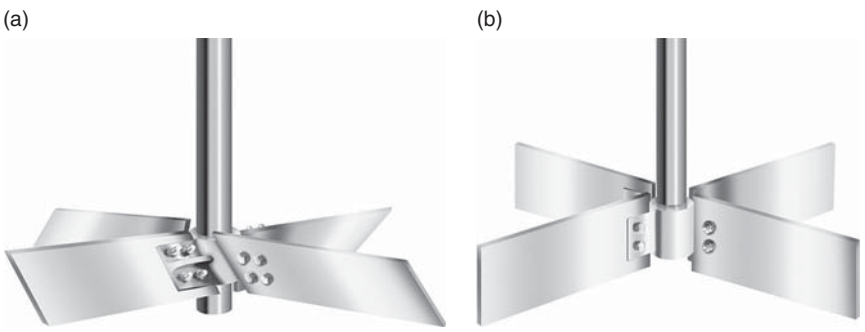

Fig. 5.2 (a) Pitched-blade turbine impeller (b) straight-blade turbine impeller. (Courtesy of Chemineer, Inc.)

Fig. 5.3 Hydrofoil mixing impeller. (Courtesy of Lightnin, SPX Corporation.)

impellers. For such a comparison to be valid, the ratio of impeller diameter to tank diameter should be between 0.2 and 0.6.

Operating an impeller at the same speed and same power means that it is also operating at the same torque. Equal torque is usually a better performance criterion than equal power for similar blending intensity. A small impeller at a higher speed would be expected to give similar mixing intensity as a large impeller at a lower speed. However, the smaller impeller would be expected to require a higher power input than the larger impeller, but both would require nearly the same torque. While power is a measure of operating cost, torque is essentially a measure of capital cost. Higher torque means a larger drive, shaft diameter and impeller. For the same torque, a pitched-blade impeller will provide greater mixing intensity than a straight-blade impeller. Comparatively, a hydrofoil impeller provides greater intensity than a pitched-blade impeller.

In food mixing applications, ease of cleaning is paramount. For most food applications, polished stainless steel is the material of choice for both tanks and mixers. Typically, more complicated impellers are required to handle a wider range of process conditions such as viscosity changes or batch levels. In general, process requirements guide the selection of mixing equipment for specific applications.

5.2.3 Mixer shafts design

Sufficient mechanical strength is the first design criterion for a mixer shaft. To avoid fatigue failure, the stresses in the shaft should be kept to levels well below the yield point, where a shaft might bend. To calculate both tensile and shear stress within the shaft, the torque and bending loads on the shaft must be estimated.

The most common liquid mixers have an overhung shaft, supported only at the top for a top-mounted mixer. For a constant shaft diameter, the point of greatest stress occurs at the lower drive bearing, which supports the mixer shaft. The maximum torque on the mixer shaft can be calculated as follows.

$$\tau = 9.55\frac{P}{N} \tag{5.1}$$

Where τ (N m) is the torque, P (W) is the motor power, and N (rpm) is the rotational speed.

Note that the motor power, and not the impeller power, is used in this equation. The assumption is that through some combination of density, viscosity, or any other upset

Table 5.1 Hydraulic force factors, f_{Hi}.

Condition	Turbine impeller	Hydrofoil impeller
	Four blades, pitched or straight	Three or four blades or marine propeller
Normal operation	1	1.5
Operation at the liquid level	2.0–3.0	2.5–3.5
Operation in boiling liquid	1.5–2.5	2.0–3.0
Operation in gas sparged systems	2.0–3.0	2.5–3.5
Large volume additions of powders	3.0–5.0	3.0–5.0

condition, all of the motor power could be applied to the mixer shaft irrespective of the power required by the impeller(s) for the design conditions.

Calculation of the bending moment on the shaft is a more complicated affair, as an estimate of the lateral hydraulic loads on the impeller or each of multiple impellers is necessary. These loads must be applied at the impeller location(s) on the shaft. If a single impeller is mounted on the shaft, all of the motor power could be delivered at that location, and only the distance from the drive to the impeller is important. If multiple impellers are on the same shaft, the motor power must first be distributed between the impellers, and then the distance to each impeller is considered in calculating the total bending moment. If two similar impellers are mounted on a single shaft, then half the motor power can be assigned to each of them. If the impellers are of different size or type, then the power for each must be calculated, and the motor power is distributed proportionately between them. For instance, if the bottom impeller requires twice the power of the upper impeller, then two-thirds of the motor power should be assigned to the lower impeller and one-third to the upper impeller. The same splits in the motor power distribution apply to other multiple impeller combinations. The following equation provides an estimate of the bending moment for typical mixing impellers:

$$M = \sum_i \frac{2.88 P_i L_i f_{\mathrm{Hi}}}{N D_i} \tag{5.2}$$

where M (N m) is the bending moment, P_i (W) is the fraction of motor power, L_i (mm) is the shaft length to the ith impeller, N (rpm) is the rotational speed, and D_i (mm) is the diameter of the ith impeller. The hydraulic force factor, f_{Hi}, depends on the application and the impeller type. Some typical values for the hydraulic force factor are listed in Table 5.1.

From a calculation for the maximum torque and an estimate of the total bending load on the shaft, shear and tensile stresses can be calculated:

$$\sigma_{\mathrm{s}} = \frac{16\sqrt{\tau^2 + M^2}}{\pi\left(\frac{d}{1000}\right)^3} \tag{5.3}$$

where σ_{s} is the shear stress (N/m^2) and d is the shaft diameter (mm).

The tensile stress σ_t (N/m^2) is calculated as follows.

$$\sigma_t = \frac{16\left(M + \sqrt{\tau^2 + M^2}\right)}{\pi\left(\frac{d}{1000}\right)^3} \tag{5.4}$$

To avoid fatigue failures in stainless steel shafts, the shear stress is typically limited to less than 40×10^6 N/m^2 and the tensile stress is limited to less than 70×10^6 N/m^2. Higher stress values may eventually result in a fatigue failure of the shaft near the drive support. Welded couplings, machined steps, keyways, or other modifications to the mixer shaft can result in failure at lower stress levels.

While high stress levels in a mixer shaft may cause the shaft to break, operating near a natural frequency or critical speed may cause the shaft to bend. Care must be taken to avoid operating a mixer near the first natural frequency of the shaft. The second natural frequency is rarely a problem. The vibration associated with the natural frequency is like the vibration of a tuning fork, but on a larger scale and at a lower frequency. The weight and length of the shaft, the weight of the impeller, along with the elastic modulus of the metal in the shaft, determine the natural frequency.

To estimate the natural frequency of a mixer shaft, the weight of the impeller(s) must be known or accurately estimated. If multiple impellers are on the same shaft, the weight of the upper impeller(s) can be resolved to end of the mixer shaft, using the following formula:

$$W_e = \sum_i W_i (L_i / L)^3 \tag{5.5}$$

where W_e is the equivalent weight (kg) at the end of the shaft of length L (mm) from the lower support bearing. The summation is for multiple impellers, with weights, W_i, and lengths, L_i, from the support bearing. The equivalent weight of the mixer shaft will also be resolved to the end of the shaft, using the density of stainless steel, the shaft diameter, and length. The following is the formula for the critical speed, N_C, in revolutions per minute (rpm).

$$N_C = \frac{5.185 \times 10^4 d^2}{L\sqrt{L + S_b}\sqrt{W_e + 1.54 \times 10^{-6} d^2 L}} \tag{5.6}$$

The equivalent weight from equation (5.5), along with the shaft length, L, shaft diameter, d, and the spacing between the support bearings, S_b, with all of these lengths in millimetres, provides an estimate for the critical speed.

Operating a mixer at speeds within 15% above or below this critical speed can cause serious vibrations, even to the point of bending or breaking the mixer shaft. Most mixers operating below a speed of about 125 rpm are usually below the first natural frequency of the shaft. Higher speed mixers may operate above the first natural frequency. When starting or stopping a mixer operating above critical speed, the shaft speed usually changes at a sufficient rate to ensure that vibrations at the natural frequency do not cause serious mechanical problems. However, operating the same mixer with a variable speed drive can cause problems, if the adjusted operating speed is near the natural frequency. For that reason,

electronic variable speed drives often prevent operation within a certain frequency or speed range, to avoid natural frequency problems.

5.2.4 Other mechanical design considerations

By knowing the torque and bending loads on the mixer shaft, other mechanical design requirements can be established. Bending load calculations can be employed to design the blade thickness for impeller blades. Torque calculations may also be used to estimate the loads on tank baffles. For design purposes, all of the torque input by the mixer must be balanced by the forces on the tank baffles.

At a more practical level, torque and bending loads must be known or specified to design a mounting structure for the mixer. Whether the mixer is supported from beams or on a tank nozzle, the support must be sufficiently strong and rigid. Strength is an obvious requirement; however, stiffness is usually found to be a more restrictive parameter. A support structure or tank nozzle may not break with a little flexibility, but only minor movement at the support can cause a long mixer shaft to move significantly. To prevent the mixer from moving too much, the support can be designed for higher loads, thus providing sufficient stiffness. Designing the support for 2.5 times the torsional load [calculated in equation (5.1)], and 3.0 times the bending load [calculated in equation (5.2)], should provide sufficient stiffness for the mixer mounting.

The selection criteria for a mixer drive, typically a gear reducer, includes not only the appropriate speed reduction from the motor speed to the mixer speed, but also power, torque, and bending. The power rating must be sufficient to handle the full motor power. The output shaft and bearings for the drive must be sufficient to handle the torque [equation (5.1)] and the bending load [equation (5.2)]. Power ratings, torque, and bending loads are specified by the gear drive manufacturers.

Electric motors must be suitable for the application. If the area is subject to frequent wash-downs, then a wash-down duty motor will be necessary. If flammable vapours or powders are handled near the mixer, explosion-proof motors are necessary.

The design and specification of all aspects of a mixer must be considered for safe and durable operation. For more information on the mechanical design of mixing equipment, see Dickey and Fasano (2004).

5.2.5 Special purpose liquid mixing equipment

Some types of liquid mixing equipment are used for specific types of applications. Typically, these applications require more than just liquid blending.

5.2.5.1 *Disperser-type mixers*

Disperser-type mixers generally fall into two categories, rotor–stator dispersers and open-style dispersers. Both rely on high rotational speeds, or more specifically, on high peripheral speeds, with impellers that create high velocity gradients in the liquids and low liquid flow rates. Unlike the mixing impellers discussed earlier, which produce bulk fluid motion to achieve uniformity, the high-shear dispersers create local conditions, near the impeller, that disperse liquids or powders into the surrounding liquid. Mixers designed for liquid uniformity are commonly used for miscible liquids, suspension of wetable or predispersed solids, or gas dispersion. When it comes to dispersing two-phase liquids, especially for emulsions, or dispersing difficult-to-wet powders, the mixers that create good liquid

uniformity may not provide sufficient local intensity for effective dispersion. Where intense local dispersion is required, disperser mixers are necessary.

Rotator–stator mixers have a rapidly rotating impeller inside a stationary housing with slots or holes through which the dispersion must pass. The types of impellers and housings can take many different forms (Figure 5.4). Usually, liquids, and solids if present, are drawn up under the rotor (rotating impeller) and then forced through the holes or slots in the stator (stationary portion of the head). By having the inlet on the underside of the head, air is less likely to be drawn down from the surface. The direction of flow into the impeller region may have advantages or disadvantages, depending on the application. When dispersing two-phase liquids, as in oil–water applications, drawing from below the impeller to prevent air entrainment may be preferable to avoid trapped air bubbles. For a powder dispersion, the ability to draw flow from above may help pull powder down from the surface, and into the disperser head. Different mixers have different capabilities, depending on auxiliary impellers and/or shafts that can rotate in either direction.

Most of the dispersion by the rotator–stator occurs in the fluid, and not as a direct result of contact with the metal surfaces. The tips of the impeller blades rotate more rapidly than the surrounding fluid, resulting in rapid acceleration into the impeller region. The motion of the impeller results in local velocity differences around each blade, creating eddies and flow patterns with more velocity gradients. A small gap between the rotating blade and the stationary housing creates a high velocity gradient in the fluid. Further, as the fluid flows through the slots or holes in the stator, acceleration and deceleration occurs. Finally, the flow-out through the slots or holes is at a velocity greater than the surrounding fluid, which also creates gradients and turbulence in the fluid.

Because of the complicated flow patterns and the typically complicated mechanisms required to achieve dispersion, testing with a specific mixer design is necessary. Usually, some combination of formulation and mixing intensity is required to achieve the desired result. Viscosity differences and interfacial tension influence liquid–liquid dispersion mixing. Wetting characteristics and particle interactions influence solid–liquid dispersion mixing.

Sometimes, a high-speed rotating blade is sufficient to accomplish dispersion. The height, number, and angle of the teeth determine the local velocity gradients and fluid pumping capacities. All applications require some combination of flow and shear; flow to move the surrounding fluid through the intense shear around the tips of the impeller blade.

In all cases, the disperser blades present some compromise in their ability to blend the bulk liquid effectively. As a liquid or dispersion becomes more viscous, bulk motion is reduced because of either liquid properties or the resulting dispersion. To handle situations where both dispersion and bulk motion are required, combinations of mixing devices are

Fig. 5.4 Rotor–stator disperser heads. (Courtesy of Silverson Machines Inc.)

encountered. Some mixers have a combination of a high-shear disperser and a high-flow or a high-viscosity impeller, such as those mentioned in the previous section.

5.2.5.2 *External re-circulation loops*

Generally, pumping liquid through an external loop and back into a tank is an ineffective and an unreliable way of mixing the liquid in the tank. The flow pattern in the tank is uncertain, which often results in short-circuiting from the inlet to the outlet. However, even with a good flow pattern, the amount of power required during pumping is typically 5 to 10 times the power required for the same amount of flow produced by mixing. If a different process function, such as rapid mixing or heat transfer, can be accomplished in the re-circulation loop, then a benefit may arise. For dispersion, the inclusion of an inline mixer in the re-circulation loop (Figure 5.5) may aid processing. Most inline mixers of this type have some pumping capabilities, but are limited to low-viscosity fluids with low flow and head requirements. Centrifugal pumps may also provide some inline dispersion capability.

5.2.5.3 *Powder addition*

Mixing devices may be designed specifically for powder addition to a liquid (Plate 5.1). Introducing dry powder directly into a region of rapid dispersion can eliminate or greatly reduce the formation of partially wetted powder agglomerates. As a rapidly rotating impeller can create a low-pressure region near the centre, dry powder can be fed directly into the powder–liquid dispersion point, as shown in the cut-away. This type of powder addition disperser can be used with fresh liquid feed or re-circulated liquid, as depicted in the re-circulation loop (Figure 5.5).

5.2.5.4 *Liquid–liquid dispersion*

For liquid–liquid dispersion, a rapidly rotating impeller may not be the most effective way of producing a fine dispersion. A valve homogeniser (Plate 5.2) forces a high-pressure

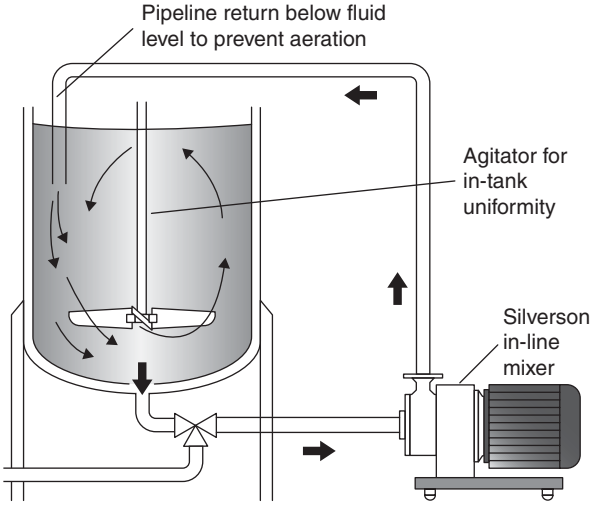

Fig. 5.5 Re-circulation loop with high-shear inline mixer. (Courtesy of Silverson Machines Inc.)

Fig. 5.6 Static mixer—sanitary. (Courtesy of Chemineer, Inc.)

liquid steam through a small gap, generating shear, impact on a ring, along with a rapid pressure change. The combined effect of the forces acting on the liquid–liquid combination passing through the homogeniser creates a fine dispersion. Although this process is often used in homogenising milk, it can be applied to other oil–water combinations also.

5.2.5.5 *Static mixers*

Other inline mixing capabilities, either in a re-circulation loop or transfer piping, can be provided by a static or motionless mixer (Figure 5.6). A static mixer has vanes or obstructions, called elements, which are designed to re-direct and divide the flow in a way that creates mixing. The mixing can be accomplished in either turbulent or laminar flow, depending on the type or length of the static mixer. A typical static mixer for a food application will have removable elements for cleaning and inspection and may have sanitary clamp connections for easy removal.

5.2.6 Food specific mixing equipment

Food mixing has some specific and unique applications, such as bread making, which are handled by special mixing equipment. Such special mixing equipment may be selected because of the mixing characteristics, past practices, or cleaning features. Some past practices have their origins in manual food handling practices that have evolved through the development of home kitchen equipment and subsequently modified for industrial applications. Often, these adaptations have attempted to duplicate home cooking on an industrial production scale.

Even the basic kitchen blender may be employed in industrial applications, especially at the bench-scale development stage. While providing the same mixing characteristics as found in many homes, duplication of the maximum mixing intensity is nearly impossible on an industrial scale. The power levels and the dispersion capability of a standard kitchen blender are rarely found anywhere in volumes larger than a few litres, and almost never in large food operations. The closest approach to such intensities is an inline, high-shear mixer, like the one in the re-circulation loop in Figure 5.5. The biggest problem with development using bench-scale blenders is that the products produced on the laboratory bench may have totally different characteristics than those produced with the same ingredients in production mixing equipment. The mixers used to develop a product should be as geometrically and operationally similar as possible to the available production mixers. The process of scale-up and development cannot be treated independently, especially when it comes to mixing. A significant amount of mixing technology is related to scale-up, because the many variables and responses expected from mixing are nearly impossible to predict without some experimentation. More information about scale-up and development testing can be found in Chapter 6.

The mixing motion created by catering scale food mixers is called planetary motion. The paddle rotates about its own axis at a relative high speed, while the axis of rotation for the paddle, rotates around the centre of the bowl. The rotation about two different axes is effective in not only mixing ingredients locally, but also in bringing ingredients from the perimeter of the bowl to the centre. Mixing equipment of this type can handle products from dry powder ingredients like flour and sugar, to liquid ingredients like milk, water, and oil. The capacity to handle batters and doughs, which have viscous or visco-elastic characteristics, along with air incorporation requires challenging mixer design. Simple rotational motion is not sufficient.

One of the unique mixing problems in food processing is the preparation of bread dough. Although bread making has been around for thousands of years, during most of that time, the kneading of dough has been an entirely manual operation. However, with bread making becoming much more of a large-scale industrial process, the kneading has taken on larger proportions. An industrial bread dough mixer (Plate 5.3) creates the kneading and stretching action by the rotation and crossover of bars inside a tub. A ball of dough is cut by the passing bars and in the process stretched to develop the gluten and distribute the leavening.

Other specific types of mixing equipment are employed in applications such as candy making, where taffy pullers, coating equipment, and other special purpose devices perform different types of ingredient or product mixing.

5.3 Powder mixing equipment

5.3.1 Ribbon blenders

Ribbon blenders are probably the most widely used powder blenders in the food industry. Although not necessarily the most effective blender for all types of powder blending, they are sufficiently versatile to allow for the successful production of many different types of blends. Ribbon blenders work best with free-flowing or slightly cohesive powders. Wet compacting powders may stall a ribbon blender, especially if the blender must be re-started during the blending process.

Ribbon blenders have helical-shaped metal blades attached to a horizontal rotating shaft. The outer pairs of blades or ribbons push material in one direction, while a second, or sometimes third, pair of blades mounted inside the first, pushes the material in the opposite direction. The direction for the ribbons is determined by the twist, or hand, of the helical blades. Blenders with a centre discharge will have pairs of outer ribbons, each pair pushing towards the centre of the blender, with inner ribbons pushing towards the ends. A blender with an end discharge will have a single pair of outer ribbons pushing towards the discharge end and an inner ribbon pushing in the opposite direction. Pushing is not an entirely adequate description for the action of the blades in a ribbon blender. The blades will push the powder material causing bulk motion, but they also cut through the material, causing relative displacement and dispersion. The combined action of bulk motion, division followed by displacement, and counter-current motion within the blender, causes mixing to take place.

The time required for complete blending after the addition of the final material should be no more than 10–15 min, and often only about 5 min. Failure to achieve a uniform blend in 10 min is usually a result of overfilling a ribbon blender. For good blending, the top edge of the ribbons should break the surface of the powder in the blender. The blender capacity stated by most manufacturers is the volume to the top of the ribbon. For best results, the blender should be filled to just over the horizontal shaft, with ribbons coming up and out of the powder; otherwise, the powder at the vertical wall of the trough may not be well

blended. Often, product quality and blending efficiency can be improved by making two well-sized batches, rather than one over-filled batch. An under-filled blender, especially a batch that does not fully engage the inner ribbon, can also be difficult to mix uniformly.

5.3.2 Paddle blenders

Paddle blenders are generally similar to ribbon blenders, except that the continuous ribbons are replaced by segmented paddles. Paddle blenders are used with free-flowing and moderately cohesive powders. In addition to handling wetter, more cohesive powders than ribbon blenders, paddle blenders aerate free-flowing powders more than ribbon blenders. The paddles can be slanted in different directions and extended to different distances from the rotating shaft, creating a complicated mixing pattern.

As for ribbon blenders, the advantages and disadvantages of paddle blenders depend on powder characteristics and application. Generally, paddle blenders reach a final blend faster than a ribbon blender, but the degree of uniformity may be slightly less. Paddle blenders are more practical for abrasive powders, where paddles may be designed for replacement. Paddle blenders are more likely to be applied in continuous blending applications than ribbon blenders. Transport in a paddle blender can be in alternating directions for more diffusive mixing.

5.3.3 Combination blenders

Several types of combination blenders are also available, combining the best features of various blender designs. A combination ribbon–paddle blender (Figure 5.7) has a continuous ribbon inside the paddles. The paddles operate near the bottom and sides of the blender trough. The ribbon provides bulk flow to ensure that all of the material passes through the paddle blades. The paddles randomise the blend effectively.

A fluidising paddle blender (Figure 5.8) uses the rotating paddles to aerate or fluidise powder for effective particle dispersion. For free-flowing powders, this fluidisation gives a more rapid and uniform blend than with most other types of horizontal rotating-shaft blenders. Multiple-shaft fluidising paddle blenders are used in some industrial applications. Many other types of industrial blenders may be employed in food processing, provided appropriate materials of construction and cleaning capabilities are considered.

Fig. 5.7 Combination ribbon–paddle agitator. (Courtesy of American Process Systems, Eirich Machines, Inc.)

Trough-type blenders can be used for either batch or continuous processing. Although the trough shape remains the same, the ratio of length to width may be different for a batch or continuous operation (Figure 5.9). Batch blenders are usually shorter and wider than continuous blenders, for the same volume. Actual blend times in batch processes are typically 3–10 min, depending on the blender type and the powder characteristics. The residence time in a continuous blender is usually only 1–3 min, again depending on the process requirements.

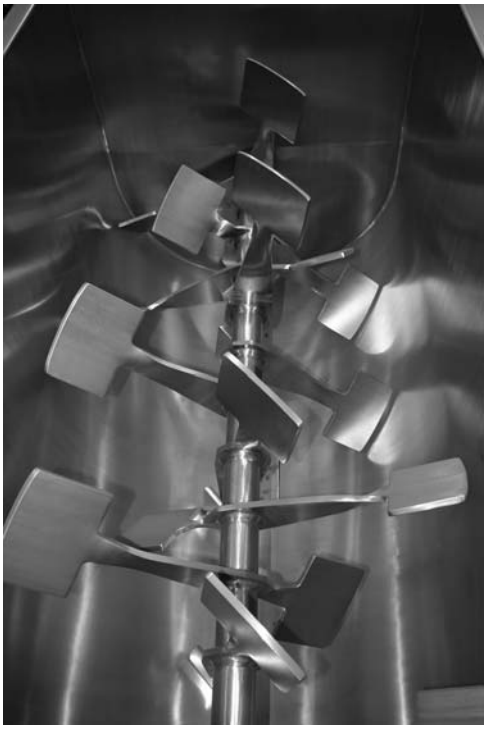

Fig. 5.8 Paddle fluidizing paddle agitator. (Courtesy of American Process Systems, Eirich Machines, Inc.)

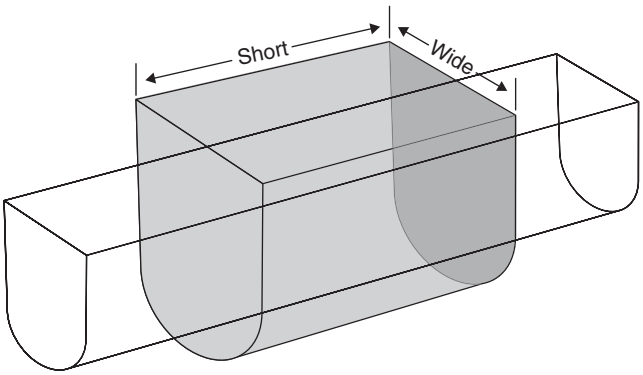

Fig. 5.9 Different blender shapes for batch or continuous blending.

5.3.4 Tumble blenders

Tumble blenders are applicable only to free-flowing powders. Types of tumble blenders include V-type, also called twin-shell blenders, double-cone blenders, and horizontal-drum blenders. Each type has advantages and limitations. The biggest advantage of most tumble blenders is that they may have few internal components and are therefore easy to empty and clean. Along with easy cleaning, the blending can be extremely uniform. With internal dispersers or nozzles, liquid addition is possible, but only if the powder remains free flowing. A limitation may be that each size blender has effectively only one useful capacity. The rated blender capacity of a tumble blender is usually half the actual volume of the blender. Over-fill and under-fill situations significantly reduce the effectiveness of the blending. Tumble blenders often require more room, especially headroom, than horizontal blenders, like ribbon and paddle blenders. Tote-type tumble blenders take advantage of the combined features of storage, blending, and handling in the same container. Tote-type blenders are of limited capacity, partly because of standard handling dimensions, but also because they must be only about half-full to allow sufficient room for effective blending. When overfilled, tumble blenders of all types fail to effectively mix the centre of the batch.

5.3.5 Loading and emptying blenders

Loading and emptying operations are important for the overall performance of all types of powder blenders. In most cases of batch blending, powder is added into the blender, either from bulk containers, bags, or other pre-weighed containers, depending on the batch size or individual ingredient quantities. For rotating-shaft blenders, such as ribbon or paddle blenders, powders are usually added with the blender running to avoid high loads associated with the starting of a filled blender. The addition of powders into an operating blender has potential safety risks and should be carried out with appropriate guards and ventilation. Bag dump stations ensure both safety and ventilation during loading of blenders.

Order and rate of addition are also important. Usually the major ingredient is added first, followed by secondary or minor ingredients, and liquids, when required. Staggered additions over time while the blender is operating or addition to multiple locations if the blender is stationary are recommended to minimise the formation of segregated regions. Pre-blending of minor ingredients with other ingredients is recommended, especially where the minor ingredient is less than 0.5%, so that the concentration will be at least a couple of percent of the pre-blended batch.

Loading a blender for continuous operation usually involves some type of conveyor. In most food applications, the feeder is a pneumatic or belt-type device, depending on the powder properties and capacity requirements. Secondary or minor ingredients should be metered into the blend using some type of weigh or screw feeder. Similarly, any liquid feeds must be monitored and controlled. Continuous operation requires greater control, but significantly increases blender capacity.

Emptying a blender should be carried out as soon as possible, once the blending process is finished. Excessive processing may result in over-blending and attrition. A delay in emptying after processing may result in compaction, which may affect discharge or segregation due to environmental vibrations. Usually, emptying a blender in continuous operation requires another conveying method to transport the product to packaging or further processing.

5.3.6 Liquid addition to powders

The simplest but least effective method of liquid addition is to pour a liquid ingredient into an operating blender, such as a ribbon or paddle blender. The important characteristic of any liquid addition is to ensure that liquid is added to moving powder and not to the blender surface. Ideally, the liquid should be sprayed or dispersed onto moving or aerated powder. Surface spray can be accomplished with a nozzle or series of nozzles. Diaphragm or peristaltic pumps can be used for a variety of liquids. A pressurised can with a dip tube may be simpler, less expensive, and easier to clean than a pump. Many tumble blenders have disperser bars or other high-speed devices to both aerate powders and disperse liquids. Viscous liquids can be difficult to disperse but may be easier to add when heated or diluted with an appropriate solvent. High-speed choppers may be used to break up any undesired agglomerates formed by the addition of liquids.

5.3.7 Sampling

Sampling a blender to identify an incomplete blend is usually done either at the outlet of the blender or at a poorly blended location in the blender. As many powders blend quickly, significant blending may occur while starting and stopping the blender to take a sample. For safety, samples should never be taken while the blender is operating. Although bulk samples may appear well blended, corners of the blender, around blender seals, or near the axis of rotation may not be adequately blended; samples and testing should focus on such locations. In a ribbon blender, poor blending is likely to be found at the corners of the blender, at the ends near the centre, at the walls of the trough if powder sticks, and along the centre shaft where ribbon supports and low velocities may create regions with slow mixing.

5.3.8 Safety

Safety is an important consideration in all types of mixing and blending equipment, especially with rotating-shaft powder blenders. Open access to the rotating components should be restricted. All blenders should be covered, at least with grates for loading or viewing. Most covers are provided with electric interlock switches to stop the blender when the cover is open or the grate is removed. Similar interlocks are needed to prevent close contact with rotating tumble blenders. Although adequate to prevent accidental contact with rotating equipment, these switches are not adequate for servicing or cleaning the blender. Appropriate lock-out and tag-out procedures must be followed to prevent serious injury.

5.3.9 Blending systems

There is a trend in industry towards integrated blending systems, where material handling, blending, and even packaging may be combined into a single package. Powder blending operations are more likely to experience problems than liquid systems, due to the unpredictability of powder characteristics. No blender type is suitable for all applications. Pilot testing is recommended to select the most appropriate system for a given application.

5.4 Equipment components

Several components are common to most mixers, whether they are used for liquids or powders. Electric motors, speed reducers, and shaft seals are used in most types of food mixers.

5.4.1 Electric motors

Electric motors drive most types of food mixers, sized appropriately for scale and rheological properties. Motors may be specifically designed for application in hazardous environments, including flammable or explosive concerns arising from volatile vapours or fine dust.

5.4.2 Speed reducers

Speed reducers are used in most industrial-size mixers to provide higher torque and more effective mixing action. Torque is a measure of the extent of rotating force that a mixer can apply to the fluid or powder being mixed. In many ways, the amount of torque that a mixer delivers is a better measure of its mixing capability than the power of the mixer. In simplest terms, torque is power divided by speed. Speed reducers are essential constant power, torque increasing devices. For example, reducing the rotational speed from a motor to a mixer with a gear drive with a 5:1 ratio will increase the torque by a factor of five, usually delivering that level of additional mixing. Loss of power due to friction or other resistances will be converted to heat. Even the effects of mixing will result in the conversion of all dissipated power into heat. Heat build-up may be either a problem or an advantage in viscous situations such as dough mixing.

The most common form of speed reduction used in food mixers is a gear reducer, as they are compact, enclosed, and relatively trouble free. Gear drives can be either inline or parallel-shaft types, where the input and output shafts are along the same axis of the drive. Some drives are right-angled, where the output shaft is at 90º to the input shaft. Each type of drive has practical advantages for a specific mixer. The internal gearing is chosen to provide the required amount of speed reduction for the specific type of mixer.

Mixers, especially powder mixers, may use either belt or chain drives. These drives also reduce the rotational speed to achieve more effective mixing. For small speed reductions, especially at higher torque, belt or chain drives can be less costly than relative capacity gear drives. Because belt and chain drives are external parts, proper guards are essential for safe operation of a mixer. In all cases, guards protecting rotating shafts or other parts of a mixer should be in place when the mixer is in operation.

5.4.3 Seals

Shaft seals and rotating seals keep food products separate from mechanical components. Static seals keep food products separate from the environment. Various kinds of simple seals are used in food applications to keep products clean and safe besides avoiding damage to mechanical equipment. Important seals are those around rotating shafts in both liquid and powder mixers.

Nomenclature

D	impeller diameter (mm)
D_i	diameter of the ith impeller (mm)
d	shaft diameter (mm)
f_{Hi}	hydraulic force factor (dimensionless)
L	shaft length (mm)
L_i	shaft length to the ith impeller (mm)
M	bending moment (N m)

N	rotational speed (rpm)
P	motor power (W)
P_i	fraction of motor power at the ith impeller (W)
S_b	bearing spacing for shaft support (mm)
W_e	equivalent weight of impellers at the end of the shaft (kg)
W_i	actual weight of ith impeller (kg)

Greek letters

π	pi (3.14159)
σ_s	shear stress (N/m^2)
σ_t	tensile stress (N/m^2)
τ	torque (N m)

References

Dickey, D.S. & Fasano, J.B. (2004). Mechanical design of mixing equipment. In: *Handbook of Industrial Mixing Science and Practice* (eds E.L. Paul, V.A. Atiemo-Obeng & S.M. Kresta). John Wiley & Sons, Inc., Hoboken, NJ, pp. 145–256.

6 Mixing scale-up

David S. Dickey

6.1 Introduction

Mixing scale-up is an empirical process that begins when the first ingredient is chosen and continues until a successful process is in production. Scale-up is repeated as recipes or ingredients change. The purpose of scale-up is to develop a process or product in an equipment size and ingredient quantity that is easily, quickly, and inexpensively managed. The challenge is to scale up the equipment and ingredients to an effective size for production, while duplicating the results obtained during development. Mixing scale-up should not be treated as an afterthought, but must be studied and tested during the development process.

Most of the guidance for mixing scale-up depends on the characteristics of the mixing process. Mixing equipment can be used to handle single-phase liquids for simple blending, multiphase immiscible liquids for dispersions or emulsions, solid–liquid systems for suspensions or dissolution, and powder-blending applications. Each type of application may have different requirements for scale-up, and within each classification, multiple scale-up options may be considered. No matter how desirable, scale-up cannot duplicate all the characteristics of a small-scale development process, but instead typically holds a single essential mixing characteristic constant. The choice of that important characteristic must be established during development.

6.2 Scale-up for fluid mixing

Scale-up of fluid mixing applications has a technical basis from dimensional analysis and similarity. Fluid properties like density and viscosity can be directly related to aspects of mixing performance. The objective of scale-up is different from either dimensional analysis or similarity, although these methods can be used to guide scale-up decisions.

6.2.1 Dimensional analysis

Dimensional analysis stems from the concept that physical quantities, related as a comparison or equality, must have the same dimensions. Thus, a time and a velocity cannot be added to find a characteristic length. However, different types of forces can be added to represent the total force acting on an object. Physical quantities such as density, velocity, or length can be associated with the dimensions of mass, length, and time, which are typically represented by M, L, and t, respectively. Thus, a velocity has the units of 'length/time' (L/t) and a force can be represented by 'mass $\times$ acceleration' (ML/t^2).

From the idea of dimensional consistency, comes the Buckingham Π theorem, which states that for every physically meaningful relationship involving n variables, there are $n - m$ dimensionless parameters, where m is the number of fundamental dimensions. Working from the Navier–Stokes equation, describing the mass and momentum balance for a Newtonian fluid, three dimensionless groups can be developed for mixing applications.

$$\text{Reynolds number:} \qquad Re \equiv \frac{D^2 N \rho}{\mu} \tag{6.1}$$

$$\text{Froude number:} \qquad Fr \equiv \frac{N^2 D}{g} \tag{6.2}$$

$$\text{Power number:} \qquad Po \equiv \frac{P}{\rho N^3 D^5} \tag{6.3}$$

The Reynolds number is a ratio of inertial to viscous forces, which at large values corresponds to turbulent flow and at low values relates to laminar or viscous flow. The Froude number is a ratio of inertial to gravitational forces, which may describe the magnitude of surface waves or vortex depth in liquid mixing applications. The power number can be developed from a ratio of pressure forces to inertial forces to provide a practical relationship between impeller power, impeller diameter, rotational speed, and fluid density. Although these groups are not often held constant as a means to scale up mixing, they do form the basis for empirical correlations that are not scale dependent. Empirical relationships between power number and Reynolds number have been developed for different types of geometrically similar impellers.

6.2.1.1 *Similarity*

Similarity is developed from physical models and can be extended to mathematical models. The simplest example of a physical model for mixing is a geometrically similar (scale) model of a mixed tank. For geometric similarity to exist, all of the linear dimensions of the small- and large-scale tanks are held to the same ratio, as shown in Figure 6.1. Geometric similarity simplifies scale-up for mixing applications such that the only remaining variable is the rotational speed of the mixer.

Kinematic (motion) similarity is a form of mechanical similarity that exists when corresponding velocities are similar. With kinematic similarity, a flow pattern can be described by dimensionless local velocities. Dimensionless velocity is the actual local velocity divided by a reference velocity. In liquid mixing equipment, this reference velocity is typically related to the impeller tip speed or peripheral velocity. However, use of tip speed is commonly expressed as the product of the rotational speed and impeller diameter, ignoring the constant π.

$$\text{Dimensionless velocity:} \qquad N_v \equiv \frac{v}{ND} \tag{6.4}$$

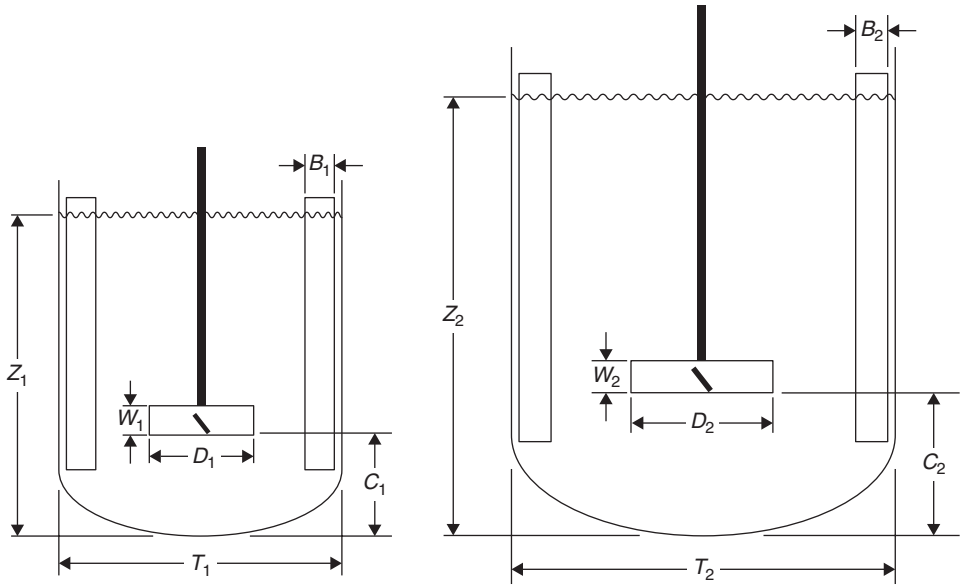

Fig. 6.1 Geometric similarity for mixed vessels.

While the details of local velocities or dimensionless velocities are rarely considered specifically for scale-up, they may be calculated by numerical methods such as computational fluid dynamics (CFD).

The importance of kinematic similarity is less about the ability to estimate local velocities for a specific application and more about the understanding of how similarity can be applied in scale-up. Kinematic similarity exists for fully turbulent mixing in geometrically similar equipment. Thus, observing a flow pattern in a scale model mixing vessel will reveal the anticipated flow pattern in a large-scale vessel. Additionally, kinematic similarity means that all local velocities are in the same proportion to the reference velocity (impeller tip speed). Doubling the impeller tip speed doubles all of the local velocities for a specific mixing vessel geometry. For scale-up, maintaining tip speed in geometrically similar systems will maintain corresponding local fluid velocities. Maintaining flow patterns and velocities can be an effective means of scale-up for fluid mixing. Conditions resulting in effective mixing in a small-scale vessel may be duplicated by maintaining equal velocity on scale-up. On a practical level, equal fluid velocities are typically observed as equal mixing intensity in different size vessels, a characteristic that can be used for scale-up.

Kinematic similarity is not the only form of mechanical similarity that can be important in mixing studies. Dynamic similarity defines conditions where forces are defined with respect to a reference force. Fluid forces can be caused by the pressure differential between the front and back of an impeller blade moving through a turbulent fluid. Other forces on an impeller blade may be caused by viscous drag. The relative importance of pressure or viscous forces depends on the operating conditions for a mixing impeller. Under turbulent conditions, inertial forces or pressure forces dominate, whereas under laminar conditions, viscous forces or drag forces dominate. The relative dominance of these forces can be

defined by the Reynolds number. The ranges for mixing Reynolds numbers are shown in the following equation.

$$\begin{aligned} &\text{Turbulent mixing :} && Re > 20{,}000 \\ &\text{Transient mixing :} && 20{,}000 > Re > 10 \\ &\text{Laminar mixing :} && Re < 10 \end{aligned} \tag{6.5}$$

6.2.1.2 *Applied scale-up*

The important differences between dimensional analysis, similarity, and scale-up are their respective purposes. Dimensional analysis may help in identifying how different variables interact with respect to each other. For instance, Reynolds number shows that trade-offs exist between impeller diameter and rotational speed with respect to fluid density and viscosity. Also, dynamic viscosity and fluid density have opposite effects on the relative magnitudes of inertial and viscous forces. Conditions showing similarity may exist over a range of operating conditions. For instance, the flow pattern in a mixing vessel remains effectively unchanged for fully turbulent conditions at different velocity magnitudes. The flow pattern, represented by the relative magnitude of velocities, remains unchanged, although the absolute magnitudes of the velocities can all change in direct proportion, for turbulent conditions. By comparison, scale-up, typically, has a specific objective. Certain conditions are expected to remain unchanged for the purpose of scale-up. Maintaining a specific velocity, as characterized by an impeller tip speed, is a practical objective for scale-up. Because of kinematic similarity, local fluid velocities remain in constant proportion to other fluid velocities; thus, all fluid velocities are the same at constant tip speed, geometric similarity, and fully turbulent conditions. Scale-up can use similarity and dimensional analysis, but for a specific condition.

Perhaps, the best way to explain these differences is by analogy to a graph (Figure 6.2). Dimensional analysis is like defining the axes of the graphs. The definition is with respect to independent and dependent variables, such as Reynolds number and power number. Impeller power number results are typically reported as a function of Reynolds number. Because Reynolds number describes the relative importance of inertial and viscous forces and power number shows the impeller response to those forces resisting rotation through the fluid, similarity is like a curve on the graph. For a given impeller geometry and geometric similarity, the impeller power number is an empirical function of the impeller Reynolds

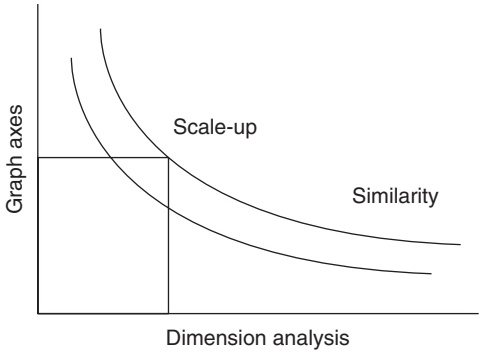

Fig. 6.2 Graphical analogy for dimensional analysis, similarity, and scale-up.

number. For scale-up, a specific condition on the graph is used to predict or maintain a required characteristic. Although constant Reynolds number is never an effective requirement for scale-up, a Reynolds number for any impeller size may be used to find the power number correlation at these conditions.

6.2.2 Scale-up with geometric similarity

Scale-up of a geometrically similar stirred vessel simplifies, because all of the length dimensions of the large-scale vessel are in direct proportion to the small-scale vessel. The only remaining variable for scale-up is the rotational speed of the mixer. Conducting development tests in a vessel that is geometrically similar to the production-scale vessel greatly simplifies many aspects of scale-up. With fully turbulent conditions in the small scale, scale-up will result in the same flow pattern in the large scale. Using a geometrically similar vessel for development—especially, using a similar impeller—avoids many of the problems caused by significant changes in mixing between development and production. Starting with or using a geometrically similar vessel to do development presumes knowledge about the production vessel size and geometry. The scale-up methods associated with non-geometric similarity is demonstrated in the example problem.

One of the biggest problems with conducting small-scale mixing tests is the ability to apply very intense mixing. Typical lab mixers and kitchen blenders have the capability of extremely intense mixing. The Waring® blender is a prime example. The maximum speed on such blenders is capable of producing at least 5 or 10 times the practical power per volume intensity of an industrial mixer. Whatever the mixer type used for development, it should be at least generally similar to the plant equipment, if not ideally geometrically similar. During development testing, mixer speed should be reduced in a series of small increments, by no more than about 10% for each increment, to determine if mixing problems develop.

Geometric similarity scale-up can be reduced to a simple expression of a correction factor for the inverse scale ratio, raised to an exponent, and applied to the successful, small-scale speed.

$$N_2 = N_1 \left(\frac{D_2}{D_1} \right)^{n'} \tag{6.6}$$

The value of the exponent, n, depends on the scale-up characteristic that is to be held constant. To hold the blend time constant with geometric similarity, the exponent is zero, so the speed remains constant.

$$N_2 = N_1 \left(\frac{D_1}{D_2} \right)^{0} = N_1 \tag{6.7}$$

While often interpreted as holding the dimensionless blend time constant, this relationship is also understood from ‘grandma’s’ baking, as a certain number of strokes with a spoon necessary to accomplish a degree of uniformity. To achieve the desired uniformity, a certain number of rotations of the impeller blade is required for a specific geometry, whatever be the rotational speed in turbulent conditions, or at equal Reynolds number in the transition range. The dimensionless blend time is sometimes called the ‘Betty Crocker®’ number. Equal blend time is an extremely difficult and, usually, an impossible scale-up criterion to achieve, as for

turbulent conditions, power increases with the impeller diameter to the fifth power. A tank with twice the volume contains 8 times the liquid, but requires 32 times the power or 4 times the power per volume for an equal blend time. The result of more practical scale-up rules is as reasonably expected; a larger tank takes longer to mix than a smaller tank.

For equal Froude numbers, geometric similarity scale-up has an exponent of one half on the scale ratio.

$$N_2 = N_1 \left(\frac{D_1}{D_2} \right)^{1/2} \tag{6.8}$$

Because Froude number relates inertial forces to gravitational forces, it may represent vortex depth or wave height on the surface of an agitated liquid. For instance, to maintain a vortex depth of one-fourth of the liquid level from the lab scale to the plant scale would require equal Froude numbers with geometric similarity. This scale-up is also extremely difficult and nearly impossible for large-scale changes. The result is that ripple height, when compared with the tank diameter, is typically less in larger tanks. The liquid that might splash out of a container at lab scale may be handled properly in production with geometric similarity and a scale-up based on equal tip speed, which results in a lower Froude number.

Equal power per volume is a practical, though a very conservative, scale-up criterion. For geometric similarity and turbulent conditions, the scale-up exponent for the inverse length ratio is two-thirds, as shown below.

$$N_2 = N_1 \left(\frac{D_1}{D_2} \right)^{2/3} \tag{6.9}$$

A power per volume scale-up might be used for equal mass transfer, especially with gas dispersion or other critical interfacial and reacting applications.

The derivation of the exponent for power per volume serves as an example of how a constant characteristic can be reduced to a speed correction, like in equation (6.6). For turbulent conditions, mixer power is proportional to fluid density, rotational speed cubed, and impeller diameter to the fifth power. Dividing by volume is a practical way of setting power in proportion to the quantity of fluid mixed [equation (6.10)].

$$\frac{\rho N_1^3 D_1^5}{V_1} = \frac{\rho N_2^3 D_2^5}{V_2} \tag{6.10}$$

$$\frac{\rho N_1^3 D_1^5}{T_1^3} = \frac{\rho N_2^3 D_2^5}{T_2^3} \tag{6.11}$$

$$N_1^3 D_1^2 = N_2^3 D_2^2 \tag{6.12}$$

$$N_2 = N_1 \left(\frac{D_1}{D_2} \right)^{2/3} \tag{6.13}$$

Volume for a cylindrical tank is proportional to the tank diameter squared times the liquid depth or tank height. Because all of the geometric ratios are in the same proportion, the volume is proportional to the tank diameter, T, cubed [equation (6.11)]. Further, the tank diameter is also proportional to the impeller diameter, which will cancel a cubed diameter in the equation for equal power per volume [equation (6.12)]. Rearranging the relationship to solve for the large-scale (subscript 2) value of the rotational speed, N, the exponent two-thirds (2/3) appears on the inverse length scale ratio [equation (6.13)]. The dimension used in the length ratio could be impeller diameter, tank diameter, or any other length dimension, because all of the ratios are the same for geometric similarity.

Scale-up for solids suspension is dependent on the properties of the solids being suspended. Hence, the exponent for equal suspension is a variable.

$$N_2 = N_1 \left(\frac{D_1}{D_2} \right)^{m'} \quad \text{where } 1 > m' > 0.5 \tag{6.14}$$

Slowly settling particles are likely to follow the flow of the fluid and may be scaled-up based on equal velocity, $m' = 1$. Rapidly settling particles will require a smaller exponent, approaching power per volume or even equal Froude number in extreme cases. Values for the solids suspension and scale-up exponent are shown in Figure 6.3.

The design settling velocity is the terminal settling velocity for the solids times the density difference, as shown below.

$$u_d = \left(\frac{\rho_p - \rho}{\rho} \right) u_t \tag{6.15}$$

As a rule-of-thumb for a particle size distribution, the settling velocity of the largest 90-percentile particle can be used for an estimate of the terminal settling velocity in the design settling velocity.

Scale-up for equal tip speed has an exponent of 1 on the inverse scale ratio, which with geometric similarity also results in scale-up for equal fluid velocity in turbulent conditions.

$$N_2 = N_1 \left(\frac{D_1}{D_2} \right)^1 \tag{6.16}$$

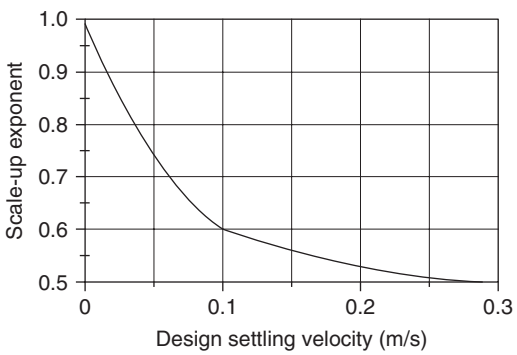

Fig. 6.3 Solids suspension scale-up exponent.

Equal fluid velocity has the effect of what is typically observed in different scale tanks as equal mixing intensity. The velocity of the fluid conveys an appearance of fluid motion and mixing intensity. This intensity does not equate to equal blend time, but rather the type of motion characteristic of adequate mixing for most blending applications. In other words, fluid motion occurs throughout the small-scale tank in much the same way it occurs in the large-scale tank. Equal fluid velocity, or a scale-up exponent of 1, also results in equal torque per volume with geometric similarity. Torque is proportional to power divided by rotational speed. Thus, torque per volume, when re-arranged like power per volume in equation (6.13), results in an exponent of two halves or 1. Equal torque per volume and equal tip speed are not the same for non-geometric similarity, as shown in the non-geometric scale-up example problem.

Equal Reynolds number would result, if the scale-up exponent were set at 2.

$$N_2 = N_1 \left(\frac{D_1}{D_2} \right)^2 \tag{6.17}$$

Although equal Reynolds number seems to result in a similar level of turbulence, it does not provide sufficient fluid motion to assure uniform mixing with any significant scale change. Thus, equal Reynolds number is not a practical scale-up criterion.

All of the practical scale-up rules for geometric similarity scale-up fall between equal tip speed and equal power per volume. The reduction in speed that occurs between the small scale and large scale is maximum for tip speed and minimum for power per volume within that range. The larger reduction in rotational speed, by holding tip speed constant, will result in a smaller large-scale mixer than the smaller reduction in speed for power per volume. However, an added degree of conservatism for the tip-speed scale-up occurs, because the Reynolds number increases. An increased Reynolds number would be equivalent to the capability of handling a higher viscosity, in proportion to the scale change. However, this effect is of little consequence for fully turbulent conditions and significant only when the small-scale tests are conducted at conditions in the transition or viscous range.

As shown in equation (6.9) for equal power per volume and equation (6.16) for equal tip speed, scale-up for geometric similarity requires only an appropriate adjustment in mixer speed, at least for turbulent mixing. The following example shows the differences between tip speed and power per volume as scale-up criteria, and also how calculations can be made to understand the effects on mixer performance.

Suppose we have a simple blending problem and have conducted a bench-scale test. The bench-scale vessel is a vertical cylinder with a flat bottom and four standard baffles. The baffles are vertical plates mounted at the wall of the vessel to prevent uncontrolled swirling of the contents and to help create top-to-bottom motion with a pitched-blade turbine impeller. The bench-scale vessel is 250 mm in diameter with a 250 mm straight side. The bench test was successfully run with a 10 L batch and a single 85 mm diameter pitched-blade turbine impeller, running at 450 rpm. The pitched-blade turbine had four blades, each mounted at 45º, with a blade width of one-fifth of the diameter of the impeller. The power number for such an impeller is 1.37. The liquid in the batch had a viscosity of 10 mPa s, and a density of 1,100 kg/m^3.

Although the dimensions of the vessel and impeller are important, the rotational speed is the variable that characterizes the mixing performance, especially for a geometrically similar scale-up. Because mixing has so many different functions, such as blending, solids

suspension, liquid dispersion, powder incorporation, and many other possible influences and combinations, no single characteristic can be used to quantify mixing performance. Often, the best insight of a mixing problem can be achieved by testing and observing in a transparent vessel. A glass or clear plastic vessel can be a highly effective bench-scale tool for developing and understanding a mixing application.

Some geometric characteristics, such as common length ratios, can help visualize a mixer. Length ratios, such as impeller-to-tank diameter ratio and blade-width-to-impeller diameter ratio, generalise the description of a mixer. Other characteristics, such as Reynolds number, power, torque, and tip speed, can describe aspects of the mixing process. For scale-up, volume-related quantities, such as power per volume and torque per volume, can describe mixing processes even at different scales. For practical calculations using convenient units of measure, correction factors are needed for dimensionless and dimensional results. A calculation for Reynolds number appears as below:

$$Re = \left(\frac{1.67 \times 10^{-5} D^2 N \rho}{\mu} \right) \tag{6.18}$$

where impeller diameter, D (mm), rotational speed, N (rpm), density, ρ (kg/m^3), and viscosity, μ (mPa s), are combined. The conversion factor, 1.67×10^{-5}, is needed only to make the units of the variables cancel. The calculated Reynolds number of 5,973 at bench scale is not fully turbulent, as defined in equation (6.5). For Reynolds numbers greater than about 900, the effect of viscosity on power is negligible for a pitched-blade turbine.

A similar calculation, equation (6.19), for power, P (W), can be developed with a conversion factor and a re-arranged form of the power number, Po, see equation (6.3), which has a dimensionless value of 1.37 for turbulent conditions with a pitched-blade turbine.

$$P = \left(\frac{N_P \rho N^3 D^5}{2.16 \times 10^{20}} \right) \tag{6.19}$$

Whereas power is commonly understood to represent the information necessary to size a motor for a mixer, torque is often a better representation of mixing intensity. Obviously, mixing a tank of liquid with a small impeller operating at a high speed can be expected to give a mixing intensity similar to a large impeller operating at a low speed. When observed with respect to the characteristics commonly viewed as mixing intensity, typically, fluid velocity, equal torque appears to give equal results for different size impellers in the same tank. Thus, torque, τ (Nm), is calculated from the power calculation.

$$\tau = 9.55 \left(\frac{P}{N} \right) \tag{6.20}$$

Other volume-related quantities such as power per volume (W/l) or torque per volume (Nm/L) can be calculated by dividing by the fluid volume (L).

Another variable of potential interest, especially related to drop or particle size in dispersions, is the impeller tip speed, v_t (m/s), which may be calculated as follows.

$$v_t = 5.24 \times 10^{-5} ND \tag{6.21}$$

A summary of these mixing dimensions and characteristics for the bench-scale test conditions is shown in Table 6.1.

Scale-up with geometric similarity to a 1,500 mm diameter production-scale tank requires the application of a 6:1 factor to all of the linear dimensions. Thus, the straight side of the tank becomes 1,500 mm and the baffle width becomes 120 mm. The impeller diameter ranges from 85 mm on the bench to 510 mm in production. With all of the plant-scale equipment dimensions defined by geometric similarity, the remaining variable, rotational speed, is selected to maintain some basic characteristic of mixing, such as tip speed or power per volume. For equal tip speed, the bench-scale rotational speed of 450 rpm is multiplied by the inverse length ratio [equation (6.16)] to obtain a production-scale speed of 75 rpm. The other operating variables of power, power per volume, torque, torque per volume, and tip speed can be calculated as for the bench-scale conditions. These values are listed in Table 6.1. Note that for an equal tip speed of 2.01 m/s, the torque per volume of 0.0060 N m/L is the same for both the bench and plant scales. Tip speed and torque per volume are the same for geometric similarity scale-up, but not for non-geometric scale-up.

Practical, but more conservative, scale-up results can be achieved by changing speed to hold power per volume constant [equation (6.9)]. In this case, the inverse scale ratio raised

Table 6.1 Geometric similarity scale-up example.

Dimensions and results	Bench-scale test conditions	Tip speed scale-up	Power/volume scale-up
Tank diameter (mm)	250	1,500	1,500
Scale ratio	1:1	6:1	6:1
Straight side (mm)	250	1,500	1,500
Actual volume (L)	10	2,160	2,160
Baffle width (mm)	20	120	120
Fluid viscosity (mPa s)	10	10	10
Fluid density (kg/m^3)	1,100	1,100	1,100
Mixer speed (rpm)	450	75	136
Impeller type	Pitched blade	Pitched blade	Pitched blade
Number of blades on impeller	4	4	4
Blade angle (°)	45	45	45
Power number	1.37	1.37	1.37
Impeller diameter (mm)	85	510	510
Impeller-to-tank diameter ratio	0.34	0.34	0.34
Blade width (mm)	17	102	102
Blade width to impeller diameter ratio	0.2	0.2	0.2
Off-bottom (mm)	100	600	600
Reynolds number	5,973	35,835	65,117
Power (W)	2.83	102	611
Power/volume (W/L)	0.283	0.047	0.283
Torque (N· m)	0.060	13.0	42.8
Torque/volume (N· m/L)	0.0060	0.0060	0.0198
Tip speed (m/s)	2.01	2.01	3.65
Motor power (W)	200	750	1,100

to the two-thirds power is multiplied by the bench-scale speed. Thus, 450 rpm is reduced to only 136 rpm, as shown in Table 6.1. With equal power per volume, both the torque per volume and tip speed increase compared to the equal tip speed results, along with the Reynolds number and rotational speed. Although a significant safety margin was used in determining a motor size in Table 6.1, the equal power per volume scale-up would require a larger motor, drive, shaft, and almost every other mixer component, including the price. As a rough guide to mixer cost, torque is closely related to the capital cost of the mixer, whereas power is related to the operating cost.

6.2.3 Scale-up without geometric similarity

Geometric similarity implies strict geometric similarity, especially for a critical variable like impeller diameter, as represented by the impeller diameter to tank diameter ratio. Even small changes in the impeller diameter result in large differences in the mixing intensity, especially when the only compensation is the speed change governed by the rules for geometric similarity. These limitations do not mean that non-geometric scale-up is impossible; it is only that different methods and 'rules' apply. These 'rules' are not exact rules, but rather rules-of-thumb, which can be applied to the calculated values for mixing characteristics.

Although not essential in all cases, a step-by-step method usually works best for scale-up with non-geometric similarity. The method may involve a couple of steps or several steps, depending on the changes in mixer geometry. The method begins with a geometric similarity scale-up from the small-scale test vessel to an equivalent vessel with the proper tank diameter. This step assures a clear understanding of the resulting scale change. After the initial scale change, further changes are usually made in only one variable at a time, such as liquid level, impeller diameter, impeller type, or number of impellers. However, changing multiple geometry and operational variables may keep a combination of characteristics, such as tip speed and torque, constant at the same time. This one-step-at-a-time method allows a check on the adequacy or appropriateness of each change. To explain and illustrate this step-by-step method, an example problem is used. The solution involves more steps than absolutely necessary to achieve scale-up, but the steps demonstrate how either existing or new mixing equipment might be evaluated.

6.2.3.1 *Example of non-geometric scale-up*

Suppose the application is the preparation of a typical water-based acidified sauce. The major liquid ingredients are water, corn syrup, and vinegar. The dry ingredients are maltodextrin (a carrier for the other dry ingredients), salt, citric acid, spices, and other ingredients, including flavourings, starch, gum, and preservatives. The bench-scale batch will be about 10 L with 5.25 L of water, 3.35 L of corn syrup, and 0.97 L of vinegar. The dry ingredients with 1,633 g of maltodextrin, 871 g of salt, 218 g of spices, and 381 g of other ingredients make up the remainder of the batch quantity. The production batch will be about 9,465 L of sauce, with 4,971 L of water, 3,167 L of corn syrup, and 919 L of vinegar as liquids. The dry ingredients will include 1,454 kg of maltodextrin, 824 kg of salt, 206 kg of spices, and 361 kg of other dry ingredients.

The bench-scale vessel is 250 mm in diameter with a 250 mm straight side for the 10 L batch. The production tank is 2,135 mm in diameter with a 2,593 mm straight side for the 9,465 L batch. The bench-scale mixer has a single 120 mm diameter pitched-blade turbine

impeller. The production tank has a mixer with two 865 mm diameter pitched-blade turbine impellers. Thus, the impeller-to-tank diameter ratio in the bench-scale vessel is 0.48, whereas that of the production tank is 0.41. These geometric differences mean that the simple relationships for speed change may not apply or may be appropriate for scale-up. The following step-by-step method for non-geometric scale-up can be used for scale-up to a known equipment design, for the design of new mixing equipment, or for evaluation of alternate mixer modifications.

- The first step is scale-up from the bench-scale mixing results to the plant-scale tank diameter with geometric similarity. This scale-up step will not account for the actual production tank volume, number of impellers, or impeller sizes. These other adjustments will be made in the following steps, with evaluation of several mixing characteristics for each case. The second column in Table 6.2 shows the bench scale, 250 mm vessel diameter, conditions for the sauce recipe, which has a viscosity of about 15 mPa s and a density of 1,090 kg/m^3. The single pitched-blade turbine in the bench scale requires a power of 4.65 W, given a power per volume (W/L) ratio of 0.465. This power translates into a torque of 0.148 N m or a torque per volume of 0.0148 N m/L at a tip speed of 1.89 m/s. Geometric similarity scale-up to a tank diameter of 2,135 mm involves a scale factor of 2,135/250, or 8.54:1. For geometric similarity, the volume is only 6,228 L, which will be adjusted in the next step. For an equal tip speed, the production-scale speed will be 35.13 rpm, with the geometrically similar 1,025 mm diameter impeller. The computed mixing characteristics are shown in the third column of Table 6.2, with the power per volume decreasing from 0.465 to 0.055 W/L, the torque per volume remaining constant at 0.0148 N m/L, and the tip speed remaining at 1.89 m/s.

Table 6.2 Non-geometric scale-up example—single impeller steps.

Dimensions and results	Bench-scale conditions	Geometric scale-up	Increased volume
Tank diameter (mm)	250	2,135	2,135
Straight side (mm)	250	2,135	2,593
Actual volume (L)	10	6,228	9,465
Fluid viscosity (mPa s)	15	15	15
Fluid density (kg/m^3)	1,090	1,090	1,090
Mixer speed (rpm)	300	35.13	35.13
Number of impellers	1	1	1
Impeller type	Pitched blade	Pitched blade	Pitched blade
Power number (each impeller)	1.37	1.37	1.37
Impeller diameter (mm)	120	1,025	1,025
Impeller-to-tank diameter ratio	0.48	0.48	0.48
Blade width (mm)	24	205	205
Blade width to impeller diameter ratio	0.2	0.2	0.2
Off-bottom (mm)	120	1,025	1,025
Reynolds number (either impeller)	5,242	44,771	44,771
Total power (W)	4.65	339	339
Total power/volume (W/L)	0.465	0.055	0.036
Total torque (N· m)	0.148	92.3	92.3
Total torque/volume (N· m/L)	0.0148	0.0148	0.0098
Tip speed (m/s)	1.89	1.89	1.89
Motor power (W)	200	1,100	1,100

- The second step involves increasing the volume in the production-scale tank to the desired capacity of 9,465 L. The large-scale tank has a larger height-to-diameter ratio than the bench-scale vessel, which is common for larger tanks. Taller, more slender tanks can be less expensive to build and easier to ship. Without changing the impeller diameter or operating speed, the mixing power, torque, and tip speed remain unchanged, but the per volume quantities are reduced. Power per volume ranges from 0.055 to 0.036 W/L and torque per volume ranges from 0.0148 to 0.0098 N m/L due to the increased volume. If the mixing requirements were related to some dispersion characteristic, then the tip speed might be the correct characteristic to hold constant. However, if mixing intensity is more important, then equal torque per volume may be appropriate for scale-up.
- The third step will add a second impeller to the mixer shaft. This step will account for the two impellers in the actual production-scale mixer and compensate for the loss in the per volume values of the previous step. When the two impellers are identical in size and type, the power and torque are effectively doubled from the single impeller case. However, to handle all cases, including different impellers, each impeller calculation should be done separately, and the results added together. Unless the impellers are less than half an impeller diameter apart, the individual power values are additive. Closely spaced impellers may require slightly less than the additive powers. The results of the dual impeller case are shown in Table 6.3. In this step, the rotational speed has been kept the same for equal tip speed, but all of the power- and torque-related quantities have doubled from the previous step.
- The fourth step changes from the geometrically similar impeller diameters, at 1,025 mm, to the actual production-scale impeller diameters, at 865 mm. In this step, the tip speed is again held constant, so the smaller impellers require a higher rotational speed

Table 6.3 Non-geometric scale-up example—dual impeller steps.

Dimensions and results	Dual impellers actual volume	Actual impellers equal tip speed	Actual impellers equal torque/volume
Tank diameter (mm)	2,135	2,135	2,135
Straight side (mm)	2,593	2,593	2,593
Actual volume (L)	9,465	9,465	9,465
Fluid viscosity (mPa s)	15	15	15
Fluid density (kg/m^3)	1,090	1,090	1,090
Mixer speed (rpm)	35.13	41.62	46.75
Number of impellers	2	2	2
Impeller type	Pitched blade	Pitched blade	Pitched blade
Power number (each impeller)	1.37	1.37	1.37
Impeller diameter (mm)	1,025	865	865
Impeller-to-tank diameter ratio	0.48	0.41	0.41
Blade width (mm)	205	173	173
Blade width to impeller diameter ratio	0.2	0.2	0.2
Off-bottom—upper impeller (mm)	1,930	1,930	1,930
Off-bottom—lower impeller (mm)	1,025	1,025	1,025
Reynolds number (either impeller)	44,771	37,789	42,449
Total power (W)	679	484	686
Total power/volume (W/L)	0.0716	0.0510	0.0723
Total torque (N· m)	185	111	140
Total torque/volume (N· m/L)	0.0195	0.0117	0.0148
Tip speed (m/s)	1.89	1.89	2.12
Motor power (W)	1,100	1,100	2,250

of 41.62 rpm. Compared with the original bench-scale conditions, the tip speed has remained constant by design at 1.89 m/s. However, the power per volume has decreased from 0.0716 to 0.0510 W/L, and the torque per volume has decreased from 0.0195 to 0.0117 N m/L. Although equal tip speed is often a reasonable and practical scale-up criterion for geometric similarity, it may be less acceptable for non-geometric similarity. Often, the equal tip speed for geometric similarity is effective, because the mixing intensity remains constant with equal torque per volume. Thus, for non-geometric scale-up, equal torque per volume may be the better scale-up requirement.

- The fifth step sets the actual dual impeller system in the production-scale tank to equal torque per volume, by increasing the rotational speed from 41.62 to 46.75 rpm. At this rotational speed, the production-scale mixer is operating at a torque per volume level of 0.0148 N m/L. This is the same torque per volume level that achieved successful results in the bench-scale sauce development. The higher tip speed would be a potential problem only if drop size or particle size in a dispersion were critical.
- The sixth step involves a practical consideration about the production-scale mixer. Mixing processes or mixing equipment are rarely so sensitive as to require speed settings like 35.13, 41.62, or 46.75 rpm. Commonly, especially in production situations, mixers operate at nominal fixed speeds corresponding to standard gear reductions and motor speeds. Thus, the production-scale mixer in this example might have been operating at a standard speed such as 56 rpm. The second column in Table 6.4 shows the mixing characteristics for the production mixer operating at 56 rpm. In most mixing applications, the required intensity is some minimum amount, above which a plateau is reached, where a little more intensity does not adversely affect the product or production. Thus, the production-scale mixer operating at 56 rpm has a torque per volume level of 0.0212 N m/L,

Table 6.4 Non-geometric scale-up example—other considerations.

Dimensions and results	Actual impellers nominal speed	Bench-scale equal torque nominal speed	Hydrofoil impellers half torque/volume
Tank diameter (mm)	2,135	250	2,135
Straight side (mm)	2,593	250	2,593
Actual volume (L)	9,465	10	9,465
Fluid viscosity (mPa s)	15	15	15
Fluid density (kg/m^3)	1,090	1,090	1,090
Mixer speed (rpm)	56	360	56
Number of impellers	2	1	2
Impeller type	Pitched blade	Pitched blade	Hydrofoil
Power number (each impeller)	1.37	1.37	0.27
Impeller diameter (mm)	865	120	1,042
Impeller-to-tank diameter ratio	0.41	0.48	0.49
Blade width (mm)	173	24	156
Blade width to impeller diameter ratio	0.2	0.2	0.15
Off-bottom—upper impeller (mm)	1,930	0	1,930
Off-bottom—lower impeller (mm)	1,025	120	1,025
Reynolds number (either impeller)	50,848	6,291	73,786
Total power (W)	1,178	8.04	588
Total power/volume (W/L)	0.124	0.804	0.0620
Total torque (N· m)	201	0.213	100
Total torque/volume (N· m/L)	0.0212	0.0213	0.0106
Tip speed (m/s)	2.54	2.26	3.06
Motor power (W)	2,250	200	1,100

as compared with 0.0148 N m/L in the bench scale. The production-scale tip speed is 2.54 m/s, as compared with 1.89 m/s for the original bench scale. Power per volume has decreased from 0.465 W/L in the bench scale to 0.124 W/L in the plant scale. Power per volume is not usually held constant, apart from gas–liquid mass transfer applications and some rapid-rate chemical reactions. The resulting reduction in power per volume for this example is not expected to be a problem.

- A possible seventh step would be to scale down from the production-scale conditions at the standard speed of 56 rpm to an equivalent torque per volume in the bench-scale vessel. These conditions are represented in the third column of Table 6.4. For equal torque per volume in both the production and bench scales, the bench-scale mixer needs to operate at 360 rpm. Operating and applying the bench-scale mixer at these conditions is likely to duplicate many successful or problem characteristics associated with moving a new recipe from the bench to production. Any effort to nearly duplicate production conditions on the bench, before going into production, will reduce the number of potential problems and failures later. Time and cost savings by doing good mixing work on the bench can be significant. Simply put, identify problems and make mistakes at the small scale, but not at large-scale production.
- Another consideration might be the effect of changing to a different type of impeller. For this example, a more efficient hydrofoil design may be considered to replace the pitched-blade turbines in the production-scale tank. For this case, direct replacement of only the impellers means that the rotational speed remains unchanged. However, because of the lower power number for the hydrofoil impellers, $Po = 0.27$, as compared with $Po = 1.37$ for the pitched blade, the hydrofoil impellers must be larger. Because hydrofoil impellers are better at creating axial flow, only half the torque may be required to duplicate the process results with pitched-blade turbines. For the same sauce application at 56 rpm, half the torque can be applied in the production tank with 1,042 mm diameter hydrofoil impellers. These impellers have a 0.49 impeller-to-tank diameter ratio, which is still practical for this application. If a change in impeller type is a serious consideration for production equipment, then the small-scale batch mixer should also be changed first. Again, testing changes in the small-scale system can save time and money, while facilitating process improvements.

The systematic and step-by-step analysis of a scale-up or mixing modification is helped by the constant evaluation of changes in mixing variables like torque per volume, tip speed, power per volume, and Reynolds number. Tracking these mixing characteristics may offer an insight into mixer performance. In most practical scale-up situations, the Reynolds number becomes larger with scale-up. Although in the turbulent range, this increase does not affect mixing intensity, moving from the transition to the turbulent range may mean that the effect of viscosity is less in the large scale. So, even scale-up with equal torque per volume or equal tip speed can have a degree of inherent conservatism in the large-scale operating conditions.

6.3 Scale-up for powder mixing

Scale-up for powder mixing is much more of an art than the perceived science of liquid mixing. By the very nature of powders, they do not have the consistent properties of an incompressible fluid, as for liquid mixing. Of major importance in the scale-up of powder mixing is the simple fact that powders can be compressed and that, as a result, the flow characteristics can change drastically. With scale-up in powder systems, as the powder depth increases, the forces exerted on the powder at the bottom are increased, often to the point of altering

the density and flow characteristics of the compacted powder. Recognising this problem with powder mixing scale-up is often the first step in understanding potential problems.

Although scale-up of powder mixing is more difficult and less consistent than scale-up of liquid mixing, some of the same basic rules do apply. The first rule is geometry; scale-up is usually best done when the type of small-scale mixer is the same as the large-scale mixer. Details of geometry are less critical in powder mixing due to changes in the powder characteristics with scale. While the impeller-to-tank diameter ratio is very important in liquid mixing, the clearance between the ribbon and shell of a ribbon blender is not so critical in powder mixing. At the same time, the gap between the ribbon and the shell can have very different effects on powder mixing scale-up, depending on how much of the powder blend sticks to the sides of the blender shell. Sometimes, a minor ingredient becomes trapped in the layer of powder on a mixer surface. The characteristics of a powder will influence the success or failure of a mixing scale-up.

With respect to powder mixing geometry, tumble blender applications should be tested and developed in small-scale tumble blenders, ribbon blender applications should be developed in small ribbon blenders, and so on. Sometimes, testing in a small-scale ribbon blender might be applied to a large-scale paddle blender, as the paddle blender is less susceptible to compaction problems encountered in large ribbon blenders. Because of the many different types of powder, blender scale-up should be done from a similar mixer with the actual powder. For new mixing equipment, most manufactures offer laboratory testing or a rental mixer for development, before purchasing a mixer.

Rotational speed is the second major issue with the scale-up of powder mixing equipment. The degree of uniformity of a blend depends more strongly on the number of revolutions made by the blender than the revolution speed. The speed of revolution decreases with increased scale. Thus, if it takes 3 min to blend a batch in a small-scale mixer, and the large-scale mixer turns at 60% (3/5) of the small-scale speed, then the expected blend time for the large-scale mixer would be five-thirds (5/3) of 3 min, that is 5 min.

Perhaps, the most difficult judgement to make with powder-blending scale-up is the critical aspect of rotational speed. Most powder-blending equipment runs at a constant speed, typically set by the equipment manufacturer. The most common and practical scale-up rotational speed is likely to achieve an equal peripheral velocity for the rotating element of the mixer, whether it is a tumble blender or a ribbon blender. This effect is the same as the equal tip-speed scale-up [equation (6.16)] for liquid blending. However, practical considerations, such as available gear reductions or standard chain drives, may cause several different size mixers to run at the same speed for one manufacturer. The same rotational speed in different size mixers will result in a range of peripheral speeds for standard mixers. The operating variable then becomes the time allowed for complete blending.

As with liquid mixing scale-up, testing and development should concentrate on the important issues with a specific product or application. Considerations such as the order of addition of ingredients can be important, especially if one ingredient is fragile, like parsley leaves. In such a case, the fragile ingredient might be added late in the process to avoid excessive mixing and damage to the ingredient. In other cases, the addition rate of a liquid might be critical in an application where rapid addition may cause excessive wetting of parts of the batch and uneven moisture in the final product. Liquid may be added by ‘plating’, which is the addition of liquid while the blender is not running. Other practical considerations may be involved in scale-up, such as loading procedures. At small scale, a scoop may be used to load the mixer. However, at the large scale, the same ingredient may be added in quantities in the order of hundreds of kilograms. Rate, order, and location of addition need to be considered during development to ensure successful scale-up.

While peripheral velocity may work well for general scale-up of many mixer types, other criteria may apply where process conditions need to be duplicated. If a paddle blender or ploughshare blender is expected to lift and fluidise the powder, then equal Froude number [equation (6.8)] or rotational speed squared times impeller diameter may be held constant for an appropriate scale-up criterion. This criterion causes the peripheral speed of the rotating equipment to increase with the size of the mixer. As with liquid mixing, equal speed is rarely practical for significant changes in mixer size.

Owing to the uncertainty in the response of different powders, the rules and methods for powder-blending scale-up are less well organised than for liquids. The effects of geometry differences are less significant in powder blending, as all size differences can have adverse or positive effects. When a mixing failure occurs at the small scale, conditions and the evident mode of failure should be noted to avoid similar or related problems at the large scale. It is only in extreme cases that greater mixing intensity poses a problem for most applications.

All scale-up begins with deciding which test condition and scale is most likely to produce useful results. Observing the effects of mixing intensity and procedures forms an integral part of developing scale-up rules or limits. Only by careful observation, common problems can be avoided and successful scale-up achieved.

Nomenclature

B	baffle width
C	impeller off-bottom clearance
D	impeller diameter
g	acceleration of gravity
l	litre
L	length dimension
m	number of dimensions
m'	exponent on solids suspension scale-up
M	mass dimension
n	number of variables
n'	exponent on geometric similarity scale-up
N	rotational speed
Fr	Froude number
Po	impeller power number
Re	Reynolds number
P	power
t	time dimension
T	tank diameter
u_d	design settling velocity
u_t	terminal settling velocity
v_t	impeller tip speed
W	blade width
Z	liquid level

Greek letters

μ	fluid viscosity (dynamic)
ρ	fluid density
ρ_p	particle density

7 Monitoring and control of mixing operations

Colette C. Fagan, P.J. Cullen and Colm P. O'Donnell

7.1 Introduction

Mixing in the food industry is employed not only to combine multiple ingredients, but also to modify the structure of foods. As discussed in Chapter 2, perfect mixing is rarely possible; consequently, mixing will be a source of variability within the manufacturing process. Within the food industry, relationships established between the quality of mixed products and the operating parameters of mixing are often empirical, and therefore, the design of mixing systems are frequently not based upon well-established scientific principles. However, as the industry trend is toward higher-level processing, a more fundamental understanding of the flow behavior within mixing systems is required.

Patwardhan and Joshi (1999) indicated an enormous scope for improvement in the mixing efficiency (mixing time per unit power consumption) by achieving a desired combination of mean and turbulent kinetic energies, at various locations within a stirred tank. Imaging and mapping the flow provides a valuable insight into the mixing process. Recent developments in imaging technologies have facilitated such insight, allowing regions of poor mixing within vessels to be identified. Computational fluid mixing (CFM) can provide very detailed predictions of flow behavior in 3D. However, proper validation of these predictions relies upon measurement techniques that furnish a commensurate degree of detail (Holden *et al.* 1998). Incomplete mixing or overmixing of a product may result in product separation, attrition and undesirable product texture. Consequently, monitoring and control of the mixing process is critical.

Process analytical technology (PAT) is a framework for innovative process manufacturing and quality assurance. The goal is to move from a paradigm of 'testing quality in' post manufacture to 'designing quality in' during manufacture. This is achieved by fundamental process understanding and controlling processes by real-time measurement of predetermined critical product quality attributes. Process industries including the petrochemical, and more recently, the pharmaceutical industry have widely adopted the framework. Blending of an active ingredient within a carrier is a critical unit operation within pharmaceutical manufacture and an identified source of variability. Sensors such as near-infrared (NIR) spectrometry have been proposed as control systems for determining the optimum mixing time, thereby reducing variability and ultimately risk. Similar approaches for the control of food mixing could be adopted by the food industry.

This chapter reviews the available techniques to study the flow patterns induced within mixing vessels and sensors which may be employed to monitor mixing progress.

7.2 Torque and power measurement

The power draw in stirred tank mixing is the most fundamental measurement of mixing (Brown *et al*. 2004). A mixing system may be characterised by a power curve, a plot of the power number (*Po*) versus the Reynolds number (*Re*) given by the following relationship.

$$Po = f(Re) \tag{7.1}$$

For a Newtonian fluid, $Po = P/\rho N^3 d^5$ and $Re = \rho N d^2/\mu$, where μ is the Newtonian viscosity, ρ is the density of the fluid, N is the impeller speed, d is the impeller diameter and P is the power requirement. When mixing Newtonian fluids in a laminar regime, the power curve can be described by:

$$Po = K_p/Re \tag{7.2}$$

where K_p is a geometrical parameter depending on the mixing system.

For a given impeller speed, equation (7.2) can be used to calculate the power requirement for similar vessel/impeller arrangements of any scale, containing any Newtonian viscous liquid (Delaplace *et al*. 2000).

As discussed in Chapter 3, for non-Newtonian fluids, the shear rate will vary through the vessel, diminishing from a maximum near the impeller, resulting in an apparent viscosity profile. To overcome this, Metzner and Otto (1957) defined an average shear rate in the vessel in such a way that the power curve in the laminar flow for both Newtonian and non-Newtonian fluids is quite similar (Delaplace *et al*. 2000).

This effective shear rate value is classically linked to the impeller rotational speed as follows.

$$\gamma_a = k_s N \tag{7.3}$$

This average shear rate value is employed to evaluate an average apparent viscosity in the Reynolds number and the power input to any non-Newtonian fluid can be easily evaluated from the Newtonian power curve using equation (7.2). Even if the Metzner and Otto (1957) concept does not allow local rheological properties of the fluid to be obtained in the whole volume of the vessel, it has been widely used and accepted, providing a useful approach for the estimation of power consumption in a mixing vessel (Delaplace *et al*. 2000).

Although some torque measurement methods take into account the individual torque contribution of each impeller, others measure an entire system's torque (Brown *et al.* 2004). Sensors, which accurately measure the torque of the mixer shaft, can provide useful information about the mixing process. It is important to ensure that the true torque arising from the resistance provided by the fluid is measured and not additional frictional loads from bearings. Non-contact torque transducers such as the Torqsense™ sensor (Sensor Technology Ltd, Banbury, Oxon, UK) provide precise dynamic measurements of rotary torque over ranges covering 0–10 mN m to 0–10,000 N m. The principle of operation of this torque transducer involves a surface acoustic wave device used as a frequency-dependent strain gauge, which measures the change in resonant frequency caused by the applied strain in the shaft. Accurate measurement of shaft rotational speed using a light beam is also recorded. Quality control personnel require that a product is within a specified range for day to day

production, this range is developed previously upon knowledge of the complete flow curve (Barnes 2001). This quality control range, whether determined by consistometers or viscosity readings from laboratory viscometers, may be predicted from torque measurements, thereby providing the benefit of real-time process monitoring. Figure 7.1 shows correlations between power law consistency index (K) and Bostwick consistency (BC) values, with torque measurements for a sauce mixed with a pilot plant scale helical ribbon mixer. Torque measurements are sensitive to small changes in bulk product consistency. Similar correlations are found between torque readings and Bostwick values for fluid foods containing large particulate matter, such as pizza sauces and sauces for ready meals, over small consistency ranges. An advantage of measuring torque is that it is capable of coping both with large particulates and high viscosity due to the scale and design respectively, of the geometry employed.

Empirical torque measurement techniques such as the farinograph, mixograph and reomixer are widely used to characterize the behavior of dough during processing. Many of these are used as 'single-point' tests, where a single parameter is often arbitrarily selected from a whole range of data acquired during the test, for example, in selecting the peak torque from a mixing trace, and then using this to correlate with performance (Dobraszczyk & Morgenstern 2003). Most of the studies using these techniques have reported results from only one or few variables (often peak time and mixing tolerance). However, with computer data acquisition and treatment, more detailed analyses can be carried out. Martinant *et al.* (1998) showed that dough formation during mixing could be consistently evaluated by 11 reproducible parameters from a mixograph. The width and height of the mixogram was related to the proportion of unaggregated proteins before the mixing peak, and to that of polymeric proteins after the dough consistency reached a maximum.

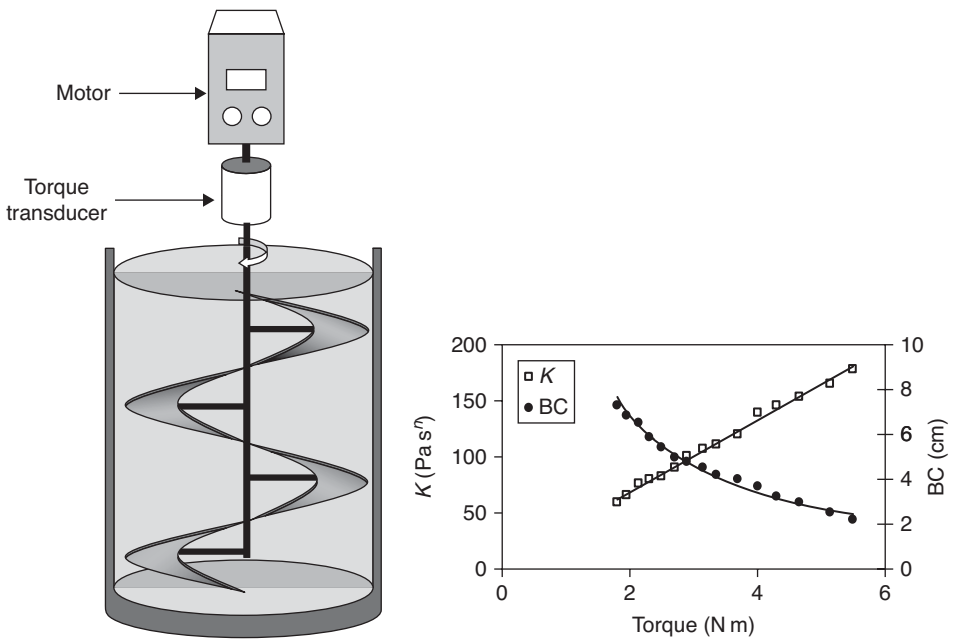

Fig. 7.1 Correlations developed between off-line consistency index K (rheometer) and Bostwick values with torque measurements for a series of tomato ketchup sample dilutions.

7.3 Flow measurement

As the turbulent flow field in stirred vessels has a highly complex structure, is three-dimensional, periodic and non-stationary with superimposed random and long-time scale fluctuations, investigations of the flow require advanced measurement techniques (Virdung & Rasmuson 2007). Flow mapping within stirred vessels may utilize single-point measuring techniques, which determine the velocity (or one of the velocity vector components) at a set point within the vessel, or whole-field measuring techniques, which determine the flow pattern simultaneously in a wider region of the bulk of the agitated fluid (Mavros 2001). Single-point measurements include anemometry techniques such as hot wire, laser and phase Doppler. Whole-field measurement techniques include particle image velocimetry (PIV) and planar laser-induced fluorescence (planar-LIF) velocimetry. High spatial resolution is desired for any flow visualization technique.

7.3.1 Hot-wire anemometry

Hot-wire anemometry (HWA) is a point-measuring technique predominantly employed for the measurement of velocity in turbulent gas and liquid flows. HWA operates using the principle of convective heat transfer from a heated wire in a fluid flow (Bruun 1995). Convection currents, which assist heat transfer from the probe, are a function of the flow properties such as velocity, fluid temperature and pressure, and physical properties of the fluid such as viscosity, density and specific heat. Hot-wire probes can operate in two modes, either in constant current or in constant temperature. In the constant current mode, the probe temperature varies, whereas in constant temperature mode, the probe resistance, and hence, temperature is kept constant. The constant temperature mode is simpler to operate in—there is less risk of wire burnout in low flow-rate systems or the risk of erroneous data being recorded in high flow-rate systems. Hence, most HWA systems operate as constant temperature anemometry (CTA), and the following discussion will focus solely on this mode. Plate 7.1 illustrates the principle of operation of CTA, which measures the rate of cooling from an electrically heated wire, maintained at a constant temperature. A current is passed through a tungsten or platinum wire of approximately 5 μm thickness, generating heat. In equilibrium this heat generation must be balanced by heat loss to the surroundings, primarily due to convection, and minor losses due to radiation and conduction to the probe support. As fluid velocity changes, the convective heat transfer coefficient will change, causing the wire temperature to change, thereby leading to a new equilibrium.

The hot wire can be said to respond according to King's Law (King 1914):

$$E^2 = A + BV^n \tag{7.4}$$

where E is the voltage across the wire, V is the velocity, and A, B and n are constants, which are determined through calibration. The constants depend, among other parameters, on fluid property values as well as the temperature difference between the sensor and the fluid (Jørgensen 1996).

In CTA the hot wire (R_w) is connected to one arm of a Wheatstone bridge (Plate 7.1) and heated by an electrical current. A servo amplifier operating as a feedback loop controls the current to the sensor so that the resistance, and consequently temperature, is maintained at a constant level, independent of the velocity, that is, cooling capacity, of the fluid. The voltage (E) applied to the top of the Wheatstone bridge provides a measure of the heat transfer

from the probe and thereby, a direct measure of fluid velocity. The sensor has a very fast response to changes in the flow due to the high gain of the servo amplifiers and the low thermal inertia of the sensor.

During calibration of the probe, the sensor is exposed to a range of known velocities and the resulting voltage outputs versus velocity measurements are generated. An algorithm based on either King's Law [equation (7.4)] or a polynomial is fitted to the calibration data in order to generate the required constant values, which characterize the relationship between voltage and velocity.

Hot-wire probes also display directional sensitivity, and therefore, systems with orthogonally arranged wires can provide data on both velocity and direction. The effective cooling velocity (U_{eff}) acting on a hot wire can be expressed by means of the normal (U_{n}), tangential (U_{t}) and binormal (U_{bn}) components, and modified by the yaw (k) and pitch (h) factors (Jørgensen 1996):

$$U_{\text{eff}}^2 = U_{\text{n}}^2 + k^2 U_{\text{t}}^2 + h^2 U_{\text{bn}}^2 \tag{7.5}$$

where k and h are determined by a directional calibration.

The bridge voltage is acquired via a fast A/D board after appropriate low-pass filtering. The data is then subjected to temperature correction, linearization and decomposition into velocity components. CTA can give point measurements of velocity and also continuous velocity time series, which can be processed into amplitude and time-domain statistics.

Cooper and Wolf (1968) used HWA, in conjunction with air as the fluid, to measure velocity profiles across impeller blades and to determine global scale-up parameters, such as pumping capacity and circulation capacity for a turbine-agitated tank with different impeller sizes. HWA was also shown to be useful for the study of air–water flow in aerated stirred tanks (Lu & Ju 1987). The turbulent flow in the impeller zone and the bulk zone of a turbine-agitated tank has also been measured by split-film HWA (Wernersson & Tragardh 2000). They found that it allowed simultaneous measurement of two velocity components in water media under conditions similar to those used in industrial fermentations and that it was possible to obtain important flow characteristics such as the statistical moments, the turbulent kinetic energy, the energy dissipation rate and turbulent time and length scales.

HWA has also been employed to study numerous other phenomena including isothermal two-dimensional channel flow (Alshamani 1980), turbulence in the upward gas flow above a gas-fluidized bed (Pemberton & Davidson 1984) and turbulent shear flows near walls (Nagano & Tsuji 1994). Sherif and Pletcher (1991) discussed the use of HWA in non-isothermal flows. They proposed a method that separated velocity and temperature signals in three-dimensional flows having small or moderate temperature fluctuations. They tested the technique in the two-dimensional region of a jet in cross flow and also by analyzing a modified version of the response equations in the core region of a fully developed pipe flow. As part of a study to investigate large-scale turbulence phenomena in compound rectangular channels, HWA revealed the presence of a quasi-periodic large-scale turbulence structure. HWA can also be used to facilitate the performance of spray driers by characterizing equipment air flow patterns (Kieviet *et al*. 1997).

7.3.2 Laser Doppler anemometry

Laser Doppler anemometry (LDA) is an optical technique for 1D, 2D and 3D point measurement of particle velocity. In the principle of LDA, a laser beam is split to form

two coherent beams which are made to cross at some point within the mixing vessel. When they cross, interference occurs between the beams, resulting in an intersection volume (Plate 7.2). A fringe pattern of high and low intensities is formed. The frequency of one of the beams is shifted, causing the fringe pattern to pulsate at steady frequency. The fringe separation (d) is determined by:

$$d = \frac{\lambda}{2\sin(\theta/2)} \tag{7.6}$$

where λ is the wavelength and θ is the angle between the two beams. When a particle passes through this region, it changes this pulsating frequency, which is measured by a detector as a Doppler shift (f_D). Particle velocity (u) may be determined from multiplying the Doppler shift by the fringe spacing.

$$u = f_D d \tag{7.7}$$

To measure two velocity components, two extra beams can be added to the optics in a plane perpendicular to the first beams. All three velocity components can be measured by two separate probes measuring two and one components, with all the beams intersecting in a common volume. Different wavelengths are used to separate the measured components. The method's particular advantages are non-intrusive measurement, high spatial and temporal resolution, non-calibration and the ability to measure in reversing flows. However, a significant limitation of the technique is that the fluid must be transparent.

LDA has been widely employed to study velocities within stirred vessels, both for various impeller designs and rheological properties. Armenante *et al*. (1997) utilized LDA to determine mean and fluctuating velocities in three directions in a closed, unbaffled, flat-bottom, water-filled cylindrical tank, where flow was generated by a six-bladed, 45º pitched-blade turbine. Kumaresan and Joshi (2006) investigated the effect of various impeller designs on the flow pattern and mixing time in stirred tanks. Li *et al*. (2005) used LDA and CFD to study the effects of scale-up. The study results indicate that the selection of a laboratory-scale vessel has little effect on the macromixing performance for the optimization of the configurations and operating conditions of an industrial-scale reactor, provided fully turbulent flow is achieved. Ducci and Yianneskis (2007) employed LDA to characterize and track a vortex within stirred vessels. Utomo *et al*. (2008) studied the flow pattern and the distribution of energy dissipation rate in a high-shear rotor–stator mixer by using LDA. They reported a good prediction of the distribution of energy dissipation rate in the tank, facilitating a better understanding of scale-up and design procedures. LDA has also been used to measure the velocities of small mica particles seeded in an optically clear model fluid in order to provide velocity vectors of rotating flows associated with dough kneading (Binding *et al*. 2003). Velocity distributions during kneading have also been examined by Yerramilli and Karwe (2004) using LDA. They determined the velocity distributions in the kneading section of a co-rotating twin-screw extruder in order to understand the mixing effectiveness of kneading blocks. Virdung and Rasmuson (2007) explored the possibility to perform LDA measurements at high solids concentrations, evaluating the effects of solid loading and particle size on the axial velocities and turbulence levels of the continuous phase in solid–liquid suspensions.

7.3.3 Phase Doppler anemometry

An extension of LDA is phase Doppler anemometry (PDA), which provides simultaneous measurement of velocity (up to three components) and particle size. Other parameters such as mass flux and concentration can also be determined. As for LDA, when a particle passes through the intersection volume formed by the two coherent laser beams, the scattered light, received by a detector, has components from both the beams. These components will interfere on the surface of the detector. As a particle moves through the measurement volume, the difference between the optical path lengths of the two components changes, this interference produces pulsating light intensity with a frequency proportional to the velocity of the particle. However, with PDA, a second detector is employed, which also receives a Doppler burst of the same frequency (Plate 7.3). The phases of the bursts received by each detector vary with the angular position of the detectors. The phase shift between these two signals is proportional to the diameter of the particle, increasing with particle size.

Guiraud *et al*. (1997) used PDA to determine local velocities and particle size in a suspension with 0.5% solids by volume in a stirred vessel agitated by an axial impeller. Ljungqvist and Rasmuson (2004) used the technique to assess slip velocities in an axially stirred vessel at two different impeller speeds in suspensions with particles of four different sizes at low volumetric concentrations. Pettersson and Rasmuson (1997) employed 3D PDA to simultaneously determine the local, instantaneous and three-dimensional velocity vectors of a fluid and suspended particles within an agitated crystalliser. Using PDA Laakkonen *et al*. (2006) validated models of bubble breakage, coalescence and mass transfer for gas–liquid dispersion within an agitated vessel.

7.3.4 Flow visualization using computer vision

Simple imaging can provide valuable insight into the mixing process. Figure 7.2 shows images of a flow field within an unbaffled tank with a Rushton turbine. The flow field is characterized by a strong circumferential motion which develops around two main vortices, one above and another below the impeller. The movements of the upper and lower vortices with respect to time may be identified from the images. These periodic oscillations are like flow instabilities which may benefit meso- and macromixing. Such approaches of flow visualization may prove to be valuable for mixing design. The addition of a coloring agent to transparent fluids facilitates flow tracking. By employing two reactive agents, it is possible to monitor both flow pattern and mixing time. Cabaret *et al*. (2007) utilized a similar technique to determine the performance of a dual-shaft mixer with viscous Newtonian liquids. They added a solution of bromocresol purple as an indicator. This indicator is yellow when pH is below 5.2 (acid color) and purple when pH is above 6.8 (alkaline color), allowing the evolution of the color from purple to yellow to be detected. They filmed this process by using a digital CCD camera. The resultant images can then be subjected to image analysis techniques in order to determine the evolution of the percentage of yellow pixels, and thereby, mixing curves. For example, the evolution of the green color brightness in the RGB (red, green and blue) model can be determined for each pixel over time and by defining a threshold for R, a pixel can be classified as either mixed or unmixed, depending on whether it is above or below the threshold value. This technique has also been utilized for the characterization of mixing patterns in co-axial mixers (Bonnot *et al*. 2007).

Computer vision and image analysis techniques have also been employed to follow stirred reactions in opaque liquids such as curd syneresis during cheese production

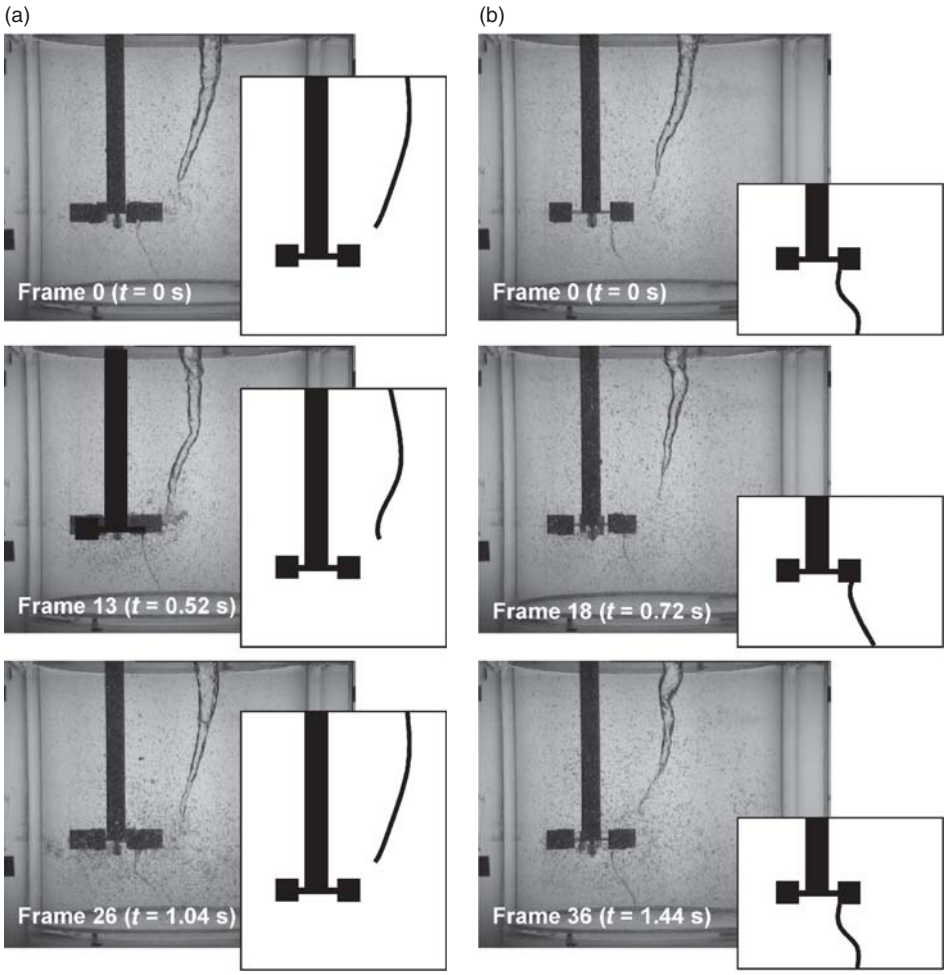

Fig. 7.2 Images of a flow field within an unbaffled tank with a Rushton turbine with sketches for: (a) upper vortex and (b) lower vortex. [Reprinted from Galletti and Brunazzi (2008) with permission from Elsevier.]

(Everard *et al*. 2007; Fagan *et al*. 2008). Everard *et al*. (2007) extracted the average RGB values from images and obtained the areas of solid curd particles and liquid whey using a thresholding image segmentation technique. They found that the technique distinguished between the effect of pH and stirring speed. They also used the resulting data to predict the moisture content of the curd particles. The curd/whey mixture can be regarded as a texture pattern which changes during processing as the volume of expelled whey increases and curd particles contract. Therefore, image texture analysis of the images was also carried out to determine whether it could be used to monitor the reaction (Fagan *et al*. 2008). Numerous image texture analysis methods were investigated, including fractal dimension (FD) and wavelet transform (WT). In FD each image is viewed as a hilly terrain whose height, at any given location, is proportional to the gray level value at that location (Chaudhuri *et al*. 1993). The FD is an indication of the roughness of the image at different

scales. WT is another well-known multi-scale analysis technique which is useful for characterising different scales of textures effectively (Simoncelli & Freeman 1995). WT parameters give a measure of the frequency content of the image on a given scale and in a given direction. Fagan *et al*. (2008) concluded that the FD models were best at predicting composition of the curd and whey during syneresis. The second best technique was WT. This indicated that multi-scale analysis techniques such as FD and WT extracted the most relevant information from images captured during syneresis.

The mixing of powders has also been widely investigated by using computer vision. Daumann and Nirschl (2008) utilized a thresholding procedure to assess the mixing efficiency of solid mixtures. Firstly, they cut the mixer wall and visible part of the shaft from the image. The fractions were then selected and the color reduced, as the position of the mixing paddles changed during the experiments. Then, based on color, a threshold for the fine-, medium- and coarse fractions was determined. Transverse mixing kinetics in a rolling drum have also been determined by image analysis (Van Puyvelde *et al*. 1999). They mixed particles of different size and color (black, orange and white) and captured images at a rate of 3.8 frames per second. Each pixel was analyzed to determine the color, and thereby, type of particle occupying each pixel. The contact of each pixel was analyzed with respect to the surrounding pixels. Contact between the two materials occurred if different color occupied pixels adjacent to one another. The total contact was calculated for the orange material and was expressed as a numerical value by calibrating the physical size represented by a pixel. The FD box counting method has also been used to follow the blending of two powders and one viscous liquid in a classical reactor, under different agitation conditions (Le Coënt *et al*. 2005).

Regardless of the method of image analysis employed, it should be noted that there is a strong influence of light intensity and camera position on image analysis, and hence, they must be standardized, as the presence of shadows or reflections can introduce errors into the results.

7.3.5 Particle image velocimetry

In contrast to LDA and HWA, PIV is a whole-field visualization technique. It can provide instantaneous quantitative velocity measurements in a cross-section of a flow by imaging small tracer particles in the flow field and analyzing the acquired digital images. PIV can measure the whole two-dimensional or three-dimensional flow field simultaneously without disturbing the flow field (Okamoto *et al*. 2000). Plate 7.4 details the principle of operation of PIV. A laser is employed to produce a light sheet which is pulsed. Images of the tracer particles in the light sheet are recorded by using a camera. The displacement of the particles between two light pulses is measured. This can be achieved by dividing the image frames into small interrogation areas and cross-correlating each pixel in the two image frames. The peak in the cross-correlation signal represents the spatial displacement that estimates the average particle displacement in the interrogation area. Velocity vectors are calculated for each interrogation area by dividing displacement by the laser pulse time interval. To achieve rapid and accurate flow velocity measurements, this time interval should be small compared to the length scales in the flow (Brown *et al*. 2004). In the case of double or multiple exposed single images, autocorrelation analysis is preformed.

PIV has been employed to study mixing in both stirred and static vessels. La Fontaine and Shepherd (1996) used a PIV system that analyzed the vessel from different aspects to study flow in a stirred vessel. They found that through analysis of the recorded images,

it was possible to expose stagnant flow regions, circulation loops and the turbulent nature of the flow. PIV has also been employed to investigate the complete velocity field in a flat-bottomed cylindrical vessel equipped with baffles and Rushton turbine impeller (Fan *et al*. 2004). They recorded sequences of instantaneous velocity fields across a vertical plane covering half of the vessel's vertical cross-section. They found that the technique revealed the near-instantaneous flow—historically considered as a double loop flow pattern—to be actually, rather complex and stochastic. The authors stated that two distinct flow patterns, namely full circulation and quick return, were also identified and that macro-instability appeared at the switching between these flow patterns. Fitch *et al*. (2005) utilized PIV in conjunction with CFD to study the effect of viscosity on the performance of an oscillatory baffled column. Results showed that it was possible to generate flow patterns by using PIV and CFD, from which the effects of viscosity on mixing could be observed. In order to quantify the effect of viscosity on mixing, they calculated the ratio between the plane-averaged axial and radial velocities. They stated that the system was found to mix sufficiently at ratio values below 3.5.

Couerbe *et al*. (2008) employed PIV to characterize the steady-state flow fields obtained in a stirred tank with a thixotropic fluid. Experiments revealed bulk flow behavior, characterized by a flow pattern in the turbulent regime at a rotation rate of eight per second and by the formation of caverns around the impeller at smaller rotation rates. It was found that as rotation rate was reduced, the pumping capacity of the impeller was reduced as well (until becoming almost zero) and that the flow was greatly re-organized, leading to poor mixing efficiency.

PIV has also been applied to the study of internal flow in bifurcation pipes (Brücker 1997). PIV was employed to provide a three-dimensional, whole-volume, and time-resolving velocity measurements at a 90º T-junction. The results showed a strong similarity of the vortical structures to that of a jet in a cross flow. He also stated that vortex breakdown in tubes is followed by a wake region, where, even at low Reynolds numbers, greater mixing was observed due to the stretching and tilting of the vortex lines and their non-linear interaction.

PIV has also been employed in various other applications including the study of local bubble size distributions, gas–liquid interfacial areas, gas hold-ups and flow velocities simultaneously from flat-blade turbine-agitated gas–liquid vessels (Laakkonen *et al*. 2005), and the characterization of suspension flow homogeneity (Hasan *et al*. 1999).

7.3.6 Planar laser-induced fluorescence

Planar-LIF imaging employs the fluorescence of an organic medium induced by a laser sheet combined with image analysis for flow visualization. It may unveil flow patterns and structures that serve as the starting point to analyze fluid mixing in stirred tanks (Arratia & Muzzio 2004). It can also be used to provide instant whole-field temperature, concentration and pH maps. The laser, which is usually a neodymium-doped yttrium aluminum garnet or Argon–ion laser, is used to form a thin sheet of light, which excites a fluorescent species within a flow. The fluorescent species is typically a tracer compound such as rhodamine B. The selection of a tracer is dependent upon its absorption wavelength being compatible with the laser excitation wavelength, a large separation between emission and excitation absorption spectra, and a high quantum efficiency to maximize signal strength (Crimaldi 2008). The emitted fluorescence is optically captured. This can be achieved by a camera with a sharp cut-off or narrow-band filter, to ensure that only fluorescence is recorded.

The level of fluorescence is known to vary with a number of experimental parameters; however, where the local excitation intensity is less than the saturation intensity, the signal (fluorescence) can be expressed as a linear function of dye concentration, laser excitation intensity and a constant that characterizes all experimental parameters. This constant value is therefore determined, by the calibration procedure, for every pixel of the camera. The captured images are then converted to concentration, temperature maps, etc., using this calibration. For liquid–liquid mixing, concentration (C) at each pixel can be determined as:

$$C \cong \frac{S}{\alpha E} \tag{7.8}$$

where S is the intensity the signal, E is the laser excitation intensity and α is the constant value determined by the calibration procedure. The technique is, however, limited to optically clean systems with a constant refractive index (Wadley & Dawson 2005).

Guillard *et al*. (2000b) developed advanced methods in planar-LIF image analysis in order to study the large-scale mixing structures obtained in a Rushton turbine-agitated reactor. They stated that while a standard statistical approach allowed the observation of tracer dispersal, a dynamic structural approach, as detailed by Guillard *et al*. (2000a), was required for deeper understanding of the three-dimensional mixing process. Arratia *et al*. (2006) used planar-LIF to examine the mixing mechanism of a Rushton impeller for a yield stress fluid, by tracking the evolution of flow microstructures. Snapshots of planar-LIF revealed the formation of lobe structures that are ejected periodically from the impeller toward the tank wall. These lobes are then stretched, folded and transported back to the impeller through the shaft in an elliptic trajectory surrounding the toroidal regions.

Recently, planar-LIF was used to study fast mixing of two liquid streams in flow channels at millimeter size (Luo *et al*. 2007) and mixing patterns associated with the bursting of isolated bubbles at the surface of gas-fluidized beds (Solimene *et al*. 2007). Wadley and Dawson (2005) used the technique to study mixing within static mixers for both turbulent and transitional flow regimes.

Szalai *et al*. (2004) investigated the mixing performance of a batch stirred tank with four Ekato Intermig® impellers using PIV, acid–base flow visualization and planar-LIF. The experimental flow patterns were compared with numerical solutions. All three techniques revealed excellent agreements between the experiments and computations.

7.3.6.1 *Combined planar-LIF and PIV*

As detailed in Plate 7.5, it is also possible to obtain synchronized planar-LIF and PIV measurements, which can provide concentration or temperature maps at the same time as velocity measurements. Uniquely, it allows both fluid and particulate flows to be determined at each location from which the shear flow experienced by the particle can be determined. This requires the introduction of a second camera to detect the laser light scattered by small particles through an optical narrow-band filter. The two LIF and PIV receivers are brought to observe the same locations by means of beam splitter optics and geometrical calibration. Law and Wang (2000) demonstrated the potential of obtaining synchronized PIV and planar-LIF measurements and stated that the two techniques could be successfully combined to capture the mean and turbulent mass transport characteristics in a mixing process.

7.3.7 Tomography

Tomography is the localized measurement of velocity, density or concentration profiles in 3D. The image is built up from an array of non-obtrusive sensors surrounding the mixing system (Brown *et al*. 2004).Various signals have been used including γ-ray, x-ray, positron and electrical resistance.

Positron emission particle tracking (PEPT) employs a single positron-emitting particle as a flow tracer, which is then tracked in 3D space and time to reveal its full Lagrangian trajectory. The method allows for probing of opaque fluids, within an opaque apparatus. The technique is particularly useful for the study of multi-phase flows, to map the flow of fluids and particles. This technology and application is discussed in detail in Chapter 10.

Electrical tomography including electrical impedance, electrical capacitance and electrical resistance use electrodes mounted on the inside walls of the mixing vessel and measure a corresponding electrical property, for example, resistance in the case of electrically conducting liquids and capacitance for non-conducting fluids (Mavros 2001). The signals from the various sensors are combined into slices or 'tomograms' to obtain a 3D representation of the flow inside the vessel. The technique has been used to investigate the flow in various process vessels for various two-phase systems (Williams *et al*. 1996; Mann *et al*. 1997; Holden *et al.* 1998; Rahimi *et al*. 1999; Wang *et al*. 2000). Electrical resistance tomography (ERT) is capable of non-invasively measuring time-evolving concentration fields, and hence mixing rates, within a stirred vessel at high spatial resolution. Moreover, the approach offers high time-wise resolution and is thus ideally suited for mixing assessment and validation against CFM predictions (Holden *et al*. 1998). Recently, Pakzad *et al*. (2008) used ERT to study the formation of caverns in the mixing of pseudoplastic fluids possessing yield stress.

Magnetic resonance imaging (MRI), as a tomographic technique, is uniquely suited to obtain both concentration and velocity profiles within process geometries (Wang *et al*. 2000). MRI has great potential to evaluate mixedness, because it is non-invasive, is applicable to a wide range of materials (opaque or transparent material) and can be operated as a real-time measurement due to its short data acquisition time (Lee *et al.* 2001). Wang *et al*. (2000) used MRI tomography to study mixing in a scraped surface heat exchanger. The mixing was quantified by velocity profiles and magnetic resonance concentration images. Lee *et al*. (2001) employed MRI tomography successfully to quantify the extent of mixing with a fluid and particle model system. In addition to the images, descriptive statistics can be used to distinguish between uniform and non-uniform mixtures. Standard deviation and coefficient of variation clearly showed the sequence of mixing for all particle loadings. Correlogram and length scale were reported as the indices for mixing and showed dramatic change as a function of number of impeller revolutions, especially at higher particle loading. MRI has also been investigated to spatially resolve and quantify mixtures of fine powders. Porion *et al.* (2004) characterized the kinematics of mixing and size segregation of dry binary mixtures (poppy seeds or sugar beads) in a shaker–mixer.

7.4 Quantification of mixing time

A number of techniques discussed above may provide a measurement of mixing time. However, for practical process control, it is critical that sensors are as simple as possible, affordable and ideally non-invasive for the food industry. NIR spectroscopy probes are often favored by the process industries due to their ability to meet these demands alongside their sensitivity to monitor fluctuations in a range of products and processes.

7.4.1 NIR spectroscopy

NIR spectroscopy is a proven technique for continuous monitoring and control of processes and product quality in both food (Huang *et al*. 2008) and pharmaceutical (Roggo *et al.* 2007) industries. Its application to process monitoring has been driven by its many advantages over traditional methods, that is, it is non-destructive requiring no sample preparation, can be employed online and can provide rapid real-time data for a range of properties from a single spectrum. Although it has been applied to the area of product quality and authenticity, NIR spectroscopy can also be applied to the monitoring of mixing systems. NIR radiation is defined as that wavelength region from 750 to 2,500 nm, lying between the visible light and the infrared light (Büning-Pfaue 2003). NIR food spectra are typically dominated by broad peaks associated water located near 970, 1,440 and 1,930 nm (Woodcock *et al*. 2008). 970 nm has been assigned to the second overtone of the O–H stretching vibration of water, with other broad peaks due to a combination of symmetric ($v1$) and antisymmetric ($v3$) stretching modes of water, and a combination of stretching ($v3$) and bending ($v2$) modes of water. These peaks mean that sophisticated multi-variate statistical techniques are required to extract relevant information from NIR spectra.

For food mixing applications, NIR spectroscopy has been predominantly applied to monitoring of dough mixing systems. The extent of mixing has a critical impact on final bread quality due to its role in ensuring flour hydration formation of the gluten network. Traditionally, the mixing of dough was monitored online by using torque sensors. However, as a range of physicochemical changes occur during dough mixing, NIR spectra can provide valuable information on the extent of mixing. Wesley *et al*. (1998) found that changes in absorbance at 1,160 and 1,200 nm followed the same trend as mixer power consumption. A diode array NIR instrument was also used to obtain an overall picture of the mixing process from the initial hydration of the flour particles through optimum dough development until overmixing had occurred, and it was found that NIR spectroscopy was shown to have considerable merit in following dough changes during mixing which were related to final bread quality and thus has the potential to be used as an online method for controlling breadmaking mixers. Aït Kaddour *et al*. (2008) investigated the potential of 2D correlation spectroscopy and moving-window 2D correlation spectroscopy to explore the time dependence of NIR spectral responses during wheat flour dough mixing. They found that it was possible to identify wavelength shifts associated with both dough 'free water' and protein secondary structure modifications.

The same group also examined the ability of NIR spectroscopy to describe the physical and chemical changes occurring during wet agglomeration of wheat flour (Aït Kaddour & Cuq 2009). They found that the spectra highlighted the modifications of the glutenin depolymerization, flour particle hydration and changes in particle size as the most important physical and chemical modifications occurring during crumbly dough mixing.

NIR spectroscopy has also been examined for monitoring of blend uniformity and segregation of dry powder blends online, predominantly, in the pharmaceutical industry. Blanco *et al*. (2002) provided an overview of NIR spectroscopy applications for monitoring blending processes. One method involved the calculation of the dissimilarity between the blend under mixing with that of a reference spectra from a homogenously mixed sample, whereas others calculated the standard deviation of a set of consecutively recorded spectra and compared it to the standard deviation of the next set of consecutively recorded spectra.

El-Hagrasy and Drennen (2006) presented an integrated approach for real-time blend uniformity assessment by using NIR spectroscopy. They developed a model for the prediction

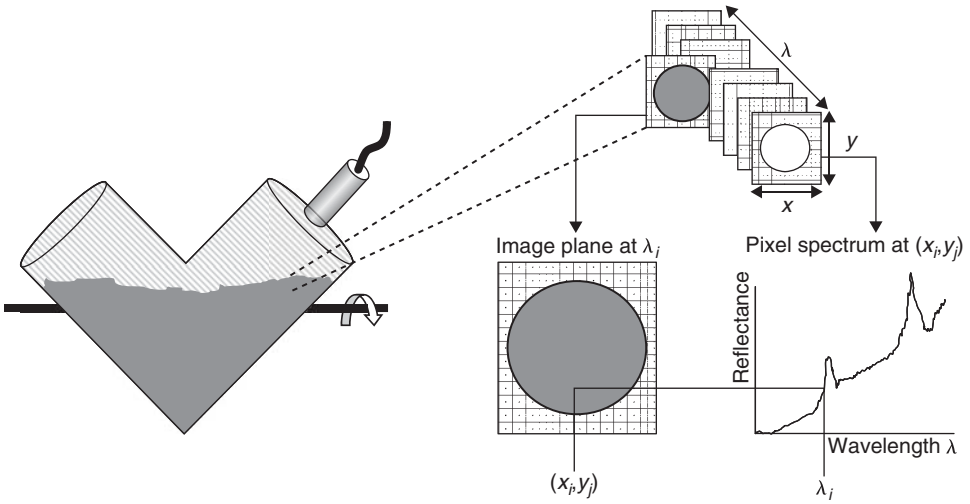

Fig. 7.3 Schematic representation of an NIR chemical imaging system for monitoring blend conformity in a V-blender. The hypercube shows the relationship between spectral and spatial dimensions.

of the end-point of blending and found that the predicted blending profiles correlated well to those determined by the UV reference analytical method. Ely *et al*. (2006) used NIR spectroscopy (1,100–2,200 nm) to monitor online low-dose, dry powder blends, mixed in a drum blender and bin blender. They monitored segregation in the drum blender by raster-scanning across the tube at specific blending times, and in the bin blender, spectra were continuously recorded through a window located on its axis of rotation. Standard deviations were calculated to determine how much the concentration of the bed was fluctuating. Results showed that univariate data analysis was ineffective at monitoring low-dose blends, as it was not possible to achieve sufficiently low detection and quantization limits; however, the application of multi-variate statistical techniques may improve the limits of detection.

7.4.2 Chemical imaging

Chemical imaging (CI) or hyperspectural imaging (HSI) is an emerging technique that integrates conventional imaging and spectroscopy to attain both spatial and spectral information from an object. By combining the chemical selectivity of vibrational spectroscopy with image visualization, CI may be used to describe ingredient concentration and distribution in heterogeneous solids, semi-solids, powders, suspensions and liquids (Gowen *et al*. 2008). Chemical images are made up of hundreds of contiguous wavebands for each spatial position of a material studied. Consequently, each pixel in a chemical image contains the spectrum of that specific position. The resulting spectrum acts like a fingerprint, which can be used to characterize the composition of that particular pixel. Chemical images, known as hypercubes, are three-dimensional blocks of data, comprising of two spatial and one wavelength dimension, as illustrated in Figure 7.3. The hypercube allows for the visualization of biochemical constituents of a sample, separated into particular areas of the image, since regions of a sample with similar spectral properties have similar chemical composition (Gowen *et al*. 2008). It is this chemical and spatial classification that has resulted in CI being identified as a potential tool for position referenced spectra, which are valuable

for the analysis of complex multi-constituent materials such as pharmaceutical tablets. The technology may be simplified for a specific product from the vast data obtained from the hypercubes to selected wavelengths of interest, facilitating the potential of the technique for process control. Recently, the technology has shown promise for monitoring the blending of pharmaceutical ingredients within a V-blender (Figure 7.3). Similarly, the technology has potential for monitoring the mixing of food powders or fluid systems.

References

Aït Kaddour, A. & Cuq, B. (2009) Inline monitoring of wet agglomeration of wheat flour using near infrared spectroscopy. *Powder Technology*, **190**(1–2), 10–18.

Aït Kaddour, A., Barron, C., Robert, P. & Cuq, B. (2008). Physico-chemical description of bread dough mixing using two-dimensional near-infrared correlation spectroscopy and moving-window two-dimensional correlation spectroscopy. *Journal of Cereal Science*, **48**(1), 10–19.

Alshamani, K.M.M. (1980). A study of turbulent flow in ducts. *The Chemical Engineering Journal*, **20**(1), 7–19.

Armenante, P.M., Luo, C., Chou, C.-C., Fort, I. & Medek, J. (1997). Velocity profiles in a closed, unbaffled vessel: comparison between experimental LDV data and numerical CFD predictions. *Chemical Engineering Science*, **52**(20), 3483–3492.

Arratia, P.E. & Muzzio, F.J. (2004). Planar laser-induced fluorescence method for analysis of mixing in laminar flows. *Industrial and Engineering Chemistry Research*, **43**(20), 6557–6568.

Arratia, P.E., Kukura, J., Lacombe, J. & Muzzio, F.J. (2006). Mixing of shear-thinning fluids with yield stress in stirred tanks. *AIChE Journal*, **52**(7), 2310–2322.

Barnes, H.A. (2001). An examination of the use of rotational viscometers for the quality control of non-Newtonian liquid products in factories. *Applied Rheology*, **11**, 89–101.

Binding, D.M., Couch, M.A., Sujatha, K.S. & Webster, M.F. (2003). Experimental and numerical simulation of dough kneading in filled geometries. *Journal of Food Engineering*, **58**(2), 111–123.

Blanco, M., Gozález Bañó, R. & Bertran, E. (2002). Monitoring powder blending in pharmaceutical processes by use of near infrared spectroscopy. *Talanta*, **56**(1), 203–212.

Bonnot, S., Cabaret, F., Fradette, L. & Tanguy, P.A. (2007). Characterization of mixing patterns in a coaxial mixer. *Chemical Engineering Research and Design*, **85**(8), 1129–1135.

Brown, D.A.R., Jones, P.N., Middleton, J.C., Papadopoulos, G. & Arik, E.B. (2004). Experimental methods. In: *Handbook of Industrial Mixing Science and Practice* (eds E.L. Paul, V.A. Atiemo-Obeng & S.M. Kresta). John Wiley & Sons, Inc., Hoboken, NJ, pp. 145–256.

Brücker, C. (1997). Study of the three-dimensional flow in a T-junction using a dual-scanning method for three-dimensional scanning-particle-image velocimetry (3-D SPIV). *Experimental Thermal and Fluid Science*, **14**(1), 35–44.

Bruun, H.H. (1995). *Hot-wire Anemometry: Principles and Signal Analysis*. Oxford University Press, New York.

Büning-Pfaue, H. (2003). Analysis of water in food by near infrared spectroscopy. *Food Chemistry*, **82**, 107–115.

Cabaret, F., Rivera, C., Fradette, L., Heniche, M. & Tanguy, P.A. (2007). Hydrodynamics performance of a dual shaft mixer with viscous Newtonian liquids. *Chemical Engineering Research and Design*, **85**(5), 583–590.

Chaudhuri, B.B., Sarkar, N. & Kundu, P. (1993). Improved fractal geometry based texture segmentation technique. *IEE Proceedings-Computers and Digital Techniques*, **140**(5), 233–241.

Cooper, R.G. & Wolf, D. (1968). Velocity profiles and pumping capacities for turbine type impellers. *Canadian Journal of Chemical Engineering*, **46**(2), 94–100.

Couerbe, G., Fletcher, D.F., Xuereb, C. & Poux, M. (2008). Impact of thixotropy on flow patterns induced in a stirred tank: numerical and experimental studies. *Chemical Engineering Research and Design*, **86**(6), 545–553.

Crimaldi, J. (2008). Planar laser induced fluorescence in aqueous flows. *Experiments in Fluids*, **44**(6), 851–863.

Daumann, B. & Nirschl, H. (2008). Assessment of the mixing efficiency of solid mixtures by means of image analysis. *Powder Technology*, **182**(3), 415–423.

Delaplace, G., Leuliet, J.C. & Ronse, G. (2000). Power requirement when mixing a shear-thickening fluid with a helical ribbon impeller type. *Chemical Engineering and Technology*, **34**(4), 329–335.

Dobraszczyk, B.J. & Morgenstern, M.P. (2003). Rheology and the breadmaking process. *Journal of Cereal Science*, **38**, 229–245.

Ducci, A. & Yianneskis, M. (2007). Vortex identification methodology for feed insertion guidance in fluid mixing processes. *Chemical Engineering Research and Design*, **85**(5), 543–550.

El-Hagrasy, A.S. & Drennen, J.K. (2006). A process analytical technology approach to near-infrared process control of pharmaceutical powder blending—Part III: quantitative near-infrared calibration for prediction of blend homogeneity and characterization of powder mixing kinetics. *Journal of Pharmaceutical Sciences*, **95**(2), 422–434.

Ely, D., Chamarthy, S. & Carvajal, M.T. (2006). An investigation into low dose blend uniformity and segregation determination using NIR spectroscopy. *Colloids and Surfaces A: Physicochemical and Engineering Aspects*, **288**(1–3), 71–76.

Everard, C.D., Fagan, C.C., O'Donnell, C.P., O'Callaghan, D.J., Castillo, M. & Payne, F.A. (2007). Computer vision and colour measurement techniques for inline monitoring of cheese curd syneresis. *Journal of Dairy Science*, **90**, 3162–3170.

Fagan, C.C., Du, C.J., O'Donnell, C.P. *et al*. (2008). Application of image texture analysis for online determination of curd moisture and whey solids in a laboratory-scale stirred cheese vat. *Journal of Food Science*, **73**, 250–258.

Fan, J., Rao, Q., Wang, Y. & Fei, W. (2004). Spatio-temporal analysis of macro-instability in a stirred vessel via digital particle image velocimetry (DPIV). *Chemical Engineering Science*, **59**(8–9), 1863–1873.

Fitch, A.W., Jian, H. & Ni, X. (2005). An investigation of the effect of viscosity on mixing in an oscillatory baffled column using digital particle image velocimetry and computational fluid dynamics simulation. *Chemical Engineering Journal*, **112**(1–3), 197–210.

Galletti, C. & Brunazzi, E. (2008). On the main flow features and instabilities in an unbaffled vessel agitated with an eccentrically located impeller. *Chemical Engineering Science*, **63**(18), 4494–4505.

Gowen, A.A., O'Donnell, C.P., Cullen, P.J. & Bell, S.E.J. (2008). Recent applications of chemical imaging to pharmaceutical process monitoring and quality control. *European Journal of Pharmaceutics and Biopharmaceutics*, **69**(1), 10–22.

Guillard, F., Trägårdh, C. & Fuchs, L. (2000a). New image analysis methods for the study of mixing patterns in stirred tanks. *The Canadian Journal of Chemical Engineering*, **78**, 273–285.

Guillard, F., Trägårdh, C. & Fuchs, L. (2000b). A study on the instability of coherent mixing structures in a continuously stirred tank. *Chemical Engineering Science*, **55**(23), 5657–5670.

Guiraud, P., Costes, J. & Bertrand, J. (1997). Local measurements of fluid and particle velocities in a stirred suspension. *Chemical Engineering Journal*, **68**(2–3), 75–86.

Hasan, O.S., Alvarez, M.M., Muzzio, F.J. & Buettner, H.M. (1999). Characterization of suspension flows using particle image velocimetry (PIV), *Paper presented at the AIChE Annual Meeting, Advanced Technologies for Fluid-Particle Systems Symposium*, Miami Beach, FL, 15–20 November 1998.

Holden, P.J., Wang, M., Mann, R., Dickin, F.J. & Edwards, R.B. (1998). Imaging stirred-vessel macromixing using electrical-resistance tomography. *AIChE Journal*, **44**, 780–790.

Huang, H., Yu, H., Xu, H. & Ying, Y. (2008). Near infrared spectroscopy for on/in-line monitoring of quality in foods and beverages: a review. *Journal of Food Engineering*, **87**(3), 303–313.

Jørgensen, F.E. (1996). The computer-controlled constant-temperature anemometer. Aspects of set-up, probe calibration, data acquisition and data conversion. *Measurement Science and Technology*, **7**(10), 1378–1387.

Kieviet, F.G., Van Raaij, J., De Moor, P.P.E.A. & Kerkhof, P.J.A.M. (1997). Measurement and modelling of the air flow pattern in a pilot-plant spray dryer. *Chemical Engineering Research and Design*, **75**(3), 321–328.

King, L.V. (1914). On the convection of heat from small cylinders in a stream of fluid: determination of the convection constants of small platinum wires with applications to hot wire anemometry. *Philosophical Transactions of the Royal Society of London. Series A, Containing Papers of a Mathematical or Physical Character*, **214**, 373–432.

Kumaresan, T. & Joshi, J.B. (2006). Effect of impeller design on the flow pattern and mixing in stirred tanks. *Chemical Engineering Journal*, **115**(3), 173–193.

La Fontaine, R.F. & Shepherd, I.C. (1996). Particle image velocimetry applied to a stirred vessel. *Experimental Thermal and Fluid Science*, **12**(2), 256–264.

Laakkonen, M., Honkanen, M., Saarenrinne, P. & Aittamaa, J. (2005). Local bubble size distributions, gas–liquid interfacial areas and gas holdups in a stirred vessel with particle image velocimetry. *Chemical Engineering Journal*, **109**(1–3), 37–47.

Laakkonen, M., Alopaeus, V. & Aittamaa, J. (2006). Validation of bubble breakage, coalescence and mass transfer models for gas–liquid dispersion in agitated vessel. *Chemical Engineering Science*, **61**(1), 218–228.

Law, A.W.-K. & Wang, H. (2000). Measurement of mixing processes with combined digital particle image velocimetry and planar laser induced fluorescence. *Experimental Thermal and Fluid Science*, **22**(3–4), 213–229.

Le Coënt, A.L., Rivoire, A., Briançon, S. & Lieto, J. (2005). An original image-processing technique for obtaining the mixing time: the box-counting with erosions method. *Powder Technology*, **152**(1–3), 62–71.

Lee, Y., McCarthy, M.J. & McCarthy, K.L. (2001). Extent of mixing in a two-component batch system measured using MRI. *Journal of Food Engineering*, **50**(3), 167–174.

Li, M., White, G., Wilkinson, D. & Roberts, K.J. (2005). Scale up study of retreat curve impeller stirred tanks using LDA measurements and CFD simulation. *Chemical Engineering Journal*, **108**(1–2), 81–90.

Ljungqvist, M. & Rasmuson, A. (2004). The two-phase flow in an axially stirred vessel investigated using phase-Doppler anemometry. *Canadian Journal of Chemical Engineering*, **82**(2), 275–288.

Lu, W.-M. & Ju, S.-J. (1987). Application of hot-film anemometry to air–water flow in aerated stirred tanks. *Chemical Engineering Communications*, **56**, 57–75.

Luo, P., Cheng, Y., Zhao, Y., Jin, Y. & Yang, W. (2007). Millisecond mixing of two liquid streams in a mixer model. *Chemical Engineering Science*, **62**(18–20), 5688–5695.

Mann, R., Dickin, F.J., Wang, M. *et al*. (1997). Application of electrical resistance tomography to interrogate mixing processes at plant scale. *Chemical Engineering Science*, **52**, 2087–2097.

Martinant, J.P., Nicolas, Y., Bouguennec, A., Popineau, Y., Saulnier, L. & Branlard, G. (1998). Relationships between mixograph parameters and indices of wheat grain quality. *Journal of Cereal Science*, **27**(2), 179–189.

Mavros, P. (2001). Flow visualization in stirred vessels: a review of experimental techniques. *Chemical Engineering Research and Design*, **79**(2), 113–127.

Metzner, A.B. & Otto, R.E. (1957). Agitation of non-Newtonian fluids. *AIChE Journal*, **3**, 3–10.

Nagano, Y. & Tsuji, T. (1994). Recent developments in hot- and cold-wire techniques for measurements in turbulent shear flows near walls. *Experimental Thermal and Fluid Science*, **9**(2), 94–110.

Okamoto, K., Nishio, S., Saga, T. & Kobayashi, T. (2000). Standard images for particle-image velocimetry. *Measurement Science and Technology*, **11**(6), 685–691.

Pakzad, L., Ein-Mozaffari, F. & Chan, P. (2008). Using electrical resistance tomography and computational fluid dynamics modeling to study the formation of cavern in the mixing of pseudo-plastic fluids possessing yield stress. *Chemical Engineering Science*, **63**(9), 2508–2522.

Patwardhan, A.W. & Joshi, J.B. (1999). Relation between flow pattern and blending in stirred tanks. *Industrial and Engineering Chemistry Research*, **38**, 3131–3143.

Pemberton, S.T. & Davidson, J.F. (1984). Turbulence in the freeboard of a gas-fluidised bed: the significance of ghost bubbles. *Chemical Engineering Science*, **39**(5), 829–840.

Pettersson, M. & Rasmuson, A.C. (1997). Application of three-dimensional phase-Doppler anemometry to mechanically agitated crystallizers. *Chemical Engineering Research and Design*, **75**, 132–141.

Porion, P., Sommier, N., Faugère, A. & Evesque, P. (2004). Dynamics of size segregation and mixing of granular materials in a 3D-blender by NMR imaging investigation. *Powder Technology*, **141**(1–2), 55–68.

Rahimi, M., Senior, P.R. & Mann, R. (1999). Image-reconstruction 3D visual modelling of stirred vessel mixing for an inclined-blade impeller. In: *Fluid Mixing 6 (IChemE Symp. Ser. no. 146)* (ed. H. Benkreira). IChemE, Rugby, UK, pp. 135–145.

Roggo, Y., Chalus, P., Maurer, L., Lema-Martinez, C., Edmond, A. & Jent, N. (2007). A review of near infrared spectroscopy and chemometrics in pharmaceutical technologies. *Journal of Pharmaceutical and Biomedical Analysis*, **44**(3), 683–700.

Sherif, S.A. & Pletcher, R.H. (1991). A hot-wire/film probe method for the measurement of turbulent stresses and heat fluxes in nonisothermal highly three-dimensional flows. *Experimental Thermal and Fluid Science*, **4**(1), 127–134.

Simoncelli, E.P. & Freeman, W.T. (1995). The steerable pyramid: a flexible architecture for multi-scale derivative computation. *Paper presented at the Proceedings of IEEE International Conference on Image Processing*, Washington DC.

Solimene, R., Marzocchella, A., Ragucci, R. & Salatino, P. (2007). Laser diagnostics of hydrodynamics and gas-mixing induced by bubble bursting at the surface of gas-fluidized beds. *Chemical Engineering Science*, **62**(1–2), 94–108.

Szalai, E.S., Arratia, P., Johnson, K. & Muzzio, F.J. (2004). Mixing analysis in a tank stirred with Ekato Intermig® impellers. *Chemical Engineering Science*, **59**, 3793–3805.

Utomo, A.T., Baker, M. & Pacek, A.W. (2008). Flow pattern, periodicity and energy dissipation in a batch rotor–stator mixer. *Chemical Engineering Research and Design*, **86**(12), 1397–1409.

Van Puyvelde, D.R., Young, B.R., Wilson, M.A. & Schmidt, S.J. (1999). Experimental determination of transverse mixing kinetics in a rolling drum by image analysis. *Powder Technology*, **106**(3), 183–191.

Virdung, T. & Rasmuson, A. (2007). Measurements of continuous phase velocities in solid–liquid flow at elevated concentrations in a stirred vessel using LDV. *Chemical Engineering Research and Design*, **85**(2), 193–200.

Wadley, R. & Dawson, M.K. (2005). LIF measurements of blending in static mixers in the turbulent and transitional flow regimes. *Chemical Engineering Science*, **60**(8–9), 2469–2478.

Wang, M., Dorward, A., Vlaev, D. & Mann, R. (2000). Measurements of gas–liquid mixing in a stirred vessel using electrical resistance tomography (ERT). *Chemical Engineering Journal*, **77**(1–2), 93–98.

Wernersson, E.S. & Tragardh, C. (2000). Measurements and analysis of high-intensity turbulent characteristics in a turbine-agitated tank. *Experiments in Fluids*, **28**(6), 532–545.

Wesley, I.J., Larsen, N., Osborne, B.G. & Skerritt, J.H. (1998). Non-invasive monitoring of dough mixing by near infrared spectroscopy. *Journal of Cereal Science*, **27**(1), 61–69.

Williams, R.A., Jia, X. & McKee, S.L. (1996). Development of slurry mixing models using resistance tomography. *Powder Technology*, **87**, 21–27.

Woodcock, T., Fagan, C., O'Donnell, C. & Downey, G. (2008). Application of near and mid-infrared spectroscopy to determine cheese quality and authenticity. *Food and Bioprocess Technology*, **1**(2), 117–129.

Yerramilli, L. & Karwe, M.V. (2004). Velocity distributions and mixing in the translational region of a kneading section in a co-rotating twin-screw extruder. *Food and Bioproducts Processing*, **82**(1), 5–12.

8 Computational fluid mixing

Chris D. Rielly and Jolius Gimbun

8.1 Introduction

8.1.1 History of CFD

Computational fluid dynamics (CFD) is an extremely powerful tool for solving problems associated with flow, mixing, heat and mass transfer and chemical reaction. Although the equations of motion for fluid flow were established in the first half of the nineteenth century (Navier 1822; Stokes 1845), it was not until the arrival of digital computers in the 1960s and 1970s that it became feasible to perform numerical simulations of complex engineering flows. In those early days, CFD was very much a research tool and most of the early work was aimed at developing numerical methods, solution algorithms and Reynolds-averaged turbulence models. However, in the 1980s, the first commercial codes emerged—for example, PHOENICS, FLUENT, FIDAP, Star-CD, FLOW3D (which later became CFX)—providing general purpose software packages for both academic and industry users. The aerospace and automotive industries were amongst the first to embrace the use of CFD in engineering design, but from the 1990s onwards, commercial codes have found widespread applications, for example, in biomedical engineering, environmental and atmospheric modelling, meteorology, chemical reaction engineering and, more recently, in the food and beverage industries. This chapter will focus on mixing vessel applications for the last two of these industry sectors, where CFD is increasingly used to provide process understanding and semi-quantitative analysis.

In their review, Norton and Sun (2006) presented a graph showing the very significant increase in the number of peer-reviewed papers related to CFD applications to food process engineering. Figure 8.1 shows an updated version of this graph containing more recent data and showing that the number of papers that specifically analyse food mixing operations using CFD is still relatively small. In contrast, there are a vast number of papers on CFD simulation of (i) other food process operations [e.g., drying, sterilisation, thermal treatment, and extrusion, many of which are described by Sun (2007)] and (ii) more conventional mixing operations in the chemicals and specialty product industries (Marshall & Bakker 2004). This chapter will outline the background knowledge required for CFD studies, present some examples of CFD modelling of mixing vessel flows and finally discuss the current difficulties in applying this approach to food mixing processes.

8.1.2 Steps towards CFD simulation of mixing processes

Although commercial CFD codes provide user-friendly, menu-driven front-ends, there is substantial work to be performed before any computation is carried out, as is shown

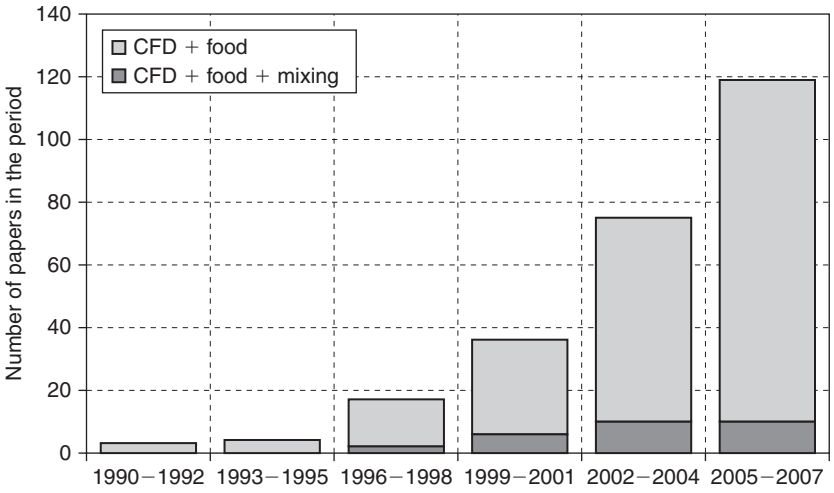

Fig. 8.1 Number of papers published on food and CFD from 1990 to 2007. Updated and enhanced version first shown by Norton and Sun (2006). (Thomson Scientific ISI Web of Knowledge[SM].)

schematically in Figure 8.2. For a mixing problem, before the software is first fired up, a number of questions should be asked, with the aim of defining suitable physical models and assumptions for the simulation.

- Is the flow one, two or three dimensional?
- Can simplifications be made to the flow domain, for example, by using planes of symmetry, periodic boundaries or axisymmetric assumptions?
- Is the flow single phase and/or single component?
- Is the liquid phase Newtonian or non-Newtonian?
- Is the flow laminar, transitional or turbulent?
- Does the flow involve heat and/or mass transfer?
- Is a detailed model of the impeller required?
- Are unsteady-state dynamics important?

These are important decisions to be made because they will affect the complexity and results of the computations. Judicious choice of simplifying assumptions can lead to drastic reductions in computing time, at the expense of only minor losses of accuracy; alternatively, inappropriate assumptions or poor selection of models can produce low-quality solutions with misleading results. This chapter will show how these decisions are implemented in a CFD environment. Although commercial CFD codes appear to give the novice user access to powerful tools, they should be used with caution and expert advice.

The next stage in setting up a simulation is to define material properties and constitutive equations, for example, to represent the effects of pressure and temperature on density or the effects of deformation rate on the apparent viscosity, that is, the rheological law. It may also be necessary to collect data and select equations to represent heat and mass transfer effects and chemical reaction kinetics (simplified kinetic schemes are often required). Information is also required for selection and setting of appropriate boundary conditions for various parts of the flow domain, as described in Section 8.2.7.

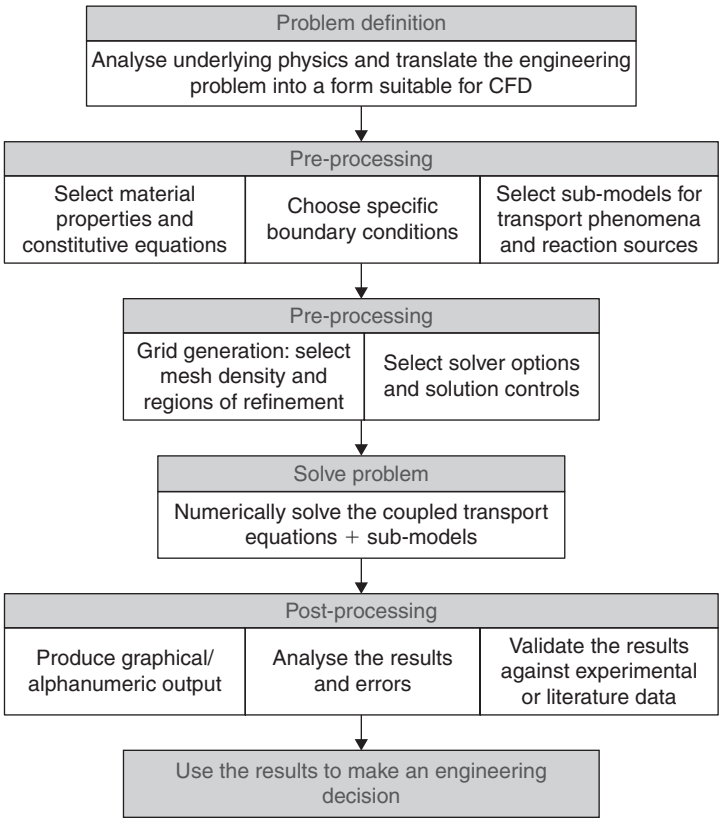

Fig. 8.2 Procedure for the solution of a mixing problem via CFD simulation.

The steps up until this point have mainly involved the collection of data and the selection, based on engineering knowledge, of appropriate constitutive and transport models. The final part of pre-processing is carried out within the software environment and involves:

- detailed definition of the internal flow domain, using the dimensions and geometry of the mixer; often this is input or imported through a Computer Aided Design (CAD)s interface;
- generation of a grid, which discretises the flow domain into a large number of control volumes; the grid does not need to have a regular structure, can be fitted around complex geometries and can be refined in regions where greater resolution is required (see Section 8.3.2);
- input of the fluid properties (often available as part of a library), selection of appropriate models to represent the flow physics and chemistry, and input of boundary and operating conditions, based on the information obtained previously and on engineering judgements with regard to suitable assumptions and simplifications;
- Initialisation of the velocity, pressure and concentration or temperature fields, either as starting guesses for an iterative solution or as initial conditions for a transient calculation (see Section 8.3.4);

- selection of suitable numerical schemes, solution monitors and controls; typically, software will contain default settings so that robust, but possibly slow and inaccurate, schemes are implemented; improved convergence rates and accuracies may be achieved by expert selection of the numerical schemes, but often this is done only after a partially converged solution has been obtained (see Sections 8.3.4 and 8.3.5).

By this point, the problem is fully specified within the computer software, although the user does not see the detailed numerics behind the code, nor is there a requirement for the user to discretise the differential transport equations which will be solved in the ensuing calculations. Typically, the user would then initialise the problem and then set the code running to converge to a solution (or for transient cases, to run for a set period of time). The progress of the solution can be monitored via residuals, which are measures of the errors in solving each of the transport equations (described in Section 8.3.5). Most codes can be set to terminate the iterations when the residuals have fallen below some prescribed value; typically, default values are supplied by the code vendor, which would mean that the solution was well enough converged for engineering design purposes.

Convergence of the numerical solution is just one aspect of obtaining an accurate solution—it means that the errors in the conservation balance equations are small, but it does not guarantee that the spatial distribution of velocities, pressures, etc. are accurately predicted. The latter should be demonstrated by grid independence studies. The initial grid that was generated is often coarse, but it can later be refined (made smaller), so that gradients in the flow are more accurately represented [see, e.g., the grid independence study reported by Aubin *et al*. (2004a)]. If the velocity and pressure fields do not change when the grid is refined, then an accurate, grid-independent solution has been obtained. In cases where the solution does change, then further grid refinement is required. Fluid mechanics know-how should be applied to increase the density of grid points in regions where strong velocity gradients might be expected, for example, close to walls or moving blades. An example of this type of grid refinement is shown in Figure 8.3: the grid spacing has been reduced around the impeller level to resolve the strong velocity gradients in this region of the discharge flow, where trailing vortices are attached to each impeller blade. This is a more intelligent use of grid refinement, rather than simply increasing the grid density at all points in the flow, and can lead to significant improvements in computational efficiency. For transient flows, time step independence should also be demonstrated by decreasing Δt until the solution stops changing. Grid and time step independence studies are laborious calculations but are necessary to demonstrate the accuracy of the solution.

Commercial CFD codes provide a wide range of post-processing options to display, visualise and analyse the flow solutions. Graphical tools allow visualisation of the flow geometry and grid distribution, as well as output of vector, contour and 3D plots of any of the flow or transport variables. Individual planes or surfaces, or profiles can be plotted and manipulated by rotation, scaling and perspective within the flow domain; transient solutions can be animated for greater visual effect and addition effects such as particle tracking can be applied to show flow patterns.

Inexpert users often stop at this point and admire their colourful graphical output. However, the job is not yet done. Expert users would attempt to validate their CFD model using experimental data, for example, obtained from small-scale equipment and preferably based on local velocity, pressure or temperature measurements. Chapter 7 discusses some methods for obtaining velocity measurements in small-scale flows, namely, laser-Doppler anemometry (LDA) and particle image velocimetry (PIV). Alternatively, some validation

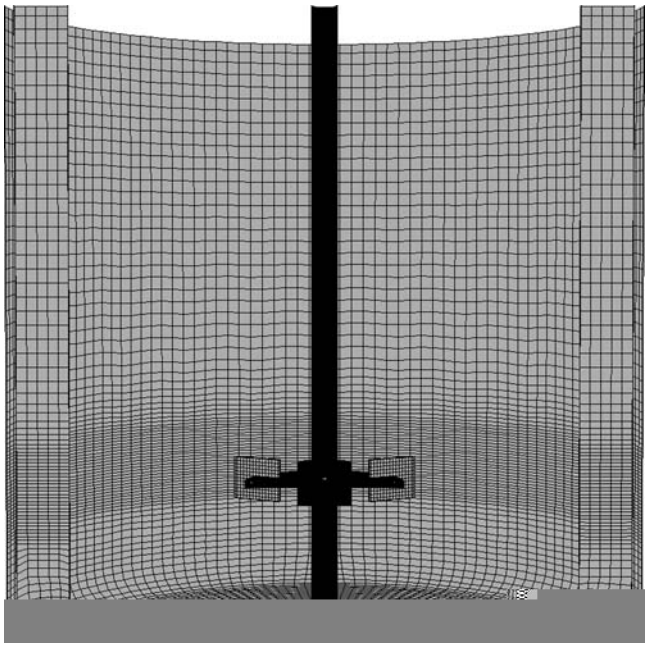

Fig. 8.3 Computational mesh shown on the wall of a stirred vessel containing a Rushton disk turbine (Gimbun 2008).

could be obtained by comparing global characteristics of the flow with experimental observations, for example, flow pattern comparison, or flow number or power number comparisons with literature values (see Section 8.4.3). By making such validation studies, the user provides an extra check that physical models, simplifying assumptions, numerical schemes and discretisation methods have been appropriately chosen. Successful validation of the CFD model at small scale generally indicates that accurate solution of the velocity, temperature and pressure fields would be obtained in larger scale, but geometrically similar equipment. Poor agreement with experimental data may suggest ways in which the simulation assumptions or models can be improved.

Finally, as is indicated in Figure 8.2, the reason for conducting the CFD simulation was to answer some questions about the fluid flow, mixing, heat transfer rate, or to design and optimise the performance of a new process. So, now the solution must be interpreted and analysed, and judgement must be exercised. Hence, it should be obvious all along the way that there is a need for fluid mechanics knowledge and physical insight to define the problem, choose suitable simulation conditions, validate and verify the result and finally interpret the solution to provide an answer to an engineering problem.

So far, a general approach has been described to simulate mixing operations using CFD. The following sections will provide basic information which will be useful in deciding how to implement the various models and methods. Section 8.2 describes the fundamental transport equations that must be solved for flows with mixing and heat transfer in the laminar and turbulent regimes; selection of suitable boundary conditions is also discussed. The numerical methods to solve these equations are then outlined in Section 8.3, and special techniques for handling impeller-driven flows are covered in Section 8.4. The latter section also presents a number of examples from the literature of studies, which have simulated

liquid flows, blending and multi-phase mixing applications. Finally, the challenges for modelling mixing operations related to food processing are discussed, and some examples of dough mixing and crystalliser design are reviewed.

8.2 Conservation equations

A key hypothesis in dealing with flow and mixing problems is that the fluid behaves as a continuum (Batchelor 2000), such that local values of the velocity, pressure and density may be defined at a point, and these properties change smoothly in space and time. In other words, the molecular structure of a gas or liquid is not considered explicitly, and the fluid is treated as a macroscopic continuum. On this basis, the governing equations of fluid mechanics may be obtained by application of the following fundamental laws.

1. *Mass conservation*: mass cannot be created or destroyed.
2. *Newton's second law*: the rate of change of momentum is equal to the sum of the forces acting on a fluid element.
3. *The first law of thermodynamics*: energy can be converted between different forms, but is neither created nor destroyed.
4. *Chemical species conservation*: atomic species are conserved, whereas molecular species can be transformed by chemical reactions, with a prescribed stoichiometry.

Detailed discussion and formulation of these transport equations can be obtained in fluid mechanics text books such as *Transport phenomena* by Bird *et al*. (2007). Here, the aim is to give the reader an insight into the general structure of these equations, which all essentially take the same form.

Consider the arbitrary control volume, V, which is fixed in space and is bounded by a surface S, shown in Figure 8.4. For any scalar property Φ, the general conservation law may be stated as:

$$\begin{matrix}\text{Rate of accumulation} \\ \text{of } \Phi \text{ Inside } V\end{matrix} + \begin{matrix}\text{Net efflux of} \\ \Phi \text{ through } S\end{matrix} = \begin{matrix}\text{Sources of} \\ \Phi \text{ inside } V\end{matrix} - \begin{matrix}\text{Sinks of } \Phi \\ \text{inside } V\end{matrix} \tag{8.1}$$

or in terms of mathematics as:

$$\int_V \frac{\partial(\rho\Phi)}{\partial t}\mathrm{d}V + \int_S (\rho \boldsymbol{u}\Phi + \boldsymbol{j}_\Phi)\cdot \mathrm{dS} = \int_V S_\Phi \mathrm{d}V \tag{8.2}$$

where $\boldsymbol{u}$ is the velocity vector, $\boldsymbol{j}_\Phi$ is the diffusive flux of Φ through surface S, Φ is the fluid density and S_Φ is the sum of sources minus sinks for Φ inside the control volume V. Note that here Φ is written as an intensive scalar quantity per unit mass and that transport of Φ across the boundary can occur by both convection and diffusion. Using Gauss' divergence theorem allows the rewriting of the flux through surface S as the volume integral of a divergence and hence:

$$\frac{\partial(\rho\Phi)}{\partial t} + \nabla\cdot(\rho\boldsymbol{u}\Phi) = -\nabla\cdot\boldsymbol{j}_\Phi + S_\Phi \tag{8.3}$$

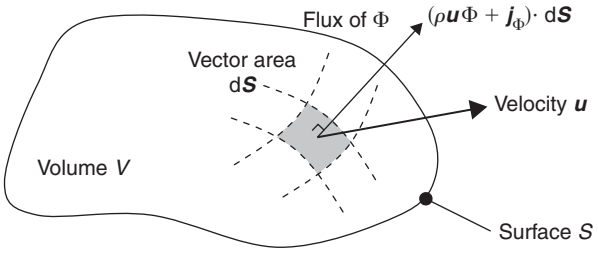

Fig. 8.4 Fixed control volume V bounded by surface S used for conservation balances.

where ∇ is the nabla or del vector operator; for example, in Cartesian coordinates:

$$\nabla = \left(\frac{\partial}{\partial x}, \frac{\partial}{\partial y}, \frac{\partial}{\partial z} \right) \tag{8.4}$$

and (x, y, z) represent the three coordinates. The LHS of equation (8.3) gives the total rate of change of Φ in a fluid particle moving at velocity $\boldsymbol{u}$; in fluid mechanics, this is known as the convective derivative or the derivative following the motion.

$$\frac{\partial(\rho\Phi)}{\partial t} + \nabla\cdot(\rho\boldsymbol{u}\Phi) = \frac{\mathrm{D}(\rho\Phi)}{\mathrm{D}t} \tag{8.5}$$

Almost all fluid mechanics simulations require the application of the general conservation statement of equation (8.3) to mass and momentum. In addition, if heat transfer occurs, resulting in non-isothermal flows, or chemical reaction takes place, then the conservation equation must also be applied to the energy and chemical species balances.

In applying such equations to predict flow and mixing in chemical and food processing operations, it is often permissible to make some simplifying assumptions. For example, the flows will often involve incompressible liquids, in which case the fluid density may be assumed to be a constant and hence may be moved outside the derivatives of equation (8.3).

8.2.1 Mass conservation

For mass conservation, there are no sources and sinks, and the scalar quantity Φ is simply equal to unity. Then, equation (8.3) becomes:

$$\frac{\partial\rho}{\partial t} + \nabla\cdot(\rho\boldsymbol{u}) = 0 \tag{8.6}$$

which is known as the continuity equation. Flows in mixing vessels generally involve an *incompressible* liquid (Φ = constant), in which case equation (8.6) reduces to:

$$\nabla \cdot \boldsymbol{u} = 0 \tag{8.7}$$

which applies to both steady- and unsteady-state flows. In Cartesian (x, y, z) coordinates, with velocity $\boldsymbol{u} = (u, v, w)^t$, equation (8.7) may be written as follows.

$$\nabla \cdot \boldsymbol{u} = \frac{\partial u}{\partial z} + \frac{\partial v}{\partial y} + \frac{\partial w}{\partial z} = 0 \tag{8.8}$$

8.2.2 Momentum conservation

Momentum is a vector quantity and so the conservation equation (8.3) must be applied in each of the coordinate directions. For example, the x-direction momentum per unit volume is ρu and hence, $\Phi = u$. In this case, the LHS of the conservation equation represents the rate of change of x-direction momentum of the fluid:

$$\frac{\partial(\rho u)}{\partial t} + \nabla \cdot (\rho \boldsymbol{u} u) = \frac{\mathrm{D}(\rho u)}{\mathrm{D}t} \tag{8.9}$$

and therefore, according to Newton's second law, the RHS of equation (8.9) must represent the sum of the forces acting on an elemental volume of fluid (VOF). The forces acting on a control VOF may be divided into two types: body forces (e.g., gravity) and surface forces (pressure or viscous stress effects). Figures 8.5 and 8.6 show the stresses acting in the x-direction, using the notation that τ_{ij} is the stress in direction j acting on face with a normal in the direction i. From these figures, it is evident that (i) differences in pressure between the shaded faces give rise to a net force and (ii) differences in viscous stresses on all six faces can result in a contribution to the net force. Hence replacing the RHS of the conservation equation by the forces per unit volume acting on the control volume yields:

$$\frac{\partial(\rho u)}{\partial t} + \nabla \cdot (\rho \boldsymbol{u} u) = -\frac{\partial p}{\partial x} - \left(\frac{\partial \tau_{xx}}{\partial x} + \frac{\partial \tau_{yx}}{\partial y} + \frac{\partial \tau_{zx}}{\partial z} \right) + \rho \boldsymbol{g}_x \tag{8.10}$$

or in all three directions, using vector notation:

$$\rho \frac{\mathrm{D}\boldsymbol{u}}{\mathrm{D}t} = -\nabla p - \nabla \cdot \boldsymbol{\tau} + \rho \boldsymbol{g} \tag{8.11}$$

where $\boldsymbol{\tau}$ is the stress tensor. Equation (8.11) is fully rigorous for incompressible fluids, typical of these found in mixing operations. Other than that it is quite general, in that it could be applied to both Newtonian and non-Newtonian fluids, by changing the constitutive equation relating the stress tensor $\boldsymbol{\tau}_{ij}$ to the deformation rate tensor $\boldsymbol{S}_{ij}$. For example, equation (8.11) can easily be extended to the special case of an incompressible Newtonian fluid (see Chapter 3) with a constant viscosity coefficient Φ.

$$\boldsymbol{\tau}_{ij} = \mu \boldsymbol{S}_{ij} = \mu \left(\frac{\partial u_i}{\partial x_j} + \frac{\partial u_j}{\partial x_i} \right) \tag{8.12}$$

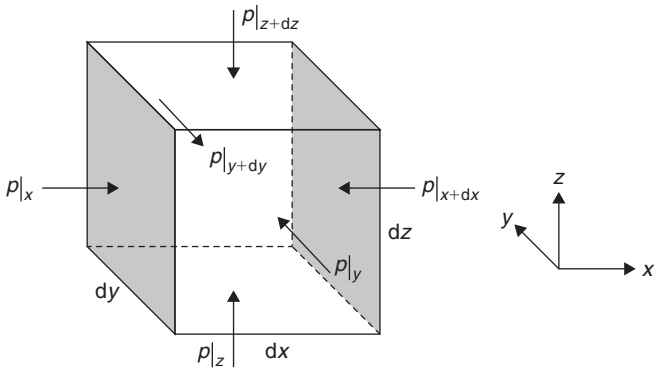

Fig. 8.5 Cartesian fluid element with a pressure gradient giving rise to normal force differences acting on its faces.

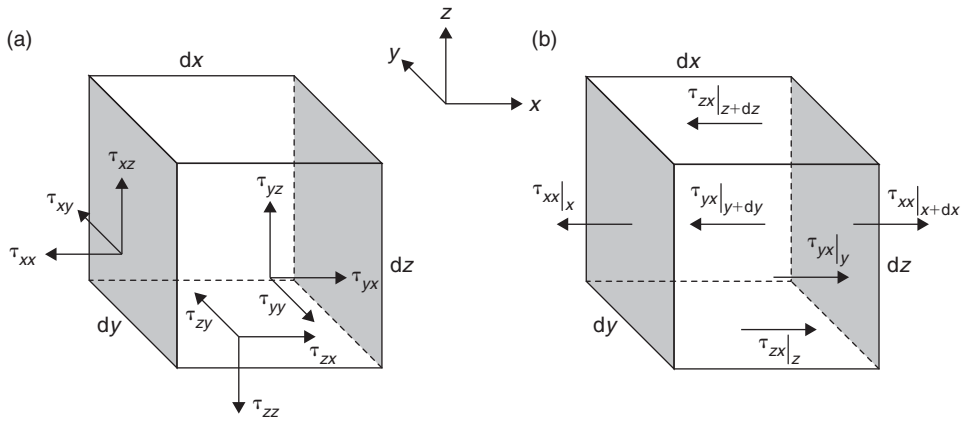

Fig. 8.6 Cartesian fluid element showing (a) the stresses acting on three of its faces and (b) the stresses that contribute to the *x*-direction force.

Use of equation (8.12), along with the incompressible continuity equation (8.7), leads to the well-known Navier–Stokes equations.

$$\rho \frac{\mathrm{D}\boldsymbol{u}}{\mathrm{D}t} = -\nabla p - \mu \nabla^2 \boldsymbol{u} + \rho \boldsymbol{g} \tag{8.13}$$

Alternatively, other constitutive models may be applied to equation (8.11) to relate the stress tensor components to velocity gradients in the flow. In these cases, the *apparent* viscosity, μ_a, of the fluid depends on the second invariant of the local deformation rates according to:

$$\mu_a = f(\dot{\gamma}) \quad \text{where } \dot{\gamma} = \sqrt{\tfrac{1}{2} S_{ij} S_{ij}} \tag{8.14}$$

where summation is implied over the repeated suffixes i and j. In commercial CFD codes, such as FLUENT, a variety of constitutive models are available to describe non-Newtonian

rheologies in the laminar flow regime, for example, power law, Carreau model, Cross model and Herschel–Bulkley model for Bingham plastics (shear thinning fluids with a yield stress). Constitutive parameters for these models must be obtained from experimental tests, as described in Chapter 4.

8.2.3 Turbulence

The conditions for laminar, transitional and turbulent flows may be distinguished according to a dimensional group known as the Reynolds number, which in general may be defined as:

$$Re = \frac{\text{inertial stresses}}{\text{viscous stresses}} = \frac{\rho UL}{\mu} \tag{8.15}$$

where U is a characteristic velocity scale and L is a characteristic length scale. In mixer designs, these are conventionally defined in terms of the impeller tip speed (proportional to ND, where N is the rotational speed, conventionally in rev/s) and the impeller diameter D.

$$Re = \frac{\rho ND^2}{\mu} \tag{8.16}$$

Typically, in stirred vessels flows, the flow is laminar for $Re < 10$ and fully turbulent for $Re > 10^4$. Thus, there is a wide range of transitional flow over $10 < Re < 10^4$, where the flow is turbulent around the impeller and relaminarises in the bulk. This is a particularly challenging area for CFD.

Turbulent flows are characterised by three-dimensional, fluctuating velocity components which lead to increased rates of transport for mass, momentum and energy. Although the equations presented in Sections 8.2.1 and 8.2.2 are valid for turbulent flow, they must be applied instantaneously and hence required to be solved using very short time and space steps to model the flow accurately. With modern computing resources, this type of direct numerical simulation (DNS) is possible for some limited cases of low Reynolds number turbulence, but for most practical applications, the number of grid and time steps required is orders of magnitude too high to be feasible. Hence, a statistical approach known as Reynolds averaging is often applied to the description of turbulence quantities [see Versteeg and Malalasekara (2007) for a more detailed account].

The Reynolds-averaged Navier–Stokes (RANS) equations result from decomposing the velocities, $\boldsymbol{u}$, and all other scalar quantities, ϕ (pressure, temperature, mass fraction), into mean and fluctuating components.

$$\boldsymbol{u} = \overline{\boldsymbol{u}} + \boldsymbol{u}' \quad \text{and} \quad \Phi = \overline{\Phi} + \Phi' \tag{8.17}$$

Time averaging the continuity equation (8.7) gives:

$$\nabla \cdot \overline{\boldsymbol{u}} = 0 \tag{8.18}$$

whereas, applying the same process to equation (8.11) generates additional Reynolds stresses, $\overline{\tau_T}$, due to the averaging of the non-linear advection terms, $\boldsymbol{u} \cdot \nabla u$.

$$\rho\frac{\mathrm{D}\bar{\boldsymbol{u}}}{\mathrm{D}t} = -\nabla\bar{p} - \nabla\cdot\overline{\boldsymbol{\tau}_{\mathrm{L}}} - \nabla\cdot\overline{\boldsymbol{\tau}_{\mathrm{T}}} + \rho\boldsymbol{g} \tag{8.19}$$

As before, the laminar stress tensor is given in terms of the mean velocity gradients by the following equation.

$$(\overline{\boldsymbol{\tau}_{\mathrm{L}}})_{ij} = \mu\left(\frac{\partial\overline{u_i}}{\partial x_j} + \frac{\partial\overline{u_j}}{\partial x_i}\right) \tag{8.20}$$

However, six new unknown quantities, the Reynolds stresses:

$$(\overline{\boldsymbol{\tau}_{\mathrm{T}}})_{ij} = (\overline{\boldsymbol{\tau}_{\mathrm{T}}})_{ji} = -\rho\overline{u_i' u_j'} \tag{8.21}$$

have now been introduced, but with no new equations to represent their transport. They represent turbulent momentum fluxes and involve statistical correlations between the various fluctuating velocity components. There is now a turbulence closure problem, with more unknowns than equations, and hence the new terms must be approximated by empirical models. One such model is based on the Boussinesq hypothesis, which draws an analogy with the laminar stress tensor in equation (8.20) and proposes:

$$(\overline{\boldsymbol{\tau}_{\mathrm{T}}})_{ij} = -\rho\overline{u_i' u_j'} = \mu_{\mathrm{T}}\left(\frac{\partial\overline{u_i}}{\partial x_j} + \frac{\partial\overline{u_j}}{\partial x_i}\right) - \frac{2}{3}\rho k\delta_{ij} \tag{8.22}$$

where μ_{T} is a turbulent or eddy viscosity, $k = \frac{1}{2}(\overline{u_i'^2} + \overline{u_j'^2} + \overline{u_k'^2})$ is the turbulent kinetic energy per unit mass and $\delta_{ij} = 0$, $i \neq j$ and $\delta_{ij} = 1$, $i = j$ is the Kronecker delta. However, this has not yet solved the turbulence closure problem, as the eddy viscosity is still unknown and has to be computed from further empirical models. In contrast to the laminar viscosity, μ, the eddy viscosity is not a material property; it depends on strain rates and eddy length scales in the flow and hence is distributed in time and space.

The two-equation $k - \varepsilon$ turbulence model is a popular method to calculate μ_{T}, where k is the turbulence kinetic energy defined earlier and ε is its dissipation rate (the rate at which the turbulence kinetic energy is converted to heat by viscous effects at the scale of the smallest eddies—the Kolmogorov scale). The standard $k - \varepsilon$ model calculates the (isotropic) eddy viscosity from:

$$\mu_{\mathrm{T}} = \rho C_\mu \frac{k^2}{\varepsilon} \tag{8.23}$$

where C_μ is a dimensionless constant. Approximate transport equations for k and ε are formulated for incompressible flow as:

$$\rho\frac{\partial k}{\partial t} + \rho\bar{\boldsymbol{u}}\cdot\nabla k = \nabla\cdot\left[\left(\mu + \frac{\mu_{\mathrm{T}}}{\sigma_k}\right)\nabla k\right] + 2\mu_{\mathrm{T}}S_{ij}S_{ij} - \rho\varepsilon \tag{8.24}$$

and

$$\rho\frac{\partial\varepsilon}{\partial t}+\rho\bar{\boldsymbol{u}}\cdot\nabla\varepsilon=\nabla\cdot\left[\left(\mu+\frac{\mu_{\mathrm{T}}}{\sigma_{\varepsilon}}\right)\nabla\varepsilon\right]+C_{1\varepsilon}\frac{\varepsilon}{k}2\mu_{\mathrm{T}}S_{ij}S_{ij}-C_{2\varepsilon}\rho\frac{\varepsilon^{2}}{k} \tag{8.25}$$

Whilst the k equation is almost exact, the ε equation contains a number of modelled terms and empirical constants. The standard $k-\varepsilon$ model contains five such constants:

$$C_{\mu}=0.09,\ \sigma_{k}=1.00,\ \sigma_{\varepsilon}=1.30,\ C_{1\varepsilon}=1.44,\ C_{2\varepsilon}=1.92 \tag{8.26}$$

which have been tuned by data fitting experiments conducted in turbulent shear flows and grid generated turbulence. It may be tempting to alter these empirical constants to obtain better agreement with experimental results, but this is not recommended as a good practice (Versteeg & Malalasekara 2007).

Thus, with such a model, the transport equations (8.24) and (8.25) may be solved to give the distributions of k, ε and the eddy viscosity via equation (8.23). Hence the unknown Reynolds stresses may be calculated from equation (8.22) for inclusion in the RANS equation (8.19).

Many variants of the standard $k-\varepsilon$ model have been proposed, amongst which are:

- The *RNG* $k-\varepsilon$ *model* was obtained from renormalization group (RGN) theory by Yakhot and Orszag (1986) and has the following features: (i) a strain-dependent term was added in the ε equation, which improves its accuracy for rapidly strained flows, such as bends and expansions; (ii) the effects of swirl are more accurately modelled, which are important features of many mixing flows; (iii) the effective viscosity is obtained from a differential equation, which better accounts for low Reynolds number effects and hence is better suited to transitional flows.
- The *realisable* $k-\varepsilon$ *model* was proposed by Shih *et al.* (1995) and differs from the standard form in that it has (i) a new expression for the calculation of the eddy viscosity, with a variable value of $C\mu$ and (ii) entirely different source and sink terms for the ε equation. It is claimed to be superior for flows that involve the spreading of planar and round jets (e.g., as in the discharge stream from an impeller) and for flows with rotation and recirculation.

In contrast, other RANS turbulence models do not make use of the Boussinesq hypothesis, with its in-built assumption of an isotropic eddy viscosity. Instead, the Reynolds stress model (RSM) solves individual transport equations for each of the six independent Reynolds stresses, plus a further conservation equation for the dissipation rate (in contrast, the standard $k-\varepsilon$ model only solves extra two equations to simulate turbulent flows). The model is too complex to present in detail here but is discussed further by Versteeg and Malalasekara (2007). As before, the closure problem forces some of the terms in the RSM equations to be modelled by empirical means. The greater number of transport equations to be solved in the RSM significantly increase the computational overhead of performing the calculations. In principle, RSM models should give improved predictions for flows that involve swirl, significant streamline curvature and rapid straining, that is, where an isotropic eddy viscosity assumption is invalid. In practice, as is described in Section 8.4.5, they have not offered great improvement for stirred mixer simulations.

Although a large number of RANS-based approaches have been proposed, there is no general model that is capable of producing accurate turbulence descriptions for a wide variety of flows. This is partly down to the difficulty in modelling both large eddies, whose direction is dependent on the geometry of the flow, and small eddies, who tend to have a more universal and isotropic character [see Kolmogorov's (1941) local isotropy assumption, which is valid for high Reynolds numbers, for a developed inertial sub-range of the energy spectrum]. A more recent approach is to resolve numerically the largest eddies in a time-dependent calculation and model only the smallest eddies, using, for example, the Boussinesq hypothesis. This is the basis of large eddy simulations (LES), which use spatial filtering and a cut-off width to separate large and small eddy effects. The resulting filtered Navier–Stokes equations may then be used to calculate explicitly the unsteady velocities of the large-scale eddies (larger than the cut-off width), whereas the small-scale eddies are represented through a subgrid-scale stress model, based on the eddy viscosity concept.

Figure 8.7 represents schematically the hierarchy of approaches to turbulence modelling. DNS uses fantastically detailed numerical simulation to resolve in time and space the motions of even the very smallest, Kolmogorov eddies in the flow, but is generally unsuitable for practical application. At the other extreme, RANS models predict only time-averaged quantities of the flow; whilst they can be tuned for certain flow pathologies, they are essentially empirical in nature and liable to provide less accurate results for flows in mixing vessels, which involve strong streamline curvature, flow separation and rapid straining. The compromise is to use LES, with a filtering scale chosen to represent the important eddy sizes; even still, practical applications at high Reynolds numbers will still involve lengthy computations, especially for wall-bounded flows.

LES is an excellent approach away from the boundary layer; however, it may not yield sufficient resolution of the near-wall flow structure, especially at high Reynolds numbers because the large eddies close to the wall are physically small in size. It is possible to resolve this near-wall flow structure using a very fine grid, but this will make the mesh requirement (and hence the computational demand) almost equivalent to that of DNS (Spalart *et al*. 1997). Inadequate grid resolution of boundary layers can severely degrade the LES approximation, and thus, separated flows may not be predicted accurately. To solve this problem, Spalart *et al*. (1997) proposed a new turbulence model called detached eddy simulation (DES), which combines both the RANS and LES models. The main idea is to combine RANS modelling with LES for applications in which the classical LES is not affordable, that is, in the boundary layers. DES reduces to RANS model in the boundary layer, thus permitting a coarser grid than for conventional LES, resulting in fewer overall mesh points and faster computation. This approach retains the full sensitivity of RANS model predictions around the boundary layer and the LES away from the wall. Despite its potential, the DES so far has not yet been used for simulating the mixing tanks.

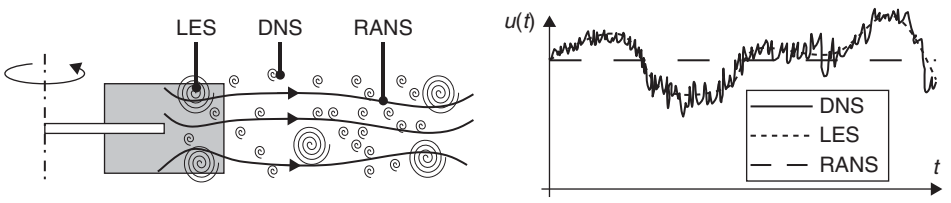

Fig. 8.7 Schematic representation of the various levels of turbulence model for implementation in CFD calculations.

8.2.4 Energy conservation

Non-isothermal flows may be modelled by solving an additional equation, based on conservation of energy. This would be necessary for flows that involve (i) heat transfer from jackets or coils; (ii) chemical reaction, which releases or consumes heat and (iii) considerable energy dissipation, which converts mechanical energy to heat through viscous effects. High-viscosity fluids, such as bread dough, are likely to experience significant temperature rises during mixing because of viscous dissipation, whereas for low-viscosity solutions, the flows can often be treated as isothermal.

For energy conservation, the quantity Φ in equation (8.3) is equivalent to the specific energy which is conveniently written as c_pT. The conductive heat flux is usually represented by Fourier's law which leads to:

$$\rho c_p \frac{\partial T}{\partial t} + \rho c_p (\boldsymbol{u} \cdot \nabla T) = \kappa \nabla^2 T + Q + E \tag{8.27}$$

where κ is the thermal conductivity, Q is a volumetric rate of heat generation (e.g., from electrical resistance heating or from chemical reaction) and the term $\boldsymbol{E} = -\boldsymbol{\tau} : \nabla \boldsymbol{u}$ represents viscous dissipation of heat. In equation (8.27), it has been assumed that the density, specific heat capacity and thermal conductivity of the fluid are constants and independent of temperature. Generally, commercial software codes will use a slightly more complex form of the energy equation, which allows for temperature-dependent physical and transport properties.

In tackling non-isothermal flow problems, it is worth considering how strongly coupled the temperature field is with the flow field. In many cases where forced convection dominates, the dissipation term is negligible compared to the enthalpy transport terms, and hence, the energy equation is effectively uncoupled from the momentum equations. In such a case, the velocity and pressure fields can be converged to a solution first, without considering temperature variations. Then the energy equation can be switched on and solved simultaneously independent of the momentum and continuity equations. On the other hand, for flows involving natural convection, the effects of temperature-dependent properties are important, and there is strong coupling between the energy and momentum equations. These types of considerations determine the order in which the equations are solved in CFD and the requirements to solve them independently or simultaneously.

8.2.5 Species transport

In chemically reacting flows, mixing operations or flows with mass transfer, the mass fractions, Y_j of the various components within a mixture may be calculated from a differential mass balance:

$$\rho \frac{\partial Y_i}{\partial t} + \rho (\boldsymbol{u} \cdot \nabla Y_i) = D_{im} \rho \nabla^2 Y_i + R_i + S_i \tag{8.28}$$

where D_{im} is the molecular diffusivity of species i in the liquid solvent, R_i is a rate of production of i per unit volume by chemical reaction and S_i represents other volumetric source terms, for example, through inter-phase mass transfer. For a mixture containing C components, there are $C - 1$ independent species transport equations because the mole fractions must add to

unity. The FLUENT manual (Fluent 2005) suggests that accuracy is best obtained by omitting the species with the largest mass fraction (often the solvent or carrier liquid phase). Equation (8.28) is based on assumption that diffusion may be modelled using Fick's law, which will be suitable for either binary cases or where the solutes are at low concentration in the liquid phase.

8.2.6 Turbulent species and energy transport

In turbulent flows, Reynolds averaging of the transport equations (8.27) and (8.28) leads to additional fluxes in the energy and species conservation equations, due to averaging of the non-linear advection terms such as $\boldsymbol{u} \cdot \nabla T$. The extra fluxes are precisely why mixers are designed to operate in turbulent flow. As before, the velocities and/or temperatures and mass fractions are written in terms of mean and fluctuating quantities, for example, in addition to equation (8.17).

$$T = \overline{T} + T' \quad \text{and} \quad Y_i = \overline{Y}_i + Y_i^{'} \tag{8.29}$$

Then, following application of the Boussinesq hypothesis, equations (8.27) and (8.28) become:

$$\rho c_p \frac{\partial \overline{T}}{\partial t} + \rho c_p (\overline{\boldsymbol{u}} \cdot \nabla \overline{T}) = \left(\kappa + \frac{\mu_{\mathrm{T}} c_p}{Pr_{\mathrm{T}}} \right) \nabla^2 \overline{T} + \overline{Q} + \overline{E} \tag{8.30}$$

$$\rho \frac{\partial \overline{Y}_i}{\partial t} + \rho (\overline{\boldsymbol{u}} \cdot \nabla \overline{Y}_i) = \left(D_{im} \rho + \frac{\mu_{\mathrm{T}}}{Sc_{\mathrm{T}}} \right) \nabla^2 \overline{Y}_i + \overline{R}_i + \overline{S}_i \tag{8.31}$$

where the default value of the turbulent Schmidt number is $Sc_{\mathrm{T}} = 0.7$ and for the turbulent Prandtl number is $Pr_{\mathrm{T}} = 0.85$. Seeing these conservation equations together, it becomes obvious that for turbulent flow the eddy transport mechanism is the same for momentum, heat and mass; the eddy thermal and mass diffusivities are approximately equal to the eddy kinematic viscosity. Thus, the eddy diffusivities for mass and heat are given by:

$$D_{iT} = \frac{\mu_{\mathrm{T}}}{\rho Sc_{\mathrm{T}}} \quad \text{and} \quad \alpha_{\mathrm{T}} = \left(\frac{\kappa}{\rho c_p} \right)_{\mathrm{T}} = \frac{\mu_{\mathrm{T}}}{\rho Pr_{\mathrm{T}}} \tag{8.32}$$

respectively.

8.2.7 Boundary conditions

The transport partial differential equations presented in the previous sections represent the general governing equations for incompressible liquid flows with heat and mass transfer. It is the boundary conditions that are imposed on each equation that makes them specific to different flow geometries and operating conditions. This section considers a range of boundary conditions that may be required to simulate flows in mixing vessels.

The vast majority of boundaries in mixing vessel flows are *impermeable walls*, at which the no-slip condition may be applied:

$$\boldsymbol{u} = \boldsymbol{u}_{\mathrm{w}} \tag{8.33}$$

where $\boldsymbol{u}_{\mathrm{w}}$ is the wall velocity vector (tank walls and baffles would have zero velocity, but the walls that constitute the surfaces of the impeller blades and shaft have a non-zero velocity). For the energy and species balance equations, wall boundary conditions can be of two types (shown here for temperature): (i) Dirichlet boundary condition:

$$T = T_{\mathrm{w}} \tag{8.34}$$

where T_{w} is a specified temperature at each point on the wall, and (ii) Neumann boundary condition:

$$\kappa \left.\frac{\partial T}{\partial n}\right|_{\mathrm{w}} = -q_{\mathrm{w}} \tag{8.35}$$

where the direction n is normal to the wall and q_{w} is a specified heat flux. For example, for insulated walls, $q_{\mathrm{w}} = 0$, or for heat transfer to an external environment at temperature T_{ex}, $q_{\mathrm{w}} = h_{\mathrm{ex}}(T_{\mathrm{w}} - T_{\mathrm{ex}})$.

For fully baffled stirred vessels, the free surface is reasonably flat and hence is often modelled using a *symmetry boundary condition* in which the normal velocity component and the tangential velocity gradients are set to zero.

$$u_{\mathrm{n}} = 0 \quad \text{and} \quad \frac{\partial u_{\mathrm{t}}}{\partial n} = 0 \tag{8.36}$$

The latter means that the shear stress on the symmetry surface is zero, which is why it corresponds approximately to a free surface condition (effects such as surface tension are not included).

In stirred tank simulations, it is also possible to reduce computation times for steady-state cases by the use of cyclic boundary conditions, making use, for example, of the fourfold symmetry of a fully baffled vessel. For steady cases (e.g., in RANS simulations, see Section 8.2.3), the flow exhibits fourfold symmetry, and therefore only one quadrant of the mixing tank needs to be considered. Figure 8.8 shows one quadrant of a stirred vessel, containing one of the four wall baffles. The two planar faces of the quadrant are set as cyclic boundary conditions: the velocity at each (r, z) position leaving the left-hand plane is set equal to that arriving at the right-hand plane, at the equivalent position.

$$\boldsymbol{u}(r, z, \theta = 0) = \boldsymbol{u}(r, z, \theta = 90^{\circ}) \tag{8.37}$$

The preceding discussion covers the range of boundary conditions that would be required for batch mixing operations. For continuous flow operations, boundary conditions are also required for liquid inlets and outlets. Inlet boundary conditions are simply specified in terms of the inlet velocity distribution, temperature and mass fraction of the various species i.

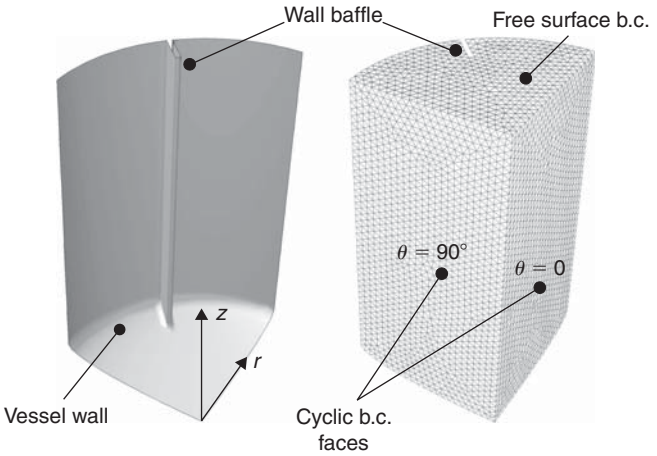

Fig. 8.8 Use of cyclic boundary conditions to reduce computational costs of simulating steady-state, fully baffled flows.

$$\text{Inlet b.c.:} \quad \boldsymbol{u} = \boldsymbol{u}_{\text{in}},\ T = T_{\text{in}} \text{ and } Y_i = (Y_i)_{\text{in}} \tag{8.38}$$

The inlet conditions may be specified using uniform values of $\boldsymbol{u}_{\text{in}}$, T_{in} and $(Y_i)_{\text{in}}$ or using inlet profiles, if they are known. Generally, the pressure does not need to be set at an inlet condition, when the inlet velocity is specified. Occasionally, the inlet velocity will not be known, in which case it will be necessary to specify the inlet pressure and a pressure at the outlet; in this case, the mass flow rate of liquid entering the tank will adjust to match the imposed pressure difference. For turbulent flow calculations using RANS models, inlet boundary conditions for k and ε are also required. An inlet value of k can be estimated from typical turbulence intensities, I, of around 5% for pipe and channel flows, and ε can be estimated using a length scale which is proportional to the diameter of the inlet pipe, D_{in}:

$$k = \frac{3}{2}(|u_{\text{in}}|\, I)^2 \quad \text{and} \quad \varepsilon_{\text{in}} = C_\mu^{3/4} \frac{k_{\text{in}}^{3/2}}{0.07\, D_{\text{in}}} \tag{8.39}$$

where $C_\mu = 0.09$ is the empirical constant used in equation (8.23).

Care needs to be taken in locating outlet boundaries, because typically for incompressible flow the boundary condition that will be imposed is zero exit gradient for the velocities, temperature or mass fraction:

$$\text{Outlet b.c.:} \quad \frac{\partial \boldsymbol{u}}{\partial n} = 0, \quad \frac{\partial T}{\partial n} = 0 \quad \text{and} \quad \frac{\partial Y_i}{\partial n} = 0,\ T = T_{\text{in}} \quad \text{and} \quad Y_i = (Y_i)_{\text{in}} \tag{8.40}$$

where n is the direction normal to the outlet boundary. Placing outlet boundaries where the velocity gradients are unlikely to be zero (or where recirculation advects materials back into the flow domain) is likely to generate erroneous results.

8.3 Numerical methods

8.3.1 Discretised solution of the flow variables

The partial differential equations which represent the various conservation statements, described in Section 8.2, can only be solved analytically for a very restricted set of cases (e.g., for some classes of one-dimensional laminar flow). Analytical solutions produce exact functional forms for the dependence of velocity and pressure on time and spatial position. Hence, they have no limits of resolution, as these functions can be evaluated at any time or space position. In practice, however, for multi-dimensional and/or unsteady flows, the equations of motion must be solved by numerical means. These methods involve the discretisation of the transport equations, so that the partial derivatives are replaced by algebraic expressions written in terms of discrete values of, for example, the velocity and pressure, at a finite number of positions in space and time. These spatial locations are distributed on the nodes of a grid which is generated by the software to fill the flow domain. The values of the flow variables (p, $\boldsymbol{u}$, T and Y_i) at the interior grid points of the flow domain are treated as unknowns, whereas those on the boundaries are either known or can be related to interior points (depending on whether Dirichlet or Neumann boundary conditions have been implemented; see Section 8.2.7). Thus, the set of partial differential equations that define the physics and chemistry of the flow system is approximated by a much larger set of algebraic equations (one for each grid position), which must be solved simultaneously to yield the discrete values of the flow variables at the grid points. Similarly, for unsteady-state problems, integration through time is advanced by making a series of finite time steps, that is, the flow variables are evaluated at discrete times as well as discrete spatial positions.

8.3.2 Grid generation

Commercial CFD software packages contain a front-end, which allows the user to specify the flow geometry, typically through a CAD type interface. The flow domain is then divided into (i) sub-volumes, in which a grid is generated and (ii) surfaces, on which boundary conditions will be applied. Grid generation is carried out by the software, under user control, and is one of the most important and time-consuming parts of conducting a CFD simulation. Construction of a high-quality grid will make for a more efficient and robust numerical solution. A high-quality grid will have:

- sufficient density of cells to capture the important flow gradients;
- cells that change slowly and smoothly in size (volume and length);
- cells that are not skewed and have an aspect ratio of around unity.

Early CFD simulations used structured grids based on simple coordinate systems and had limited ability to mesh around complex geometries. More recently, unstructured grids and multi-block grids have allowed a mesh to be generated inside most geometries.

Structured grids are generated by dividing a single or multiple blocks of the flow volume into hexahedral elements, which can be logically addressed using (i, j, k) indices in the computational domain (these indices do not need to align with the coordinate system, but the solution will be more accurate if they are aligned with the flow direction). This structure reduces the memory size required, allows for more efficient numerical solution and

permits higher-order discretisation scheme (i.e., QUICK, third order), and hence a greater accuracy which is not applicable to the unstructured grid. Moreover, the hexahedral elements can tolerate greater skewness and elongation without affecting the stability of the solution, and they are subject to smaller numerical diffusion errors than tetrahedral elements. They are, however, not suited to all geometries and can require considerable user skill to generate satisfactory distributions of the grid points.

Unstructured grids are based on dividing the volume into hexahedral or tetrahedral elements, which are fitted to the geometry of the flow domain. They are easier to generate automatically for arbitrary geometries. Typically, the user defines the mesh spacing on the boundaries and the software generates the distribution of internal grid points. Unstructured grids require more memory and have longer computation times than structured grids. Figure 8.9 shows a simple example of meshes generated inside a cylindrical flow domain using either hexahedral or tetrahedral cells.

Hybrid grids combine the best features of both structured and unstructured grids, making use of both hexahedral and tetrahedral elements in different blocks within the flow domain. The grids points do not need to match each other at the interfaces between blocks, which allows greater flexibility in matching the grid and the flow geometry.

8.3.3 Discretisation

Converting the partial differential equations of Section 8.2 to a set of algebraic equations is achieved by a process known as discretisation. There are three basic ways to discretise the

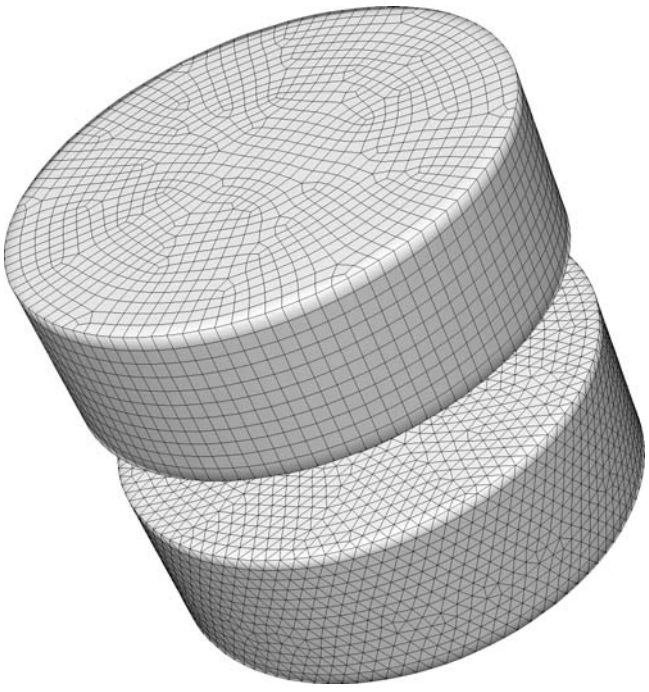

Fig. 8.9 An illustration of the difference between a hexahedral unstructured mesh (upper) and a tetrahedral unstructured mesh (lower).

transport equations: finite difference, finite volume and finite element. Although the latter exhibit more stability than finite-volume methods (Huebner *et al.* 1995), they have mainly found applications in specialist codes, such as those for non-Newtonian and visco-elastic flows, for example, POLYFLOW. Finite differences are amongst the oldest methods of approximating partial differential equations, but they suffer from the problem that (i) conservation of scalar quantities is not necessarily achieved, unless great care is taken and (ii) they are restricted to simple cell element geometries. The finite-volume method overcomes both of these disadvantages, which is why it is widely applied in commercial CFD packages (e.g., PHOENICS, FLUENT and CFX). Within the software, the expert user is able to choose details of the numerical scheme to be applied. Formal discretisation of the transport equations by the user is not required because the software does this automatically for either the default or user-specified schemes.

8.3.4 Finite-volume discretisation methods

As an example of discretisation based on the finite-volume method, consider a simplified steady-state 1D transport equation for a conserved scalar quantity Φ, with a diffusion coefficient Γ_Φ and a volumetric source term S_Φ.

$$\frac{\partial}{\partial x}(\rho u\Phi) = \frac{\partial}{\partial x}\left(\Gamma_\Phi \frac{\partial \Phi}{\partial x}\right) + S_\Phi \tag{8.41}$$

The control volume in Figure 8.10 is centred at node P at which all the flow variables are stored. Here the quantity Φ is advected into, or out of, the control volume from neighbouring nodes W and E, through the faces labelled w and e.

The finite-volume approximation ensures that Φ remains properly conserved by first integrating the transport equation over the control volume, making use of the divergence theorem to convert volume integrals to fluxes through surfaces.

$$[(\rho u\Phi)_e - (\rho u\Phi)_w]A = \left[\left(\Gamma_\Phi \frac{\partial \Phi}{\partial x}\right)_e - \left(\Gamma_\Phi \frac{\partial \Phi}{\partial x}\right)_w\right]A + \int_V S_\Phi \mathrm{d}V \tag{8.42}$$

The terms on the LHS represent the net advective fluxes of Φ leaving through faces e and w, whereas the first two terms of the RHS represent the diffusive fluxes. These fluxes at the faces e and w have to be determined in terms of the flow variable values stored at the nodes E and W; the source volume integral in equation (8.42) can be written simply as $S_{P\Phi}V_P$, where $S_{P\Phi}$ is a linearised function of Φ_P and V_P is the volume of cell P. The gradients in the

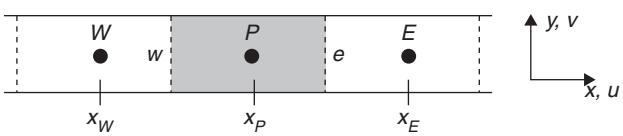

Fig. 8.10 A simple one-dimensional grid for finite-volume analysis.

diffusive flux terms can be represented by central differences to give second-order accurate schemes.

$$\left(\frac{\partial \Phi}{\partial x}\right)_e = \frac{\Phi_E - \Phi_P}{x_E - x_P} \tag{8.43}$$

The advective fluxes are related to Φ values at the nodes by various interpolation schemes, depending on the local Peclet number, $Pe = \rho u L/\Gamma$, using:

- central differencing ($Pe = 0$) for pure diffusion;
- upwind differencing ($Pe >> 1$) for advection dominated flows;
- hybrid and power-law differencing ($0 < Pe < 10$);
- higher-order methods, for example, QUICK (Leonard 1979) based on weighted averages of second-order upwind and central interpolations, which is more accurate on structured grids.

First-order differencing using upwind or power-law schemes are often suitable for flows that are aligned with the grid direction, but for the complex 3D flows in mixing vessels, this is unlikely to happen. Therefore, second-order schemes should be employed to yield more accurate results (although at greater computational expense and reduced stability) for a given grid spacing. To overcome some of the stability issues, it is a good practice initially to start CFD mixing simulations using a first-order scheme and run a few iterations to achieve a partially converged solution. Then the differencing is switched to a second-order scheme and the simulation is run until fully converged.

8.3.5 Solver methods

Whatever differencing scheme is chosen, the result is that equation (8.42) can be linearised and written in terms of the Φ values at neighbouring points (the number depends on the form of grid chosen). In the simple example of Figure 8.10, the resulting equation would be:

$$a_P \Phi_P = a_E \Phi_E + a_W \Phi_W + S_{\Phi c} \tag{8.44}$$

where a_P, a_E and a_W are coefficients that can be written in terms of known quantities and $S_{\Phi c}$ is a constant related to the source terms. Even for a multi-dimensional flow problem, an equation similar to equation (8.44) can be written, expressing $a_P \Phi_P$ as a linearised sum of values at its neighbouring nodes.

$$a_P \Phi_P = \sum_{\text{neighbours}} a_i \Phi_i + S_{\Phi c} \tag{8.45}$$

There will be one such algebraic equation for each grid node and for each conserved quantity in the flow. This large, but sparse, system of linear algebraic equations must be solved simultaneously to give the discrete values of each flow variable on all the grid points. For small mesh sizes, a solution by matrix inversion may be feasible, but for realistic CFD simulations containing several thousand grid points, an iterative solution is required, for example, using the Gauss–Siedel method (Versteeg & Malalasekara 2007). The iterative

solution proceeds slowly, but is susceptible to divergence, and hence, the changes in the calculated values of Φ have to be controlled using under-relaxation. After each iteration, the old value of scalar Φ^{old} is updated by adding the required change $\Delta\Phi$ multiplied by an under-relaxation factor α_Φ.

$$\Phi^{\text{new}} = \Phi^{\text{old}} + \alpha_\Phi \Delta\Phi \tag{8.46}$$

For $\alpha_\Phi = 1$, the value of $\Delta\Phi$ would give a new Φ^{new} that exactly satisfied equation (8.45) at that grid point; but this can lead to too rapid changes and divergence. Use of under-relaxation with $0.1 < \alpha_\Phi < 1$ leads to a slower but more stable convergence. Usually, small under-relaxation factors would be set for each variable during the initial stages of iteration to avoid divergence problems. Then as a converged solution is approached, the under-relaxation factors can be increased for faster convergence. At each iteration, the residual or the error in equation (8.45) can be computed and summed over all cells to monitor the progress towards convergence.

$$R = \sum_{\text{cells}} R_P \quad \text{where } R_P = \left| \sum_{\text{neighbours}} a_i \Phi_i + S_{\Phi c} - a_P \Phi_P \right| \tag{8.47}$$

The magnitude of R depends on the scalar variable Φ that is examined, and therefore, it is usual to normalise the residuals in some way, for example, by dividing by the residual after a small number of iterations (typically 5). For velocity components and pressure, an engineering-quality solution would be obtained when the normalised residuals fall below 10^{-3}–10^{-4}.

Commercial packages offer a choice between two basic types of iterative solutions.

- *Segregated solver*: each flow variable (u, v, w and p) is solved sequentially over the whole grid for each iterative step.
- *Coupled solver*: at each iteration, the flow variables (u, v, w and p) are solved together for each cell, before moving to other cells in the grid.

The coupled solver requires more memory than the segregated solver, but the number of iterations needed for convergence can be a lot smaller. In terms of solution accuracy, the difference is not substantial for a well-converged solution. The segregated solver approach is appropriate for incompressible flows, such as those found in fluid mixing applications. For fluid flow problems, there are four unknowns (three velocity components and pressure: u, v, w and p) and four equations (three momentum equations and continuity). The segregated solver starts from guessed values of the velocity and pressure fields (or using values from the previous iteration) and sequentially computes the new values of the velocity components from the momentum equations. However, these are not likely to satisfy the remaining continuity equation, and there is a further problem because there is no natural equation that can be used to update the pressure. A standard way around this difficulty is to use the semi-implicit method for pressure-linked equations (SIMPLE) algorithm by Patankar (1980), which calculates a correction term based on the continuity equation to compute the updated pressure value. This ensures both convergence of the pressure field and that mass conservation is satisfied. Additionally, commercial codes will offer alternative pressure–velocity coupling methods, such as SIMPLE-consistent (SIMPLEC; Vandoormaal & Raithby 1984),

which may improve convergence for some turbulent flow problems and pressure-implicit with splitting of operators (PISO; Issa 1986) for transient flow simulations.

The final stage before performing an iterative solution is to provide the starting guesses for all the flow variables. This is a process known as initialisation and involves specifying values of, say, u, v, w and p at all grid locations, or in each sub-volume, in the flow domain. Often these starting guesses would all be zero; alternatively known approximate values can be patched in at appropriate grid positions to reduce the number of required iterations or to force the flow in a particular direction. Once initialisation is complete, iteration can proceed until convergence has been achieved. It is also more convenient to prepare separate coarse and fine grids for a given geometry. The initial simulation may be carried out using the coarser grid, and its result is then used to initialise the fine grid. Such a practice is the first step in checking grid dependence and can minimise the overall computation time.

8.4 Application of CFD to stirred tank modelling

8.4.1 Mixing operations

Stirred tank mixers typically comprise cylindrical vessels, with dished bottoms, containing a centrally located shaft and one or more impellers; in turbulent flows, the tank should be equipped with four wall baffles, which are designed to convert the swirling flow generated by the impeller to axial and radial flow components, thereby giving improved top-to-bottom mixing. In cases where the aspect ratio (height to diameter ratio) is greater than 1, the mixing can be improved by using two or more impellers operating on the same shaft; these impellers do not need to be of the same diameter or design and could fulfil quite different agitation duties. For low Reynolds number ($Re < 10$) laminar flows, the motion generated by the impeller is highly damped by viscous effects and does not extend far from the blades. In these cases, large diameter impellers are required that pass close to the walls of the tank. Hence, baffles are unnecessary and, in fact, make mixing worse: regions of almost stagnant flow are found in front and behind the wall baffles, and they limit the VOF that can be visited by a large diameter impeller.

Prior to the application of CFD, mixing operations were generally designed making use of empirical rules based on data gained from small-scale experimental investigations. The most successful rules have been formulated using dimensional analysis, to scale up results obtained on geometrically similar vessels and impeller systems. Often, however, there are uncertainties in deciding a suitable scale-up rule, and hence, errors can occur in extrapolating the results to large, industrial-scale vessels. Moreover, with this approach it is not possible to predict or optimise the tank and impeller design using different geometries, and it would be expensive and time consuming to investigate all these possibilities through experimental studies. Therefore, the potential of CFD is to allow the engineer to explore a much wider design space by simulating a variety of geometries and operating conditions and predicting the process outcome. Still, there will be a need for experimental validation and verification, but once this is completed, there should be confidence that simulations conducted for similar cases, or different scales of operation, should be accurate.

8.4.2 Representation of the impeller

Modelling of turbulence flows in stirred tanks is difficult because the flow structures are often turbulent, highly three dimensional and cover a wide range of spatial and temporal

scales. These flows are transient because trailing vortices are formed in the wake of the blades so that the flow varies periodically close to the impeller (Yianneskis *et al*. 1987). In addition, stirred tanks containing wall baffles or fixed internals, such as heating coils or dip pipes, are challenging to simulate using CFD because the shape of the flow domain is not fixed in time. As the impeller rotates relative to the stationary walls and baffles, the geometry of the flow changes; in a fixed inertial frame of reference, the flow is unsteady due to the periodic passage of the impeller blades. Special precautions must be used to generate a grid, which discretises the changing fluid volume and captures the impeller motion. Adaptive grids, which change with the moving boundaries of the flow domain, are feasible to construct, but there are better and more efficient approaches used in the field of stirred tank modelling.

Before the mid-1990s, most stirred tank CFD models made use of a black-box approach to represent the impeller. An internal boundary was defined to coincide with the swept surface of the impeller, and boundary conditions for the mean velocity components and turbulence quantities (k and ε) were imposed at specified inlets to represent the discharge flow; the suction sides of the swept surface were set as outlet boundary conditions, as indicated in Figure 8.11. Although this is a very simple approach, it requires detailed experimental data for all the flow variables in close proximity to the blades. Mean velocities and k values may be obtained from LDA measurements (Derksen *et al*. 1999) or in more recent times from PIV (Khan *et al*. 2006); ε values are much more difficult to measure and may have to be estimated indirectly from the turbulence kinetic energy and an assumed length scale (Wu & Patterson 1989):

$$\varepsilon = A\frac{k^{3/2}}{(3\Lambda^2)^{1/2}} \tag{8.48}$$

where $A = 0.85$ is a constant and Λ is the integral length scale estimated as $W/2$ and W is the impeller blade width.

The $(\overline{u},\overline{v},\overline{w},k,\varepsilon)$ experimental data are tangentially averaged and time averaged and applied as inlet conditions to the boundary. As shown in Figure 8.11, for the case of a Rushton disk turbine, they represent the discharge stream as an axisymmetric swirling radial jet; for other impeller types, different surfaces of the swept volume would be defined as inlet and outlet flows to represent the discharge and suction sides, respectively. However, as the data are time averaged, there is no possibility to include any details of the trailing vortex structure, which follows each blade—such structures were first observed experimentally by Van't Riet and Smith (1975) and characterised by Yianneskis and Whitelaw (1993); they have an important effect on the power reduction and the breakage of drops and bubbles.

Although the method has short computation times and yields fairly accurate predictions of the mean flow patterns (Ranade & Joshi 1990; Kresta & Wood 1991), it is time consuming to collect experimental data for new impellers and for each change in geometry or tank dimensions. Moreover, these data cannot be obtained for large-scale vessels, or for multiphase flows, which rather restricts the application of the method to small-scale, single-phase operations. Therefore, the black-box approach is not an *a priori* design tool and has now been superseded by techniques based on moving meshes.

A better and more explicit approach is to generate an accurate 3D model of the impeller geometry and to mesh this with a grid that moves at the impeller rotational speed (Marshall & Bakker 2004). For an unbaffled vessel (with no tank internals), the flow is steady state in a

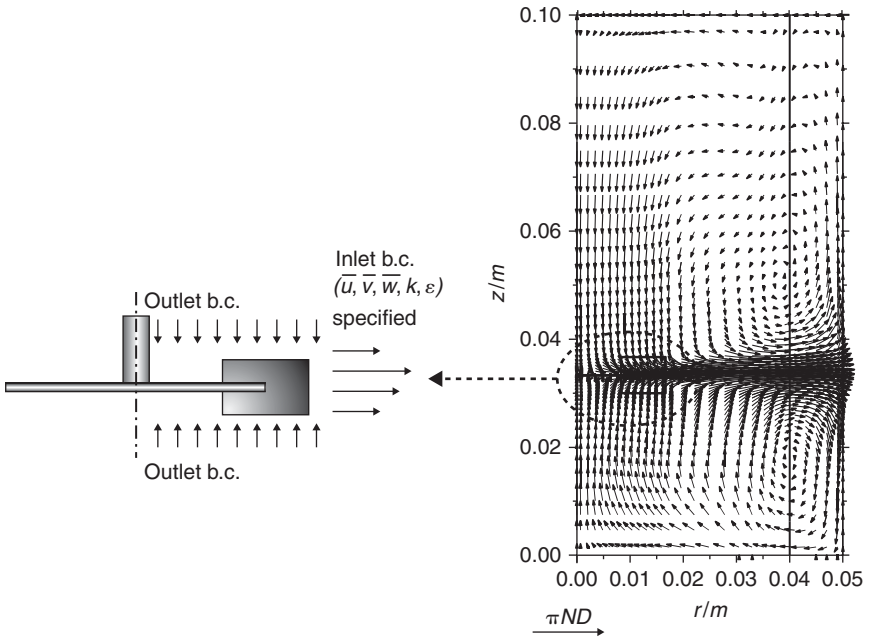

Fig. 8.11 Black-box approach to impeller modelling using prescribed boundary conditions on the swept surface of the blades.

rotating frame of reference with a rotational speed that matches the impeller N (rev/s). Thus in the rotating frame, the impeller appears stationary, and the wall of the tank moves in the opposite direction with a linear velocity πNT, where T_d is the tank diameter. The momentum equations can then be numerically solved allowing for the additional Coriolis effects that result from the use of a non-inertial (accelerating) frame of reference. This method of using a single rotating frame is valid only for axisymmetric tank geometries, with no internal components and smooth walls. An example of such a simulation by Haque *et al.* (2006) is presented in the following section, where the effects of free surface modelling are also discussed.

For baffled vessels (or tanks containing other stationary internals), a similar approach may be employed using two grids, as is illustrated in Figure 8.12: (i) an inner grid that moves with the impeller in a rotating frame of reference, as described earlier and (ii) an outer grid that is stationary with respect to the walls and baffles, which are at rest. The inner grid is usually contained within a cylinder that surrounds the impeller; its radius should extend beyond the blade tips and outside the region where the trailing vortices are found, but not as far as the baffles; the height should be sufficient to contain the impeller and any features of the trailing vortices for axial and mixed flow impellers; see for example, Schäfer *et al*. (1998). The momentum and continuity equations are solved on the inner grid using a rotating frame of reference and on the outer grid in a stationary frame of reference. The results at the interface from the inner grid become boundary conditions for the outer grid, and vice versa. This approach can be extended to cases with multiple impellers, on different shafts, operated at different rotational speeds; one rotating reference frame would be required for each impeller.

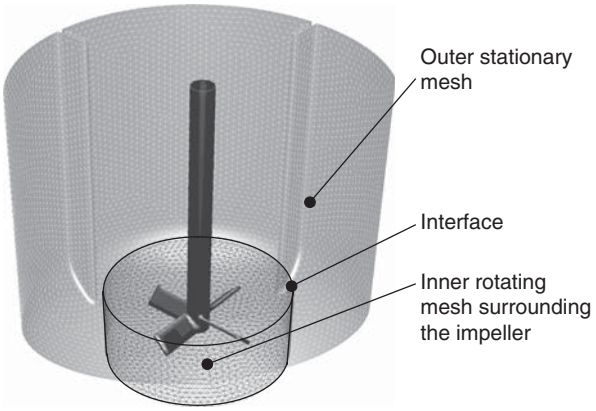

Fig. 8.12 MRFs representation using a rotating grid around the impeller itself and a stationary grid to mesh the walls and baffles.

There are two methods for passing information for the boundary conditions at the grid interface using either a sliding mesh (SM) or multiple reference frame (MRF) model. In the SM formulation, the inner grid rotates at the impeller speed and continually passes angle-dependent information to the outer stationary grid and vice versa. This occurs as a sequence of steps in which the transport equations are solved iteratively between the inner and outer grids until convergence is obtained; the inner grid then slides or clicks to a new angular position and the iterative process starts once more, passing information between the two grids. In this way, the solution is fully time dependent and models the detailed motion of the impeller relative to the baffles and tank wall. The cells at the interface between the inner and outer grids do not always line up, and hence, interpolation is required during the passing of information—this is known as a non-conformal interface. The SM method requires a transient calculation and is the most detailed and accurate method of modelling the impeller rotation; it should be used when there are strong interactions between the baffles and the blade. However, SM simulations are very computationally demanding and typically it will take several (10–20) impeller revolutions for the solution to come to a periodically stationary state; a further 10–20 rotations may be required to collect statistical data and so quite long transient calculations have to be performed. If only time-averaged flow quantities (e.g., flow number, power number, mixing time; see Section 8.4.3) are required, then it is unnecessary to account for the periodic motion of the impeller blades and a simplified, steady-state model would suffice, which leads to the MRF method.

In the MRF model, the inner mesh does not move relative to the outer mesh, and so there is a steady-state transfer of information across the interface (Luo *et al.* 1994). Thus, the impeller is modelled at only one position relative to the baffles, which is acceptable where the blade–baffle interactions are weak. This is often the case in stirred tank flows, where the periodic effects are found only in the vicinity of the impeller; the flow in the outside region is essentially steady (Khan *et al*. 2004). This approximation may be verified by noting the changes in the MRF simulations for two different impeller orientations relative to the baffles. There is a very significant saving in the computational overhead using the MRF model because the simulation is now steady state. Furthermore, interpolation across the interface can be avoided using a conformal interface between the inner and outer grids, so that the cells on either side match up.

The *mixing plane model* is a variant of the MRF method in which information at the interface is azimuthally averaged before it is passed to the other grid zone. Any tangential variations in the flow variables are removed, so that effectively the average for all impeller blade positions is passed to the outer grid. Any asymmetry in the outer geometry, for example, due to dip pipes, or wall inlets and outlets, cannot be correctly taken into account using the mixing plane model, and hence, it has not found widespread applications in mixing tank simulations (Marshall & Bakker 2004).

In summary, both the SM and MRF approaches may be used to construct *a priori* models of the flows generated by the impeller, without the need for experimental data as boundary conditions. Although the SM model gives the most accurate representation of the rotating impeller, it is too computationally expensive to use for most situations and there appears to be little benefit in applying it with a RANS turbulence model. In contrast, LES simulations are inherently unsteady and must be performed on 360º flow domains (no cyclic boundaries) and require SM representations of the impeller. For these reasons, LES computational times are very long and the method has yet to have significant impact on the routine design of large-scale equipment; nevertheless, as described in Sections 8.4.5–8.4.7, LES is the most promising route to successful simulations. The MRF model is a simplification that ignores blade–baffle interactions to yield a steady-state simulation of the flow, but includes a detailed prediction of the flows around individual impeller blades. With sufficient grid resolution, details of the trailing vortices can be modelled accurately with MRF.

8.4.3 Prediction of mixer performance characteristics

One of the first stages in designing a stirred tank mixing operation is to calculate the required power input to obtain a given process result. For example, the specific power input per unit volume (P/V in W/m^3) determines the mixing time, the mass transfer coefficient and may determine the distribution of solids in a vessel. The impeller power draw can be characterised by a dimensionless *power number*:

$$Po = \frac{P}{\rho N^3 D^5} = f(Re,\ Fr) \tag{8.49}$$

which is a function of the Reynolds number defined in equation (8.16) and the Froude number for unbaffled tanks, as the shape of the surface vortex is determined by gravitational acceleration, g.

$$Fr = \frac{N^2 D^2}{g} \tag{8.50}$$

At high Reynolds numbers ($Re > 10^4$) in baffled vessels, the power number is a constant. Empirical relations of the form of equation (8.49), or constant values of Po at high Re, are available for standard impeller types and geometries (Hemrajani & Tatterson 2004), but they do not always extend to a wide range of diameters ratios, D/T_d, or clearance ratios, C/T, or to new impeller designs. For these cases, the power number can be quite successfully predicted by CFD from a torque balance on either the shaft and impeller blades, or the tank wall and baffles. This torque, Γ, results from an integration of the shear stress and

pressure differences acting on these surfaces and is related to the power input by the following equation.

$$P = 2\pi N\Gamma \tag{8.51}$$

In principle, the power input could also be obtained from a volume integral of the turbulence kinetic energy dissipation rate, ε, which is predicted directly in RANS simulations and can be calculated from LES. There is also viscous dissipation due to the mean flow velocity gradients, but this term usually makes a negligible contribution to the overall power input in turbulent flows.

$$P = \rho \int_V \varepsilon \, \mathrm{d}V \tag{8.52}$$

In practice, however, RANS models significantly under-predict the turbulence quantities, and hence, the total power input is not accurately obtained from equation (8.52). In both laminar and turbulent mixer applications, equation (8.51) is the preferred method to calculate power draw from the integrated torque on the impeller and shaft.

The *flow number* is a dimensionless measure of the strength of the discharge stream generated by the impeller. It is defined in terms of the volumetric flow rate, Q, obtained by integrating the velocity distribution over the parts of the swept surface through which the discharge stream passes. For example, for a Rushton disk turbine, this surface would be a cylinder with diameter of just greater than the impeller diameter D and a height just greater than the blade width W (the region marked as in inlet boundary condition in Figure 8.11).

$$Fl = \frac{Q}{ND^3} = f(Re) \tag{8.53}$$

For high Reynolds number flows, Fl is a constant whose value can be obtained by integrating velocity profiles, measured experimentally by LDA or PIV (see Chapter 7), or more straightforwardly from CFD simulations. If the surface for integration is moved away from the impeller swept surface, then larger flow numbers result, because they include the effects of entrainment into the impeller discharge stream. This type of flow number is a measure of the circulation flow inside the vessel, rather than the flow emanating from the impeller itself. The concept of the discharge flow gives a good qualitative indication of the impeller's ability to generate fluid motion, but is not particularly useful in the design of mixing systems, unless it can be directly linked to blend times or solids suspension criteria.

The dimensionless mixing time is another global characteristic of a stirred tank agitator that has been traditionally measured by experiment, but which is now *potentially* accessible by CFD simulation. In experimental studies, the mixing is quantified by the time required for the concentration fluctuations of a tracer material to have decayed to within 5% of the final well-mixed concentration (95% mixing time, θ_{95}). Salt or dye concentration are commonly used to mark the tracer, and detection is then by conductivity probe, optical absorption or visual observation. The dimension mixing time is as follows.

$$N\theta_{95} = f(Re) \tag{8.54}$$

At high Reynolds numbers, the dimensionless mixing time is a constant. There have been many attempts to calculate this mixing time, by solving the species transport equation, to

predict the transient distribution of a tracer that has been added to a developed flow inside a stirred tank. These types of simulations are discussed further in Section 8.4.6.

8.4.4 Simulation of unbaffled or partially baffled stirred tanks

For high Reynolds number turbulent flows, most industrial mixing vessels would be equipped with a set of four wall baffles, which redirect the swirling flow generated by the impeller to produce axial and radial velocity components and improved top-to-bottom mixing. Glass-lined vessels are an exception and may contain only one or two beavertail baffles, which are suspended from the reactor head. Some mixing vessels used in food processing may also operate without baffles because of CIP cleaning requirements. For low Reynolds number mixing operations (viscous systems) in the laminar or transitional regimes, internal obstructions may make mixing slower, and hence, vessels are often operated without baffles.

For unbaffled, or partially baffled, vessels the flow contains strong tangential velocity components, and a surface vortex tends to form at all but the lowest impeller speeds. Hence, the free surface is far from flat, and it would be inappropriate to represent this boundary using a symmetry condition, as described in Section 8.2.7.

The first studies of unbaffled vessels ignored the surface vortex feature of the flow [e.g., Armenante *et al*. (1997) who studied vessels with a lid], but more recent works have attempted to simulate the free surface shape using, for example, the VOF method first proposed by Hirt and Nichols (1981). This is a form of two-phase simulation, which tracks the VOF f, using a transport equation. A single set of momentum and continuity equations are solved for either the gas phase ($f = 0$), the liquid phase ($f = 1$), or the mixture ($0 < f < 1$); mean physical and transport properties are calculated from the value of f. For no interphase mass transfer, the VOF equation simplifies to the following equation.

$$\frac{\partial f}{\partial t} + (\boldsymbol{u} \cdot \nabla f) = 0 \tag{8.55}$$

In practice, the change from gas to liquid is not abrupt, and hence, specialised methods have to be applied to sharpen and interpret the interface (Rudman 1997). VOF methods can take surface tension effects at the interface into account, although typically, they should not be important for stirred tank flows because the Weber number (a ratio of inertial to surface tension effects) is often much greater than unity.

$$We = \frac{\rho N^2 D^3}{\sigma} >> 1 \tag{8.56}$$

Haque *et al*. (2006) implemented such a VOF model within ANSYS CFX-5.7 to simulate the flow in an unbaffled tank agitated by a Rushton disk turbine (Figure 8.13), which was modelled using a single rotating frame of reference (see Section 8.4.2). Their simulations showed that both the shear stress transport (SST: a hybrid $k - \varepsilon/k - \omega$ formulation) and the Reynolds stress (RSM) turbulence models gave reasonable predictions of the mean velocity fields and the surface shape of the central vortex, when compared to experimental measurements and a simplified forced/free-vortex model by Nagata (1975). The SST model was shown to be more successful than the standard $k - \varepsilon$ model in predicting the tangential velocity distribution, which is the key to correct prediction of the surface vortex shape.

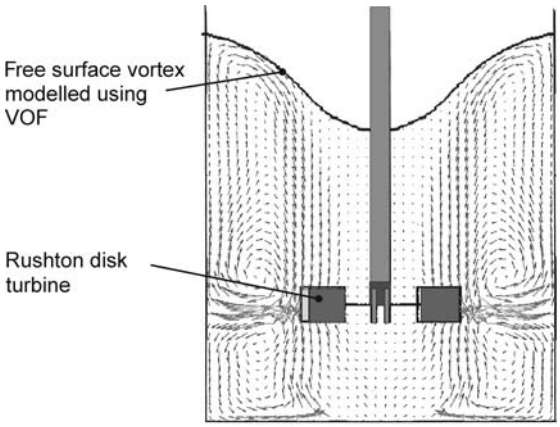

Fig. 8.13 Mean velocity vector map and surface profile for an unbaffled tank, predicted by Haque *et al*. (2006) using a VOF model. [Reprinted with permission from Haque *et al*. (2006). Copyright American Chemical Society.]

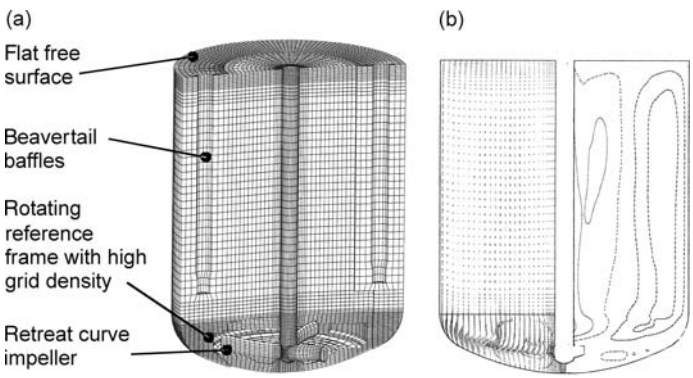

Fig. 8.14 (a) Grid and geometry used by Campolo *et al*. (2002) and Campolo and Soldati (2002) to model an industrial-scale vessel. (b) The mean velocity field and streamlines for the retreat curve impeller. [Reprinted with permission from Campolo *et al*. (2002) and Campolo and Soldati (2002). Copyright American Chemical Society.]

There are only a few studies to date of stirred vessels that are partially baffled by dip pipes, beavertails of finger baffles. Campolo *et al*. (2002) and Campolo and Soldati (2002) presented a comparison of the flows generated by a retreat curve impeller and a turbofoil turbine in an industrial-scale vessel (12.5 m^3) containing two beavertail baffles, over a range of Reynolds numbers in the transitional and turbulent regimes (Figure 8.14). An SM model was applied to take into account the interaction between the two baffles and the impeller blades. The standard $k - \varepsilon$ turbulence model was selected and the free surface was assumed to be flat, such that it could be modelled as a zero shear stress boundary condition. It could be argued that it would have been better to use a VOF model in this case because free surface vortices have been observed in the wake of the beavertail baffles (Li *et al*. 2004). Campolo's results were successfully validated by comparison of the calculated power number against experimental measurements; the impeller performance was characterised by

the flow number, and the advantages and disadvantages of retrofitting the vessel with a turbofoil to replace the retreat curve impeller could be clearly identified in terms of the flows and circulations generated in the upper parts of the vessel. The simulations clearly showed that reducing the bottom clearance of the impeller produced a more radial discharge stream.

In a similar study, Li *et al*. (2004) simulated a retreat curve impeller with a single cylindrical baffle, using the SST turbulence model but again with a flat free surface. Their mean velocity predictions were successfully validated at the 20-L scale using LDA measurements. However, as is common with RANS models, the turbulence kinetic energy, and hence the dissipation rate, were significantly under-predicted by CFD. Li *et al*. (2005) took this validated model and examined scale-up from tank volumes of 0.5–20 L to mimic the process development in pharmaceuticals manufacture. Their work suggested that the macro-mixing characteristics of lab-scale vessels should be approximately the same as in an industrial-scale reactor, so long as turbulent flow can be maintained.

8.4.5 Simulation of single-phase flow in baffled stirred tanks

Many researchers (Ranade & Joshi 1990; Harris *et al.* 1996; Brucato *et al.* 1998a; Jones *et al*. 2001; Patwardhan 2001; Jaworski & Zakrzewska 2002; Aubin *et al.* 2004a,b; Ochieng & Onyango 2008) have applied RANS-based turbulence models (mainly $k-\varepsilon$ model) to simulate flow in a fully baffled stirred tank. Following comparisons with LDA or PIV measurements, these authors have generally found that CFD gives a satisfactory prediction of the axial and radial mean velocity components and flow patterns. However, the tangential velocity components are reported to be variously under- or over-predicted, whereas the turbulence kinetic energy, k, and the turbulence energy dissipation rate, ε, are under-predicted by RANS CFD models. Aubin *et al*. (2004a) carried out a detailed review of the recent literature and also made their own investigations of different impeller representations, turbulence models and discretisation schemes. She showed that changing the impeller representation from MRF to SM had only a small effect on the radial and axial velocity components near the impeller, which were in good agreement with LDA data, as shown in Figure 8.15. The difference from experimental values in the calculated circulation numbers was less than 10% and power numbers were predicted within 5% (from the torque on the blades and shaft). Also, the impeller model made no significant improvement to the tangential velocity or turbulence kinetic energy, k, predictions. First-order upwind discretisations were found to give the worst estimates of k, although even higher-order schemes were under-predictive. Similarly, changing from the standard $k-\varepsilon$ to the RNG $k-\varepsilon$ or RSM models did not improve the turbulence predictions for k. Thus, although RANS models successfully predict mean flow patterns, their ability to predict k (and by inference ε) is poor.

Figure 8.16 shows a comparison of the CFD simulation of a Rushton disk turbine (Ng *et al*. 1998), using an SM and the standard $k-\varepsilon$ RANS turbulence model. Fine grid resolution around the blades (around 10 grid points across the blade width are required) and the use of the SM allows the trailing vortices to be visualised in the wake of each turbine blade. The turbulence kinetic energy, k, is a maximum in the core of these vortices, but the comparison with LDA measurements in Figure 8.16b shows that in the region $0.2 < r/T < 0.3$, k is under-predicted by about 50%, which is a common problem for RANS models. Despite this deficiency, the mean flow patterns and velocity components are rather well predicted in Ng *et al*.'s (1998) simulations.

Harris *et al*. (1996) and Jaworski and Zakrzewska (2002) have studied more advanced RANS models, such as the RSM, but these also suffer from similar difficulties in predicting

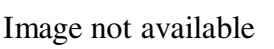

Fig. 8.15 Standard $k - \varepsilon$ and higher-order upwind discretisation: (a) MRF model and (b) SM model, compared to LDA data (c). [Reprinted from Aubin *et al*. (2004a) with permission from Elsevier.]

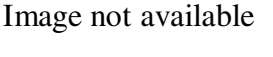

Fig. 8.16 (a) CFD SM simulations of a Rushton disk turbine performed by Ng *et al*. (1998) using a standard $k - \varepsilon$ RANS model. (b) Comparison with angle-resolved LDA measurements. [Reprinted from Ng *et al*. (1998) with permission from Elsevier.]

the turbulence quantities. Armenante *et al*. (1997) reported good predictions of the mean velocities and turbulence using an algebraic stress model (ASM), but their simulations used a black-box approach (see Section 8.4.2) and cannot be considered an *a priori* calculation. The ASM is a simplification of the RSM, which proposes a set of approximate algebraic equations that relate the Reynolds stresses. Other than the study by Armenante *et al*. (1997), the ASM model has not been extensively tested and validated for prediction of turbulent flows in stirred tanks.

Fig. 8.17 LES simulations of a Rushton disk turbine performed by Derksen and Van den Akker (1999). (Reproduced with permission from John Wiley & Sons, Inc.)

It is well known from the literature that LES can predict excellently the time-averaged mean and turbulence flows (Revstedt *et al*. 1998; Derksen & Van den Akker 1999; Derksen 2001; Hartmann *et al*. 2004; Yeoh *et al*. 2004; Jahoda *et al*. 2007; Li *et al*. 2007; Tyagi *et al*. 2007; Yapici *et al*. 2008). LES is a three-dimensional numerical simulation of turbulent flow where large eddies are resolved and the effects of subgrid-scale eddies, which are more universal in nature, are modelled. An example of two flow snapshots is shown in Figure 8.17; the instantaneous structure of the trailing vortex system behind each blade is clearly visible, as is the interaction of the discharge stream with the baffle. LES, to some extent, tends to over-predict the turbulent kinetic energy (Hartmann *et al*. 2004), but generally, it predicts turbulent flows much better than RANS models. However, full LES simulations are still very expensive to solve. For example, Alcamo *et al*. (2005) needed 33 days to solve an LES of an unbaffled tank on a Pentium IV 3 GHz computer. Earlier, Derksen (2001) reported that it took a month (up to 44 h per impeller revolutions) to solve the LES of a baffled stirred tank on a cluster of four parallel processors.

It is also possible to solve the turbulence flow in stirred tanks directly using the exact Navier–Stokes equations without any modelling, but this requires a grid and time step that resolves even the smallest eddies. Such a method is known as a DNS. Recently, DNS has been applied to predict the turbulence flows in a stirred tank by Verzicco *et al*. (2004) and Sbrizzai *et al*. (2006). These authors concluded that DNS predicts the turbulence-related quantities such as turbulent kinetic energy and turbulent energy dissipation rate much better than RANS model. However, both works only involved a low Reynolds $Re = 1{,}636$ (a transitional flow) in an unbaffled tank, suggesting that DNS for a baffled stirred tank at high Reynolds number is still far from the reach of current computer resources.

8.4.6 Mixing and blending simulations

Accurate prediction of mean velocity and turbulence k and ε fields is only the first stage in using CFD as a practical design tool for mixing operations that involve species transport,

chemical reaction and phase dispersion. Clearly, the deficiencies of RANS models in predicting the energy dissipation rate in single-phase flows is likely to impact on the simulation of these more complex processes. As an example, for blending operations, a standard correlation for the 95% batch mixing time is (Ruszkowski 1994):

$$\theta_{95} = 5.91\,\varepsilon^{-1/3}\left(\frac{T_\mathrm{d}}{D}\right)^{1/3} T_\mathrm{d}^{\,2/3} \tag{8.57}$$

which suggest the importance of at least the mean dissipation rate (Nienow 1997). In gas–liquid or liquid–liquid dispersion, the breakage kinetics and equilibrium bubble (droplet) size are related to the maximum local dissipation rate.

Ochieng and Onyango (2008) demonstrated the difficulties in predicting the 95% mixing time from CFD simulations using a standard $k-\varepsilon$ RANS model, applying the SM method. The blending process was simulated by solving equation (8.31) to follow the transient concentration variations of a tracer that had been released as a point source in the flow. The mixing time was calculated from the concentration variations at a single point in the flow, as described in Section 8.4.3 and was compared to (i) experimental measurements based on conductivity and decolourisation of a reactive indicator and (ii) empirical correlations, such as equation (8.57). The measured mixing times and those predicted by literature correlations agreed to within 10%. In contrast, the CFD predicted times were around 100% longer, despite the fact that the mean velocity fields agreed well with LDA measurements. Nevertheless, Ochieng and Onyango (2008) were able to deduce the qualitative effects that reducing the impeller off-bottom clearance gave shorter mixing times.

Bujalski *et al.* (2002) performed mixing simulations of Rushton turbine, using a $k-\varepsilon$ RANS model and found that the mixing time was very sensitive to the tracer concentration monitoring point; in contrast, experimental θ_{95} measurements do not show the same level of sensitivity to probe location in fully turbulent flows. For many of their monitoring locations, the mixing times were significantly over-predicted by a factor of about 2. Montante *et al.* (2004) were able to make satisfactory predictions of θ_{95} using a RANS-based CFD model, for a multiple impeller system, but were able to do so only by adjusting the value of the turbulent Schmidt number in equation (8.31). For many turbulent flows, a value of $Sc_\mathrm{T} = 0.7$ is applied, but Yimer *et al.* (2002) have reported that improvements in the concentration field predictions can be obtained using lower values. Montante *et al.* (2004) had to reduce the turbulent Schmidt number to an exceptionally low value, $Sc_\mathrm{T} = 0.1$, to match the experimental mixing times. Examination of equation (8.32) shows that reducing Sc_T increases the eddy diffusivity and hence becomes an *ad hoc* correction to the under-prediction of the turbulence quantities, k and ε. The generality of this approach for stirred tank flows has not yet been demonstrated.

Yeoh *et al.* (2005) used an LES turbulence model to predict tracer dispersion and mixing times in a vessel agitated by a Rushton turbine and obtained very good agreement with experimental values of θ_{95} and estimates obtained from literature correlations. They attributed this success to the fact that their LES generated flow fields were very well validated in terms of the mean and rms fluctuating velocity distributions. The latter, of course, are related to the turbulent diffusivity of the tracer. Notably, their implementation of the species transport equation (8.31) used $Sc_\mathrm{T} = 0.8$, which is close to the default value for turbulent shear flows. Their results support the conclusion that the main problem with RANS simulations of mixing processes is that the turbulence quantities are under-predicted. A further

problem associated with mixing time calculations is numerical diffusion, which results from inaccurate discretisation methods and has a strong effect on the solution of the species transport equation, smearing out concentration gradients more quickly than would be expected by laminar diffusion alone.

8.4.7 Multi-phase simulations

As noted in Section 8.4.1, there are many industrial examples of multi-phase mixing operations in the chemical, biochemical and food industries. In principle, multi-phase systems also can be simulated using the techniques of CFD, although clearly the physics of these flows is considerably more complicated. The discussion of Section 8.4.4 described one technique for dealing the two-phase (gas–liquid) flows using the VOF approach. This is suitable for cases where each phase can be treated as continuous, with an identifiable and fairly simple shape of interface. The previous example in Section 8.4.4 was of an unbaffled vessel with a free surface vortex. However, for phase dispersion and suspension operations, there will be well-defined dispersed and continuous phases, with many interfaces, and the VOF method would be quite impractical. Other approaches are described below.

At low volume fractions (<10%) of dispersed phase, it is possible to perform Eulerian–Lagrangian particle tracking calculations. The background continuous fluid flow is obtained by solving the single-phase (Eulerian) equations, as previously described in Section 8.2; a Lagrangian equation of motion for the particles is then formulated, for example (Rielly & Marquis 2001):

$$\boldsymbol{F} = \rho_p \frac{\mathrm{D}_p \boldsymbol{v}}{\mathrm{D}t} = \rho_f \frac{\mathrm{D}_f \boldsymbol{u}}{\mathrm{D}t} - \rho_l C_M \left(\frac{\mathrm{D}_p \boldsymbol{v}}{\mathrm{D}t} - \frac{\mathrm{D}_f \boldsymbol{u}}{\mathrm{D}t} \right) - \rho_f C_L (\boldsymbol{v} - \boldsymbol{u}) \times \boldsymbol{\omega} - \frac{3}{4} \frac{\rho_f C_D}{d_p} (\boldsymbol{v} - \boldsymbol{u}) |\boldsymbol{v} - \boldsymbol{u}| - (\rho_p - \rho_f) \boldsymbol{g} \tag{8.58}$$

which relates the particle velocity vector $\boldsymbol{v}$ to the fluid velocity vector $\boldsymbol{u}$ and includes effects such as the pressure gradient, added mass effect and lift, drag and buoyancy forces. This equation can be integrated through time to yield individual particle tracks; the stochastic effects of particle interactions with eddies can also be included, as shown in Figure 8.18.

By following a large number of particles, the dispersed-phase volume fraction distributions, as well as time histories for how the particles sample, the turbulence and strain rate fields can be deduced. Figure 8.18 shows how inhomogeneous the flow environment is in a stirred vessel, with very large peaks in the dissipation and strain rate as the particle passes through the impeller region.

Commercial software is also able to implement two-way coupling between continuous- and dispersed-phase flows: Eulerian continuous phase and Lagrangian discrete phase are run alternately until the momentum exchanges are converged. The method is limited to low volume fractions because it does not include the effects of momentum exchanges through particle–particle collisions. If the flows involved heat and mass transfer between the dispersed and continuous phases, then these effects can be included in the same way as interphase momentum exchange.

For higher volume fractions, it is less time consuming and better to use an Eulerian–Eulerian two-fluid model. Both the dispersed and continuous phases are assumed to behave as interpenetrating continua represented locally by their phase volume fractions. The continuity and momentum equations are then written separately for each phase and additional

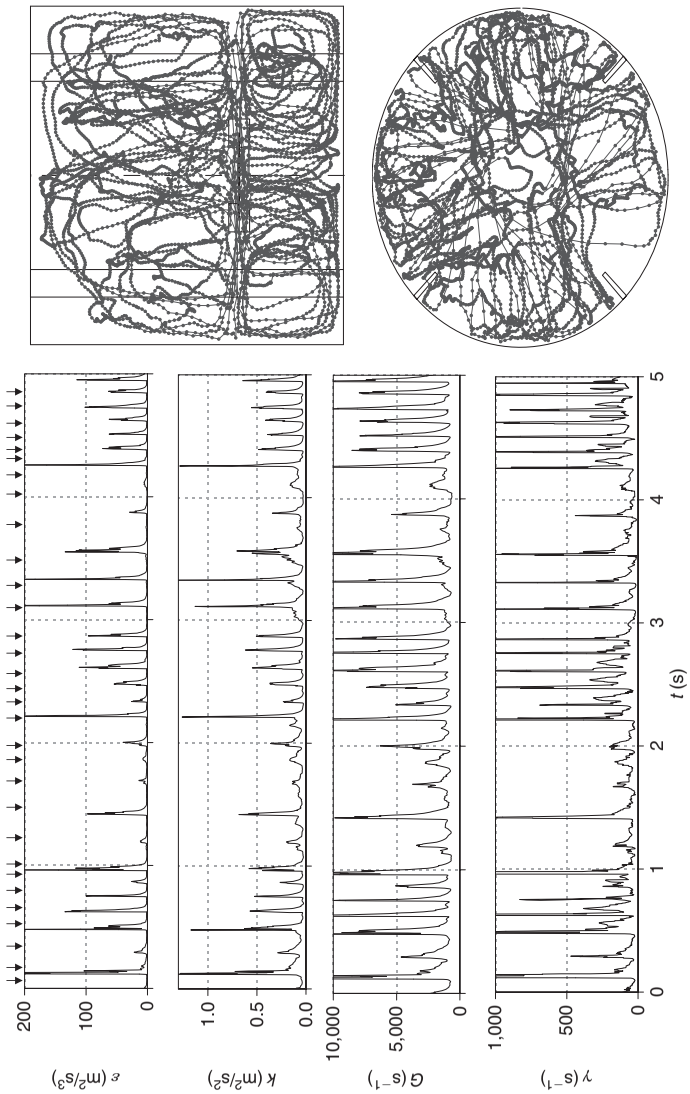

Fig. 8.18 Lagrangian particle tracking in a stirred vessel.

terms are included for the effects of momentum exchange (predominantly drag) between the two phases (Elgobashi & Abou-Arab 1983). A similar approach can be applied to the energy and species transport equations, except that now the exchange terms represent heat or mass transfer between the phases. The implementation of RANS-based turbulence models is much more complex in multi-phase flows: the averaging of the momentum equations for each phase produces a much larger number of unknowns (in the single-phase case, the six Reynolds stresses are the only unknowns generated by the averaging process), which have to be modelled empirically (Simonin & Viollet 1990). Furthermore, although there is no restriction on the range of dispersed-phase volume fractions that can be modelled, the effects of particle–particle collisions are not included—in Eulerian granular multi-phase models (Ding & Gidaspow1990), these effects can be included through a solids pressure term.

Solids suspension in a liquid phase is probably the easiest mixing operation to simulate, given that typically both size and volume fraction of the dispersed phase will be known; in contrast, in gas–liquid flows, the volume fraction and bubble size are not known at the outset of the calculation, and hence, this represents the most challenging case. Montante and Magelli (2005) carried out a thorough study of CFD modelling methods to predict the solids distribution in tanks agitated by multiple Rushton turbines and pitched-blade impellers. They concluded that dilute solid–liquid systems (<6% v/v) can be fairly well predicted, so long as (i) the single-phase mean velocity field is accurate and (ii) the drag coefficient is corrected to allow for the effects of turbulence (Brucato *et al*. 1998b). They recommended the use of the mixture turbulence model in which the two phases are assumed to share the same k and ε. In addition, there were some minor improvements for higher volume fractions when the effects of particle–particle interaction were included through the granular multi-phase model. It should be noted that all such solid–liquid CFD simulations need to be conducted above the just-suspended speed of the particles (Zwietering 1958) because the physics of particle settling, saltation and resuspension which occur in the boundary layer at the base of the tank, are not included in the model.

As noted previously, LES models are much better equipped to simulate the turbulence in a stirred tank flow but at very considerable computational cost. This has deterred all but a few from performing solid–liquid calculations based on LES. An exception is presented by Derksen (2003), who simulated a 1% v/v fraction of 300 μm diameter particles agitated by a Rushton disk turbine. The liquid flow was obtained using LES on a grid of some 14 million cells; Lagrangian tracking of almost 7 million particles was carried out over 10–20 impeller revolutions, with 2,800 time steps per revolution and both two-way coupling and particle–particle interactions were included; importantly, the latter were required to keep the particles in suspension, even though the impeller speed was above the just-suspended condition. Guha *et al*. (2008) recently presented a comparison between (i) solid–liquid CFD simulations based on Eulerian–Eulerian RANS models and Derksen's (2003) LES particle tracking and (ii) experimental measurements from computer automated radioactive particle tracking (CARPT). LES was shown to improve the prediction of fluid tangential mean velocities, but there were significant discrepancies in the particle velocities at the impeller level. Slip velocities from the Eulerian–Eulerian model were very much smaller than those obtained via LES, which is rather significant because the inter-phase momentum exchange (drag) depends directly on this quantity. Despite this finding, the solids concentrations at the impeller level were broadly similar for both CFD models, with the LES predicting slightly lower values. Thus although solid–liquid simulations can be conducted, there are still a number of uncertainties related to the physics of these flows, particularly with respect to

particle–particle and particle–impeller interactions. There are even issues about the calculation of the drag coefficient for such flows: Montante and Magelli (2005) recommended correction of the drag coefficient to allow for local turbulence levels (Brucato *et al*. 1998b) but not for local solids volume fraction (Crowe *et al*. 1998), whereas Derksen (2003) makes the opposite recommendation, which seems to be the more conventional thinking.

Simulations of gas–liquid flows are more complex still because the bubble size is not known *a priori* and results from a balance of breakage and coalescence events, depending on local energy dissipation rates. The first gas–liquid simulations assumed a constant bubble size, based on either experimental evidence or chosen as a fitting parameter to match the gas hold distribution or velocity measurements. They then proceeded to formulate the problem in a very similar way to the solid–liquid case, sometimes even using the same drag laws as for solid particles. For example, Montante *et al.* (2007) chose a bubble size of around 1–2 mm diameter with a terminal velocity of around 0.12 m/s (quite small for an agitated air–water flow) and successfully validated their predicted liquid-phase velocity distributions against two-phase PIV measurements. The experimental mean gas volume fraction of about 1.6% was also predicted by CFD, but distributions of local hold-ups were not available for comparison.

As shown experimentally by Barigou and Greaves (1992) and Laakkonen *et al*. (2005, 2007), the distribution of bubble sizes varies inside the stirred tank depending on the spatial position. Generally, bubble sizes around the impeller discharge stream are the smallest due to breakage caused by the high turbulence dissipation rates. Knowledge of bubble sizes is necessary in a two-phase CFD model because they affect the momentum exchange through drag. In addition, local bubble sizes and the local gas volume fraction are required for the calculation of the interfacial area, which is an important variable in designing an aerated stirred tank to achieve a required rate of gas–liquid mass transfer. Relaxing the assumption of a constant and uniform bubble size requires a new level of sophistication in CFD modelling, to account for the dynamics of breakage and coalescence events. A rigorous approach would be to couple the two-phase fluid dynamics simulations, for example, using an Eulerian–Eulerian continuum model, with a population balance equation (PBE) to represent the evolution of the bubble size distribution. The solution of the PBE is not a trivial task because it requires detailed knowledge of kinetics for the breakage and coalescence events and for the distribution of bubbles that result from each breakage. Equation (8.59) shows how the local bubble size distribution by number, $n(L)$, evolves in time; in solving such an equation, $n(L)$ has to be represented as a set of discrete size classes or the moments of the distribution. Either approach results in a set of equations derived from equation (8.59), which have to be solved for every computational cell in the flow domain.

$$\frac{\partial(n(L))}{\partial t} = \underbrace{\int_L^\infty \beta(L,\lambda)g(\lambda)n(\lambda)\mathrm{d}\lambda}_{\text{birth due to breakage}} + \underbrace{\frac{L^2}{2}\int_0^L \frac{F((L^3-\lambda^3)^{1/3},\lambda)n((L^3+\lambda^3)^{1/3})n(\lambda)}{(L^3-\lambda^3)^{2/3}}\mathrm{d}\lambda}_{\text{birth due to coalescence}} \quad (8.59)$$
$$- \underbrace{g(L)n(L)}_{\text{death due to breakage}} - \underbrace{n(L)\int_0^\infty F(L,\lambda)n(\lambda)\mathrm{d}\lambda}_{\text{death due to coalescence}}$$

The results for the mean bubble size, d_{32}, from the PBE are passed back to the fluid flow calculation and affect the drag between the phases; the kinetic terms, $\beta(L,\lambda)$, $g(L)$ and

Image not available

Fig. 8.19 Local gas hold-up (vol%) and Sauter mean bubble diameter d_{32} (mm) in an agitated gas–liquid flow. [Reprinted from Laakkonen *et al*. (2007) with permission from Elsevier.]

$F(L,\lambda)$ are all related to the local hydrodynamics, mainly through the dissipation rate, ε. Thus, the Eulerian–Eulerian two-fluid calculation is coupled to the PBE solution. This type of approach is still in its infancy, although some promising results have been generated so far by workers such as Montante *et al*. (2008), Laakkonen *et al*. (2007) and Gimbun *et al.* (2009). Figure 8.19 shows some example results from Laakkonen *et al*. (2007) for the gas hold-up and bubble size distributions; the latter are rather far from uniform, and the distribution of bubble sizes has a significant effect on the local mass transfer coefficient and interfacial area.

Thus, very significant advances have been made in recent years in developing better and more realistic multi-phase models, yet they come with a substantial computational overhead and are not yet usable for industrial design purposes. A coupled CFD–PBE solution inevitably requires the application of RANS turbulence models to limit the computational cost of the velocity field calculations, yet these are known to suffer from deficiencies in their ability to predict the dissipation rate. Unfortunately, this is precisely the quantity that determines the local kinetics within the PBE, which makes this an exciting area for future developments.

8.5 Application to food mixing operations

8.5.1 Challenges for simulation of food processes

Figure 8.1 showed that CFD has been increasingly applied within the food industries, and Sun (2007) presents a very wide range of examples in his book *Computational Dynamics in Food Processing*. However, there are relatively few literature publications related to food mixing, whereas in contrast, there are numerous CFD studies of a wide range of mixing unit operations in chemical and biochemical engineering. Several of these have been described and discussed in previous sections. So, what has held back the application of CFD to food mixing processes? The following sections provide a personal view of the challenges in applying CFD in this area.

8.5.1.1 *Knowledge of physical and transport properties*

Many food materials are complex mixtures, containing a structure which is irreversibly (occasionally reversibly) affected by shear and elongation, leading to non-Newtonian behaviour and possibly elastic effects. Standard commercial software allows the treatment of shear thinning and yield stress materials, but more complex visco-elastic behaviour (typical of pastes and doughs) is much more difficult to characterise experimentally and requires more specialised numerical approaches, for example, through the add-on module to POLYFLOW. Doughs, for example, are mixed to align proteins and develop structure; deformation coupled to chemistry results in a material that changes its rheology and properties during mixing, which is a real difficulty in fluid flow modelling. Other pastes and dispersion that thicken due to mixing and heat transfer are also problematic to simulate. Where chemical reactions occur in food mixtures, their specific rate laws are often unknown, and hence, it may be impossible to include important chemistry within the simulation.

8.5.1.2 *Transitional flows*

The vast majority of the flows discussed in Section 8.4 were in the fully turbulent flow regime. But with viscous fluids, such as are common in food processes, it is likely that the flow is transitional, in the range $10 < Re < 104$, or even that the Reynolds number changes during mixing, due to heat transfer and/or thickening. Some low *Re* turbulence models are better suited to weakly turbulent flows, but there has not really been enough research to assess their applicability in transitional cases (the stirred tank mixer is unusual in that the range of transitional flow is rather large, and it is not uncommon to find a turbulent type flow close to the blade tips, which relaminarises in the bulk of the tank).

8.5.1.3 *Complex mixer geometries*

The standard representations of the impeller for a cylindrical stirred vessel were discussed in Section 8.4.2. The best of these techniques, SM and MRF, require that the rotating blades are enclosed in a simple surface, which is usually a volume of revolution. Industrial dough mixers and planetary mixers involve intermeshing blades, for which there is no way of defining non-overlapping moving reference frames. Therefore, remeshing, adaptive meshs or superposition techniques are required, and typically, these will be available only in bespoke or specialist software. Even then, simplifications to the mixer geometry may be required to make the simulation tractable. Some further examples of these specialist techniques are given in Section 8.5.2.

8.5.1.4 *High volume fraction multi-phase mixtures*

Economic optimisation of process equipment generally requires intensive operation at high dispersed-phase fraction, which maximises specific kinetic rates (e.g., of mass transfer or chemical reaction). The Lagrangian tracking technique of Section 8.4.7 is restricted to low volume fractions ($<10\%$), although with some additional effort, two-way coupling can be included; inclusion of particle–particle collisions involves simultaneous tracking of the particles, which makes this technique infeasible for highly concentrated dispersions. Although the Eulerian–Eulerian methods (see Section 8.4.7) are more easily implemented for high volume fractions, they do not include particle–particle collision effects. Therefore, simulation of important processes, for example, secondary nucleation by crystal–crystal or crystal–impeller collisions is not yet possible at high solids fractions.

Realistic simulations of industrial food mixing operations may involve one or more of the difficulties discussed above, but nevertheless, some progress can be made by using simplifying assumptions, which can be tested out against experimental evidence. The approach really needs to be that doing something is better than doing nothing. The following sections give a selection of recent examples, where researchers have been pushing the boundaries to ever more complicated simulations relevant to food mixing operations.

8.5.2 Examples of food applications

As noted in Section 8.1.1, despite the ubiquitous use of CFD for the analysis of food processes, there are relatively few examples of applications to food mixing operations. Most of the applications are related to homogenisations, bioreactors, crystallisation and modelling of viscous fluid mixing. Commercial CFD code without modification are often not capable of dealing with the complex fluid flow of food mixtures, especially when it is related to viscous fluid and particle/bubble dynamics. Connelly and Kokini (2007) provide a recent review, which highlighted advances in only three areas related to food: (i) high-viscosity non-Newtonian blending; (ii) visco-elastic dough mixing in simplified mixer geometries and (iii) crystallisation and nano-particle production. These are amongst the first attempts at addressing some of the issues raised in Section 8.5.1.

CFD has been applied to model two-phase flow in bioreactors for shear thinning xanthan fermentations by Venneker *et al*. (2002) and Laakkonen *et al*. (2006). Venneker implemented a one-way coupled PBE to model a lab-scale bioreactor and found satisfactory predictions for the local gas hold-up, except around the impeller region. Laakkonen employed a coupled CFD–PBE approach for modelling the mass transfer in a lab- and pilot-scale bioreactors. They obtained good predictions of the local bubble size but only by adjusting the constants within the breakage and coalescence kernel. This practice is essentially empirical and is not fully predictive for cases where the experimental data is not available. They also reported a satisfactory prediction of the mass transfer coefficient.

Tanguy's group at the Ecole Polytechnique de Montreal have for many years studied finite-element simulations of low Reynolds number flows in helical ribbon and corotating screw extruders. These flow geometries are characterised by narrow gaps and one or more moving parts which rotate relative to each other, and hence, advanced meshing techniques are required. Giguere *et al*. (2006) reviewed the recent history of finite-volume or finite-element methods to deal with complex moving geometries. Quasi-steady simulations on a number of meshes, which represent the geometries at each time step, are feasible but cumbersome to implement; of order 100 separate meshes may be required to model the impeller throughout the period of its motion. Improved strategies include: (i) allowing the mesh to deform between time steps and only remeshing highly skewed or high aspect ratio elements; (ii) the mesh superposition technique (MST) which involves combining a static and dynamic mesh (Avalosse *et al*. 2002) and is implemented in the commercial solver POLYFLOW; and (iii) the fictitious domain method by Bertrand *et al*. (1997), which is similar to MST, but enforces the kinematics of the moving boundary in a different way.

Giguere *et al*. (2006) applied the fictitious domain method coupled with a mesh refinement strategy to a helical ribbon mixer and obtained satisfactory agreement with experimentally measured power inputs for a Newtonian liquid. Iranshahi *et al*. (2006) included a mixing time calculation within their study of a Paravisc impeller (a hybrid of an anchor and a double helical ribbon). As noted in Section 8.4.6, solution of the species transport equation is problematic and prone to numerical diffusion effects. An alternative way to represent

mixing is by particle tracking and trajectory analysis of a large number of massless particles which are released from a single point and then advected in the flow. A mixing time can then be evaluated from the decay of the intensity of segregation, which is related to spatial variance of the concentration of particles. In Iranshahi *et al*.'s (2006) work, the predicted mixing times were within 6% of experimentally measured values, and the method allowed the mixing efficiency of the Paravisc to be compared with more conventional low Reynolds number impeller types.

Fictitious domain and MST impeller representation methods have also been applied to the simulation of dough mixing operations. The first attempts, for example, by Jongen *et al*. (2000) assumed Newtonian behaviour in a simplified 2D geometry but were still able to assess the different relative amounts of rotation and shear and elongational deformation that were imposed on the dough during mixing. These deformations have an important effect on the alignment of proteins inside the dough and hence on the development of the visco-elastic structure which is so important in determining the texture of the baked loaf. Connelly and Kokini (2004) took this further by examining the effects of the fluid rheological properties (Newtonian, shear thinning inelastic, constant viscosity linear visco-elastic and non-linear visco-elastic fluids) on the deformation rate fields generated in a simplified 2D model of a dough mixer, modelled using a rotating frame of reference. The streamline contours and flow pattern were similar for each rheology, but the choice of constitutive equation led to differences in the deformation rates, particularly in the narrow gap between the moving blade and the walls. The amount of elongational flow, important for structure development, was found to depend on the constitutive model. Nevertheless, the results indicated regions of the device where mixing was poor and deformation rates were low.

Connelly and Kokini (2006a) extended their previous 2D work to a more realistic 3D geometry, namely a simplified version of the Farinograph, which is a sigma blade used for characterisation of flours and for determining water absorption. The mixer features two non-intermeshing sigma blades, as shown in Figure 8.20. MST was applied to mesh around the moving blades and both Newtonian and shear thinning fluids were examined. Although the flow patterns were in good agreement with LDA data, the predicted shear rates were an order of magnitude too low when compared to experimental measurements at similar positions in the flow. Poor refinement of the meshing technique close to the blades was one reason for this underestimate. Connelly and Kokini (2006b) performed further CFD mixing studies in the Farinograph geometry, based on tracking of 10^4 particles that were initially segregated in the two halves of the mixer. Figure 8.21a shows the initial configuration and Figures 8.21b–d show the situation after three cycles; around the blades, the particles appear more homogeneous, but near the top of the Farinograph, the mixture remains highly segregated. Although CFD simulations have the capabilities to model the flows, deformation and mixing rates in these complex geometries, more work is still required before they can be used for thorough analysis of the mixing performance. A further simplification used in Connelly and Kokini's studies is that the mixer runs full of fluid. In practice, however, dough mixers seldom run full, and the dough itself is thrown around the mixer, resulting in a very complex free surface flow. Treatment of this type of dynamic free surface flow is beyond current capabilities.

Some food processes involve a crystallisation stage. Indeed simulation of crystallisation processes and, in particular, the prediction and control of the crystal size distribution is a subject of much current research. PBEs equivalent to equation (8.59), but including the additional effects of nucleation and crystal growth, have to be solved in conjunction with the equations describing the hydrodynamics to predict the evolution of the crystal sizes in a batch vessel. In addition, the supersaturation, which provides the driving force for nucleation and

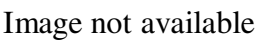

Fig. 8.20 Mesh used in the POLYFLOW simulation of a Farinograph sigma-blade dough mixer (Connelly & Kokini 2006a). (Reproduced with permission from John Wiley & Sons, Inc.)

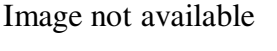

Fig. 8.21 Assessment of mixing from particle tracking in the POLYFLOW simulation of a Farinograph sigma-blade dough mixer (Connelly & Kokini 2006a): (a) the initial configuration of 10,000 particles and (b–d) their positions after three revolutions of the impeller. (Reproduced with permission from John Wiley & Sons, Inc.)

growth, may result from chemical reaction, cooling or anti-solvent addition. The supersaturation is likely to be non-uniformly distributed in space, but in principle, it can be calculated by solving energy and species transport equations in addition to the fluid flow modelling. Thus, these processes are amongst the most complicated that have been studied by CFD methods. One simplification that can be used is that the crystals are often small so that they follow the fluid motion, and hence, only single-phase flow calculations are necessary.

Wei *et al*. (2001) applied a moment-based population balance (based on nucleation and growth only) to predict the mean and standard deviation of the crystal size distribution produced from a semi-batch precipitation of barium sulphate. (Ba_2SO_4 is a much studied model system, due to detailed knowledge of its kinetics and thermodynamics.) Their predicted Sauter mean sizes compared well to experimental measurements, when both the feed time and impeller speed were varied, demonstrating that such studies have the potential to design and optimise semi-batch reactive crystallisations. However, as Rielly and Marquis (2001) have pointed out, reliable and detailed knowledge of the local kinetics of reaction, growth, nucleation and agglomeration is often missing for systems of practical or commercial importance. There is much debate about the suitable forms for kinetic rate laws, even for something as simple as growth—external mass transfer and surface reaction effects can lead to a variety of rate laws, which depend on the local supersaturation and crystal size.

The moment transport equations used by Wei *et al*. (2001) run into closure problems for processes that involve agglomeration or crystal breakage. A more advanced method, the quadrature method of moments (QMOM), replaces each of the integral expressions for the moments by a quadrature approximation using a small number of weights and abscissas. Marchisio *et al*. (2003) described how QMOM may be applied to systems that exhibit agglomeration and breakage, using simplified kernels. Later, Gavi *et al*. (2008) successfully applied QMOM, coupled with micro-mixing model and a RANS CFD model, to predict the size of nano-agglomerates of Ba_2SO_4 formed in an impinging jet micro-reactor. Comparisons with experiments were favourable (at the low barium excesses used) but required further testing for conditions where agglomeration is more likely to occur.

8.6 Closing remarks

This chapter has outlined the procedures for approaching CFD simulation and has discussed the underlying equations and numerical methods which are built into commercial packages. The more specialised methods for simulating stirred tank flows are described, and applications to single-phase flow simulations are also discussed. More complex methods to deal with multi-component mixing situations and multi-phase flows are presented, and examples from the literature have been analysed. The intention has been to emphasise at each stage the need for a good fundamental understanding of fluid mechanics and transport processes, so that justified decisions are made about the simplifying modelling assumptions, approximations and boundary conditions. Commercial CFD packages have been made much more user-friendly in recent years, but they are not intended for the novice who has little or no knowledge of fluid mechanics.

Very significant advances have been made in the last 30 years in the numerical solution of the equations of fluid motion using CFD methods, and yet there are still a very large number of problems to be solved to make it an easily accessible tool that is routinely applied for design and optimisation in food mixing. The final section of this chapter discussed some of the barriers to the application of CFD to realistic mixing processes used in the food and allied industries, but it also looked at some recent studies which aimed to address at least some of these issues. In many cases, it is not simply the lack of computing power that is the problem—admittedly, turbulent flows modelled with LES or DNS require very significant resources—but rather that there are real difficulties in characterising the evolving non-Newtonian multi-phase behaviour of many food products, representing the complex geometries of some food mixers, dealing with unknown chemistry or incomplete

knowledge of reaction rates and simulating high volume fraction dispersed phases or complex free surface shapes. The accuracy of any prediction is only as good as the underlying chemistry and physics, and hence, as knowledge improves in these areas it is expected that CFD will emerge as a useful tool for food applications in just the same way that it has already been accepted in other engineering fields.

Nomenclature

a_i	coefficients
c_p	specific heat capacity
C	impeller off-bottom clearance
$C_{1\varepsilon}$	dimensionless constant in equations
$C_{2\varepsilon}$	dimensionless constant in equations
C_μ	dimensionless constant in equations
D	impeller diameter
D_{im}	molecular diffusivity of species i in the fluid
E	viscous dissipation rate
f	volume of fluid (liquid volume fraction)
Fr	dimensionless Froude number
g	gravitational acceleration
h	space step
h_{ex}	heat transfer coefficient
I	turbulence intensity
j_Φ	flux of scalar quantity Φ
k	turbulence kinetic energy
L	characteristic length scale
N	impeller speed (rev/s)
Pe	Peclet number
Po	dimensionless power number
q	heat flux
Q	specific rate of heat generation
r, z, θ	cylindrical polar coordinates
R	residual
R_i	rate of production of species i
Re	Reynolds number
S	surface area
S_i	sources of species i
$\boldsymbol{S}_{ij}$	rate of deformation tensor
S_Φ	source of Φ
t	time
T_{d}	tank diameter
T	temperature
$\boldsymbol{u}$	fluid velocity vector $(u, v, w)^t$
U	characteristic velocity scale
V	volume
W	impeller blade width
We	Weber number

x, y, z cartesian coordinates
Y_i mass fraction of species i

Greek

ε turbulence energy dissipation rate
$\dot{\gamma}$ strain rate
Γ diffusivity of scalar Φ
κ thermal conductivity
Λ integral length scale
μ fluid viscosity
Φ a general scalar quantity
Φ' fluctuating value of Φ
$\overline{\Phi}$ mean value of Φ
ρ fluid density
σ surface tension
σ_k dimensionless constant in equations
τ_{ij} stress tensor
σ_ε dimensionless constant in equations

Subscripts

ex external
in inlet
L laminar
n normal
T turbulent
w wall

References

Alcamo, R., Micale, G., Grisafi, F., Brucato, A. & Ciofalo, M. (2005). Large-eddy simulation of turbulent flow in an unbaffled stirred tank driven by a Rushton turbine. *Chemical Engineering Science*, **60**, 2303–2316.

Armenante, P.M., Luo, C., Chou, C., Fort, I. & Medek, J. (1997). Velocity profiles in a closed, unbaffled vessel: comparison between experimental LDV data and numerical CFD predictions. *Chemical Engineering Science*, **52**, 3483–3492.

Aubin, J., Fletcher, D.F. & Xuereb, C. (2004a). Modelling turbulent flow in stirred tanks with CFD: the influence of the modelling approach, turbulence model and numerical scheme. *Experimental Thermal and Fluid Science*, **28**, 431–445.

Aubin, J., Le Sauze, N., Bertrand, J., Fletcher, D.F. & Xuereb, C. (2004b). PIV measurements of flow in an aerated tank stirred by a down- and an up-pumping axial flow impeller. *Experimental Thermal and Fluid Science*, **28**, 447–456.

Avalosse, T., Rubin, Y. & Fondin, L. (2002). Non-isothermal modeling of corotating and contra-rotating twin screw extruders. *Journal of Reinforced Plastics and Composites*, **21**, 419–429.

Barigou, M. & Greaves, M. (1992). Bubble-size distributions in a mechanically agitated gas–liquid contactor. *Chemical Engineering Science*, **47**, 2009–2025.

Batchelor, G.K. (2000). *An Introduction to Fluid Dynamics*. Cambridge University Press, Cambridge, UK.

Bertrand, F., Tanguy, P.A. & Thibault, F. (1997). Three dimensional fictitious domain method for incompressible fluid flow problems. *International Journal for Numerical Methods in Fluids*, **25**(6), 719–736.

Bird, R.B., Stewart, W.E. & Lightfoot, E.N. (2007). *Transport Phenomena.* John Wiley & Sons, Inc., New York.

Brucato, A., Ciofalo, M., Grisafi, F. & Micale, G. (1998a). Numerical prediction of flow fields in baffled stirred vessels: a comparison of alternative modelling approaches. *Chemical Engineering Science*, **53**, 3653–3684.

Brucato, A., Grisafi, F. & Montante, G. (1998b). Particle drag coefficients in turbulent fluids. *Chemical Engineering Science*, **53**, 3295–3314.

Bujalski, J.M., Jaworski, Z., Bujalski, W. & Nienow, A.W. (2002). The influence of the addition position of a tracer on CFD simulated mixing times in a vessel agitated by a Rushton turbine. *Chemical Engineering Research and Design*, **80**, 824–831.

Campolo, M. & Soldati, A. (2002). Appraisal and fluid dynamic efficiency of retreated-blade and turbofoil impellers in industrial-size CSTRs. *Industrial and Engineering Chemistry Research*, **41**, 1370–1377.

Campolo, M., Paglianti A. & Soldati, A. (2002). Fluid dynamic efficiency and scale-up of a retreated blade impeller CSTRs. *Industrial and Engineering Chemistry Research*, **41**, 164–172.

Connelly, R.K. & Kokini, J.L. (2004). The effect of shear thinning and differential viscoelasticity on mixing in a model 2D mixer as determined using FEM with particle tracking. *Journal of Non-Newtonian Fluid Mechanics*, **123**, 1–17.

Connelly, R.K. & Kokini, J.L. (2006a). 3D numerical simulation of the flow of viscous Newtonian and shear thinning fluids in a twin sigma blade mixer. *AIChE Journal*, **52**(10), 3383–3393.

Connelly, R.K. & Kokini, J.L. (2006b). Mixing simulation of a viscous Newtonian liquid in a twin sigma blade mixer. *Advances in Polymer Technology*, **25**(3), 182–194.

Connelly, R.K. & Kokini, J.L. (2007). Examination of the mixing ability of single and twin screw mixers using 2D finite element method simulation with particle tracking. *Journal of Food Engineering*, **79**, 956–969.

Crowe, C., Sommerfeld, M. & Tsuji, Y. (1998). *Multiphase Flows with Droplets and Particles*. CRC Press, Boca Raton, FL.

Derksen, J. & Van den Akker, H.E.A. (1999). Large eddy simulations on the flow driven by a Rushton turbine. *AIChE Journal*, **45**(2), 209–221.

Derksen, J.J. (2001). Assessment of large eddy simulations for agitated flows. *Chemical Engineering Research and Design*, **79**(A9), 824–830.

Derksen, J.J. (2003). Numerical simulation of solids suspension in a stirred tank. *AIChE Journal*, **49**(11), 2700–2714.

Derksen, J.J., Doelman, M.S. & Van den Akker, H.E.A. (1999). Three-dimensional LDA measurements in the impeller region of a turbulently stirred tank. *Experiments in Fluids*, **27**, 522–532.

Ding, J. & Gidaspow, D. (1990). Bubbling fluidization model using kinetic theory of granular flow. *AIChE Journal*, **36**(4), 523–538.

Elgobashi, S.E. & Abou-Arab, T.W. (1983). A two-equation turbulence model for two-phase flows. *Physics of Fluids*, **26**, 931–938.

Fluent. (2005). *Fluent 6.2 User Guide*. ANSYS Inc., Canonsburg, PA.

Gavi, E., Marchisio, D.L. & Barresi, A.A. (2008). On the importance of mixing for the production of nanoparticles. *Journal of Dispersion Science and Technology*, **29**(4), 548–554.

Giguere, R., Bertrand, F. & Tanguy, P.A. (2006). A three-dimensional mesh refinement strategy for the simulation of fluid flow with a fictitious domain method. *Computers and Chemical Engineering*, **30**(3), 453–466.

Gimbun, J., Rielly, C.D. & Nagy, Z.K. (2009). Modelling of mass transfer in gas–liquid stirred tanks agitated by Rushton turbine and CD-6 impeller, *13th European Conference on Mixing*, London.

Guha, D., Ramachandran, P.A., Dudukovic, M.P. & Derksen, J.J. (2008). Evaluation of large eddy simulation and Euler–Euler CFD models for solids flow dynamics in a stirred tank reactor. *AIChE Journal*, **54**(3), 766–778.

Haque, J.N., Mahmud, T. & Roberts, K.J. (2006). Modeling turbulent flows with free-surface in unbaffled agitated vessels. *Industrial and Engineering Chemistry Research*, **45**, 2881–2891.

Harris, C.K., Roekaerts, D., Rosendal, F.J.J. *et al.* (1996). Computational fluid dynamics for chemical reactor engineering. *Chemical Engineering Science*, **51**, 1569–1594.

Hartmann, H., Derksen, J.J., Montavon, C., Pearson, J., Hamill, I.S. & van den Akker, H.E.A. (2004). Assessment of large eddy and RANS stirred tank simulations by means of LDA. *Chemical Engineering Science*, **59**, 2419–2432.

Hemrajani, R.R. & Tatterson, G.B. (2004). Mechanically agitated vessels. In: *Handbook of Industrial Mixing, Science and Practice* (eds E.L. Paul, V.A. Atiemo-Obeng & S.M. Kresta). John Wiley & Sons, New Jersey, pp. 345–390.

Hirt, C.W. & Nichols, B.D. (1981). Volume of fluid (VOF) method for the dynamics of free boundaries. *Journal of Computational Physics*, **39**, 201–225.

Huebner, K.H., Thornton, E.A., & Byron, T.D. (1995). *The Finite Element Method for Engineers*, 3rd edn. Wiley Interscience, New York.

Iranshahi, A., Heniche, M., Bertrand, F. & Tanguy, P.A. (2006). Numerical investigation of the mixing efficiency of the Ekato Paravisc impeller. *Chemical Engineering Science*, **61**(8), 2609–2617.

Issa, R.I. (1986). Solution of implicitly discretized fluid flow equations by operator splitting. *Journal of Computational Physics*, **62**, 40–65.

Jahoda, M., Mostek, M. & Kukukova, A. (2007). CFD modelling of liquid homogenization in stirred tanks with one and two impellers using large eddy simulation. *Chemical Engineering Research and Design*, **85**(A5), 616–625.

Jaworski, Z. & Zakrzewska, B. (2002). Modelling of the turbulent wall jet generated by a pitched blade turbine impeller: the effect of turbulence model. *Chemical Engineering Research and Design*, **80**, 846–854.

Jones, R.M., Harvey III, A.D. & Acharya, S. (2001). Two-equation turbulence modeling for impeller stirred tanks. *Journal of Fluids Engineering*, **123**, 640–648.

Jongen, T. (2000). Characterization of batch mixers using numerical flow simulations. *AIChE Journal*, **46**(11), 2140–2150.

Khan, F.R., Rielly, C.D. & Hargrave, G.K. (2004). A multi-block approach to obtain angle-resolved PIV measurements of the mean flow and turbulence fields in a stirred vessel. *Chemical Engineering Technology*, **27**, 264–269.

Khan, F.R., Rielly, C.D. & Brown, D.A.R. (2006). Angle-resolved stereo-PIV measurements close to a down-pumping pitched-blade turbine. *Chemical Engineering Science*, **61**, 2799–2806.

Kolmogorov, A.N. (1941). The local structure of turbulence in incompressible viscous fluid for very large Reynolds numbers. *Doklady Akademii Nauk SSR*, **30**, 301–305.

Kresta, S.M. & Wood, P.E. (1991). Prediction of the three-dimensional turbulent flow in stirred tanks. *AIChE Journal*, **37**, 448–460.

Laakkonen, M., Moilanen, P., Miettinen, T. *et al*. (2005). Local bubble size distributions in agitated vessel comparison of three experimental techniques. *Chemical Engineering Research and Design*, **83**, 50–58.

Laakkonen, M., Moilanen, P., Alopaeus, V. & Aittamaa, J. (2006). Dynamic modeling of local reaction conditions in an agitated aerobic fermenter. *AIChE Journal*, **52**, 1673–1689.

Laakkonen, M., Moilanen, P., Alopaeus, V. & Aittamaa, J. (2007). Modelling local gas–liquid mass transfer in agitated vessels. *Chemical Engineering Research and Design*, **85**(A5), 665–675.

Leonard, B.P. (1979). A stable and accurate convective modelling procedure based on quadratic upstream interpolation. *Computer Methods in Applied Mechanics and Engineering*, **19**, 59–98.

Li, M., White, G., Wilkinson, D. & Roberts, K.J. (2004). LDA measurements and CFD modeling of a stirred vessel with a retreat curve impeller. *Industrial and Engineering Chemistry Research*, **43**, 6534–6547.

Li, M., White, G., Wilkinson, D. & Roberts, K.J. (2005). Scale up study of retreat curve impeller stirred tank using LDA and CFD. *Chemical Engineering Journal*, **108**(1–2), 81–90.

Li, Z.P., Gao, Z.M. & Smith, J.M. (2007). Large eddy simulation of flow fields in vessels stirred by dual Rushton impeller agitators. *Journal of Chemical Engineering of Japan*, **40**, 684–691.

Luo, J.Y., Issa, R.I. & Gosman, A.D. (1994). Prediction of impeller-induced flows in mixing vessels using multiple frames of reference. *IChemE Symposium Series*, No. 136, pp. 549–556.

Marchisio, D.L., Vigil, R.D. & Fox, R.O. (2003). Quadrature method of moments for aggregation-breakage processes. *Journal of Colloid and Interface Science*, **258**(2), 322–334.

Marshall, E.M. & Bakker, A. (2004). Computational fluid mixing. In: *Handbook of Industrial Mixing, Science and Practice* (eds E.L. Paul, V.A. Atiemo-Obeng & S.M. Kresta). John Wiley & Sons, New Jersey, pp. 257–344.

Montante, G. & Magelli, F. (2005). Modelling of solids distribution in stirred tanks: analysis of simulation strategies and comparison with experimental data. *International Journal of Computational Fluid Dynamics*, **19**(3), 253–262.

Montante, G., Paglianti, A. & Magelli, F. (2004). Liquid homogenization characteristics in vessels stirred with multiple Rushton turbines mounted at different spacings. CFD study and comparison with experimental data. *Chemical Engineering Research and Design*, **82**(A9), 1179–1187.

Montante, G., Paglianti, A. & Magelli F. (2007). Experimental analysis and computational modelling of gas–liquid stirred vessels. *Chemical Engineering Research and Design*, **85**(A5), 647–653.

Montante, G., Horn, D. & Paglianti, A. (2008). Gas–liquid flow and bubble size distribution in stirred tanks. *Chemical Engineering Science*, **63**(8), 2107–2118.

Nagata, S. (1975). *Mixing: Principles and Applications.* Halstead Press, Tokyo, Japan.

Navier, C.L.M.H. (1822). Memoire sur les lois du mouvement des fluides. *Memoires de L'Academie Royale des Sciences de L'Institut de France*, **6**, 389–440.

Ng, K., Fentiman, N.J., Lee, K.C. & Yianneskis, M. (1998). Assessment of sliding mesh CFD predictions and LDA measurements of the flow in a tank stirred by a Rushton impeller. *Chemical Engineering Research and Design*, **76**, 737–747.

Nienow, A.W. (1997). On impeller circulation and mixing effectiveness in the turbulent flow regime. *Chemical Engineering Science*, **52**, 2557–2565.

Norton, T. & Sun, D.W. (2006). Computational fluid dynamics (CFD) – an effective and efficient design and analysis tool for the food industry: a review. *Trends in Food Science and Technology*, **17**, 600–620.

Ochieng, A. & Onyango, M.S. (2008). Homogenization energy in a stirred tank. *Chemical Engineering and Processing*, **47**(9–10), 1853–1860.

Patankar, S.V. (1980). *Numerical Heat Transfer and Fluid Flow*. Hemisphere, Washington, DC.

Patwardhan, A.W. (2001). Prediction of flow characteristics and energy balance for a variety of downflow impellers. *Industrial and Engineering Chemistry Research*, **40**, 3806–3816.

Ranade, V.V. & Joshi, J.B. (1990). Flow generated by a disc turbine. Part II. Mathematical modelling and comparison with experimental data. *Chemical Engineering Research and Design*, **68**, 34–50.

Revstedt, J., Fuchs, L. & Tragardh, C. (1998). Large eddy simulations of the turbulent flow in a stirred reactor. *Chemical Engineering Science*, **53**, 4041–4053.

Rielly, C.D. & Marquis, A.J. (2001). A particle's eye view of crystallizer fluid mechanics. *Chemical Engineering Science*, **56**, 2475–2493.

Rudman, M. (1997). Volume-tracking methods for interfacial flow calculations. *International Journal for Numerical Methods in Fluids*, **24**, 671–691.

Ruszkowski, S. (1994). A rational method for measuring blending performance and comparison of different impeller types, *Proceedings of the 8th European Mixing Conference*, Institute of Chemical Engineers, Rugby, U.K., pp. 283–291.

Sbrizzai, F., Lavezzo, V., Verzicco, R., Campolo, M. & Soldati, A. (2006). Direct numerical simulation of turbulent particle dispersion in an unbaffled stirred-tank reactor. *Chemical Engineering Science*, **61**, 2843–2851.

Schäfer, M., Yianneskis, M., Wächter, P. & Durst, F. (1998). Trailing vortices around 45º pitched-blade impeller. *AIChE Journal*, **44**, 1233–1245.

Shih, T.H., Liou, W.W., Shabbir, A., Yang, Z. & Zhu, J. (1995). A new $k-\varepsilon$ eddy viscosity model for high Reynolds number turbulent flows. *Computers and Fluids*, **24**(3), 227–238.

Simonin, O. & Viollet, P.L. (1990). Prediction of an oxygen droplet pulverization in a compressible subsonic coflowing hydrogen flow. *Numerical Methods for Multiphase Flows*, **91**, 65–82.

Spalart, P.R., Jou, W.-H., Strelets, M. & Allmaras, S.R. (1997). Comments on the feasibility of LES for wings, and on a hybrid RANS/LES approach, *Advances in DNS/LES, 1st AFOSR International Conference on DNS/LES*, Greyden Press, Columbus, OH, 4–8 August.

Stokes, G.G. (1845). On the theories of internal friction of fluids in motion. *Transactions of the Cambridge Philosophical Society*, **8**, 287–305.

Sun, D.W. (2007). *Computational Fluid Dynamics in Food Processing.* CRC Press, Taylor & Francis Group, Boca Raton, FL.

Tyagi, M., Roy, S. & Harvey, A.D. (2007). Simulation of laminar and turbulent impeller stirred tanks using immersed boundary method and large eddy simulation technique in multi-block curvilinear geometries. *Chemical Engineering Science*, **62**(5), 1351–1363.

Vandoormaal, J.P. & Raithby, G.D. (1984). Enhancements of the SIMPLE method for predicting incompressible fluid flows. *Numerical Heat Transfer*, **7**, 147–163.

Van't Riet, K. & Smith, J.M. (1975). The trailing vortex system produced by Rushton turbine agitators. *Chemical Engineering Science*, **30**, 1093–1105.

Venneker, B.C.H., Derksen, J.J. & Van den Akker, H.E.A. (2002). Population balance modeling of aerated stirred vessels based on CFD. *AIChE Journal*, **48**, 673–685.

Versteeg, H.K. & Malalasekara, W. (2007). *An Introduction to Computational Fluid Dynamics. The Finite Volume Method.* Pearson Education, Harlow, U.K.

Verzicco, R., Fatica, M., Iaccarino, G. & Orlandi, P. (2004). Flow in an impeller-stirred tank using an immersed-boundary method. *AIChE Journal*, **50**, 1109–1118.

Wei, H., Zhou, W. & Garside, J. (2001). Computational fluid dynamics modeling of the precipitation process in a semibatch crystallizer. *Industrial and Engineering Chemistry Research*, **40**, 5255–5261.

Wu, H. & Patterson, G.K. (1989). Laser Doppler measurements of turbulent flow parameters in a stirred mixer. *Chemical Engineering Science*, **44**, 2207–2221.

Yakhot, V. & Orszag, S.A. (1986). Renormalization group analysis of turbulence: I. Basic theory. *Journal of Scientific Computing*, **1**(1), 1–51.

Yapici, K., Karasözen, K., Schäfer, M. & Uludag, Y. (2008). Numerical investigation of the effect of the Rushton type turbine design factors on agitated tank flow characteristics. *Chemical Engineering and Processing*, **47**, 1346–1355.

Yeoh, S.L., Papadakis, G., Lee, K.C. & Yianneskis, M. (2004). Large eddy simulation of turbulent flow in a Rushton impeller stirred reactor with sliding-deforming mesh methodology. *Chemical Engineering and Technology*, **27**, 257–263.

Yeoh, S.L., Papadakis, G. & Yianneskis, M. (2005). Determination of mixing time and degree of homogeneity in stirred vessels with large eddy simulation. *Chemical Engineering Science*, **60**, 2293–2302.

Yianneskis, M. & Whitelaw, J.H. (1993). On the structure of the trailing vortices around Rushton turbine blades. *Chemical Engineering Research and Design*, **71**, 543–550.

Yianneskis, M., Popiolek, Z. & Whitelaw, J.H. (1987). Experimental study of the steady and unsteady flow characteristics of stirred reactors. *Journal of Fluid Mechanics*, **175**, 537–555.

Yimer, I., Campbell, I. & Jiang, L-Y. (2002). Estimation of the turbulent Schmidt number from experimental profiles of axial velocity and concentration for high-Reynolds-number jet flows. *Canadian Aeronautics and Space Journal*, **48**, 195–200.

Zwietering, T.N. (1958). Suspending of solid particles in liquid by agitators. *Chemical Engineering Science*, **8**, 244–253.

9 Immiscible liquid–liquid mixing

Fotis Spyropoulos, P.W. Cox and Ian T. Norton

9.1 Introduction

Good examples of immiscible liquid–liquid systems are emulsions which are normally either an oil-in-water system such as salad dressings, soups, sauces, mayonnaise, skin creams, emulsion-based paints, etc. (Walstra 1993; Campbell *et al*. 1996), or a water-in-oil system such as margarines, low-fat spreads, butter, etc. (Livingston & Norton 1997; Rousseau & Hodge 2005). These immiscible liquids can be 'mixed' to give finely divided included phases. This is achieved in an emulsification step often known as homogenisation (Walstra 1993). These processes normally use high shear devices and require high energy input. However, even by significantly increasing the shear forces and energy input, the emulsion droplet sizes reach a limiting value. This is commonly found to be in the order of 0.5–1 μm (Walstra 1993; McClements 1999). The reason for this limiting behaviour will be discussed as will strategies to produce much smaller droplets, nano-emulsions, in which the structure is kinetically trapped with limiting concentrations of surfactant (Henry *et al*. 2008).

Once mixing has stopped, emulsion droplets will quickly cream or sediment, and additionally, as the 'naked' interfaces come into contact, coalescence occurs and two bulk liquid phases are eventually formed (Dickinson 1989). To prevent these types of instabilities, in water and oil systems, a surfactant (also known as an emulsifier) is added to the formulation to stabilise the interface and stop naked interfaces from coming into contact after the homogenisation step. The amount of surfactant used needs to be high enough to cover the surface of the droplets, and the process has to be designed to give enough time for the surfactant to cover the interface before droplets contact each other (Walstra 1993; McClements 1999) normally in low shear regions after the homogenisation step.

Emulsifiers can be charged to induce charge repulsion between droplets, or be polymeric in nature (e.g., proteins) to induce steric stabilisation (Dickinson & McClements 1996), or be aggregated at the interface so inducing a rheological stability, that is, giving an elastic interface. In addition, particles can be placed at the interface to give stability; this is known as Pickering stabilisation (Pickering 1907). The energy of adsorption for particles is 10s to 1,000s kT; thus once they are present at the interface, they cannot be removed during a thermal or mechanical process (Binks 2002).

One of the key roles of emulsions in fabricated products is to control the texture, appearance, in use properties (spreading, etc.), oral response in terms of both the physical interactions (mouth coating) and flavour (Malone *et al*. 2003; Lian *et al*. 2004) or fragrance

release. For instance, oils can be included to give a particular structure such as a particulate gel (as is the case in mayonnaise) (Foegeding *et al*. 1995; Clark *et al*. 2001) or to give appearance properties (as in the case of the whiteness of milk or skin care products). The droplets can be flocculated into a network to give spreading properties as in emulsion paints (Hofland 1997) and the way the emulsion dilutes and breaks down in the mouth (Malone *et al*. 2003).

Other types of immiscible liquids that will be discussed in some detail in this chapter are:

- 'water-in-water emulsions', which are formed when two biopolymers are mixed together in water;
- air-filled emulsions;
- double emulsions.

9.2 Emulsion types and properties

9.2.1 Kinetically trapped nano-emulsions

There have been many good reviews on simple emulsions, both water-in-oil and oil-in-water. It is not our intention to repeat these reviews here; however, a new development worth discussing is that there is a great interest in introducing low levels of oil into products for either mouthfeel reasons (Dillon 1996) or to carry micronutrients (McClements & Decker 2000; Mason *et al*. 2006). In order to do this without changing the appearance of the product, oil droplets of less than 40 nm are required. This could be achieved with microemulsions (Hoar & Schulman 1943). However, there are a number of problems with using this approach: they require large quantities of emulsifier, causing off flavours, astringency, etc., when consumed; they are thermodynamically stable and so are very difficult to destabilise when required to release flavours and/or nutrients in use; and the emulsifiers traditionally used are synthetic and not allowed in foods in many countries.

Potentially, the best way of including low levels of oil is by incorporating kinetically trapped nano-emulsions. These emulsions can be designed to breakdown and release the active ingredient at the desired rate and in the appropriate place (i.e., in the mouth or stomach). However, they need to be stable when being transported and stored before use, and preferably be stabilised with natural emulsifiers such as proteins. What has prevented the widespread introduction of this type of emulsion is that they are very difficult to manufacture, and often unstable. Attempts have been made to produce nano-emulsions by increasing the pressure in the homogenisation step (Olson *et al*. 2004). This has resulted in sub-micron droplets but not in stable nano-emulsions (i.e., droplets with diameter below 100 nm). It seems that beyond a certain point, more energy input in the homogeniser simply result in greater heating with little or no change in droplet size (Schubert & Engel 2004).

The question that needs to be addressed (Henry *et al*. 2008) is: what is the rate-limiting step in the mechanism? Currently, it is unknown whether the droplet size is limited by the efficiency of the droplet break-up (suggesting that the only way to get smaller droplets is to find new homogenisation processes), or is it a consequence of the emulsifier used (in which case there is a physical chemical limit to the final droplet size), or is limited by the back reaction (i.e., coalescence) in the process (in this case, it is the rate at which the emulsifier reaches the naked interface produced in the homogenisation process that determines the final droplet size). As the droplets become smaller, the Laplace pressure increases and

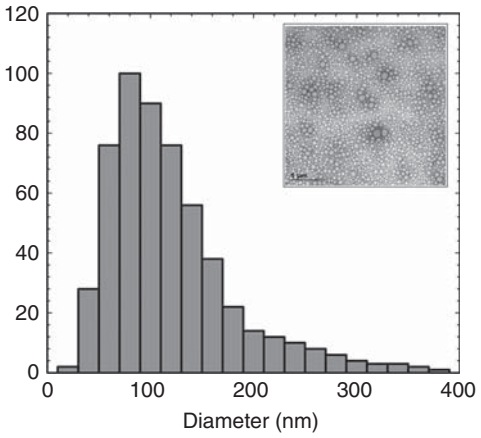

Fig. 9.1 Transmission electron micrograph (TEM) and droplet size (diameter) of a nano-emulsion.

Ostwald ripening becomes a potential coarsening mechanism as oil moves from the small droplets to the larger ones (Walstra 1996).

Henry *et al*. (2008) reported the work carried out to understand the production and long-term stability of nano-emulsions for use in the food industry. They showed that sub-micron emulsion droplets could be produced (Figure 9.1) in a high-pressure impinging jet device. Emulsions produced using triglyceride oils were stable over many weeks or months. This stability was explained as a consequence of the insolubility of the oil in the water and a lack of micellar-driven ripening. More work is required in this area, which seems very likely over the next few years.

9.2.2 Pickering emulsions

The concept of using particles as surfactants is not new and was first reported by Pickering (1907). Pickering emulsions share the same stabilisation requirements of the common emulsions, that is, protection of the naked interface to prevent coalescence and minimisation of either creaming or sedimentation to the original bulk phases (Walstra 1993). However, in the Pickering systems, the interface is not necessarily covered but has a (near to) close packed arrangement of particles, which reside at some depth within the interface of the emulsion or foam (see Section 9.2.4 regarding air-filled emulsions). It is the depth of the particle's final position, as defined by its wettability (Sacanna *et al*. 2007), that in turn controls the angle of curvature for the colloidally stabilised droplet. The particle and its effects can be described by:

$$E = \Pi r^2 \gamma (1 \pm \cos\theta)^2 \tag{9.1}$$

where E is the energy of attachment of a particle to an interface, r is the particle radius, γ is the interfacial tension and θ is the particle contact angle (Figure 9.2a). This equation remains central to colloid stabilisation of droplets as it describes the relevant considerations surrounding particle-stabilised emulsions.

From equation (9.1), it can be seen that the energy of attachment to an interface is large (up to thousands of kT) and is highly dependent on the interfacial tension, which not only

changes the binding energy directly but also changes the contact angle and therefore the position of the particle in the interface (Figure 9.2). In foods, the interfacial tension and the effect of solid particles on emulsion stability are manipulated by the addition of low-molecular-weight emulsifiers. The addition of emulsifier may then help modify the high binding energy of particles, which is a problem for foods because at some point in their product cycle, food emulsions must break to either deliver nutrients or sensorial response, and so permanent constructs are not ideal. Because of this, each of the terms used within equation (9.1) will be discussed in isolation before a unified description is attempted later.

9.2.2.1 *Particle wettability*

Equation (9.1) describes the position of the stabilising particle at rest within an interface, that is, the particle's interfacial angle [denoted as θ in Figure 9.2 and equation (9.1)]. Both Binks (2002) and Rousseau (2000) describe this as analogous to the hydrophilic–lipophilic balance (HLB) of the small molecules stabilising common emulsions. This is represented schematically in Figure 9.2. In Figure 9.2a, the particle's relative hydrophobicity defines its position in the interface and therefore the curvature of the interface (Figure 9.2b). At $\theta = 90º$, the energy of attachment becomes maximal as the hydrophobicity/hydrophilicity of the particle is equal, but the curvature is minimal. Away from $\theta = 90º$, the energy of attachment is reduced and the angle of curvature increases, and therefore, the size of stabilised droplets decreases (Figure 9.2b). At large distances from $\theta = 90º$, that is, below $\theta = 20º$ or above $\theta = 160º$, the angle of contact or perhaps more correctly the apparent HLB becomes too small for the majority of the particles to exist at the interface, and so gross partitioning to a respective phase occurs and the emulsifier action diminishes (Aveyard *et al.* 2003). However, as mentioned earlier, the contact angle of any particle can be manipulated by adding low-molecular-weight emulsifiers. This then allows food grade particles to be used.

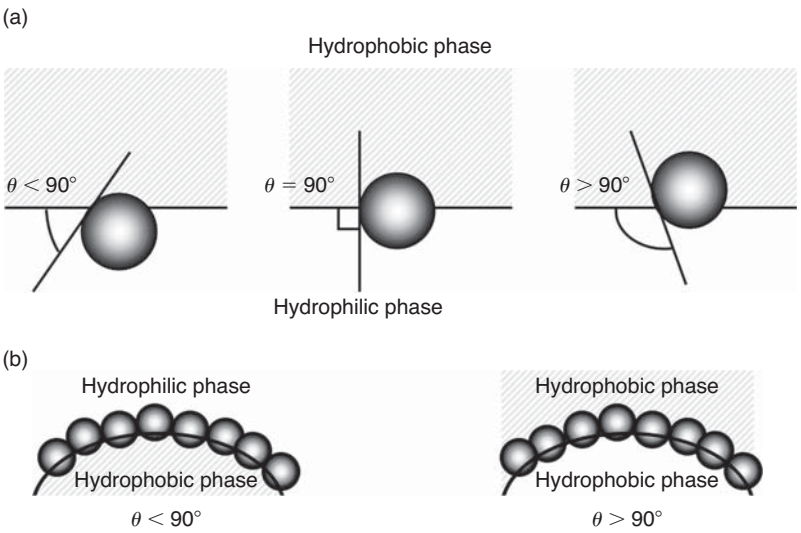

Fig. 9.2 Interfacial contact angles for Pickering particles. (a) The likely positions of three particles with differing wettability at an interface. (b) The effect of the contact angle (θ), seen in (a), upon interfacial curvature.

9.2.2.2 *Particle size and number*

Equation (9.1) implicates the stabilising particle's size in the energy of attachment: as the size of the stabilising particle increases, the energy of attachment of the particle increases. This implies that larger particles should be used if stability is required. However, the particle size will also influence the overall droplet size, and so there is a limited ratio of droplet size to particle size that are of practical use. As the radius of the stabilising particles diminishes, the energy of attachment decreases to a point where it mimics that of a common emulsion stabilised by small molecules and so may be manipulated to have a controllable meta-stability. To reach this level of control within the structure requires particles of a similar size to the amphiphilic molecules the particles were intended to replace (Binks 2002; Aveyard *et al*. 2003). This implies that the use of nano-particles will be of considerable use in the future.

One parameter that needs to be considered is the number or density of the particles at the stabilised interface. As the number of particles at an interface rises, not only does the stability increase, as the curvature of the droplet is reinforced by the properties of the particles, but also the available free interface diminishes and so does the probability of coalescence. Although for non-mixed systems the rate at which particles reach an interface is slower than for surfactants (Pichot *et al*. 2008), this is not necessarily true for mixed systems where the particles are swept to the interface and once there they are unlikely to leave and so re-expose the naked interface in the process. As the interface becomes populated by particles, it becomes more rigid. This has a detrimental effect in mixed systems because the time for film drainage decreases as there is decreased surface flattening as droplets collide, and there are reports that propose that solid particles may puncture the interface during flow. The result is then an increased coalescence rate in flow. Once the interface is fully covered, then coalescence is stopped.

9.2.2.3 *Naturally occurring Pickering emulsions*

Particle-stabilised emulsions have been used in industry (Hunter *et al*. 2008), for example, in cosmetics, pharmaceutics, oil recovery, wastewater treatment, whipped cream and ice cream (Brooker 1986, 1993).

In creams and ice cream, fat crystals are used as the particles to give the emulsion stabilisation (Rousseau 2000). This has an advantage that when the food products are consumed, the heating process in the mouth can be used to melt the crystals and cause the emulsion to break and release flavours and nutrients. In both of these examples, the fat particles do not act alone at the interface as they contain milk proteins and a range of low-molecular-weight emulsifiers. These proteins and emulsifiers affect the interfacial tension and thus the position of the particle within the interface. This naturally occurring interplay of stabilisation processes has yet to be fully explored, although Pichot *et al*. (2008) have explored the role that Pickering stabilisation might have in a mixed food grade emulsifier systems (silica, at edible concentrations and monoolein) and have clearly shown the counterbalance between the two systems and the level of control which such an approach could deliver to a production process.

9.2.2.4 *Monodispersion and meta-stability*

In almost all of the studies published on Pickering emulsions, the stabilising particles used have been exquisitely prepared to have as narrow a range of particle size as possible (Binks

& Lumsdon 2001). Unfortunately, nature or more usually large-scale industrial production isn't so obliging, and particle sizes and digestibility may be too broad for a well-controlled process to be achieved at a significant scale; indeed the two examples described above are bulk commodities and notoriously difficult to make, either at bench or industrial scale. Owing to the scale of manufacture, the use of expensive, finely made monodispersed particles in such applications is impossible, and so microstructural design of new products will in many ways remain empirical.

Similarly, for food products the stability of the particle networks is important. The provision of meta-stability to silica-stabilised emulsions has been discussed in terms of particle size and number, but has also been introduced for systems where fat causes the Pickering effect. Indeed the use of fat along with protein particles (Murray & Ettalaie 2004) for the Pickering stabilisation of foods is probably the route future research will take (along with small molecular weight co-emulsifiers). Using fat and/or protein is an attractive prospect, not just due to their digestibility, but their controllable meta-stability. Although the mechanisms of breakage differ between the two classes—that is, fat crystals melt and are removed from the interface, presumably by shear effects, whereas protein particles are small enough to have an approachable energy of removal as defined earlier—both can break appropriately in the mouth or gastrointestinal (GI) tract and not during manufacture, distribution or storage. So, these two systems along with the emerging use of co-surfactant look to be promising areas for the future.

9.2.3 Double emulsions

Double or duplex or multiple emulsions are emulsions of complex microstructure where the droplets of the dispersed phase themselves contain even smaller dispersed droplets. These systems, also referred to as 'emulsions of emulsions' or 'emulsified emulsions' or 'liquid emulsion membranes', are of two major types: water-in-oil-in-water ($W_1/O/W_2$) and oil-in-water-in-oil ($O_1/W/O_2$) double emulsions. For example (Plate 9.1), in the case of a $W_1/O/W_2$ multiple emulsion, small aqueous droplets W_1 (primary emulsion internal droplets) are dispersed in oil O (primary emulsion matrix phase) and this water-in-oil (W/O) emulsion (primary emulsion) itself is dispersed as large droplets in the continuous aqueous phase W_2 (double emulsion matrix). Finally, double emulsions can be further classified depending on the number of internal droplets in the primary emulsion (W_1 in Plate 9.1), which can range from one large internal droplet ('core–shell' type) to a large number of internal droplets. A typical *W/O/W* double emulsion stabilised by monomeric emulsifiers will consist of inner *W/O* droplets of 0.5–2 μm in size and double *W/O/W* droplets (the outer phase) of 10–60 μm (Garti 1997).

9.2.3.1 *Advantages and applications of double emulsions*

Double emulsions were first described at the beginning of the last century (Seifriz 1925). Despite the early interest in these systems, their potential superiority over the conventional *O/W* or *W/O* emulsions has only been recognised in relatively recent years. One of the major advantages of *W/O/W* (or *O/W/O*) double emulsions is their potential of acting as microcarriers of hydrophilic (or lipophilic) ingredients entrapped in their internal droplets. Depending on the application, these ingredients can then be released from the inner to the outer water (or oil) phase by a controlled and sustained mechanism or even stay entrapped in the inner phase during a specific process (e.g., during oral processing).

The advantages of using double emulsions in food applications are mainly related to their capability to encapsulate (or entrap), in their internal droplets/compartments, substances that

are then slowly released (Garti 1997; Mezzenga 2007; Muschiolik 2007). On this basis, several food formulations have been patented, such as creams, spreads, salad dressings, confectionary, etc. (Suzuki *et al*. 1991; Taki *et al*. 2007). Double emulsions can also be used in the food industry where an external water phase is more acceptable in terms of palatability than an oil one (Matsumoto *et al*. 1976). Further food applications are related to the development of low-fat (calorie) formulations; *W/O/W* systems have the same volume fraction of the dispersed phase and the same texture as a simple *O/W* emulsion, but with a lower fat content, due to the existence of the aqueous compartments in the food globules (Gaonkar 1994). The personal care industry has also acknowledged the great potential of this technology for delivery of actives (Tokimitsu *et al*. 1990; Herb *et al*. 1999; Araújo Macian *et al*. 2007). Additionally, possible applications of double emulsions for drug delivery or controlled drug release purposes have been demonstrated (Engel *et al*. 1968; Kim *et al*. 1995; Cole & Whateley 1997). Finally, the technology shows promise in the detoxification or removal of toxic materials from wastewater (Ho *et al*. 1982; Pickering & Southern 1997) and the slow and controlled release of materials such as fertilizers and pesticides for agricultural uses (Garti & Aserin 1996).

9.2.3.2 *Formation of double emulsions*

The formation of double emulsions is usually a one- or two-step process. The early 'one-step' techniques were based on the concept that a double emulsion is a mesophase between *O/W* and *W/O* emulsions. Such a mesophase is achieved by increasing the temperature of an emulsion consisting of non-ionic emulsifiers or by mixing two different types of emulsifiers (Dokić & Sherman 1980; Matsumoto 1983).

Owing to the empirical and somewhat 'accidental' nature of such one-step preparations and the growing need for better control over the complex microstructure of double emulsions, the so-called two-step emulsification processes were later adopted (Muschiolik 2007). In the case of a *W/O/W* double emulsion, the first stage involves the preparation of a *W/O* simple emulsion, with a large excess of hydrophobic emulsifier, by strong homogenisation to form the smallest possible droplets. In industry, this stage is usually carried out using mechanical devices (such as high-speed blenders, high-pressure homogenisers and colloid mills), which subject the liquids to violent agitation. In the second stage, the *W/O/W* double emulsion is formed by gentle addition of the *W/O* to water in the presence of a hydrophilic emulsifier. The second emulsification stage is usually carried out under gentle conditions in order to avoid the rupture of the internal droplets (Muschiolik 2007).

Recent advances in emulsification techniques are now used for the preparation of double emulsions. Most of the techniques reported here have found use as the second emulsification step in the 'two-step' emulsification processes of double emulsions. Even though there is room for improvement, these novel techniques have been found to produce fairly monodispersed systems under relatively mild conditions, which understandably is beneficial for the formation of double emulsions.

Membrane emulsification

Membrane emulsification is a low-energy process with good control over the droplet size and size distribution (van der Graaf *et al*. 2005; Muschiolik 2007), which uses an applied pressure to force the dispersed phase to permeate through a membrane into the continuous phase. The shear stress is lower than in conventional emulsification processes because small droplets are formed directly by permeation of the dispersed phase through the micropores.

The distinguishing feature of this process is that the droplet size of the resulting emulsion is controlled primarily by the choice of the membrane and not by the generation of turbulent droplet break-up (Charcosset *et al*. 2004).

More recently, variations of the technique, such as 'cross-flow' and 'rotating' membrane emulsification (Schadler & Windhab 2006; Vladisavljević & Williams 2006), have emerged in order to assist the detachment of the droplets formed on the membrane surface thus reducing the droplet size in the resulting emulsion.

Microchannel emulsification

In microchannel emulsification process, droplets are produced by forcing the to-be-dispersed phase through the microchannels in a silicone plate with well-defined geometries. This technique is particularly useful for the second step in double emulsion formation as no excessive mechanical shear is involved. Furthermore, microchannel emulsification opens up the possibility of preparing emulsions of high monodispersity (Sugiura *et al*. 2004). The preparation of uniform and tailored droplets can be of importance for food application, to regulate the release kinetics with more precision and for special applications where standardised particle sizes are necessary (e.g., capsule formation) (Muschiolik 2007). A clear advantage of this technique is the high entrapment yields associated with it; Sugiura *et al*. (2004) reported *W/O/W* entrapment yields as high as 91%.

A distinct disadvantage of microchannel emulsification is the low production rates usually associated with the process. However, it is believed that microchannel emulsification can be scaled up and meet industrial production rates by using larger microchannel plates and multiple microchannel plates (Sugiura *et al*. 2004).

Microfluidic devices

Double emulsions can be formed using microfluidic devices in two stages. Initially, the aqueous (or oil) internal drops are formed periodically upstream at a hydrophobic (or hydrophilic) junction (e.g., T-junction); then, in a continuing series, organic droplets enclosing the aqueous droplets are formed downstream at a hydrophilic (or hydrophobic) junction. Okushima *et al*. (2004) described a very interesting microfluidic device capable of producing multiphase systems of high reproducibility, narrow size distribution of droplets (low coefficient of variation = 2.7%) at high flow rates (up to 2.5×10^3 drops/s). Furthermore, by adjusting the relation between break-up rates at the two junctions, the number of enclosed droplets can be precisely controlled.

Microcapillary devices

Microcapillary devices, in their more simple form, consist of two coaxially aligned cylindrical capillary tubes where the dispersed (inner capillary) and continuous (outer capillary) phases of the to-be emulsion are flowing. Formation of the emulsion is the result of the hydrodynamic focusing of the dispersed phase, as it exits the inner capillary through an orifice, by the converging flow of the continuous phase. A microcapillary device that generates double emulsions in a single step, allowing precision control of the outer and inner drop sizes as well as the number of droplets encapsulated in each larger droplet has been recently reported (Utada *et al*. 2005).

The production of double emulsions by this method is limited by the drop formation frequency, which varies from 100 to 5,000 Hz. Increasing the production rate for the use of microcapillary devices in industrial scale requires the operation of parallel devices (Whitesides &

Stroock 2001). Furthermore, the size of the drops obtained using these devices is limited to the characteristic cross section of the capillaries (a few microns) to avoid clogging problems.

High- and low-pressure homogenisers

High-pressure homogenisation is the most common method of producing fine emulsions in the food industry. It reduces the droplet size of a coarse emulsion, made by traditional methods (e.g., high-speed mixers), and it has been proven to be an effective first-stage process in the formation of double emulsions. Owing to the high shear introduced into the system, its use in the second stage is usually avoided (Muschiolik 2007).

Nonetheless, there have been some publications on double emulsion formation using high- or low-pressure homogenisation processes. Benichou *et al*. (2002) report on the production of *W/O/W* double emulsions using a high-pressure homogeniser with a 'dual feed' cell. Here, the finely dispersed *W/O*-phase was emulsified in the external *W*-phase by mixing in the emulsification chamber under dynamic pressures of up to 600 atm (Benichou *et al*. 2002). Low-pressure emulsification, using a homogeniser with a special orifice valve operating at low pressures $\leqslant$1 MPa (in comparison to those involved in high-pressure homogenisation), has also been reported to successfully produce stable double emulsions (Muschiolik *et al*. 2006). The inclusion yields for the double emulsions produced by this technique were found to be over 90% and not too far from those obtained using a more 'gentle' emulsification process such as membrane emulsification.

Coaxial jet electrospray

In electrospray techniques, emulsification takes place by smoothly stretching the dispersed liquid interface by the action of electrical forces until its characteristic length reaches a critical value (usually in the micro- or nano-metric range) and the interface breaks by capillary instabilities yielding an emulsion rather than monodisperse drops. Multiple emulsions ($O_1/W/O_2$) with monodispersed droplets have been produced by the coaxial jet electrospray technique (Marín *et al*. 2007). This method is able to reach the sub-micron scale if the dielectric host liquid (O_2-phase), the conductive liquid (*W*-phase) and the insulating liquid (O_1-phase) are carefully selected. The conductive liquid (*W*-phase) is injected through an annular gap between two needles, whereas the inner insulating one (O_1-phase) is injected though the inner needle. Conductive liquids with high viscosity are required for the dispersion in the outer insulating *O*-phase. This technique has the capability to generate droplets with diameters in the sub micro-metre range depending on the conductivity of the liquid (Marín *et al*. 2007).

9.2.3.3 *Stability of double emulsions*

The main physicochemical mechanisms by which destabilisation of a double emulsion may occur are related to either the specific interactions between the mixture of emulsifiers used for its formation or the existence of an osmotic pressure difference between the internal droplets and the continuous phase.

For instance, a $W_1/O/W_2$ emulsion contains both water-in-oil and oil-in-water-type emulsions and therefore requires the presence of at least two emulsifiers, one that is predominantly hydrophobic, stabilising the primary W_1/O emulsion, and one that is predominantly hydrophilic, stabilising the secondary O/W_2 emulsion. The hydrophobic and hydrophilic emulsifiers are added to the oil and continuous aqueous phases, respectively. These two emulsifiers may interact at the external water/oil interface and interfere with each other's

stabilising performance. This leads to the overall destabilisation of the double emulsion according to one or a combination of all of the following scenarios: (i) coalescence of the oil droplets (primary emulsion) leading to larger droplets, with subsequent creaming; (ii) coalescence of the dispersed inner droplets of the primary emulsion, resulting in coarser double emulsions and (iii) coalescence of the inner droplets with the outer phase due to rupture of the thin film that forms between the external and the inner small droplets.

In addition, the stability of a double emulsion (e.g., $W_1/O/W_2$) can be seriously compromised by the existence of an osmotic pressure difference between the external continuous water phase (W_2) and the inner small water droplets (W_1).

The stability of a multiple emulsion is therefore greatly dependent upon such parameters as the choice of the emulsifier (or emulsifier mixture) and the control of the osmotic gradient.

Choice of emulsifier

Mixtures of monomeric surfactants. In multiple systems (e.g., *W/O/W*), and because the curvatures of the two types of monolayers are opposite, a mixture of monomeric surfactants is normally used, one of low *HLB* and another of high *HLB*, to stabilise the internal (*W/O*) and external (*O/W*) interfaces, respectively. However, the presence of two different surfactants is a major source of instability in multiple emulsions because they tend to migrate from one interface to another, thus considerably shortening the emulsion lifetime (Ficheux *et al*. 1998).

Polymeric emulsifiers. Owing to the aforementioned limitations of monomeric surfactants, there is a need for amphiphilic structures that would provide additional stabilisation to the thermodynamically metastable emulsions. The use of naturally occurring polymeric emulsifiers, such as gums and proteins, has long been known in practice. These macromolecules might adsorb at the interface in a slow process, but once adsorbed, they form an interfacial layer comprising loops and tails, well anchored into the oil and aqueous phases. Both naturally occurring and tailor-made polymeric emulsifiers are known to provide better interfacial coverage and furthermore to increase the stability of an emulsion by steric stabilisation or, if charged macromolecules are used, by electrostatic stabilisation.

Solid particles as emulsifiers. The ability of solid particles of colloidal size to kinetically stabilise emulsions, in the same way that surfactant molecules can, has been demonstrated since the beginning of the last century (Pickering 1907; also see Section 9.2.2). Unlike low-molecular-weight surfactants, solid particles in Pickering emulsions are irreversibly (the energy required to remove it is very high ~2,750 kT) anchored at the oil/water interface, providing a mechanical barrier against coalescence (Arditty *et al*. 2004).

The use of solid particles in the formation of double emulsions offers increased stability because, unlike monomeric surfactants, migration of particles from the inner to the outer interface, or vice versa, is expected to be minimal after emulsion formation (Binks 2002). Both *W/O/W* and *O/W/O* double emulsions stabilised solely by solid particles have been reported (Barthel *et al*. 2003). The *W/O* and *O/W* interfaces are stabilised by particles only differing in their hydrophobicity and the produced double emulsions are claimed to be stable against coalescence for over a year (Barthel *et al*. 2003). Careful selection of the particles, used for the formation of these systems, as well as careful manipulation of their surface properties (hydrophobic/hydrophilic properties) are crucial for enhanced stability.

What has yet to generate any significant interest in the scientific community is the use of a mixture of particles and monomeric surfactants acting as the emulsifier in multiple

(but also simple) emulsions. By using such an approach, and if the mixture of emulsifiers is carefully selected, what arises is the potential of precisely controlling the positioning of the particles on the interface (by effecting their contact angle θ), via carefully regulating the surfactant concentration in the mixture. The same particles could therefore be used to stabilise both *W/O* and *O/W* interfaces only by changing the surfactant concentration in the system and in effect the curvature of the interface between the oil and the water phases.

Control of osmotic pressure

A great source of instability in double emulsions (e.g., *W/O/W*) is the Laplace pressure associated with the small internal droplets, which results in water diffusing from the inner to the outer water phase. There are two mechanisms suggested in the literature for the transport of water and/or water-soluble addenda through the oil phase in a *W/O/W* emulsion, resulting in swelling or shrinking of the inner water droplets and finally inversion to an *O/W* emulsion. The two mechanisms put forward by Kita *et al*. (1977) are: (i) transport of molecules through a 'thin lamellae' of surfactants which partially form in the oil layer due to fluctuation of its thickness and (ii) transport of molecules across the oil layer by being incorporated in 'reverse micelles'. Colinart *et al*. (1984) have suggested one more possible way for the water transport, which occurs via hydrated surfactants. Wen and Papadopoulos (2001) observed single $W_1/O/W_2$ double emulsion globules through capillary video microscopy and suggested that the water transport process, when the W_1 droplets were at visual contact with the W_2 phase, is controlled by transportation through a 'thin lamellae' of surfactants, whereas for non-contacting W_1 and W_2 phases, the process is controlled by transportation via 'reverse micelles'.

9.2.4 Air-filled emulsions

This section addresses two new and potentially important developments in emulsion science, and although the bulk of this chapter covers the formation, processing and properties of emulsions, an important consideration is the incorporation of gas as an air-filled emulsion, which have the potential for immense benefit in microstructural design. The definition of an 'air-filled emulsion' does require careful thought and description. However, the simplest way to think about these structures is to consider air as an immiscible liquid, which as an emulsion has the physical size and surface chemistry and are intended to extend the functionality of the foams, now termed air-filled emulsions, into new areas.

In air-filled emulsions, the air/water interface is modified so that rupture and coarsening are reduced, and the emulsion may flow and disperse within a bulk medium in a similar fashion to a traditional oil/water system. Importantly, the new functionality that air-filled emulsions can offer for food systems is a route to a reduction in fat or calorie density (Norton *et al*. 2007).

The overriding limitations of creating this new class of emulsion are Ostwald ripening and creaming. Creaming of the emulsion depends on a number of parameters and is described by the following relation (Langevin 2000):

$$V = \frac{2R^2(\rho_g - \rho_l)g}{9\eta} \tag{9.2}$$

where V is the creaming (or in other situations, sedimentation) rate, R is the radius of the air cell, ρ_g is the density of the gas phase, ρ_l is the liquid-phase density, g is the acceleration due to gravity and η is the bulk fluid viscosity. Obviously, a number of terms in equation (9.2) are beyond manipulation, for example, g, ρ_g and ρ_l. However, sufficient terms still remain so that a plausible and now tested design may be considered. Explicitly, manipulation of the air cell size and the relative viscosity between the air and the continuous phase might be made to minimise the creaming of air-filled cells. Most obviously, setting of the bulk phase as seen in bread or cakes would eliminate this concern. Similarly, a reduction of the radius of the air cells would also reduce the creaming rate, as well as affecting the emulsion viscosity and importantly the mouthfeel of the emulsion.

For small molecular weight surfactants, the operational space for manipulating the radius is somewhat limited Tchuenbou-Magaia et al., 2009. The route chosen to stabilise the air cells was to use proteins to act as the interfacial stabilising material (Damodaran 2005).

Recently, a novel class of proteins, the hydrophobins (Wösten *et al*. 1993; Wessels 1997), have been identified as having unique properties at air/water and water/oil interfaces. These proteins are ubiquitous in the filamentous fungi and perform a variety of physiological roles. However, when exposed to interfaces, they will aggregate from the liquid phase to form a gelled protein layer with strong elastic properties (Wilde *et al*. 2004; Cox *et al*. 2007). These papers add a cautionary note to the use of proteins mixed with surfactants; this is discussed further below.

Tchuenbou-Magaia et al. (2009) recently showed that hydrophobin-rich extracts from *Trichoderma reesei* could be used to stabilise both water and oil droplets at the same time with up to 60% air within the emulsion (70% final phase volume). A mean air cell size of 5 μm was produced. These air droplets were remarkably stable over time and were sufficiently robust to withstand manipulation after the emulsion was made, for example, spooning from the container and shearing in a rheometer. However, challenges remain and although creaming (even after reasonably long storage) was not a significant factor, concerns over coalescence and Ostwald ripening will need to be addressed. During the experiments, an initial period of ripening and subsequent insignificant loss from the emulsions was observed. This was followed (after approximately 24 h) by an extended period of stability, up to months, where the coarsening process was arrested and the emulsion remained triphasic. The effect was explained by the physical properties of the hydrophobins, as once assembled, the protein aggregate and cross-link to form a continuous layer around the air or oil droplet.

In other work the order of addition of the hydrophobins was found to be important. If the protein extract was added to the oil and then the water slowly added (along with entrained air), then the characteristic 5 μm air droplets did not form, although if the usual routine of adding the protein to the water was followed, then air droplets could be formed. These findings are starting to reveal a potential manufacture process. Care needs to be taken that the manufacturing schedules account for quiescent holding of product to allow for maturation, the energy input for the formation of the emulsions must be controlled and the exposure of the stabilising protein to the differing interfaces must be controlled. Or, indeed, the use of mixed emulsifiers for the different phases might be explored although protein/surfactant mixtures have been identified as potentially weakening interfaces (Wilde *et al*. 2004).

Certainly, all of these concerns are easily addressed. A variety of foods undergo a holding time to allow for their microstructure to form, for example, ice cream; the new technologies, such as rotating membranes, are now offering low-energy emulsification processes, and if it is appropriate to use mixed emulsifiers, then split stream processing (two fractions of the

final product are prepared independently and mixed later in the manufacturing process) might overcome the potential problems of mixing at interfaces. If and when these considerations are addressed, then air-filled emulsions will offer the ultimate 'low-fat' ingredient.

9.2.5 Water-in-water emulsions

Aqueous biopolymer mixtures are commonly used in a variety of industrial formulations to impart a specific flow behaviour, texture, appearance and, where required, tactile and oral properties to products (Tolstoguzov 1996; Lundin *et al*. 2000; Norton & Frith 2001). It has been long appreciated that biopolymers when mixed in aqueous solutions often phase separate to give two immiscible phases that mainly contain water (Albertsson 1995), hence the term 'water-in-water' emulsions. Phase separation in these aqueous two-phase systems results in microstructures often compared to those found in conventional oil-in-water (*O/W*) or water-in-oil (*W/O*) emulsions. Recent work concluded that biopolymer emulsions are governed, to a great extent, by the same physical principles, including the rules for droplet break-up and droplet coalescence, as for conventional emulsions, and can be treated as such both in theory and in practice (Foster *et al*. 1996). When phase separation occurs in the absence of an applied flow field, the included phase normally forms spherical domains, the size of which usually ranges between 2 and 20 μm (Norton & Frith 2001).

Nonetheless, some differences between conventional emulsions and aqueous two-phase biopolymer systems do exist, and they usually arise from the fact that both the immiscible phases in the latter systems are mainly water. Exceptional features of water-in-water emulsions are the partial miscibility and very small interfacial tension between the two immiscible water phases. Interfacial tensions for liquid biopolymer–biopolymer interfaces were shown to be in the range of a few micro Newtons per metre (Forciniti *et al*. 1990; Ding *et al*. 2002, 2005). Additionally, in the case of water-in-water emulsions, there is no need for stabilising the emulsion droplets against creaming or sedimentation as the densities of the two (mainly water) phases are essentially the same, and therefore, both types of instability are rather slow processes (Aymard *et al*. 2000; Ding *et al*. 2002). In contrast to conventional water–oil emulsions, stabilisation against coalescence in water-in-water emulsions cannot be achieved by using surfactants because, due to the absence of a hydrophobic phase in the system, they show no preference in adsorbing at the water–water droplet interface and tend to remain in the bulk water phases in self-aggregated form (micelles). Therefore, in water-in-water emulsions, and because droplets coming in contact do coalesce (Ding *et al*. 2002) in the same way as oil or water droplets in classical *O/W* or *W/O* emulsions, gelation, of one or both of the phases, is used to kinetically trap the emulsion structure and induce long-term stability (Lorén *et al*. 2001). This kinetic stability can then be used to induce structural breakdown as the product is used, for example, eating (Norton *et al*. 2006b) or application to skin.

The quality of water-in-water emulsion-based products often depends on the morphology and structure of these mixtures, which in turn strongly depends on the interfacial tension between the two immiscible phases. It is consequently very important to understand the phase behaviour, rheological behaviour and other factors affecting phase morphology and structure of such systems (e.g., effects of processing).

9.2.5.1 *Phase separation*

General considerations and thermodynamic aspects

As already mentioned, limited miscibility in aqueous mixtures of biopolymers is a relatively common phenomenon and so is frequently encountered in industrial formulations,

either because the system naturally contains mixed polymers (e.g., food applications) or because mixtures of polymers are used to impart certain properties. Sometimes applications involving aqueous biopolymer mixtures take advantage of the phase separation phenomena (e.g., aqueous two-phase partitioning; Albertsson 1995), whereas at other times what is required is a single-phase system, in which case phase separation is an unwanted side-effect. However, regardless of whether phase separation is a desirable or undesirable event, it is essential to know when it takes place and which are the (system-specific) parameters that affect it.

But why is phase separation such a common phenomenon in aqueous mixed biopolymer systems? The answer to this question lies within the thermodynamics of these systems. Miscibility in a multicomponent system is governed by the free energy of mixing and therefore the entropy and enthalpy of mixing. In a mixture of small molecules (or low-molecular-weight components), the large entropy of mixing is the dominating factor resulting in complete miscibility. However, in a system containing relatively large components (such as a high-molecular-weight biopolymer aqueous mixture), the much lower entropy of mixing per unit weight no longer dominates and demixing can occur. Although this is entropically unfavourable, the enthalpy term is advantageous, as ultimately the molecules prefer to have neighbours of similar structure. This is, particularly true when, as the temperature is lowered the molecules start to interact and order. It is these interactions between the segments of the different polymers that dominate the free energy of mixing. If the interaction between the segments is repulsive (Zeman & Patterson 1972), phase separation occurs above certain polymer concentrations, and the two polymers will collect separately in two opposite phases—what is known as 'segregative type' of phase separation (Piculell & Lindman 1992). If, however, the interaction between the two polymers is attractive, as is the case between two oppositely charged polyelectrolytes, the two polymers will collect in the same phase and the result is a system with one phase enriched in both polymeric components existing in equilibrium with another phase poor in both—what is known as an associative type of phase separation (Piculell & Lindman 1992).

The presence of charged groups on one of the polymers has a profound influence on the phase behaviour (Perrau *et al*. 1989). If no added salt is present in the system, the counterions resulting from the dissociating polyelectrolyte are forced to follow their parent macromolecules into the phase in order to render the system electroneutral. The resulting entropic disadvantage of segregating the co-ions is so large that phase separation is often suppressed (Piculell *et al*. 1995). Addition of salt to the system reduces the impact of this increased entropic term, and phase separation increases as the salt concentration increases (Perrau *et al*. 1989; Piculell & Lindman 1992; Piculell *et al*. 1995).

Phase diagrams

In water-in-water emulsions, knowledge of the polymers' compositions where phase separation is taking place as well as the composition of polymers in the co-existing phases is essential. The composition of polymers needed to induce phase separation in an aqueous biopolymer mixture can be determined by the cloud point method (Aymard *et al*. 2000). Alternatively, the composition of the separated phases can be measured by direct chemical and/or physical analysis (Pudney *et al*. 2004).

The obtained polymer compositions of a water-in-water emulsion can then be used to produce the phase diagram of the system; for example, Figure 9.3 shows a phase diagram for a segregative aqueous mixture. The solid curve is called the phase curve or binodal,

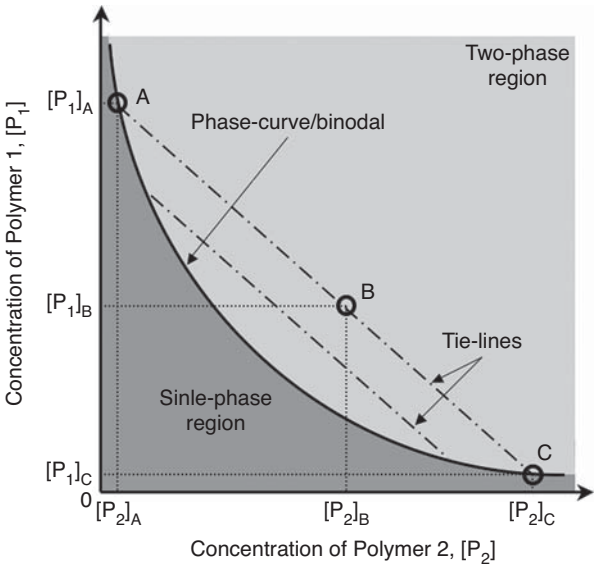

Fig. 9.3 Phase diagram of a segregating Polymer 1–Polymer 2 aqueous biopolymer mixture.

and it represents the borderline between systems that are completely miscible (single-phase region) and those that exhibit phase separation (two-phase region). For example, an aqueous mixture containing polymer concentrations depicted by point B will phase separate giving two co-existing phases of concentrations depicted by points A and C.

Before leaving the phase diagram, there is one further consideration worth covering—that of phase volume. As with any phase diagram, moving the composition of the system along a tie-line changes the relative volumes of the resulting co-existing phases, according to the relative lengths of the tie-line to the binodal, but the composition of the polymeric components in these individual phases remains the same. Therefore, at the middle point of the tie-line, a water-in-water emulsion with co-existing phases each occupying 50% of the system's volume will be produced. It is in this region that the microstructure of the system becomes 'confused' as both phases are in volumetric balance and both exhibit the same tendency towards becoming the continuous phase. As a result, bi-continuous systems are often observed. As with oil/water systems, on either side of the midpoint the phase with the greatest phase volume forms the continuous phase. This region of bicontinuity can occur over phase volume ranges as high as 10% (Foster *et al.* 1996). This is consistent with the lower interfacial tension in the mixed biopolymer system, which is discussed later.

Modelling of demixing in water-in-water emulsions

Modelling of the phase behaviour of polymers in aqueous solutions was first attempted by Flory (also known later as the Flory–Huggins theory) in his pioneering work (Flory 1953). Even though its accuracy was later proven poor, the general concept of the theory is still considered to grasp the gross thermodynamic features of these mixtures (Cowie 2001). Since then, the ability to predict the phase behaviour of water-in-water emulsions has received a great deal of attention both for fundamental reasons and also to facilitate the use of such systems in engineering processes (Tolstoguzov 1996).

Mechanisms of demixing

The mechanism(s) by which phase separation occurs needs to address both the initial stages of phase separation and the processes by which ripening of the phase structure occurs.

Phase separation is driven via two mechanisms, either nucleation and growth or a spinodal decomposition (Butler 2002). A reduction in temperature reduces the entropy of the mixture, leading to an increased incompatibility in the system. In biopolymer systems, molecular ordering often occurs resulting in increased molecular weight, giving a reduced entropy penalty for the formation of two phases and may also change the Flory–Huggins interaction (χ) parameters (Lorén *et al*. 2001). In fact, in gelatin/maltodextrin (Aymard *et al*. 2000; Lorén *et al*. 2001; Norton & Frith 2001; Williams *et al*. 2001), a system that has been widely studied, it has been suggested that depending on the composition of the mixture and the temperature history applied to it, either of the above mechanisms can drive the separation process. However, ordering-induced phase separation is the dominant mechanism (Williams *et al*. 2001).

As with synthetic polymers, it is possible to construct a spinodal on the phase diagram (Figure 9.4), which separates the metastable and unstable regions of the two-phase system. If we then start with a homogeneous mixture and change the conditions so as to move into the two-phase region, then the mechanism by which two phases are formed depends on the position relative to the spinodal. If, after the change in conditions, the mixture lies within the spinodal line on the phase diagram (i.e., in the unstable region, point A in Figure 9.4) then the mechanism of separation will be via spinodal decomposition. However, if we move to a position between the spinodal and the binodal (the metastable region, point B in Figure 9.4), then phase separation will follow a mechanism involving nucleation and growth.

Once the droplets have formed, they can start to ripen. Ultimately, in many systems, if this process is allowed to continue unchecked, then bulk phase separation is expected. Light scattering evidence (Butler & Heppenstall-Butler 2001) indicates that the increase in

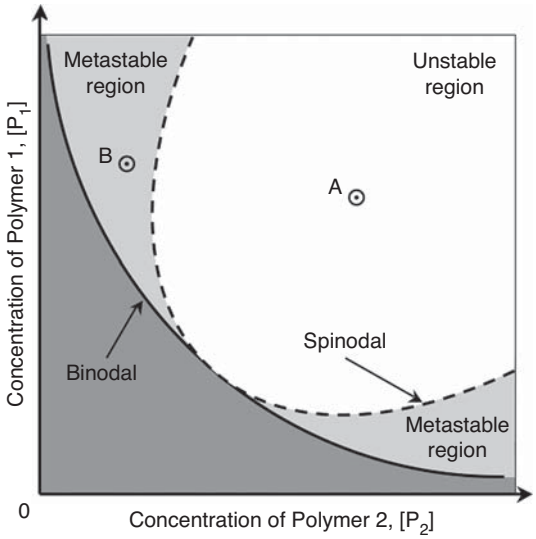

Fig. 9.4 Phase diagram and spinodal line separating the metastable and unstable regions of the two-phase system.

size goes as $t^{0.5}$ suggesting a diffusion-controlled mechanism, as might be expected. As the system continues to ripen, then microscopic evidence shows that a coalescence of droplets also occurs (Foster *et al*. 1996).

9.2.5.2 *Interfacial tension*

The morphology and structure of water-in-water emulsions strongly depend on the interfacial tension between their co-existing phases (Ding *et al*. 2002). Surprisingly enough, there are only a few studies in the open literature reporting on the interfacial tension in aqueous phase-separated polymer–polymer systems (Bamberger *et al*. 1984; Ding *et al*. 2002, 2005). This is primarily due to the fact that techniques used for the measurement of interfacial tensions in conventional *O/W* or *W/O* emulsions (such as spinning or pendant drop) either cannot be used or give poor accuracy. The reason for this is the low interfacial tensions in water-in-water emulsions and the very small density differences between the co-existing phases in these systems.

Recently, a number of groups (Guido & Villone 1999; Wolf *et al*. 2000; Ding *et al*. 2002) have adopted the approach of measuring droplet deformation in a controlled applied flow field to calculate interfacial tensions in a number of different systems. The technique involves observation of single drop deformation in an applied flow field and the relaxation of shape after cessation of flow, and thus avoids problems associated with small density differences. These data are then used in combination with knowledge of the flow behaviour of the two biopolymer phases and models for the drop deformation to give the interfacial tension (Guido & Villone 1999).

The calculated interfacial tensions have been found to be in the range of 0.5–500 μN/m (Ding *et al*. 2002), that is, two to three orders of magnitude lower than in typical oil/aqueous systems (Zaslavsky 1995). This is mainly because in water-in-water emulsions, the interface is formed by two high water content (~80–90%) phases. It is quite interesting to ponder the meaning of an interface in a biopolymer de-mixed system, more than 90% of which is solvent that can move unhindered between the phases. As yet, there is almost nothing known regarding the structure of the interface between these aqueous phases, mainly because the techniques for studying this require more contrast than is available in biopolymer mixtures.

What has been reported (Bamberger *et al*. 1984; Forciniti *et al*. 1990) though is that interfacial tension in aqueous biopolymer mixtures depends on the molecular weight and total concentration of both polymers in the system. Furthermore, it has been found that interfacial tension experimental data can be correlated either with the tie-line length (TLL) or with the difference between the concentrations of the polymers in the co-existing phases (Bamberger *et al*. 1984; Forciniti *et al*. 1990; Ding *et al*. 2002). The interfacial tension in these systems has also been found to somewhat depend on the concentration of additives such as salts (Bamberger *et al*. 1984).

9.2.5.3 *Rheological behaviour*

In order to facilitate the use of biopolymer mixtures in industrial applications, knowledge of their flow properties and morphology during flow processing is of great importance (Lundin *et al*. 2000, Norton & Frith 2001). For this reason, rheological investigation of aqueous biopolymer mixtures (or aqueous biopolymer 'blends') has been extensively performed (Stokes *et al*. 2001; Wolf *et al*. 2001; Wolf & Frith 2003; Ding *et al*. 2005). The apparent viscosity of these aqueous two-phase systems depends on the viscosity of the continuous phase, the viscosity ratio (λ), the chemical compositions of the individual phases

(Wolf & Frith 2003) and the phase volume of the dispersed phase, and generally increases with increasing phase volumes of the dispersed phase (Wolf & Frith 2003). Hence, aqueous biopolymer mixtures exhibit a shear viscosity/composition dependence pattern similar to that of conventional *O/W* and *W/O* emulsions (Pal 2001).

The blend viscosity also depends on the phase sense. As a result, at the phase inversion composition, the viscosity of water-in-water emulsions should 'change'. For this reason, there have been reports in the literature where the phase inversion composition (under shear) is deduced from rheo-optical investigations (Wolf & Frith 2003) of the blends or calculated by simple empirical models (Utracki 1991).

Finally, the shear viscosity of aqueous biopolymer mixtures has been found to depend on the blend morphology (microstructure) under shear. The relationship between microstructure and rheology in two-phase polymer mixtures has been the subject of a number of studies (Utracki 1991; Ziegler & Wolf 1999; Jeon & Hobbie 2001; Wolf & Frith 2003). A plethora of different structures have been reported for aqueous biopolymer blends under shear, ranging from simple droplet-like morphologies to systems where string-like phases develop (Jeon & Hobbie 2001; Wolf & Frith 2003).

9.2.5.4 *Kinetic trapping*

The phase morphology and structure in many biopolymer mixtures can be kinetically trapped by the gelation of one or both of the phases. Using droplet size measurements obtained through turbidity measurements, it has been demonstrated that gelation of one or both phases will arrest the process of ripening of the phase structure (Williams *et al*. 2001). By variation of the quench depth, it then becomes possible to produce biopolymer gel 'composites' with a range of trapped microstructures and properties (Norton & Frith 2001).

When biopolymer mixtures are subjected to industrial processes, the additional factor of a flow history is superimposed on the phase separation/gelation history. This can of course have quite dramatic effects on the final microstructures and textures produced. A considerable literature already exists on this subject for biopolymers (de Carvalho & Djabourov 1997; Wolf *et al*. 2000). In mixed systems, the simplest effect of shear while separation, molecular ordering and gelation are occurring is to reduce the particle size of the included phase and to stabilise the microstructure while the kinetic trapping occurs. This can be used to make a phase-separated biopolymer system that has droplet sizes in the range of 1–10 μm (Foster *et al*. 1996).

Application of shear to biopolymer mixtures undergoing gelation can also influence the phase sense of the system and in some cases induce phase inversion. For instance, if gelation of both phases in a mixed system (7% gelatin/9.5% maltodextrin) is induced quiescently, we consider the mixture will normally form a gelatin continuous composite (Foster *et al*. 1996). In the liquid state, the application of shear does not cause any phase inversion. However, if shear is applied as the mixture is cooled through the gelation temperature, then a phase inversion to a maltodextrin continuous system occurs. This is believed to occur because, as the mixture is cooled, the gelatin orders first and the viscosity of its phase increases and becomes greater than that of the maltodextrin-rich phase. As with oil/water emulsions and polymer blends, the application of shear to such a mixture leads to the phase with the highest viscosity becoming the included phase (Han *et al*. 1998). By confirming the idea with other concentrations and different biopolymer mixtures, it appears that this general rule for *O/W* emulsions and blends seems to hold true in mixed biopolymers as well (Foster *et al*. 1996).

Under certain conditions of applied shear or elongational flow, it is possible to use gelation to trap the dispersed phase in an anisotropic morphology (Antonov *et al*. 1980; Wolf & Frith 2003). Once these asymmetric particles have been formed, they will exhibit different rheological properties to those possessing a quiescently cooled, spherical phase structure; see Section 9.2.5.3.

9.3 Future challenges

9.3.1 Better mechanistic understanding of the emulsification process(es)

At the moment, there is no detailed mechanistic understanding of emulsion formation and behaviour in the homogenisation or emulsification processes. This is not to say that the individual steps have not been identified, that is, break up via tip streaming and stretching in elongational flow or that coalescence is a consequence of droplets coming together with film drainage. Nonetheless, the challenge that remains is to work out the relative importance of the different steps in the mechanism and how these change according to the process used, that is, impinging jets or high-pressure homogenisation with a valve. Some initial work has been reported by Schubert and Engel (2004) who developed a technique to study the relative rates of break-up and back coalescence in defined flow fields, for example, turbulence. This is a challenge still for oil and water emulsions, but when we consider other more complex emulsions, the challenge is even greater. For air-filled emulsions, the steps in the mechanism are not clear; for instance, how can an air cell break up in flow when the relative viscosities of the two phases are so different? With a Pickering-stabilised emulsion, partial coverage of the interface increases the rate of coalescence in turbulent flow; however, when the surface is fully covered with particles, coalescence is arrested. Thus future challenges are to understand why this happens, what the detailed mechanisms are including how the particles get to and enter the interface. For instance with crystallising particles, do they get swept to the interface and then are wetted or do they crystallise at the interface, and does the droplet size determine the particle size or does the particle size determine the droplet size?

9.3.2 Improved emulsification processes

As mentioned throughout this chapter, the emulsification processes have been designed from a standpoint of the more shear is introduced into a mixture of oil and water the smaller the final droplet size will become. Thus the approach has been to increase the energy input into the system by increasing the pressure of the process—homogenisation. This hypothesis is clearly limited as the amount of energy required to increase the surface area of the emulsion is less than 1% of the total energy input with the rest of the energy converted to heat. This fundamental assumption is now being challenged. As the mechanistic understanding is growing, processes will be developed to control and influence the rate-limiting step. Nanoemulsions using food grade materials and limited amounts of emulsifiers that are kinetically trapped for delivery of bioactives will prove a future challenge. Obviously, using classical homogenisation/emulsification processes is not the way forward. However, for bulk production of consumer goods, the current microchannel techniques are not going to be scalable for some considerable time. These techniques have shown that production of droplets in the nano-scale is possible. A scale-up of these processes will form a future challenge.

Smaller, more intense processes will be required for distributed manufacture. As people want their products personalised for both personal care and food, the market will become more segmented. This will be for diet and health needs and for their personal care requirements. As energy and environmental issues grow in importance, more energy-efficient processes will be required and will challenge the emulsion engineers. Gentler processes are necessary and a significant challenge will be to deliver delicate molecules to specific points in the human GI tract, and many of the microstructures needed are delicate and are damaged by the shear in the process.

Double emulsions offer great opportunities; however, the process for their production is a challenge. The first (inner) emulsion needs to have small droplet, at most a few microns, which need to be stable through the second emulsification process. High shear emulsification processes are problematic as they cause damage to the inner phase and leakage. There are a few reports about ways around this problem but there is work still to be done. The double emulsions need to be stabilised over long periods of time with zero mixing of the two water or oil phases. If this is not achieved, then any segregated molecules will not survive.

9.3.3 Designed emulsions for improved nutrition and health

Emulsions can be used to impact on nutrition and health of the public (Norton *et al*. 2006a, 2007). This can be achieved via a reduced calorific food in which emulsions are designed to give all the sensory properties of high-fat products with lower calorific content and the addition and delivery of micronutrients in a way that is not detectable to the consumer. These have been discussed in detail in the double emulsion and air-filled emulsion sections of this chapter. A challenge will be to design these more complex emulsions in such a way as they are stable on storage but behave in the mouth to 'fool' the senses. This will require emulsions to be designed to have the required rate of breakdown and flavour release while coating bio-surfaces and imparting the required tribological response.

9.3.4 Reduced use of surfactants for environmental reasons

Emulsions with lower surfactant levels and/or natural surfactants will be required in order to reduce the 'chemicals' going into the environmental and thus reduce the environmental impact. The replacement of synthetic surfactants with natural unmodified materials will be a challenge in itself, as will the use of Pickering stabilisation, which will play a key role in this area as Pickering emulsions allow reduced usage of surfactants. One of the challenges will be to find particles that are environmentally acceptable. It is most likely that these natural particles will be mixed with emulsifiers. The study of particles and surfactants in combination has been of academic interest for more than 100 years. However, the use of such systems is limited as a consequence of the difficulty of processing. One of the major problems is that as the emulsion interface is stretched in the process, the particles cannot move faster enough to cover the interface and give stability. This results in 'naked' interface which causes coalescence in the process.

References

Albertsson, P.-Å. (1995). Aqueous polymer phase systems: properties and applications in bioseparation. In: *Biopolymer Mixtures* (eds S.E. Harding, S.E. Hill & J.R. Mitchell). Nottingham University Press, Nottingham, UK, pp. 1–12.

Antonov, Y.A., Grinberg, V.Y., Zhuravskaya, N.A. & Tolstoguzov, V.B. (1980). Liquid two-phase water-protein-polysaccharide systems and their processing into textured protein products. *Journal of Texture Studies*, **11**, 199–215.

Araújo Macian, K., Villa Nova Silva, L., Pedroso de Oliveira, A.P. & Gesztesi, J.-L. (2007). A multiple emulsion excipient for cosmetic actives. *EP1786387*.

Arditty, S., Schmitt, V., Giermanska-Kahn, J. & Leal-Calderon, F. (2004). Materials based on solid-stabilized emulsions. *Journal of Colloid and Interface Science*, **275**, 659–664.

Aveyard, R., Binks, B.P. & Clint, J.H. (2003). Emulsions stabilised solely by colloidal particles. *Advances in Colloidal and Interface Science*, **100–102**, 503–546.

Aymard, P., Williams, M.A.K., Clark, A.H. & Norton, I.T. (2000). A turbidimetric study of phase separating biopolymer mixtures during thermal ramping. *Langmuir*, **16**, 7383–7391.

Bamberger, S., Seaman, G.V.F., Sharp, K.A. & Brooks, D.E. (1984). The effects of salts on the interfacial tension of aqueous dextran-poly(ethylene glycol) phase systems. *Journal of Colloid and Interface Science*, **99**, 194–200.

Barthel, H., Binks B.P., Dyab, A. & Fletcher, P. (2003). Multiple emulsions. *US2003175317*.

Benichou, A., Aserin, A. & Garti, N. (2002). Double emulsions stabilized by new molecular recognition hybrids of natural polymers. *Polymers for Advanced Technologies*, **13**, 1019–1031.

Binks, B.P. (2002). Particles as surfactants – similarities and differences. *Current Opinion in Colloid and Interface Science*, **7**, 21–41.

Binks, B.P. & Lumsdon, S.O. (2001). Pickering emulsions stabilized by monodisperse latex particles: effects of particle size. *Langmuir*, **17**, 4540–4547.

Brooker, B.E. (1986). The development of structure in whipped cream. *Food Microstructure*, **5**, 277–285.

Brooker, B.E. (1993). The stabilisation of air in foods containing air – a review. *Food structure*, **12**, 115–122.

Butler, M.F. (2002). Mechanism and kinetics of phase separation in a gelatin/maltodextrin mixture studied by small-angle light scattering. *Biomacromolecules*, **3**, 676–683.

Butler, M.F. & Heppenstall-Butler, M. (2001). Phase separation in gelatin/maltodextrin and gelatin/maltodextrin/gum arabic mixtures studied using small-angle light scattering, turbidity, and microscopy. *Biomacromolecules*, **2**, 812–823.

Campbell, I., Norton, I.T. & Morley, W. (1996). Factors controlling the phase inversion of oil-in-water emulsions. *Netherlands Milk and Dairy Journal*, **50**, 167–182.

Charcosset, C., Limayem, I. & Fessi, H. (2004). The membrane emulsification process – a review. *Journal of Chemical Technology & Biotechnology*, **79**, 209–218.

Clark, A.H., Kavanagh, G.M. & Ross-Murphy, S.B. (2001). Globular protein gelation – theory and experiment. *Food Hydrocolloids*, **15**, 383–400.

Cole, M.L. & Whateley, T.L. (1997). Release rate profiles of theophylline and insulin from stable multiple w/o/w emulsions. *Journal of Controlled Release*, **49**, 51–58.

Colinart, P., Delepine, S., Trouve, G. & Renon, H. (1984). Water transfer in emulsified liquid membrane processes. *Journal of Membrane Science*, **20**, 167–187.

Cowie, J.M.G. (2001). *Polymers: Chemistry & Physics of Modern Materials*, 2nd edn. Nelson Thornes, Cheltenham, UK.

Cox, A.R., Cagnol, F., Russell, A.B. & Izzard, M.J. (2007). Surface properties of class II hydrophobins from *Trichoderma reesei* and influence on bubble stability. *Langmuir*, **23**, 7995–8002.

Damodaran, S. (2005). Protein stabilization of emulsions and foams. *Journal of Food Science*, **70**, 54–66.

de Carvalho, W. & Djabourov, M. (1997). Physical gelation under shear for gelatin gels. *Rheologica Acta*, **36**, 591–609.

Dickinson, E. (1989). Food colloids – an overview. *Colloids and Surfaces*, **42**, 191–204.

Dickinson, E. & McClements, D.J. (1996). *Advances in Food Colloids*. Blackie Academic & Professional, Glasgow, UK.

Dillon, P.M. (1996). Be equipped to cut the fat. *Food Formulating*, available online: http://www.microfluidicscorp.com

Ding, P., Wolf, B., Frith, W.J., Clark, A.H., Norton, I.T. & Pacek, A.W. (2002). Interfacial tension in phase-separated gelatin/dextran aqueous mixtures. *Journal of Colloid and Interface Science*, **253**, 367–376.

Ding, P., Pacek, A.W., Frith, W.J., Norton, I.T. & Wolf, B. (2005). The effect of temperature and composition on the interfacial tension and rheology of separated phases in gelatin/pullulan mixtures. *Food Hydrocolloids*, **19**, 567–574.

Dokić, P. & Sherman, P. (1980). Study on thermal induced phase inversion of concentrated *O/W* emulsions stabilized by various tween emulsifiers. *Colloid and Polymer Science*, **258**, 1159–1163.

Engel, R.H., Riggi, S.J. & Fahrenbach, M.J. (1968). Insulin-intestinal absorption as water-in-oil-in-water emulsions. *Nature*, **219**, 856–857.

Ficheux, M-F., Bonakdar, L., Leal-Calderon, F. & Bibette, J. (1998). Some stability criteria for double emulsions. *Langmuir*, **14**, 2702–2706.

Flory, P.J. (1953). *Principles of Polymer Chemistry*. Cornell University Press, Ithaca, NY.

Foegeding, E.A., Bowland, E.L. & Hardin, C.C. (1995). Factors that determine the fracture properties and microstructure of globular protein gels. *Food Hydrocolloids*, **9**, 237–249.

Forciniti, D., Hall, C.K. & Kula, M.R. (1990). Interfacial-tension of polyethyleneglycol-dextran-water systems-influence of temperature and polymer molecular-weight. *Journal of Biotechnology*, **16**, 279–296.

Foster, T.J., Brown, C.R.T. & Norton, I.T. (1996). Phase inversion of water-in-water emulsions. In: *Gums and Stabilisers for the Food Industry 8* (eds G.O. Phillips, P.A. Williams & D.J. Wedlock). Oxford University Press, Oxford, pp. 297–306.

Gaonkar, A.G. (1994). Stable multiple emulsions comprising interfacial gelatinous layer, flavour-encapsulating multiple emulsions and low-no fat products comprising the same. US Patent No. 5332595, July 26.

Garti, N. (1997). Progress in stabilization and transport phenomena of double emulsions in food applications. *Lebensmittel-Wissenschaft und-Technologie*, **30**, 222–235.

Garti, N. & Aserin, A. (1996). Double emulsions stabilized by macromolecular surfactants. *Advances in Colloid and Interface Science*, **65**, 37–69.

Guido, S. & Villone, M. (1999). Measurement of interfacial tension by drop retraction analysis. *Journal of Colloid and Interface Science*, **209**, 247–250.

Han, C.D., Sun, J.S., Chuang, H.K. & Lee, J.K. (1998). Prediction of equilibrium polymer blend morphology in dispersed two-phase flow and comparison with experiment. *Polymer Engineering and Science*, **38**, 1154–1166.

Henry, J.V., Frith, W.J., Fryer, P.J. & Norton, I.T. (2008). Kinetically trapped food grade nano-emulsions. *Foods & Food Ingredients Journal of Japan*, **213**(3), 192–196.

Herb, C.A., Chen L.B., Chung, J.B. *et al*. (1999). Water-in-oil-in-water compositions. *US5942216*.

Ho, W.S., Hatton, T.A., Lightfoot, E.N. & Li, N.N. (1982). Batch extraction with liquid surfactant membranes: a diffusion controlled model. *AIChE Journal*, **28**, 662–670.

Hoar, T.P. & Schulman, J.H. (1943). Transparent water in oil dispersions: the oleopathic hydromicelle. *Nature*, **152**, 102–103.

Hofland A. (1997). Making paint from alkyd emulsions. In: *Technology for Waterborne Coatings*, *ACS Symposium Series 663* (ed. J.E. Glass). American Chemical Society, Washington, pp. 183–195.

Hunter, T.N., Pugh, R.J., Franks, G.V. & Jameson, G.J. (2008). The role of particles in stabilising foams and emulsions. *Advances in Colloid and Interface Science*, **137**(2), 57–81.

Jeon, H.S. & Hobbie, E.K. (2001). Shear viscosity of phase-separating polymer blends with viscous asymmetry. *Physical Review E*, **63**, 061403 (1–5).

Kim, C.-K., Kim, S-C., Shin, H.-J. *et al*. (1995). Preparation and characterization of cytarabine-loaded w/o/w multiple emulsions. *International Journal of Pharmaceutics*, **124**, 61–67.

Kita, Y. Matsumoto, S. & Yonezawa, D. (1977). Viscometric method for estimating the stability of w/o/w type multiple phase emulsions. *Journal of Colloid and Interface Science*, **62**, 87–94.

Langevin, D. (2000). Influence of interfacial rheology on foam and emulsion properties. *Advances in Colloid and Interface Science*, **88**, 209–222.

Lian, G.P., Malone, M.E., Homan, J.E. & Norton, I.T. (2004). A mathematical model of volatile release in mouth from the dispersion of gelled emulsion particles. *Journal of Controlled Release*, **98**, 139–155.

Livingston, R.M. & Norton, I.T. (1997). Edible spread with aqueous phase with non-gelling thickener system and low protein content. *US5656322*.

Lorén, N., Hermansson, A.-M., Williams, M.A.K. *et al*. (2001). Phase separation induced by conformational ordering of gelatin in gelatin/maltodextrin mixtures. *Macromolecules*, **34**, 289–297.

Lundin, L., Norton, I.T., Foster, T.J., Williams, M.A.C., Harmansson, A.-M. & Bergström, E. (2000). Phase separation in mixed biopolymer systems. In: *Gums and Stabilisers for the Food Industry 10* (eds P.A. Williams & G.O. Phillips). Royal Society of Chemistry, Cambridge, UK, pp. 167–180.

Malone, M.E., Appelqvist, I.A.M. & Norton, I.T. (2003). Oral behaviour of food hydrocolloids and emulsions. Part 1. Lubrication and deposition considerations. *Food Hydrocolloids*, **17**, 763–773.

Marín, Á.G., Loscertales, I.G., Márquez, M. & Barrero, A. (2007). Simple and double emulsions via coaxial jet electrosprays. *Physical Review Letters*, **98**, 014502 (1–4).

Mason, T.G., Wilking, J.N., Meleson, K., Chang, C.B. & Graves, S.M. (2006). Nanoemulsions: formation, structure, and physical properties. *Journal of Physics: Condensed Matter*, **18**, 635–666.

Matsumoto, S. (1983). Development of W/O/W-type dispersion during phase inversion of concentrated W/O emulsions. *Journal of Colloid and Interface Science*, **94**, 362–368.

Matsumoto, S., Kita, Y. & Yonezawa, D. (1976). An attempt at preparing water-in-oil-in-water multiple-phase emulsions. *Journal of Colloid and Interface Science*, **57**, 353–361.

McClements, D.J. (1999). *Food Emulsions – Principles*, *Practice and Techniques*. CRC Press, Boca Raton, FL.

McClements, D.J. & Decker, E.A. (2000). Lipid oxidation in oil-in-water emulsions: impact of molecular environment on chemical reactions in heterogeneous food systems. *Journal of Food Sci*ence, **65**, 1270–1282.

Mezzenga, R. (2007). Equilibrium and non-equilibrium structures in complex food systems. *Food Hydrocolloids*, **21**, 674–682.

Murray, B.S. & Ettalaie, R. (2004). Foam stability: proteins and nanoparticles. *Current Opinion in Colloid and Interface Science*, **9**, 314–320.

Muschiolik, G. (2007). Multiple emulsions for food use. *Current Opinion in Colloid and Interface Science*, **12**, 213–220.

Muschiolik, G., Scherze, I., Preissler, P., Weiss, J., Knoth, A. & Fechner, A. (2006). Multiple emulsions – preparation and stability, *Proceedings of the 13th World Congress of Food Science and Technology*, *IUFoST World Congress*, pp. 123–137 (doi: 10.1051/IUFoST:20060043).

Norton, I.T. & Frith, W.J. (2001). Microstructure design in mixed biopolymer composites. *Food Hydrocolloids*, **15**, 543–553.

Norton, I.T., Fryer, P.J. & Moore, S. (2006a). Product/process integration in food manufacture: engineering sustained health. *AIChE Journal*, **52**, 1632–1640.

Norton, I.T., Frith, W.J. & Ablett, S. (2006b). Fluid gels, mixed fluid gels and satiety. *Food Hydrocolloids*, **20**, 229–239.

Norton, I.T., Moore, S. & Fryer, P.J. (2007). Understanding food structuring and breakdown: engineering approaches to obesity. *Obesity Reviews*, **8**, 83–88.

Okushima, S., Nisisako, T., Torii, T. & Higuchi, T. (2004). Controlled production of monodisperse double emulsions by two-step droplet breakup in microfluidic devices. *Langmuir*, **20**, 9905–9908.

Olson, D.W, White, C.H. & Richter, R.L. (2004). Effect of pressure and fat content on particle sizes in microfluidized milk. *Journal of Dairy Science*, **87**, 3217–3223.

Pal, R. (2006). Rheology of high internal phase ratio emulsions. *Food Hydrocolloids*, **20**(7), 997–1005.

Perrau, M.B., Iliopoulos, I. & Audebert, R. (1989). Phase separation of polyelectrolyte/nonionic polymer systems in aqueous solution: effects of salt and charge density. *Polymer*, **30**, 2112–2117.

Pichot, R., Spyropoulos, F. & Norton, I.T. (2008). Mixed-emulsifier stabilised emulsion: investigation of the effect of monoolein and hydrophilic silica particle mixtures on the stability to coalescence. *Journal of Colloid and Interface Science*, **329**(2), 284–291.

Pickering, P.J. & Southern, C.R. (1997). Clean-up to chirality – liquid membranes as a facilitating technology? *Journal of Chemical Technology and Biotechnology*, **68**, 417–424.

Pickering, S.U. (1907). Emulsions. *Journal of the Chemical Society*, **91**, 2001–2021.

Piculell, L. & Lindman, B. (1992). Association and segregation in aqueous polymer/polymer, polymer/surfactant, and surfactant/surfactant mixtures: similarities and differences. *Advances in Colloid and Interface Science*, **41**, 149–178.

Piculell, L., Bergfeldt, K. & Nilsson, S. (1995). Factors determining phase behaviour of multi component polymer systems. In: *Biopolymer Mixtures* (eds S.E. Harding, S.E. Hill & J.R. Mitchell). Nottingham University Press, Nottingham, UK, pp. 13–35.

Pudney, P.D.A., Hancewicz, T.M., Cunningham, D.G. & Brown, M.C. (2004). Quantifying the microstructures of soft solid materials by confocal Raman spectroscopy. *Vibrational spectroscopy*, **34**, 123–135.

Rousseau, D. (2000). Fat crystals and emulsion stability – a review. *Food Research International*, **33**, 3–14.

Rousseau, D. & Hodge, S.M. (2005). Stabilization of water-in-oil emulsions with continuous phase crystals. *Colloids and Surfaces A – Physicochemical and Engineering Aspects*, **260**, 229–237.

Sacanna, S., Kegel, W.K. & Philipse, A.P. (2007). Thermodynamically stable Pickering emulsions. *Physical Review Letters*, **98**, 158301 (1–4).

Schadler, V. & Windhab, E.J. (2006). Continuous membrane emulsification by using a membrane system with controlled pore distance. *Desalination*, **189**, 130–135.

Schubert, H. & Engel, R. (2004). Product and formulation engineering of emulsions. *Chemical Engineering Research & Design*, **82**(A9), 1137–1143.

Seifriz, W. (1925). Studies in Emulsions. III–V. *Journal of Physical Chemistry*, **29**, 738–749.

Stokes, J.R., Wolf, B. & Frith, W.J. (2001). Phase-separated biopolymer mixture rheology: prediction using a viscoelastic emulsion model. *Journal of Rheology*, **45**, 1173–1191.

Sugiura, S., Nakajima, M., Yamamoto, K. *et al*. (2004). Preparation characteristics of water-in-oil-in-water multiple emulsions using microchannel emulsification. *Journal of Colloid and Interface Science*, **270**, 221–228.

Suzuki, K., Uehara, K. & Omura, H. (1991). Oil-in-water-in-oil doubly emulsified fat or oil composition. *EP0425958 A2*.

Taki, J., Isomura, T., Kanda, K., Kawahara, A., Maruyama, K. & Kusumoto, S. (2007). $W_1/O/W_2$-type double emulsion dressing and method for production thereof. *WO2007043678*.

Tchuenbou-Magaia, F.L., Norton, I.T. & Cox, P.W. (2009). Hydrophobins stabilised air-filled emulsions for the food industry. Food Hydrocolloids, doi:10.1016/j.foodhyd.2009.03.005

Tokimitsu, I., Kobayashi, K., Uzu, A. & Arisawa, M. (1990). Cosmetic composition of double emulsion type. *EP0391124*.

Tolstoguzov, V.B. (1996). Application of phase separated biopolymer systems. In: *Gums and Stabilisers for the Food Industry 8* (eds G.O. Phillips, P.A. Williams & D.J. Wedlock). Oxford University Press, Oxford, UK, pp. 151–160.

Utada, A.S., Lorenceau, E., Link, D.R., Kaplan, P.D., Stone H.A. & Weitz, D.A. (2005). Monodisperse double emulsions generated from a microcapillary device. *Science*, **308**, 537–541.

Utracki, L.A. (1991). On the viscosity-concentration dependence of immiscible polymer blends. *Journal of Rheology*, **35**, 1615–1637.

van der Graaf, S., Schroen, C.G.P.H. & Boom, R.M. (2005). Preparation of double emulsions by membrane emulsification – a review. *Journal of Membrane Science*, **251**, 7–15.

Vladisavljević, G.T. & Williams, R.A. (2006). Manufacture of large uniform droplets using rotating membrane emulsification. *Journal of Colloid and Interface Science*, **299**, 396–402.

Walstra, P. (1993). Principles of emulsion formation. *Chemical Engineering Science*, **48**, 333–349.

Walstra, P. (1996). Emulsion stability. In: *Encyclopedia of Emulsion Technology*, Vol. 4 (ed. P. Becher). Marcel Dekker Inc., New York, pp. 1–62.

Wen, L.-X. & Papadopoulos, K.D. (2001). Effects of osmotic pressure on water transport in $W_1/O/W_2$ emulsions. *Journal of Colloid and Interface Science*, **235**, 398–404.

Wessels, J.G.H. (1997). Hydrophobins: proteins that function at an interface. *Trends in Plant Science*, **1**, 9–15.

Whitesides, G.M. & Stroock, A.D. (2001). Flexible methods for microfluidics. *Physics Today*, **54**, 42–48.

Wilde, P., Mackie, A., Husband, F., Gunning, P. & Morris, V. (2004). Proteins and emulsifiers at liquid interfaces. *Advances in Colloid and Interface Science*, **108–109**, 63–71.

Williams, M.A.K., Fabri, D., Hubbard, C. *et al*. (2001). Kinetics of droplet growth in gelatin/maltodextrin mixtures following thermal quenching. *Langmuir*, **17**, 3412–3418.

Wolf, B. & Frith, W.J. (2003). String phase formation in biopolymer aqueous solution blends. *Journal of Rheology*, **47**, 1151–1170.

Wolf, B., Scirocco, R., Frith, W.J. & Norton, I.T. (2000). Shear-induced anisotropic microstructure in phase-separated biopolymer mixtures. *Food Hydrocolloids*, **14**, 217–225.

Wolf, B., Frith, W.J., Singleton, S., Tassieri, M. & Norton, I.T. (2001). Shear behaviour of biopolymer suspensions with spheroidal and cylindrical particles. *Rheologica Acta*, **40**, 238–247.

Wösten, H.A.B., de Vries, O.M.H. & Wessels, J.G.H. (1993). Interfacial self-assembly of a fungal hydrophobin into a hydrophobic rodlet layer. *Plant cell*, **5**, 1567–1574.

Zaslavsky, B.Y. (1995). *Aqueous Two-Phase Partitioning*, *Physical Chemistry and Bioanalytical applications*. Marcel Dekker, New York.

Zeman, L. & Patterson, D. (1972). Effect of the solvent on polymer incompatibility in solution. *Polymer Incompatibility*, **5**, 513–516.

Ziegler, V. & Wolf, B.A. (1999). Viscosity and morphology of the two-phase system PDMS/P(DMS-ran-MPS). *Journal of Rheology*, **43**, 1033–1045.

10 Solid–liquid mixing

Mostafa Barigou

10.1 Introduction

Mechanically agitated vessels are used in the formulation and manufacture of a wide variety of food products. A typical configuration of a stirred vessel is shown in Figure 10.1. Solid–liquid systems are the most common of those processed in these vessels. The reasons for processing solid–liquid systems in mixing equipment of this type include: (i) promotion of heat/mass transfer or chemical reaction between the solid and liquid phases; (ii) creation and maintenance of a relatively uniform dispersion of settled or floating solid particles in a fluid; (iii) promotion of particle dissolution or crystal growth; (iv) use of gentle, low shear action of the mixer to suspend the particles and cause inter-particle collisions to promote flocculation in a low-intensity turbulence field; and (v) establishing a uniform particle distribution in an effluent stream when a vessel is emptied. Typical solid–liquid applications in the food industry include suspension withdrawal from a stirred vessel used as a premixer or holding vessel, crystallisation, fermentation, dissolution, development of structure, rehydration of dried solids and mixing of fine powders in liquids. These systems represent a very high proportion (~80%) of mixing applications in the entire process industries. The design of mechanically agitated vessels for solid–liquid mixing, however, still remains as much an art as a science, and for many applications, it cannot be carried out from first principles.

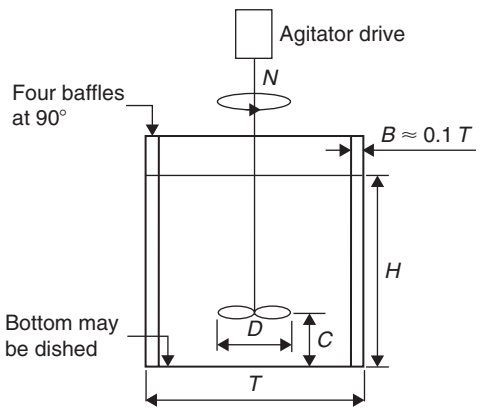

Fig. 10.1 Typical configuration of a stirred vessel used for solid–liquid mixing.

Suspensions can generally be categorised into two broad classes on the basis of their particle size: (i) fine particle suspensions in which particles are fairly uniformly distributed in the liquid with little separation occurring; and (ii) coarse suspensions in which the solid phase, if heavier than the liquid, tends to separate out. Though such a classification is evidently not very clear-cut, as it is influenced by a number of other factors including solids loading and the nature of the flow field, it serves as a useful practical basis for classifying the general behaviour of solid–liquid suspensions. Food particles in particular are usually large (typically 1–25 mm) and the suspending medium may be a viscous and/or non-Newtonian fluid and may itself consist of a dispersion of small particles (e.g., colloidal to 10s of microns size).

It is worth noting that virtually all the knowledge in this field has stemmed from chemical engineering research. Therefore, food-related materials have not been used in the majority of the published works. In particular, non-Newtonian materials have not received sufficient attention and large particles of the order of a centimetre or more which are more relevant to food applications have not been researched in any significant way. However, most of the mixing rules that have been established can usually be applied as a first approximation to the design of food mixing operations, although some experimentation and pilot study using the actual systems may often be necessary.

The solid particles discussed here will be assumed to be stable in suspension and do not influence the rheology of the suspending fluid. Notwithstanding any particle attrition caused by inter-particle and particle–impeller interactions or even fluid shear, the particles are considered to be present as separate entities and not as flocs or weak agglomerates whose stability is affected by the mechanical mixing process. The discussion in this chapter will focus mostly on the suspension of the larger type of particles. Fine particles which tend to form rheologically complex pseudo-homogeneous slurries are briefly addressed in a separate section. The ingestion and dispersion of fine powders and floating particles in liquids is beyond the scope of this chapter.

10.2 Regimes of solids suspension and distribution

The state of suspension in a stirred vessel can be defined in a number of ways. In a design or scale-up problem, it is important to use the appropriate definition and correlation as different processes require different degrees of suspension. The basic common states of suspension are described in the following sections in the order of increasing homogeneity.

10.2.1 State of nearly complete suspension with filleting

Most of the solid particles are suspended while a small fraction is allowed to loosely aggregate and form fillets on the base of the vessel in relatively stagnant regions behind baffles, in corners or below the agitator. This state of suspension may sometimes be acceptable provided the fillets do not grow and the solids do not cake. This, however, would be undesirable in operations such as crystallisation or where mass/heat transfer is involved.

10.2.2 State of complete particle motion

No fillets exist, and solids that are not suspended are in a state of motion along the base of the vessel. These particles will have considerably reduced mass/heat transfer coefficients than the suspended ones because of their non-uniform exposure to the liquid. Such

a condition, however, is sufficient in some cases such as the dissolution of highly soluble solids even if only a relatively small fraction of solids are suspended.

10.2.3 State of complete off-bottom suspension

In this state, all solids are suspended and no particle remains at the bottom of the vessel for more than 1 or 2 s approximately, a condition known as Zwietering's criterion (Zwietering 1958). Under this 'just suspended' condition, the maximum solid area is exposed to the fluid but there are usually concentration gradients in the vessel, and there may be a significant region of clear liquid near the top. Much of the mixing research in this area has been devoted to the determination of the minimum agitation speed, N_{js}, necessary to achieve this state of suspension. As such, N_{js} is one of the most important design requirements. This is usually measured in a well-illuminated, transparent vessel by gradually increasing the impeller speed until the condition is visually satisfied. It should be noted, however, that whilst the concept of N_{js} is simple, its accurate measurement is not, especially under conditions of high solids concentration, as generally found in real industrial processes, or where a third gas phase is also present. Determination of N_{js} tends to be somewhat subjective and measurements by different workers can differ by a significant margin. However, in a given experiment, a single experimentalist can achieve results with a good precision.

Complete suspension is often an energy-intensive operation with power requirements of the order of $1\,\mathrm{kW\,m^{-3}}$ being rather common, depending on impeller and vessel geometry. A more relaxed definition of N_{js} would include the state of nearly complete suspension with filleting, as described above. As power dissipation is proportional to N^3, this state of suspension offers substantial savings in power requirement compared to Zwietering's criterion, which may more than outweigh the deficiency in suspended solids.

10.2.4 State of homogeneous or uniform suspension

Homogeneous suspension exists when the solids are practically uniformly distributed throughout the vessel volume, that is, there are no solids concentration gradients, and for a polydisperse system, the particle size distribution should also be approximately the same everywhere. This condition is required when it is necessary to obtain uniform treatment of all the particles, when a suspension must be discharged at a constant concentration for sampling, for further processing, or for packaging. The process result that the mixing has to achieve is that the discharge from the vessel should enable homogeneous filling of packaging lines, for example, meat/vegetable pieces in a sauce or fruit particles in yoghurt. Another example would be in a crystalliser where a non-uniform solids distribution may cause high local supersaturation levels and hence a non-uniform crystal growth which is undesirable.

In general, a considerably higher power input is required to achieve a state of homogeneous suspension than just complete suspension. Such an increase in power demand is higher for faster settling particles, as shown in Table 10.1. Food particles are often nearly neutrally buoyant, and this should make homogeneity easier to achieve than in many other industrial processing applications, where it is not usually economically feasible. In many such cases, however, the minimum condition of suspending all particles in the fluid is sufficient to satisfy the process requirements, and thus, industrial suspensions in the process industries are often designed to operate under a heterogeneous régime, that is, at N_{js} or slightly above it. Consequently, studies reported in the literature have focussed greatly on the determination of N_{js}.

Table 10.1 Illustration of power requirement for different suspension criteria and settling velocities.

	Power ratio		
State of suspension	**u_∞ = 0.51–3.05 mm s^{-1} Easy problem**	**u_∞ = 20.3–40.6 mm s^{-1} Moderate problem**	**u_∞ = 81.3–305 mm s^{-1} Difficult problem**
Complete particle motion	1	1	1
Complete off-bottom suspension	2	3	5
Homogeneous suspension	4	9	25

Source: Adapted from Oldshue (1983).

At the high impeller speeds generally required to achieve homogeneity, however, there is the additional possible problem of surface aeration. Considerable amounts of air can be drawn into the vessel, which can have negative effects on the process, especially when mixing very viscous fluids or fluids with an apparent yield stress. Under such conditions, surface aeration must be guarded against to avoid a severe entrapment of unwanted air in the suspension which can cause great difficulties, including the mass/heat transport limitations that may ensue due to a blanketing of the particle surfaces.

Whilst solids tend to suspend fairly uniformly across the radius of the vessel at agitation speeds above N_{js}, vertical homogeneity is much harder to achieve; the vertical distribution is usually non-uniform and is generally characterised by a local maximum occurring above the impeller plane giving rise to what is sometimes called a 'belly plot' (Barresi & Baldi 1987). Visual observation is most commonly used to measure N_{js}, as discussed earlier, but is also used in practice to qualitatively gauge the degree of homogeneity. This is a crude but rapid procedure which enables a quick basic comparison to be made between different geometries or processing conditions, and can enable salient features and problems to be identified such as stagnant areas and solids accumulation. Whilst visual observation becomes increasingly more difficult at high solids loadings due to the increased opacity of the system, the method is still useful in acquiring a rough picture of the general flow patterns. Good lighting is essential, and the addition of food dyes and the use of photography and/or video can also help.

A quantitative description of homogeneity is harder to formulate, however. The degree of homogeneity can be quantified in terms of the coefficient of variation, a statistical parameter defined as:

$$C_v = \frac{\sigma}{\bar{C}} = \frac{\sqrt{\dfrac{1}{n-1}\sum_{i=1}^{n}(C_i - \bar{C})^2}}{\bar{C}} \tag{10.1}$$

where σ is the standard deviation, $\bar{C}$ is the mean solids concentration in the vessel, C_i is the local solids concentration of sample i, and n is the number of samples (Rieger *et al.* 1988). Whereas σ gives a measure of how different the values are from each other and from the mean $\bar{C}$, C_v is a measure of the spread of the distribution relative to its mean; the larger the C_v, the more significant is the σ relative to the mean.

The state of homogeneous suspension is difficult to achieve and to measure in practice. It has been proposed that a suspension should be assumed homogeneous when the height of the suspended particle layer, otherwise called *cloud height*, reaches 90% of the liquid height (Zlokarnik 2001). The liquid layer above this is usually particle free. A 100% uniform suspension would imply $C_v = 0$; this would be impractical because of the particle-free layer near the surface. In practice, therefore, homogeneity is usually deemed adequate if $C_v \leqslant 0.05$.

Whilst the definition of the coefficient C_v is simple, its measurement is far from trivial. The method requires a large number of local measurements of solids concentration, something not readily achievable in practice. Withdrawal of samples has been attempted in the past, but it is fraught with problems as it is difficult to achieve representative isokinetic sampling in most regions of the vessel (Nasr-El-Din *et al*. 1996). So far, other attempts at local measurements have been mainly confined to the investigation of axial solid concentration profiles at relatively low concentrations using intrusive conductivity or capacitance probes (Yamazaki *et al*. 1986; Barresi & Baldi 1987; Mak *et al*. 1997; Montante *et al*. 2001, 2002; Brunazzi *et al*. 2004). A non-intrusive electrical resistance tomography technique has also been developed but suffers from a lack of resolution (Mann *et al*. 2001). There are, however, no instruments that can be used to reliably probe concentrated suspensions and provide detailed pointwise measurements of solids concentration. A better more reliable criterion for uniformity of suspension is also missing. Thus, more research is needed on the experimental front to help the development of the theory in this area.

Positron emission particle tracking (PEPT) is a novel technique, which is unique in flow visualisation terms, being able to examine flow phenomena in three dimensions that could not be observed as effectively by using other techniques. It is particularly useful for the study of multiphase flows, to map the flow of fluids and the flow of particles, where one component can be labelled and its behaviour observed. The method has been successfully applied recently to the study of solid–liquid mixing in stirred vessels and has also been used to study the flow of solid–liquid food suspensions in pipes (Barigou *et al*. 2003; Barigou 2004).

PEPT uses a single positron-emitting particle as a flow tracer, which is then tracked in 3D space and time to reveal its full Lagrangian trajectory. The method allows probing of opaque fluids and within opaque apparatus, a distinct advantage over advanced optical methods such as laser Doppler velocimetry (LDV) and particle image velocimetry (PIV). The positron camera uses two position-sensitive detectors between which the system under study is mounted, as shown in Figure 10.2. A positron-emitting radioactive tracer is introduced into the flow. Once emitted from the nucleus, a positron annihilates with an electron, releasing energy in the form of two back-to-back γ-rays travelling at 180º. Each detector captures incident γ-rays over an area of $59 \times 47\,\text{cm}^2$ and determines their interaction coordinates. Only coincidence events in which γ-rays are simultaneously detected by both detectors are recorded. By a triangulation process of multiple events, it is possible to reconstruct the three-dimensional position of the particle and thus its trajectory over time, as shown in Figure 10.3. The complexity of the trajectory is itself a characteristic of the mixing process and is dictated by many factors including impeller design, fluid rheology, and flow regime. By analysing the particle trajectory, a lot of quantitative information can be obtained including the 3D space occupancy, local particle concentration, and local phase velocities. Further details of the technique can be found in Barigou (2004) and Parker *et al*. (2002).

The accuracy of PEPT has been independently ascertained by comparison with 2D PIV measurements in turbulent water in a stirred vessel and via accurate mass continuity calculations throughout the vessel (Barigou *et al*. 2009; Pianko-Oprych *et al*. 2009). PEPT has

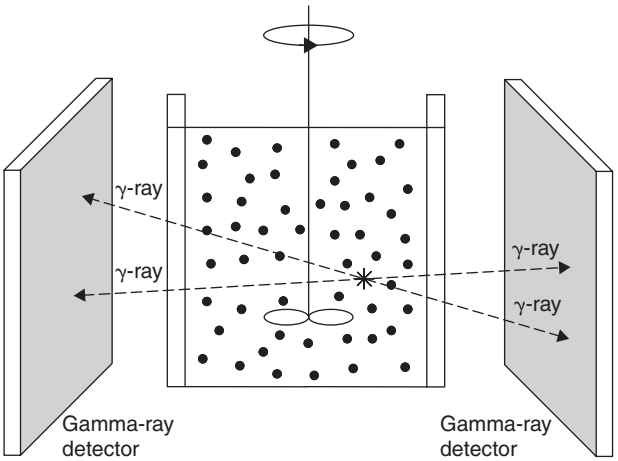

Fig. 10.2 Schematic diagram of PEPT set-up.

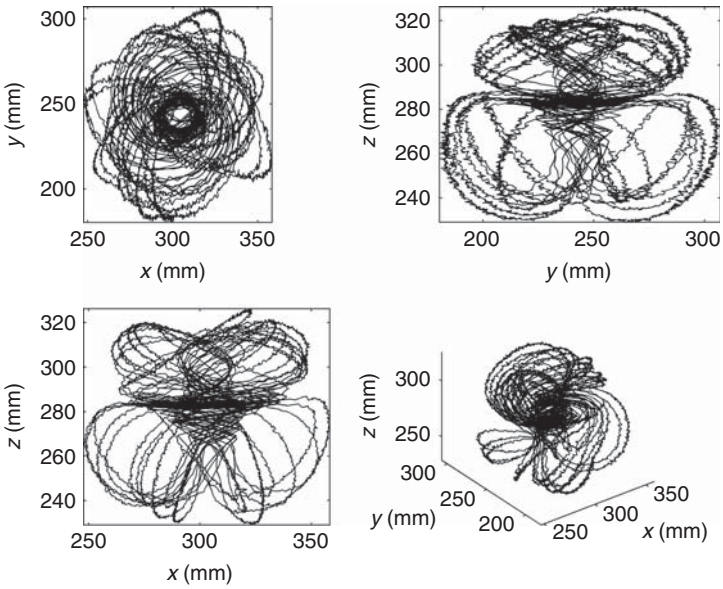

Fig. 10.3 Short sample of PEPT tracer trajectory in a non-Newtonian industrial slurry stirred by a PBT (3 min). PEPT experiments are usually run over a considerable period of time (*ca.*, 1 h), which depends amongst other factors on vessel size to acquire the full trajectory of the solid or liquid phase, long enough for ergodicity to be safely assumed in a turbulent flow system.

recently been used to determine the 3D velocity field as well as solids distribution developed during the mixing of monodisperse and polydisperse slurries consisting of glass particles from 1 to 3.30 mm, at mass concentrations varying from 5% to 40%, in a vessel agitated by a pitched blade turbine (PBT). For the first time, it has been possible by selective labelling to determine the full 3D local velocity field and spatial distribution of the liquid phase and of each individual particle size fraction. No other technique is capable of discerning the motion of different sizes of particle when a distribution of sizes is involved (Barigou *et al.* 2009; Guida *et al.* 2009).

Information on particle *slip velocities* is also of real value to processing applications involving the transfer of heat or mass, such as in the sterilisation of particulate food mixtures or chemical reactions. PEPT allows estimations of time-averaged particle slip velocities to be obtained by tracking the solid and liquid phases separately one at a time and determining their local velocities, albeit it does not measure the velocities of the two phases simultaneously, and does not measure any rotational slip component or turbulent fluctuations, but these are only relevant in very complex turbulent flows. PEPT can identify regions of poor slip velocity, and thus, enables the evaluation of impeller effectiveness in optimising heat and mass transfer. For example, recent results have shown that larger glass particles generally have higher apparent slip velocities than smaller ones; in particular, in the impeller discharge stream, they are approximately twice as large. Thus, PEPT has proved to be a powerful technique in probing stirred vessels in general but is showing particularly a great and unique capability for the study of solid–liquid mixing (Barigou 2004; Barigou *et al*. 2009; Guida *et al*. 2009).

10.3 Prediction of minimum speed for complete suspension

The minimum impeller speed to produce complete off-bottom suspension has been an issue receiving attention in the literature for decades. For example, Brujes *et al*. (1998) compiled most of the correlations for estimating N_{js} published over a 40-year span, and tested them against experimental measurements obtained in baffled and unbaffled tanks of microcapsule suspensions. Since then, many more papers have been published on the topic. Many workers have measured N_{js} using different instruments and approaches, but Zwietering's approach remains the most popular (Zwietering 1958).

Zwietering's classical correlation which stands as a reference in the field was developed from dimensional analysis and was based on experiments covering by far the widest range of fluid and particle properties, particle size and concentration, impeller type and size, and vessel geometry. Thus:

$$N_{js} = S\nu^{0.1} d_p^{0.2} \left(\frac{g\Delta\rho}{\rho_L} \right)^{0.45} D^{-0.85} X^{0.13} \tag{10.2}$$

where S is a shape factor, that is, dimensionless parameter which accounts for geometrical effects including impeller type, impeller off-bottom clearance, and impeller-to-tank diameter ratio; d_p is particle diameter; D is impeller diameter; ρ_L is liquid density; g is gravitational acceleration; $\Delta\rho$ is solid–liquid density difference; X is solids concentration by weight $\times 100$; and ν is liquid kinematic viscosity. Subsequent independent studies (Nienow 1968; Baldi *et al*. 1978; Rao *et al*. 1988) generally corroborated Zwietering's correlation for process conditions similar to those covered by Zwietering. For conditions very different from Zwietering's equation (10.2) may be much less reliable, and where a state of complete off-bottom suspension is deemed essential, it is advisable to measure N_{js} experimentally if at all possible.

10.3.1 Influence of physical properties

Zwietering's correlation which is based on turbulent flow, indicates a low dependence on fluid viscosity ($\nu^{0.1}$), which is expected in a turbulent flow field. However, results on

suspensions where the liquid is viscous are scarce. Shamlou (1993) reported, on the basis of some limited experimental data obtained in high-viscosity liquids, that N_{js} values estimated by correlations such as Zwietering's are too high by as much as a factor of 2.5. Using Newtonian liquids, Ibrahim and Nienow (1994) found that at viscosities of about 1 Pa s, the Zwietering correlation fails to predict N_{js} with as much as 90% error. The influence of the suspending fluid rheology on solids suspension generally has received scant attention in the literature. In the processing of particulate food mixtures, the particles are quite often suspended in a non-Newtonian fluid which can have a complex rheology, for example, fruit particles in yoghurt. When the suspending medium is non-Newtonian, the hydrodynamic field inside a stirred vessel becomes even more complex with a non-uniform viscosity field. Recently, we observed both experimentally and using computational fluid dynamics (CFD) that large glass particles ($d_p = 4.5$ mm) seem to suspend better and distribute better in a carboxymethyl cellulose (CMC) solution compared to pure water in a vessel agitated by a PBT (Pianko-Oprych *et al*. 2006). This could be due to the increased drag experienced by the particles in such a shear-thinning fluid, as discussed in Section 10.4.2. Despite their industrial importance, these rheologically complex suspensions have been inadequately researched and are not well understood.

The low dependence on particle size ($d_p^{0.2}$) has been confirmed for particles in the range 0.2–1 mm. For solids smaller than 0.2 mm, higher exponents have been reported, but as N_{js} seems to fall off more rapidly than equation (10.2) suggests, the latter expression is still considered to give conservative predictions (Baldi *et al*. 1978). For d_p greater than about 1 mm, however, there are indications in the literature that N_{js} may be insensitive to particle size, but these have not been widely confirmed. On the other hand, it has been reported that Zwietering's correlation is not as reliable at high d_p/T values (Atiemo-Obeng *et al*. 2004). The latter situation is especially relevant to food applications where particles tend to be large; little information exists on the suspension of such coarse particles especially in viscous and non-Newtonian media.

The solid–fluid density difference, $\Delta\rho$, is the property with the largest influence on N_{js}. Its exponent reflects the effect of the settling velocity of the solids. The exponent on D represents the influence of scale. The effects of settling velocity and scale are discussed in more detail in Sections 10.4 and 10.5, respectively.

10.3.2 Influence of solids concentration

The dependence on X seems fairly small, but it has been reported that Zwietering's correlation is not as reliable at low solids concentrations below 2 vol% and high concentrations above 15 vol% (Atiemo-Obeng *et al*. 2004). As discussed above, though a lot of work has been done on measuring N_{js}, there is still a need for considerably more high-quality experimental data in which both N_{js} and local energy dissipation rates are measured. This is needed to improve the prediction of N_{js} through better understanding of particle lift-off from a stationary bed of particles and particle settling, especially in rheologically complex media where information is scarce.

10.3.3 Influence of geometric parameters

The influence of impeller design, impeller size *D/T*, impeller off-bottom clearance *C/T*, and vessel configuration are represented by the dimensionless parameter S in equation (10.2). Graphs of S as a function of *T/D* and *T/C* have been presented by Zwietering (1958) and

Nienow (1968) for three different impellers (propeller, disc turbine, and flat paddle) in flat-base cylindrical vessels equipped with four baffles of $0.1T$ width, where liquid height is equal to tank diameter, that is, $H = T$ (Figure 10.1). These data can be represented by a correlation of the form:

$$S = p\left(\frac{T}{D}\right)^q \tag{10.3}$$

where the constants p and q are a function of impeller design and T/C. Values of S for other types of agitators have also been reported (Nienow 2000; Atiemo-Obeng *et al*. 2004). Such data show that S is generally smaller for smaller C/T values, that is, at low off-bottom clearances, and at larger D/T values, that is, when using wider impellers, but only up to a practical limit beyond which performance declines. The data also show that axial flow agitators, that is, propellers and hydrofoil impellers such as Lightnin A310 and Chemineer HE3, shown in Figure 10.4, are the best performers as they have the lowest N_{js} values and by far the lowest power dissipation rates. These high-efficiency impellers develop a stronger axial flow field near the base of the vessel where particles deposit, than radial (disc turbine, flat paddle) or mixed flow (PBT) impellers (Figure 10.4). Such an axial flow is effective in lifting off particles and suspending them and enables these impellers to cope better when positioned at relatively high clearances. Their low power demand is relatively independent of D/T, which means that larger impeller diameters with lower rotational and tip speeds can be used to minimise damage to shear-sensitive particles. Large D/T ratios combined with low clearances, however, lead to a weak axial flow causing particle accumulation in the centre directly beneath the agitator, and should be avoided.

As discussed above, axial flow impellers used in the down-pumping mode are known to be the most energy efficient in just suspending solids, that is, they achieve solids suspension with less power dissipation. Some more recent studies, however, have shown that up-pumping axial hydrofoil impellers provide considerable advantages over down-pumping ones in single-phase mixing (Aubin *et al*. 2001) and in three-phase gas–solid–liquid mixing (Nienow 1999). In the down-pumping mode, one circulation loop is produced and velocities in the upper part of the vessel are very weak, resulting in poor mixing in that region. In the up-pumping mode, fluid circulation in the upper part of the tank is considerably improved as two distinct circulation loops are established which is beneficial to gas retention and dispersion.

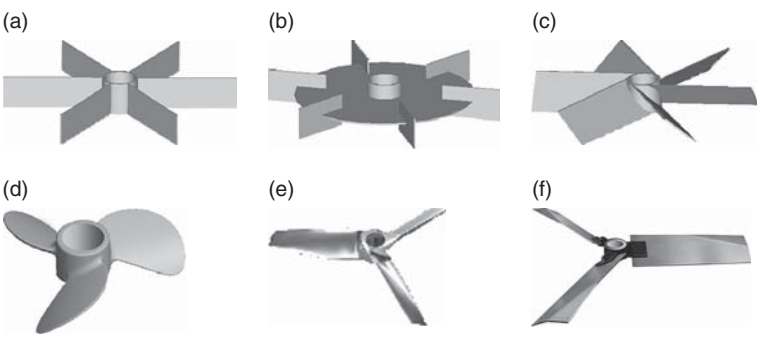

Fig. 10.4 Common impellers used in solid–liquid mixing: (a) flat paddle; (b) disc turbine; (c) pitched blade turbine (PBT); (d) marine propeller; (e) Lightnin A310 hydrofoil; (f) Chemineer HE3 hydrofoil.

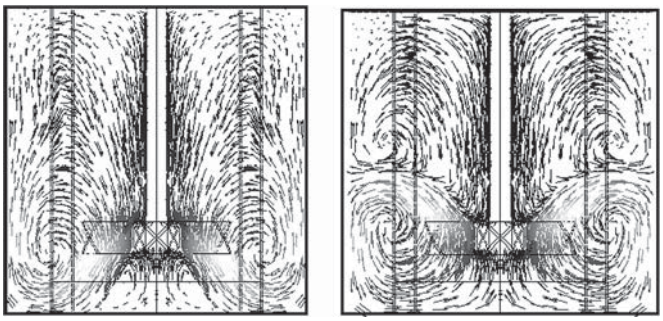

Fig. 10.5 CFD simulation of solid-phase velocity field in an aqueous pseudo-plastic CMC solution: 5 wt% glass beads, $d_p = 4.5$ mm, $T = 287$ mm, $D = T/2$, $C = T/4$, $N_{js} = 600$ rpm. The up-pumping PBT generates two flow loops rotating in opposite directions compared to a single flow loop generated in down-pumping.

When dispersing solids, however, it is not entirely clear what the pumping direction does to the 3D distribution of the particles and, hence, to the homogeneity of the suspension. In our recent work on the suspension of large glass particles (1–3.30 mm) in water, a uniformity index based on the variance of the local solids concentration in the vessel measured by the PEPT technique showed that, overall, a down-pumping PBT achieves a significantly better homogeneity than an up-pumping PBT (Guida *et al*. 2009). In a different CFD study using glass particles of 4.5 mm in a pseudo-plastic CMC solution, the CFD simulated flow field was characterized by a single flow loop for a down-pumping PBT, and two flow loops rotating in opposite directions for an up-pumping PBT, as shown in Figure 10.5 (Pianko *et al*. 2006). In this case, the particles trapped in the lower flow loop fall down with high velocities towards the base, while particles entrained in the upper flow loop rise towards the surface. The presence of two such flow loops seemed to achieve a better radial as well as axial distribution of the solids, so that in the CMC solution, an up-pumping PBT appeared to produce a better solids distribution than a down-pumping PBT, which appeared to be consistent with visual observation of the suspension in the vessel.

As pointed out earlier, a uniform distribution of the solids is important for some processes such as crystallisation and when the vessels are used for semi-batch feeds for subsequent processing to obtain uniform treatment of all the particles. In addition, when the suspending liquid is viscous leading to transitional flow, such impellers are known to exhibit almost radial flow, and in this case again, it is not entirely clear *à priori* which pumping configuration would be more advantageous both in suspending the solids and achieving a good spatial distribution.

Data reported by Guerci *et al*. (1986) suggest that N_{js} is more easily achieved in dished bottom vessels (~20% lower) and vessels equipped with a draught tube, as they have smaller S values than flat-based vessels, but deep dishes are usually less energy efficient because of the proximity of the impeller tip to the base. In this respect, however, there is no significant difference between different dish shapes, for example, hemispherical or elliptical.

It should also be pointed out that whilst the use of more than one impeller improves solids distribution, this should not have any significant effect on N_{js} as the settled solids would only feel the effect of the action of the bottom agitator. Power draw, however, would increase proportionally to the number of agitators used. Varying the liquid height also has no effect on N_{js} as the hydrodynamics associated with particle lift-off from the sediment on the bottom of the vessel remain unaffected.

10.4 Hydrodynamics of particle suspension and distribution

The three-dimensional flow field inside a mechanically agitated vessel displays complex features depending on the mixer configuration used and the physical properties of the phases involved. The regime of flow is determined by the impeller Reynolds number defined as:

$$Re = \frac{\rho_L N D^2}{\mu} \tag{10.4}$$

where μ is the fluid dynamic viscosity. The flow field generated by the agitator is such that particles are lifted off the bottom of the vessel and dispersed throughout the vessel volume. Even when the flow field is fully turbulent (i.e., $Re > 2 \times 10^4$), the spatial distribution of the local energy dissipation and turbulent shear rates is highly non-uniform. Energy dissipation is highest in the impeller flow region, being an order of magnitude greater than the mean value in the tank, and consequently much lower in the bulk circulation region comprising the remainder of the vessel.

The process of particle suspension and dispersion consists initially of particle lift-off from the base of the vessel (i.e., suspension) followed by dispersion into the bulk of the liquid. The mechanisms of particle lift-off and suspension are governed by the flow field adjacent to the base of the vessel, whereas the general flow pattern in the bulk dictates the way particles are held in suspension and distributed in 3D space. Attempts have been made to develop physical and theoretical models capable of explaining particle suspension. Such models, however, have in the main considered particles that are already in suspension or just about to be lifted at the base of the vessel. These two situations are distinctly different, and it is important to treat them as such because the fluid mechanics which facilitate particle lift-off are undoubtedly different from those needed to maintain the particles in suspension and distribute them.

Particle lift-off from a stationary bed of particles at the bottom of the vessel occurs as a result of the drag and lift exerted by the moving fluid. The flow near the base has been described as boundary layer flow, which causes particles to be swept across the base of the vessel (Bourne & Zabelka 1980). Once small fillets of particles have been formed, particle lift-off is usually seen to be caused by sudden turbulent bursts originating in the turbulent bulk flow above. There is no complete theory of turbulent flow phenomena, but Kolmogorov's theory of isotropic turbulence has been exploited to some advantage in analysing fluid–particle interactions in this type of flow (Kolmogorov 1941a,b). Turbulent kinetic energy is cascaded down chains of turbulent eddies of progressively smaller scales to very small isotropic eddies where ultimately viscous dissipation to heat can occur. The smallest scale of turbulence, or the smallest eddy size, is characterised by the Kolmogorov length scale, λ, given by:

$$\lambda = \left(\frac{\nu^3}{\varepsilon} \right)^{1/4} \tag{10.5}$$

where ε is the local rate of energy dissipation measured in $\mathrm{W\,kg^{-1}}$. λ is also known as the Kolmogorov microscale of turbulence, below which most of the energy dissipation occurs as viscous forces dominate. In a stirred vessel containing a low-viscosity liquid such as water, λ is typically of the order of $\sim 10\,\mu\mathrm{m}$ near the impeller and $\sim 30\,\mu\mathrm{m}$ in the bulk.

Fluid–particle interactions in turbulent flow are dependent on the relative size of eddies and the particles. Eddies relatively large compared to a particle will tend to entrain it, and if the particle density is close to that of the fluid, there will be little relative motion. An eddy smaller than the particle will not be able to entrain it, and the eddy will act on the particle surface, possibly resulting in some erosion. It is, therefore, the large eddies (near the base) generated by the impeller motion which are responsible for the suspension of particles. Consequently, different agitator designs and configurations yield different flow signatures, that is, generate different convective flows and, thus, achieve different levels of solids suspension at the same power input. Once suspended, neutrally buoyant or nearly neutrally buoyant particles, as pointed out above, will follow the motion of the fluid. It is then relatively easy to keep them in suspension and distribute them throughout the vessel volume. Heavier particles, however, will have significant velocities relative to the fluid and will tend to settle out, so the fluid flow field must be such that the combined fluid drag and lift generated are sufficient to keep them suspended. At high solids concentrations, once particles are suspended, they significantly damp fluid turbulence and, consequently, greater energy inputs are necessary to achieve and maintain suspension.

The complex nature of the flow field in a stirred vessel is such that there is no fundamental theory to describe the process of particle suspension. The overall behaviour of such a stirred medium is the result of the complex interaction occurring between solid particles and liquid turbulence: fluid turbulence anisotropy, large differences in eddy length scales, particle dynamics, and spatial distribution of these factors as well as their consequences for the local fluid–particle interactions and turbulence modulation make a detailed description difficult to achieve at present. Therefore, simplifications are adopted, the nature of which depends on the specific objective. A number of semi-empirical approaches have been suggested, but none of them have been successful in quantitatively modelling particle suspension. The hydrodynamics of suspension in rheologically complex fluids are even less well understood and a great deal of work is needed.

10.4.1 Particle slip velocity

As pointed out above, a particle with a density different from that of the fluid will travel at a velocity u relative to the fluid, known as slip velocity. A number of quantities are defined on the basis of the slip velocity such as particle Reynolds number and drag coefficient, as shown below. Such a velocity, therefore, is needed for hydrodynamics as well as mass/heat transport calculations. In a mechanically agitated suspension, the definition of slip velocity can be further complicated by the possible superimposition of other components of motion, namely rotation of the particle relative to the fluid and turbulent fluctuations of the particle in complex situations of turbulence. In a stirred suspension, u will be a function of particle size and will vary from point to point, and a representative mean value is *à priori* difficult to estimate even if local values were known. Attempts to measure it or estimate it on the basis of Kolmogorov's theory have not been successful. In practice, however, it has been customary in stirred vessels to take the free *terminal settling velocity* of the particle, u_∞, as a representative of its mean slip velocity. This assumption, albeit crude, seems, for example, to give reasonable mass transfer predictions at N_{js} but not above it (Nienow 2000).

10.4.2 Particle settling and drag

The settling tendency of the particles has a dominating influence on the behaviour of the suspension and is greatly affected by the solid–fluid density difference. The free particle

terminal settling velocity has been used to classify suspension problems into easy, moderate, or difficult, as illustrated in Table 10.1. It is also used as an estimate for the mean slip velocity as discussed above and as such is an important parameter which deserves some attention. To understand how particles settle in fluids, it is important to understand fluid drag in both Newtonian and non-Newtonian fluids and how to estimate the settling velocity of particles in these fluids.

10.4.2.1 *Drag force and drag coefficient*

When a particle in a fluid is in relative motion to it, the *drag* is defined as that component of the resultant force acting on the particle in the direction of the relative motion. The total (or profile) drag force acting on a particle in a fluid is made up of two contributions: the *form* (or *pressure*) drag, arising from the non-uniform pressure distribution on the particle, and the *skin friction* (or *viscous*) drag, the force on the particle due to the fluid shear stress at the surface. The total drag force F on a particle is made dimensionless by use of the drag coefficient C_D defined as:

$$C_D = \frac{F}{\frac{1}{2}\rho_L u^2 A} \tag{10.6}$$

where A is the area of the particle's projection on a plane normal to the direction of relative motion. For a spherical particle, A is the area of the circle having the sphere diameter d_p and hence the following equation results:

$$F = C_D\left(\frac{1}{2}\rho_L u^2\right)\left(\frac{\pi d_p^2}{4}\right) \tag{10.7}$$

Both contributions to the profile drag can be calculated if the pressure and shear stress distributions around the particle are known. The shear stress and pressure distributions can, in principle, be derived by solving the continuity and momentum equations. General solutions do not exist, however, and numerical solutions are often sought even at low Reynolds numbers. A detailed treatment of this subject for Newtonian fluids can be found in Clift *et al.* (1978) and Lareo *et al.* (1997). Of particular interest to food applications is the motion of particles in non-Newtonian fluids and a good treatise can be found in Lareo *et al.* (1997) and Chhabra (2006). The following sections, however, give a summary of the main results.

10.4.2.2 *Drag on a sphere in a Newtonian fluid*

In general, both skin friction and form drag depend on the particle Reynolds number defined as:

$$Re_p = \frac{\rho_L u d_p}{\mu} \tag{10.8}$$

Therefore, C_D is a function of Re_p but also depends on factors such as particle shape and surface roughness, the turbulence in the fluid, and the acceleration of the fluid relative to the particle. Theoretical treatments are in general difficult, and it is very often necessary to

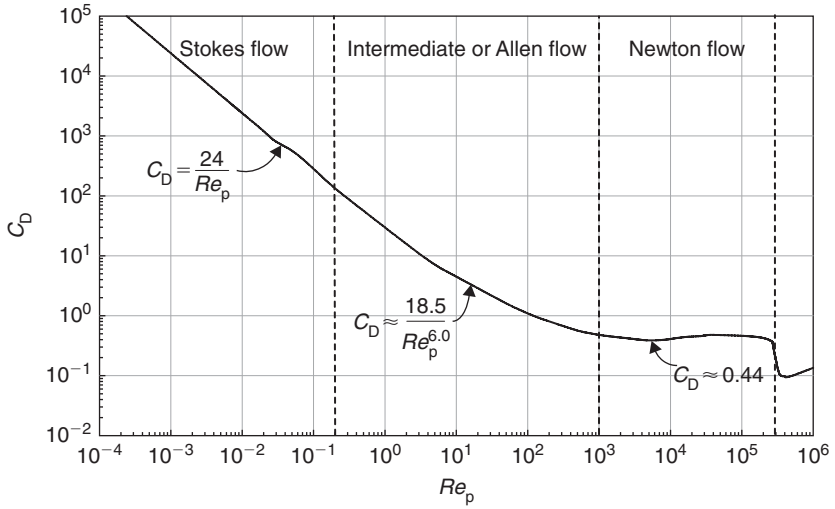

Fig. 10.6 Standard drag curve for a sphere.

rely on experimental data. Such data for drag are most conveniently represented in graphical form by plotting C_D versus Re_p. The drag curve for a rigid sphere is called the *standard drag curve* and is shown in Figure 10.6. It should be noted that in stirred vessels, C_D for large particles ($d_p > \sim 1.5$ mm) is higher than shown by the standard drag curve due to the high level of turbulence, so a value of 1.0 instead of 0.44 should be used in Newton's flow (Nienow 2000).

For a sphere moving in creeping flow, that is, $Re_p \leqslant 0.2$, the well-known Stokes law ($F = 3\pi\mu d_p u$) and equation (10.7) lead to the following relationship, a different form of Stokes law:

$$C_D = \frac{24}{Re_p} \tag{10.9}$$

Many empirical expressions, often highly complex, have been suggested for C_D throughout the standard drag curve. These have been reviewed and critically evaluated by Clift *et al.* (1978).

10.4.2.3 *Drag on a sphere in a non-Newtonian fluid*

Power law fluids

These fluids are very common in food applications and are described by the constitutive equation:

$$\tau = k\dot{\gamma}^n \tag{10.10}$$

where τ is shear stress, $\dot{\gamma}$ is shear rate, k is the consistency index, and n is the power law or flow behaviour index. The model is used to describe the widely familiar shear-thinning (or pseudo-plastic) food fluids with $n < 1$, such as concentrated fruit juices, fruit

Table 10.2 Numerical values of $Z(n)$ for a sphere in creeping flow (Chhabra and Richardson, 1999).

	Shear thickening				**Newtonian**	**Shear thinning**								
n	1.8	1.6	1.4	1.2	1.0	0.9	0.8	0.7	0.6	0.5	0.4	0.3	0.2	0.1
$Z(n)$	0.261	0.390	0.569	0.827	1.002	1.14	1.24	1.32	1.382	1.42	1.442	1.458	1.413	1.354

Source: Chhabra and Richardson (1999).

and vegetable purées, cream, and is also used to describe the much rarer behaviour of shear-thickening (or dilatant) fluids with $n > 1$, such as starch suspensions and some types of honey. A simple dimensional analysis would show that

$$C_D = f(Re_p, n) \tag{10.11}$$

Thus, C_D is a function of the power law index n and the corresponding particle Reynolds number is now defined as follows:

$$Re_p = \frac{\rho_L u^{2-n} d_p^n}{k} \tag{10.12}$$

For a power law fluid in creeping flow, the drag coefficient can be expressed in terms of Stokes law [equation (10.9)] using a correction factor $Z(n)$ as shown below:

$$C_D = \frac{24}{Re_p} Z(n) \tag{10.13}$$

The numerical values of $Z(n)$ are listed in Table 10.2 for both shear-thinning and shear-thickening behaviour. The data show that shear thinning increases drag whereas shear thickening reduces it.

Experimental results and numerical simulations indicate that creeping flow in shear-thinning liquids occurs up to $Re_p \sim 1.0$. For shear-thickening liquids, creeping flow occurs up to $Re_p \sim 0.2$–0.5.

Numerical predictions of the drag coefficient of a sphere in a power law liquid are available up to $Re_p = 130$. Thus, C_D can be estimated with a maximum error of 10% using the following expressions for shear-thinning liquids developed by Graham and Jones (1994):

$$C_D = \frac{35.2(2)^n}{Re_p^{1.03}} + n\left(1 - \frac{20.9(2)^n}{Re^{1.11}}\right) \quad 0.2(2)^n \le Re_p \le 24(2)^n \tag{10.14}$$

$$C_D = \frac{37(2)^n}{Re_p^{1.1}} + 0.25 + 0.36n \quad 24(2)^n \le Re_p \le 100(2)^n \tag{10.15}$$

Experimental results are available in the literature for Re_p values up to 1,000 and $0.38 \leqslant n \leqslant 1$ (Chhabra 1990). It is found, however, that the standard drag curve for

Newtonian liquids adequately correlates the results in power law liquids in the region $1 \leqslant Re_p \leqslant 1{,}000$ within $\pm 30\%$. Non-Newtonian effects also diminish with increasing Re_p and predictions using the standard drag curve improve accordingly.

Viscoplastic fluids

This type of fluid appears to require a yield shear stress, τ_y, that has to be exceeded before fluid flow takes place. A number of models exist, with the Bingham plastic and the Herschel–Bulkley types being the most popular.

Bingham plastic fluid

Examples of food materials of this type include tomato paste, margarine, vegetable fats, and molten chocolate. The constitutive equation for a Bingham plastic fluid is as follows.

$$\begin{aligned} \tau &= \tau_y + \eta_B \dot{\gamma} \quad \tau \geq \tau_y \\ \dot{\gamma} &= 0 \qquad\qquad \tau < \tau_y \end{aligned} \tag{10.16}$$

The constant η_B is known as the plastic viscosity. Numerical finite-element simulations of a sphere in creeping flow in a Bingham plastic liquid have suggested the use of a correction factor such that (Lareo *et al*. 1997):

$$C_D = \frac{24}{Re_B} Z \tag{10.17}$$

in which Re_B is the Bingham Reynolds number ($Re_B = \rho_L u d_p / \eta_B$) and Z is a function of the Bingham number $Bi = \tau_y d_p / \eta_B u$, thus:

$$Z = 1 + a(Bi)^b \tag{10.18}$$

where $a = 2.93$, $b = 0.83$ for Bi values up to 1,000. Note that as Bi decreases, Z tends to 1 (i.e., Newtonian flow). The higher drag ($Z > 1$) in a viscoplastic medium is due to the combined effects of viscosity and yield stress. The criterion for creeping flow in viscoplastic liquids is found to be the Bingham Reynolds number, the upper limit for which is as follows:

$$Re_{B\,max} \approx 100 Bi^{0.4} \tag{10.19}$$

Thus, the greater the Bi (i.e., the greater τ_y) the higher is the upper Reynolds number for creeping flow.

Herschel–Bulkley fluid

Examples of food materials of this type include yoghurt, potato puree, soft cheeses, and fruit jams. This is also called the generalised power law model as it represents power law behaviour with an apparent yield stress, that is:

$$\begin{aligned} \tau &= \tau_y + k\dot{\gamma}^n \quad \tau \geq \tau_y \\ \dot{\gamma} &= 0 \qquad\qquad \tau < \tau_y \end{aligned} \tag{10.20}$$

The following semi-empirical correlation has been proposed for C_D (Atapattu *et al.* 1995):

$$C_D = \frac{24}{Re_p}(1 + Bi^*) \tag{10.21}$$

where Bi^* is the modified Bingham number given by $Bi^* = \tau_y/k(u / d_p)^n$. This correlation covers the range $10^{-5} \leqslant Re_p \leqslant 0.36$, $0.25 \leqslant Bi^* \leqslant 280$, $0.43 \leqslant n \leqslant 0.84$.

Beyond creeping flow, drag data are reasonably well represented by the standard drag curve for Newtonian liquids. Thus, the non-Newtonian effects seem to be much more important at low Re_p values; they gradually diminish as inertial effects become more and more significant.

In conclusion, equations (10.13), (10.17), and (10.21) should be used to estimate drag in creeping flow in power law, Bingham and Herschel–Bulkley liquids, respectively. Beyond creeping flow, the use of the standard drag curve for Newtonian fluids gives predictions as accurate as any correlations available in the literature. There are at present insufficient reliable experimental or theoretical data available on particle drag in viscoelastic fluids and, in consequence, it is not yet possible to interpret and/or correlate experimental results in terms of measurable rheological properties.

10.4.2.4 *Particle terminal settling velocity*

When a solid particle settles under gravity in a stationary fluid, it undergoes an initial acceleration after which it attains its constant terminal settling velocity, u_∞. The terminal velocity is approached very rapidly in Newtonian and power law fluids. For example, a particle settling in creeping flow will reach u_∞ after a distance equivalent to only a few particle diameters. The velocity of a particle settling in a gravitational field will increase until the drag force becomes equal to the apparent weight of the particle (particle weight − buoyancy force), that is:

$$F = \left(\frac{\pi d_p^3}{6}\right)(\rho_p - \rho_L)g \tag{10.22}$$

and equating this with equation (10.7) gives:

$$C_D = \frac{4gd(s-1)}{3u_\infty^2} \tag{10.23}$$

where $s = \rho_p/\rho_L$. For a sphere settling in creeping flow in a Newtonian liquid, Stokes law leads to the following equation:

$$u_\infty = \frac{gd_p^2(\rho_p - \rho_L)}{18\mu} \tag{10.24}$$

For a power law liquid, in creeping flow (i.e., $Re_p < \sim 1$), equations (10.7), (10.13), and (10.22) lead to the following equation:

$$u_\infty\big|_{\mathrm{PL}} = \left[\frac{g d_\mathrm{p}^{n+1}(\rho_\mathrm{p}-\rho_\mathrm{L})}{18kZ(n)}\right]^{1/n} \tag{10.25}$$

Note that when $n = 1$, equation (10.25) reduces to equation (10.24), putting $k = \mu$, and $Z(n) = 1$. In a shear-thinning liquid, u_∞ shows a greater sensitivity to the particle diameter d_p and the solid–liquid density difference $(\rho_\mathrm{p} - \rho_\mathrm{L})$ than in a Newtonian liquid.

In general, to calculate u_∞ for a given sphere/fluid combination, it is necessary to determine C_D which is a function of Re_p and hence of u_∞. This difficulty can be circumvented by introducing the particle Archimedes number, Ar, which is independent of u_∞ and is defined as:

$$Ar = C_\mathrm{D} Re_\mathrm{p}^{2/(2-n)} = \frac{4}{3}\frac{g d_\mathrm{p}^{(2+n)/(2-n)}(\rho_\mathrm{p}-\rho_\mathrm{L})\rho_\mathrm{L}^{n/(2-n)}}{k^{2/(2-n)}} \tag{10.26}$$

Note that for $n = 1$, the above definition gives the Archimedes number for a sphere in a Newtonian liquid (with $k = \mu$) which is given by the following equation:

$$Ar = C_\mathrm{D} Re_\mathrm{p}^2 = \frac{4}{3}\frac{g d_\mathrm{p}^3(\rho_\mathrm{p}-\rho_\mathrm{L})\rho_\mathrm{L}}{\mu^2} \tag{10.27}$$

For a given sphere diameter and density, and power law liquid, Ar can be calculated using equation (10.26). The particle Reynolds number can then be expressed in terms of Ar and n as follows:

$$Re_\mathrm{p} = aAr^b \quad a = 0.1\times e^{0.51/n} - 0.73n;\ b = (0.954/n) - 0.16 \tag{10.28}$$

The above values were obtained from experimental data covering the ranges $0.4 \leqslant n < 1$, $1 \leqslant Re \leqslant 1000$, and $10 \leqslant Ar \leqslant 10^6$ subject to an average error of 14% and a maximum error of 21% (Lareo *et al.* 1997).

As drag outside creeping flow is only slightly affected by non-Newtonian characteristics, the use of correlations for u_∞ in Newtonian liquids leads to only marginally larger errors in power law liquids. It should be noted that in viscoplastic liquids, estimation of terminal velocity requires an iterative solution as the unknown u_∞ appears in all the groups involved (C_D, Re_p, Bi^*).

10.4.2.5 *Effects of particle shape on terminal settling velocity and drag*

Drag on particles is strongly influenced by their shape and orientation to the flow which must be specified before the drag force can be estimated. In consequence, the drag force on non-spherical particles is much more difficult to determine than for spheres, and often the effect of shape on particle settling must be determined experimentally. Experimental data for non-spherical particles are presented in the same way as for a sphere, that is, in the form of a drag curve representing $\log(C_\mathrm{D})$ versus $\log(Re_\mathrm{p})$. The particle Reynolds number for a non-spherical particle is based on d_V, the diameter of an equivalent sphere having the same volume as the non-spherical particle. A different curve is obtained for each particle shape

and for each orientation. For Newtonian liquids, data exist in the literature for a number of different shapes, for example, cylinders, plates, discs, etc. (Clift *et al*. 1978).

Spheroidal particles (oblates and prolates) have been studied in pseudo-plastic and dilatant liquids for Reynolds numbers up to 100 over the range $0.4 \leqslant n \leqslant 1.8$. For a given Reynolds number and aspect ratio (minor/major axis), the drag on an oblate particle is less than on a sphere of equal volume, whereas it is higher for a prolate particle. A summary of the relevant literature is given by Lareo *et al*. (1997) and Chhabra and Richardson (1999).

As observed for a sphere, in the creeping flow regime, the drag on a non-spherical particle in shear-thinning liquids is higher than in Newtonian liquids under otherwise identical conditions. As Re_p increases, the shear-thinning effect (i.e., the n effect) diminishes. In dilatant liquids, the drag is lower than in Newtonian liquids. Results concerning other particle shapes (cylinders, rectangular prisms, discs, cones) settling at their terminal velocity in power law media have been published, but no general correlation has emerged yet (Chhabra 1996). There is at present rather a paucity of data concerning the drag on non-spherical particles in viscoplastic and viscoelastic liquids.

The problem discussed above relates to the motion of a single isolated particle in an effectively infinite medium. The boundaries of the fluid container in which the particle is settling will also affect its terminal velocity. To characterise a multiple particle system, single particle behaviour should be understood, but most solid–liquid suspensions are of such a high solid fraction that single particle data are not usually sufficient. Such details are beyond the scope of this chapter, and the reader is referred to more specialised publications such as Chaabra (2006) and Lareo *et al*. (1997).

10.5 Scale-up of solid–liquid mixing

An important aspect in the design of mixing equipment is scale-up, which requires extrapolation of results from the laboratory or pilot scale to the industrial size, on the assumption that the *principle of similitude* is respected. This principle depends on three types of similarity: geometric similarity, kinematic similarity, and dynamic similarity, as discussed in Chapter 6. In stirred vessels, however, the principle of similitude can be difficult to implement due to a number of practical reasons. In an operation such as solid–liquid suspension, the size of the particles remains the same while the equipment is scaled-up. Furthermore, it is not always possible to have the large and small vessels geometrically similar, and in scaling up impellers, it may not be possible to maintain exact geometric similarity of blade thickness and impeller hub dimensions. Strictly speaking, geometric similarity extends to the actual surface roughnesses of the model and prototype, which must be in the same ratio as the rest of the linear dimensions. In many cases, the model roughness cannot be made small enough for complete similarity. Scale-up of mixing in non-Newtonian fluids has its own added difficulties as the apparent viscosity varies with shear rate. Changes in the apparent viscosity can shift the Reynolds number into the transitional or laminar flow regimes, which affect other dimensionless groups such as power number and pumping number. Most of the literature has dealt with Newtonian systems, whereas only limited design information is available for non-Newtonian systems.

Furthermore, even if geometric similarity is obtainable, dynamic similarity and kinematic similarity are usually not, so that the scale-up results are not always fully predictable. As in most engineering problems, the designer must rely on a considerable amount of judgement and experience.

In solid–liquid mixing, the objective of scale-up would be to determine the design and operating conditions necessary to maintain the same suspension quality at considerably different scales. Whilst general criteria do exist for the simpler categories of mixing problems, much less is known about the scale-up of solid–liquid mixing operations. A general criterion of the form:

$$ND^a = \text{constant} \tag{10.29}$$

has been proposed for complete off-bottom and homogeneous suspensions, where geometrical similarity can be assumed (Zlokarnik 1991; Tatterson 1994). Note that the scale-up parameter in equation (10.29) can be equally the impeller diameter D or the vessel diameter T.

In turbulent flow, the power number

$$Po = \frac{P}{\rho_L N^3 D^5} \tag{10.30}$$

is constant, being a function only of impeller design and vessel geometry, that is:

$$P \propto N^3 D^5 \tag{10.31}$$

and the power per unit volume is thus as follows:

$$\frac{P}{V} \propto \frac{N^3 D^5}{T^3} \propto N^3 D^2 \tag{10.32}$$

Equations (10.29) and (10.32) lead to:

$$\frac{P}{V} \propto D^{2-3a} \tag{10.33}$$

implying that on scale-up, the specific power consumption will increase for $a < 2/3$, decrease for $a > 2/3$, and remain unchanged for $a = 2/3$.

In particular, when $a = 1$, that is, when scaling up at constant impeller tip speed (πND = constant), there is much less specific power dissipation at the larger scale as $P/V \propto D^{-1}$. Scale-up at constant specific power, however, leads to a substantial increase in impeller tip speed as $\pi ND \propto D^{1/3}$, even though the impeller rotational speed N obviously reduces substantially. Note that the reduction in N on scale-up at constant P/V leads to longer mixing (or blending) times in larger vessels. Trying to maintain the same mixing time in the full-scale unit as in the pilot-scale vessel is usually impractical; however, a moderate increase in blending time in the larger vessel reduces the power requirement to a reasonable level. Such tradeoffs are often necessary in scaling up mixing equipment.

Zwietering's correlation [equation (10.2)] gives $N_{js} \propto D^{-0.85}$ which translates into:

$$\left(\frac{P}{V}\right)_{js} \propto D^{-0.55} \tag{10.34}$$

Table 10.3 Illustration of the dramatic effects of different scale-up rules.

Model parameters	Scale-up factor (*i.e.*, D_P/D_M or T_P/T_M)	Prototype parameters		
		P/V = constant	πND = constant	Re = constant
$\frac{P_P}{P_M}$ [a]	10	1,000	100	0.1
$\frac{(P/V)_P}{(P/V)_M}$	10	1	0.1	0.0001
$\frac{N_P}{N_M}$	10	0.215	0.1	0.01
$\frac{(\pi ND)_P}{(\pi ND)_M}$	10	2.15	1	0.1
$\frac{Re_P}{Re_M}$	10	21.5	10	1

[a] M = model; P = prototype.

implying a large reduction in power on scale-up. Scaling up at constant specific power input is a conservative approach but might lead to unnecessarily oversized equipment and, thus, uneconomic design.

Another scale-up criterion that is sometimes mentioned in the general mixing literature is that of constant impeller Reynolds number [equation (10.4)]. This rule leads to drastic reductions in specific power input ($P/V \propto D^{-4}$), impeller speed ($N \propto D^{-2}$), as well as impeller tip speed ($\pi ND \propto D^{-1}$). Such a rule appears to be unrealistic for most oper-ations and is usually not recommended (Wilkens *et al.* 2003). Note, however, that scaling up at either constant P/V or constant πND increases Re substantially.

Table 10.3 illustrates the dramatic effects of scale-up on power dissipation, impeller speed, impeller tip speed, and impeller Reynolds number, assuming geometric similarity is obeyed. The case considered highlights the difficulties in maintaining complete similarity as well as the impact that the choice of scale-up rule has on the full-scale unit.

Bourne and Hungerbuehler (1980) showed that a homogeneous suspension could be maintained in a continuous crystalliser at constant impeller tip speed, that is, $a = 1$. Later, Voit and Mersmann (1986) noted that the values of a reported in the literature ranged from 0.5 to 0.9.

Buurman *et al.* (1986) studied complete and homogeneous suspensions in a large vessel ($T = 4.26$ m). For complete suspension, they proposed constant specific power input as the scale-up criterion, that is, $N_{js} \propto D^{-2/3}$. They also attributed the differences in scale-up criteria for off-bottom suspension available in the literature, at least partly, to incorrect scaling of the impeller blade thickness. In a homogeneous suspension, the largest eddies, that is, fluid circulation, also play a role, as expected from the theory of turbulence. This means that on a large scale homogeneous suspension is attained at a lower specific power input.

Rieger *et al.* (1988) proposed scaling up weakly homogenous suspensions at constant P/V (i.e., $a = 2/3$) and highly homogeneous suspensions at constant impeller tip speed (i.e., $a = 1$). From work on the vertical distribution of solids in multiple radial or axial impeller systems, Magelli *et al.* (1990, 1991) and more recently Montante *et al.* (2003) arrived at a value of $a = 0.93$. Mak and Ruszkowski (1990) and Mak *et al.* (1997) suggested a value of $a = 2/3$, that is, constant specific power, for solids mixed by a PBT. Very

recently, Angst and Kraume (2006) obtained $a = 0.52–0.86$ from an experimental study, whereas Ochieng and Lewis (2006) suggested that suspensions with low solids loadings scale up at constant impeller tip speed, but for high solids loading (10%), turbulence intensity influences the solids suspension and the scale-up may be based on constant *P/V*.

It is evident from the above brief review of the literature that solid suspensions are difficult to scale up, as there are conflicting data and rules being reported. Though the differences in the values of *a* reviewed above might not seem substantial at first sight, they do lead to major differences in power consumption when considerable changes of scale are involved.

There is no one simple and consistent scale-up rule that can deliver the same suspension quality over a wide range of suspension properties, vessel geometries, and impeller types and sizes. The above results also seem to point to the conclusion that the scale-up methods used to predict N_{js} are not necessarily suited for predicting solids uniformity in the vessel. Much research is therefore needed to develop the science in this area. In the meantime, tackling the problem of scale-up will have to rely as much on experience as on existing scientific knowledge.

Furthermore, nearly all the work reported in the literature has been limited to systems with mono-sized, dense, small particles at low concentrations in Newtonian flows. Little has been done on large nearly-neutrally buoyant particles in viscous Newtonian or non-Newtonian fluids, as is the case in many food processing applications. Much less is known about the hydrodynamics and mixing of these systems. The materials to be mixed in these applications can be very important economically, and the cost of equipment for high-viscosity applications is higher than for low-viscosity ones because mixing equipment costs rise sharply with increasing viscosity. Whilst the above knowledge base can serve to provide broad guidelines for equipment design and operation, it is not immediately obvious, however, how much of it is directly applicable to these even more complex situations.

10.6 Damage to food particles in suspension

Another aspect of solid–liquid mixing in food processing that has also received little attention is the mechanical damage to food particles in suspension that may result from the stirring action of the impeller. It is possible that comminution or attrition of the particles might be such that the overall quality of the product is affected.

Attrition is the unwanted breakdown of particles within a process, mainly as a consequence of collisions with other particles or parts of the equipment, that is, impeller blades or vessel walls. Attrition can also result from intense shear in the carrier fluid. The hydrodynamic stress on particles in stirred vessels can be important. Damage due to hydrodynamic forces in stirred vessels, often loosely referred to as ‘shear effect’, can be of some significance in food applications where solids are particularly delicate, but this does not seem to have been addressed in the literature. In laminar flow, soft particles may be deformed and even damaged by large shear stresses in the same way that liquid droplets are deformed and broken. In turbulent flow, however, fluid–particle interactions are governed by the relative size of eddies and the particles. Eddies larger than a particle will tend to entrain it causing no significant damage to it. Eddies smaller than the particle will not be able to entrain it but will act on the particle surface possibly resulting in damage. Particles larger than Kolmogorov’s scale are affected by normal stresses resulting from turbulent velocity fluctuations. Particles smaller than Kolmogorov’s scale are affected by shear stress related to the local energy dissipation rate. Unfortunately, no rigorous description of the

complex turbulent hydrodynamics near a particle surface has been presented and it is, therefore, difficult to estimate shear stresses on particles.

These effects are also undesirable in agglomeration and crystallisation processes. When solids are merely suspended in a liquid, the size and surface area of the particles exposed to the liquid are fixed, as is the total volume of suspended solids. At high shear rates, however, agglomerates may be broken up, and with fragile or sensitive materials the particles themselves may be degraded, their diameter reduced, and new surface area created. This is especially important in fermentations and similar operations in which biological cells may be destroyed if the local shear rates in the vessel are too high. A lot of work has been reported on the damage caused to cells in liquid suspension in fermenters, but little has been done to quantify the effect of hydrodynamic forces on solid particles in suspension, and in particular, food particles.

In a rare contribution to this area of work, Wang *et al.* (2002) measured the damage caused to cooked potato during processing in a continuous scraped surface heat exchanger, which is similar in principle to a mechanically agitated vessel. The material was cut into 7 mm cubes and suspended in a CMC solution whose rheology was described by the power law model [equation (10.10)]. The particle concentration used was rather low at 3.6 particles per kg of liquid, however. Even then, it was shown that a severe reduction in particle size can occur when the particle tissue is soft (i.e., when the cooking time is high in the case of potatoes). The evidence suggested that particle damage was due primarily to particle–blade collisions. A higher liquid viscosity did not offer any protective effect to the particles. The degree of particle attrition was directly affected by the rotor speed, which determined the collision frequency, and particle residence time, which determined the total number of collisions experienced by each particle.

Much of the relevant work reported to date, however, has been in relation to crystallisation processes. The relevant mechanisms involved are abrasion, which is the removal of material much smaller than the particle, and fragmentation/breakage of a particle into smaller parts. Abrasion requires lower impact energy and tends to prevail in crystal suspensions (Mazzarotta 1992).

Crystallisation is widely used in food manufacture, for example, in the production of sugars such as sucrose and glucose, food additives such as salt, and in the processing of food products such as chocolate and ice cream. Crystals tend to have regular shapes, for example, cubic and tetragonal. Crystal shape is important because it affects other properties such as the angle of repose of stacked crystals and rate of dissolution. Crystal size uniformity is also important because a non-uniform crystal mixture is visually unattractive, the different sizes tend to segregate, and separating the mother liquor from the solids is more difficult. Attrition is the only source of new crystals that is independent of supersaturation. This hydrodynamic phenomenon has a significant effect on nucleation kinetics and hence on the crystal size distribution.

A good treatise on crystal attrition can be found in various works such as Fasoli and Conti (1973), Chianese *et al.* (1986), Shamlou *et al.* (1990), Synowiec *et al.* (1993), and Gahn and Mersmann (1995). Though a number of attrition rates have been defined, such as the number of abrasion fragments produced per abrading particle (Fasoli & Conti 1973; Nienow & Conti 1978; Synowiec *et al.* 1993), the mass-abrasion rate of the fragments (Chianese *et al.* 1986), and the initial rate of fragment generation (Shamlou *et al.* 1990), no generally accepted method for quantifying attrition has emerged. In addition to generating large amounts of small fragments, crystal attrition also affects their size distribution as well as their shape. The breakage functions commonly adopted to describe the product of comminution events are not applicable to attrition because fracture which leads to a bimodal size

distribution predominates (Kelly & Spottiswood 1982). Encouraging results were obtained by Mazzarotta (1992) using a model combining abrasion and fracture. However, information about the morphology of crystals which have been subjected to attrition has been limited to qualitative observations gleaned from photographs of the abraded crystals and fragments (Fasoli & Conti 1973; Conti & Nienow 1980).

Attrition due to particle interactions with the walls of the vessels is only significant when there are flow constrictions present, for example, when the impeller is installed close to a solid boundary such as when large *D/T* ratios are used, or when inserts are used. In the absence of such flow constrictions, at low solids concentrations, inter-particle interactions are rare and relatively weak, and most damage that occurs is due to particle collisions with the impeller blades.

The frequency of particle–impeller collisions, ω, is assumed to be proportional to: (i) the frequency f of particle passage through the impeller volume, represented by the impeller volumetric discharge divided by the vessel volume, $f = ND^3/V$; (ii) the probability p of collision during a passage, $p = Nu_\infty$; and (iii) the mean solids concentration in the vessel, $\bar{C}$ as shown below (Nienow 2000):

$$\omega \propto \frac{ND^3}{V} \times p \times \bar{C} \tag{10.35}$$

The amount of particle damage due to attrition is assumed to be proportional to the energy of impact, E, which in turn is assumed to be proportional to N^2D^2. For a given fluid–solid system, there is a minimum level of energy that is required at impact before any significant particle damage can occur. Beyond that level, the rate of particle attrition J is then given by the following equation (Nienow 2000):

$$J \propto \omega E \propto \frac{P}{V} N \tag{10.36}$$

The energy threshold for particle damage to occur needs to be assessed in a controlled experiment using appropriate mechanical testing equipment. Therefore, a higher power input and increasing agitation speed by the use of smaller *D/T* ratios, for example, will increase the rate of particle damage. Note, however, that as discussed in Section 10.5, N decreases on scale-up and hence particle damage would be expected to be lower in larger vessels. This implies that the use of large *D/T* ratios and minimum power input—for example, by using high-efficiency hydrofoil impellers (Figure 10.4)—would help to minimise particle damage. Conversely, in a crystallisation process it may be desirable to promote particle–impeller collisions, and in that case, the dissipation of higher power inputs using smaller impellers would be recommended.

In concentrated suspensions, inter-particle collisions would be more frequent and their effects on particle integrity would become predominant, again provided the impact energy levels are high enough. In that case, the rate of particle damage has been described as follows (Nienow 2000):

$$J \propto \bar{C}^2 \left(\frac{P}{V}\right)^{3/2} d_p^6 \tag{10.37}$$

Equation (10.37) suggests that the rate of particle attrition is highly sensitive to particle size and solids concentration. Therefore, concentrated systems with larger particles would generate a lot of attrition, provided the solids are soft enough or conversely the impact energies are high enough. Specific power input is again a key to controlling particle damage, as J is very sensitive to P/V in this case.

10.7 Fine particle slurries

Fine particles tend to form reasonably homogeneous suspensions and are usually treated as such. At high solid concentrations, particles under normal agitation conditions have low settling velocities compared to the liquid flow velocities. Under conditions of turbulent flow, particles are maintained in suspension by the eddies in the liquid. In general, such conditions tend to prevail in practice, unless the liquid is highly viscous as may be the case for food slurries. Concentrated suspensions often tend to exhibit a non-Newtonian behaviour, and they behave essentially as single-phase pseudo-plastic liquids. Existing models for describing them are based on the principles of continuum mechanics using an effective density and viscosity for the suspension.

Amongst the situations where non-Newtonian behaviour is most important is the suspension of polydisperse slurries. As the concentration of solids increases, the suspension more and more takes on the character of a shear-thinning (pseudo-plastic) fluid caused by the presence of a large amount of fine particles. Such a behaviour is often described by the power law model [equation (10.10)]. Typically, the suspension first becomes moderately shear thinning and as the concentration increases, this behaviour is enhanced, that is, the consistency index k steadily increases reflecting an increase in viscosity and the power law index n is reduced showing further departure from Newtonian behaviour. Above a certain concentration, the suspension becomes viscoplastic, that is, n becomes so small (typically at $n < 0.2$) that it exhibits an apparent yield stress like a Herschel–Bulkley fluid [equation (10.20)]. Now both k and τ_y increase with increasing solids concentration, a situation which is quite common. In certain cases, for example, starch suspensions, the slurries may exhibit dilatant behaviour and, contrary to a shear-thinning fluid, the apparent viscosity increases with the rate of shear. Transparent polymer solutions with this behaviour do not exist, and current industrial practice in this area is based entirely on trial and error, as there is little fundamental knowledge of the hydrodynamics of these systems and no rational rules to determine process parameters and equipment design.

The fact that these slurries tend to exhibit a non-Newtonian behaviour means that the detailed flow patterns of these systems can be difficult to predict. Even though these slurries are widely used, relatively little work has been done to understand how to mix them properly. The main reason for the lack of understanding of their behaviour is due to their opaque nature, as most techniques developed to characterise the mixing of fluids are optical (e.g., LDV and PIV) and so require translucent materials. In order to understand these fluids, it has been commonly assumed that knowledge of the rheology of the slurry enables the prediction of its behaviour. This of course assumes that the slurry behaves like a single-phase fluid of the same rheology, an assumption that is yet to be fully proven. Based on this assumption, conservative predictions can be made that allow processes and equipment to be designed, but further understanding is needed to enable a more rational design approach.

The rheological complexities of non-Newtonian slurries can lead to a variety of difficulties including most importantly changes in viscosity during processing. Shear-thinning slurries, for example, will be viscous to start with; then once the shear rate is increased, the

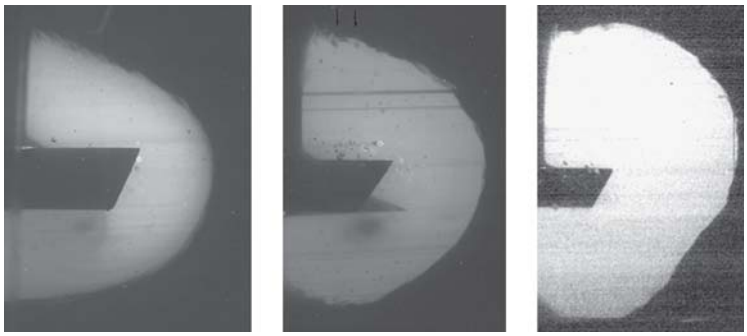

Fig. 10.7 Cavern visualisation by PLIF in an aqueous carbopol solution of Herschel–Bulkley rheology stirred by a down-pumping PBT: both cavern shape and size change as a function of Reynolds number; cavern size increases, and at higher *Re* values the cavern reaches the vessel wall and base and is confined to grow in the upper part of the vessel. [Reprinted from Adams and Barigou (2007) with permission from Elsevier.]

viscosity drops dramatically, as well as being different in different parts of the mixing tank. Shear-thickening slurries will behave in exactly the opposite manner. In these situations, it is difficult to determine the correct operating conditions and equipment set-up to achieve optimum ways of mixing.

In the mixing of viscoplastic slurries which exhibit an apparent yield stress, the impeller creates a 'cavern' within which liquid is in flow, but in the bulk where the shear stresses are below the yield stress, the fluid is stagnant, a phenomenon that can be disastrous for many mixing operations. Some work has been done on measuring the size of caverns in transparent yield stress fluids using 2D visualisation methods (Elson 1990). Nienow and Elson (1988) used x-rays in a shear-thickening slurry; this method only gave rough estimates of flow patterns, however. Recently, a planar laser-induced fluorescence (PLIF) technique and CFD were used to visualise and study caverns in transparent non-Newtonian fluids, as shown in Figure 10.7 (Adams & Barigou 2007). The PLIF technique also gave a measure of the rate of fluid mixing within such caverns, a problem not studied before.

Similarly, 'pseudo-caverns' are formed when other fluids are agitated such as shear-thinning fluids or even highly viscous Newtonian fluids, especially in the laminar and transitional flow regimes. Outside a pseudo-cavern, the fluid is in motion but the velocities are small. The presence of stagnant zones in viscous or non-Newtonian fluids is detrimental to mixing, heat and mass transfer and should be avoided. For a proper understanding and design of these processes, it is essential to establish the size of the cavern region as a function of fluid rheology and agitation conditions. This is a real industrial problem, but progress in this area has been hampered by the lack of techniques suitable for 3D flow visualisation in these complex fluids, which are usually opaque.

A number of theoretical cavern/pseudo-cavern models have been proposed based on the cylindrical, spherical, and toroidal shape, as shown in Figure 10.8. These have been recently reviewed and compared to CFD predictions and experimental PLIF measurements, with the toroidal shape model giving the better agreement in terms of shape and size for both caverns and pseudo-caverns (Adams & Barigou 2007). Fluid mixing inside caverns is relatively fast near the centre but very slow near the boundary, where the shear stress approaches the apparent yield stress. CFD predictions of cavern size and shape were very good at low Reynolds numbers in the laminar and transitional regimes but not at higher Reynolds numbers.

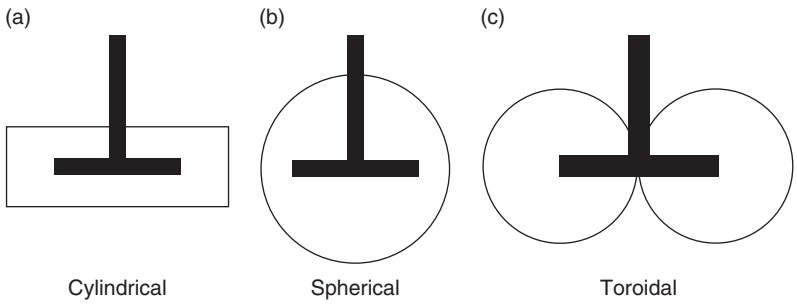

Fig. 10.8 Proposed model shapes of caverns and pseudo-caverns.

The cylindrical cavern model, although simplistic in terms of cavern shape representation, gave a good approximation to cavern size but only at low Reynolds numbers. The spherical cavern model of Amanullah *et al*. (1998) for a yield stress fluid did not fit the cavern shape well and overestimated the cavern size. This model was extended by Adams and Barigou (2007) to a toroidal cavern shape, giving a better agreement with experimental measurements.

The toroidal cavern model of Amanullah *et al*. (1998) agreed reasonably well with CFD simulations of pseudo-caverns formed in a power law fluid at low Reynolds numbers, where the pseudo-cavern is confined to a small region around the impeller. As the impeller speed is increased and flow moves further into the transitional regime, however, CFD predicts that the pseudo-cavern expands into the tank and adopts a much more complex shape than a toroid.

The main reason for the lack of understanding of the behaviour of these slurries is due to their opaque nature, as pointed out above. The novel PEPT technique described earlier has been recently used to study the 3D flow of industrial slurries inside a mechanically agitated vessel and, in particular, inside the cavern region formed around the impeller (Barigou *et al*. 2009). PEPT was successful in delineating the cavern region inside opaque industrial slurries exhibiting an apparent yield stress, as shown in Figure 10.9. The flow field inside the cavern is mainly tangential which suggests poor mixing but is also characterised by a complex toroidal motion. The radial and axial velocity components, even though small, seem to dictate the shape and size of the cavern. PEPT has proved to be a very powerful technique for studying these complex opaque systems in a quantitative way.

Nomenclature

a	exponent in equation (10.29)
Ar	Archimedes number
Bi	Bingham number
C	impeller off-bottom clearance (m)
C_D	drag coefficient
C_i	solids concentration in sample i ($kg\,m^{-3}$)
C_v	coefficient of variation
$\bar{C}$	mean solids concentration ($kg\,m^{-3}$)
d_p	particle diameter (m)
D	impeller diameter (m)

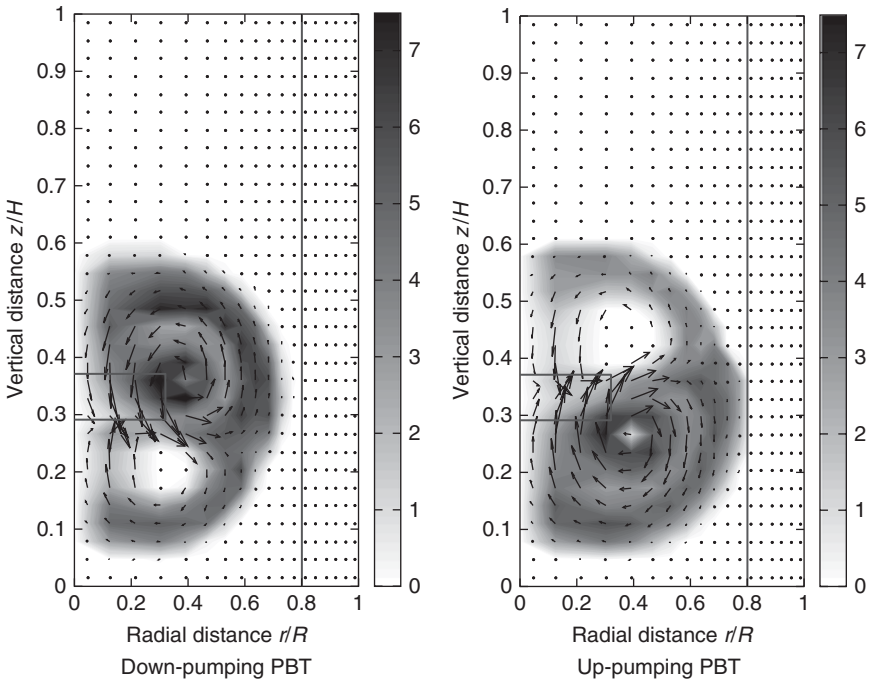

Fig. 10.9 PEPT tracer occupancy distribution delineating cavern region around a PBT in a Herschel–Bulkley type slurry: grey scale denotes azimuthally averaged occupancy and vectors denote azimuthally averaged *r*–*z* velocity. Occupancy is obtained by dividing the vessel volume into small cells and calculating the fraction of time spent by the tracer particle in each cell during the experiment. Within each cavern, there are toroidal zones of intensive tracer motion depicted by a high level of occupancy and blank areas which the PEPT tracer in this instance did not visit. These blank areas are not stagnant regions but zones of complex toroidal fluid motion.

F	drag force (N)
g	gravitational acceleration ($\mathrm{m\,s^{-2}}$)
H	liquid height in vessel (m)
J	rate of particle attrition [number/(volume × time)]
k	flow consistency index ($\mathrm{Pa\,s^{n}}$)
n	flow behaviour index
N	impeller speed ($\mathrm{s^{-1}}$)
N_{js}	minimum agitation speed for complete suspension ($\mathrm{s^{-1}}$)
P	power dissipation (W)
Po	power number
Re	impeller Reynolds number
Re_{B}	Bingham Reynolds number
Re_{p}	particle Reynolds number
S	shape factor
T	tank diameter (m)
u	particle slip velocity ($\mathrm{m\,s^{-1}}$)
u_{∞}	terminal settling velocity ($\mathrm{m\,s^{-1}}$)
V	volume of vessel contents ($\mathrm{m^3}$)
X	solids concentration by weight × 100
Z, $Z(n)$	correction factor

Greek symbols

$\Delta\rho$	solid–fluid density difference ($kg\,m^{-3}$)
ε	local rate of energy dissipation ($W\,kg^{-1}$)
η_B	plastic viscosity (Pa s)
$\dot{\gamma}$	shear rate (s^{-1})
λ	Kolmogorov length scale (m)
μ	dynamic viscosity (Pa s)
ν	kinematic viscosity ($m^2\,s^{-1}$)
ω	frequency of particle–impeller collisions (number/time)
ρ_L	fluid density ($kg\,m^{-3}$)
ρ_p	particle density ($kg\,m^{-3}$)
σ	standard deviation ($kg\,m^{-3}$)
τ	shear stress (Pa)
τ_y	yield stress (Pa)

References

Adams, L. & Barigou, M. (2007). CFD analysis of caverns and pseudo-caverns developed during mixing of non-Newtonian fluids.*Chemical Engineering Research and Design*, **85**, 598–604.

Amanullah, A., Hjorth, S.A. & Nienow, A.W. (1998). A new mathematical model to predict cavern diameters in highly shear thinning power law liquids using axial flow impellers. *Chemical Engineering Science*, **53**, 455–469.

Angst, R. & Kraume, M. (2006). Experimental investigations of stirred solid–liquid systems in three different scales: particle distribution and power consumption. *Chemical Engineering Science*, **61**, 2864–2870.

Atapattu, D.D., Chhabra, R.P. & Uhlherr, P.H.T. (1995). Creeping sphere motion in Herschel–Bulkley fluids: flow field and drag. *Journal of Non-Newtonian Fluid Mechanics*, **59**, 245–265.

Atiemo-Obeng, V.A., Penney, W.R. & Armenante, P. (2004). Solid–liquid mixing. In: *Handbook of Industrial Mixing* (eds E.L. Paul, V.A. Atiemo-Obeng & S.M. Kresta), Chapter 10. John Wiley, New Jersey, pp. 543–584.

Aubin, J., Mavros, P., Fletcher, D.F., Bertrand, J. & Xuereb, C. (2001). Effect of axial agitator configuration (up-pumping, down-pumping, reverse rotation) on flow patterns generated in stirred vessels.*Chemical Engineering Research and Design*, **79**, 845–856.

Baldi, G., Conti, R. & Alaria, E. (1978). Complete suspension of particles in mechanically agitated vessels. *Chemical Engineering Science*, **33**, 21–25.

Barigou, M. (2004). Particle tracking in opaque mixing systems: an overview of the capabilities of PET and PEPT.*Chemical Engineering Research and Design*, **82**, 1258–1267.

Barigou, M., Fairhurst, P.G., Fryer, P.J. & Pain, J.P. (2003). Concentric flow regime of solid–liquid food suspensions: theory and experiment. *Chemical Engineering Science*, **58**, 1671–1686.

Barigou, M., Chiti, F., Pianko-Oprych, P., *et al*. (2009). Using positron emission particle tracking (PEPT) to study mixing in stirred vessels: validation and tackling unsolved problems in opaque systems. *Journal of Chemical Engineering of Japan*, in press.

Barresi, A. & Baldi, G. (1987). Solid dispersion in an agitated vessel. *Chemical Engineering Science*, **42**, 2949–2956.

Bourne, J.R. & Hungerbuehler, K. (1980). An experimental study of the scale-up of a well-stirred crystallizer. *Transactions of the Institute of the Chemical Engineers*, **58**, 51–58.

Bourne, J.R. & Zabelka, M. (1980). The influence of gradual classification on continuous crystallisation. *Chemical Engineering Science*, **35**, 533–542.

Brujes, L., Legrand, J. & Carnelle, G. (1998). Complete suspension of microcapsules in baffled and unbaffled stirred tanks. *Chemical Engineering and Technology*, **21**, 735–744.

Brunazzi, E., Gallettii, C., Paglianti, A. & Pintus, S. (2004). An impedance probe for the measurements of flow characteristics and mixing properties in stirred slurry reactors. *Chemical Engineering Research and Design*, **82**, 1250–1257.

Buurman, C., Resoort, G. & Plaschkes, A. (1986). Scaling-up rules for solid suspension in stirred vessels. *Chemical Engineering Science*, **41**, 2865–2871.

Chhabra, R.P. (1990). Motion of spheres in power law (viscoinelastic) fluids at intermediate Reynolds numbers: a unified approach. *Chemical Engineering and Processing*, **28**, 89–94.

Chhabra, R.P. (1996). Hydrodynamics of non-spherical particles in non-Newtonian fluids. In: *Handbook of Applied Polymer Processing Technology* (eds N.P. Cheremisinoff & P.N. Cheremisinoff), Chapter 1. Marcel-Dekker, New York, pp. 1–46.

Chhabra, R.P. (2006). *Bubbles, Drops and Particles in Non-Newtonian fluids*, 2nd edn. CRC Press, Boca Raton, FL.

Chhabra, R.P. & Richardson, J.F. (1999). *Non-Newtonian Flow in the Process Industries: Fundamentals and Engineering Applications.* Butterworth-Heinemann, Oxford, UK.

Chianese, A., Di Cave, S. & Mazzarotta, B. (1986). Secondary nucleation by abrasion of potassium sulphate, *Proceedings of the World Congress of Chemical Engineering*, Vol. 11, Tokyo, Japan, 21–25 September, p. 937.

Clift, R., Grace, J. & Weber, M.E. (1978). *Bubbles, Drops and Particles*. Academic Press, New York.

Conti, R. & Nienow, A.W. (1980). Particle abrasion at high solids concentration in stirred vessels-II, *Chemical Engineering Science*, **35**, 543–547.

Elson T.P. (1990). The growth of caverns formed around rotating impellers during the mixing of a yield stress fluid. *Chemical Engineering Communications*, **96**, 303–319.

Fasoli, U. & Conti, R. (1973). Crystal breakage in a mixed suspension crystallizer. *Kristall Technik*, **8**, 931–946.

Gahn, C. & Mersmann, A. (1995). The brittleness of substances crystallized in industrial processes, *Powder Technology*, **85**, 71–81.

Graham, D.I. & Jones, T.E.R. (1994). Settling and transport of spherical particles in power-law fluids at finite Reynolds number. *Journal of Non-Newtonian Fluid Mechanics*, **54**, 465–488.

Guerci, D., Conti, R. & Sicardi, S. (1986). *Proceeding of the International Colloquium on Mechanical Agitation*, ENSIGC, Toulouse, France, pp. 3–8 to 3–24.

Guida, A., Fan, X., Parker, D.J., Nienow, A.W. & Barigou, M. (2009). Positron Emission Particle Tracking in a mechanically agitated solid-liquid suspension of coarse particles. *Chemical Engineering Research and Design*, **87**, 421–429.

Ibrahim, S.B. & Nienow, A.W. (1994). The effect of viscosity on mixing pattern and solid suspension in stirred vessels, *Proceeding of the 8th European Conference on Mixing*, *IChemE Symposium Series*, **136**, 25–32.

Kelly, E. G. & Spottiswood, D.J. (1982). *Introduction to Mineral Processing.* Wiley, New York, pp. 113–123.

Kolmogorov, A. (1941a). Dissipation of energy in the locally isotropic turbulence. *Comptes Rendus de l'Académie des Sciences de l'URSS*, **32**, 16–18.

Kolmogorov, A. (1941b). The local structure of turbulence in incompressible viscous fluid for very large Reynolds' numbers. *Comptes Rendus de l'Académie des Sciences de l'URSS*, **30**, 301–305.

Lareo, C., Fryer, P.J. & Barigou, M. (1997). The fluid mechanics of two-phase solid–liquid food flows. *Food and Bioproducts Processing*, **75**, 73–105.

Magelli, F., Fajner, D., Nocentini, M. & Pasquali, G. (1990). Solid distribution in vessels stirred with multiple impellers. *Chemical Engineering Science*, **45**, 615–625.

Magelli, F., Fajner, D., Nocentini, M., Pasquali, G., Ditl, P. & Marisko, V. (1991). Solids concentration distribution in slurry reactors stirred with multiple axial impellers. *Chemical Engineering and Processing*, **29**, 27–32.

Mak, A.T.C. & Ruszkowski, S.W. (1990). Scaling-up of solids distribution in stirred vessels. *IChemE Symposium Series*, No. 121, pp. 379–395.

Mak, A.T.C., Yang, S. & Ozcan-Taskin N.G. (1997). The effect of scale on the suspension and distribution of solids in stirred vessels, *9th European Conference on Mixing*, Paris, March 1997 [*Récents Progrès en Génie des Procédés*, Lavoisier, Paris, Vol. 11, pp. 97–104].

Mann, R., Stanley, S., Vlaev, D. & Wabo, E. (2001). Augmented-reality visualization of fluid mixing in stirred chemical reactors using electrical resistance tomography. *Journal of Electronic Imaging*, **10**, 620–629.

Mazzarotta, B. (1992). Abrasion and breakage phenomena in agitated crystal suspensions. *Chemical Engineering Science*, **47**(12), 3105–3111.

Montante, G., Micale, G., Magelli, F. & Brucato, A. (2001). Experiments and CFD predictions of solid particle distribution in a vessel agitated with four pitched blade turbines.*Chemical Engineering Research and Design*, **79**, 1005–1010.

Montante, G., Pinelli, D. & Magelli, F. (2002). Diagnosis of solids distribution in vessels stirred with multiple PBTs and comparison of two modelling approaches. *The Canadian Journal of Chemical Engineering*, **80**, 665–673.

Montante, G., Pinelli, D. & Magelli, F. (2003). Scale-up criteria for the solids distribution in slurry reactors stirred with multiple impellers. *Chemical Engineering Science*, **58**, 5363–5372.

Nasr-El-Din, H.A., MacTaggart, R.S. & Masliyah, J.H. (1996). Local solids concentration measurement in a slurry mixing tank. *Chemical Engineering Science*, **51**, 1209–1220.

Nienow, A.W. (1968). Suspension of solid particles in turbine-agitated baffled system. *Chemical Engineering Science*, **23**, 1453–1459.

Nienow, A.W. (1999). The versatility of up-pumping, wide-blade hydrofoil agitators, *Proceedings of the 3rd International Symposium on Mixing in Industrial Processes*, Osaka, Japan, 19–22 September, pp. 173–180.

Nienow, A.W. (2000). The suspension of solid particles. In: *Mixing in the Process Industries* (eds N. Harnby, M.F. Edwards & A.W. Nienow), Chapter 16, 2nd edn, Butterworth-Heinemann, Oxford, pp. 364–393.

Nienow, A.W. & Conti, R. (1978). Particle abrasion at high solids concentration in stirred vessels. *Chemical Engineering Science*, **33**, 1077–1086.

Nienow, A.W. & Elson T.P. (1988). Aspects of mixing in rheologically complex fluids. *Chemical Engineering Research and Design*, **66**, 5–15.

Ochieng, A. & Lewis, A.E. (2006). Nickel solids concentration distribution in a stirred tank. *Minerals Engineering*, **19**, 180–189.

Oldshue, J.Y. (1983). Fluid mixing technology and practice. *Chemical Engineering*, **90**, 82–108.

Parker, D.J., Forster, R.N., Fowles, P. & Takhar, P.S. (2002). Positron emission particle tracking using the new Birmingham positron camera. *Nuclear Instruments and Methods in Physics Research. Section A*, **477**, 540–545.

Pianko-Oprych, P., Adams, L., Nienow, A.W. & Barigou, M. (2006). CFD simulation of solid–liquid suspension in Newtonian and power law liquids, *Proceedings of the 12th European Conference on Mixing*, Bologna, Italy, 27–30 June, pp. 503–510.

Pianko-Oprych, P., Nienow, A.W. & Barigou, M. (2009). Positron Emission Particle Tracking (PEPT) compared to Particle Image Velocimetry (PIV) for studying the flow generated by a pitched-blade turbine in single phase and multi-phase systems. *Chemical Engineering Science*, in press.

Rao, K.S.M.S.R., Rewattkar, V.B. & Joshi, J.B. (1988). Critical impeller speed for solid suspension in mechanically agitated contactors. *AIChE Journal*, **34**, 1332–1340.

Rieger, F., Ditl, P. & Havelkova, O. (1988). Suspension of solid particles – concentration profiles and particle layer on the vessel bottom, *Proceedings of the 6th European Conference on Mixing*, Pavia, Italy. BHRA, Cranfield, UK, pp. 251–258.

Shamlou, P.A. (1993). Suspension of particles in liquids in stirred vessels. In: *Processing of Solid–Liquid Suspensions* (ed. P.A. Shamlou). Butterworth-Heinemann, Oxford, UK, pp. 273–286.

Shamlou, P.A., Jones, A.G. & Djamarani, K. (1990). Hydrodynamics of secondary nucleation in suspension crystallization. *Chemical Engineering Science*, **45**, 1405–1416.

Synowiec, P., Jones, A.G. & Shamlou, P.A. (1993). Crystal break-up in dilute turbulently agitated suspensions. *Chemical Engineering Science*, **48**, 3485–3495.

Tatterson, G.B. (1994). *Scale-up and Design of Industrial Mixing Processes.* McGraw-Hill, New York.

Voit, H. & Mersmann, A.B. (1986). General statement for the minimum stirrer speed during suspension. *German Chemical Engineering*, **9**, 101–106.

Wang, Y.Y., Russell, A.B. & Stanley, R.A. (2002). Mechanical damage to food particles during processing in a scraped surface heat exchanger. *Food and Bioproducts Processing*, **80**, 3–11.

Wilkens, R.J., Henry, C. & Gates, L.E. (2003). How to scale-up mixing processes in non-Newtonian fluids. *Chemical Engineering Progress*, **99**, 44–52.

Yamazaki, H., Tojo, K. & Miyanami, K. (1986). Concentration profiles of solids suspended in a stirred tank. *Powder Technology*, **48**, 205–216.

Zlokarnik, M. (1991). *Dimensional Analysis and Scale-up in Chemical Engineering.* Springer Verlag, Berlin.

Zlokarnik, M. (2001). *Stirring: Theory and Practice.* Wiley-VCH, Weinheim, Germany.

Zwietering, N.TH. (1958). Suspending of solid particles in liquid by agitators. *Chemical Engineering Science*, **8**, 244–253.

11 Gas–liquid mixing

J.K. Sahu and Keshavan Niranjan

11.1 Introduction

Food materials are multi-components and invariably, multi-phase systems; thus, mixing occurs in innumerable instances. Mixing is one of the most commonly encountered unit operations in food industry. Despite being so, it would not be inaccurate to suggest that mixing mechanisms, especially those operating within food systems, are least understood. A wide variety of food mixers are now available with equally wide ranging capabilities. A significant proportion of current research efforts in food and pharmaceutical sectors is directed toward the development of new and novel mixing devices for food and pharmaceutical materials. A glance at some of the recent issues of food abstracts reveals that several new mixers with special design feathers continue to be developed and patented. Although these devices are undoubtedly effective for many applications, it is extremely difficult to decipher and analyze their action on food materials, partly because of the complex properties of food systems that can themselves vary during mixing. As a result, developments in mathematical modeling of food-mixing processes are meager, if existent. Establishment of procedures for proper design and scale-up are lacking, and it is virtually impossible to devise a relationship between mixing conditions and mixing quality. This chapter deals with characteristics of food mixing in general, objectives and mechanics of gas–liquid mixing, dynamics and size distributions of bubbles in mixing, equipment designs and ultrasound in gas dispersions and applications in food aeration.

11.2 Gas–liquid dispersion operations

In suspending solids, the size and the surface area of the solid particles exposed to the liquid are fixed, as is the total volume of suspended solids. In gas–liquid or liquid–liquid dispersion operations, by contrast, the size of the bubbles or drops and the total interfacial area between the dispersed and continuous phases vary with conditions and degree of agitation. New area must constantly be created against the force of the interfacial tension. Drops and bubbles are continually coalescing and being re-dispersed. In most gas dispersion operations, bubbles rise through the liquid pool and escape from the surface and must be replaced by new ones.

11.2.1 Characteristics of dispersed phase—mean diameter

Despite these variations, a basic relationship exists between the hold-up ϕ (volume fraction of dispersed phase in the system), the interfacial area 'a' per unit volume and the bubble

or drop diameter D_p. If the total volume of the dispersion is taken as unity, the volume of dispersed phase, by definition, is ϕ. If all the drops or bubbles were spheres of diameter D_p, their total volume would be:

$$\frac{\pi N D_p^3}{6} = \phi \tag{11.1}$$

where N is the number of drops or bubbles. The total surface area of the drops or bubbles in this volume would be as shown below.

$$\pi N D_p^2 = a \tag{11.2}$$

Dividing equation (11.1) by equation (11.2) and rearranging, we get the following equation.

$$D_p = \frac{6\phi}{a} \tag{11.3}$$

In actual practice, the drops or bubbles differ in size and are not spherical. However, for a given value of 'ϕ' and 'a', an equivalent average diameter D_s can be defined similar to equation (11.3) as follows.

$$D_s = \frac{6\phi}{a} \tag{11.4}$$

Diameter D_s in equation (11.4) is also known as the volume surface mean diameter or Sauter mean diameter.

11.2.2 Gas dispersion—bubble behavior

In a quiescent liquid, a single bubble arising from a submerged circular orifice will be a sphere if the flow rate is small. Under these conditions, the bubble's diameter D_p can be calculated as follows, by equating the net buoyant force on the bubble to the opposing drag force at the edge of the orifice. The net buoyant force, acting upward, is:

$$F_b - F_g = \frac{g\pi D_p^3}{g_c 6}(\rho_L - \rho_V) \tag{11.5}$$

where g ($m\,s^{-2}$) is the gravitational acceleration, g_c ($m\,s^{-2}$) is the Newton's law proportionality factor, ρ_L ($kg\,m^{-3}$) is the density of liquid, ρ_V ($kg\,m^{-3}$) is the density of vapor, F_b (N) is the total buoyant force and F_g (N) is the force of gravity.

The drag force F_D (N) is given by:

$$F_D = \pi D_0 \sigma \tag{11.6}$$

where D_O (m) is the orifice diameter and σ (dyn cm^{-1}) is the interfacial tension.

When the bubble becomes large enough, then drag force is no longer strong enough to keep the bubble attached to the edge of the orifice; at this point, the opposing forces become equal, and the bubble is detached from the orifice. The bubble diameter D_p can be found out by combining equations (11.5) and (11.6), and solving for D_p, we get the following equation.

$$D_p = \left[\frac{6D_0\sigma g_c}{g(\rho_L - \rho_V)}\right]^{1/3} \tag{11.7}$$

At very low flow rates, the bubbles formed are slightly smaller than predicted by equation (11.7) because some of the gas stays behind when the bubbles leave. At higher flow rates, D_p is greater than the predicted values because of additional gas that enters during separation of bubble from the orifice. At still higher rates, the gas stream appears to be at continuous jet, which actually consists of large closely spaced irregular bubbles and disintegrates into a cloud of smaller bubbles of few inches above the orifice. In stirred tanks or unstirred bubble columns, the average bubble size actually depends on the superficial velocity in the equipment and on the power dissipation rather than the orifice size of the perforated pipe.

Bubbles change in shape from spherical to ellipsoidal to lens-shaped, as their diameter increases. Larger bubbles often rise in spiral paths at terminal velocities that are almost constant and independent of their size.

11.2.3 Gas dispersion in agitated vessels

Gas is normally fed to a processing vessel through the open end of a submerged pipe, through a sparger, or through a porous ceramic or metal plate. Sometimes the gas, by itself, provides sufficient agitation for the liquid; more commonly, a motor-driven turbine impeller is used to disperse the gases and circulate the liquid and bubbles through the vessel. Figure 11.1 shows the schematic diagram of a turbine impeller commonly used in food industry. The typical geometrical proportions of the impeller are given below.

$$\frac{D_a}{D_t} = \frac{1}{3}, \quad \frac{H}{D_t} = 1, \quad \frac{J}{D_t} = \frac{1}{12} \tag{11.8}$$

$$\frac{E}{D_t} = \frac{1}{3}, \quad \frac{W}{D_a} = \frac{1}{5}, \quad \frac{L}{D_a} = \frac{1}{4} \tag{11.9}$$

For low gas hold-up ($\phi < 0.15$), the following dimensionless equations are available for gas dispersion in pure liquids by a six-blade turbine impeller. The average bubble diameter D_s in millimeters is given by:

$$D_s = 4.15\frac{(\sigma g_c)^{0.6}}{(Pg_c/V)^{0.4}\sigma_L^{0.2}}\phi^{0.5} + 0.9 \tag{11.10}$$

where V (m^3) is the volume of the gas, σ (dyn cm^{-1}) is the interfacial tension, σ_L (kg m^{-3}) is the density of liquid in gas–liquid dispersion and P (kW) is the power.

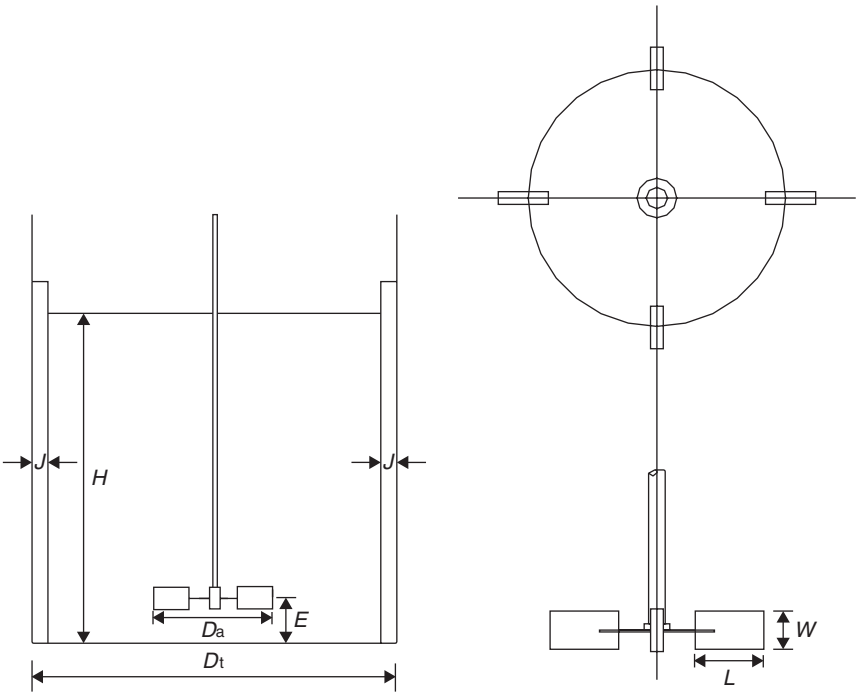

Fig. 11.1 Measurements of turbine. [Rushton *et al.* (1950).]

The average bubble diameter does not change with stirrer speed and is usually in the range of 2–5 mm. Smaller bubbles are formed in the high shear region near the tip of the impeller, but they collapse rapidly, and the average size is determined by the balance between coalescence and break-up in the rest of the tank. Theory for turbulent break-up of drops indicates that the size should vary with the group $(\sigma g_c)^{0.6}/(Pg_c/V)^{0.4}\sigma_L{}^{0.2}$, but the other terms in equation (11.10) were determined empirically. The term $\phi^{0.5}$ reflects the importance of bubble coalescence, which is more frequent at high gas hold-up.

The interfacial area can be calculated from the average bubble size D_p and the hold-up ϕ, as follows:

$$a = 1.44\frac{(Pg_c/V)^{0.4}\sigma_L^{0.2}}{(\sigma g_c)^{0.6}}\left(\frac{V_s}{u_t}\right)^{1/2} \tag{11.11}$$

where, a is the interfacial area (m^2), V_s ($m\,s^{-1}$) is the superficial velocity of gas (volumetric gas feed rate divided by the cross-sectional area of the vessel) and u_t ($m\,s^{-1}$) is the bubble rise velocity in stagnant liquid.

Equation (11.11) underestimates the area in mixing vessels operated at high impeller numbers, because additional gas is drawn into the liquid by surface aeration. Combining equations (11.7), (11.10) and (11.11) leads to the following dimensional equation for the gas hold-up.

$$\phi = \left(\frac{V_s\phi}{u_t}\right)^{1/2} + 0.216\frac{(Pg_c/V)^{0.4}\sigma_L^{0.2}}{(\sigma g_c)^{0.6}}\left(\frac{V_s}{u_t}\right)^{1/2} \tag{11.12}$$

In equations (11.10)–(11.12), all quantities involving the dimension of length are in millimeters.

The terminal velocity in equations (11.11) and (11.12) does not change much with diameter for bubbles larger than 1 mm, and a value of $0.2\,\mathrm{ms}^{-1}$ can be used for gases in water or similar pure liquids. For air bubbles in electrolyte solutions, coalescence is greatly retarded and the average bubble size can be much less than in pure water, with corresponding increases in interfacial area and gas hold-up.

11.3 Power input to turbine dispersers

An important consideration in design of an agitated vessel is the power required to drive the impeller. When the flow of the tank is turbulent, the power requirement can be estimated from a dimension power number *Po* defined by:

$$P_o = \frac{P g_c}{n^3 D_a^5 \rho_L} \tag{11.13}$$

where P (kw) is the power, n ($\mathrm{rev\,s}^{-1}$) is the rotational speed, D_a (m) is the diameter of the impeller and σ_L ($\mathrm{kg\,m}^{-3}$) is the density of liquid in gas–liquid dispersion.

The power consumed by a turbine impeller dispersing a gas is less than that indicated by equation (11.13) for agitating just liquids. The ratio of the power when gas is present to that for the liquid alone depends mainly on the superficial gas velocity and to some extent on the stirrer speed, tank size, impeller diameter and properties of the liquid.

The study of Dickey (1981) covers the higher range of gas velocities, and in this region the relative power generally decreases with increasing stirrer speed as well as with increasing gas velocity. This work and some of others show that P_g varies with about 2.1–2.9 power of the stirrer speed as compared to 3.0 power for liquids. The exponent for stirrer speed depends on gas velocity and other variables and no simple correlation is available. In the region of high gas velocities, P_g/P_o also depends on the ratio of impeller diameter to tank size. For $D_a/D_t = 0.4$, the values of P_g/P_o are lower by about 0.03–0.10 than those for $P_g/P_o = 0.33$. The main effect of using a larger impeller is that greater volumes of gas can be dispersed at a given stirrer speed.

Data for relative power consumption have often been presented as a function of a dimensionless aeration number $N_{ae}=q_g/nD_a{}^3$, where q_g ($\mathrm{m^3\,s^{-1}}$) is the total gas flow and ND_a^3 is a measure of the flow rate of liquid from the impeller. When N_{ae} is increased by increasing q_g, P_g/P_o decreases. However, when N_{ae} is increased by decreasing n, P_g/P_o generally increases (high-velocity region) or remains unchanged (low-velocity region).

The decrease in power with gassing is not just an effect of the lower average density of the gas–liquid dispersion, as the gas hold-up ϕ is generally 10% or less when P_g/P_o is reduced to 0.5. The decrease in power is associated with the formation of gas pockets behind the turbine blades (van't Riet & Smith 1973). Bubbles are captured in the centrifugal field of vortices that form behind the horizontal edges of the blades, and coalescence leads to large cavities that interface with normal liquid flow.

The change in power dissipation with gassing must be allowed for in the design of large units. An agitator drive chosen to handle the torque for a gassed system could be overloaded if the system has to operate occasionally with no gas flow, and a dual-speed drive might be needed. Also, a good performance sometimes requires constant power dissipation per unit volume, and scaled-up may lead to different values of V_s and P_g/P_o.

11.4 Gas handling capacity and loading of turbine impeller

If the gas throughput to a turbine-agitated vessel is progressively increased, the impeller eventually floods and can no longer disperse the gas effectively. The flooding point is not as distinct a transition as in a packed column, and various criteria for flooding have been proposed. One definition of flooding based on visual inspection is when most of the bubbles rise vertically between the turbine blades rather than being dispersed radially from the tips of the blades (Dickey 1981). The critical gas velocity for this transition $V_{s.c}$ was found to be proportional to the power per unit volume dissipated by the stirrer with a slight effect of tank size. Using data from tanks of 1.54 and 0.29 m diameter, and velocities up to 75mm s^{-1}, the following dimensional equation was obtained:

$$V_{s.c} = 0.144\left(\frac{P_g}{V}\right)\left(\frac{D_t}{1.5}\right)^{0.17} \tag{11.14}$$

where P_g/V is in watts per meter cube, D_t is in meters and $V_{s.c}$ is in millimeter per second. The effect of D_t is somewhat uncertain as it is based only on two sizes, and for a conservative scale-up, this factor could be ignored. Of course, conditions close to flooding may not be optimum for mass transfer, as bubbles coalescencing in the regions away from the impeller could greatly reduce the surface area.

11.5 Bubbles in foods

The presence of bubbles in a number of food products such as bread, champagne, ice cream and beer has dominated the perception of product quality. The inclusion of bubbles in foods permits the creation of very novel structures, while offering lighter alternatives in terms of calories. Manufacturers generally find that most products manage to gain a positive market image by highlighting bubbles. It is generally recognized that the mechanisms governing the formation and stability of such structures are very complicated, because the recipes often contain a number of ingredients that undergo very complex interactions during processing as well as storage. At the same time, there is also recognition of the fact that these complex interactions between ingredients have not been adequately researched. A significant body of published information exists on the formation of porous structures in bread and their relation to the processes adopted to mix the dough (Chiotellis & Campbell 2003; Martin *et al.* 2004). However, such studies in relation to the whole range of other bubble-containing food products such as cakes, creams in biscuits, ice cream and so on, are very sketchy.

11.6 Methods for mixing gas in liquid

11.6.1 Mixing by mechanical agitation under positive pressure

Beating a material to induce air entrapment and produce a foam is a relatively common process. Beating machines, comprised of a mixing bowl and a motor-driven whisker, are generally used for the purpose. The mechanical energy generated within the system by impeller rotation results in the dispersion of gas bubbles. Larger air bubbles are initially incorporated

from the head space, and their sizes diminish as agitation proceeds (Prins 1988). Air can be incorporated by this process into a range of liquid foods having different viscosities.

Mixing operations in food industry can be carried out batchwise or continuously. When whipping occurs in an open bowl by a rotating whisk, the amount of liquid (or continuous phase) is fixed, but air supply is unlimited. In this case, the amount of air taken up by the material is related to the apparatus geometry and the physicochemical properties of the material (Prins 1988). Air content and bubble size distribution (BSD) of the dispersion at any given moment during aeration will depend on the balance between the rates of entrainment and disengagement of gas between the headspace and continuous phase (Campbell & Mougeot 1999; Massey *et al.* 2001). Headspace pressure and whisk speed are important process parameters in such mechanically agitated processes. The whisk speed must be kept above the minimum speed for air entrainment and below values that cause the destruction of structure. Rolling vortices of liquid formed on the surface entrain gas and the bubbles formed are captured into the bulk by liquid circulation. Increasing headspace pressure will often reduce the time taken to achieve a set level of air incorporation (Cheng 1992). Continuous processes are being increasingly employed by the food industry for forming bubble-containing structures in soft solids, as well as for dissolving gases such as carbon dioxide in liquids and syrups to produce beverages. In most processes, the gas dissolution occurs under pressure and the bubbly structure is formed when excess dissolved gas desorbs upon pressure release. Mass transfer principles, therefore, play an important role in structure formation. Carbonated beverages are produced in specific mixing equipment called carbonators. This equipment allows close contact between carbon dioxide and the liquid. The pressure of the system, gas solubility, time and area of contact, as well as the presence of other gases in the mixture are the main factors determining the degree of carbonation. A typical carbonator is shown in Figure 11.2. It is noteworthy that the carbon dioxide can either be dissolved directly into concentrated sugar syrup, or be dissolved in water prior to syrup addition (Mitchell 1990). Ice cream is normally aerated during freezing, either by injecting air under pressure in a continuous freezer or by blending air pockets during freezing in a batch process. The shearing process that accompanies freezing reduces the size of the larger air bubbles, just as the fat globules coalesce. The type of freezer and the operating conditions employed will ultimately influence dispersion properties: generally, continuous operation generates smaller air bubbles than batch processes (Goff & Clarke 2004).

11.6.2 Mixing by mechanical agitation under vacuum

This process is based on applying vacuum to a liquid or a continuous phase in order to allow dissolved gases to come out of solution (Wolfe 1995). The foam formed is normally cooled to generate a solidified structure in which the bubbles are trapped. In the case of confectionery mixes, air is injected into the mix to reduce the dispersion-specific gravity. Individual pieces are then shaped and directed to the vacuum tunnel held at around 0.03 atm. Some bubbles may well be lost during shaping. The remaining bubbles expand to cause a 6–10 fold increase in the volume of the shaped product (Jones 1995).

11.6.3 Steam-induced mixing

Steam-induced mixing is applied to a range of food products. An example is the application of dry heat inside an oven to bread dough or cake batter. A porous structure is formed that is largely influenced by steam generation, although thermal expansion of other gases and CO_2 desorption also play a critical role (Campbell & Mougeot 1999). The structure

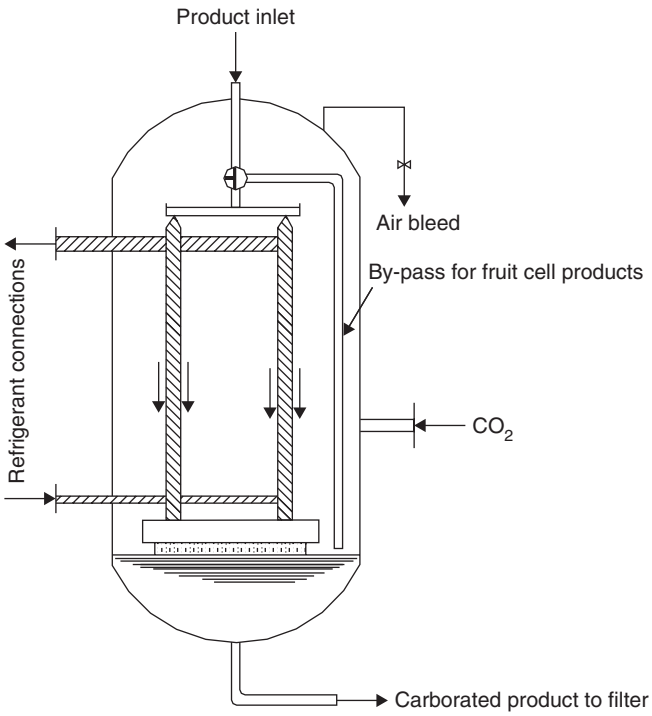

Fig. 11.2 Typical carbonator (Mojonnier carbo-cooler). [Mitchell (1990), with kind permission of Springer Science and Business Media.]

of breakfast cereals, such as wheat flakes and puffed rice, and popcorn are also formed by this method, which consists of introducing material pellets into a toasting oven, where the material stays exposed to temperatures up to 300ºC for 30–90 s. This exposure results in the formation of steam in the pellets that escapes against a resisting pressure to cause puffing, which is a significant volume expansion of up to 20 times the original pellet size (Kent & Evers 1994). When corn is subjected to high heat, the water inside the kernel vaporizes. This steam expands, causing the disruption of the hard pericarp, and forms a highly porous structure of what is commonly known as popcorn (Matz 1984).

As an alternative to the above method, cereal puffing can also be accomplished by a puffing gun. The process relies on the immediate transfer of the heated cereal containing superheated steam from a high to a low pressure, allowing water condensation and consequent expansion. The suddenness at which pressure transition occurs is the key parameter determining the porosity (Kent & Evers 1994). The popular array of milk-based foamed coffee products found in every coffee shop has a common characteristic contributing to its appeal: a milky frothy head. Milk foams are traditionally generated by injecting steam through a nozzle into milk contained in a cup. Air is essentially entrained from the headspace due to high surface turbulence, and the dispersion is stabilized by biochemical changes accompanying a steep increase in milk temperature. The extent of air entrainment and the nature of the dispersion formed are critically dependent on the nozzle design. A variety of designs are commercially available, including the one where the air is entrained by venture action through a pipe having one end open to the atmosphere and the other end connected to the tip of the steam injector. The exact mechanism by which the dispersions formed are stabilized

is not clearly understood, and further research is needed in this area. The direct immersion of foods in hot oil, that is, frying, also generates steam within the exposed material. An example is the commercial production of potato crisps. As the potato slices pass through the fryer, they are exposed to temperatures around 180–200ºC. The high temperature causes the water in the slices to evaporate, leaving behind voids that play a critical role in characterizing the crispiness of the final product (Matz 1984).

Extrusion is used in a range of products from cereals to crisp snacks and sugar confectionery. However, its most representative application is in breakfast cereals. In extrusion cooking, the raw material is conveyed through a rotating screw while being compressed, and then it is sheared at high temperatures and pressures to form a plasticized mass. As this mass passes through a die at the end of the screw, the temperature and pressure are suddenly reduced, when moisture evaporation in the channeled strips forms a honeycombed structure (Kent & Evers 1994). Extruded product properties are much dependent on an array of interrelated operational parameters (such as temperature, pressure, die diameter, screw configuration and available water), which complicates the control of the structure. Low-temperature extrusion has been applied in the manufacture of ice cream. It involves the conveying of ice cream mix at −5ºC through a refrigerated screw extruder. As the ice cream leaves the extruder at low temperature, the hardening step is eliminated and the ice cream can be taken directly to the cold store. The manufacture of ice cream by this process also generates smaller air bubbles than conventional freezing, as the low temperature will result in a reduction in the coarsening of air bubbles and ice crystals (Clarke 2004). Low-temperature extrusion of chocolate has also been patented though no commercially available products are known to be produced by this method (Mackley 1994).

11.6.4 Other gas–liquid mixing methods

The mixing methods discussed so far are largely reliant on physical changes occurring within the product, which may be either mechanically or thermally induced. However, chemical reactions leading to the evolution of CO_2—for example, yeast metabolism during fermentation or the decomposition of baking soda—are mainly responsible for structure development in universally appreciated foods such as bread and cakes. Sodium bicarbonate and phosphates can be thermally activated at temperatures above 90ºC. This decomposition results in the formation of carbon dioxide and water vapor, which in turn causes volume expansion of the product (Bennion & Bamford 1997). The unique texture of bread is achieved through gas incorporation and bubble manipulation within the dough during mixing, proving and baking. Proving is the defining operation of the whole process during which yeast metabolizes flour sugars into CO_2. This gas diffuses into bubbles, previously incorporated in the mixing stage, and expands the dough (Chiotellis & Campbell 2003). In crumpet production, the batter expands due to the formation of CO_2 during fermentation; the larger bubbles then escape, leaving behind a population of small nuclei. The water in the batter evaporates into the nuclei during hot plate baking at 200–230ºC to form a series of vertical cones (Pyle 2005).

11.7 Characterization of bubble-containing structures

11.7.1 Gas hold-up

Gas hold-up (ϕ) is a common measure of the level of bubbles present in liquid foods. It is normally defined as the volume fraction of gas based on the dispersion volume, but

commonly expressed as a percentage. Gas hold-up values in bubble-containing liquid foods range from 15% to 20%, for example, in milkshakes, to over 90% in extruded products such as popcorn and rice cakes (Campbell & Mougeot 1999). Experimentally, gas hold-up can be estimated by the density difference between the bubble-containing dispersion and the material forming the continuous phase. This is most commonly achieved by completely filling, covering and weighing a cup, first with the continuous phase (m_i), then with the bubble-containing dispersion (m_f), and using the following equation.

$$\phi = \left(1 - \frac{m_f}{m_i}\right) \times 100 \tag{11.15}$$

This standard procedure can be applied to liquids and pastes having medium to high viscosity, such as ice cream and whipped cream (Massey *et al.* 2001; Lau & Dickinson 2005; Jakubczyk & Niranjan 2006), where the dispersion is stable and air release during the measurement process is negligible. In the case of solid foams such as aerated chocolate, where it is difficult to sample a defined volume, the flotation method is more suitable (Haedelt *et al.* 2005). The mass of an aerated material is noted (m_f) and placed in a corked glass cylinder filled with water. The total weight is noted as m_a and the weight of the container filled with water alone is noted as m_c. The density of the solid foam is then calculated as:

$$\phi_f = \frac{\rho_w \rho_f}{m_f + m_c - m_a} \tag{11.16}$$

where ρ_w is the density of water (kg m^{-3}) and m_f is the mass of solid foam (kg). Gas hold-up is then calculated by comparing the density of the aerated solid foam (ρ_f) with the gas-free density, that is, density of the continuous phase (ρ_i), as follows.

$$\phi = \left(1 - \frac{\rho_f}{\rho_i}\right) \times 100 \tag{11.17}$$

In more fragile systems, such as aqueous foams forming a head on a clear liquid (e.g., draft beer, cappuccino), where even careful foam manipulation can induce significant air release, the gas hold-up in the foam at any instant can be measured by noting the height of the foam (h_f), the height of the clear liquid taken initially (h_i) and the height of the clear liquid at the instant (h_l) (all heights being measured in a vessel of uniform cross-sectional area), and calculating the hold-up by using the following equation.

$$\phi = \left(\frac{h_f - h_i}{h_f - h_i}\right) \times 100 \tag{11.18}$$

A number of instrumental methods have also been developed to measure hold-up directly. Bisperink *et al.* (1992) observed good agreement between ϕ values read by an optical probe and those estimated by using equation (11.18). Ultrasound-based techniques have also been applied to measure the specific gravity of food batters, which is a promising

method because it avoids sampling procedures in a manufacturing environment (Fox *et al.* 2004). In systems with high air content, such as egg white foam, the term 'overrun' is most commonly used to characterize the level of aeration.

Overrun (OR) represents the additional air added to the material and it is related to gas hold-up as follows (Campbell & Mougeot 1999).

$$\mathrm{OR} = \frac{\phi}{100 - \phi} \times 100 \tag{11.19}$$

In other words, the overrun represents the fraction of gas based on the clear volume of the continuous phase. During the process of bubble inclusion, the gas hold-up varies with time. In most systems, the gas hold-up increases initially, reaches a peak and then drops. A maximum gas hold-up of 48% was observed after 9 min of whipping UHT cream in a standard device, followed by a decrease for longer whipping times (see Figure 11.3) (Jakubczyk & Niranjan 2006). Similar profiles have been reported in the cases of cake batter whipping (also shown in Figure 11.3), formation of high sugar containing egg albumen foams for a range of sugar concentrations and aeration of a model maltodextrin solution (Bee & Prins 1986; Massey *et al.* 2001; Lau & Dickinson 2005). This trend in gas hold-up variation can be attributed to physical or chemical changes occurring in the continuous phase during shearing. Such changes include the irreversible fat droplet aggregation in the case of whipping cream or the irreversible denaturation of proteins adsorbed at the gas–water interface during the whipping of protein solutions (Halling 1981; Walstra 1984).These observations suggest that, for a set of operating conditions in a given aerator, there is an optimum holding time that will give the desired level of bubble inclusion in a product. It is important to note that this optimum time does not necessarily have to coincide with the time taken for the hold-up to peak. For instance, a given product may not be able to sustain such a high level of bubble fraction if, for instance, it has to be baked in an oven.

The optimum time clearly depends on the desired product quality as perceived by a consumer. Very long holding times often result in loss of quality, as do very short holding

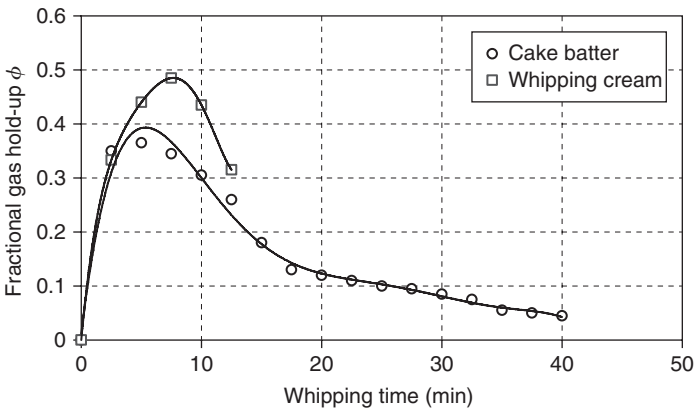

Fig. 11.3 Fractional gas hold-up profile during the whipping of cream at atmospheric pressure and at 380 rpm for cake batter at 3 bar, 5 revs^{-1}. [Massey *et al.* (2001) and Jakubczyk and Niranjan (2006).]

times. It is thus very important in a manufacturing environment to relate operating variables with the desired dispersion characteristics, which include texture, mouthfeel and so on. The transient variation in gas hold-up in any given system can be accounted for by considering the instantaneous rate of change of hold-up to be determined by a balance between the rate of hold-up formation and that of hold-up loss. The rate of formation of hold-up depends on the method used to form bubbles within the system, that is, whether the bubbles are whipped into the headspace or whether they are generated by chemical/biochemical reactions. Massey *et al.* (2001) proposed a mechanistic model for the time dependency of gas hold-up entrapped in cake batter, when the batter was aerated in a pressure whisk. This model successfully described the experimental data for a range of whisk speeds and headspace pressures. Two mechanisms were considered for the formation of bubbles which can potentially be entrapped in the batter: a primary mechanism where entrapped bubbles are directly entrained from the headspace during whisking, and a secondary mechanism involving the break-up of larger bubbles entrained from the headspace.

The loss of entrapped bubbles was considered to occur mainly due to coalescence of the bubbles, which subsequently escaped from the system. On the basis of these assumptions, the following correlation was derived and shown to be valid, where the empirical parameters k_1, k_2, k_3 and k_4 were determined to fit the equation to the experimental data.

$$\phi = \left[\frac{k_1}{k_4} + \frac{k_2}{k_4 - k_3} e^{-k_3 t} - \left(\frac{k_1}{k_4} + \frac{k_2}{k_4 - k_3} e^{-k_4 t}\right)\right] \times 100 \tag{11.20}$$

Just as operating time influences the extent of bubble build-up in a system, the operating conditions, and more importantly, the method used to create the dispersion, also influence the development of gas hold-up. During the process of generating bubbles in tempered chocolate by applying vacuum, the gas hold-up was observed to increase with the application of higher vacuum levels when the vacuum application time was maintained at the same value (Haedelt *et al.* 2005). This was explained by considering the mechanism of gas volume build-up under vacuum: the gas solubility in the chocolate decreases proportionally to the pressure, which in turn, increases the volume of gas desorbed from the chocolate. Assuming that the dissolved gases were initially at a level corresponding to the solubility of air components (mainly, N_2 and O_2) at atmospheric pressure, the following model was deduced, which related the gas hold-up (ϕ) with operating pressure under vacuum (P).

$$\frac{\phi}{100 - \phi} = RT(H - k)\left(\frac{1}{P} - 1\right) \tag{11.21}$$

In the above equation, k is a model constant, R is the ideal gas constant, T is the temperature and H is a pseudo-Henry's constant. These examples illustrate how, once the mechanisms underlying gas incorporation are identified, it is possible to establish a relationship between operating parameters and the level of gas inclusion.

11.7.2 Bubble size distribution

BSD is one the most difficult parameters to measure and analyze. However, its evolution with time is of great importance because it is closely linked to the product quality as

perceived by a consumer (Halling 1981; Campbell & Mougeot 1999). In some systems, a uniform bubble size may be desirable (e.g., bread dough and cake batter), which improve baking characteristics, whereas in others, a wide spread in the distribution may be advantageous to achieve specific mouthfeel responses.

In general, the distribution observed in any dispersion depends on the operating conditions such as pressure, agitation speed and temperature, as well as the chemical nature of the gas. It may be noted that a number of gases, apart from air, are used commercially—for example, carbon dioxide, nitrogen and its oxides, helium and other inert gases. As mentioned in Section 11.7, there are four mechanisms by which the bubbles can be formed: (i) by entrapping a sparged gas and dispersing it with mechanical agitation; (ii) by entraining air during steam sparging; (iii) by allowing bubbles to be formed by chemical and biochemical reactions and (iv) by dissolving a gas and lowering the pressure to release it. The BSDs resulting from the first two methods strongly depend on the hydrodynamics prevailing in the equipment, whereas the rate of gas generation, the gas solubility and its variation with pressure play a critical role in the latter two methods. Methods commonly used to determine bubble sizes in dispersions include the following.

1. Photographic techniques.
2. Measurement of bubble penetration length through optical probes.
3. Measurement of bubble volume using ultrasound sampling probes.
4. Freezing dispersions and visualizing cross-sections.

Bubble sizes have been traditionally examined by taking conventional photographs of dispersions, often through container walls, and analyzing them by using image analysis software. The accuracy of this technique can be compromised by the fact that inferences are drawn on a three-dimensional structure based on two-dimensional images, normally assuming symmetry. Further, it can be difficult to obtain sharp images. Moreover, wall and curvature effects can also introduce errors into the measurement. Nevertheless, it is relatively cost-effective, and a number of dispersions, such as dough and batters, have been examined using ordinary photography.

Recent developments in image analysis software have turned this method into a faster and more efficient technique (Hepworth *et al.* 2004). Ultrasound reflective spectroscopy application in the analysis of bubbly liquids has been known for many years. This technique is based on the transmission of ultrasound waves through dispersion, and measuring the velocity and attenuation spectra.

The interpretation of these signals yields information on bubble sizes and gas hold-up. However, the application of this technique to dispersions having bubble concentration greater than 0.1% is complex and not yet fully developed (Kulmyrzaev *et al.* 2000). Bisperink *et al.* (1992) developed a foam analyzer for the measurement of foam properties, based on an optical fiberglass probe that is moved through the foam while emitting a signal that depends on the medium surrounding it, thus permitting highly localized measurement of BSDs. However, techniques involving probes often require a dilute system and are intrusive.

More recently, x-ray tomography has emerged as a valuable tool for imaging a number of cellular food products such as strawberry mousse and chocolate muffins (Lim & Barigou 2004). This technique is non-invasive and non-destructive, avoiding laborious sample treatments, and is particularly suited in the analysis of fragile bubble-containing foods. The contrast obtained in this technique between the continuous and gas phases is based on their density difference. When used in conjunction with a suitable image analysis software

Table 11.1 Typical bubble sizes and measurement methods used in the analysis of aerated foods microstructure.

Material	Technique	Bubble size (μm)	Reference
Bread dough	Freezing of sample and slicing	20–50 g	Martinet *et al.* (2005)
Whipped cream	Photography and image analysis	10–40	Jakubczyk and Niranjan (2006)
Model cake batter	Photography and image analysis	20–50	Massey *et al.* (2001)
Macro-aerated chocolate	X-ray tomography	600–1,400	Haedelt *et al.* (2005)
Milk foam	CLSM	M 60–100	Silva and Niranjan (2006, unpublished data)
Beer	Optical probe	20–120	Bisperink *et al.* (1992)
Beer	Photography	137–190	Hepworth *et al.* (2004)
Whey protein solution	Ultrasonic reflectance spectroscopy	10–160	Kulmyrzaev *et al.* (2000)

(e.g., Imagine Pro ®Plus Software, The Proven Solution™), it can successfully visualize bubble-containing sections giving information on bubble numbers and size distribution in aerated chocolates. However, with equipment currently available, the application of x-ray is limited to relatively stable structures and bubble sizes generally over 50 μm (Haedelt 2005). Confocal scanning laser microscopy (CLSM) is a promising technique to characterize food dispersion. In a laser scanning confocal microscope, a laser beam is passed through a light source aperture and is then focused by an objective lens into a small focal volume within a fluorescent specimen. A fluorescent dye added to the sample enables the visualization of the product structure. The identification of different components partitioned within the product by dye manipulation and image overlapping is also possible by this technique. As this method is fast and does not demand laborious sample preparation, it is suitable for BSD determination and dynamic microstructural examination in complicated structures like albumen foams (Lau & Dickinson 2004) and emulsions containing egg, sugar and milk proteins (Martinet *et al.* 2005). Examples of typical bubble sizes encountered in foods are given in Table 11.1.

Processing parameters influence not only gas incorporation into the product, but also its microstructure. An understanding of the relationship between process parameters and BSD is essential to establish the operating conditions needed to obtain the desired product quality. Bread is the oldest and one of the most popular aerated foods consumed all over the world. This makes it one of the most extensively studied aerated food products. The effect of mixing bread dough under partial vacuum was studied by Campbell *et al.* (1998) who observed that BSD was not significantly influenced by the vacuum level, though the number of bubbles per unit of dough volume decreased with reduced mixing pressure. Chiotellis and Campbell (2003) modeled the evolution of BSD in bread dough during proving for different temperatures and yeast concentrations, predicting an increased growth rate for higher temperatures and increasing yeast levels.

11.7.3 Rheological characterization

The overall stability of a dispersed system is primarily affected by its rheology. The aerated lifetime of solidified structures such as chocolate and extruded cereals is up to years,

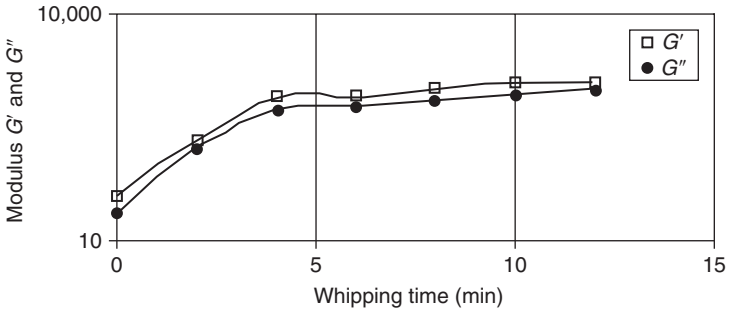

Fig. 11.4 Evolution of viscous and elastic moduli (G' and G'', respectively) with time during whipping of dairy cream (frequency: 2.2 rad s^{-1}). [Jakubczyk and Niranjan (2006), with permission from Elsevier.]

whereas systems such as whipped cream will hold air for a few hours. The head of a beer or cappuccino, which are low-viscosity aqueous foams, will collapse in minutes. Campbell and Mougeot (1999), and before them Prins (1988), recognized that aeration is a physical process in which the rheological and interfacial properties play key roles. However, these properties, particularly the former, change during the course of aeration. Rheology can therefore be a useful tool in the assessment of structural changes occurring in a product during processing.

Dynamic oscillatory shear testing over a wide range of frequencies can provide information not easily obtained by other methods. Although this technique has traditionally been used to yield information on the fundamental structural characteristics of the food, a number of recent papers attempt to relate parameters such as the complex viscosity amplitude to sensory attributes such as perceived thickness in the mouth (Gunasekaran & Ak 2000). Dynamic oscillatory testing can also be applied to bubble-containing dispersions, its reliability depending on the dispersions remaining stable during the tests. Dynamic oscillatory tests have been performed on whipped cream and cake batters not only to assess their rheological properties, but also to trace the way these properties change during the course of aeration (Massey 2002; Jakubczyk & Niranjan 2006). Even though a continuous phase may be purely viscous, bubble incorporation tends to make the dispersion viscoelastic. All whipped creams studied by Jakubczyk and Niranjan (2006) exhibited viscoelastic behavior, with an increase in elastic and viscous moduli observed during whipping attributed to the presence of bubbles and the clustering of fat globules (Figure 11.4). Massey (2002) also reported on the creation of a stronger viscoelastic system while aerating cake batter by mechanical beating. The results are in agreement with those obtained for the aeration of maltodextrin solutions (Bee & Prins 1986). Although such data provide insight into the structural changes occurring in these products during bubble inclusion, there is a lack of knowledge concerning the relationship between multi-phase rheology and consumer perception (mouthfeel).

As one of the main reasons to incorporate bubbles into foods is to impart particular textural characteristics, the rheological characterization of the dispersion is absolutely critical to the nature of the dispersion formed, as well as to the product quality. For example, increasing the viscosity of the continuous phase can be detrimental to air incorporation by slowing surfactant diffusion to interface; however, it favors stability of the dispersion already formed by retarding liquid drainage (Halling 1981; Lau & Dickinson 2004). The relative viscosity—defined as the ratio of the viscosity of the dispersion to that of the

continuous phase—has been reported to increase with gas hold-up (Bee & Prins 1986). However, the opposite, that is, a decrease in relative viscosity with increasing hold-up between these parameters, was observed in low-viscosity aqueous protein system by Britten and Lavoie (1992). These discrepancies can be explained by the model proposed by Llewellin *et al.* (2002a,b), who suggested the existence of two different flow regimes, based on the extent of bubble distortion occurring under applied stress–strain conditions. The extent of distortion is characterized by the capillary number $Ca = \eta_0 a\gamma/\Gamma$, where η_0 is the viscosity of the continuous phase; a is the radius of the relaxed undeformed bubble; γ is the strain rate and Γ is the surface tension. The capillary number is a measure of the equilibrium deformation of the bubbles in a given stress field. For low values of Ca, bubbles remain more or less spherical and distort the flow around them considerably, thereby increasing the viscosity with hold-up. On the contrary, when Ca is high, bubbles get distorted and provide a high free-slip surface, so that the viscosity decreases with increasing hold-up. Llewellin *et al.* (2002a,b) developed a generalized constitutive equation to describe the evolution of viscosity with gas hold-up that takes into account the two possible situations. The solution of this equation for oscillatory flow, for example, in a concentric cylinder where the imposed torque varies sinusoidally, has also been derived by Llewellin *et al.* (2002a,b):

$$\eta_r = \frac{1}{3}\sqrt{9 - 30\varepsilon + 25\varepsilon^2 + \frac{(450b + 750)\varepsilon + (225b^2 - 625)\varepsilon^2}{25 + 36C_d^2}} \tag{11.22}$$

where η_r is the viscosity of the continuous phase; ε is the fractional gas hold-up (i.e., ϕ /100) and b is an experimentally fitted parameter found to take the value 9. Ca_d is known as dynamic capillary number, which measures the steadiness of the flow by giving the ratio of the bubble relaxation time to the time-scale over which the strain rate changes appreciably, and is defined as:

$$C_{a_d} = \lambda\omega \tag{11.23}$$

where ω is the angular frequency of the torque and λ is the relaxation time.
The parameter k increases with the volume fraction of the dispersed phase (approximately 1 for limit of a solitary bubble in an infinite pure liquid). For $Ca_d >> 1$ and $Ca_d << 1$, equation (11.22) reduces to the following equation.

$$\lambda = \frac{k\eta_r}{T} \tag{11.24}$$

Figure 11.5 compares the experimental values of η with those calculated using equation (11.22) for $Ca_d << 1$, with $b = 3.8$, a value deduced for best fit between experimental data and model values (Niranjan *et al.* 2005). Llewellin *et al.* (2002a,b) stated a value of 9 for the parameter b, which was based on experimental data obtained using golden syrup. The difference between the values of b obtained for the two cases can be attributed to the difference between the rheology of the continuous phases: while golden syrup is essentially Newtonian, cake batter is a weakly viscoelastic system, as characterized by Massey (2002). Relating the viscosity of the continuous phase with the viscosity of the dispersed system is a

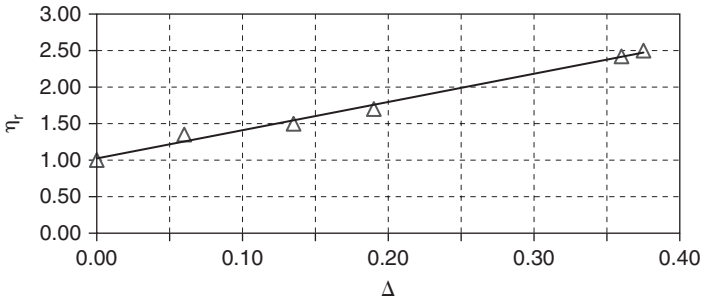

Fig. 11.5 Fitting of equation (11.22) to experimental data on cake batter (aerated at 300rev min^{-1} and at atmospheric pressure); Δ, relative viscosity (experimental); —, relative viscosity (predicted). [Niranjan *et al.* (2005).]

sound approach to model the evolution of viscosity with gas hold-up. There is evidence that this approach works when the continuous phase is Newtonian; however, further modeling is needed to take into account more complicated continuous-phase rheological behavior:

$$\eta_r = \begin{cases} 1+b; C_d << 1 \\ 1-\dfrac{5\varepsilon}{3}; C_d >> 1 \end{cases} \tag{11.25}$$

where η_r is the relative viscosity.

11.8 Role of gases and specific ingredients in characterizing interfacial and rheological properties

Aerating a liquid will only result in the formation of foam if a surfactant is present. The role of the surfactant is to stabilize gas bubbles within the liquid matrix by adsorbing at the gas–liquid interface. As discussed earlier, it is well established that process or operating parameters influence hold-up development, and the stability and morphology of disperse systems. However, ingredients in the food system, their physicochemical properties and the way they interact are just as important in bubble interface stabilization. The rate of liquid drainage from a foam, for instance, will be determined by the viscosity of the serum. This can be manipulated, for example, by adding ingredients that will promote an increase in viscosity to retard drainage. Relevant examples are the addition of guar gum to whipping cream, or sugar to egg albumen mixes (Smith *et al.* 2000; Lau & Dickinson 2004). In protein-stabilized foams, protein flexibility is critical to the molecule functionality in stabilizing interfaces (Halling 1981; Lemeste *et al.* 1990). This has important consequences in the development and stability of dairy foams and emulsions, where the heat treatment received by the material can define its foamability and dispersion properties. A symbiotic effect between native and denatured proteins on the emulsifying properties of whey proteins isolate blends has been observed by Britten *et al.* (1991). Though most studies on protein adsorption at interfaces have been conducted in solutions having a single well-characterized protein, evidence has emerged in recent years that film properties in mixed protein systems

are much more complex than in single protein systems. Competitive adsorption to the air–serum interface has been reported even below the denaturation temperature in protein mixtures, and is dependent not only on protein properties, but also on environmental factors such as pH, ionic strength and protein concentration (Dickinson 1999; Zhang *et al.* 2004). Fat also plays a key role in the behavior of food foams. Depending on its physical state and size distribution in the continuous phase, the fat may act as stabilizer or destabilizer of aqueous foams, for instance, by competing with and even displacing proteins at the gas–liquid interface (Pilhofer *et al.* 1994). In whipped cream, the initial cream temperature is crucial to air incorporation by whipping normally below 4ºC to ensure partial crystallization of the fat droplets. The shear induced during whipping of cream can lead to droplet coalescence and bubble formation. Long-term stability in whipped cream will ultimately result from the formation of a three-dimensional network of aggregated fat droplets surrounding the air cells (Jakubczyk & Niranjan 2006). Gas retention in bread is a function of gluten, the flour protein. The interaction between added fat and flour components also plays a key role in gas retention. Gluten must be sufficiently extensible to allow loaf rising, while sufficiently strong to prevent gas escaping and consequent loaf collapsing. Added fat interaction with flour components and quantity of sugars in the dough during fermentation will also have a significant effect on the structure of the final product (Kent & Evers 1994). Overrun and BSD in ice cream will depend not only on the type of freezer and its operating conditions, but also on product formulation. Amount of fat, and type and level of emulsifier will affect the extent of destabilized fat that stabilizes the air cells (Goff & Clarke 2004). The type of gas used to create structure in any given food will depend on the specific requirements. An example is the use of CO_2 in carbonated beverages. CO_2 is one of the few gases suitable to provide the characteristic effervescence in soft drinks. Owing to its non-toxicity and lack of taste, it will not affect safety and flavor of the final product. Its availability and moderate cost make it suitable for industrial use. Additionally, its solubility in aqueous solutions allows an acceptable retention of the gas in solution at atmospheric pressure and room temperature (Mitchell 1990). In general, the type of gas used has a significant impact on the dispersion characteristics. The use of air is avoided in a number of products, particularly those containing fat, because of the susceptibility of certain ingredients to oxidation. Often, carbon dioxide, nitrogen or one of the inert gases such as helium or argon is utilized. Haedelt (2005) investigated the effect of the type of gas used—CO_2, N_2, N_2O and Ar—on the bubble-containing structures formed in chocolates. He reported that the solubility of the gas played a very critical role in the structure formed. When gases having higher solubility in chocolate (e.g., CO_2 and N_2O) were used, the bubbles formed tended to be larger and the dispersion, in general, tended to contain a higher fraction of bubbles. The use of relatively low solubility gases (N_2 and Ar) resulted in the formation of dispersions containing much smaller bubbles; correspondingly, the fractional hold-up of bubbles was also significantly lower. Based on this study, he postulated that highly soluble gases form macro-aerated structures, whereas low solubility gases form micro-aerated structures. The gas used is therefore a structure-developing aid.

11.9 Stability of foams and solidification of bubbly dispersions

Stability is the most important property of a bubble-containing product: once the desired characteristics for the product have been achieved, the structure must be retained at least

until product consumption. Destabilization processes can combine in various ways and at various rates between foam formation and phase separation; thus, the reference to foam stability must be accompanied by the specific mechanism under observation (Halling 1981). In general, the following phenomena can be distinguished when a liquid foam is allowed to stand (Prins 1986):

1. coalescence of gas bubbles;
2. disproportionation of gas bubbles;
3. liquid drainage;
4. creaming of gas bubbles.

Both liquid drainage and creaming result in the loss of liquid from the foam matrix and are generally determined by the rheological properties of the foam serum, and to a certain extent, by the foam network itself (Halling 1981; Prins 1986; Lau & Dickinson 2005). These processes involve flow, that is, relative movement between gas bubbles and the serum. In foams containing spherical bubbles or low gas fraction, the movement of bubbles is greater than the movement of liquid and individual bubbles can cream at a rate depending on the balance between buoyancy force and viscous resistance. On the contrary, when liquid movement is more pronounced than bubble movement (e.g., in polyhedral foams), drainage mechanisms predominate (Prins 1988). Bubble rise can be slowed down, though not completely stopped, by increasing the viscosity of the serum phase. Gas bubbles coalescence results in an increase in mean bubble size and a decrease in the number of bubbles, with a decrease in air content. Coalescence is ultimately determined by the stability and attractive/repulsive forces between the thin liquid films surrounding air bubbles (Prins 1988). Disproportionation occurs through gas diffusion between bubbles having different sizes. The excess internal pressure within any bubble, also known as the Laplace pressure (ΔP), is inversely proportional to the bubble diameter. Thus, the dissolved gas concentration at the interface of a smaller bubble will be greater than that at the interface of a larger bubble. This promotes mass transfer and therefore a net loss of gas from the smaller to the larger bubble. The rate of disproportionation will depend on the Laplace pressure, the solubility of the gas and other geometric factors (Halling 1981). Foam stability is most commonly monitored by following its collapse and liquid drainage. Both are macroscopic properties and can be easily measured. These properties are not directly related to microscopic events, such as drainage occurring from lamellae, but they allow a description of foam behavior over time and, in conjunction with the transient development of BSD, yield a complete description of foam destabilization mechanisms (Halling 1981; Bisperink *et al.* 1992; Patino *et al*. 1995; Lau & Dickinson 2005). The common parameter characterizing foam stability is half-life time for liquid drainage or foam collapse (Deeth & Smith 1983; Britten & Lavoie 1992; Patino *et al*. 1995). Liquid drainage from foams has been described in the literature by the following empirical equations (Halling 1981; Elizalde *et al.* 1991; Patino *et al*.1995):

$$\frac{dV'}{dt} = K_2 V' \tag{11.26}$$

$$\frac{dV'}{dt} = K_2 V'^2 \tag{11.27}$$

where, V' is the total volume of liquid in the foam at time t, and K_1 and K_2 are empirical constants. Equations (11.26) and (11.27) successfully described drainage in pure ovalbumin and casein foams, respectively, generated by air sparging, with drainage rate constant K_2 used as a stability parameter to compare foams generated at different temperatures and pH values (Patino *et al*. 1995). Other authors, however, have suggested that such empirical equations do not describe foam behavior completely over their life spans: drainage is slower than values predicted by either equation (11.26) or (11.27) (Halling 1981; Elizalde *et al.* 1991). An empirical model proposed by Elizalde *et al.* (1991) fitted experimental data on liquid drainage with time for different protein solutions, and has been used in the investigation of drainage from dairy protein foams (Britten & Lavoie 1992) and egg albumen foams (Lau & Dickinson 2005).

$$V_l(t) = \frac{V_{max} \times t}{B + t} \tag{11.28}$$

In the above equation, V_{max} and B are empirically determined parameters representing the maximum volume of liquid drained and the time taken to drain a volume of $V_{max}/2$, respectively. B can be used as a parameter to assess the relative stability of different foams where liquid drainage can be represented by equation (11.26). It is necessary to note that the measurements of the rates of foam collapse and liquid drainage yield no information on the dynamic changes occurring within the foam structure: bubbles grow and shrink by disproportionation, move and coalesce with each other, and all these are reflected on changes in foam morphology and BSD. An understanding of the destabilization mechanisms operating between formation and collapse will only be complete if an analysis of the microstructural changes is incorporated. Some of the techniques can also be used to monitor transient variations in BSDs during destabilization. The above description of foam destabilization mechanisms is only applicable to liquid foods. In solid dispersions, these mechanisms are significantly slowed down, or even eliminated. As mentioned earlier, solid matrices such as aerated confectionery will hold air for years. Structure stabilization occurs, for example, in chocolate foams, when the product is cooled to solidify and trap the bubbles formed within. The baking of cake and bread dough is another example of how a bubble-containing structure formed during mixing and proving is stabilized when starch gelatinization is induced by the high temperatures prevailing in baking ovens.

11.10 Ultrasound in gas mixing and applications in food aeration

Many foods consist of air bubbles or cells distributed in a viscoelastic liquid or solid matrix, for example, ice cream, whipped cream, confectionery, bread dough and desserts. The shelf life, texture and appearance of these foods are strongly influenced by the size and concentration of the bubbles they contain. It is therefore important to prevent changes in the characteristics of the bubbles over time (German & McCarthy 1989). There is currently a lack of analytical techniques capable of providing information about bubble characteristics in aerated foods (Bee *et al.* 1989; Dickinson 1992). This is because many aerated foods are optically opaque or have delicate structures that are easily damaged by physical manipulation (Halling 1981). For this reason, there is a pressing need to develop new analytical techniques to non-invasively pro-

vide information about bubble characteristics in aerated foods (German & McCarthy 1989). These techniques are required in the laboratory for fundamental studies aimed at improving understanding of the relationship between bubble characteristics and bulk properties of aerated foods. They are also needed in the factory as online sensors for monitoring the properties of foods during manufacture, storage and handling (Haley & Mulvaney 1995).

Recent studies have demonstrated that magnetic resonance imaging (MRI) is a powerful technique for studying the microstructure of aerated foods (German & McCarthy 1989). Nevertheless, the widespread application of this technique in the food industry is currently limited, because it is relatively expensive, requires highly skilled operators and is not easily adapted for online monitoring. Recently, techniques based on the backscattering of laser light from particles suspended in a fluid have become commercially available (Lasentecä, Redmond, WA). Techniques based on this technology may also be useful for characterizing aerated foods. Studies have shown that ultrasonics can be used to provide valuable information about food properties such as structure, composition and physical state (McClements 1995, 1997). Ultrasonic instruments have major advantages over alternative technologies because they can be fully automated, are capable of rapid and precise measurements and are easily adapted to online applications.

It has been known for many years that ultrasound can be used to determine the size and concentration of air bubbles in very dilute systems. Nevertheless, recent preliminary studies have shown that information about bubble characteristics in concentrated systems can be obtained if the ultrasonic wave is reflected from the surface of the sample, rather than transmitted through it (Fairley 1993; Fairley *et al.* 1991).

The propagation of ultrasonic waves through aerated liquids has been investigated both theoretically and experimentally by Kulmyrzaev *et al.* (2000). Results indicate that the acoustic impedance spectra of aerated liquids, which can be measured non-destructively by reflecting ultrasonic waves from their surfaces, are sensitive to changes in bubble size and concentration. Good qualitative agreement was found between experimental measurements and theoretical predictions; however, more theoretical and experimental research is required to render the ultrasonic reflectance spectroscopy technique more quantitative. The ultrasonic scattering needs to be extended to account for concentrated bubbly liquids containing relatively large bubbles suspended in a viscoelastic medium. So far this has proved to be extremely difficult because of the complexity of the physical processes that occur when an ultrasonic wave propagates through a concentrated suspension of strong scatterers. In addition, a better model system is required for the experiments that have stable droplets, whose size and concentration can be carefully controlled and measured. Despite these limitations, preliminary results suggest that the ultrasonic technique may prove to be a useful online sensor for monitoring the properties of aerated food samples.

References

Bee, R.D.C. & Prins, A. (1986). Behaviour of an aerated food model. In: *Food Emulsions and Foams* (ed. E. Dickinson). Royal Society of Chemistry, Cambridge, UK, pp. 128–143.

Bee, R.D., Clement, A. & Prins, A. (1989). Behavior of an aerated food model. In: *Food Emulsions and Foams* (ed. E. Dickinson). The Royal Society of Chemistry, Cambridge, UK.

Bennion, A.B. & Bamford, B.S.T. (1997). *The Technology of Cake Making.* Chapman and Hall, London, UK.

Bisperink, C.G.J., Ronteltap, A.D. & Prins, A. (1992). Bubble-size distributions in foams. *Advances in Colloid and Interface Science*, **38**, 13–32.

Britten, M. & Lavoie, L. (1992). Foaming properties of proteins as affected by concentration. *Journal of Food Science.*, **57**, 1219–1222.

Britten, M., Giroux, H.J. & Rodrigue N. (1991). Emulsifying properties of whey–protein and casein composite blends. *International Dairy Federation, Special Issue*, **9303**, 368–374.

Campbell, G.M. & Mougeot, E. (1999). Creation and characterisation of aerated food products. *Trends in Food Science Technology*, **10**, 283–296.

Campbell, G.M., Rielly, C.D., Fryer, P.J. & Sadd, P.A. (1998). Aeration of bread dough during mixing: effect of mixing dough at reduced pressure. *Cereal Food World*, **43**, 163–167.

Cheng, L.M. (1992). *Food Machinery for the Production of Cereal Foods, Snack Foods and Confectionery*. Ellis Horwood Ltd., Chichester, UK.

Chiotellis, E. & Campbell, G.M. (2003). Proving of bread dough. I. Modelling the evolution of the bubble size distribution. *Food Bioproduction Processing*, **81**, 194–206.

Clarke, C. (2004). *The Science of Ice Cream.* Royal Society of Chemistry, Cambridge, UK.

Deeth, H.C. & Smith, R.A.D. (1983). Lipolysis and other factors affecting the steam frothing capacity of milk. *Australian Journal of Dairy Technology*, **38**(1), 14–19.

Dickey, D.S. (1981). Turbine agitated gas dispersion: power, flooding and hold-up. In: *Advances in Biotechnology* (ed. M. Moo-Young), Vol. 1. Pergamon Press, New York, p. 483.

Dickinson, E. (1992). *An Introduction to Food Colloids*. Oxford University Press, Oxford.

Dickinson, E. (1999). Adsorbed protein layers at fluid interfaces: interactions, structure and surface rheology. *Colloids and Surfaces B: Biointerfaces*, **15**(2), 161–176.

Elizalde, B.E., Giaccaglia, D., Pilosof, A.M.R. & Bartholomai, G.B. (1991). Kinetics of liquid drainage from protein-stabilized foams. *Journal of Food Science*, **56**, 24–26.

Fairley, P. (1993). Ultrasonic characterization of areated foods. Ph.D. Thesis, University of Leeds, UK.

Fairley, P., McClements, D.J. & Povey, M.J.W. (1991). Ultrasonic characterization of aerated foodstuffs, *Ultrasonics International Conference Proceedings*, p. 79.

Fox, P., Smith, P.P. & Sahi, S. (2004). Ultrasound measurements to monitor the specific gravity of food batters. *Journal of Food Engineering*, **65**, 317–324.

German, J.B. & McCarthy, M.J. (1989). Stability of aqueous foams; analysis using magnetic resonance imaging. *Journal of Agriculture and Food Chemistry*, **37**, 1321–1326.

Goff, H.D. & Clarke, C.J. (2004). Effects of structural attributes on hardness and melting rate of ice cream. *Ice Cream 2: 2nd IDF Symposium on Ice Cream*, Thessaloniki, Greece. International Dairy Federation, Brussels.

Gunasekaran, S. & Ak, M.M. (2000). Dynamic oscillatory shear testing of foods: selected applications. *Trends in Food Science Technology*, **11**, 115–127.

Haedelt, J. (2005). An investigation into bubble inclusion into liquid chocolate. Ph.D. Thesis, School of Food Biosciences, University of Reading, Reading, UK.

Haedelt, J., Pyle, D.L., Beckett, S.T. & Niranjan, K. (2005). Vacuum-induced bubble formation in liquid-tempered chocolate. *Journal of Food Science*, **70**, 159–164.

Haley, T.A. & Mulvaney, S. J. (1995). Advanced process control technique for the food industry. *Trends in Food Science and Technology*, **6**(4), 103–110.

Halling, P.J. (1981). Protein-stabilized foams and emulsions. *CRC Critical Reviews in Food Science and Nutrition*, **15**, 155–203.

Hepworth, N.J., Hammond, J.R.M. & Varley, J. (2004). Novel application of computer vision to determine bubble size distributions in beer. *Journal of Food Engineering*, **61**(1), 119–124.

Jakubczyk, E. & Niranjan, K. (2006). Transient development of whipped cream properties. *Journal of Food Engineering*, **77**, 79–83.

Jones, L. (1995). Aeration of boiled sweets: a review of available methods. *The Manufacturing Confectioner*, **75**(10), 47–52.

Kent, N.L. & Evers, A.D. (1994). *Technology of Cereals: An Introduction for Students of Food Science and Agriculture.* Elsevier Science Ltd, Kidlington, Oxford.

Kulmyrzaev, A., Cancelliere, C. & Mc Clements, D.J. (2000). Characterization of aerated foods using ultrasonic reflectance spectroscopy. *Journal of Food Engineering*, **46**, 235–241.

Lau, C.K. & Dickinson, E. (2004). Structural and rheological properties of aerated high sugar systems containing egg albumen. *Journal of Food Science*, **69**, 232–239.

Lau, C.K. & Dickinson, E. (2005). Instability and structural change in an aerated system containing egg albumen and invert sugar. *Food Hydrocolloids*, **19**(1), 111–121.

Lemeste, M., Colas, B., Simatos, D., Cross, B., Courthaudon, J.L. & Lorient, D. (1990). Contribution of protein flexibility to the foaming properties of casein. *Journal of Food Science*, **55**, 1445–1447.

Lim, K.S. & Barigou, M. (2004). X-ray micro-computed tomography of cellular food products. *Food Research International*, **37**, 1001–1012.

Llewellin, E.W., Mader, H.M. & Wilson, S.D.R. (2002a). The constitutive equation and flow dynamics of bubbly magmas. *Geophysical Research Letters*, **29**(24), 23-1–23-4.

Llewellin, E.W., Mader, H.M. & Wilson, S.D.R. (2002b). The rheology of a bubbly liquid. *Proceedings of the Royal Society of London Series A Mathematical, Physical and Engineering Sciences*, **458**, 987–1016.

Mackley, M.R. (1994). Cold extrusion of chocolate. Patent 9220477.

Martin, P.J., Chin, N.L. & Campbell, G.M. (2004). Aeration during bread dough mixing. II. A population balance model of aeration. *Food Bioproducts Processing*, **82**, 268–281.

Martinet, V., Valentini, C., Casalinho, J., Schorsch, C., Vaslin, S. & Courthaudon, J.L. (2005). Composition of interfacial layers in complex food emulsions before and after aeration: effect of egg to milk protein ratio. *Journal of Dairy Science*, **88**, 30–39.

Massey, A.H. (2002). *Air Inclusion Mechanisms and Bubble Dynamics in Intermediate Viscosity Food Systems*. School of Food Biosciences, University of Reading, Reading, MA.

Massey, A.H., Khare, A.S. & Niranjan, K. (2001). Air inclusion into a model cake batter using a pressure whisk: development of gas hold-up and bubble size distribution. *Journal of Food Science*, **66**(8), 1152–1157.

Matz, S.A. (1984). *Snack Food Technology.* AVI Publishing Co. Inc., Westport, CT.

McClements, D.J. (1995). Advances in the application of ultrasound in food analysis and processing. *Trends in Food Science and Technology*. **6**, 293–299.

McClements, D.J. (1997). Ultrasonic characterization of foods: principles methods and applications. *CRC Critical Reviews in Food Science and Nutrition*. **37**, 1–46.

Mitchell, A.J. (1990). *Formulation and Production of Carbonated Soft Drinks.* Blackie, Glasgow, UK.

Niranjan, K., Khare, A.S. & Silva, S.F.J. (2005). Bubbles in foods: creating structure out of thin air. *7th World Congress of Chemical Engineering*, Glasgow, UK.

Patino, J.M.R., Delgado, M.D.N. & Fernandez, J.A.L. (1995). Stability and mechanical strength of aqueous foams containing food proteins. *Colloids and Surfaces A: Physicochemical and Engineering Aspects*, **99**(1), 65–78.

Pilhofer, G.M., Lee, H.C., McCarthy, M.J., Tong, P.S. & German, J.B. (1994). Functionality of milk-fat in foam formation and stability. *Journal of Dairy Science*, **77**, 55–63.

Prins, A. (1986). Some physical aspects of aerated milk-products. *Netherlands Milk Dairy Journal*, **40**(2–3), 203–215.

Prins, A. (1988). Principles of foam stability. In: *Advances in Food Emulsions and Foams* (eds E. Dickinson & G. Stainsby). Elsevier Applied Science Publishers Ltd., Barking, UK, pp. 91–119.

Pyle, D.L. (2005). Crumpet structures experimental and modelling studies. *Food and Bioproducts Processing*, **83**, 81–88.

Rushton, J.H. Costich, E.W. & Everett, H.J. 1950. Power characteristics of mixing impellers Part I. *Chemical Engineering Progress*, **46**, 395–404.

Smith, A.K., Goff, H.D. & Kakuda, Y. (2000). Microstructure and rheological properties of whipped cream as affected by heat treatment and addition of stabilizer. *International Dairy Journal*, **10**, 295–301.

van't Riet, K. & Smith, J.M. (1973). The behaviour of gas–liquid mixtures near the Rushton turbine blades. *Chemical Engineering Science*, **28**, 1031–1037.

Walstra, P. (1984). *Dairy Chemistry and Physics*. John Wiley, New York.

Wolfe, T.L. (1995). Vacuum aeration. *The Manufacturing Confectioner*, **75**(5), 97–98.

Zhang, Z., Dalgleish, D.G. & Goff, H.D. (2004). Effect of pH and ionic strength on competitive protein adsorption to air/water interfaces in aqueous foams made with mixed milk proteins. *Colloids and Surfaces B: Biointerfaces*, **34**, 113–121.

12 Evaluation of mixing and air bubble dispersion in viscous liquids using numerical simulations

Kiran Vyakaranam, Maureen Evans, Bharani Ashokan and Jozef L. Kokini

12.1 Introduction

Mixing, as a unit operation in processing, is used for blending of ingredients, improvement of the rate of heat transfer, facilitation of chemical reactions, creation of structure, addition of energy in order to create or break molecular bonds, etc. The mixing mechanisms occurring in food and polymer processing equipment can be broadly characterized into 'dispersive' and 'non-dispersive' (or extensive) (Wang & Manas-Zloczower 2001). Dispersive mixing is the reduction in size of a cohesive component within a continuous fluid. Examples include dis-agglomeration of solid particles and break-up of immiscible droplets and gas bubbles dispersed in a continuous fluid. Non-dispersive or extensive mixing can be further categorized as 'distributive' or 'laminar.' Distributive mixing is the process of material re-arrangement and is related to the material residence time distribution; whereas, laminar mixing deals with the affine stretching and folding of material elements and is characterized by the strain distribution functions (Meijer & Jannsen 1994).

In the food industry, mixing processes often involve highly viscous fluids like wheat flour dough, batters, and syrups. The mixing mechanisms include distribution of ingredients, laminar shear and elongation, and dispersion of agglomerates or air. For example, Bloksma (1990a) identified three main steps in the mixing of wheat flour dough. The first step is the homogenous distribution of the ingredients throughout the mixture to enable proper hydration of the flour particles, and to facilitate the release of the starch and protein, and allow gluten formation. The second step is dough development, which involves the application of mechanical energy to stretch the long glutenin molecules, thus imparting to the dough, its machineability and gas retention properties (MacRitchie 1986; Bloksma 1990a). The third step during mixing of dough is the incorporation and dispersion of air. Air incorporation and dispersion during mixing of dough, results in formation of air bubbles acting as nuclei for gas cells formed in dough through fermentation and leavening agents (Hosney 1985; MacRitchie 1986; Bloksma 1990a,b; Eliasson & Larsson 1993). Gas bubbles also act as nucleating sites for gas cells during direct and indirect expansion of extruded foods, resulting in the crispy structure. Thus, the efficiency of the mixing process in a batch or a continuous mixer, or in an extruder can be evaluated by looking at the ability of the machine to distribute ingredients, stretch the dough molecules, and disperse air bubbles or cohesive clumps.

The evaluation of dispersive and distributive mixing parameters is essential for scale-up and design of commercial mixers. Numerical simulation of mixing processes provides a non-intrusive way to compute the various mixing parameters in order to compare and

identify geometries that are similar in mixing performance and efficiency. In this chapter, we first look at the various quantitative measures that have been previously established to characterize dispersive and distributive mixing flows. Then we briefly discuss the governing equations and the finite element Method (FEM) techniques used to calculate these measures and summarize the results for batch and continuous mixers with varying geometries and material rheology. Finally, we analyze the dispersion of bubbles and drops in a continuous mixing device using FEM simulations of the flow.

12.2 Measures of mixing and evaluation of flow

There are several measures to characterize mixing, both extensive and dispersive. Mixing efficiencies in different flows created by different mixing equipment geometries can be compared by using the kinematic parameters developed by Ottino (1989) and the dispersive mixing index proposed by Yang and Manas-Zloczower (1992).

12.2.1 Efficiency of stretching

A kinematic analysis of laminar stretching has been developed (Ottino 1989) in which the capacity of the flow to stretch and fold the interfaces of material elements is quantified by calculating the stretching of infinitesimal vectors (2D flows) and surfaces (3D flows). A global efficiency of mixing is then estimated by analyzing the stretching of a statistically large number of material points in the flow domain.

Let Ω^0 and Ω denote the domain of a homogenous liquid at times 0 and t, respectively. If a material point P has a position $\boldsymbol{X}$ in Ω and $\mathbf{x}$ in Ω^0, the motion of the fluid is then described by the following equation.

$$\boldsymbol{x} = \chi(\boldsymbol{X},t) \tag{12.1}$$

The deformation of a material fiber $\mathrm{d}\boldsymbol{X}$ in Ω^0 with a unit orientation $\boldsymbol{M}$ into a material fiber $\mathrm{d}\boldsymbol{x}$ with a unit orientation $\boldsymbol{m}$ at a time t is defined as:

$$\mathrm{d}\boldsymbol{x} = \boldsymbol{F} \cdot \mathrm{d}\boldsymbol{X} \tag{12.2}$$

where $\boldsymbol{F}$ is the deformation gradient tensor. The equivalent relation for the deformation of an area element $\mathrm{d}\boldsymbol{a}$ with orientation $\boldsymbol{n}$ into $\mathrm{d}\boldsymbol{A}$ with an orientation $\boldsymbol{N}$ in a 3D flow is given as given below.

$$\mathrm{d}\boldsymbol{a} = (\det \boldsymbol{F}) \cdot (\boldsymbol{F}^{-1})^T \ \mathrm{d}\boldsymbol{A} \tag{12.3}$$

The strain is then measured as:

$$\lambda = \lim_{|\mathrm{d}\boldsymbol{X}|\to 0} \frac{|\mathrm{d}\boldsymbol{x}|}{|\mathrm{d}\boldsymbol{X}|} \ \eta = \lim_{|\mathrm{d}\boldsymbol{A}|\to 0} \frac{|\mathrm{d}\boldsymbol{a}|}{|\mathrm{d}\boldsymbol{A}|} \tag{12.4}$$

where λ and η are called the length stretch and the area stretch, respectively. The efficiency of the flow to stretch and fold the material is quantified using λ and η. The instantaneous stretching efficiencies for d$\boldsymbol{X}$ and d$\boldsymbol{A}$ are given as:

$$e_\lambda(\boldsymbol{X},\boldsymbol{M},t)=\frac{D\ln\lambda/Dt}{(\boldsymbol{D}:\boldsymbol{D})^{1/2}}\quad e_\eta(\boldsymbol{X},\boldsymbol{N},t)=\frac{D\ln\eta/Dt}{(\boldsymbol{D}:\boldsymbol{D})^{1/2}} \tag{12.5}$$

where $\boldsymbol{M}=\mathrm{d}\boldsymbol{X}/|\mathrm{d}\boldsymbol{X}|$ and $\boldsymbol{N}=\mathrm{d}\boldsymbol{A}/|\mathrm{d}\boldsymbol{A}|$.
In equations (12.5), $\boldsymbol{D}$ is the rate of strain tensor and $(\boldsymbol{D}:\boldsymbol{D})^{1/2}$ is the magnitude of $\boldsymbol{D}$. For an incompressible Newtonian fluid, the viscous dissipation is given by $\boldsymbol{\tau}:\boldsymbol{D}=2\mu(\boldsymbol{D}:\boldsymbol{D})$, and hence, the local instantaneous efficiency in equations (12.5) gives the fraction of dissipated energy that is used to stretch the material. The local instantaneous efficiency has a range between -1 and 1.

The time-averaged stretching efficiencies are then calculated as shown below.

$$\left\langle e_\lambda\right\rangle(\boldsymbol{X},\boldsymbol{M},t)=\frac{1}{t}\int_0^t e_\lambda(\boldsymbol{X},\boldsymbol{M},t')\mathrm{d}t'\quad\left\langle e_\eta\right\rangle(\boldsymbol{X},\boldsymbol{N},t)=\frac{1}{t}\int_0^t e_\eta(\boldsymbol{X},\boldsymbol{N},t')\mathrm{d}t' \tag{12.6}$$

The time-averaged mixing efficiency can be used to classify flows into (a) flows with no re-orientation where the efficiency decays with time as t^{-1}, (b) flows with partial re-orientation but with the time-averaged efficiency, still decaying as t^{-1}, and (c) flows with strong re-orientation but with the time-averaged efficiency tending to a constant value (Figure 12.1) (Ottino 1989).

12.2.2 Dispersive mixing efficiency

Dispersion of agglomerates and drops in flow will require the application of enough mechanical stress to overcome the interfacial forces holding the particles together. It has been shown from fundamental drop break-up studies that this mechanical stress required for break-up depends on the type of flow. Pure elongational or irrotational flows are more effective in breaking up of droplets and agglomerates than flows of simple shear type, and thus, a parameter to quantify the ratio of rotational and irrotational flow components is useful in analyzing the dispersive ability of a flow (Grace 1982; Bentley & Leal 1986;

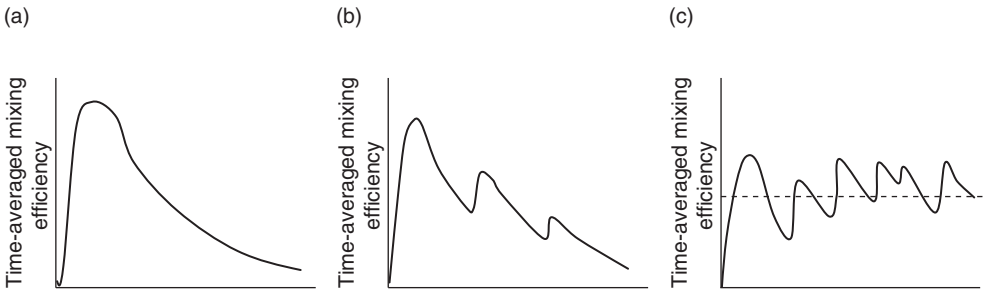

Fig. 12.1 Typical behavior of time-averaged mixing efficiency. [Reprinted from Ottino (1989) with permission from Cambridge University Press.]

Manas-Zloczower & Feke 1988, 1989). Cheng and Manas-Zloczower (1990) introduced a parameter λ_{MZ} called the 'mixing index,' defined as:

$$\lambda_{MZ} = \frac{|\mathbf{D}|}{|\mathbf{D}| + |\mathbf{\Omega}|} \tag{12.7}$$

where $\mathbf{D}$ and $\mathbf{\Omega}$ are the rate of deformation and vorticity tensors, respectively. The dispersive ability of a mixing device can then be characterized by the combination of the distributions of mixing index and the shear stresses. The value of λ_{MZ} ranges from 0 for pure rotation to 0.5 for simple shear, to 1.0 for pure elongation. It should be noted that the Manas-Zloczower mixing index defined above is not frame invariant. Flow type parameters that are frame invariant were reviewed by Connelly and Kokini (2003) for mixing index. The computation of these frame-invariant mixing indices required the use of high-density meshes, thus greatly increasing the computational costs, while giving information similar to the non-frame-invariant mixing index.

12.2.3 Distributive mixing efficiency

The distribution of material points in the mixer can be quantified using the segregation scale, $S(t)$. First, the concentration between M pairs of material points in the mixer separated by a distance $|r|$ is correlated, using a coefficient $R(|r|)$ defined as:

$$R\left(|r|\right) = \frac{\sum_{j=1}^{M} (c_j^{'} - \overline{c}) \cdot (c_j^{''} - \overline{c})}{MS^2} \tag{12.8}$$

where c_j' and c_j'' are the concentrations of the points of the jth pair, $\overline{c}$ is the average concentration of all the points, and S is the standard deviation. If ξ is chosen such that $R(\xi,t) = 0$ when $r = \xi$, then the segregation scale $S(t)$ is given by the following equation.

$$S(t) = \int_0^{\xi} R(r,t)dr \tag{12.9}$$

The parameter $S(t)$ is a good indicator of the average size of the segregated regions on a global scale and cannot detect local defects in flow (Connelly & Kokini 2007).

The deviation in the distribution of a cluster of minor ingredient particles from an ideal, random distribution is given by the cluster distribution index:

$$\varepsilon = \frac{\int_0^{\infty} [c(r) - c(r)_{ideal}]^2 dr}{\int_0^{\infty} [c(r)_{ideal}]^2 dr}, \tag{12.10}$$

where $c(r)$ is the coefficient of probability density function, and the value of ε varies from 0 for an ideal distribution to 1 where all the points in the cluster are at the same position.

12.3 Governing equations for calculation of flow

For an incompressible and isothermal fluid flow, the velocity profiles are obtained by solving the continuity and conservation of momentum equations given by:

$$\nabla \cdot \boldsymbol{v} = 0 \tag{12.11}$$

$$\nabla \cdot \sigma + \rho \boldsymbol{f} = \rho \left(\frac{\partial \boldsymbol{v}}{\partial t} + \boldsymbol{v} \cdot \nabla \boldsymbol{v} \right) \tag{12.12}$$

where ρ is the fluid density and $\boldsymbol{f}$ is the external body force per unit mass. The stress tensor $\boldsymbol{\sigma}$ is the sum of the isotropic pressure (P) and an extra stress tensor ($\boldsymbol{T}$).

$$\sigma = -P\boldsymbol{I} + \boldsymbol{T} \tag{12.13}$$

In a non-isothermal flow situation, the equation for conservation of energy has to be solved in order to get the temperature profiles.

$$\rho C(T) \cdot \left(\frac{\partial T}{\partial t} + \boldsymbol{v} \cdot \nabla T \right) = \boldsymbol{T} : \nabla \boldsymbol{v} + r - \nabla \cdot q \tag{12.14}$$

In equation (12.14), $C(T)$ is the heat capacity as a function of the temperature, r is the volumetric heat source, q is the heat flux, and $\boldsymbol{T}$:$\nabla \boldsymbol{v}$ describes the viscous heating.

The analysis of flow would be complete only with an appropriate constitutive equation to calculate the stress tensor of equation (12.3). For a generalized Newtonian fluid in an isothermal flow, the stress tensor $\boldsymbol{T}$ is given as a function of the rate of deformation tensor $\boldsymbol{D}$ and the viscosity function $\mu(\dot{\gamma})$, where $\dot{\gamma}$ is the local shear rate calculated from the rate of deformation tensor.

$$\boldsymbol{T} = 2\mu \mathbf{D} \tag{12.15}$$

$$\dot{\gamma} = \sqrt{2tr(\mathbf{D}^2)} \tag{12.16}$$

For a Newtonian fluid, the viscosity function would reduce to a constant value μ_0, called the Newtonian or zero-shear-rate viscosity. Several models are available for shear-dependant viscosity of polymeric fluids, with the power-law and the cross models being the most frequently used ones. The power-law model for viscosity is given by:

$$\mu = m(\dot{\gamma})^{n-1} \tag{12.17}$$

where m is the consistency factor and n is a property of the fluid material called the power-law index. A Newtonian fluid would be a special case, where m is equal to the Newtonian viscosity μ_0 and n would be equal to 1. A modified cross model was used to model the steady shear data of 0.11% carbopol solution (Prakash 1996) and is given by the following equation.

$$\mu = \mu_0 (1 + k\dot{\gamma})^{n-1} \tag{12.18}$$

12.4 CFD approaches for simulation of mixing flows

12.4.1 Finite element method

The solution of the set of equations consisting of the conservation of mass and momentum, the energy equation (for non-isothermal problems), and the appropriate constitutive equation for a complex mixing flow is usually not obtainable using analytical methods. Instead, numerical and computational methods are used to solve complex flow profiles. In particular, the finite element method has been effectively used to solve problems involving highly viscous fluids in complex mixer flows (Dhanasekharan & Kokini 2000, 2003; Connelly & Kokini 2003, 2004, 2006a,b, 2007).

There are three main steps involved in solving a flow problem using FEM (Reddy 1993).

- The flow volume or the domain of the problem is constructed as a mesh made of several sub-domains called finite elements.
- The physical processes are approximated over each finite element using polynomial functions and algebraic equations relating the physical quantities at the element nodes.
- The equations for each finite element are assembled and solved using continuity and/or balance of physical quantities across the elements.

The equations of motion are simplified by assuming the inertia terms to be negligible and are solved for the velocity, pressure, and stress tensor values over the entire flow domain Ω. The set of finite element equations are then given by:

$$\int_{\Omega} (-\nabla p + \nabla . \boldsymbol{T} + \boldsymbol{f}) . \boldsymbol{u} \, \mathrm{d}\Omega = 0, \quad \forall u \in V \tag{12.19}$$

$$\int_{\Omega} (\nabla . \boldsymbol{v}) q \, \mathrm{d}\Omega = 0, \quad \forall q \in P \tag{12.20}$$

where V and P are the function spaces of the velocity and pressure fields, respectively, and $\boldsymbol{u}$ and q are weighting functions. Several computational fluid dynamics (CFD) software are available which solve the set of independent algebraic equations. In most of the researches cited in this chapter, the numerical simulations were conducted using the Polyflow CFD software (Fluent Inc., Lebanon, NH). A typical flow problem would include the following steps: building the mixer geometry and converting it into an FEM mesh, using the mesh generator, Gambit; defining the flow boundaries, material properties, numerical parameters, and operating conditions using the Polydata interface; solving for velocity profiles using the FEM solver, Polyflow; calculating the various mixing measures from the velocity data using a post-processor, FLPost/Fieldview.

12.4.2 Techniques to handle moving parts

The Polyflow FEM solver is primarily designed for simulating applications that involve isothermal/non-isothermal, 2D and 3D, steady-state and time-dependant viscous and viscoelastic fluid flows. In case of mixer geometries with moving paddle elements causing a continuously changing geometry of the flow domain, Polyflow uses a mesh superposition

technique (MST), wherein the moving element and the flow domain are meshed separately and superimposed (Connelly & Kokini 2006a). The equation of motion is then modified using a penalty term H and is given by:

$$H(\boldsymbol{v}-\bar{\boldsymbol{v}})+(1-H)(-\nabla P+\nabla.T+\rho\boldsymbol{g}-\rho\boldsymbol{a})=0 \tag{12.21}$$

where $\boldsymbol{v}$ is the velocity, $\bar{\boldsymbol{v}}$ is the local part velocity, P is the pressure, T is the extra stress tensor, $\rho\boldsymbol{g}$ is the volume force, and $\rho\boldsymbol{a}$ is the acceleration. The penalty term H is a step function with a value set equal to 1 for all nodes on a moving part and equal to 0 for all nodes in the fluid volume. In such a scenario, the mass conservation equation is also modified using a relative compression factor β:

$$\nabla.v+\frac{\beta}{\mu}\Delta P=0 \tag{12.22}$$

where μ is the local viscosity.

12.5 FEM numerical simulation of batch mixer geometries

12.5.1 3D numerical simulation of flow in a Brabender Farinograph®

The Farinograph is a low shear rate model batch mixer used for flour testing. It has two non-intermeshing asymmetrical sigma blades rotating in opposite directions in a 3:2 speed ratio. Plate 12.1 shows the FEM mesh of the bowl and the sigma blades. Connelly and Kokini (2006a) performed steady-state, isothermal simulations on three different fluid models in the Farinograph—a Newtonian corn syrup, a 2% carboxymethyl cellulose (CMC) solution, and a 0.11% carbopol solution. The shear-dependant viscosities of the CMC and carbopol solutions were fitted with the power-law and modified cross model respectively, using the experimental data. The effect of increasing shear thinning on the trends in the velocity profiles was shown to be consistent with the experimental results of Prakash and Kokini (2000). Plate 12.2 shows the mixing index for the three fluid models at blade angular positions of 180º and 270º, respectively. An increase in shear thinning showed an increase in shearing at the blade edges and in the region between the blades while worsening the mixing in the regions away from the blades. The dispersive mixing index was highest in the region swept by the blades which had high values of shear rate and mixing index.

12.5.2 Analysis of mixing in 2D single-screw and twin-screw geometries

Connelly and Kokini (2007) analyzed mixing in a 2D axial cross-section of the Readco® 2″ continuous processor (Readco Inc., York, PA), neglecting the flow along the barrel length. The differences in mixing efficiency between a single paddle and two interacting paddles were studied by comparing the distributive mixing, segregation and the dispersive mixing in the 2D single-screw and twin-screw mixers. The single paddle geometry was meshed using a rotating reference frame technique where the barrel or the outer boundary of the mixer rotates around a fixed paddle, while the twin-screw geometry was meshed using MST. (Figure 12.2).

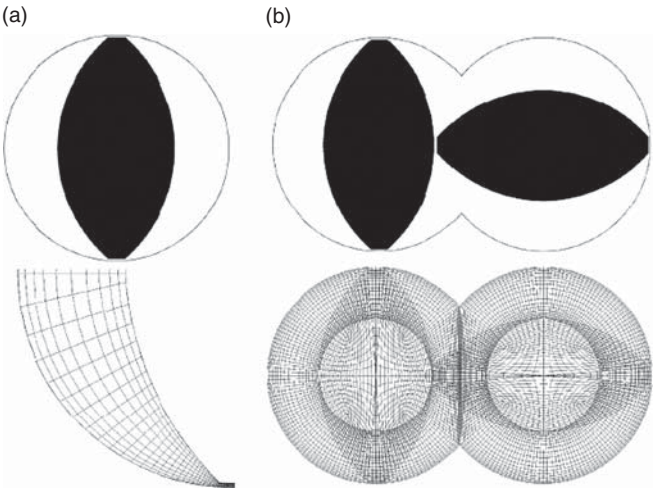

Fig. 12.2 FEM meshes for flow simulations: (a) single-screw mixer in the rotating reference frame and (b) twin-screw mixer with MST. [Reprinted from Connelly and Kokini (2007) with permission from Elsevier.]

The mixing simulations were run with a Carreau model for dough using a mixed Galerkin FEM simulation in Polyflow (Dhanasekharan *et al*. 1999). The area and magnitude of elongational flows was greater in the twin screw when compared to the single screw. Specifically, in the twin-screw geometry, the mixing index and shear stress values were lowest in areas separated from the paddle interaction, while the highest mixing index and shear stress values were generally found in the paddle intermeshing regions.

Analysis of the distributive mixing showed that the twin-screw geometry had a better cluster distribution index for an initial position of the cluster just behind the blade tip in the leftmost flow domain, whereas for a material cluster initiating in the middle of the leftmost flow domain, both single-screw and twin-screw geometries showed weak distribution. The single-screw mixer showed cyclic distribution indicating that the material points were unable to leave the streamlines. The stretching in the single-screw mixer remains at a constant level after an initial increase, while it increases exponentially with time in the twin-screw mixer. The instantaneous efficiency of the single-screw mixer oscillates around zero, indicating the periodic stretching and compression of the same material points. In contrast, the instantaneous efficiency of the twin-screw mixer is always positive, indicating that the material points are continuously re-oriented in the intermeshing region due to the splitting of the flow by the second paddle.

These simulations were useful in showing that the twin-screw mixer showed substantially higher mixing efficiency as compared to the single-screw geometry. However, 3D simulations of the full-length mixer are needed to account for the axial flow disturbances caused by mixer design, for example, staggered mixing elements.

12.6 3D numerical simulation of twin-screw continuous mixer geometries

3D Numerical simulation of the mixing of a generalized Newtonian fluid were performed in a full-length kneading section of the Readco continuous processor with nine paddle

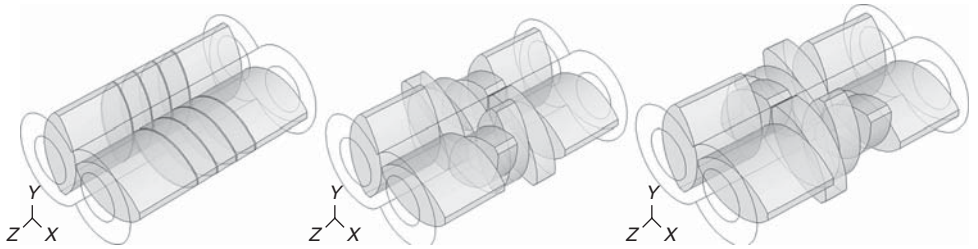

Fig. 12.3 Paddle configurations of the full nine paddle pair geometry: (a) flat, (b) 45F, and (c) 45R.

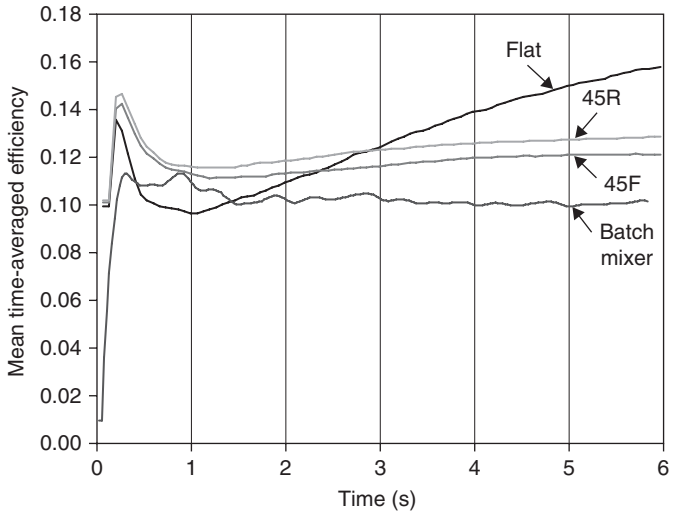

Fig. 12.4 Time-averaged efficiencies for various paddle configurations of the Readco mixer in comparison to the Farinograph during mixing of a Newtonian corn syrup at 100 rpm.

pairs. First, the velocity and pressure profiles were calculated for a Newtonian corn syrup with a viscosity of 53 P and a density of 1,409 kg/m^3. The flow data was calculated for every 10º movement of the paddles for 10 rotations at 3 different screw speeds (1 rpm, 50 rpm, and 100 rpm) and the mean logarithm of the length of stretch, instantaneous mixing efficiency, time-averaged mixing efficiency and normalized segregation scale were evaluated for 3 different screw configurations and compared with the Farinograph data.

12.6.1 Distributive mixing efficiency in a 3D mixing geometry

Figure 12.3 shows three different paddle configurations of the full-length mixing region of the Readco mixer. By staggering the three center paddle element pairs, three different configurations providing differences in the overall pressure drop and flow profiles were obtained. The first configuration (flat) has all paddle elements aligned parallel to each other, while the other two have the center three paddle elements aligned at a successive rotation of 45º in a forward (45F) or a reverse direction (45R), respectively.

Figure 12.4 shows the time-averaged efficiencies of the three continuous mixer geometries with the Farinograph. At the start of the mixing process, the efficiency shows a

sharp rise for all the geometries before settling at a steady value. It can be seen that changing the mixer geometries causes the mixing efficiencies to evolve differently. At shorter residence times, both the staggered configurations (45F and 45R) show greater efficiencies. However, at longer times, they equilibrate to a lower value compared to the flat configuration, which shows a steady increase. The mixing efficiency of the batch mixer shows a greater periodicity but a lesser average value at the end of 10 rotations (or 6 s) in comparison to the continuous mixer geometries.

An increase in the screw speed resulted in a decrease in the time-averaged instantaneous mixing efficiency, as shown in the Plate 12.3. The efficiency was the highest at a screw speed of 1 rpm compared to 50 and 100 rpm and the batch mixer due to the high value of material residence time at the slow speed allowing for greater stretching and folding of the material. Among all the three configurations studied, the flat configuration is the closest in terms of efficiency when compared to the batch mixer. However, a better mixing performance would need a matching of all the mixing measures including length of stretch, segregation scale and dispersive mixing index.

12.6.2 Evaluation of dispersive mixing in 3D continuous mixer geometry

The Manas-Zloczower dispersive mixing index [equation (12.7)] was calculated from the flow data. Plate 12.4 shows the contour maps of the mixing index and the shear rate on a vertical cross-sectional plane at the eighth paddle of each paddle configuration at 100 rpm. A mixing index value of greater than 0.7 indicates greater elongational flows and better dispersion. For all the paddle configurations, these high values of mixing index are found in the plug flow regions between the paddle and the barrel wall, and the intermeshing regions. However, the intensity of these regions is higher for the staggered configurations. Apart from the mixing index, corresponding high values of shear stress are also needed for effective dispersion. It can be seen from the contour maps (Plate 12.4) that the highest shear rates (and hence, shear stress for the Newtonian fluid under consideration) occur in the intermeshing regions. Hence, dispersive mixing ability of the staggered configurations is greater due to the higher mixing index values in the intermeshing regions.

Plate 12.5 shows the dispersive mixing index contours evaluated for a shear thinning 2% carboxymethyl cellulose in a shortened mixer of two paddle pairs. It shows the distribution of the flow type for three screw configurations. The stagger angle between the successive paddle elements was 0º (2×), 45º (2 × 45) or 90º (2 × 90) and the material flow rate and the screw speed were the operational variables studied. The mixing indices were calculated for points throughout the volume of the mixer after one full rotation of the paddles. In all three mixer configurations (2×, 2 × 45 and 2 × 90), the greatest number of points had a mixing index of around 0.5 or 0.1, indicating most of the flow to be in the simple shear or rotational flow region. Points in the elongational flow region (mixing index > 0.7) are significantly fewer and the density of this region will play an important role in the dispersion of bubbles and drops as will be discussed in the next section.

A comparison between the different mixer configurations shows the stagger-less configuration (2×) as having greater density of rotational flow, as well as in the region of elongational flow while the ninety degree staggered configuration (2 × 90) has the greatest collection of points with a mixing index near 0.5 and thus has the potential for more shear flow. It can be seen from Figure 12.5 that the change of screw speed did not significantly affect the distribution of the dispersive mixing index. It will however affect the distribution

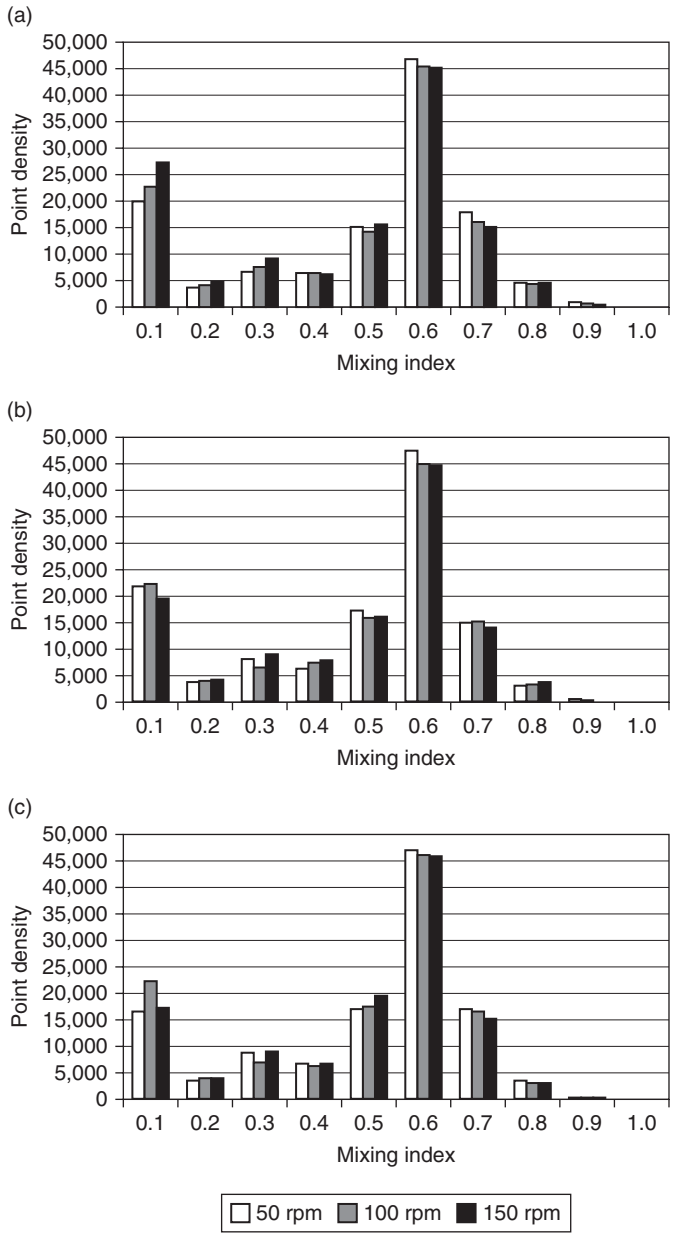

Fig. 12.5 Mixing index density distribution for 2× configuration at different screw speeds during mixing of a shear thinning 2% CMC solution in a two paddle continuous mixer: (a) 2×, (b) 2 × 45, and (c) 2 × 90.

of shear stresses that cause the dispersion of bubbles and drops in flow; therefore, in order to determine the dispersive ability of the mixer, the combined effects of screw configuration (which influences the flow type) and the screw speed (which influences the flow strength) have to be studied. In addition, increasing the length of the mixer to a full nine paddle pairs will have an impact on the local distribution of the mixing index.

12.7 Prediction of bubble and drop dispersion in a continuous mixer

Bubbles and immiscible drops suspended in a fluid undergoing flow will deform and break up, if the flow strength is sufficiently large. In highly viscous flows, the deformation and break-up of a bubble or drop is governed by a dimensionless ratio called the capillary number (*Ca*):

$$Ca = \frac{\mu\dot{\gamma}}{\sigma} r \tag{12.23}$$

where μ is the viscosity of the continuous medium (food matrix), $\dot{\gamma}$ is the local shear rate, r is the bubble radius and σ is the surface tension of the food matrix (Meijer & Janssen 1994; Risso 2000). The capillary number can be defined as the ratio of viscous forces acting to deform the drop, to the interfacial forces acting to restore its spherical shape. When the viscous forces are large enough that the drop can no longer maintain a stable deformed shape, it breaks up. The determination of these break-up conditions is fundamental to the design of efficient dispersion processes.

Several researchers have studied numerically and experimentally the deformation and break-up of isolated drops in simple two-dimensional flows, in order to establish the critical value of the capillary number (Ca_{cr}) or the point at which the flow strength is strong enough to cause the drop deformation to become unsteady leading to break-up. (Grace 1982; Acrivos 1983; Bentley & Leal 1986; Khakhar & Ottino 1986).

For any given drop diameter, the Ca_{cr} is a function of the viscosity ratio of the continuous and discontinuous phases (p) and the flow type parameter (α), which is a quantification of the shear and extensional characters of the flow (Grace 1982; Risso 2000). The relation between Ca_{cr} and the viscosity ratio p has been developed for a range of two-dimensional planar flows of the form:

$$\boldsymbol{e} = \frac{1}{2}(1+\alpha)\begin{pmatrix} 0 & 1 & 0 \\ 1 & 0 & 0 \\ 0 & 0 & 0 \end{pmatrix} \quad \text{and} \quad \boldsymbol{\omega} = \frac{1}{2}(1-\alpha)\begin{pmatrix} 0 & 1 & 0 \\ -1 & 0 & 0 \\ 0 & 0 & 0 \end{pmatrix}, \quad \text{where } -1 \le \alpha \le 1 \tag{12.24}$$

where $\boldsymbol{e}$ and $\boldsymbol{\omega}$ are the dimensionless rate of deformation and vorticity tensors, respectively. The value of α ranges from -1 for pure rotation, to 0 for simple shear and 1.0 for pure elongation. Thus, a simple shear flow would have equal contributions of rotation and elongation, whereas values of $\alpha > 0$ would cause the elongation to be greater than rotation.

At very small viscosity ratios ($p \to 0$) involving highly viscous fluids in the continuous phase, the drop elongates to a slender body shape prior to break-up. In such a case, Ca_{cr} for simple shear flow ($\alpha = 0$) is given by:

$$Ca_{cr} \approx 0.0501 p^{-2/3} \tag{12.25}$$

and for flows with $0 < \alpha \le 1.0$,

$$Ca_{cr} = \frac{0.145 p^{-(1/6)}}{a^{1/2}} \tag{12.26}$$

For the case of $\alpha = 1.0$ or pure elongation, equation (12.26) would transform into the following equation.

$$Ca_{cr} = 0.145p^{-(1/6)} \tag{12.27}$$

The correlations between equations (12.25) and (12.27) have been validated by experiments and these show that a slight deviation in the flow character from simple shear would drastically reduce the flow strength required for drop break-up (Grace 1982; Bentley & Leal 1986). Thus, for dispersing drops in systems with very low viscosity ratios, it is desirable to have more elongational flows. Flows in continuous mixing devices are a complex distribution of shear and elongation, depending on the paddle element configurations (Connelly & Kokini 2003). Flow type distribution in mixing devices has been quantified in various mixing simulation studies using the Manas-Zloczower mixing index (λ_{MZ}) defined in equation (12.7) (Li & Manas-Zloczower 1994; Connelly & Kokini 2006a, 2007). The mixing index λ_{MZ} quantifies the ratio of shear and elongational flows and is related to the flow type parameter α by the following equation.

$$\lambda_{MZ} = \frac{1+\alpha}{2} \tag{12.28}$$

The value of λ_{MZ} ranges from 0 for pure rotation, to 1.0 for pure elongation, with 0.5 denoting simple shear flow.

FEM simulations were performed on the mixing of a highly viscous Newtonian corn syrup ($\mu \sim 1{,}200$ Pa s) in the full-length nine paddle pair mixing region of the Readco mixer in order to obtain the distribution of the capillary numbers (flow strength) and the mixing indices (flow type). Figure 12.6 shows the capillary numbers calculated from the maximum shear rates encountered by a 400 μm air bubble in the entire mixer volume with a flat configuration (Vyakaranam & Kokini 2008). It can be seen that the maximum possible capillary numbers fall well below the required critical value for break-up in simple shear flow for the corn syrup–air system under consideration (~1,833) and above the value for elongational flow (~2.046), suggesting that the distribution of elongational flows is critical for dispersion.

A study of the distribution of the dispersive mixing index and shear rates showed the variation of elongational flow at different cross-sections along the length of the mixer. Plate 12.6 shows the contour maps of shear rate and mixing index at the first, fourth and eighth paddle elements of the flat configuration. The density of elongational flow is the highest in the center region of the mixer, around the fourth paddle element, with the intermeshing regions showing high values of shear rates as well as mixing index.

The staggering of paddle elements also has an effect on changing the flow type distribution. Figures 12.7a–c show plots of the mixing index versus the capillary number for points at the three different locations in the mixer having a mixing index greater than 0.8. It can be seen that the density of these points is the greatest for the flat configuration and lowest for the 45° reverse stagger configuration (45R), suggesting higher break-up in the staggerless configuration.

The effect of process parameters like stagger angle and the screw speed on the distribution of flow type in a mixing device is critical information that will help in the design of mixers with better dispersive abilities.

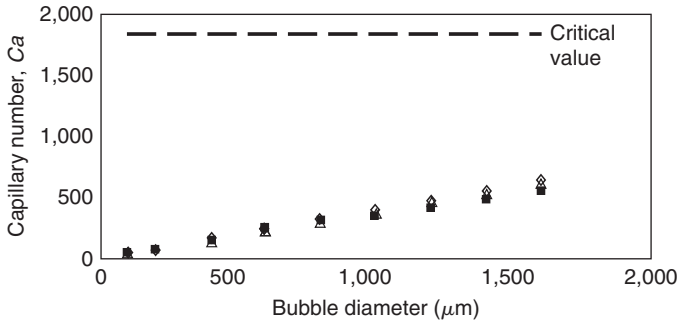

Fig. 12.6 Maximum Ca observed for flat configuration at 75 rpm plotted against the Ca_{cr} for simple shear and pure extension.

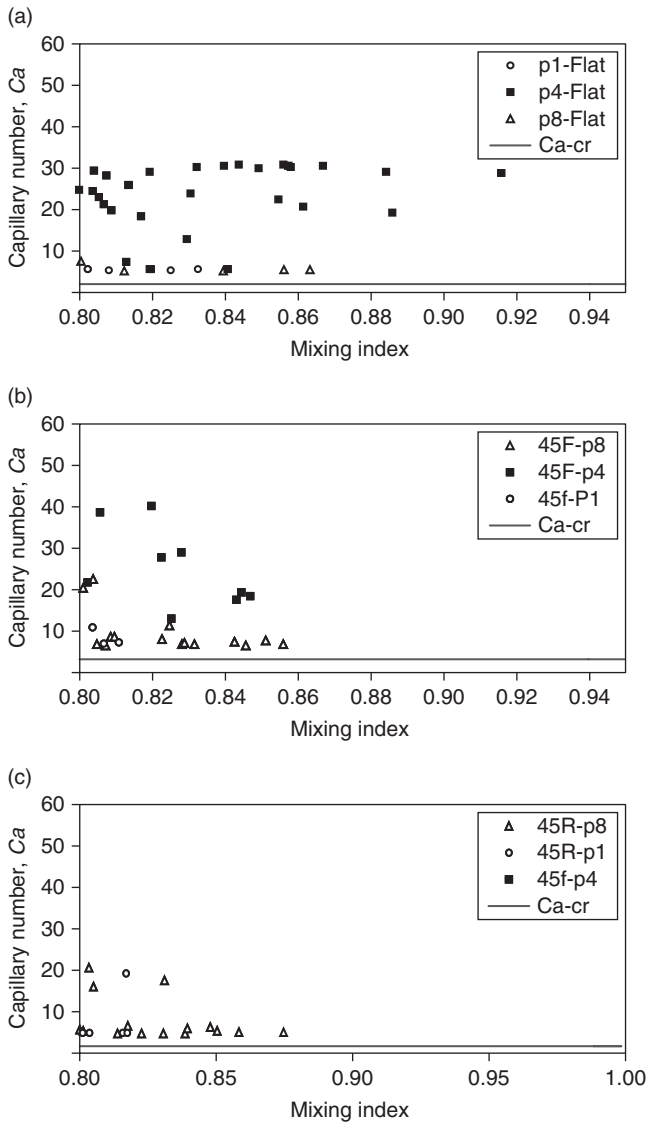

Fig. 12.7 Capillary number for mixing index >0.8: (a) flat configuration, (b) 45F configuration, and (c) 45R configuration, 75 rpm, bubble diameter 400 μm.

12.8 Summary

Numerical simulations using the FEM are an effective, cost-saving and non-intrusive way for analyzing and comparing the distributive and dispersive mixing ability of batch and continuous mixing devices. The dispersive and distributive mixing abilities of various mixer geometries have been studied during the mixing of model high-viscosity Newtonian and non-Newtonian fluids. Although there has been some work done (Dhanasekharan & Kokini 2000; Connelly & Kokini 2004), further investigations could focus on solving viscoelastic fluid flows in such mixing devices, thus bringing the knowledge much closer to real food systems. An analysis of dispersive mixing indices has been shown to be useful in predicting break-up of bubble and drops in viscous continuous mixing flows.

Acknowledgments

The authors would like to thank the USDA Cooperative State Research, Education and Extension Service research for their support through the National Research Initiative grants # 2001-35503-10127 and 2003-35503-13907.

They would also like to acknowledge Dr. Robin Connelly, University of Wisconsin–Madison, for her valuable suggestions during the preparation of the manuscript.

References

Acrivos, A. (1983). The breakup of small drops and bubbles in shear flows. *Annals of New York Academy of Sciences*, **404**(1), 1–11.

Bentley, B.J. & Leal, L.G. (1986). An experimental investigation of drop deformation in steady, two-dimensional linear flows. *Journal of Fluid Mechanics*, **167**, 241.

Bloksma, A.H. (1990a). Rheology of the breadmaking process. *Cereal Foods World*, **35**(2), 228.

Bloksma, A.H. (1990b). Dough structure, dough rheology and baking quality. *Cereal Foods World*, **35**(2), 237.

Cheng, J.J. & Manas-Zloczower, I. (1990). Flow field characterization in a banbury mixer, *International Polymer Processing*, **5**(3), 178–83.

Cheng, H. & Manas-Zloczower, I. (1997). Chaotic features of flow in polymer processing equipment-relevance to distributive mixing. *International Polymer Processing*, **12**(2), 83.

Connelly, R.K. & Kokini, J.L. (2003). 2D numerical simulation of differential viscoelastic fluids in a single-screw continuous mixer: application of viscoelastic finite element methods. *Advances in Polymer Technology*, **22**(1), 22.

Connelly, R.K. & Kokini, J.L. (2004). The effect of shear thinning and differential viscoelasticity on mixing in a model 2D mixer as determined using FEM with particle tracking. *Journal of Non-Newtonian Fluid Mechanics*, **123**(1), 1.

Connelly, R.K. & Kokini, J.L. (2006a). 3D numerical simulation of the flow of viscous Newtonian and shear thinning fluids in a twin sigma blade mixer. *Advances in Polymer Technology*, **25**(3), 182.

Connelly, R.K. & Kokini, J.L. (2006b). Mixing simulation of a viscous Newtonian liquid in a twin sigma blade mixer. *AIChE Journal*, **52**(10), 3383.

Connelly, R.K. & Kokini, J.L. (2007). Examination of the mixing ability of single and twin screw mixers using 2D finite element method simulation with particle tracking. *Journal of Food Engineering*, **79**(3), 956.

Dhanasekharan, M., Huang, H., & Kokini, J.L. (1999).Comparison of the observed rheological properties of hard wheat flour dough with the predictions of the Giesekus–Leonov, the White–Metzner, and the Phan–Thien Tanner models, *Journal of Texture Studies*, **30** (5), 603–623.

Dhanasekharan, M. & Kokini, J.L. (2000). Viscoelastic flow modeling in the extrusion of a dough-like fluid. *Journal of Food Process Engineering*, **23**(3), 237.

Dhanasekharan, M. & Kokini, J.L. (2003). Design and scaling of wheat dough extrusion by numerical simulation of flow and heat transfer. *Journal of Food Engineering*, **60**(4), 421.

Eliasson, A.C. & Larsson, K. (1993). *Cereals in Breadmaking: A Molecular Colloidal Approach*, Marcel Dekker, Inc., New York.

Grace, H.P. (1982). Dispersion phenomena in high viscosity immiscible fluid systems and application of static mixers as dispersion devices in such systems. *Chemical Engineering Communications*, **14**, 225.

Hosney, R.C. (1985). The mixing phenomena. *Cereal Foods World*, **30**(7), 453.

Khakhar, D.V. & Ottino, J.M. (1986). Deformation and breakup of slender drops in linear flows. *Journal of Fluid Mechanics*, **166**, 265.

Li, T. & Manas-Zloczower, I. (1994). Flow field analysis of an intermeshing counterrotating twin screw extruder. *Polymer Engineering and Science*, **34**(7), 551.

Manas-Zloczower, I. & Feke, D.L., (1988). Analysis of agglomerate separation in linear flow fields. *Intenational Polymer Processing Journal*, **II**(3/4), 185.

Manas-Zloczower, I. and Feke, D.L., 1989. Analysis of agglomerate rupture in linear flow fields. *Intenational Polymer Processing Journal*, **IV**(1), 3.

Meijer, M.E.H. & Janssen, J.M.H. (1994). Basic concepts. In: *Mixing and Compounding of Polymers: Theory and Practice* (eds I. Manas-Zloczower & Z. Tadmor). Carl Hanser Verlag, New York.

Ottino, J.M. (1989). *The Kinematics of Mixing: Stretching, Chaos, and Transport*. Cambridge University Press, Cambridge.

Prakash, S. (1996). Characterization of shear rate distribution in a model mixer using laser Doppler anemometry. Ph.D. Thesis, Department of Food Science Rutgers University, New Brunswick, NJ, p. 315.

Prakash, S. & Kokini, J.L. (2000). Estimation and prediction of shear rate distribution as a model mixer. *Journal of Food Engineering*, **44**(3), 135.

Reddy, J.N. (1993). An introduction to the finite element method (ed. J.N. Reddy) 2nd edn. McGraw-Hill, New York.

Risso, F. (2000). The mechanisms of deformation and breakup of drops and bubbles. *Multiphase Science and Technology*, **12**, 1.

Vyakaranam, K.V. & Kokini, J.L. (2008). Study of the dynamics and size distributions of air bubbles during mixing in a continuous food mixer. In: *Bubbles in Food2: Novelty, Health and Luxury* (eds G. Campbell, M. Scanlon & L. Pyle). AACC Press, St.Paul, MN.

Wang, W. & Manas-Zloczower, I. (2001). Temporal distributions: the basis for the development of mixing indexes for scale-up of polymer processing equipment. *Polymer Engineering and Science*, **41**(6), 1068–1077.

Yang, H.H. & Manas-Zloczower, I. (1992). 3D Flow field analysis of a Banbury mixer. *Proceedings of the International Congress on Rheology*, p. 408.

13 Particulate and powder mixing

John J. Fitzpatrick

13.1 Introduction

The food industry produces a wide variety of particulate mixtures, including soups, cakes, baby foods, custard, cereal mixes and spice mixes, which combine a wide variety of ingredients such as sugars, flour, dairy powders, salt, dried cereals, vegetables and fruits. The mixing of these particulate ingredients involves the movement of the ingredients throughout each other, in an effort to produce a uniform concentration of each component throughout the mix. Mixing of dry particulates and powders is a common operation in many industries, thus the basic principles of mixing and equipment used are common amongst most applications including food powders, although each application may have certain issues that are of particular relevance. Consequently, this chapter describes many of the important aspects of particulate mixing and concludes with a section concentrating on aspects that are of special relevance to food particulate mixtures.

13.2 Characterisation of particulate mixtures

13.2.1 Types of mixtures

13.2.1.1 *Perfect mixtures*

A perfect mixture is produced by positioning individual particles to obtain a uniform concentration of each ingredient throughout the mix. For example, consider a 50:50 mix of black and white particles. A perfect mixture of these black and white particles is illustrated in Figure 13.1a. This is produced by selectively positioning black and white particles in specified adjacent positions. In practice, commercial mixers cannot do this, as they do not select individual particles and place them in specific positions relative to other particles.

13.2.1.2 *Random mixtures*

In a random mixture, the probability of finding a particle of any component is the same at all positions in the mixture and is equal to the proportion of that component in the mixture as a whole. Figure 13.1b illustrates a random mixture of the same black and white particles. Here, a toss of a coin decides if a space is filled by a black or white particle. From looking at the figure, there appears to be a similar number of particles in the top half as the bottom half or in the right half as the left half because the probability of finding a black particle anywhere in the mix is the same. Industrial mixers strive to produce random mixtures by inducing motions in the particles to randomly disperse particles throughout each other.

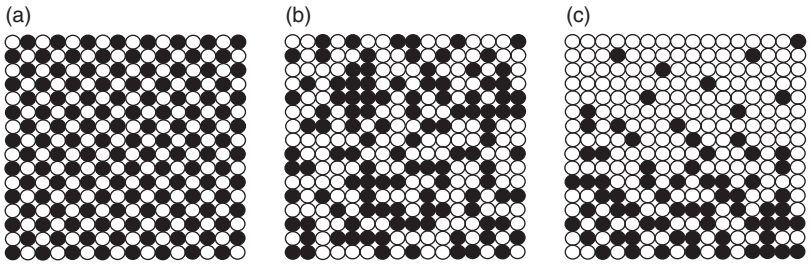

Fig. 13.1 Mixture types: (a) perfect mixture, (b) random mixture and (c) segregating mixture.

13.2.1.3 *Segregating mixtures*

This is a mixture where there is a greater probability of finding a given component's particles in one region of the mix. Figure 13.1c illustrates a segregating mix, where it is obvious that there are more black particles than white particles in the bottom half, that is, there is a segregation of black particles towards the bottom half.

13.2.1.4 *Ordered mixtures*

These may occur in cohesive mixes containing larger sized ingredients and smaller sized ingredients. An ordered mix is where the smaller ingredient particles effectively coat the larger particles. This may result in a better mix than a random mix because the smaller particles are, in a sense, positioned onto the larger particles due to the cohesion between the particles. However, it may also lead to a segregated mix if the action of the mixer is unable to uniformly distribute the small particles throughout the mix because of strong cohesion between small and large particles.

13.2.2 Mixture quality

The job of a mixer is to try and achieve a uniform composition of component ingredients throughout the whole mix. For example, if 20 samples were taken randomly from throughout the mix then all should have the exact same composition. In practice, this is not achieved and deviations will exist between the composition of the samples and mean composition of the whole mix. Mixture quality is a quantitative assessment of these deviations. The smaller the deviations, the better will be the mixture quality. Assessment of mixture quality is presented in Section 13.3.

13.3 Assessment of mixture quality

13.3.1 Sampling

The purpose of taking samples is to estimate the mixture quality of the whole volume of material from analysing a small proportion of it (the samples). It should be noted that mixture quality will depend on the size of samples taken, the number of samples taken, the positions from where the samples are taken and the sampling procedure used, as described below.

13.3.1.1 *Sample size*

Sample size refers to the physical size of the sample, that is, its mass or volume. It is very important and will have a significant effect on mixture quality. The smallest sample size is at the size of the smallest particle. At this scale of scrutiny, there is no mixture. On the other hand, the largest sample size is the contents of the entire mixer. At this scale of scrutiny, the mixture quality is the same as the composition. As a result, there is a greater probability of measuring a better mixture quality as sample size increases. This leads to the question of what sample size should be selected. The answer to this is the scale of scrutiny implemented by the user or the sample size used by the consumer. This could be the size of a teaspoon, a capsule, a tablet or a 25 kg bag. Thus, an adequate mixture quality must be achieved at the sample size used by the consumer.

13.3.1.2 *Sampling procedure*

First of the all, the following two 'golden rules of sampling' proposed by Allen (1981) should be considered.

- Samples should be taken from a moving stream.
- Samples should be randomly taken from throughout the whole mixture.

For continuous mixers, the first rule is easy to implement as a mixture is continuously leaving the mixer. For batch mixers, this involves taking samples at the end of mixing during mixture discharge. However, in practice, sampling of the powder stationary bed inside the mixer is often done, especially if it is required to evaluate mixture quality at discrete times during the batch mixing operation. There are a number of devices for taking a sample from a stationary bed of powder, such as a sampling thief and pneumatic lance. The problem with these devices is that they may bias the sample, for example, a device may preferentially sample smaller particles. Consequently, care must be taken with the use of these devices. Biasing of the sample by the sampling technique may be seen by assessing the component concentration values of the samples. If there is a tendency for most of them to be either greater or lesser than the target concentration, this may suggest biasing by the sampling technique, provided that samples are taken randomly from throughout a batch.

The second rule of random sampling of the entire mixture is very important in case a segregated mix is produced. For example, if a mix is partially segregated from top to bottom, then taking samples only from the top is not representative of the whole mix. It is very important that the samples taken are representative of the whole mix because these samples are used to determine the mixture quality of the whole mix.

13.3.1.3 *Number of samples*

The variance in measured mixture quality will be influenced by the number of samples taken with small sample numbers leading to higher variance in mixture quality. Consider measuring the mixture quality from a small number of samples, such as four. If this was repeated, say 5 times, then a significant variation in the measured mixture quality would be noted. If the same test was repeated with a higher sample number of say 20, then the variance in mixture quality would be reduced. This variance in mixture quality will become smaller and smaller with more samples (Weinekötter & Gericke 2000), as illustrated in Figure 13.2. Consequently, it is required to choose a sufficient number of samples to reduce the effect of this source of variation. In practice, it is common practice to take at least 20–30 samples.

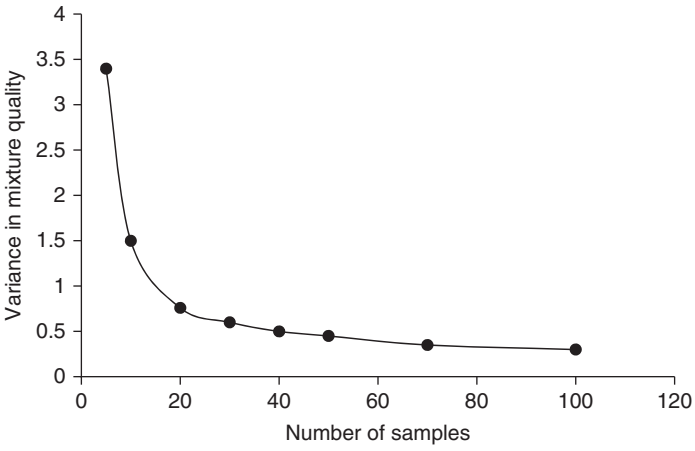

Fig. 13.2 Reduction in the variance in mixture quality with increase in the number of samples used to determine mixture quality.

13.3.1.4 *Analysing the samples*

This usually involves measuring the composition of one or more key components within the mix. It should be kept in mind that these analytical techniques will have their own intrinsic variance, which should be assessed independently.

Let us now consider N samples being taken randomly from throughout the whole mixture and the sample size is at the scale of scrutiny of the user. The samples are then analysed to determine the composition of a key component. Statistical techniques are then applied using the sample data to quantitatively assess mixture quality. Below are some of the approaches used for assessing mixture quality.

13.3.2 Sample variance and standard deviation

The variance S^2 is given by:

$$S^2 = \frac{\sum_{i=1}^{N}(y_i - \mu)^2}{N} \tag{13.1}$$

where N is the number of samples, y_i is the composition of the component in sample i and μ is the mean composition or the composition of the component in the whole mix, which is usually a known value. In some cases, the mean may not be known. In these cases, the mean can be estimated by evaluating the sample mean, and the sample variance can then be estimated from equation (13.1) with $N - 1$ in the denominator. The lower the sample variance or standard deviation (S), the better will be the mixture quality.

From considerations above, the sample variance may include significant variance from the sampling procedure and analytical techniques, in addition to that due to the mixture, that is

$$S^2 = S^2_{\text{mixture}} + S^2_{\text{sampling}} + S^2_{\text{analytical}} \tag{13.2}$$

13.3.3 Lacey and Poole indices of mixture quality

For a binary mixture, upper and lower limits of variance are given as follows:

$$\text{Upper limit (completely segregated):} \quad \sigma_0^2 = p(1-p) \tag{13.3}$$

$$\text{Lower limit (randomly mixed):} \quad \sigma_R^2 = \frac{p(1-p)}{n} \tag{13.4}$$

where p is the fraction of the component in the mixture and n is the number of particles in each sample.

The Lacey and Poole mixing indices use these values along with the sample variance and standard deviation.

$$\text{Lacey mixing indes} = \frac{\sigma_0^2 - S^2}{\sigma_0^2 - \sigma_R^2} \tag{13.5}$$

In practical terms, the Lacey mixing index is the ratio of mixing achieved to mixing possible. A Lacey index of zero would represent complete segregation and a value of unity would represent a completely random mixture.

$$\text{Poole mixing index} = \frac{S}{\sigma_R} \tag{13.6}$$

A Poole mixing index of 1 represents a random mixture.

13.3.4 Relative standard deviation

Relative standard deviation (RSD), also known as the coefficient of variation (CoV), is often used as a measure of mixture quality and is defined as follows.

$$\text{RSD} = \frac{S}{\mu} \tag{13.7}$$

RSD is more useful in providing an insight into how the target component concentration influences mixture quality. As the target component concentration becomes smaller, sample variance tends to decrease due to the smaller values of concentration and this can hide the reality that mixture quality tends to get worse with decreasing target component concentration (Weinekötter 2007). Consequently, RSD is better for comparing mixture quality when trying to evaluate the influence of target component concentration on mixture quality. It is commonly used in the pharmaceutical industry where the active pharmaceutical ingredient is often a small proportion of the mix.

13.3.5 Estimating the true variance (σ^2) from the random sample variance (S^2)

σ^2 is the true variance or the variance obtained if all samples that make up the entire volume of the mix were measured. This is the variance that one would like to estimate. The

random sample variance S^2 becomes more meaningful if it can be evaluated how accurately it describes the unknown true variance. Statistical techniques can be applied to state the probability of locating the true variance within a confidence interval, that is:

there is $x\%$ confidence that the true variance σ^2 lies within the range

$$\sigma_{\mathrm{L}}^2 < S^2 < \sigma_{\mathrm{U}}^2$$

These techniques can evaluate the upper and lower limits for a desired confidence interval, provided samples have been taken randomly from the entire mixture (it is very important that a procedure has been used for random sampling of the entire mixture). Two commonly used statistical techniques are outlined below.

13.3.5.1 *Student's t-test statistics*

When more than 50 samples are taken (i.e., $N > 50$), the distribution of variance values can be assumed to be normal, that is, if the sample variance was measured many times, it would be distributed normally. In this case, the student's t-test statistics can be used to evaluate the upper and lower limits for a given percentage confidence as follows.

$$\begin{aligned} \sigma_{\mathrm{U}}^2 &= S^2 + \left(t \times S^2 \sqrt{\frac{2}{N}} \right) \\ \sigma_{\mathrm{L}}^2 &= S^2 - \left(t \times S^2 \sqrt{\frac{2}{N}} \right) \end{aligned} \tag{13.8}$$

For a given percentage confidence, the t-test statistical tables are used to evaluate t for a given number of samples N. For example, at 95% confidence level, $t = 2.0$ for $N = 60$. Also note that as the number of random samples increases, the gap between the upper and lower limits decreases.

13.3.5.2 *Chi-square statistics*

When less than 50 samples are taken (i.e., $N > 50$), the distribution of variance values may not be normally distributed and is likely to be a χ^2 (chi-square) distribution. In this case, the upper and lower limits are not symmetrical. These limits are given by:

$$\begin{aligned} \sigma_{\mathrm{U}}^2 &= \frac{S^2(N-1)}{\chi_{1-\alpha}^2} \\ \sigma_{\mathrm{L}}^2 &= \frac{S^2(N-1)}{\chi_{\alpha}^2} \end{aligned} \tag{13.9}$$

where the chi-square values $\chi^2_{1-\alpha}$ and χ^2_{α} are read from the chi-square statistical table. This table requires the degrees of freedom and the α value. The degrees of freedom is $N - 1$. The α value depends on the level of confidence. For example, for a 90% confidence range, $\alpha = 0.5[100 - 90]/100 = 0.05$. For a 95% confidence range, $\alpha = 0.5[100 - 95]/100 = 0.025$.

13.3.6 Assessing if satisfactory mixture quality is achieved

1. Firstly, this requires the manufacturer to specify what is meant by satisfactory mixture quality. This should be presented probabilistically as the percentage of all samples that must fall within a specified upper and lower limit of the mean composition, that is *y*% of all samples have compositions within $\mu \pm L_{spec}$
   Note that, here, all samples refer to the entire batch being sampled. For example, suppose the mean composition of ingredient A with a sample size of 2 g is 0.3 g, it is required that 99% of all samples in the mix must fall within 0.005 g of the mean value.
2. Then, the mixture quality of the mix is measured and statistically analysed by evaluating the sample variance and the upper and lower limits for which there is a very high probability that the true variance lies within these limits, as described above.
3. If the whole batch were to be sampled, then the composition of the samples would be normally distributed around the mean composition. If the true standard deviation ($\sigma = \sqrt{\sigma^2}$) is known (usually is not known), then the normal distribution statistical tables can be used to estimate the percentage of all samples that will have a composition within a given range of the mean (μ). For example,
   95.4% of all samples will have compositions within $\mu \pm 2\sigma$
   99.7% of all samples will have compositions within $\mu \pm 3\sigma$
   As the true standard deviation is not known, the upper or lower limit (whichever is more important, usually the upper) calculated above (Section 13.3.5) is used instead of the true standard deviation.
4. Finally, the calculated range around the mean in step (3) is now compared to the specified range around the mean in step (1). If the calculated range is less than the specified range about the mean, then the mixture is of satisfactory quality, that is, it is within specification. For example, if it is required that 99.7% of all samples have compositions within $\mu \pm L_{spec}$, then $\mu \pm 3\sigma < \mu \pm L_{spec}$ or $\sigma < L_{spec}/3$, where $\sigma = \sigma_U$

13.3.7 'Baking a cake' method of assessing mixture quality

Oftentimes, in industry including the food industry, the above fundamental approach to assessing mixture quality is not used because it is considered too cumbersome and it requires an understanding of statistics and its application. Instead, the mix is assessed by applying it to its final application and evaluating if the final application is satisfactory. For example, for a cake mix, cakes are baked using the mix and the mixture quality is assessed by assessing the quality of cakes that are baked from the mix.

13.3.8 Influence of particle size and powder cohesiveness on mixture quality

The smaller the particle size of the ingredients, the more intimately they will be mixed which can lead to a higher quality mix. This is demonstrated by equation (13.4), where the

variance obtained for a random binary mix decreases with increase in the number of particles n. As particle size decreases, the number of particles in a given sample increases and thus the variance of a random mix decreases leading to a higher quality mix.

Increasing powder cohesiveness reduces the flowability of the powder which reduces the rate at which individual powder particles can mix, which can increase the time required to obtain a specific mixture quality. Furthermore, powder cohesiveness may result in clumps of particles not being broken up, with individual particles in the clump not being mixed, and this can limit the mixture quality attained.

Particle size influences powder cohesion, especially when size is reduced below $100\,\mu$m, with smaller size leading to a more cohesive powder. From the above, reducing particle size results in a greater potential for achieving a higher quality mix; however, this depends on the mixer's ability to liberate all the particles from any powder clumps. Reducing particle size will require longer mixing times because of powder cohesion and the fact that there are more particles to mix.

13.4 Mixing mechanisms

The mixing mechanisms have been traditionally described as:

- diffusion;
- convection;
- shearing.

The use of these words has been derived from our much greater knowledge of fluid mixing. However, powders are a lot different to fluids. The basic powder particle is much greater in size than the equivalent molecule in fluid mixing. In fluids, molecules randomly move around due to Brownian motion and diffuse from locations of high to low concentrations. There is no such thing as an equivalent Brownian motion in powders giving rise to diffusion. As a result, the powder particles require a motion to be imposed on them in order to get them to move and for mixing to occur. Therefore, all powder mixers have some sort of devices that induce powder motion, which may be container rotation or movement of paddles within the powder.

13.4.1 Convection or macromixing

This refers to the gross movement of a group of powder particles from one position to another. This is sometimes referred to as macromixing. This occurs in convective mixers due to the movement of mixing elements and can occur in tumbler mixers when material cascades.

13.4.2 Diffusion or micromixing

This refers to random motions of individual particles that result in micromixing as individual particles randomly disperse throughout the mixture. Unlike fluids, the powder particles must first be set in motion by some external action. There are different forms of diffusive motion, some of which are given below.

Random motion due to aeration/fluidisation: Powder particles may become aerated during tumbling or by fluidisation, and as a consequence, they randomly move around and mix.

Random motion at moving interfaces: Powder layers moving over each other during convection will experience an expansion in volume at the interface giving the particles more freedom to randomly move and mix.

13.4.3 Shearing

This occurs when a slip failure plane develops in the powder and a chunk of powder is moved down or slips down along this plane. This can occur in convective mixers and high shear mixers where mixing elements shear the powder. This may also be caused by tumbling where a layer of powder avalanches down along a slip plane. Shearing results in both convective and diffusive mixing where a chunk of powder moves (convective mixing), but the chunk may become aerated and the volume will expand at the interface leading to diffusive mixing where particles can move across the shear zone.

13.4.3.1 *High shear mixing*

This can lead to break-up of cohesive aggregates into the individual particles that constitute the aggregate and allows the mixing of the individual particles.

13.5 Segregation or demixing

13.5.1 Segregation

When particles to be mixed have the same physical properties, then a random mixture will be obtained if the particles are mixed for long enough. However, if the properties are different, then the particles may demix or segregate where particles with the same physical property separate out and collect in one part of the mixture. The major property difference causing segregation is difference in particle size, although differences in particle density can also cause segregation.

Segregation is a very important consideration and a real problem in the industry. Some mixers may not be able to form a random mixture because of segregation mechanisms occurring in the mixer. Some mixers may even demix a mixture due to the dominance of segregation mechanisms acting in a particular mixer. For example, a rotating cylindrical mixer will demix a mixture of dry spheres if they have a difference in particle size. In mixers in which a segregation mechanism is present, the mixing and demixing may progress at different rates over time until an equilibrium is reached where both rates equal each other. In between, mixture quality may initially improve with mixing time but may then disimprove after a certain mixing time due to the segregation rate. Figure 13.3a illustrates a typical decrease in sample variance with mixing time, whereas Figure 13.3b illustrates the competition between the mixing rate and the segregation rate, where the sample variance first decreases with time to a minimum before increasing until equilibrium is achieved. Mixing times greater than required to achieve the minimum variance is sometimes referred to as ‘overmixing’. (Overmixing can also refer to powders being mixed for a time greater than that required to attain satisfactory mixture quality with the powders being degraded over time, for example, by particle breakage.)

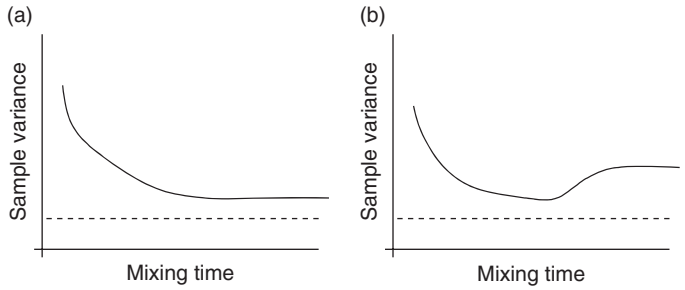

Fig. 13.3 (a) Typical variation of sample variance with mixing time. (b) Sample variance displays a minimum due to interaction between the rate of mixing and segregation. Solids lines represent a best fit curve through the sample variance data points. Dashed lines represent the true variance of a completely random mix.

Even more important are the steps that follow mixing, such as emptying the mixer, mixture transport, charging and discharging hoppers and silos, and further processing. These may introduce segregation mechanisms that can demix a mixture. For example, in filling a silo from the top with a mixture containing ingredients with different size particles, a heap will be created. Big particles have a greater tendency to roll down along the surface of the heap to the silo wall surface, and the smaller particles tend to congregate near the centre. On emptying in funnel flow discharge, the smaller ingredients will leave first resulting in demixing.

Segregation takes place due to the preferential motion of particles with similar properties, in particular, particle size. A summary of a number of segregation mechanisms is given below (Williams 1990; Rhodes 2002).

13.5.1.1 *The rolling heap*

This is where big particles tend to roll down the slope of the heap while smaller particles congregate more towards the centre. This is important in filling silos and containers and forming stockpiles.

13.5.1.2 *Trajectory*

Consider a mass of particles moving around a corner. The bigger particles require a greater radius of turn than the smaller particles because of the momentum associated with their greater mass. This is important when emptying mixers or moving from one conveyor to another at right angles. It is potentially important in any operation where there is a change in direction in the conveying of the particles and the particles are free to move.

13.5.1.3 *Percolation of fines*

If vibration is applied to a bed of powder, the smaller particles tend to sift or percolate through the voids created between the bigger particles. This can commonly occur during transport in trucks, trains and ships due to the vibrations induced. This will lead to more fine particles at the bottom of the container and more larger particles on the top.

13.5.1.4 *Elutriation*

Gas moving through an expanded or fluidised bed of particles tends to preferentially drag small particles upwards because they are lighter and have greater surface area per unit mass

for drag forces to lift the particles. Elutriation may also occur if the particles have different densities. Consider same size particles but with different densities. The less dense particles are lighter and will be elutriated upwards more easily than the heavier denser particles. Elutriation can occur where particles are aerated. For example, when filling powder into a silo, air currents are generated that entrain fine particles into it in the headspace. They may settle only when filling has been completed, and thus settle as a segregated layer on the top of the heap.

There are a number of segregation tests available to give some insight into the segregation tendency of a mix; however, each test relates to a specific segregation mechanism. For example, there are two ASTM standard methods (D6940-03 and D6943-03), the first relating to the rolling heap mechanism and the second relating to the fluidisation mechanism.

13.5.2 Reducing segregation

The main methods for trying to reduce segregation are described below.

13.5.2.1 *Reduce the difference in particle size*

As difference in particle size is the main cause of segregation, reducing this difference in size should reduce segregation. An acceptable size difference is difficult to determine, as it will depend on other factors such as the magnitude of particle size and the cohesiveness of the powder particles. However, it does not take much difference in particle size to segregate a free flowing powder, for example, a size ratio of 1.3 (big/small) will result in significant segregation.

13.5.2.2 *Increase the cohesion of powders*

Increased cohesion forces between powder particles will restrain individual particles from moving freely and segregating. Increased cohesion can be achieved by reducing particle size or adding small quantities of liquid. Reducing particle size increases total particle contact area, which can greatly increase surface attractive force interactions. Segregation is generally not a serious problem when all the particles are less than 30 μm.

13.5.2.3 *Change process to eliminate segregation mechanisms from taking place*

Eliminate and redesign locations in the process layout where segregation can occur, for example, conveying belts should not be split off at right angles.

13.5.2.4 *Mix when needed*

Mix only when the mix is needed. Instead of mixing followed by transport and storage before packing, it is better to transport, store and finally mix prior to packing. This can eliminate mixture transport, filling and emptying operations that may induce segregation. For some food powders, it may be necessary to pack some of the ingredients separately and allow the consumer mix the powders at the point of use.

13.5.2.5 *Agglomerate/granulate the mix*

Once the mix is satisfactorily formed, then produce granules by getting powder particles to stick together and form bigger particles called granules. Once particles are stuck together, they cannot segregate.

13.6 Powder mixing equipment

Powder mixers can be classified as batch and continuous mixers with batch being by far the most commonly used in the food industry. The most common batch mixers can be classified as tumbling mixers and convective mixers. Other batch mixers include gravity silo mixers and pneumatic mixers. Detailed discussion of these mixers is reported by Muzzio *et al*. (2004). Below is a summary of common mixers used in the food industry.

13.6.1 Tumbling mixers

A tumbling mixer consists of a closed vessel rotating about its axis. Common shapes for the vessels are double cone and V-shape, as illustrated in Figure 13.4. These vessels are typically around half full of particulate material. Mixing is achieved predominantly by random motion where particles roll down along a sloping surface, and these mixers can achieve very good mixture quality. Tumbling mixers provide a low shear environment. This may limit their potential when trying to mix cohesive powders as the shear may not be sufficient to break up chunks of powder and liberate individual powder particles for mixing. Another potential problem with these mixers is that they may not be effective if the mixture has a tendency to segregate.

13.6.2 Convective mixers

Convective mixers consist of a static shell in which the powder is circulated around by rotating blades, paddles or screws. These are very commonly used in the food industry. Mixing consists of convective, diffusive and shear mechanisms. The rotation of the mixing elements gives rise to convective transport of chunks of powder around the mixer by the mixing element. Shear and diffusive transport take place as these chunks of powder shear and interdisperse with each other causing individual powder particles to randomly move from point to point. It is desirable to have elements that can move the powder in many different directions so as to more easily obtain a random mix. These mixers can mix a wide range of bulk solids from free flowing material to cohesive material, as the rotation of mixing elements are able to create much higher shear environments than tumbler mixers. Another major advantage of convective mixers is that they are not prone to segregation because the convective motions induced by the mixer elements overcome any segregation motions. Convective mixers that are very commonly used in the food industry are the ribbon mixer with helical blades (Figure 13.5) and the plough mixer, and combinations of these mixers.

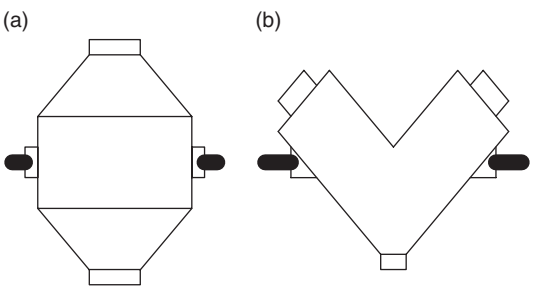

Fig. 13.4 Tumbling mixers: (a) double cone and (b) V blender.

A somewhat different type of convective mixer is the Nauta mixer (Figure 13.6) in which an orbiting screw lifts powder from the base of a conical hopper and progresses it around the hopper wall.

The Forberg mixer (Figure 13.7) is another type of convective mixer that induces a fluidised zone and is sometimes referred to as a fluidised zone mixer. It consists of twin drums that have two counter-rotating agitators with specifically angled paddles that sweep the entire bottom of both mixer drums.

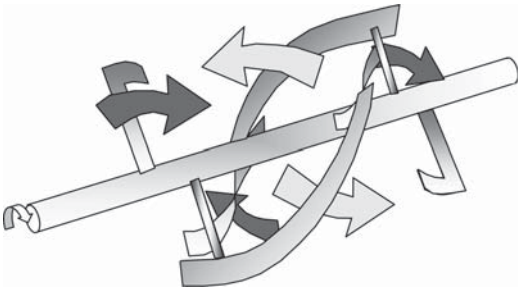

Fig. 13.5 Mixing elements in a ribbon convective mixer.

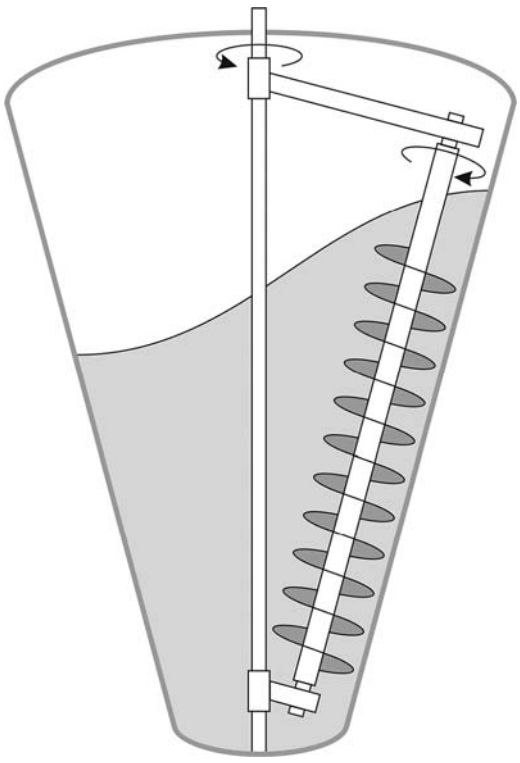

Fig. 13.6 Nauta orbital screw mixer.

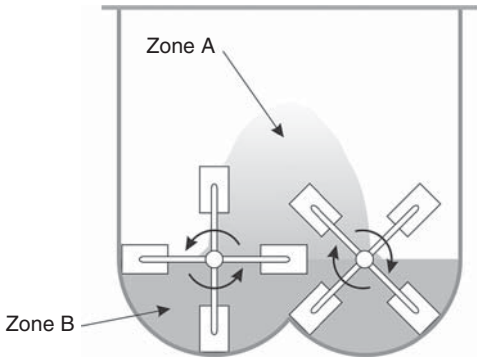

Fig. 13.7 Forberg mixer.

The material in the mixer moves in a horizontal counter-clockwise direction at the perimeter while simultaneously moving both left and right in the centre. The material in Zone B is in its normal gravimetric state as it is being moved and disbursed. In Zone A, a fluidised zone is created that effectively lifts the ingredients to an almost weightless state allowing them to move freely and randomly, regardless of particle size and density. The interaction of the two zones allows every particle to move rapidly to a highly homogenous mix in short mixing times.

13.6.3 High shear mixers

High shear mixers are convective mixers that are used in the mixing of very cohesive powders. They have special mixing elements that induce high shear stresses in the powder. These high stresses are predominantly used to break up very cohesive agglomerates so that the individual particles within these agglomerates can be liberated to mix with other particles.

13.6.4 Sigma blade mixers

Sigma blade mixers consist of two troughs and each contain a rotating sigma blade mixing element. The material is loaded into the mixer up to about 50–60% of its load capacity. Liquid spray devices are located above the blades. The blades are counter-rotating, overlapping as they fold and shear the material. These mixers are predominantly used for producing doughs and highly viscous pastes.

13.6.5 Continuous mixers

In a continuous mixing process, the ingredients are continuously fed into and through the mixer to continuously produce mixed product. Continuous mixers are basically accurate ingredient feeders, which feed the ingredients into a small mixing chamber. The accuracy of the ingredient feeders is critical as they will have a major influence on mixture quality. If the ingredient feeders are sufficiently accurate, then the mixing elements in the chamber need to provide only radial mixing to mix the ingredient streams. Short mixing chambers and residence times are required to do this. In practice, fluctuations in feed rates occur, thus the mixing elements usually impose some motion in the axial direction to try and counteract any perturbations in the feed rates (Weinekötter & Gericke 2000).

13.7 Mixer selection and process design

13.7.1 Specification of mixture quality requirement

In designing a process that involves the mixing of particulate solids, a specification should be drawn up for the quality of mixing required. To do this, it is necessary to specify three quantities:

- scale of scrutiny;
- allowable variation from the mean composition;
- frequency or probability with which this variation may be exceeded.

The scale of scrutiny is the smallest amount of material within which the quantity of mixing is important. For example, if the mixture is to be used to fill nutraceutical capsules, each capsule should have the necessary mixture quality. The allowable variation from the mean composition and the frequency with which this variation may be exceeded can be decided only by considering the purpose for which the mixture is used or the consequences if the amount of a certain component is above or below its mean value. In some cases, it may be prescribed by law or specified by standards.

13.7.2 Mixer selection

The following factors are useful to consider in selecting from the mixers described above. The first part is to consider batch or continuous mixing. Both have different advantages and disadvantages which can readily determine which approach is best.

13.7.2.1 *Batch versus continuous*

Batch mixing is the traditional form of mixing; however, continuous mixers have many advantages including:

- much smaller mixing equipment is required (even high throughput continuous mixers are compact);
- short residence time in mixer (as there is always only a small amount of material being mixed in the mixer at any time);
- mixing is simpler;
- less likely to have segregation problems.

The major disadvantages with continuous mixing are as follows.

- It requires high quality accurate powder feeding of components into the mixer (the whole continuous mixing process depends on this).
- It requires high quality automation to monitor and control powder feed rates.
- There is a lower limit on production output, typically 100 kg/h.
- There is a lower limit on the feed rate of any ingredient, typically 300 g/h. Below this limit, it is difficult to control the constancy of the feed with any accuracy.
- There is usually a limit on the number of ingredients that can be fed into the mixing chamber.

The advantages of batch processes include the following.

- Feeding is relatively easy. It is just a matter of weighing out each component and placing them in the mixer. The mixer will mix them all together.
- Automation is simpler.
- Batch mixers are much more versatile with regard to the number of ingredients that can be mixed.
- Batch mixers are also much more versatile with regard to how often the mix recipe is changed.

13.7.2.2 *Segregation tendency*

If the particles tend to segregate, then tumbler mixers may not be suitable. Specify a convective type mixer, such as a ribbon mixer or a plough mixer, or a continuous mixer and design the rest of the process so as to minimise the amount of segregation occurring in the subsequent handling of the mixture.

13.7.2.3 *Mixing of cohesive powders*

Convective mixers are more suitable than tumblers for mixing cohesive powders. The mixing elements can deliver much higher shear to break up the powder into individual particles. For the mixing of very cohesive powders that tend to form cohesive agglomerates, it is necessary to break up the agglomerates so as to mix the particles that constitute the agglomerate. In this situation, it is necessary to use mixers that can provide sufficient shear to break the agglomerates, thus higher shear mixers may be necessary. Tumbling mixers are not suitable, as these are more likely to promote agglomeration. One problem with higher shear is that it may also break down friable particles.

13.7.2.4 *Mixing of shear sensitive particulates*

As tumbling mixers create a low shear environment, they are more suitable for mixing shear sensitive particulates.

13.7.3 Process design

Once a mixer is selected, it is necessary to evaluate if the mixer can obtain the specified mixing performance in terms of mixture quality required. Pilot-scale tests can be performed where a sufficient number of samples are taken after a number of mixing times. From these samples, the mixture quality can be evaluated (as outlined in Section 13.3) as a function of mixing time, as illustrated in Figure 13.3. This will give an indication if the mixer can provide the required mixture quality and roughly how long the mixing time should be. Mixing times in batch mixers are usually not that long, typically of the order of minutes. This pilot-scale testing can also be used to evaluate if any particle size degradation is taking place. It may be necessary to reduce the speed of mixing elements to reduce such particle breakage.

The major costs associated with mixing is the capital cost (which is related to the size of the mixer), the energy requirement (which is related to mixer size and how often it is used) and the labour cost. The size or volume of the mixer is often determined by the size of the batch to be processed. The batch mixing cycle time is usually not the rate-limiting step in an overall batch process, and consequently, mixers may be idle for a significant amount of time. Thus, there is the possibility of specifying a smaller mixer and using it multiple times

during the time allowable for the rate-limiting step. This could reduce the mixer capital cost. However, the disadvantage with this is that it will require more weighing, filling and discharging and this will result in greater labour costs. Consequently, there is a trade-off between mixer capital cost and labour operating cost. In the food industry, mixer sizing may be more complex, as the same mixer may be required to mix a number of different ingredient recipes.

Currently, there are no mathematical modelling techniques available that can be applied in the process design of particulate mixers. There are scale-up rules and procedures that can be applied to approximately scale up the performance obtained in a pilot-scale mixer to that at industrial scale (Muzzio *et al*. 2004).

13.8 Other factors affecting mixing process design in dry food processing

Up to now, the major focus has been on achieving satisfactory mixture quality and the mixers that are used to achieve this. There are other factors in the mixing of food particulate material that are also very important in the overall design of mixing processes (Brennan *et al*. 1990; Barbosa-Canovas *et al*. 2005; Clement & Prescott 2005). These include the following.

13.8.1 Hygiene and cleaning

Food safety is of paramount importance in the food industry; thus dry powder processing operations should not contaminate the product or allow conditions facilitating microbial growth. Consequently, it is important to use appropriate cleaning regimes and to use equipment with proper hygienic design.

The choice of cleaning procedure depends firstly on whether dry cleaning or wet cleaning is to be used. Dry cleaning is preferred as wet cleaning introduces water and the risk of microbial growth. For powders having a water activity below 60%, little or no growth will occur and dry cleaning is a possibility. Furthermore, dry cleaning is applicable for cleaning powder contact surfaces where:

- remaining dry material is in a loose form and not crusted onto equipment surfaces;
- there are no problems with cross-contamination with a subsequent batch;
- remaining dry material presents no risk of microbial growth due to moisture content, temperature and prevailing relative humidity;
- dry material is non-hygroscopic and non-sticky.

Otherwise, wet cleaning methods are required. The subgroup on dry materials handling of the European Hygienic Equipment Design Group (EHEDG) provide guidelines on dry cleaning and wet cleaning methods and hygienic equipment design criteria (Hauser *et al*. 2002). At the end of wet cleaning operations, it is very important that the equipment is totally dried to prevent microbial growth and subsequent contamination of product. Product contact surfaces should be smooth and resistant against dry material contact and against liquids used in wet cleaning. Product contact surfaces should be free of crevices or pinholes that could allow material to penetrate and be difficult to clean. A roughness standard of Ra $< 0.8\,\mu$m is recommended.

13.8.2 Addition of multiple ingredients with large variation in properties

In the food industry, many ingredient mixes consist of many different ingredients. Consequently, it is a requirement to try and obtain a satisfactory mixture quality for all these ingredients in the mix. Some ingredients may be considered minor ingredients and be present as a small mass fraction of the overall mix. As a rule of thumb, an ingredient should not be added into a mixer if its content is less than 0.5% of the overall contents of the mixer. Instead, it should be premixed with a smaller amount of other ingredients and then mixed with the remainder of the ingredients in the large mixer.

The larger the number of ingredients in the mix the more difficult it is to assess mixture quality. Consideration has to be given to which key component concentrations in the mix should be measured. Oftentimes, this is done by measuring the concentration of component(s) that are there in small amounts or components that are critical to the functioning of the mix or that are simply easier to measure analytically.

Furthermore, the food industry deals with a whole variety of particulates with different sizes, shapes and strengths. Sizes range from fine cohesive micron sized powders to particulates with millimetre and centimetre sizes, such as dried fruit fragments. This can lead to major segregation issues where particulates with differences in size or density are segregating, for example, due to vibrations during transport. Producing particulates with similar sizes, or agglomerating ingredients or reducing vibration during transport can all help to reduce these segregation problems.

13.8.3 Addition of ingredients in liquid form

In the food industry, some ingredients are added in liquid form to a dry mix. For example, a mixer may have a number of spray devices, such as spray bars, located above the mix onto which the liquid is sprayed, as the mixing is taking place. The wetted particles are transported into the bulk of the mix, and the liquid is distributed throughout the mix. At the end of mixing, a dry powder still exists but with a higher liquid content. Convective mixers are usually used for this because liquid addition will make the mix more cohesive and convective mixers are able to supply sufficient shear to overcome the cohesiveness.

One of the problems associated with this is the ability of the mixer to distribute the liquid uniformly around the mix and provide adequate mixture quality of the components within the mix. It may also increase the cohesiveness and stickiness of the powder. One particular problem is that wetted particles may become sticky and stick to the chamber wall if they encounter the wall of the mixer while still being sticky. This will lead to a gradual build up of a crust on the wall of the mixer. This is a loss of material and also represents an additional cleaning problem requiring wet cleaning. Overcoming this problem depends on the design of the spray system coupled with the convective motion to ensure that distribution of liquid away from the wetted particles has been achieved before these particles encounter the chamber wall. This involves investigating how this problem is influenced by the type of spray device used, its location, spray configuration, droplet sizes and liquid flow rate.

13.8.4 Dust prevention and control

Dust generation can lead to a number of problems for food powders. These can be summarised as follows: (i) health problems, in particular allergy problems; (ii) contamination and plant hygiene issues due to dust settling and sticking onto equipment and (iii) fire/explosion

hazards. Owing to their biological origin, there is always the possibility that a food powder may contain biological active components, such as enzymes, that may be harmful and may produce allergy problems. Consequently, this may lead to the imposition of stricter dust exposure limits. During the mixing operation, dust generation should not be a problem as the mix is contained in the mixer. The problem may occur during charging and discharging of the mixer where the bulk solids may contact air and become entrained in the air. Entrapment in air is a strong function of particle size especially as the particle size decreases below 100 μm. As a result, for smaller sized dusty powders it is important to ensure that the powders are contained from outside air during charging and discharging of the mixer.

References

Allen, T. (1981). *Particle Size Measurement*, 3rd edn. Chapman & Hall, London.

Barbosa-Canovas, G., Ortega-Rivas, E., Juliano, P. & Yan, H. (2005). Mixing. In: *Food Powders: Physical Properties, Processing, and Functionality* (eds G. Barbosa-Canovas, E. Ortega-Rivas, P. Juliano & H. Yan). Kluwer Academic, New York.

Brennan, J.G., Butters, J.R., Cowell, N.D. & Lilley A.E.V. (1990). Mixing and emulsification. In: *Food Engineering Operations* (ed J.G. Brennan), 3rd edn. Elsevier, UK.

Clement, S.A. & Prescott, J.K. (2005). Blending, segregation and sampling. In: *Encapsulated and Powdered Foods* (ed. C. Onwulata). Taylor & Francis, London.

Hauser, G., Mager, K., Maller, R.R. *et al*. (2002). EHEDG document no 22. General hygienic design criteria for the safe processing of dry particulate materials. *Trends in Food Science and Technology*, **12**, 296–301.

Muzzio, F.J., Alexander, A., Goodridge, E.S. *et al*. (2004). Solids mixing. In: *Handbook of Industrial Mixing* (eds E. Paul, V. Atiemo-Obeng & S. Cresta). Wiley, New Jersey.

Rhodes, M. (2002). Mixing and segregation. In: *Introduction to Particle Technology* (ed M. Rhodes). Wiley, New York.

Weinekötter, R. (2007). Degree of mixing and precision for continuous mixing processes. *PARTEC 2007—International Congress on Particle Technology*, Nuremberg, Germany.

Weinekötter, R. & Gericke, H. (2000). *Mixing of Solids*. Kluwer Academic, Boston, MA.

Williams, J.C. (1990). Mixing and segregation in powders. In: *Principles of Powder Technology* (ed. M.J. Rhodes). Wiley, Chichester, UK.

This page intentionally left blank

Index

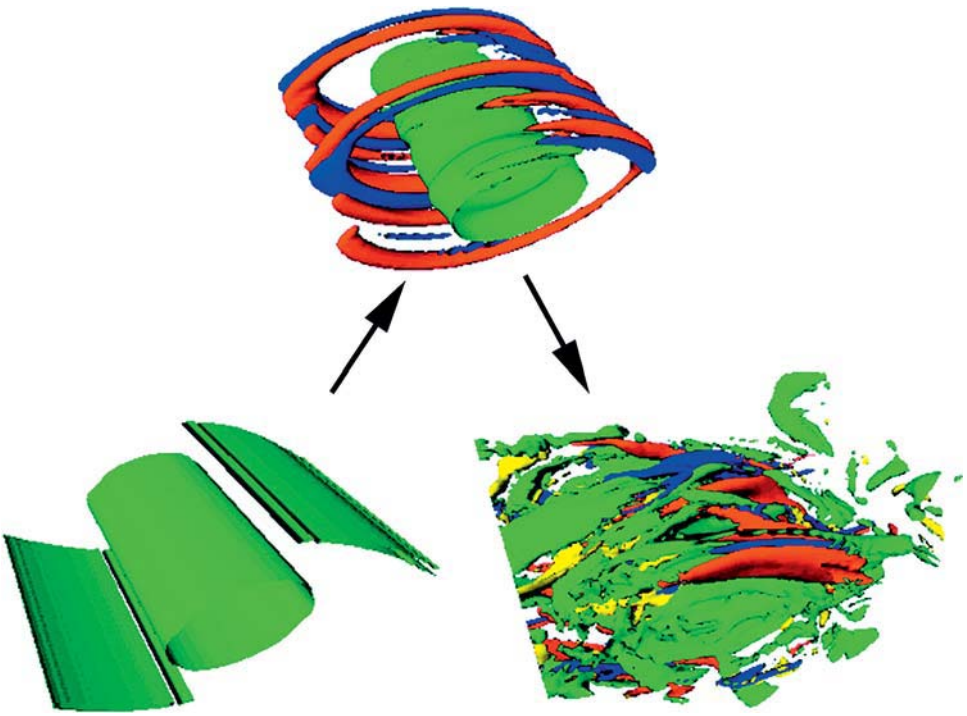

Plate 3.1 Isosurfaces of spanwise vorticity (green), streamwise vorticity of opposite signs (red and blue) and absolute value of vertical vorticity (yellow) for a simulation with $Re = 750$, $Pr = 1$ and $Ri(0) = 0.05$ at three characteristic times (t_{2dmax}): when the two-dimensional perturbation has maximal amplitude, when the kinetic energy associated with the three-dimensional perturbation is 1% of the kinetic energy associated with the two-dimensional perturbation and when the dissipation within the flow is maximal. [Reprinted with permission from Peltier and Caulfield (2003), © 2003 by Annual Reviews.]

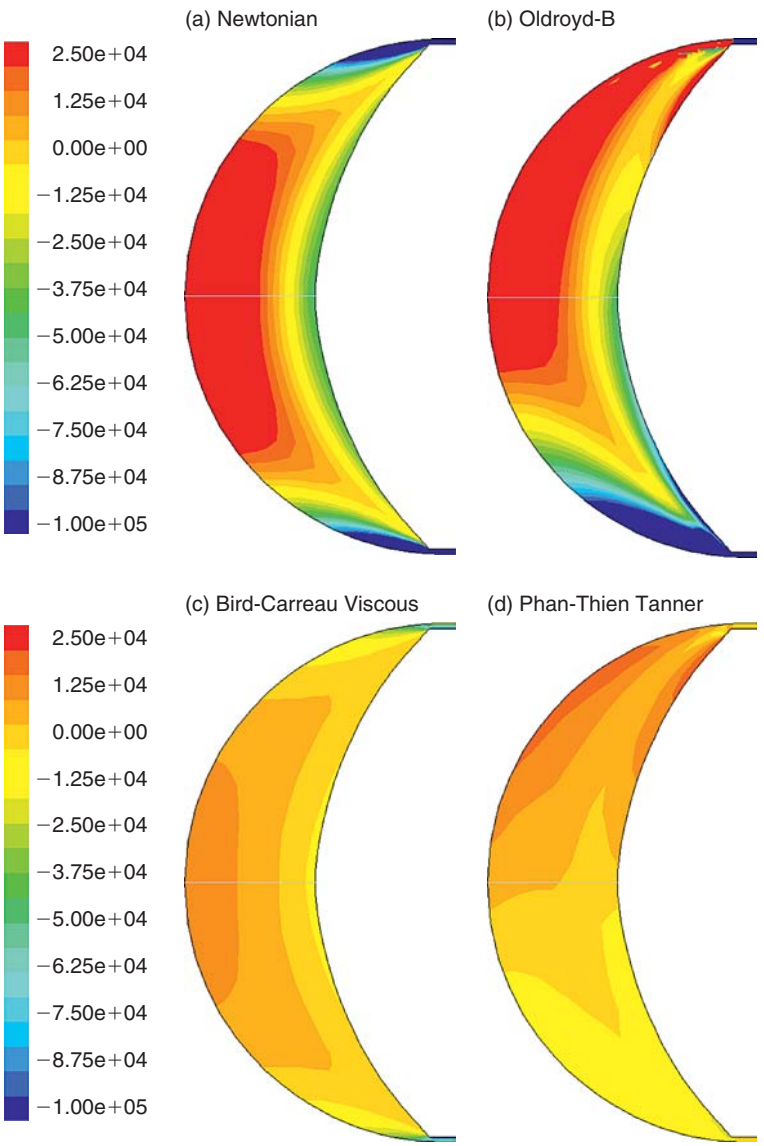

Plate 4.1 Effects of viscoelasticity on the shear stress distributions around an impeller blade. [Reprinted from Connelly and Kokini (2004) with permission from Elsevier.]

Plate 5.1 Powder disperser for addition to liquids. (Courtesy of Quadro Engineering Corp.)

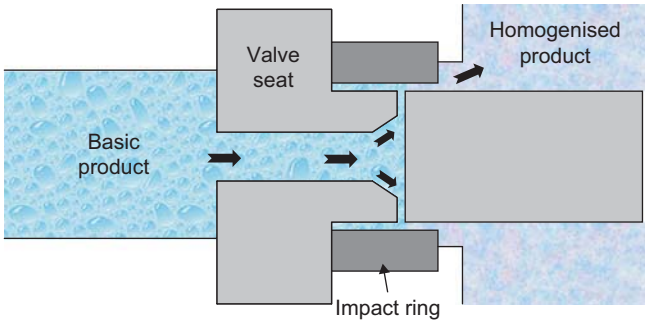

Plate 5.2 Valve homogeniser.

Plate 5.3 Industrial bread dough mixer. (Courtesy of Shaffer Manufacturing.)

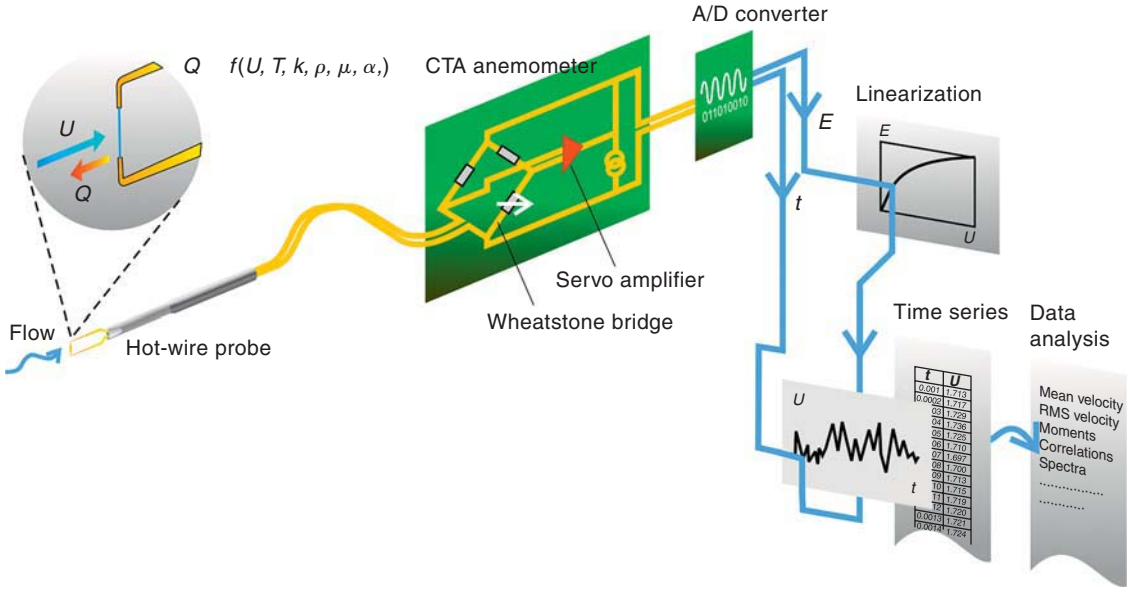

Plate 7.1 Measurement principle of a HWA system operating in constant temperature mode. (Courtesy of Dantec Dynamics Limited, Bristol, UK.)

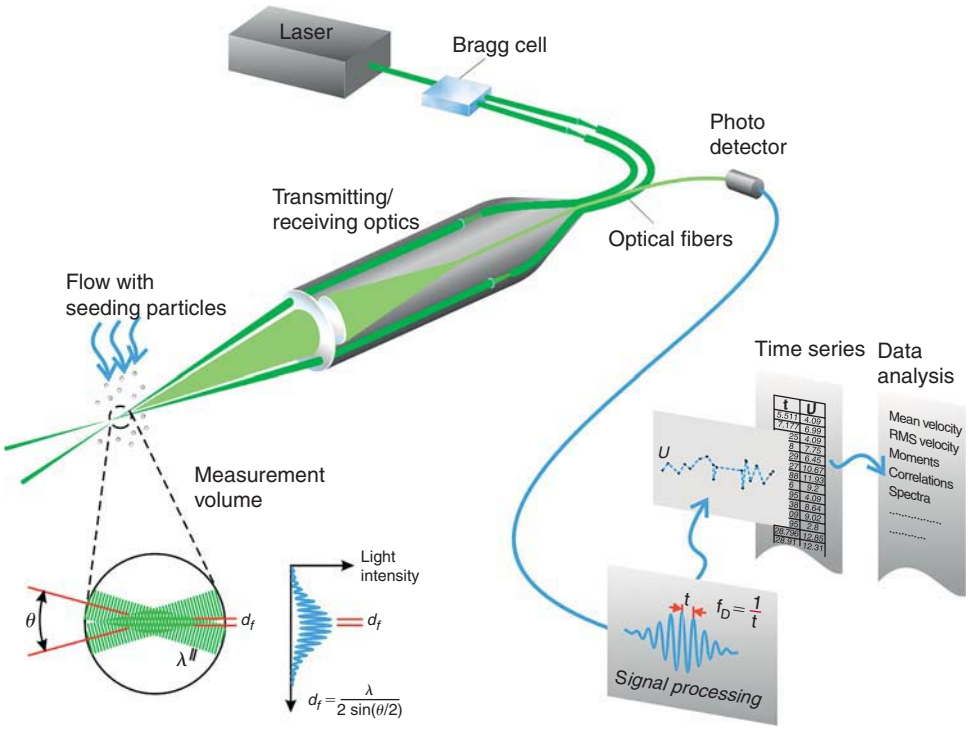

Plate 7.2 Measurement principle of an LDA system showing two intersecting beams forming a fringe pattern. (Courtesy of Dantec Dynamics Limited, Bristol, UK.)

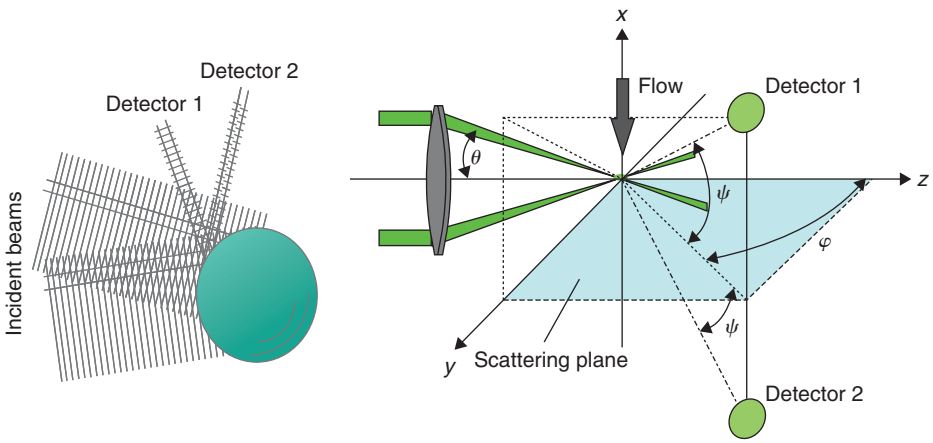

Plate 7.3 Detector set-up and general coordinate system used for PDA, and schematic showing how interference patterns at two photodetectors will differ by a certain phase. (Courtesy of Dantec Dynamics Limited, Bristol, UK.)

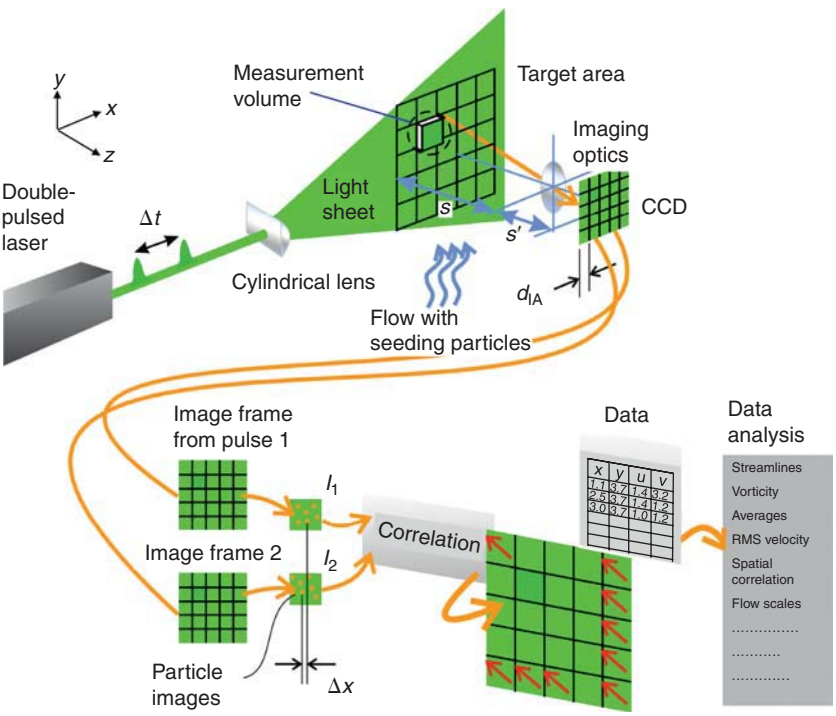

Plate 7.4 Measurement principle of PIV. (Courtesy of Dantec Dynamics Limited, Bristol, UK.)

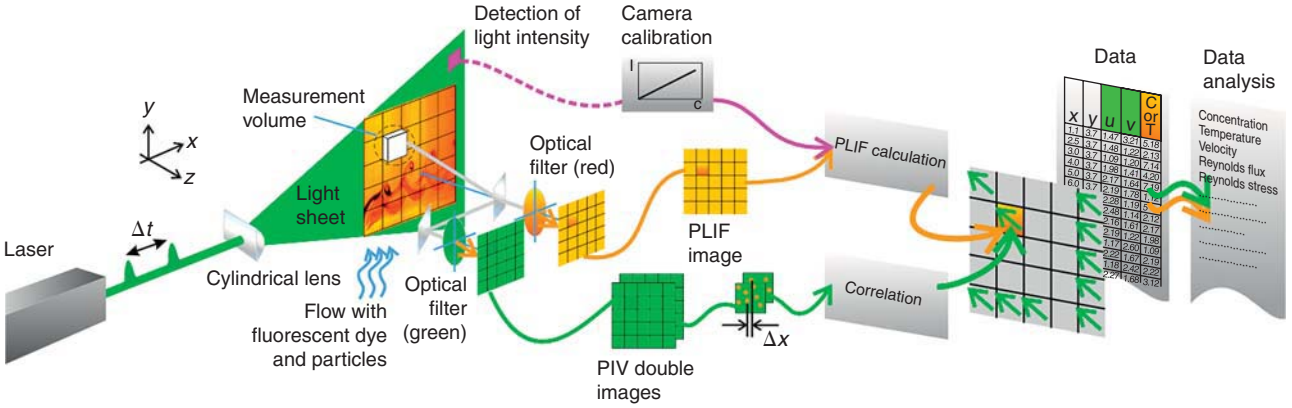

Plate 7.5 Measurement principle of a planar-LIF system incorporating PIV measurements. (Courtesy of Dantec Dynamics Limited, Bristol, UK.)

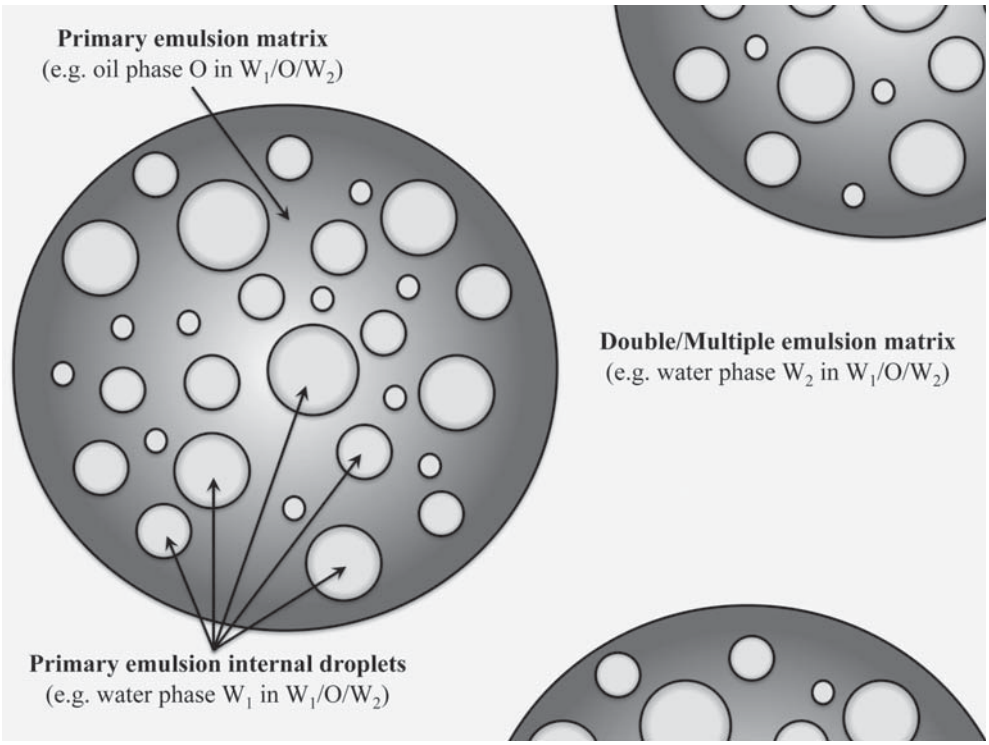

Plate 9.1 Schematic representation of a $W_1/O/W_2$ double emulsion.

Image not available

Plate 12.1 Shear rate contours on a plane across the center of the bowl at $y = 4.225$ cm for (a) Newtonian corn syrup, (b) 2% CMC, and (c) 0.11% carbopol. [From Connelly and Kokini (2006a). Reproduced with permission from John Wiley & Sons, Inc.]

Image not available

Plate 12.2 Mixing index (λ_{MZ}) contours on a plane across the center of the bowl at $y = 4.225$ cm for (a) Newtonian corn syrup, (b) 2%CMC, and (c) 0.11% carbopol. [From Connelly and Kokini (2006a). Reproduced with permission from John Wiley & Sons, Inc.]

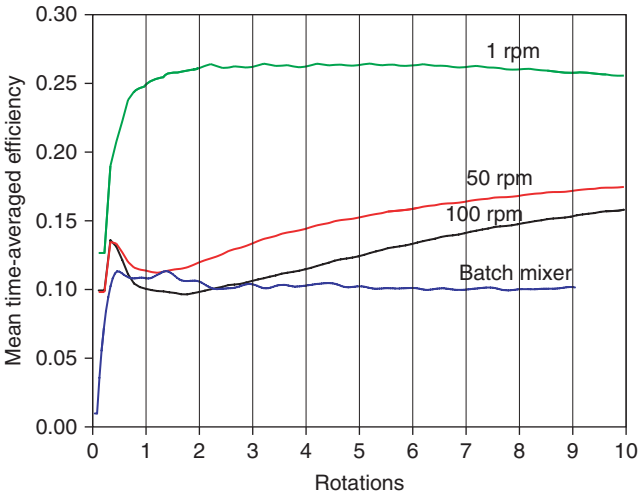

Plate 12.3 Time-averaged efficiencies of flat configuration for various screw speeds for 10 rotations in comparison to the Farinograph during mixing of a Newtonian corn syrup at 100 rpm.

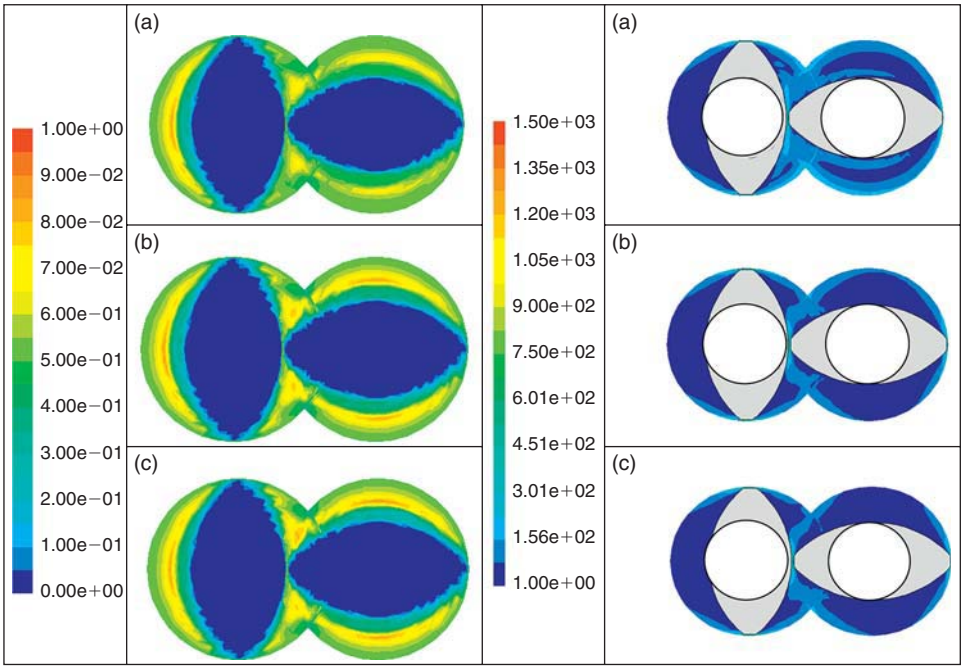

Plate 12.4 Dispersive mixing index contours of Newtonian fluid at the eighth paddle pair for (a) flat, (b) 45F, and (c) 45R configurations.

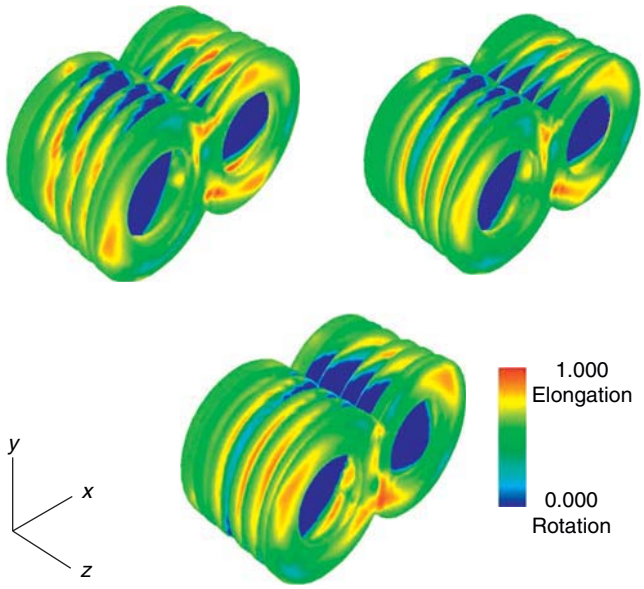

Plate 12.5 Mixing index contours for 2× configuration at different screw speeds during mixing of a shear thinning 2% CMC solution in a two paddle continuous mixer.

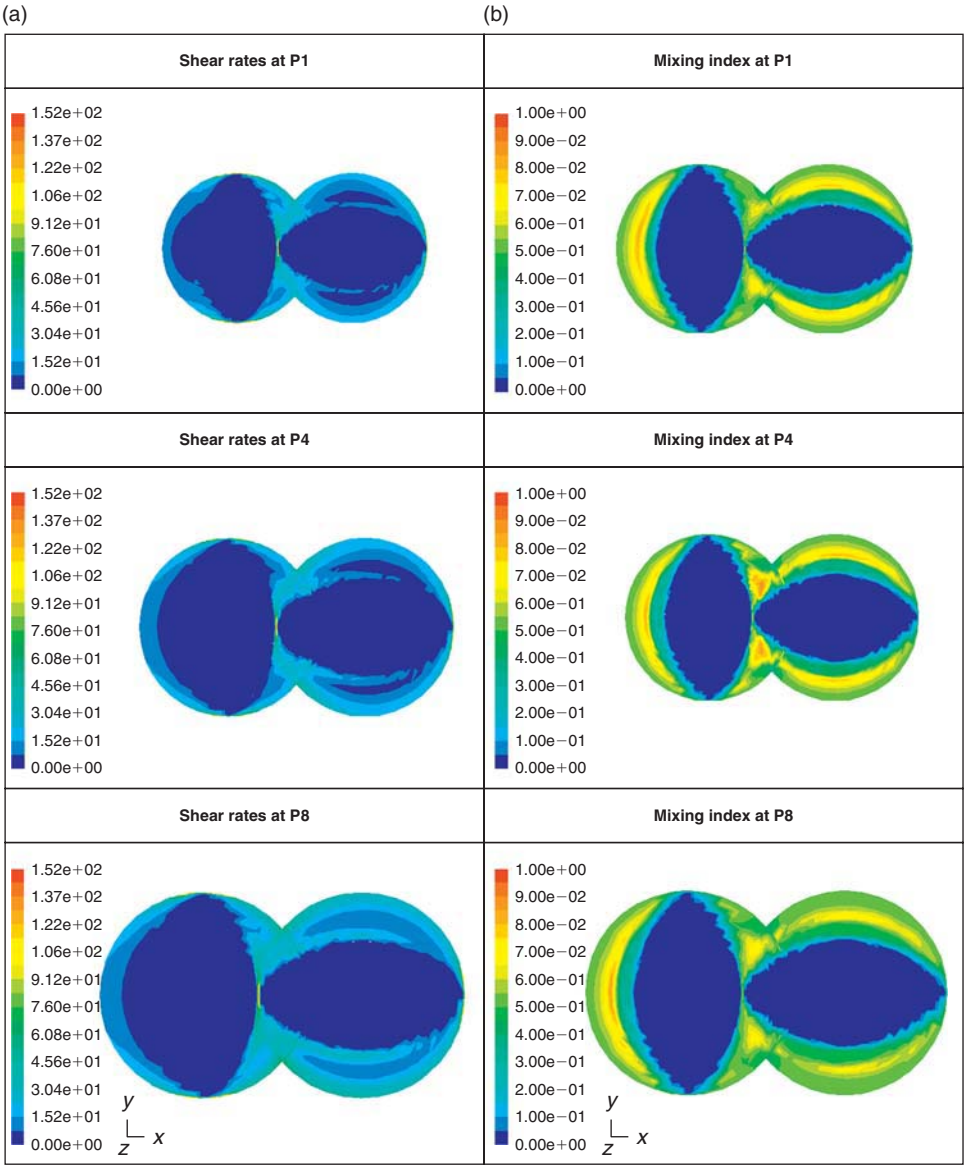

Plate 12.6 (a) Shear rate and (b) mixing index contour maps at the three axial positions for flat configuration.